

**ANALYSIS OF HEAT DISSIPATION FROM
RAILWAY AND AUTOMOTIVE FRICTION BRAKES**

A thesis submitted for the degree of Doctor of Philosophy

By
Gordon Paul Voller

Department of Mechanical Engineering, Brunel University

2003

Abstract

The thesis presents research into the understanding and improvement of heat dissipation from friction brakes. The investigations involved two brake types, considered to be the most thermally loaded and therefore most challenging; axle mounted high speed railway and commercial vehicle disc brakes. All three modes of heat transfer (conduction, convection and radiation) and airflow characteristics have been analysed experimentally and theoretically in order to increase the understanding of heat dissipation. Despite the very practical aspects of this research, a 'generic heat transfer approach' was applied, enabling wider engineering applications of the results.

Experimental analyses conducted on a specially developed Spin Rig allowed measurements of cooling and airflow characteristics for different designs. Methodologies have been developed to determine thermal contact resistance, heat transfer coefficients, emissivity and aerodynamic (pumping) losses. Established values and relationships compared very favourably with theoretical work. Analytical, FE and CFD analyses were employed to further investigate design variations and perform sensitivity studies. Inertia dynamometer route simulations provided disc temperatures for validation of the overall work.

Recommendations have been made for optimising heat dissipation, by proposing practically acceptable and economically viable design solutions. A proposed ventilated disc design efficiency ratio allows large, high speed ventilated disc designs, to be efficiently and accurately evaluated and compared, providing a valuable disc design optimisation tool.

The determination of the methodologies, parameters and functions defining cooling characteristics, enable heat dissipation to be predicted confidently and accurately for brakes and other engineering assemblies at early design stages.

Acknowledgements

The author would like to thank Dr. Marko Tirovic, Lecturer in the Department of Mechanical Engineering, Brunel University, for his continuous encouragement, guidance and criticism. Gratitude is expressed to the technicians in the Department of Mechanical Engineering, Brunel University, for their professional advice and assistance, in particular Mr. Brian Dear, Mr. Len Soanes, Mr. Clive Barrett and Mr. Keith Withers.

Gratitude is extended to Mr. Roy Morris and Mr. Peter Gibbens of ArvinMeritor (UK) and Mr. John Watson and Mr. Alastair Roberts of SabWabco (UK) for their support and interest in the project.

Finally, the author would like to thank his family and Ms. Tania Rueda Cornejo for their invaluable support and encouragement throughout.

Gordon Paul Voller

March 2003

Contents

| | |
|---|-----------|
| Nomenclature | viii |
| Chapter 1 Introduction and Research Objectives | 1 |
| 1.1 Introduction | 1 |
| 1.2 Main Brake Types Studied | 2 |
| 1.3 Research Objectives | 3 |
| Chapter 2 Literature Survey | 5 |
| 2.1 Introduction | 5 |
| 2.2 Friction Braking Development | 6 |
| 2.3 Studies of Heat Dissipation | 7 |
| 2.3.1 Convective Heat Dissipation | 7 |
| 2.3.1.1 Convective Heat Transfer Coefficient Equations | 8 |
| 2.3.1.2 Cooling Parameters | 10 |
| 2.3.2 Conductive Heat Dissipation | 11 |
| 2.3.2.1 Thermal Contact Resistance | 11 |
| 2.3.2.2 Conductive Heat Transfer Coefficient | 14 |
| 2.3.3 Radiative Heat Transfer | 16 |
| 2.4 Experimental Studies of Brake Cooling | 16 |
| 2.4.1 Temperature | 16 |
| 2.4.2 Airflow | 19 |
| 2.5 Studies of Heat Dissipation Optimisation | 20 |
| 2.6 Numerical Analysis | 22 |
| 2.6.1 Finite Element Methods | 22 |
| 2.6.2 Computational Fluid Dynamic Methods | 27 |
| 2.7 Summary | 29 |
| Chapter 3 Experimental Apparatus and Test Components | 31 |
| 3.1 Introduction | 31 |
| 3.1.1 Road and Track Tests | 31 |
| 3.1.2 Dynamometers | 32 |
| 3.2 Spin Rig | 34 |
| 3.2.1 Design Brief | 35 |
| 3.2.2 Design and Specification | 35 |
| 3.2.3 Equipment | 39 |
| 3.2.3.1 Torque and Rotational Velocity Measurement | 39 |
| 3.2.3.2 Signal Processing and Data Logging | 40 |
| 3.2.3.3 Heating System | 41 |
| 3.3 Measurement and Instrumentation | 43 |
| 3.3.1 Temperature Measurements | 44 |
| 3.3.1.1 Thermocouples | 44 |
| 3.3.1.2 Radiation Thermometry | 46 |
| 3.3.2 Airflow Measurements | 48 |

| | |
|---|------------|
| 3.3.2.1 Air Velocity | 48 |
| 3.3.2.2 Airflow Visualization | 50 |
| 3.3.3 Bolt Force Measurement | 50 |
| 3.4 Test Components | 51 |
| 3.4.1 Commercial Vehicle Brake | 52 |
| 3.4.2 TGV Brake | 56 |
| Chapter 4 Disc Brake Airflow | 60 |
| 4.1 Introduction | 60 |
| 4.2 Analytical Airflow Analysis | 60 |
| 4.2.1 Velocity Diagrams | 63 |
| 4.2.2 Pumping Power | 66 |
| 4.3 Vane Design | 68 |
| 4.3.1 Blade Width | 70 |
| 4.3.2 Number of Blades | 70 |
| 4.3.3 Blade Under Filling and Over Filling | 71 |
| 4.4 Airflow around Disc | 71 |
| 4.4.1 Experimental Measurements | 72 |
| 4.4.2 CFD Modelling | 78 |
| 4.4.2.1 Commercial Vehicle Brake Disc | 78 |
| 4.4.2.2 TGV Railway Brake Disc | 82 |
| 4.5 Pumping Loss Measurement | 87 |
| 4.5.1 Experimental Procedure | 87 |
| 4.5.2 Commercial Vehicle Brake Disc | 90 |
| 4.5.3 TGV Railway Brake Disc | 93 |
| 4.6 CFD Pumping Loss Prediction | 95 |
| 4.6.1 Commercial Vehicle Brake Disc | 96 |
| 4.6.2 TGV Railway Brake Disc | 98 |
| 4.7 Summary | 99 |
| Chapter 5 Convective Heat Dissipation | 101 |
| 5.1 Theoretical Background | 101 |
| 5.2 Convective Heat Transfer Coefficients and Relationships | 104 |
| 5.3 Cooling Constants | 110 |
| 5.4 Measurement of Commercial Vehicle Disc Cooling | 113 |
| 5.4.1 Comparison of Disc Designs | 118 |
| 5.4.2 Influence of Wheel Assembly on Disc Cooling | 121 |
| 5.4.3 Convective Heat Transfer Coefficients | 123 |
| 5.5 Measurement of TGV Railway Disc Cooling | 125 |
| 5.5.1 Influence of Rotational Speed on Disc Cooling | 129 |
| 5.5.2 Influence of Vane Design on Disc Cooling | 133 |
| 5.6 CFD Analysis of Convective Heat Transfer Coefficients | 133 |
| 5.6.1 Commercial Vehicle Disc | 134 |
| 5.6.2 TGV Railway Disc | 140 |

| | |
|--|------------|
| 5.7 Summary | 146 |
| Chapter 6 Conductive Heat Dissipation | 148 |
| 6.1 Introduction | 148 |
| 6.1.1 Theoretical Background | 149 |
| 6.1.2 Influencing factors | 151 |
| 6.2 Bolt Clamping Force Determination | 152 |
| 6.2.1 Theoretical Calculation | 152 |
| 6.2.2 Experimental Measurement | 153 |
| 6.3 FE Analysis of Contact Pressure | 155 |
| 6.4 Contact Pressure Measurement and FE Results Verification | 160 |
| 6.5 Measurement of Thermal Contact Resistance | 166 |
| 6.5.1 Experimental Set-up | 166 |
| 6.5.2 Experimental Procedure | 169 |
| 6.5.3 The Influence of Interface Pressure and Temperature | 171 |
| 6.6 Summary | 174 |
| Chapter 7 Radiative Heat Dissipation | 176 |
| 7.1 Theoretical Background | 176 |
| 7.1.1 Emissivity | 178 |
| 7.1.2 View Factors | 179 |
| 7.2 Surface Emissivity of Brake Discs | 180 |
| 7.2.1 Literature Data | 180 |
| 7.2.2 Emissivity Measurements | 181 |
| 7.2.3 Radiative Heat Transfer Coefficients | 188 |
| 7.3 FE Modelling of Radiative Heat Dissipation | 190 |
| 7.3.1 Analysis of Modelling Methods | 190 |
| 7.3.2 Secondary Radiation | 193 |
| 7.4 Summary | 196 |
| Chapter 8 Cooling Performance Simulation and Validation | 198 |
| 8.1 Introduction | 198 |
| 8.2 Modelling Methods | 198 |
| 8.2.1 Software Packages | 199 |
| 8.2.2 Model Solution | 199 |
| 8.2.3 Model Optimisation | 200 |
| 8.3 Commercial Vehicle Route Simulation | 203 |
| 8.3.1 Duty | 203 |
| 8.3.2 FE Modelling | 204 |
| 8.3.3 Analytical Temperature Prediction | 207 |
| 8.3.4 Dynamometer Test | 208 |
| 8.3.5 Results Comparison | 209 |
| 8.4 TGV Route Simulation | 210 |
| 8.4.1 Duty | 210 |
| 8.4.2 FE Modelling | 211 |

| | |
|---|------------|
| 8.4.3 Dynamometer Tests | 213 |
| 8.4.4 Results Comparison | 214 |
| 8.5 Investigation of Temperature Measurements and Predictions | 215 |
| 8.5.1 Rubbing Thermocouple Measurement Response | 215 |
| 8.5.2 Thermoelastic Instability Influence on Brake Temperatures | 221 |
| 8.6 Contribution of Modes of Heat Transfer to Disc Heat Dissipation | 223 |
| 8.6.1 Commercial Vehicle Disc | 224 |
| 8.6.2 TGV Disc | 228 |
| 8.7 Summary | 229 |
| Chapter 9 Heat Dissipation Improvement and Optimisation | 231 |
| 9.1 Objectives | 231 |
| 9.2 Analysis of Methods to Improve Heat Dissipation | 232 |
| 9.2.1 Airflow and Convection | 232 |
| 9.2.2 Conduction | 234 |
| 9.2.3 Radiation | 235 |
| 9.3 Commercial Vehicle Brake Assembly | 236 |
| 9.3.1 Wheel Carrier Ventilation | 236 |
| 9.3.2 Thermal Contact Resistance | 243 |
| 9.3.3 Simulation of Modified CV Wheel Assembly | 245 |
| 9.3.3.1 Component Materials | 246 |
| 9.3.3.2 Thermal Contact Resistance and Cross Flow | 248 |
| 9.4 TGV Railway Disc | 250 |
| 9.4.1 Ventilated Brake Disc Efficiency Ratio | 251 |
| 9.4.2 Disc Design Comparison | 256 |
| 9.5 Summary | 260 |
| Chapter 10 Conclusions and Recommendations | 262 |
| 10.1 Introduction | 262 |
| 10.2 Conclusions | 262 |
| 10.3 Recommendations for Further Work | 267 |
| | |
| List of References | |
| Appendix A Material Properties | |
| Appendix B Brake Components | |
| Appendix C Temperature Prediction | |
| Appendix D Spin Rig Design | |
| Appendix E SabWabco Dynamometer Test Schedule | |

Nomenclature

| | | |
|---------------|--|-----------------|
| A | cross sectional area | m^2 |
| b | cooling rate; blade width | $s^{-1}; m$ |
| d | diameter | m |
| c | distance along radius | m |
| c_p | specific heat | J/kgK |
| e | radius of curvature | m |
| E | modulus of elasticity | N/m^2 |
| F_o | Fourier number | - |
| F | force | N |
| F_i | preload | N |
| G | modulus of rigidity | N/m^2 |
| h | thermal heat transfer coefficient | W/m^2K |
| I | moment of inertia | m^4 |
| J | radius of gyration | kgm^2 |
| k | thermal conductivity | W/mK |
| K | constant | - |
| l | characteristic length | m |
| m | mass | kg |
| \dot{m} | mass flow rate | kg/s |
| M | bending moment | Nm |
| n | rotational speed | min^{-1} |
| n_b | number of stops | - |
| n_s | factor of safety | - |
| Nu | Nusselt number | - |
| P | pressure | N/m^2 |
| Pr | Prandtl number | - |
| q | energy | J |
| q' | thermal flux | W/m^2 |
| Q | power | W |
| r | radius | m |
| R | thermal resistance | m^2K/W |
| Ra | surface roughness | μm |
| Re | Reynolds number | - |
| s | time | s |
| t | thickness | m |
| T | temperature | K |
| U | velocity component | m/s |
| \dot{V} | volumetric flow rate | m^3/s |
| V | velocity component | m/s |
| x | distance; Cartesian co-ordinate | m |
| y | Cartesian co-ordinate | m |
| z | height; Cartesian co-ordinate | m |
| α | thermal diffusivity | m^2/s |
| β | proportion of heat conducted to rotor | - |
| $\beta_{1,2}$ | blade angle | $^\circ$ |
| γ | braking force transmitted to front axle | - |
| δ | boundary layer thickness | m |
| ϵ | emissivity | - |
| ζ | fraction of rotational energy to kinetic energy of vehicle | - |
| η | efficiency ratio | - |
| θ | angle | $^\circ$ |
| λ | parameter, $\lambda = t_d/(\alpha_d s_b)^{1/2}$ | - |
| μ | coefficient of friction | - |
| ν | kinematic viscosity | m^2/s |
| ρ | density | kg/m^3 |
| σ | stress; Stefan-Boltzmann constant | $N/m^2; m^2K^4$ |

| | | |
|----------|-------------------------------------|----------|
| τ | Torque | Nm |
| Φ | half apex angle of thread | ° |
| ϕ | lead angle | ° |
| Ψ | parameter, $\Psi = n_b \pi / 2 t_d$ | m^{-1} |
| ω | angular velocity | rad/s |
| f | function | - |

Subscripts

| | |
|----------|----------------|
| 1 | inner diameter |
| 2 | outer diameter |
| avg | average |
| b | braking |
| cond | conduction |
| conv | convection |
| C | carrier |
| D | disc |
| f | fluid |
| h | hydraulic |
| i | initial |
| o | interval |
| p | pad |
| ps | pad support |
| r | radial |
| rad | radiation |
| rel | relative |
| s | surface |
| w | whirl |
| ∞ | ambient |

Introduction and Research Objectives

1.1 Introduction

Braking is one of the most important and safety critical elements of vehicle control. For rail and automotive vehicles to operate safely, it is paramount to provide a stable and effective brake system that can decelerate or stop the vehicle as required. This thesis is concerned with the dry friction disc brake, which is the configuration found in most braking systems due to its superior braking efficiency and reliability. To achieve adequate brake operation, acceptable temperatures must be maintained during all service conditions. The thesis deals with the heat dissipation phenomenon, which is essential for the safe and efficient operation of all brakes.

Throughout a heavy-duty single brake application, virtually all the thermal energy is absorbed by the brake disc and pad, the short braking time does not allow significant heat dissipation. Brake disc thermal capacity must be sufficient to ensure acceptable temperature rise. If temperatures are allowed to become too high, deterioration of the brake structural integrity and friction performance will take place. For repeated brake applications or drag braking, the brake disc must be able to dissipate the thermal

energy that is generated. Adequate brake cooling is necessary to keep the brake temperature within a safe operating range.

By design, friction brakes generate thermal energy and can achieve very high temperatures. It is the duty of the brake designer to ensure that adequate heat dissipation is provided in all expected vehicle service conditions. This can only be achieved by studying all the modes of heat dissipation; convection, conduction and radiation. Sufficient brake cooling must be achieved since excessive thermal loading can result in brake fade, surface cracking, judder and high wear of the friction pair. High temperatures can also lead to overheating of brake fluid, seals and other components. The complex design requirements are difficult to satisfy and extensive research, development and testing are required.

1.2 Main Brake Types Studied

The research has mainly concentrated on two brake types considered to be the most thermally loaded and therefore most challenging; axle mounted high speed train disc brakes and commercial vehicle disc brakes. Different designs of these brake types have been analysed.

Railway Brakes – Axle Mounted High Speed Train Discs

High speed train discs must be capable of absorbing large amounts of heat in emergency brake applications from maximum speed. Heat dissipation during braking is low and therefore it is crucial to ensure low initial brake temperatures. This can only be achieved with good cooling characteristics, since brake mass must be kept to a minimum to ensure low unsprung mass. It must also be taken into consideration that emergency braking from maximum speed is relatively rare, however the brake system must be capable of performing this duty without excessive thermal loading. Ventilated brake discs are commonly employed for their good cooling qualities, however this type of brake disc can generate substantial pumping losses when rotating at high speed. The effects are very serious because a high number of discs (usually 4 discs per axle) rotating at high speed (up to 2000 min⁻¹) require very high levels of power, just for disc rotation. This has resulted in the development of numerous ‘low loss’ ventilated disc designs and the use of solid discs. Obviously, a

very fine balance of low pumping losses and good cooling characteristics are necessary to satisfy braking and power consumption requirements for all vehicle routes.

Automotive Brakes – Commercial Vehicle Discs

Compared to passenger cars, commercial vehicles have a much higher wheel load to wheel diameter ratio. This inevitably limits the size of the brake system that can be installed. Commercial vehicle speeds are usually lower than passenger cars, which combined with larger wheels, substantially reduce disc rotational speeds. Brake applications are often more frequent and combined with high axle loads results in the generation of large amounts of thermal energy, which have to be dissipated in a confined space at lower rotational speeds, with a restricted supply of cool air.

1.3 Research Objectives

The phenomenon of heat dissipation from friction brakes is very complex and requires carefully planned research, combining detailed literature study and analytical, numerical and experimental techniques. It is important to ensure that research results are of a generic nature, applicable to other brake designs and have wider engineering applications. At the same time, analysis must be orientated to finding ways of improving and optimising brake cooling using practically acceptable and economically viable methods.

Based on previous considerations, literature studies, suggestion of industrial partners involved, and taking into account financial and time limitations imposed upon the project, the following research objectives have been set:

- To establish values of contact resistance, heat transfer coefficients and emissivity values for main brake areas.
- To establish the main parameters influencing the above coefficients and recommend functions defining appropriate relationships.
- To study analytical, numerical and experimental techniques used in determining brake heat dissipation and airflow characteristics.

- To perform sensitivity analyses and make recommendations for appropriate brake thermal modelling and experimental measurements.
- To compare different modes of heat dissipation and make recommendations for optimal brake designs.
- To validate overall work by performing a number of route simulations.

Meeting the above research objectives will lead to a better understanding of all the modes of heat dissipation and aerodynamic losses from friction brakes. With this understanding, higher performance brakes can be designed in a shorter time, with more predictable performance limits and lower testing requirements. This will reduce development costs and risks, increasing brake manufacture's competitiveness, and overall vehicle performance.

Literature Survey

2.1 Introduction

The field of brake cooling has been a subject of research since the 1950s and consequently many papers can be found on the subject. Since the use of the first brake, vehicle speeds and weights have steadily increased. These increases lead to braking energy rise resulting in higher brake temperatures, necessitating further research. However, the published research is fragmented and applied to specific cooling problems or brake designs.

Initially, analytical techniques were used to predict brake temperatures during cooling, which were limited to steady-state analysis and simple geometries. Now brake thermal research has been dominated by finite element analysis and more recently, computational fluid dynamics. The objective of this chapter is to present an extensive review of previous work in the area of dry friction brake heat dissipation and associated topics. Literature specific to areas of investigation has been referenced in the relevant section of the thesis. The area of friction heat generation and resulting brake temperature has also been researched and used in brake cooling

performance simulation (Chapter 8). As it is not directly associated with brake cooling analyses, this topic is discussed, with relevant literature in Appendix C.

2.2 Friction Braking Development

The problem of safe vehicle braking became apparent at the beginning of self-propelled vehicle development. Newcomb and Spurr (1970) highlighted the story of 1769 when the Frenchman, Cugnot, made the first self-propelled steam road vehicle. The vehicle had a top speed of about 5 km/h and demolished a wall because of braking system failure. The story goes that hot embers and boiling water spilled everywhere; Cugnot was arrested and sent to prison.

Early combustion engine car brake systems were also inadequate, Benz pressed a small block against a drum and Daimler used spoon brakes acting on the rear tyres. A reliable and contamination resistant brake system was not developed until 1903 when Daimler introduced the first internal drum brake. In the 1920s cars became much faster, the need for improved braking became apparent and vehicle braking systems evolved to hydraulic brakes on all four wheels. The first car of any consequence to use hydraulic brakes at all four wheels was the 1921 Duesenberg of the U.S. (Freudenberger 1999).

The main disadvantage of the drum brake is its non-linear relationship between brake torque and pad/disc friction coefficient, which is exaggerated by the poor cooling characteristics of the design. Temperature rise causes drum expansion increasing pedal travel, soft pedal feel and improper contact between drum and brake shoe lining. The need for improved braking systems led to the development of the disc brake, which has a more linear relationship between brake torque and pad/disc friction coefficient and far superior cooling characteristics. The first disc brake was patented in 1902 by F. Lanchester. However, interest in the design was not established until it was introduced at the UK 1951 International Motor Show and later when the Jaguar C-Type won the 1953 Le Mans fitted with Dunlop disc brakes. During the 1950s the disc brake became more commonplace on cars. Present day road vehicles (passenger cars and commercial vehicles) are fitted with disc brakes at the front wheel as standard and discs fitted to the rear wheels are increasingly more common.

George Westinghouse invented the first version of the railway air brake in 1869, acting on a tread (wheel) brake. The tread brake method has many disadvantages including limited energy capacity, high wheel tread wear and accelerated tread damage. Since then train speeds have increased dramatically and more advanced disc braking has been employed. Operation at 200 km/h has existed since the 1970s and in 1989 TGV (Train à Grande Vitesse) trains were running at 300 km/h. In 1990 TGV set a new world record travelling at 515.3 km/h. In order to provide the necessary braking energy capacity for the new generation of high-speed trains TGV incorporated four brake discs on each trailer axle (Russell and Williams 1990) and later wheel mounted discs on power cars (replacing tread brakes).

The development of the motorcycle brake was much slower than that of the car. The first drum brake was introduced in 1935 by BMW on the BMW R 32. At the Tokyo Show of 1968 Honda unveiled the CB750F, fitted with the first disc brake.

2.3 Studies of Heat Dissipation

In the brake disc heat is generated at the friction surface and conducted through the brake assembly, where it is dissipated. All three modes of heat transfer; convection, conduction and radiation are introduced and studied in this section. Their characteristics related to heat dissipation from friction brakes are described and analytical equations given for the prediction of heat transfer by each mode.

2.3.1 Convective Heat Dissipation

The convective heat transfer coefficient (h_{conv}) is a function of geometry, rotational speed and temperature, which influences the flow pattern and velocity of the airflow over its surface. The geometry of the brake is generally broken down into regions defining simple shapes. For each area, h_{conv} can be determined using equations found in the literature. The brake disc geometry can be divided into a rotating disc (for the friction surfaces) and rotating cylinders (for the rim and hat sections). In addition, for the ventilated disc the channels can be defined as rectangular channels.

2.3.1.1 Convective Heat Transfer Coefficient Equations

Equations describing convective heat transfer for each area of the brake disc are shown in Table 2.1. Measurement of laboratory experiments have established Nusselt equations for each surface region, where:

$$Nu = \frac{h_{conv}l}{k} \quad (2.1)$$

Where l is the characteristic length (generally the disc radius or ventilation channel hydraulic length), k is the thermal conductivity of air and h_{conv} is the convective heat transfer coefficient. The rotating Reynolds number (Re_o) and cross flow Reynolds number (Re_t) are given by the following equations:

$$Re_o = \frac{\omega r^2}{\nu} \quad (2.2)$$

$$Re_t = \frac{vr}{\nu} \quad (2.3)$$

Where, r is the disc outside radius and ν is the cross flow velocity. When the disc is ventilated, it acts like a fully shrouded impeller, pumping air through the ventilation channels. Before a Nusselt value can be found for the ventilation channels of the disc, the mean velocity in the ventilation channel must be determined using the hydraulic diameter. The hydraulic diameter is defined as the average ratio of four times the cross sectional flow area (wetted area) divided by the wetted perimeter (Limpert 1975). Table 2.2 shows published equations used to determine average vane velocity.

Table 2.1 Convective heat transfer coefficients

| Equation number | Description | Equation | Critical Re Number | Reference |
|-----------------|--|---|-------------------------------------|--|
| (2.4) | Cylinder rotating in still air | $h_{conv} = \frac{0.02 Re_o^{0.75} k_{air}}{1 - 0.67 Re_o^{-0.125} d}$ | - | (Kohto 1984), (Fukano and Matsui 1986) |
| (2.5) | Cylinder rotating in still or moving air | $Nu = 0.06 \{2 Re_o^2 + 4 Re_t^2\}^{\frac{1}{3}}$ | - | (Morgan and Dennis 1972), (Day 1998), (Newcomb 1979), (Sheridan, Kutchev et al. 1988) |
| (2.6) | Disc rotating in still air | $Nu = 0.36 Re_o^{0.5}$ | Re < 240000, laminar | (Cobb and Saunders 1955), (Day 1998), (Newcomb 1979) |
| (2.7) | Disc rotating in still air | $Nu = 0.015 Re_o^{0.8}$ | Re > 240000, turbulent | (Cobb and Saunders 1955), (Day 1998), (Newcomb 1979) |
| (2.8) | Disc rotating in still air | $h_{conv} = 0.7 \left(\frac{k_{air}}{d} \right) Re_o^{0.55}$ | Re < 240000, laminar | (Limpert 1975) |
| (2.9) | Disc rotating in still air | $h_{conv} = 0.04 \left(\frac{k_{air}}{d} \right) Re_o^{0.8}$ | Re > 240000, turbulent | (Limpert 1975) |
| (2.10) | Disc rotating in still air | $Nu = 0.0195 Re_o^{0.8}$ | - | (Dennis, Newstead et al. 1970), (Sheridan, Kutchev et al. 1988) |
| (2.11) | Disc rotating in still air | $h_{conv} = 0.399 k_{air} \left(\frac{w}{v_{air}} \right)^{0.5} Pr^{0.43}$ | - | (Dorfman 1963), (Fukano and Matsui 1986) |
| (2.12) | Disc rotating in a cross flow | $Nu = 0.0436 \left[\frac{Re_t}{Re_o} \right]^{0.74} Re_o^{0.8}$ | - | (Morgan and Dennis 1972), (Day 1998), (Sheridan, Kutchev et al. 1988) |
| (2.13) | Used for all free surfaces in still air | $Nu = 0.037 Re_o^{0.8}$ | - | (Dennis, Newstead et al. 1970), (Grieve, Barton et al. 1998), (Koetnuyom, Brooks et al. 2000) |
| (2.14) | Vane | $Nu = 0.024 \left[1 + \left(\frac{d_h}{l} \right)^{\frac{2}{3}} \right] Re_o^{0.8} Pr^{0.45}$ | Factorise by 1.7 for turbulent flow | (Hausen 1950), (Day 1998), (Newcomb 1979) |
| (2.15) | Vane | $Nu = 0.045 Re_t^{0.8} \left(\frac{d_2}{2} \right)^{0.2} + \frac{6.6 d_2}{2}$ | - | (Sisson 1978), (Sheridan, Kutchev et al. 1988) |
| (2.16) | Vane | $h_{conv} = 0.023 \left[1 + \left(\frac{d_h}{l} \right)^{0.67} \right] Re_t^{0.8} Pr^{0.33} \left(\frac{k_{air}}{d_h} \right)$ | Re > 10000, turbulent | (Kreith 1986), (Limpert 1975) |
| (2.17) | Vane | $h_{conv} = 1.86 (Re_t, Pr)^{\frac{1}{3}} \left(\frac{d_h}{l} \right)^{0.33} \left(\frac{k}{d_h} \right)$ | Re < 10000, laminar | (Kreith 1986), (Limpert 1975) |

Table 2.2 Vane velocity equations

| Equation number | Vane inlet velocity [m/s] | Vane outlet velocity [m/s] | Vane average velocity [m/s] | Reference |
|-----------------|---|--|--|---------------------------------|
| (2.18) | $u_{in} = 0.171n(d_2^2 - d_1^2)$ | $u_{out} = u_{in} \left(\frac{A_{in}}{A_{out}} \right)$ | $u_{avg} = \frac{u_{in} + u_{out}}{2}$ | (Day 1998), (Newcomb 1979) |
| (2.19) | $u_{in} = 0.0158n(d_2^2 - d_1^2)^{\frac{1}{2}}$ | $u_{out} = u_{in} \left(\frac{A_{in}}{A_{out}} \right)$ | $u_{avg} = \frac{u_{in} + u_{out}}{2}$ | (Limpert 1975) |
| (2.20) | - | - | $u_{avg} = \frac{(-0.02 + 0.0091d_1 - 0.00002d_1^2)^{\frac{1}{2}} \omega d_2}{2}$ | (Sheridan, Kutchey et al. 1988) |
| (2.21) | - | - | $u_{avg} = \frac{\pi d_2 n}{60} (-0.0201 + 0.2769 \times d_1 - 0.0188 \times d_1^2)^{\frac{1}{2}}$ | (Sisson 1978) |

2.3.1.2 Cooling Parameters

An alternative approach is to define cooling parameters for an actual brake assembly on the vehicle. Results indicate that a ‘cooling body’ can be expressed as (Newcomb and Millner 1965):

$$b = b_o + Kv^{0.8} \quad (2.22)$$

The term b_o involves a conduction and natural convection component and the $Kv^{0.8}$ is the forced convective component where v is the linear velocity of the vehicle and K is a constant relating to the geometry of the body. A comparison between the cooling rates of a solid disc and two ventilated discs of similar outside diameters (280 mm) were made on a dynamometer. The solid disc was 12.5 mm in thickness and had a mass of 5.7 kg. One ventilated disc was made from cast iron with a mass of 17.4 kg, the other ventilated disc was made of aluminium alloy coated with steel and had a mass of 3.1 kg, both discs had a thickness of 6.25 mm excluding the vane. Table 2.3 shows experimental values of b . The cooling rates were determined by bringing the disc to a uniform temperature of 300° to 400°C by drag braking and cooling.

Table 2.3 Experimental values of b (Newcomb and Millner 1965)

| Disc | $10^3 b$ [s ⁻¹] |
|----------------------|-----------------------------|
| Solid cast-iron | 2.36 |
| Ventilated cast-iron | 2.91 |
| Ventilated aluminium | 4.96 |

2.3.2 Conductive Heat Dissipation

Heat generated at the friction surface of the disc is conducted through the disc to the disc flange area. Heat is then conducted to the hub and, or wheel assembly. The rate of heat conduction through a solid object is governed by the cross section area, material properties (conductivity, specific heat and density) and temperature.

2.3.2.1 Thermal Contact Resistance

Thermal conductivity is very important in the investigation of conductive heat transfer through assemblies. The value of thermal contact resistance (TCR) at the interface between two mating surfaces depends on the surface roughness, material properties, temperature and pressure at the interface, and also the type of interstitial medium. In general, TCR will increase with increased surface roughness, reduced interface pressure and increased material hardness.

There is much published work in the area of TCR, though this has not applied to brake cooling. In order to predict the TCR across a given area, the number and average size of the micro-contacts that make up the apparent contact area must be accurately predicted. Greenwood and Williams (1966) proposed one of the first models to predict contact area known as the GW model, which can be summarised as an elastic micro-contact model. McCool (1986) has compared several models and reports that the GW model gives good results. The GW model has been modified by McCool (1986) using the random process model of rough surfaces. The modified version of the GW model has been applied by McWaid and Marschall (1992) to predict TCR and results compare well with experimental data.

The GW model does not take into account the presence of surface films, which may take the form of natural oxidation, liquid, powder, foil or plating. Research in the area of oxidation has been summarised by Madhusudana and Fletcher (1986). A

generally accepted conclusion is that oxide films, unless sufficiently thick, do not appreciably increase the TCR. Lambert, Fletcher, et al. (1995) investigated the TCR of anodised coatings, noticing that TCR drops after the break up of the oxide layer (due to deformation of the base metal) allowing flow through the cracks in the oxide. Unless the oxide layer is thicker than the mean height of the surface peaks, oxide layers will not appreciably increase the TCR. Mian, Al-Astrababi et al. (1979) have shown experimentally that TCR increases with the film thickness and the ratio of the total film thickness to the mean surface roughness. TCR was found to decrease with increased loading and mean surface roughness.

To decrease the TCR, the air within interstitial areas at the contact interface can be replaced with a medium of higher conductance. Interstitial fillers may take the form of grease, metal foil, wire screens or powders. Indium foil and silicon grease appear to be the best materials in this category (Madhusudana and Fletcher 1986). It has been shown that thermal conductive conductance (the reciprocal of TCR) can be increased up to a factor of seven, by inserting a metallic foil at the interface (Cengel 1998), see Figure 2.1.

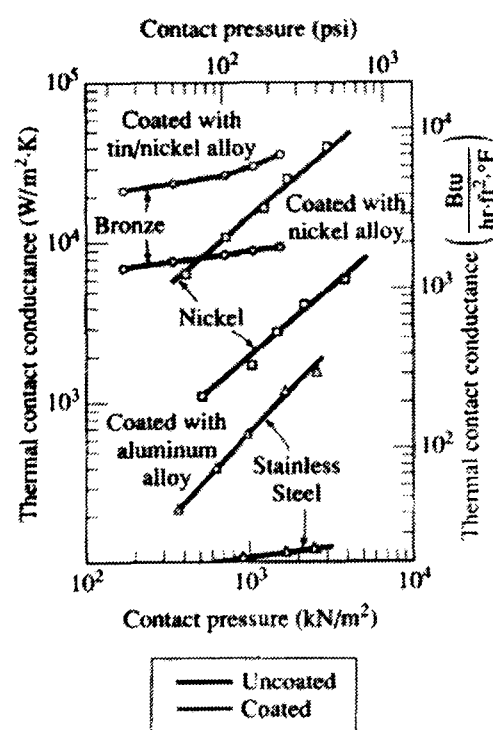


Figure 2.1 Effect of metallic coatings on thermal contact conductance (Cengel 1998)

Foils, greases and powders are difficult to apply during component assembly and plating mating surfaces may be the most convenient method of enhancing thermal conductivity. Mikic and Carnasciali (1970) analysed the effects of plating material on TCR. Results showed that considerable reduction of TCR could be achieved with

plating. Stainless steel plated with copper of a thickness of the order of the contact size radius, will reduce resistance by more than an order of magnitude.

Reduction of TCR by metallic coatings has been analysed by Antonetti and Yovanovich (1985). It was found that a silver layer can reduce the TCR of nominally flat, rough, contacting nickel specimens by as much as an order of magnitude; and that for a given layer thickness, the smoother the bare contacting surface the greater the enhancement will be.

Madhusudana and Fletcher (1986) report on experimental observations regarding the sensitivity of conductance to direction of heat flow. This phenomenon, known as thermal rectification, is observed in dissimilar mating surfaces. It is generally accepted that the thermal rectification is caused by the distortion of the contact surface due to local temperature gradients. Experiments on stainless steel/stainless steel contact observed a large directional effect when one surface was bead blasted and the other lapped; the conductance was higher when the heat flowed from the rougher to the smoother surface. Conductance through stainless steel/aluminium contact showed higher conductance in the SS→Al direction, the same was found for copper, a higher conductance was found in the SS→Cu direction, stainless steel being the harder material in both cases.

Determining TCR becomes more complex when bolts or rivets fasten the two materials. These are the most common methods of mechanical connection and are often found in braking systems. The interface pressure in this case is non-uniform, the highest being near the bolt or rivet shank, and reducing away from the centre line. The thermal contact resistance in this case is dependent on the plate thickness, bolt or rivet thickness and size of contact zone. Mittelbach, Vogd et al. (1994) presented experimental interface pressure distributions and thermal conductance data for a bolted joint, see Figure 2.2. Results show that thermal conductance is a function of plate thickness ratio. The actual area of contact will be circular in shape, with the contact pressure decreasing with distance from the bolt centre line. The area of actual contact zone is directly associated with TCR. This implies that the heat transfer

through a bolted joint is dependent upon the pressure distribution at the joint as well as the macroscopic and microscopic contact resistance.

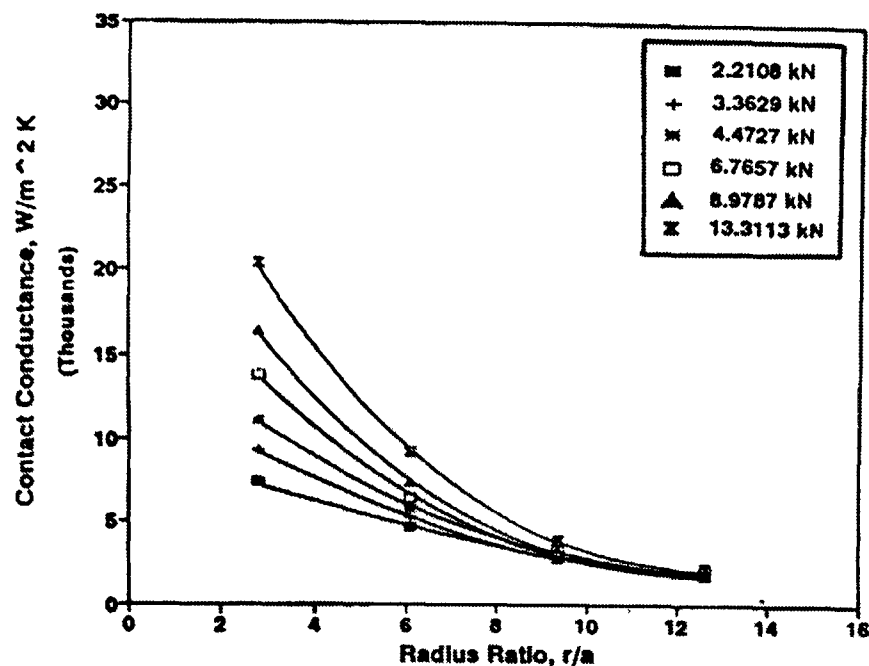


Figure 2.2 Contact conductance as a function of dimensionless radius for a plate thickness $t_1/t_2 = 4/3$ (Mittelbach, Vogd et al. 1994)

2.3.2.2 Conductive Heat Transfer Coefficient

From various experimental data on brake discs, it has been found most efficient to quantify the conduction of heat to the hub as an apparent heat transfer rate (the reciprocal of TCR). Quantified values were determined by Fukano and Matsui (1986) by changing the apparent rate of heat transfer to the hub and by comparing with experimental values. In a certain vehicle test the calculation corresponded best with the experimental results when the apparent heat transfer rate to the hub was $712 \text{ W/m}^2\text{K}$.

Morgan and Dennis (1972) found that conduction coefficients are extremely variable for the theoretical prediction of brake temperatures and comparison with experimental data. Cetinkale and Fishenden (1951) suggested that the contact coefficient is likely to change dramatically with time or with subsequent dismantling and reassembly during servicing. Sheridan, Kutchev et al. (1988) modelled the conduction heat transfer that exists between the disc flange and the hub and wheel by doubling the convective heat transfer coefficients used on the disc friction surfaces. An even more simple approach was taken by D'Cruz (D'Cruz 1989) using a blanket heat transfer coefficient of $100 \text{ W/m}^2\text{K}$ to all free surfaces.

Aikawa and Winer (1994) and McWaid and Marschall (1992) have published the test procedure used for thermal contact resistance measurement. The apparatus shown in Figure 2.3 consists of a vertical column composed of the bolted test specimens, a heat flow meter and heat sink. The heat flow through the specimens is kept constant by using a heating element attached to the top of the first specimen. A constant temperature heat sink is used to remove energy from the bottom of the test column. To allow examination of the temperature gradient at the specimen, interface thermocouples are placed into the specimens at known axial locations. A heat flow meter is used in order to measure actual heat flow through the column. The heat flow meter is fabricated from a standard reference material with a known thermal conductivity. To determine the temperature gradient, thermocouples are placed into the heat flow meter at known axial locations. The heat flow meter is necessary because of difficulties determining the power input via the heater. The thermal contact resistance is determined using the temperature gradient and area taken at the sample interface. It is assumed that there are no losses in the system between the specimen and the heat flow meter. Convection and radiation losses are reduced by shielding and keeping the operating temperature to a minimum.

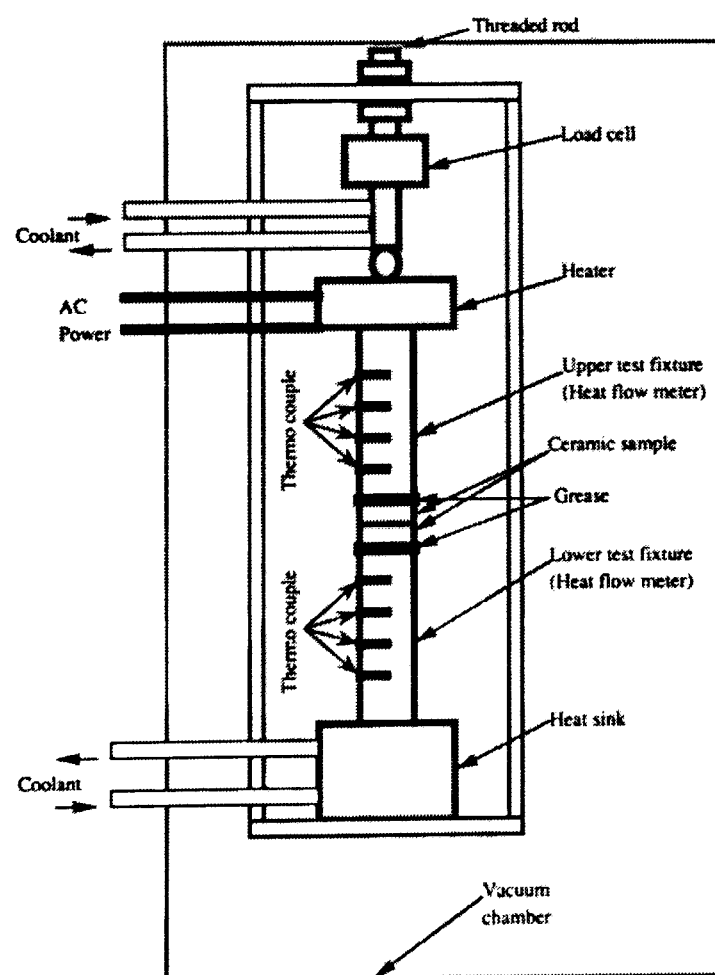


Figure 2.3 Thermal contact resistance test rig (Aikawa and Winer 1994)

2.3.3 Radiative Heat Transfer

Radiative heat transfer is a function of surface emissivity and more so temperature (to the fourth power). Until only very recently radiative heat transfer has been neglected or greatly simplified in brake cooling analysis. Brake temperatures were lower in the early period of brake analysis and available modelling techniques less complex. However, today's brake temperatures can reach much higher values with the use of new materials and high performance designs. That, along with more complex modelling requires radiative heat transfer to be included in thermal analysis.

In a comparison of theoretical and experimental data by Morgan and Dennis (1972) radiation losses were neglected as radiation was thought to be responsible for only a very small fraction of total heat losses. However, in the discussion of the alpine simulation test it is stated that radiation was probably quite significant at the high temperatures reached in this test (up to 700°C). Radiation losses were also neglected by Fukano and Matsui (1986), and Sheridan Kutchev et al. (1988) in their disc temperature calculations. Allowance for radiation is given in temperature predictions by Limpert (1975) and Newcomb (1979), with Limpert recommending an emissivity value of 0.55 for cast iron discs. Noyes and Vickers (1969) provided for radiative heat transfer in FEA simulation by assuming all emissivity to be 0.8 with a background temperature of 38°C.

2.4 Experimental Studies of Brake Cooling

Experimental measurement techniques related to brake cooling described in the literature have been reviewed because of their relevance to the experimental part of the thesis.

2.4.1 Temperature

The most common methods of temperature measurement in industrial and research environments are resistance temperature detectors (RTDs), thermocouples, and infrared sensors. Thermocouples have been used in most brake temperature analysis due to their ruggedness, operating temperatures, small size, response, cost and availability.

Embedded thermocouples have been used to measure the temperatures of sliding mechanical components, but Kennedy (1984) has concluded that they cannot give a true indication of surface temperature peaks. The thermocouples have a limited transient response owing to their mass and distance from the points of intimate contact, and their emplacement close to the contact may change the flow of frictional heat. Although these problems are not as severe with fast response micro-thermocouples, embedded thermocouples maybe more useful for the measurement of the bulk temperatures within the sliding bodies and not contact temperatures. It must be remembered that the permanently fixed thermocouples measure temperature at one particular point, and this specific point may not be representative of the average temperature. Lee and Barber (1994) used six chromel-constantan thermocouples press-fitted though holes drilled 1.5 mm below the disc surface for brake temperature measurement. The outer halves of the holes were filled with cast iron rods. Readings for the disc temperatures were extracted via slip rings. The depth of the thermocouple from the friction surface will affect the response, Daudi (1998) conducted experimental measurements based on thermocouples that were mounted closer to the friction surface (1 mm below).

Newcomb and Millner (1965) obtained temperature measurements from a test vehicle using copper-constantan thermocouples mounted midway in the brake disc below the middle of the rubbing path and the hub. The thermocouple outputs were collected by slip-ring units mounted to the wheels. Some measurements were also made using rubbing thermocouples attached to the dust shields. Cooling rates determined in this manner were found identical to those derived from the embedded thermocouples. Bailey, Buckingham et al. (1991) have also used embedded thermocouples and slip rings amplified by a circuit rotating with the disc. This arrangement reduced noise problems associated with slip rings. It was noted that the embedded thermocouples demonstrated slow response time and low temperature readings as they are not quite at the surface of the disc. Basch, Fash et al. (2000) also used embedded thermocouples with slip rings to evaluate thermally sprayed aluminium brake discs.

Dynamic thermocouples are contacting bodies themselves or part of them (Kennedy 1984). They act to create a thermocouple junction at the sliding interface. The

technique has been used for suitable dissimilar sliding metals but the e.m.f. produced is the weighted average of all temperatures across the sliding thermocouple junction. Qi, Noor et al. (2002) have showed that exposed thermocouples with open and closed hot junctions can provide useful data on the interaction between pad and disc. The closed junction can record the pad surface temperature during braking, the open junction can detect when the disc and pad are in contact locally, and indicate the formation of an interfacial layer (tribo-layer) at the interface of the brake friction pair.

The thermal mass of a contact sensor, the process of conducting heat from the object into the sensor, and associated thermal resistance at the point of contact can limit response time (Young 2000). Because of their non-contacting nature, infrared temperature sensors can respond almost instantaneously to temperature changes, permitting measurement of fast moving objects or objects whose temperature changes rapidly. Dubensky (1986) used infrared techniques for obtaining temperatures on brake discs. An Inframetric scanner was used and temperature patterns were recorded on videotape. This technique can provide detailed inputs for finite element techniques. This technique was also used by Bailey, Buckingham et al. (1991) and Dufrenoy and Weichert (1995) with results agreeing well with test data. From thermal imaging work carried out on a brake dynamometer Grieve Barton et al. (1998) used the emissivity value 0.4 for cast iron and aluminium MMC discs. Radiative heat transfer was not used on the ventilation channel interior of the ventilated disc because of its enclosed nature.

Eisengraber, Grochowicz et al. (1999) compared different methods for the determination of disc brake temperature on a dynamometer and stated that the usage of a pyrometer at the friction surface is only possible when the disc surface emissivity can be permanently corrected. The measured emissivity (ϵ) of the disc surface during the tests ranged between 0.15-0.9 ($\epsilon = 0.9$ during hot spot formation).

2.4.2 Airflow

Airflow is an important factor of heat dissipation from friction brakes. Air heated by the brake assembly surface is transported away from the brake assembly by airflow and replaced with cooler air. Airflow also directly influences convective heat transfer coefficients, which increase with air velocity.

Several results have been published for the ventilation channel velocity of a rotating disc, however methods of measurement are not discussed or are unclear. Sisson (1978) measured the average air velocity for a range of rotational speeds for a model disc with an inside diameter of 140mm, an outside diameter of 267 mm and 40 straight radial vanes of 25.4 mm width. A linear relationship was established; at 1000 min^{-1} average vent velocity was 7.3 m/s. A 72 curved fin disc produced by Hayes Lemmerz (Daudi 1999) with an inside diameter of 165 mm and an outside diameter 280 mm, showed a power curve relationship between rotation and vane velocity. The average airflow through the vane was measured to be 0.3 m/s at 700 min^{-1} . Krusemann and Schmidt (1995) applied CFD analysis to major wheel arch components (excluding the wheel and tyre) of an automotive vehicle travelling at a constant velocity of 120 km/h (1224 min^{-1}), an average mass flow rate of air through the ventilated channel was shown to be 0.04 kg/s giving an average airflow velocity of 2.5 m/s. From the above data, it can be established that predicted and measured airflow vary considerably from one set of findings to another.

The use of smoke to visualize the flow in wind tunnels was first adopted by L. Mach (Vienna, 1893) and E. J. Marey (Paris, 1899). The important advances toward the eventual use of smoke visualization as a research tool began in the 1930s with the work of A. M. Lippish (Darmstadt, 1937) and F.N.M. Brown (Notre Dame, 1937). A large number of materials have been used to generate smoke including; tobacco, rotten wood, titanium chloride, water vapour and oil vapour. Smoke particles must be small enough so they closely follow the flow pattern being visualized but also large enough to scatter a sufficient amount of light. Kerosene oil smoke is commonly used; the smoke generator generally uses an oil drip feed onto strip heater mounted inline with a blower to force the smoke through a tube (Goldstein 1996).

Kubota, Hamabe et al. (2000) investigated the airflow through ventilated brake disc cooling channels using a one-tenth scale model of a wheel unit incorporating a disc brake assembly submersed in a water tank. Flow through the ventilation channels were visualised by photographing the movement of a tracer through the fins, showing a relationship between rotor shapes and cooling performance.

2.5 Studies of Heat Dissipation Optimisation

Many methods of optimising heat dissipation from brake discs have been published and are mainly concerned with increasing the airflow around the disc surface.

Newcomb and Millner (1965) measured the cooling rates of a small saloon car fitted with and without dust shields. At low speeds the effect of removing dust shields is small but at 32 km/h the cooling rate is increased by 15% and above this speed 30%, showing that the elimination of dust shields can increase the cooling rate by approximately 30% at cruising speed. It is noted however that the reduced life of disc and pad due to particles of road debris outweigh the cooling advantages.

Cooling rates were also compared on cars fitted with solid wheels and wire wheels; little improvement of cooling rates resulted. Blanking off the small air vents in the front wheels of the car to prevent additional air flow from the inside to the outside of the wheel caused little change to the cooling rates of the disc up to a speed of approximately 64 km/h. Above this speed, an increase in cooling was measured, which was approximately 10% at 113 km/h. On the same car measurements of cooling rates were made with the engine bonnet and wings removed. The cooling rate of the exposed disc was only 13% higher. During these test it was noted that rain had little effect on the cooling rates.

The convective cooling capacity of a brake can be improved by increasing the effective surface area of the disc and by increasing the convective heat transfer coefficient. The heat transfer coefficient can be improved through better airflow ducting to the brake as well as through the interior vanes of the disc. Tests have shown (Limpert 1975) that straight vanes are inferior to the curved cooling vanes of a ventilated disc. Under identical test conditions, the curved vane disc produced

steady-state power capacities that were approximately 12% higher than the straight vane disc. Further improvements in cooling capacity may be achieved with axial as well as radial cooling passages as indicated in Figure 2.4. The increased cooling is achieved by the larger surface area and increasing convective heat transfer coefficients are expected. Comparison analysis shows that standard ventilated discs exhibit higher temperatures during the cooling down period than the axial/radial disc. Axial/radial ventilated discs exhibit advantages over radial ventilated discs only during a large number of repeated brake applications.

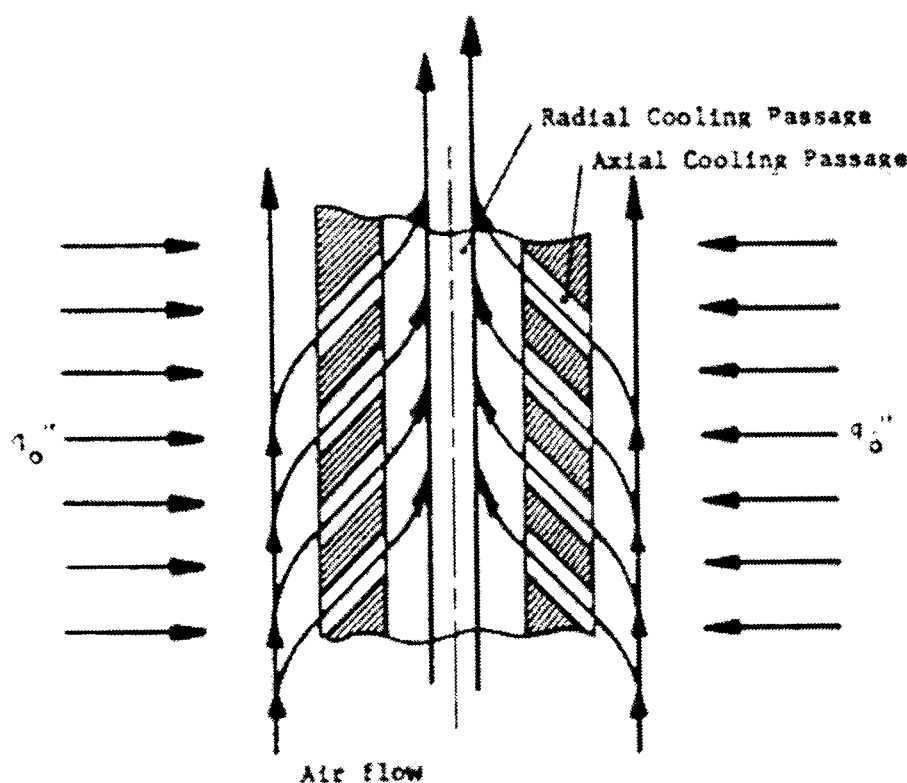


Figure 2.4 Ventilated disc with axial cooling passages (Limpert 1975)

Kubota, Hamabe et al. (2000) found that the air velocity through the ventilation channels increases in proportion to the inner radius of the disc. In addition to the wider opening area resulting from a larger inner radius, it is thought that the offset ($R_{in}-R_{out}$) of the disc works to promote smooth introduction of cooling air into the ventilation channels, increasing air velocity. Alternately arranging two different length fins increases cooling air inlet area resulting in a higher air velocity, however there is an optimum fin length when considering the surface area of the ventilation channels. The air velocity was found to increase through the ventilation holes with the use of alternate gourd-shaped fins and short, straight fins, see Figure 2.10.

Sheridan (1988) showed a comparison of measured and calculated plateau temperatures for a mountain descent with a steel wheel and aluminium wheel with

more than twice the vent area of the steel wheel. The benefits of the increased cooling flow rate through the aluminium wheel and increased conductive heat dissipation through the hat section to the wheel are shown in the reduced brake temperatures.

2.6 Numerical Analysis

The analytical solutions given in Appendix C assume the disc geometry can be approximated by a semi-finite slab with a heat flux varying linearly with time applied at each of its two faces. The assumptions include that; the disc is homogenous, cooling occurs at the friction surface, deceleration is constant and disc material thermal properties are constant with temperature. Most braking systems involve complex geometry, and transient boundary conditions and thermal properties, which cannot be solved analytically. In such cases, sufficiently accurate results must be obtained by computer using numerical methods. Numerical solution methods are based on solving the governing differential equations together with the boundary conditions.

2.6.1 Finite Element Methods

Abbas, Cubbitt et al. (1969) were one of the first to use an FE model to predict brake temperatures. A half section of the disc is shown in Figure 2.5. Simplification is achieved by assuming the brake temperature does not vary through the disc thickness at any point, reducing it to a one-dimensional problem. Comparison of the computer program's results and experimental results for a single stop show good agreement.

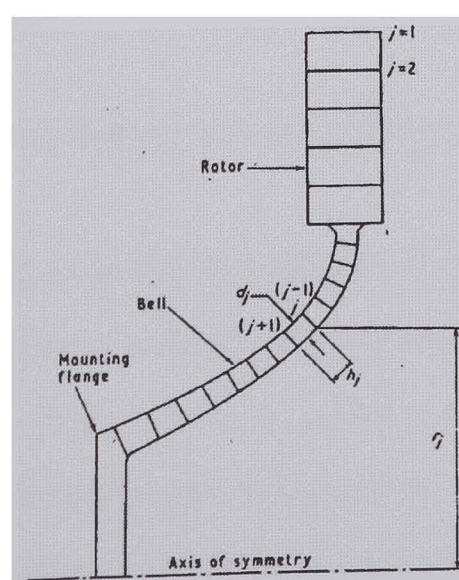


Figure 2.5 Half-section of hypothetical brake disc (Abbas, Cubbitt et al. 1969)

Morgan and Dennis (1972) created a rectangular mesh of parallelepiped elements over the cross section of the disc. Sets of linear, simultaneous equations were solved, which allowed for convenient solution of transient temperatures. Comparison with experimental results showed reasonable agreement although the cooling was slightly over predicted, probably due to the effective cross flow velocity being lower than the vehicle velocity used in the model.

Noyes and Vickers (1969) produced an FE model for a vented disc undergoing 97 km/h fade stops. The disc was split at its lines of symmetry (using half a vane and ventilation channel) producing a 4.5° segment, shown in Figure 2.6. The three-dimensional (3-D) model was approximated with parallelepiped elements containing 104 nodes. Comparisons of predicted results with measured temperatures on the Pikes Peak descent showed that measured temperatures lag appreciably behind predicted surface temperatures. This is reported to be due to the high thermal resistance of the brake linings in which the measuring thermocouples were embedded.

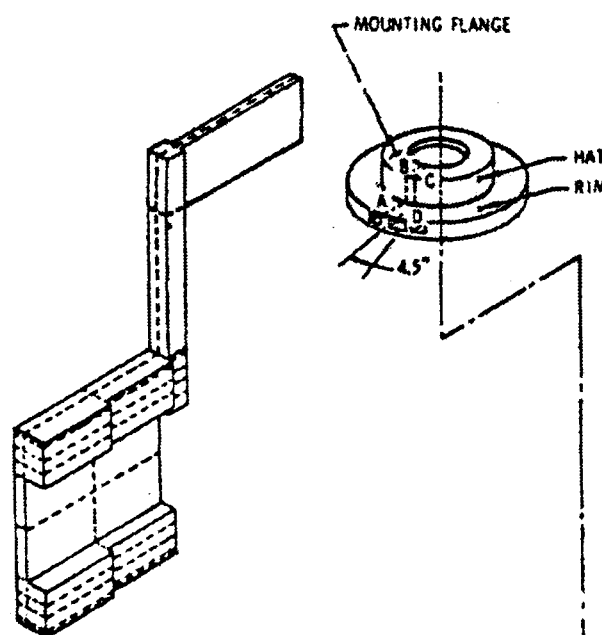


Figure 2.6 Half vane segment model (Noyes and Vickers 1969)

Day and Newcomb (1984) incorporate the effects of interface pressure distribution, material wear and thermal expansion on the dissipation of frictional energy from the interface of an annular disc brake. It is suggested that conventional methods of thermal analysis have been limited by the assumption of a uniform heat flux over the friction interface. Braking friction is simulated using FE techniques by dividing up individual brake applications into a number of time steps over which the combined

influence of pressure, temperature and wear was predicted. Calculated temperature, interface contact and pressure, and wear distributions are compared with observed and measured experimental results.

Fukano and Matsui (1986) created a similar FE model, however a whole vane was included in the model, see Figure 2.7. This is not the smallest segment of symmetry possible resulting in an increase of computing costs.

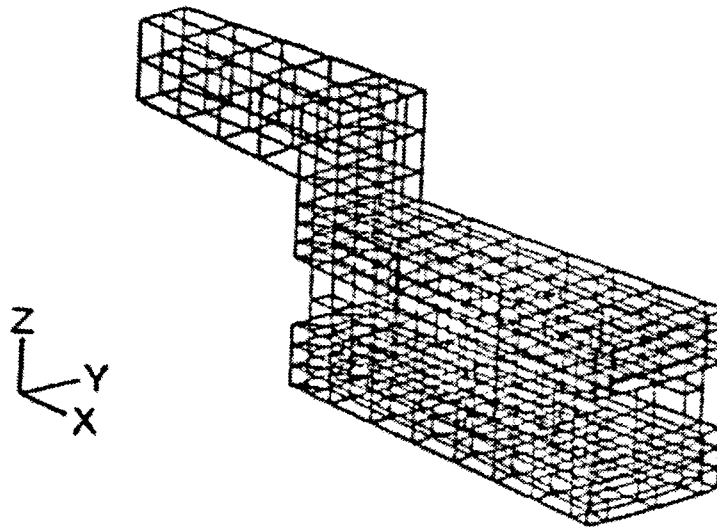


Figure 2.7 Full vane segment mesh (Fukano and Matsui 1986)

Sheridan, Kutchev et al. (1988) carried out different modelling approaches for the thermal analysis of disc brakes. A one-dimensional model provided peak surface as well as bulk temperatures. A steady state 2-D model of the entire brake system predicted plateau temperatures during a multi-stop driving schedule and finally, a complex 3-D transient model was used to obtain detailed local disc temperature distributions for any stopping sequence. For the 3-D model convective heat transfer coefficients were derived for each area of the disc. To simulate the conductive heat transfer that exists between disc flange and hub and wheel, the heat transfer coefficients were double those used on the disc cheeks. A heat flux varying with time was imposed on the disc cheek faces. Radiation energy exchange was assumed to be zero. All models compared well to experimental measurements.

D'Cruz (1989) created a 3-D model using the rotational symmetry of the vent and vanes, similar to Fukano and Matsui (1986) resulting in 194 twenty noded brick elements and a total of 1530 nodes. Radiation energy exchange was assumed to be

zero and a blanket convective film coefficient of $100 \text{ W/m}^2\text{K}$ was applied to all free surfaces except along lines of symmetry. A time dependent heat flux was applied to the braking surfaces of the disc. Transient heat transfer and stress analysis was carried out using the ABAQUS FE package.

Barozzi, Nobile et al. (1989) modelled a railway brake disc, analysing a 36° symmetrical section; cooling fins were ignored to further simplify the model. Cubic 8-noded brick type elements were used amounting to 1275 nodes. Again, the ABAQUS FE package was used to analyse temperature distribution and thermal stresses.

Bailey, Buckingham et al. (1991) carried out FE studies using ABAQUS FE package with a full 3-D model of a passenger car brake disc. Temperature distributions measured during dynamometer testing by a thermal imaging camera were mapped onto the disc surface, the disc consisted of 2640 nodes. Heat loss from the disc was simulated using surface heat transfer coefficients of $100 \text{ W/m}^2\text{K}$ from all free faces. It was assumed that conductive heat losses at the mating surfaces of the disc were equal to convective heat losses.

Day, Tirovic et al (1991) discussed how many of the thermal problems associated with brake friction pairs can be analysed in terms of localized frictional heat generation. A 2-D axisymmetric model was used to predict temperature distributions in the brake disc. The disc distortion was modelled in a 3-D pad/disc assembly model, where gap elements were used to connect the pad friction surface to a 'rigid' disc surface. FE methods were used to indicate that uniform friction interface pressure distribution is very important in minimizing brake thermal problems.

Kao, Richmond et al. (1993) used an FE technique to predict hot spot formation. An axisymmetric model was used consisting of the disc, pads and pad baking plates. Special four node interface elements were developed, which link the rotational disc element on one side and stationary ring sector pad elements on the other. The frictional heat generation and wear characteristics were incorporated into this element.

Dufrenoy and Weichert (1995) conducted FE analysis using ANSYS FE software to predict railway disc brake temperatures taking into account the friction surface variations. A half cross section of the disc is modelled with the cross section of one of the pads. Meshing has been refined near the region of high thermal gradients. Assumption of uniform circumferential heat flux distribution allows a 2-D axisymmetric model to be used and then to study only one half of the structure. A comparison with a 3-D model was carried out to validate these assumptions.

The ABAQUS FE package was used by Grieve, Barton et al. (1998). A 3-D model of a 10° segment of a ventilated front disc, hub and wheel for a typical medium sized passenger car was generated. Quadratic brick elements were used so as to include one vent and two half vanes giving a total of 1824 nodes. The disc wheel and hub are combined into one solid model to enable conductive heat transfer. Sensitivity studies to investigate the thermal resistance between the disc and hub and the hub and wheel surfaces revealed that little or no thermal resistance was apparent owing to mechanical clamping of the wheel to the hub and disc. The wheel was truncated in order to reduce the complexity of the model as shown in Figure 2.8. Convective heat transfer coefficients were calculated and used for all free surfaces. Radiative heat transfer was also modelled except at the vane.

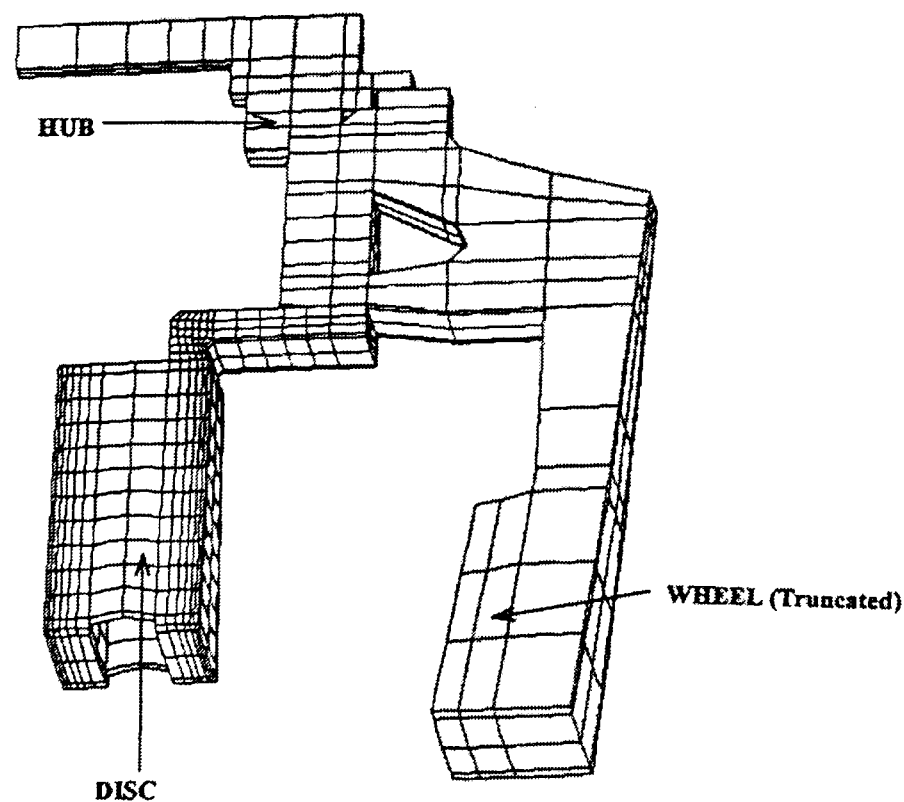


Figure 2.8 Segment FE mesh of a vented brake disc, hub and truncated wheel
(Grieve, Barton et al. 1998)

2.6.2 Computational Fluid Dynamic Methods

Computational fluid dynamics (CFD) is the latest technique used for brake cooling analysis and temperature prediction. This method can analyse the airflow through complex rotating brake geometry and provide convective heat transfer coefficients for all brake surfaces.

Kruseman and Schmidt (1995) used the STAR-CD CFD code to simulate the airflow through the brake disc in order to optimise cooling, see Figure 2.9. CFD analysis gave a new fundamental insight into the behaviour of the airflow through the disc. The simulation of geometric modifications is also presented and provides a good estimation of disc cooling potential.

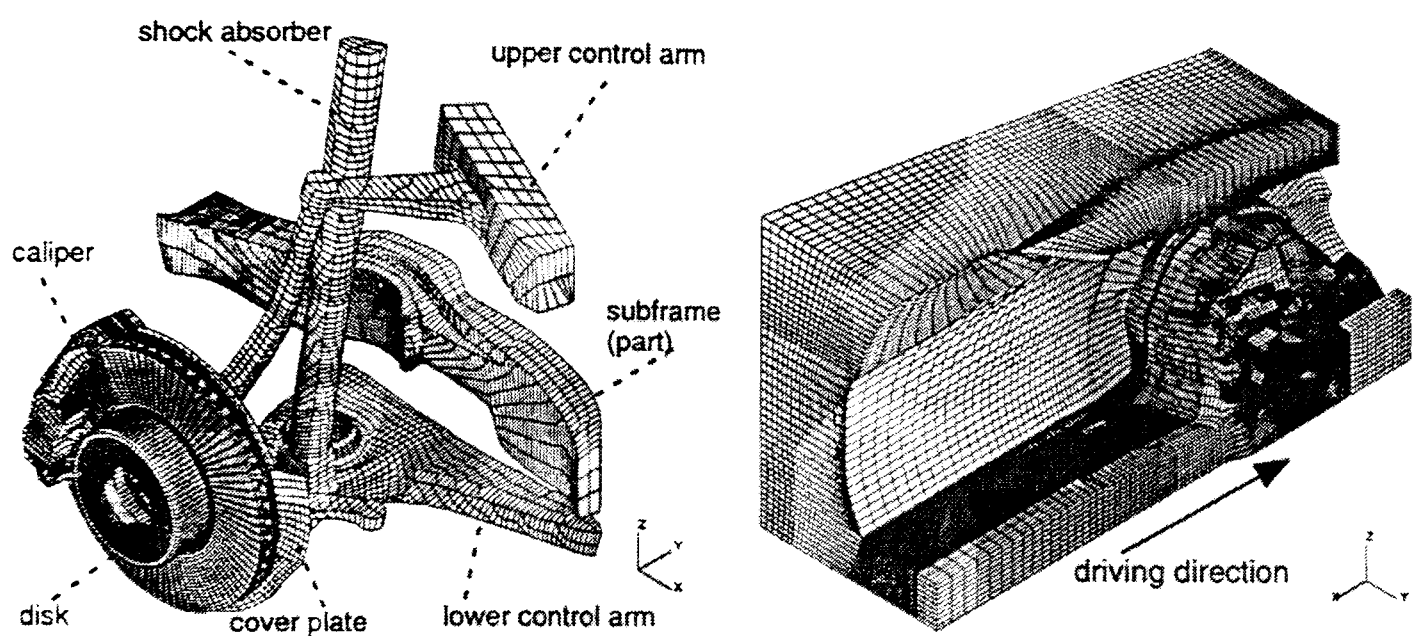


Figure 2.9 CFD mesh of a brake disc and surrounding components (Krusemann and Schmidt 1995)

Axon, Garry et al. (1999) developed a 3-D CFD model of a wheelhouse cavity. Both stationary and rotating wheels were considered and comparisons made with wind tunnel tests.

A Paper published by Basara, Beader et al. (2000) determines the influence of turbulence models on the development of the unsteadiness the airflow around an isolated wheel. The paper is presented by AVL who are developing CFD software for rotating parts, such as ventilated brake discs, using moving meshes.

Daudi and Narain (2000) used CAE prediction and experimental verification to determine the maximum temperature of a ventilated automotive disc. FEA was used to verify structural strength, and Fluent CFD software was used to find the highest airflow velocity through the vane and the heat transfer coefficient. ABAQUS software used the heat transfer coefficients to predict the temperature of the disc. The analysis assumes heat is removed by airflow only and zero heat flow was assumed through hub. The CAE analyses correctly predict the temperature difference trends corresponding to disc design changes but temperature predictions are much higher than experimental results.

Kubota, Hamabe et al. (2000) performed parametric studies based on an analysis of airflow through discs. Brake cooling performance is determined by the airflow around the wheel unit and the airflow through the disc vanes. A one-tenth-scale model of a wheel unit incorporating a disc is tested in a water tank. Findings show the air velocity through the ventilation channels increased in proportion with the disc inner radius and alternately arranging fins of two different lengths increased the ventilation channel inlet, which in turn increased velocity. Velocity through the vanes increases with gourd-shaped vanes and short straight vanes, see Figure 2.10. CFD results compared well with the water tank results. It was also found that increasing the number of fins achieves a more uniform stress distribution.

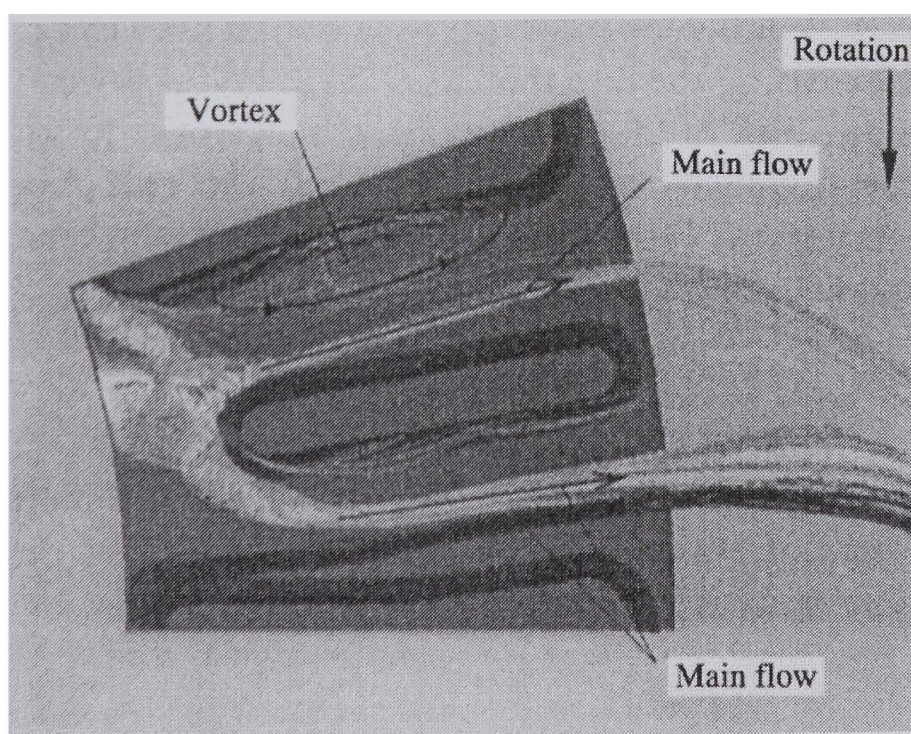


Figure 2.10 CFD predicted airflow through gourd-shaped and short straight vanes of a ventilated disc (Kubota, Hamabe et al. 2000)

CFD analysis is used to a great extent in the design of hydrodynamic pumps. A computer-aided design system has been developed by Goto, Nohmi et al. (2002) for hydraulic parts of pumps including impellers. The key technologies include 3-D CAD modelling, automatic grid generation, CFD analysis, and a 3-D inverse design method. The design system is directly connected to a rapid prototyping production system and a flexible manufacturing system composed of a group of DNC (direct numerical control) machines. The use of this novel design system leads to a drastic reduction of the development time of pumps having high performance, reliability, and innovative "Blade Design System" design concepts.

Surface flow patterns generated with oils have been used in centrifugal pump design for many years. Hamkins and Bross (2002) have showed how modern image analysis methods allow quantitative predictions of the corresponding pressure distributions by analysing surface flow patterns. The surface flow patterns can be used to confirm CFD results and improve boundary conditions.

The author of this thesis has published three papers on the topics of brake cooling analysis of automotive disc brakes (Voller and Tirovic 2002), improving cooling of commercial vehicle brakes (Tirovic and Voller 2002) and optimisation of heat dissipation from commercial vehicle brakes (Tirovic and Voller 2002). The work is based on experimental and numerical analyses, most of which will be discussed throughout the thesis.

2.7 Summary

The problems of adequate brake cooling are associated with all brake types and heat dissipation has attracted much investigation and research. The experimental and theoretical results were limited with the tools available at the time. Most of the recent published work has been fragmented and the efforts concentrated on the specific problem, design or heat transfer mode.

Conduction is the least studied mode of heat dissipation from brakes. From published research on TCR at the interface of two mating components, the effect of interface condition has been shown but not directly related to brake components. Brake

interface conditions vary due to corrosion and dismantling and re-assembly procedures. Different material combinations also complicate the issue. Published research, dealing with brake thermal modelling, takes a simplified approach to conductive heat dissipation, applying general heat transfer coefficients to brake areas conducting heat to adjacent parts.

A number of published papers deal with convective cooling from specific disc areas. Research has also been focused on the heat transfer in the channels of ventilated discs. Comparison of the suggested approaches show that, although similar heat transfer coefficients can be obtained in some cases, in other cases differences can be substantial. More recent approaches have been published using CFD methods to predict airflow around the vehicle's front ventilated disc brakes. Most of the published work relates to automotive applications. Available data is insufficient to offer a reliable guide regarding the heat transfer coefficients that should be used for railway brake thermal analyses. Limited published data shows that ventilated railway discs can cause substantial aerodynamic losses, and a compromise with cooling must be achieved.

Radiative cooling has often been neglected in published brake thermal analyses, even though at higher temperatures radiation is a very significant mode of heat dissipation. It is interesting to note the substantial differences of published cast iron disc surface emissivity; values range from 0.15 to 0.9. Again, available data is very limited and insufficient for adequate modelling of radiative heat losses. It is particularly important to accurately model this mode of heat dissipation, because of its significant influence at the high temperatures reached by new disc and pad materials and high performance designs.

Experimental Apparatus and Test Components

3.1 Introduction

The experimental study of friction brakes is generally conducted on a dynamometer or test vehicle. The dynamometer is used to design and develop a brake for a range of duties. However the brake is only one component of a vehicle system and so vehicle tests are necessary to test and tune the braking system for a specific vehicle.

3.1.1 Road and Track Tests

Brake measurements on vehicles are very valuable, however they are prone to substantial external factors including ambient temperature, wind speed and direction, road surface, dirt and spray from the road, and driver. These factors mean there are often considerable differences between dynamometer and vehicle tests and comparing results is difficult. The cost of vehicle testing is also high, requiring a specially instrumented vehicle, test driver, test track facilities and good weather conditions. Vehicle testing is still vital for final evaluation of system design and brake approval and test tracks specifically for braking have been developed.

There are many test tracks in use, such as MIRA and Millbrook, in the UK and abroad. Details are given on one of the newest, Idiada, Spain, which is made up of an acceleration stretch of 960 m and a braking area with surfaces of different coefficients of friction, see Figure 3.1 and Table 3.1.

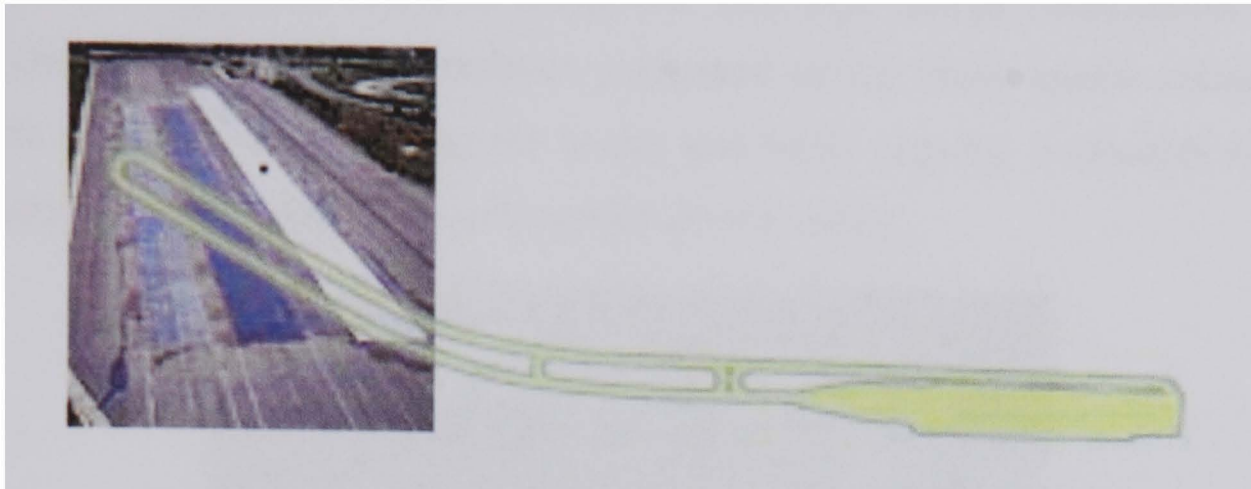


Figure 3.1 Four surface brake test track, IDIADA, Spain

Table 3.1 Coefficient of friction values for the track surfaces, IDIADA, Spain

| Surfaces | μ [-] | Length [m] |
|-----------------------|-----------|------------|
| High-friction asphalt | 0.8 | 200 |
| Treated concrete | 0.4 | 200 |
| Basalt slabs | 0.3 | 200 |
| Ceramic tiles | 0.1 | 250 |

3.1.2 Dynamometers

Tests are used to represent all aspects of vehicle brake application, maximum brake duty, friction evaluation, drag and repeated brake applications and cooling. Dynamometers can provide fast, accurate repeatable tests unaffected by road or weather conditions. High torques are achieved during braking and dynamometers are usually of the inertia type, using a flywheel as the main source of energy during braking. Typically, the braking torque of a passenger vehicle can amount to 5000 Nm and a typical motor used on an inertia dynamometer produces a maximum of 1500 Nm (Slevin and Smales 2002). A range of flywheels can be fitted to the dynamometer depending on torque requirement. In Figure 3.2 the brake disc is situated on the left and flywheels are clearly shown at the centre of the picture. The motor is used to add to or subtract torque from the flywheel to interpolate between available flywheels and constantly adjust torque during testing. Constant torque

adjustment compensates for mechanical losses, rolling resistance, wind resistance, work done on a gradient and vehicle loading.

The disadvantages of inertia dynamometers are that they are expensive to purchase and run, their operation requires manpower and high energy consumption. Also, small changes in brake characteristics performed during brake system refining are difficult to detect. Furthermore, for health and safety reasons, extraction fans are necessary to remove brake dust and vapours during testing.

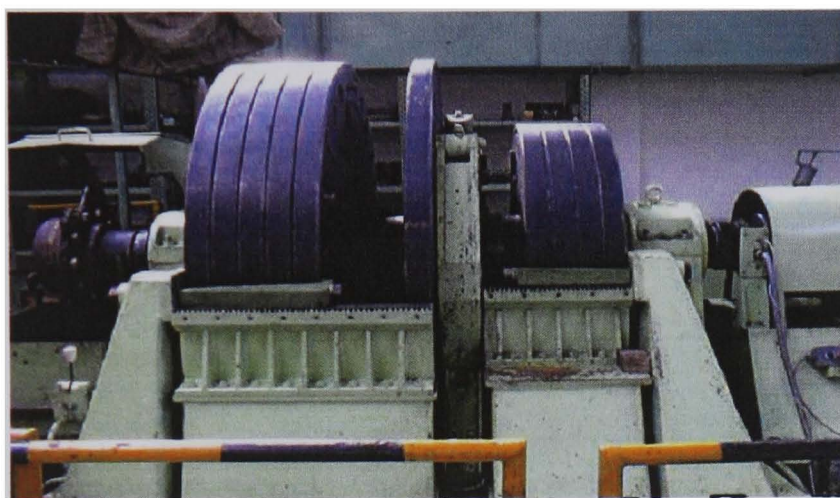


Figure 3.2 Inertia brake dynamometer, Motor vehicle research institute, CZ

Railway discs require particularly high inertia brake dynamometers. The Sabwabco inertial dynamometer test facility is shown in Figure 3.3. Discs or whole axles are mounted on special frames (shown in Figure 3.3), allowing more efficient operation (frames can be prepared while other tests are running).

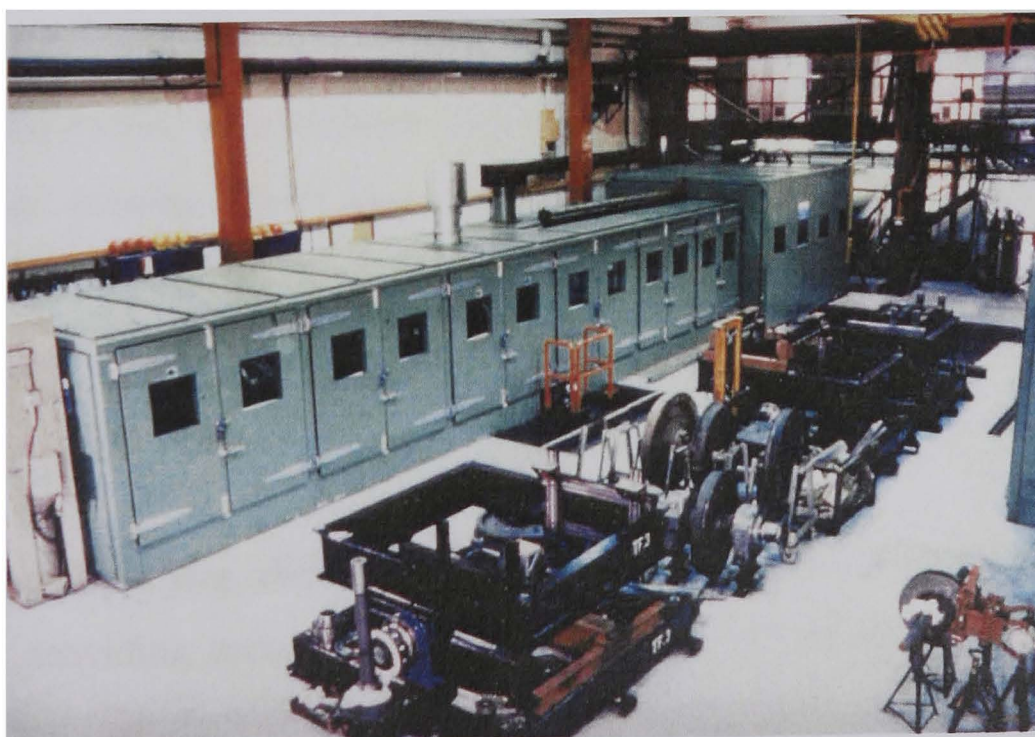


Figure 3.3 SabWabco's R1 inertia brake dynamometer test facility, UK

Investigations of friction brake heat dissipation from vehicles and dynamometers are confronted with problems of accuracy, repeatability and cost. Most of the friction brake applications are performed in the thermoelastic instability regime, which causes variation of interface pressure and heat generation at the disc/pad interface throughout braking. Hot spots are created making it difficult to determine surface temperatures and measured results usually vary, often to a high degree, for otherwise identical brake applications (initial temperature, speed, load, deceleration). Figure 3.4 clearly shows the hot bands generated by hot spots on the disc surface. During the brake cooling period, these influences are reduced as temperature dissipates towards an average temperature.

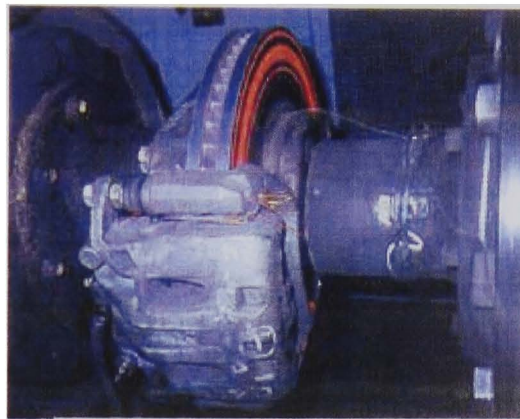


Figure 3.4 Hot bands on disc surface (Chemical 2002)

Specialised brake test rigs have been developed to allow for more accurate, repeatable and specific brake measurement with reduced cost. Different test rigs have been designed focusing on areas of hydraulic and pneumatic systems, calliper fatigue, parking brake fatigue, operating loads (Kruger, Boss, et al. 1990) and airflow analysis (Wild 1989). To overcome the problems of brake cooling measurement and achieve more accurate brake heat dissipation and pumping loss measurement, a dedicated Spin Rig test facility was developed.

3.2 Spin Rig

The developed Spin Rig, shown in Figure 3.5, allows brake assemblies to be heated and cooled, providing accurate heat dissipation measurements and airflow analysis. The design and manufacture of the Spin Rig has been conducted in conjunction with the thesis research project during the three-year time period provided. Careful

planning has been necessary to ensure that the Spin Rig was completed with sufficient time remaining for brake testing.

3.2.1 Design Brief

A design brief was prepared based on the research objectives, further use by industry, the available time and financial constraints. Nevertheless, the Spin Rig can accommodate and provide accurate measurements for a variety of research areas:

- Aerodynamic losses of brakes (and wheels)
- Airflow and cooling of brakes (with and without wheels)
- Heat transfer and interaction of brakes and wheels
- Other applications where torque and speed measurements are required
- Other studies of heat transfer problems

The development and commissioning of the Spin Rig is detailed in Appendix C

3.2.2 Design and Specification

The Spin Rig (Figure 3.5 and Figure 3.6) has a simple, in-line arrangement of the brake disc, torque transducer, speed sensor and electric motor. The disc is heated using electric heaters or gas flame heaters. Cooling characteristics are studied by rotating the brake disc at different rotational speeds. Temperatures are measured throughout the tests using rubbing and imbedded thermocouples, as well as infrared sensors. Uniform heating ensures high test repeatability. The Spin Rig also enables the determination of ventilated disc ‘pumping losses’ by measuring the torque required to spin the disc at different rotational speeds, which is crucial for high-speed railway disc brakes. Airflow measurements are conducted with a handheld anemometer velocity.

The Spin Rig can accommodate a range of brake discs, from motorbike discs up to high speed train discs. The Spin Rig guarding has clearance for a diameter of 1 metre providing room to mount a wheel carrier, wheel, tyre and calliper up to a mass of 250 kg. This capacity allows the investigation of the influence of brake component design, material and condition of contact surface on brake cooling.



Figure 3.5 Spin Rig for studying airflow and heat dissipation from brakes

The Spin Rig is aimed at experiments related to brake heat dissipation and flow characteristics and not for studies of friction couple or brake structural integrity. Compared to dynamometers, achieving high disc temperatures is more difficult on the Spin Rig. In addition, the heat is not generated by rubbing the friction pads against the disc surface, which results in a different condition of these surfaces compared with discs used on dynamometers and vehicles. However, the above effects can be taken into consideration by adequate measurements and calculations. As a result, the prediction of 'real friction brake' temperatures can be very accurate. Spin Rig tests are much cheaper to prepare and run than brake dynamometer or vehicle tests, due to much lower cost and complexity of the equipment, lower energy consumption and manpower required. Figure 3.6 and Table 3.2 shows the Spin Rig specification.

Table 3.2 Spin Rig specification

| | |
|--|-----------------------------------|
| Motor speed | 0 – 2000 min ⁻¹ |
| Motor power | 7.5 kW |
| Maximum transducer torque | 50 Nm (running) |
| | 70 Nm (overload) |
| Maximum rotating assembly mass | 250 kg |
| Maximum rotating diameter | 1.05 m |
| Main shaft bearing type (SKF) | 7314B (motor side) |
| | 7315B (wheel side) |
| Flame heater | Gas/air torch |
| Electrical heater airflow | 30 – 500 SLPM |
| Maximum combined heater power | 8 kW |
| Maximum electrical heater temperature | 750 °C |
| Main power requirements | 415V A.C., 50 Hz, 3-phase at 22 A |
| Heater power requirements | 230 V A.C, 50 Hz |
| Torque transducer full scale output | ± 5 V |
| Speed full scale F/V converter output | ± 10 V |
| Data acquisition channels | 16 |
| Input full scale range | ± 0.05 V, ± 0.5V, ± 5V, ± 10 V |
| Maximum sample period | 1 ms (1 kHz) |
| Dimensions, H x W x L | 1.5 x 2.45 x 1.75 m |
| Spin Rig mass | 250 kg |

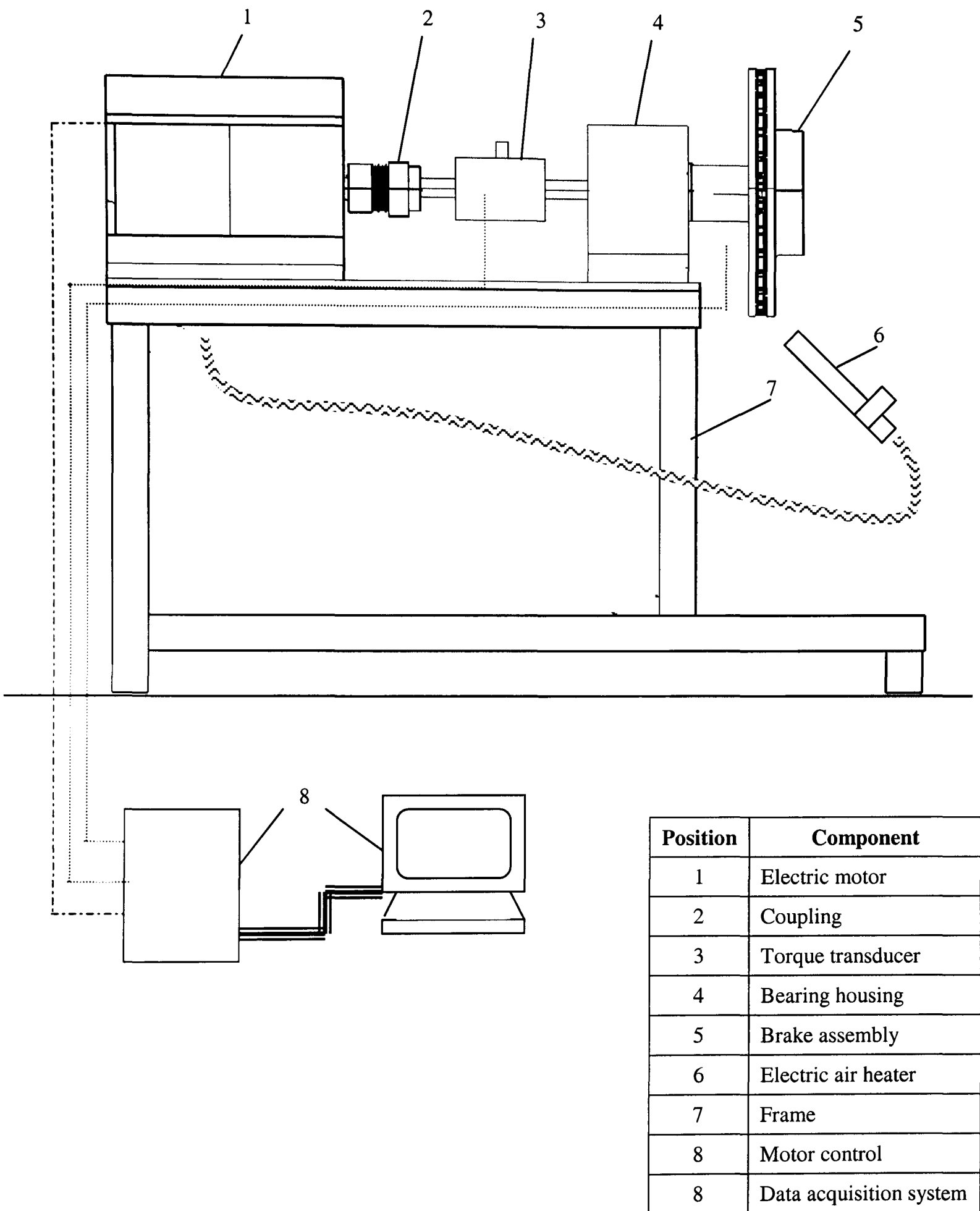


Figure 3.6 Spin Rig layout

3.2.3 Equipment

The Spin Rig is fitted with apparatus for heating the brake assembly and instrumentation for the measurement and logging of temperatures, rotational speed and torque. Details are given in this section.

3.2.3.1 Torque and Rotational Velocity Measurement

The Spin Rig (Figure 3.6) is fitted with an inline torque transducer; see Figure 3.7 and Table 3.3. The transducer consists of a housing containing the measuring shaft with free shaft ends. On the measuring shaft there is a torsion distance with strain gauges and signal amplifier employing induction technology. It can be used to measure static and dynamic torque and rotational speed. Rotational speed is measured using digital pulses at 60 pulses per revolution.

Table 3.3 Torque transducer 0160 DM specification

| | |
|------------------------------------|--------------------------|
| Torque rating | 50 Nm |
| Maximum rotation speed | 12,000 min ⁻¹ |
| Overload capacity | 1.3 x rated torque |
| Break capacity | > 5 x rated torque |
| Bearing life | 20,000 hours |
| Speed transducer | 60 pulses |
| Linearity deviation | < 0.1 % of full scale |
| Output | ± 5.0 V at rated torque |
| Operating temperature range | 0 to 70 °C |

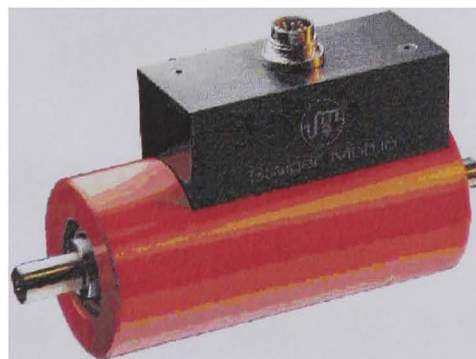


Figure 3.7 Torque transducer 0160 DM, Dr. Staiger, Mohilo + Co GmbH, Germany

3.2.3.2 Signal Processing and Data Logging

The torque and speed of the shaft are measured by the torque transducer. This unit outputs ± 5 V for ± 50 Nm of torque and a frequency proportional to speed of rotation, 2 kHz = 2000 min⁻¹. The torque voltage is fed directly to the data acquisition card of the Spin Rig computer. The speed frequency is fed into a frequency/voltage converter, the resultant 0 to 10 V output is then fed to the data acquisition card of the Spin Rig computer. The data acquisition card is a National Instruments 6023E PCI card with 16 single ended, 8 differential channels and 2 output channels. The input range is ± 0.05 V, ± 0.5 V, ± 5 V or ± 10 V with a maximum sampling rate of 1000 Hz. A dedicated Spin Rig program has been written to view channel outputs and log the data as a comma space variable file.

Data acquisition of the thermocouples measurements have been performed with a dedicated data logger designed for thermocouple input. Signal processing of the thermocouple output requires cold junction compensation, signal amplification and linearization. The RS Datascan 2200 data acquisition system has been used, see Figure 3.8, providing software configurable inputs, on-board processor to pass data to the host PC in engineering units, and a RS-232 computer interface. Sixteen channel inputs are individually configurable for dc voltage, thermocouple and 4 to 20 mA. Cold junction compensation provides direct thermocouple measurement.

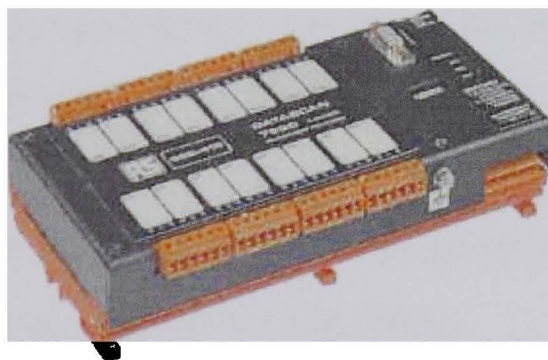


Figure 3.8 RS Datascan 2200 data acquisition system

Orchestrator by Measurement Systems Ltd., UK is the monitoring and recording software used with the RS Datascan, a real time data acquisition software for Microsoft Windows NT. Orchestrator provides integrated data acquisition, monitoring, data logging, and report generation. It interfaces with the Datascan device from which it imports the data to a real time memory database. This data is

processed and redirected to other tasks such as alarm monitors, data loggers, real time calculators, and trend displays.

3.2.3.3 Heating System

The Spin Rig is fitted with a 4 kW industrial high temperature air heater, shown in Figure 3.9. It is designed for continuous high temperature operations up to 650°C, supplying an airflow rate up to 1400 l/min. Hot air flowing over the rotating disc provides uniform heating and can be switched off instantly ready for cooling measurement. This method of heating is suited to the ventilated disc, which has a large surface area for heating. Inductive heating methods were considered (discussed in Appendix D) but cost were too high.

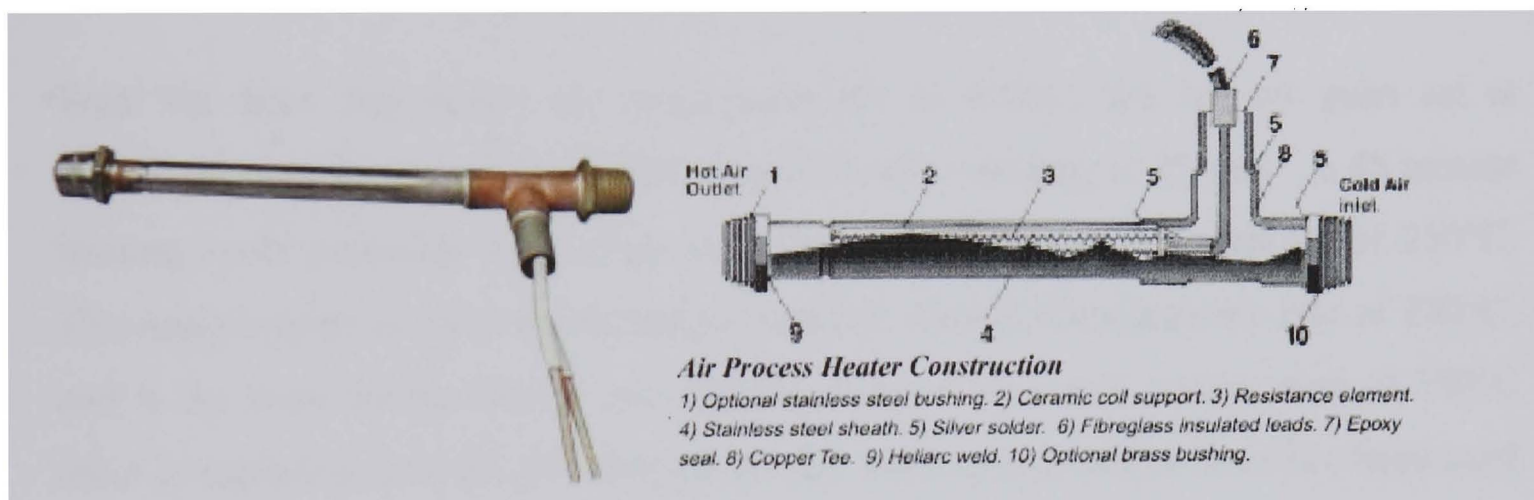


Figure 3.9 Hot air heater, Hawco Ltd, UK

A problem associated with the air heater is high heat loss. Hot air flows over the disc surface with little of the heat transfer from the air to the disc. Also the disc dissipates heat to the atmosphere and to adjacent components during the heating phase, these losses make the air heater relatively inefficient. To use the heated air more efficiently it must flow over more of the disc surface to transfer heat and the disc requires insulating to avoid heat loss during the heating phase.

To substantially reduce losses a heater box has been manufactured to control the hot airflow and insulate to the disc during the heating phase, see Figure 3.10. A Teflon insulating disc is also fitted between the shaft flange and the disc adaptor to reduce heat flow from the disc back to the shaft. The heater box is design to accommodate two hot air guns each providing an extra 2 kW of heating power. The box ducts the hot air from the Spin Rig air heater as it exits the disc vane; hot air is guided back over the rubbing surface of the disc, finally exiting at the top of the heater box

through ventilation holes. The hot air guns provide additional hot airflow over the rubbing faces of the disc. Total heating power is equal to 8 kW.

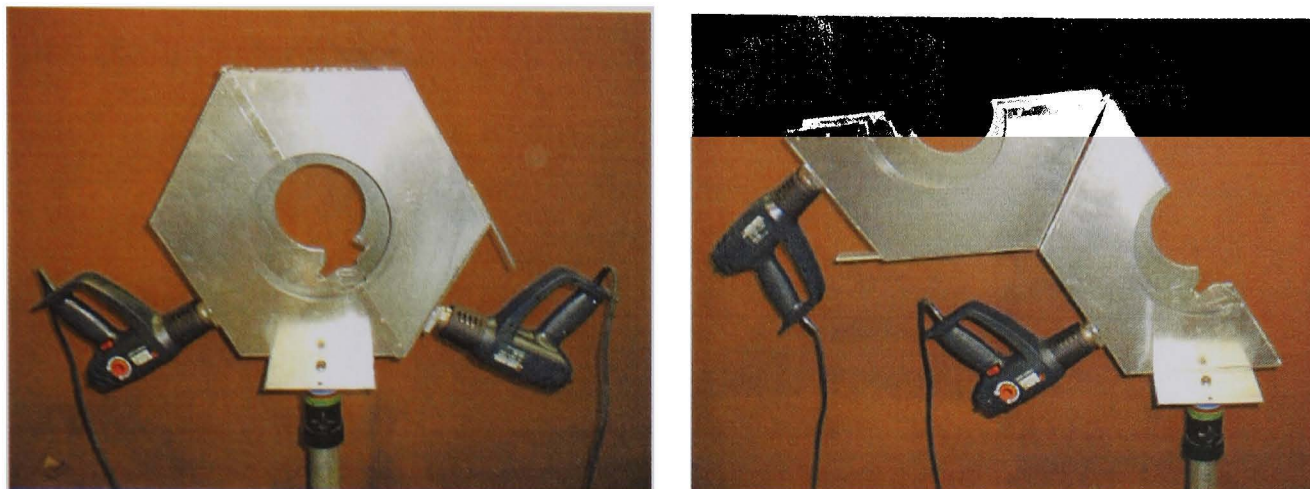


Figure 3.10 Heater box with additional air heaters

With the Spin Rig heater air temperature set to 600°C , the hot air guns set at maximum output, airflow set to 45 l/m and the disc rotating at 25 min^{-1} , a 45 minute heating cycle produces an average commercial vehicle disc temperature of 250°C . The temperatures reach a steady state condition. This is a temperature rise of 230°C , and is the limit for the hot air disc heating method (at a disc temperature of 250°C there is sufficient heat for the analysis of disc cooling and this method has been used for the cooling analysis of the commercial vehicle disc in this project).

For tests requiring higher disc temperatures, an air/gas torch has been used. The flame heating allows controllable localised heat input and uniform heating with the disc rotating through the flame. Surface temperatures of up to 600°C can be achieved with this method.

The large thermal capacity of the TGV railway disc, see Section 3.4.2, meant that the disc could not be heated using the hot-air heaters. The disc mass is three times greater than the commercial vehicle disc, and assuming that the losses are the same, the TGV disc would take three times longer to heat. This was impractical, and too much heat would be conducted through to the Spin Rig shaft and bearings. To overcome this problem the disc was heated in an industrial oven before being mounted to the Spin Rig, see Figure 3.11. The oven temperature was set to 500°C and the disc left to soak at this temperature for three hours. The disc was placed in a metal frame to ease handling. A chain and crane were used to mount the disc to the Spin Rig shaft. The

mounting procedure took approximately 20 minutes by which time the disc temperature was 300°C, which was sufficient for testing.



Figure 3.11 Industrial oven used to heat TGV railway disc

3.3 Measurement and Instrumentation

The measurement system used to provide information about the physical value of the variable being measured generally comprises of several elements, as shown in Figure 3.12. All measuring instruments have a primary transducer, this gives an output that is a function of the input to the measuring instrument. It is common that the transducer will give an output in an inconvenient form; the thermocouple output for example is a non-linear increase of $\mu\text{V}/^\circ\text{C}$. Signal processing is used to enhance output of a transducer in some way. Processing can include linearization, amplification, and filtering. The final stage of measurement is transmission of the processed signal for visualization and recording.

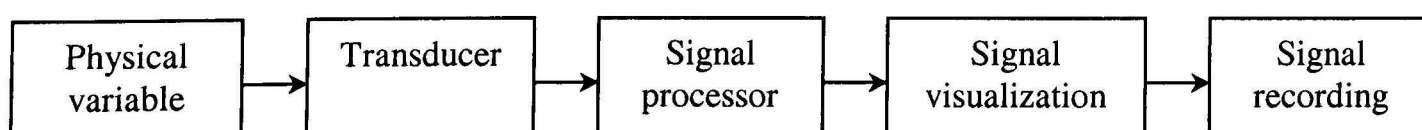


Figure 3.12 Elements of a measuring system

Measurement system selection is dependent on the physical property to be measured, working conditions, level of accuracy, sensitivity, output and recording requirements. The physical properties measured during the study of disc brake cooling included; temperature, air velocity, torque and angular velocity.

3.3.1 Temperature measurements

The two most common ways of measuring temperatures in industrial and research environments are resistance temperature detectors (RTDs) and thermocouples. To determine the most appropriate device several factors should be considered as outlined in Table 3.4 (Sulciner 1999):

Table 3.4 Properties of RTDs and thermocouples

| Property | RTD | Thermocouple |
|---------------------------|-------------|--------------|
| Temperature [°C] | -200 to 500 | -250 to 1200 |
| Response time | Seconds | Milliseconds |
| Sheath size diameter [mm] | 3 - 6 | > 1.5 |
| Accuracy [°C] | > ± 2 | < ± 2 |

Thermocouples have been proven to be the most suitable method of thermometry for brake temperature measurement and have been used extensively throughout the experimental analysis in this project. They have many advantages, performing well over the brake operating temperature range and in rugged conditions, they have fast response time, are small in size, relatively inexpensive and simple to use.

3.3.1.1 Thermocouples

The K-type (Chromel/Alumel) thermocouple was chosen, which is a good general purpose thermocouple. It is a low cost thermocouple with good resistance to oxidation and owing to its popularity is available in a wide variety of probes.

Brake temperatures

The embedded thermocouples used throughout this project are K-type welded tip glass fibre insulated thermocouples, with two metre long thermocouple wire insulated with a varnish impregnated glass fibre sleeving, the tip welding prevents oxidation.

Rubbing thermocouples are available in various designs, see Figure 3.13, some designs incorporate a floating shoe onto which a miniature thermocouple is mounted. The shoe is mounted to a spring steel arm. Spring pressure setting may be adjusted by means of a setscrew and lock nut. Other designs incorporate a flattened copper bead brazed to an extension cable to form a grounded hot junction secured by a spot welded clip onto a spring steel arm. A graphite tip is also available similar to the copper bead design.

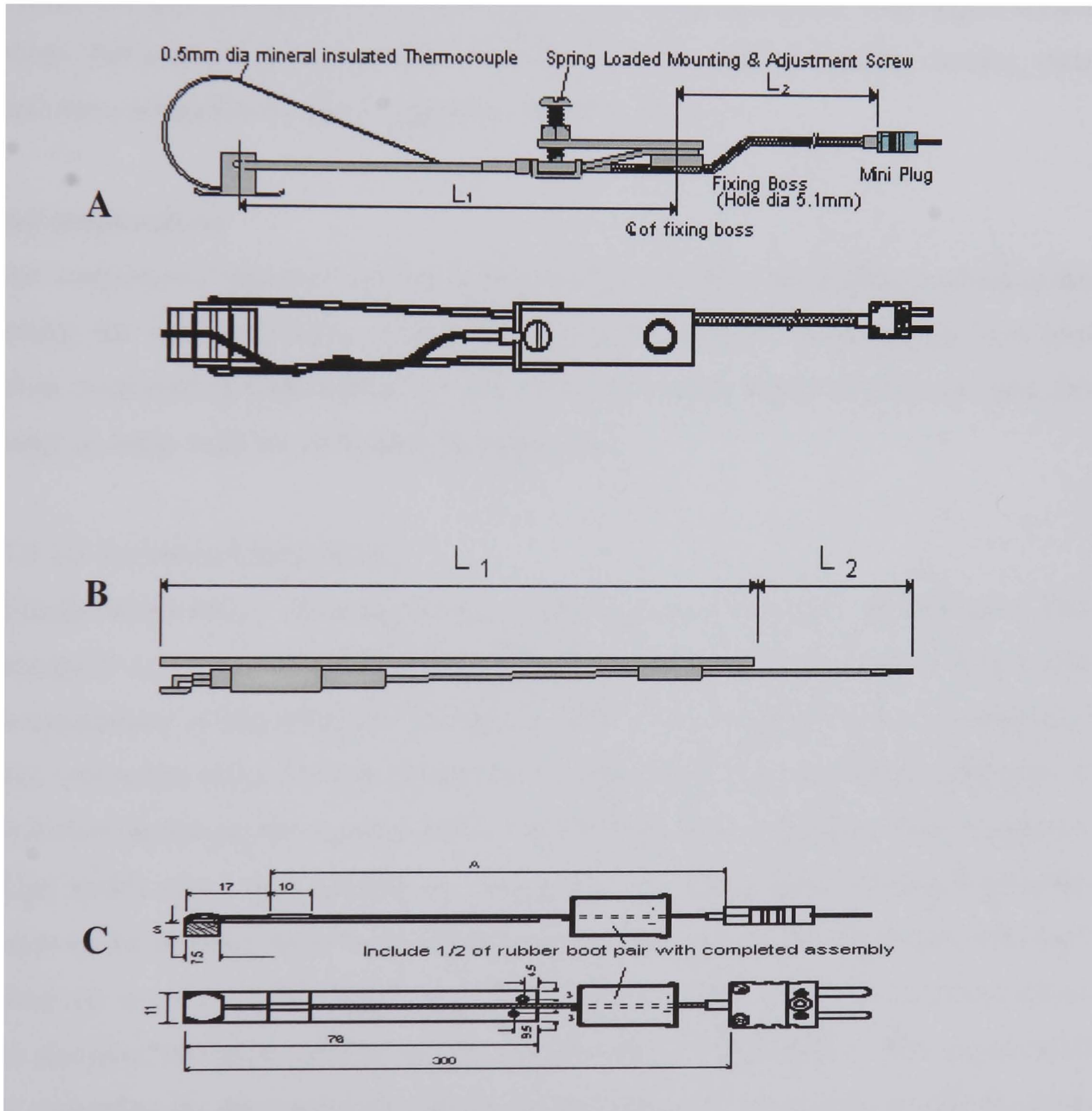


Figure 3.13 Rubbing thermocouple types, A) low friction sled, B) copper tip, C) graphite tip, UTL, Kent, UK

Rubbing thermocouples have been used extensively for brake testing but not without their problems. Rubbing thermocouples will generate some heat due to friction, see Chapter 5, they are also prone to wear, permitting the thermocouple tip to score the

brake disc. The brake temperature must conduct through the shoe or bead leading to relatively long response times, but this is not a problem for measuring the cooling rates achieved on the Spin Rig.

Spin Rig temperatures

The K-type welded tip glass fibre insulated thermocouples have been used to monitor the Spin Rig bearing temperature. A self-adhesive PTFE glass cloth pad is used to locate the thermocouple. These have been used in conjunction with liquid crystal strips that respond to temperature fluctuations. They can be used on moving parts and show temperature values in increments of 5° steps.

Air temperatures

Air temperature measurement has been performed close to the rubbing surface of the brake, the disc ventilation channel inlet and exit; ambient temperatures have also been measured. K-type welded tip glass fibre insulated thermocouples are used, the same as those used for embedded measurements.

3.3.1.2 Radiation Thermometry

Energy is emitted by all bodies having a temperature greater than absolute zero. This energy is a function of temperature, permitting the temperature measurement by the measurement of the radiation. The major part of the frequency spectrum measured lies within the infrared range. Radiation thermometers have one major advantage in that they do not require contact with the hot body in order to measure its temperature. This makes them very suitable for measuring high temperature and moving bodies such as the rotating brake disc; furthermore no wear denotes a longer life. However, their use is not straightforward because the radiation emitted from a body depends on its material, surface condition and the temperature being measured. This dependence is quantified by the emissivity (discussed in Chapter 7). Radiation is also absorbed by carbon dioxide, ozone and water vapour molecules and is scattered by atmospheric dust and water droplets. Therefore all radiation thermometers have to be carefully calibrated for each application.

Radiation thermometry use has been investigated and compared with rubbing thermocouples for the measurement of brake temperatures. Two types of infrared

sensor have been selected for their small size, versatility and low cost; the Calex Convir MT20 two-piece fixed head infrared thermometer, see Figure 3.14(a), and the hand held Raytec ST60 infrared thermometer, see Figure 3.14(b). Their specifications are given in Table 3.5. The Calex two-piece infrared thermometer consists of a miniature sensing head and separate electronics. The sensor is housed in stainless steel and is small enough to fit between the disc brake and the wheel. The Raytec handheld device reads surface temperature without the need to carefully position the probe or interfere with the object being measured.

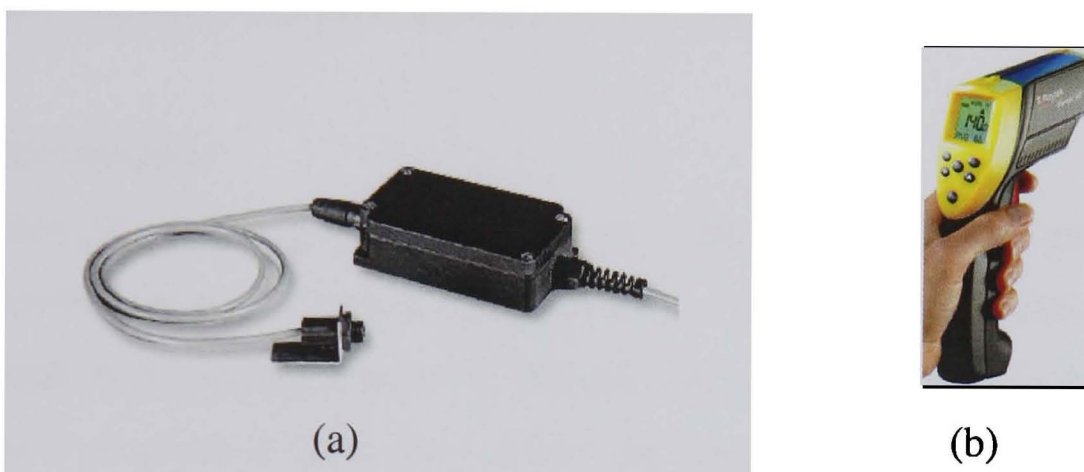


Figure 3.14 Radiation thermometers, (a) Calex two-piece and (b) Raytec handheld

Table 3.5 Infrared thermometer specifications

| Property | Calex Convir MT20 | Raytek ST60 |
|--|---------------------------------------|----------------------------------|
| Measurement range | 0 to 500 °C | -32 to + 600 °C |
| Emissivity adjustability | 0.2 to 1.0 | 0.1 to 1.0 |
| Response | 150 ms | 500 ms |
| Ambient temperature | 0 to 85 °C | 0 to 50 °C |
| Output | Type K, J Thermocouple, 0 to 5 VDC | Digital display resolution 0.1°C |
| Optical resolution (distance from object:measurement diameter) | 2:1 | 30:1 |

To determine the emissivity of the material to be measured a list of common emissivity values are given by the sensor manufacturer (see Chapter 7). To gain extra precision a thermocouple probe device in contact with the surface can be used and the emissivity setting adjusted until the infrared reading agrees with the contact reading.

3.3.2 Airflow Measurements

The study of airflow around the disc is an integral part of understanding convective heat dissipation. To fully investigate the airflow around the disc, flow patterns have been investigated. Flow visualization can be performed by measuring the three velocity components at a single point using a triple sensor hot wire anemometer or rotating a single sensor and taking sample measurements at three orientations. Simple qualitative methods included using yarn tufts or smoke and still camera, as described in Chapter 2. Areas of interest are the airflows due to disc ventilation pumping and surface air velocities. A full-bore flow meter cannot be fitted into the ventilation channel of the disc, and so single measurements are necessary.

3.3.2.1 Air Velocity

For reasons of availability and ease of use, a hand held hot wire anemometer has been used throughout. The sensor probe head is 7 mm in diameter and can be used to give a mean flow measurement over the diameter. In taking one measurement slight variations in position or turbulence in the flow could affect readings (Baker 2001). In addition the probe may modify the flow in the ventilation channel. However, the flow around a rotating disc and wheel assembly will not be greatly affected because of the small scale of the probe. The hot-wire anemometer measures a fluid velocity by sensing heat convected away from the hot wire by the fluid. The core of the anemometer is an exposed hot wire maintained at a constant temperature. The heat lost to fluid convection is a function of the fluid velocity. By measuring the change in the electrical current required to maintain a constant wire temperature, the heat lost is obtained and converted to fluid velocity. A Velocicalc Plus 8386 handheld device has been used throughout the project (see Figure 3.15 and Table 3.6) and is ideal for measuring various air velocities around the brake assembly, providing good comparative data.

Table 3.6 Airflow meter, Velocicalc Plus specifications model 8386

| Velocity From Thermal Sensor (all models): | |
|---|-----------------------------------|
| Range | 0 to 50 m/s |
| Accuracy | ± 3.0 % of reading or ± 0.015 m/s |
| Resolution | 0.01 m/s |
| Instrument Temperature Range: | |
| Operating | -10 to 60 °C |
| Operating (Electronics) | 5 to 45 °C |
| Storage | -20 to 60 °C |
| Resolution | 0.1 °C |
| Accuracy | ± 0.3 °C |
| Relative Humidity: | |
| Range | 0 to 95 % rh |
| Accuracy | ± 3 % rh |
| Resolution | 0.1 % rh |
| Meter Probe Dimensions (all models): | |
| Probe Length | 1016 mm |
| Probe Diameter of Tip | 7.01 mm |
| Probe Diameter of Base | 10.03 mm |



Figure 3.15 Airflow meter, Velocicalc Plus 8386, TSI Inc., USA

3.3.2.2 Airflow Visualization

Flow visualization in this research has been conducted with an SP Teknik AB, RG-100 smoke generator, see Figure 3.16. The smoke generator was available for use on this project and is of convenient dimensions for brake disc analysis. The smoke generator vaporizes odina oil and pumps it through a flexible pipe to a nozzle. The smoke generator has an on/off control at the nozzle. The oil feed is controllable to govern the amount of smoke produced. A digital camera has been used to capture the smoke patterns generated by the airflow, giving information on the flow pattern around the brake assembly.

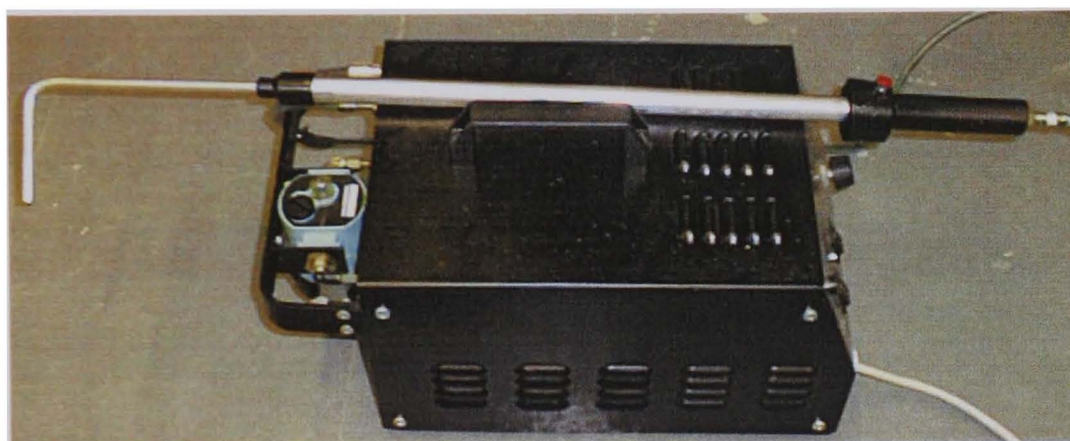


Figure 3.16 SP Teknik AB airflow visualization smoke generator

3.3.3 Bolt Force Measurement

To fully analyse conductive heat dissipation through brake assembly components the clamping forces must be known. To measure the bolt force, a low profile force washer has been used in conjunction with a digital meter (see Chapter 6). The low profile force washer is a stainless steel construction load cell with a through hole design for the measurement of bolt forces. Supplied by Procter and Chester (Meas) Ltd., the load cell type T.W.S 25TE is shown in Figure 3.17(a). The digital meter is manufactured by Kosmos, model Micra-C, and custom configured for the load cell displaying load in imperial tons, see Figure 3.17(b).



(a)



(b)

Figure 3.17 Bolt force (a) F.W.S 25TE Load cell and b) Kosmos Micra-C digital meter

3.4 Test Components

The problems of adequate heat dissipation are associated with all brake types, but they are particularly severe in the case of commercial vehicles (CVs) and high speed trains.

Compared to passenger cars, CVs have a much higher wheel load to wheel diameter ratio. This inevitably limits the size of the brakes that can be installed. The CV speeds are usually lower than passenger cars and combined with larger wheels, substantially reduce disc rotational speeds. However, brake applications are often more frequent (e.g. mountain descent). High axle loads result in the generation of large amounts of thermal energy, which have to be dissipated in a confined space at lower rotational and transversal air speeds, with a restricted supply of cool air (Tirovic and Voller 2002). For these reasons the CV brake is an obvious area of study.

High speed train discs must be capable of absorbing large amounts of heat in emergency brake applications from maximum speed. Heat dissipation during braking is low; it is therefore crucial to ensure low initial brake temperatures. This can only be achieved with good cooling characteristics, since brake mass must be kept to a minimum to ensure low unsprung mass. Ventilated brake discs are commonly employed for their cooling qualities, however when these types of brake disc rotate at high speed, they cause substantial pumping losses. The effects are very serious, since a single ventilated disc with radial vanes would require, just for rotation, in excess of 10 kW at maximum vehicle speed (300 km/h, corresponding to about 2000 min^{-1}). Obviously, this is not acceptable, because at 4 discs per axle, with 26 braked axles, over 1 MW of power per train would be required, just to rotate the discs. Therefore, a different approach is required and numerous 'low loss' disc designs have been developed. Current vehicle designers and railway operators require that this power does not exceed 1 kW per disc, but the disc must maintain good convective cooling properties. Obviously, a very fine balance of low pumping losses and good cooling characteristics is required at all speeds.

3.4.1 Commercial Vehicle Brake

For the study of automotive brake heat dissipation Brunel University have collaborated with ArvinMeritor Heavy Vehicle Braking Systems, UK, who provided a range of commercial (CV) braking components. ArvinMeritor is a global supplier to the automotive industry, providing a broad range of integrated systems, modules and components to OEMs. The CV brake assembly studied is designed for a Renault vehicle (see Figure B1), consisting of the brake disc, wheel carrier, wheel and tyre. Figure 3.18 shows the assembly and Table 3.7 the component details. The calliper has not been shown.

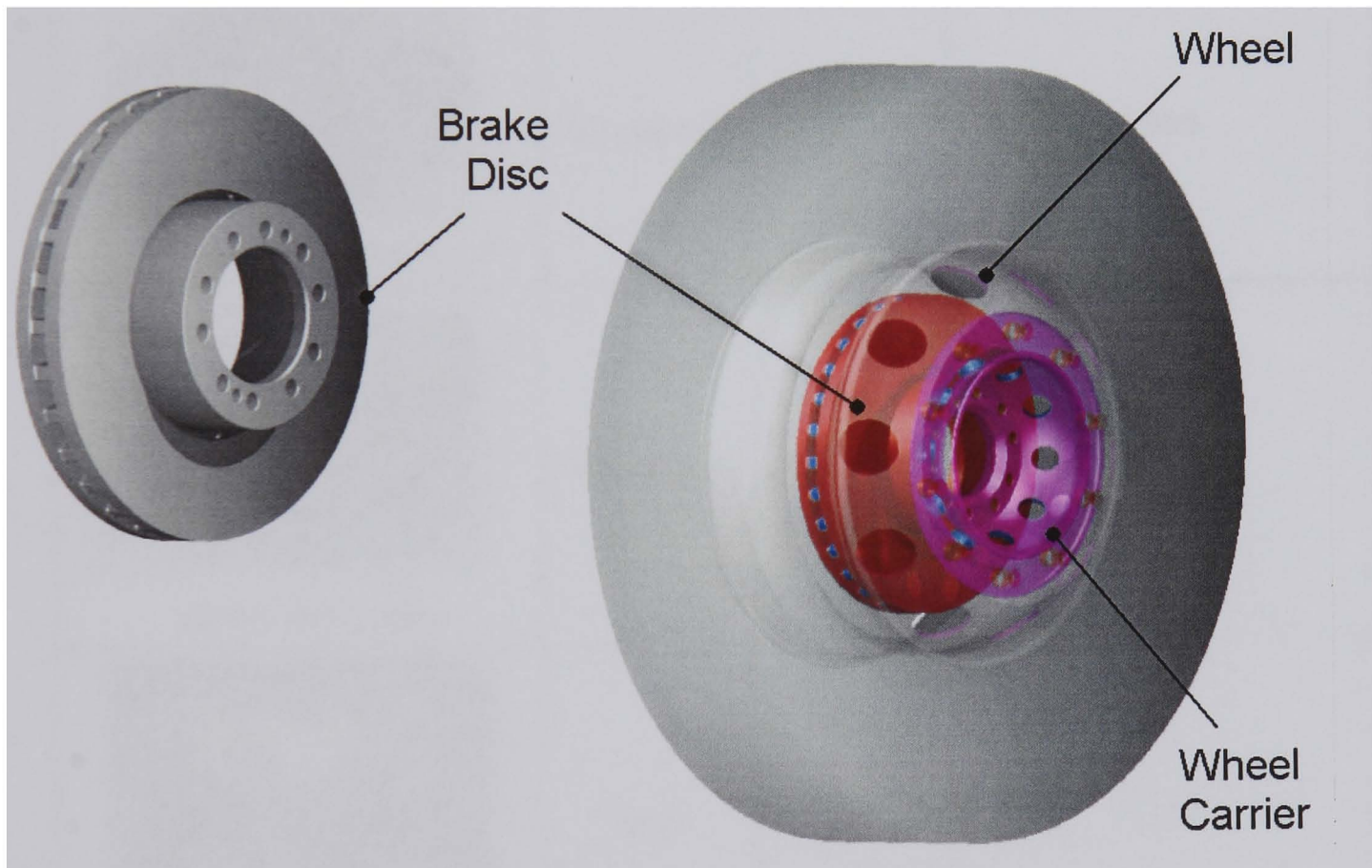


Figure 3.18 Commercial vehicle wheel assembly

Table 3.7 Commercial vehicle brake design characteristics

| Component | Material | Mass [kg] | Nominal Outside Diameter [m] |
|---|-----------------|-----------|------------------------------|
|  Disc | Grey cast iron | 33 | 0.434 |
|  Wheel Carrier (standard) | SG cast iron | 21.5 | 0.390 |
|  Wheel Carrier (modified) | SG cast iron | 20.5 | 0.390 |
|  SAF wheel Carrier | SG cast iron | 18.5 | 0.390 |
|  Steel wheel | Steel | 35 | 0.570 |
|  Aluminium wheel | Aluminium alloy | 26.5 | 0.570 |

Several types of brake disc are available in relation to the ventilation design; see Table 3.8, all of which have been studied. Drawings of the discs are shown in Appendix B.

A detailed drawing of the standard radial disc is shown in Figure 3.19. All discs are manufactured from grey cast iron (see Appendix A) and have the same external dimensions, giving them very similar masses and surface areas. The average surface areas are given in Table 3.9, detailing the areas dissipating heat to surrounding air (wetted area) and the areas conducting heat.

Table 3.8 Description of disc designs

| Disc type | Drawing number | Description |
|-------------|----------------|---|
| Standard | B1.1 | 30 straight radial vanes, inboard inlet |
| Anti-coning | B1.2 | 30 radial vanes, outboard inlet to reduce coning |
| Curved | B1.3 | 30 curved vanes, designed to provide improved cooling performance without adding weight over comparable dimensioned straight vane discs |
| Pillar | B1.4 | 30 pillar vanes to increase cooling at low speeds, outboard inlet to reduce coning |

Table 3.9 Average surface areas of the standard CV disc

| Surface | Area [m ²] |
|-----------------------------------|------------------------|
| Total | 0.631 |
| Total 'wetted' | 0.565 |
| Friction faces | 0.207 |
| Rim | 0.040 |
| Vane | 0.240 |
| Top hat | 0.078 |
| Total conductive (flange – holes) | 0.066 |

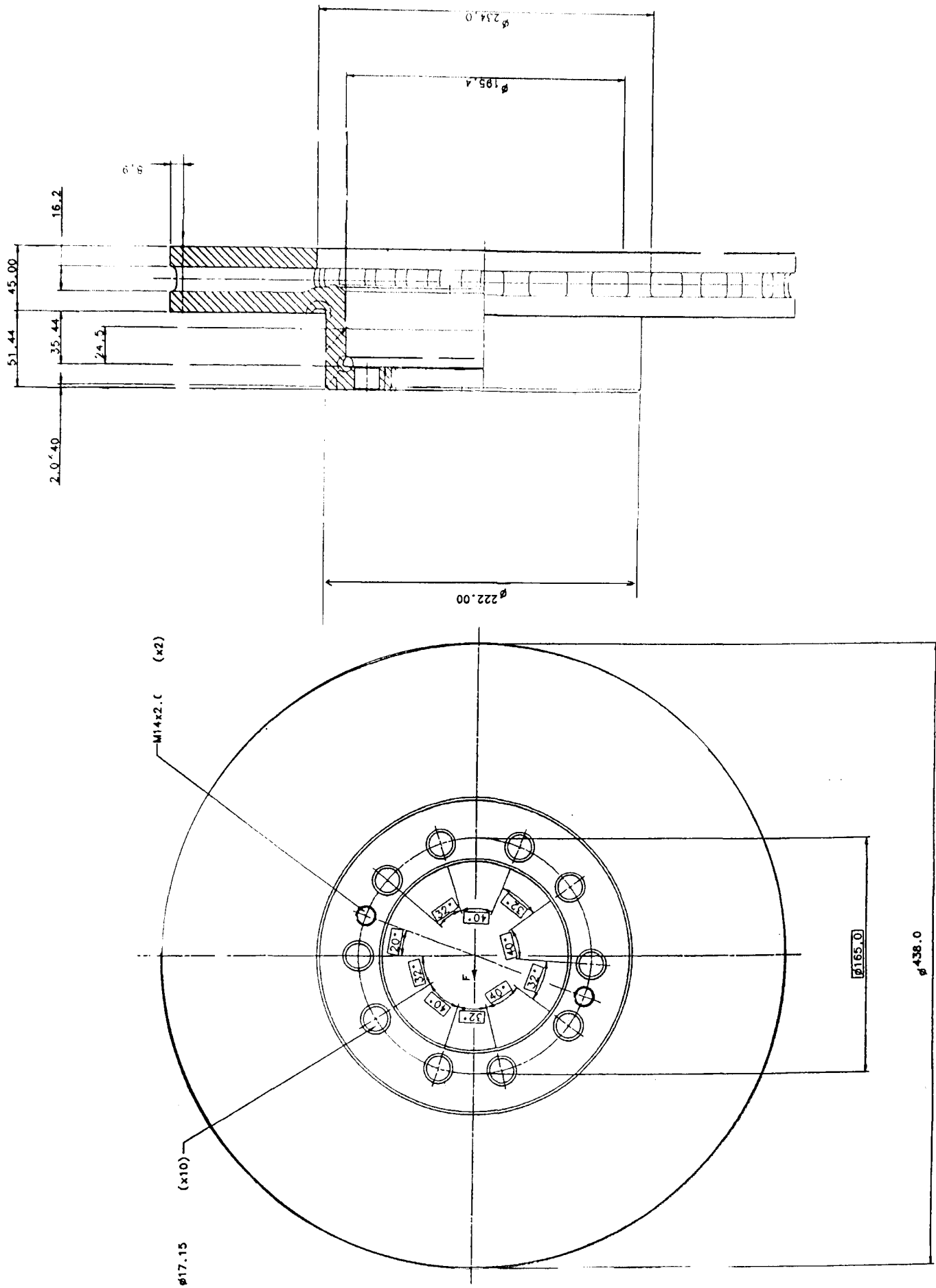


Figure 3.19 ArvinMeritor standard radial CV brake disc drawing

The CV disc design features the disc and hat as one piece. Two disc forms are used: the standard (hat attached to the outboard friction face) and anti-coning (hat attached to the inboard friction face). Disc coning may have serious consequences on disc and pad wear, noise and vibration.

The wheel carrier is a standard design; a modified version has been studied as well as a new ventilated SAF wheel carrier. The wheel is available in two materials, aluminium and steel, the aluminium wheel has a thicker wall thickness and reduced ventilation hole diameter. The tyre is a standard type and although available has not been used in Spin rig tests. It was considered that the tyre does not influence disc cooling in still air conditions.

3.4.2 TGV Brake

For the railway brake heat dissipation aspect of the study, Brunel University collaborated with SabWabco (UK) Ltd., and they have provided a ventilated axel mounted TGV (Train à Grande Vitesse) high speed railway disc and a modified hub (original hub no available). SabWabco are a supplier of complete brake systems, brake products, wheels and couplings for rail vehicles.

The TGV is a high speed train that travels at speeds up to 320 km/h (200 mile/h), see Figure B2. It is fitted with a variety of discs depending on service conditions. The railway brake disc studied in this project is mounted to the axle of the frequently stopping train; four discs are fitted on each axle.

The TGV disc brake consists of a hub, ventilated disc and retaining ring, the assembly is shown in Figure 3.20 and a detailed drawing of the assembly is shown in Figure 3.21. The assembly was mounted to the Spin Rig shaft using a specially designed adaptor; Table 3.10 shows the details of the components. The disc surface areas are given in Table 3.11, detailing the areas dissipating heat to surrounding air (wetted area) and the areas conducting heat.

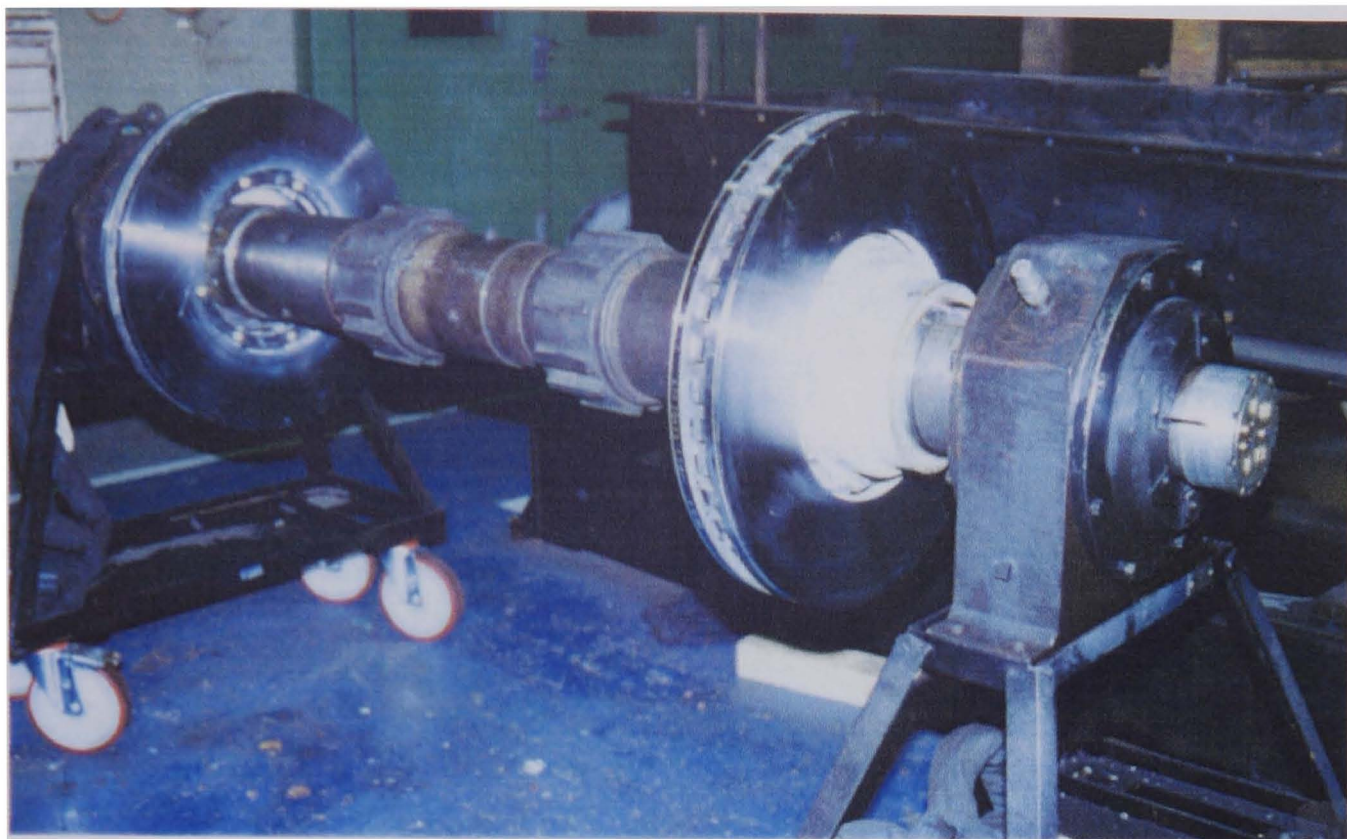





Figure 3.20 TGV axle mounted brake disc assembly, ready for dynamometer tests

Table 3.10 TGV brake design characteristics

| Component | Material | Mass [kg] | Nominal Outside Diameter [m] |
|--|----------------------|-----------|------------------------------|
|  Disc | Cast steel (15CDV06) | 91 | 0.640 |
|  Hub and adaptor | Forged steel | 49 | 0.280 |
|  Retaining ring | Steel (15CDV06) | 2 | 0.330 |

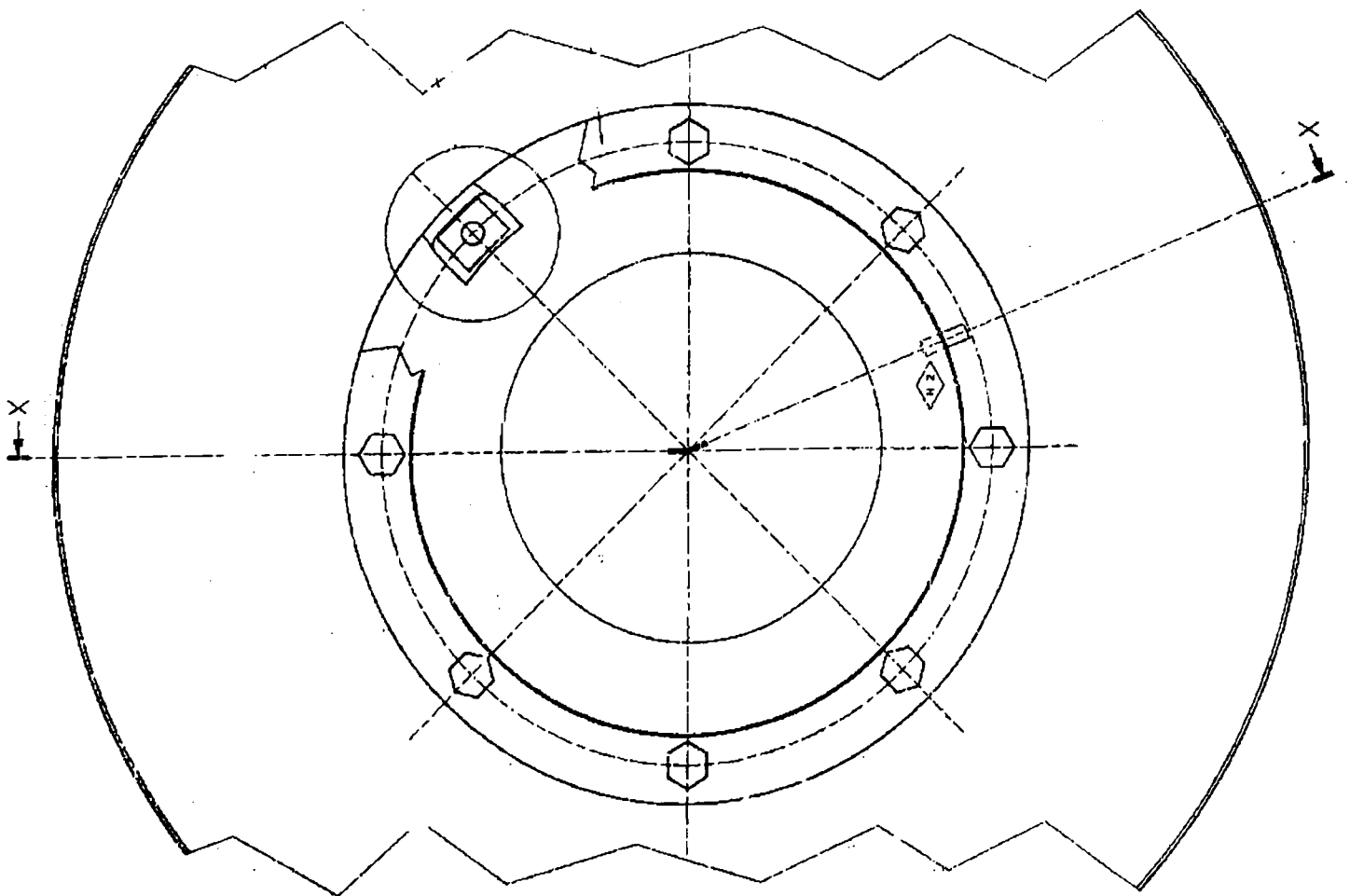
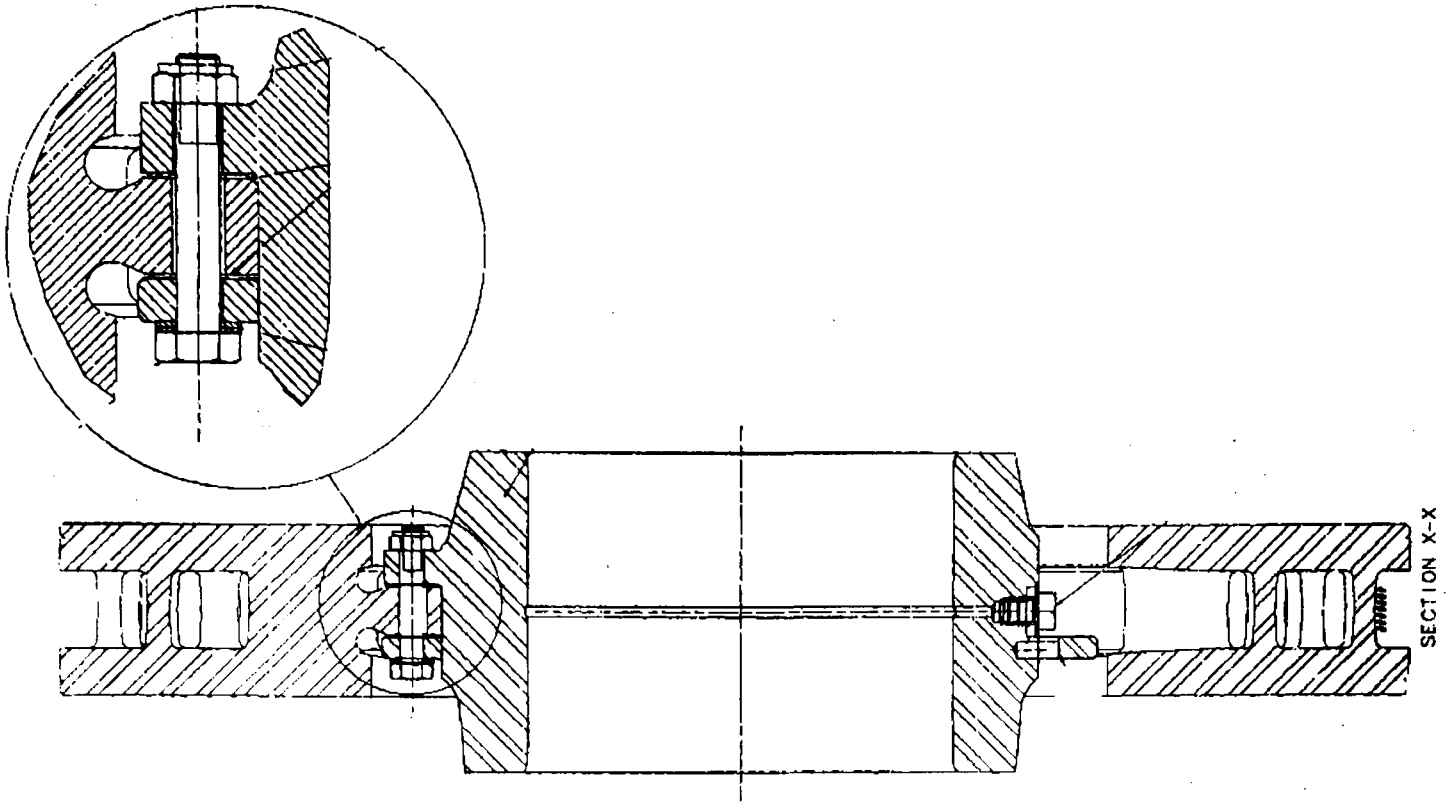


Figure 3.21 SabWabco TGV axle mounted railway brake disc assembly used

Table 3.11 Average surface areas of the TGV disc

| Surface | Area [m ²] |
|-------------------------|------------------------|
| Total | 1.308 |
| Total 'wetted' | 1.306 |
| Friction faces | 0.451 |
| Rim | 0.092 |
| Vane | 0.763 |
| Total conductive (lugs) | 0.002 |

The vane design of the TGV disc can be seen in Figure B8. The design incorporates vanes and pillars to provide optimum cooling with low pumping loss, which is an important factor in the design of railway brake discs. The vanes pump air through the disc and over the pillars. The disc is fixed to the hub by eight lugs. A retaining ring is used to clamp the disc to the hub, see Figure 3.20. Slip washers are placed at the interface of the disc lugs and ring and disc lugs and hub. The slip washers allow thermal expansion of the disc during service, reducing stresses in the assembly. The retaining ring almost completely blocks the vane inlet on one side affecting the cooling performance of the disc (see Figure 3.21).

Disc Brake Airflow

4.1 Introduction

Air heated by the brake assembly surface is transported away from the brake assembly by airflow in the region and gets replaced by cooler air. Heat dissipation increases with temperature difference between the brake surface and surrounding air. Airflow also directly influences convective heat transfer coefficients (h_{conv}), with h_{conv} increasing with air velocity. Railway ventilated disc brakes rotate at high speed, which causes substantial pumping power requirements. These effects are very serious; a single ventilated disc with radial vanes would require excessive power just for rotation. This chapter is dedicated to the analysis of airflow in the region of the brake, to enable better understanding and improvement this process, which is crucial for disc cooling. To achieve this, airspeed and pumping losses have been studied using analytical, experimental and numerical methods.

4.2 Analytical Airflow Analysis

Near the surface of a rotating disc, air flows mainly in the direction tangential to rotation. An additional component of airflow is caused by the centrifugal forces due

to rotation. Accordingly, ambient air moves from the surroundings towards the surface of the disc (Wagner 1948). According to Von Kármán (Kármán 1946), the velocity components, U_r (radial) and U_t (tangential), of the air flowing in the radial and tangential direction inside the boundary layer are given approximately by the equations (4.1) and (4.2):

$$U_r = r\omega \left[1.026 \frac{x}{\delta} \left(1 - \frac{x}{\delta} \right)^2 \left(1 + 2 \frac{x}{\delta} \right) - \frac{1}{2} \left(\frac{x}{\delta} \right)^2 \left(1 - \frac{x}{\delta} \right)^2 \right] \text{ if } x \leq \delta \quad (4.1)$$

$$U_t = r\omega \frac{1}{2} \left[\left(2 + \frac{x}{\delta} \right)^2 \left(1 - \frac{x}{\delta} \right)^2 \right] \text{ if } x \leq \delta \quad (4.2)$$

Where, r represents the radial distance from the axis, x the axial distance from the disc, ω is the angular velocity, and δ , the boundary layer thickness, is given by the equation (4.3):

$$\delta = 2.58(\nu/\omega)^{\frac{1}{2}} \quad (4.3)$$

Where, ν is the kinematic viscosity of air. The brake disc is also subject to external airflow. A moving vehicle provides airflow to the disc, causing a cross flow over the disc surface. The cross flow is generally restricted, firstly by the vehicle structure (body panels, wheel arch), secondly by the wheel assembly (wheel, dust shields, suspension components, etc.) and thirdly by the ground effect.

Ventilation of the brake disc represents the primary system designed to improve brake disc cooling, by pumping air through the disc ventilation channels and providing a larger wetted area for convective heat dissipation. The ventilated brake disc acts like a rotodynamic radial flow pump, more commonly known as the centrifugal fan or impellor. There are six types of centrifugal fan in common use, as shown in Figure 4.1:

- Aerofoil blade (AF)
- Backward curved blade (BC)
- Backward inclined blade (BI)
- Radial tip blade (RT)
- Forward curved blade (FC)
- Radial blade (RB)

Figure 4.1 shows the vane configurations with their corresponding pumping efficiencies (η_p) as defined by equation (4.4), where Q_a is the power of the air pumped by the fan and Q_b is the power to rotate the fan. The centrifugal fan with AF blades has the best pumping efficiency and the most complex blade design. For the centrifugal fan, the aerofoil lift contributes only by a small proportion of the pressure produced and the improvements due to airfoil blades are not as pronounced as they are for axial flow fans. The RB design is the least efficient in pumping and has the simplest blade design. The 90° blade angle at the leading edges results in poor flow conditions. An advantage of the RB design is that it is bi-directional unlike the other designs, which are designed to operate in one direction only. On a vehicle a single RB disc can be fitted to either the right hand or left hand side. For this reason and manufacturing simplicity, the RB design is the most common design for disc brakes.

$$\eta_p = \frac{Q_a}{Q_b} \quad (4.4)$$

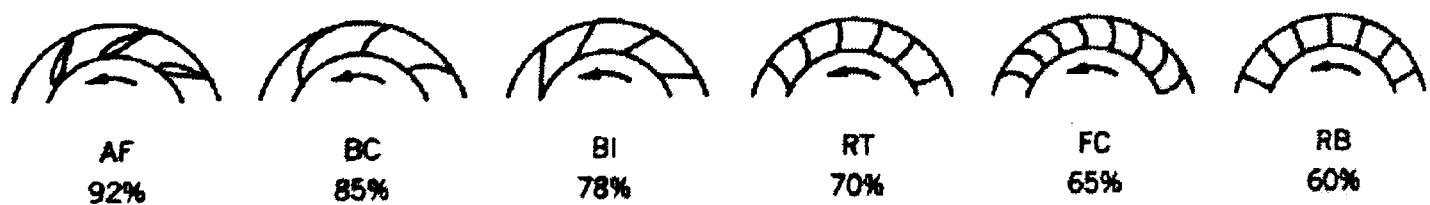


Figure 4.1 Six blade shapes commonly used in centrifugal fans and their approximate efficiency (Bleier 1998)

The flow pattern for the RB design begins as the airflow enters the disc axially and then turns 90° into a radial direction as it enters the ventilation channel. The air leaves the channel in a circumferential direction as shown in Figure 4.2. The

operating principle is a combination of two effects: centrifugal force and deflection of airflow by the vanes. As the brake disc rotates together with the air inside the cooling channels, the air is subject to centrifugal force, this is the main cause for the outward flow of air. The air moving from the channel inlet to the channel outlet causes a pressure drop at the channel inlet drawing more air into the channel. The change in static pressure is only enough to overcome resistance to the motion and so the variation of fluid density is negligible, and air maybe regarded as incompressible. Air deflection only has a strong influence on the flow pattern and performance in the case of the FC blade design.

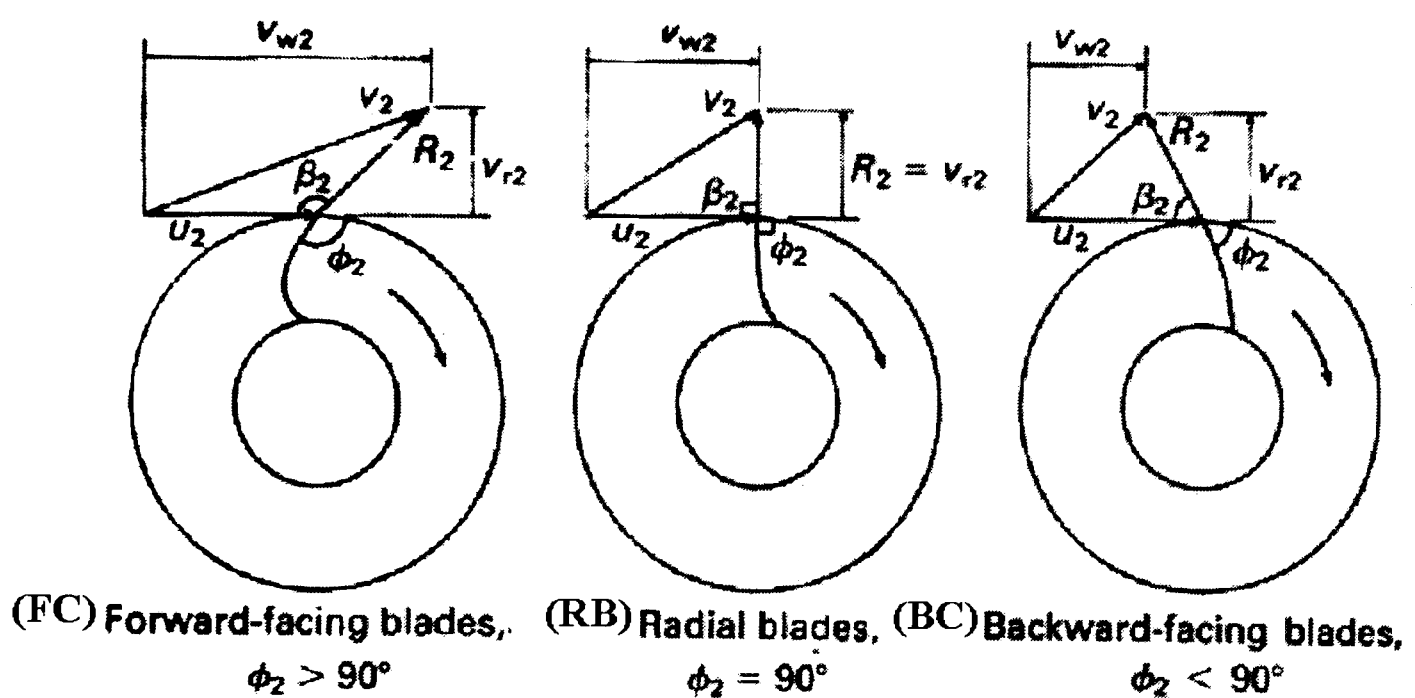


Figure 4.2 Outlet angle of centrifugal fan blades (Massey and Ward-Smith 1998)

4.2.1 Velocity Diagrams

Figure 4.2 and Figure 4.3 show the velocity diagrams for the rotating disc in still air at the leading and trailing edges of the vane. From the diagrams, velocity calculations can be derived. The vector sum of the air velocity (R) and the blade velocity (U) result in the absolute air velocity (V). This is true for the leading (1) and trailing edges (2). Figure 4.2 shows the outlet vector diagrams for different outlet angles, assuming that there is no discrepancy between the direction of relative velocity R_2 and the outlet edge of the blade. The airflow exit vector triangle is dependent on the outlet angle of the centrifugal fan. The outlet blade angle is defined by ϕ_2 . V_{w2} is the velocity of whirl, the component of absolute velocity in the direction tangential to the

vane circumference. There are no guide vanes at the ventilation channel inlet; the air therefore enters the centrifugal fan at right angles to the blade velocity (U). This means the V_w component is equal to zero at the inlet (V_{w1}) (Figure 4.3).

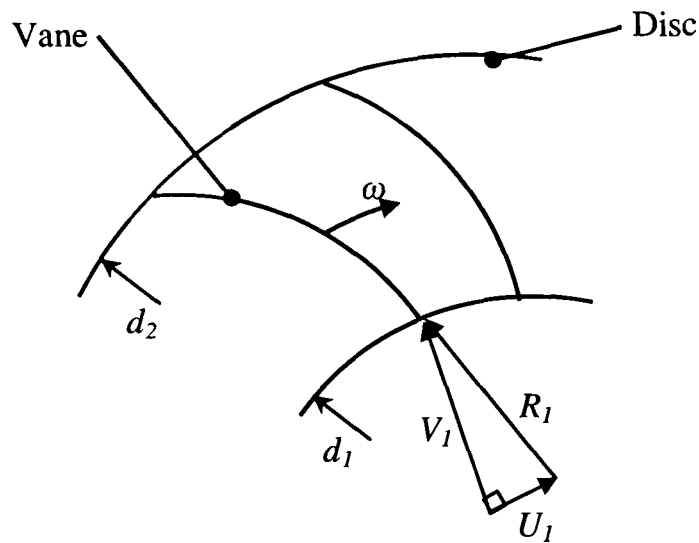


Figure 4.3 Centrifugal fan velocity diagram for the leading edge (Massey and Ward-Smith 1998)

At the leading edge the following conditions exist in most cases (Bleier 1998):

The cylindrical area, A_1 , through which the airflow will pass, can be derived from the blade width (b_1):

$$A_1 = \pi b_1 d_1 \quad (4.5)$$

The blade velocity, U_1 :

$$U_1 = \frac{d_1 \omega}{2} \quad (4.6)$$

The absolute air velocity (V_1) is perpendicular to the area, A_1 and can be derived from the total volumetric flow rate (\dot{v}):

$$V_1 = \frac{\dot{v}}{A_1} \quad (4.7)$$

The blade angle, β_1 can be calculated from:

$$\tan \beta_1 = \frac{V_1}{U_1} \quad (4.8)$$

At the blade tip the following conditions exists:

The cylindrical area of A_2 :

$$A_2 = \pi b_2 d_2 \quad (4.9)$$

The blade velocity, U_2 :

$$U_2 = \frac{d_2 \omega}{2} \quad (4.10)$$

The absolute air velocity, V_2 , can be resolved into two components: a radially outward component (V_{2r}) and a circumferential component (V_{2c}):

$$V_{2r} = \frac{\dot{v}}{A_2} \quad (4.11)$$

$$V_{2c} = K \frac{P_s}{\omega d_2} \quad (4.12)$$

Where P_s is the static pressure. The constant K contains two correction factors for hydraulic and circulatory flow losses, which can only be estimated.

The V_{2c} component cannot be calculated accurately because of hydraulic and circulatory flow losses. The hydraulic losses are the pressure losses due to friction as the air flows across the disc surfaces. The circulatory flow is the rotation of air within the ventilation channel. Air particles within this space lag behind the rotation of the ventilation channels reducing the pressure in the ventilation channel.

An increase in the angles β_1 and β_2 results in an increase in air volume and static pressure but in a decrease in efficiency. However, if the angle becomes too large circulatory flow will become excessive.

The blade angle β_2 can be calculated from:

$$\tan \beta_2 = \frac{V_{2r}}{U_2 - V_{2c}} \quad (4.13)$$

4.2.2 Pumping Power

Since the torque about a fixed axis must be equal to the rate of increase of angular momentum about that axis, the torque on the fluid must be equal to the angular momentum of the fluid leaving the rotor per unit time minus the angular momentum of the fluid entering the rotor per unit time. Therefore (Massey and Ward-Smith 1998):

$$\tau = \int V_{w2} r_2 d\dot{m} - \int V_{w1} r_1 d\dot{m} \quad (4.14)$$

This expression only involves the conditions at the inlet and outlet and therefore is independent of losses from bearings and air friction or air turbulence.

$$\begin{aligned} \tau\omega &= \int V_{w2} \omega r_2 d\dot{m} - \int V_{w1} \omega r_1 d\dot{m} \\ \tau\omega &= \int V_{w2} U_2 d\dot{m} - \int V_{w1} U_1 d\dot{m} \\ \tau\omega &= U_2 V_{w2} \int d\dot{m} - U_1 V_{w1} \int d\dot{m} \\ \tau\omega &= \dot{m} (U_2 V_{w2} - U_1 V_{w1}) = Q_{pump} \end{aligned} \quad (4.15)$$

As previously mentioned, the component V_{w1} is equal to zero, therefore the expression becomes:

$$Q_{pump} = \dot{m} U_2 V_{w2} \quad (4.16)$$

For the radial vane disc the V_{w2} component is equal to the U_2 component, see Figure 4.2, thus the power equation is modified to:

$$Q_{pump} = \dot{m}U_2^2 \quad (4.17)$$

The above equation been used to determine Q_{pump} (ventilated brake disc pumping losses) for the standard radial vane CV disc and Figure 4.4 shows the power curve, at the rotational speed of 2000 min^{-1} Q_{pump} is 550 W. The theoretical calculation of pumping losses will be compared with experimental measurements and CFD predictions.

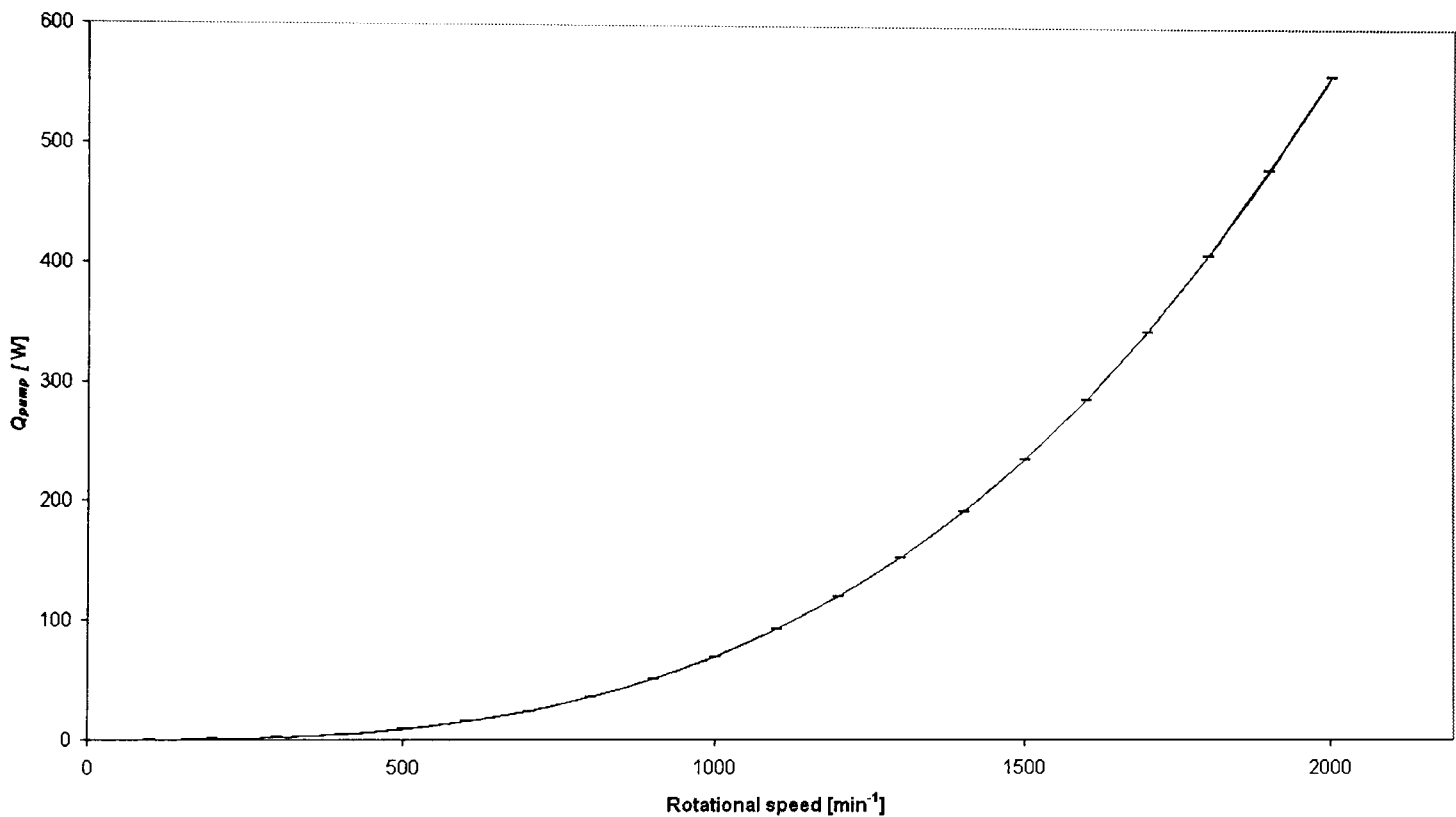


Figure 4.4 Theoretical standard CV disc ventilation channel pumping power

In order to compare the pumping performance of a ventilated disc at one rotational speed (1) to another rotational speed (2), the following rules generally apply to all types of fans (Bleier 1998). These relationships are useful in ventilated disc design for performance prediction and modelling validation.

The volume rate of flow (\dot{v}) varies directly with the rotational speed (n):

$$\frac{\dot{v}_2}{\dot{v}_1} = \frac{n_2}{n_1} \quad (4.18)$$

The static pressure (P_s) varies with the square of the rotational speed:

$$\frac{P_{s2}}{P_{s1}} = \left(\frac{n_2}{n_1} \right)^2 \quad (4.19)$$

Q_{pump} varies with the cube of the rotational speed:

$$\frac{Q_{pump2}}{Q_{pump1}} = \left(\frac{n_2}{n_1} \right)^3 \quad (4.20)$$

4.3 Vane Design

When designing a ventilated disc, the required outside diameter and inside diameter can be calculated from the required thermal capacity, available space, disc thickness and airflow requirements; n , \dot{v} and P_s , enabling ventilated disc cooling and pumping efficiency to be achieved. Equation (4.21) can be used to calculate the inside diameter (d_1):

$$d_{1,\min} = 10^3 \sqrt[3]{\frac{\dot{v}}{n}} \quad (4.21)$$

To calculate the outside diameter, the following equation can be used:

$$d_{2,\min} = \frac{18000}{n} \sqrt{P_s} \quad (4.22)$$

From the above equations, it can be seen that air volume increases with the inside diameter. The static pressure will only be produced after the air has entered the channel and flowed to the outside diameter.

Further formulae are available relating the centrifugal fan performance with disc size. These fan relationships can only be used if the two fans are geometrically in

proportion. D_1 is the outside diameter of known rotor performance; D_2 is the outside diameter of the modified rotor (Bleier 1998).

\dot{v} varies as the cube of the size:

$$\frac{\dot{v}_2}{\dot{v}_1} = \left(\frac{D_2}{D_1} \right)^3 \quad (4.23)$$

P_s varies as the square of the size:

$$\frac{P_{s2}}{P_{s1}} = \left(\frac{D_2}{D_1} \right)^2 \quad (4.24)$$

Q_{pump} varies as the fifth power of the size:

$$\frac{Q_{pump2}}{Q_{pump1}} = \left(\frac{D_2}{D_1} \right)^5 \quad (4.25)$$

For changes in the outside diameter only there is a modification to the above fan laws.

\dot{v} varies as the square of the size:

$$\frac{\dot{v}_2}{\dot{v}_1} = \left(\frac{D_2}{D_1} \right)^2 \quad (4.26)$$

P_s varies as the square of the size:

$$\frac{P_{s2}}{P_{s1}} = \left(\frac{D_2}{D_1} \right)^2 \quad (4.27)$$

Q_{pump} varies as the fourth power of the size:

$$\frac{Q_{pump2}}{Q_{pump1}} = \left(\frac{D_2}{D_1} \right)^4 \quad (4.28)$$

Equations (4.26) to (4.28) are of sufficient accuracy for practical purposes (Bleier 1998).

4.3.1 Blade Width

The airflow enters the ventilated brake disc axially and then decelerating turns through 90° to a radial direction. The air stream tends to follow its inertia by moving across the blade width (b), 'crowding' the back plate reducing the airflow entering the ventilation channels. Smooth curves can improve the condition. Bleier (1998) has empirically calculated the maximum recommended blade width:

$$b = 0.46d_1 \quad (4.29)$$

However smaller blade widths are often used in fan designs when less air volume is required. A reduced blade width, which may be used when there is limited space for the brake disc, will result in less deceleration or even acceleration during the right-angled turn. Acceleration will take place when:

$$b \leq 0.22d_1 \quad (4.30)$$

4.3.2 Number of Blades

The channel between the blades must be narrow enough to give good guidance to the air stream but needs to be wide enough so that resistance to the airflow is not too high. Inserting partial blades in the outer portion of the annular space will reduce the channel where it is largest, providing a more uniform distance between the channels. However, tests on such configurations show that this will not improve pumping

performance, because the increased number of blade edges increase turbulence in the airflow (Bleier 1998).

4.3.3 Blade Under Filling and Over Filling

Under filling is a method of achieving an increase in flow. The increase in exit area causes an increase in the tangential component V_w . Over filling does not change the area but increases the efficiency by making the exit smoother, flow increases by lowering friction and turbulence (Nelik 1999), see Figure 4.5.

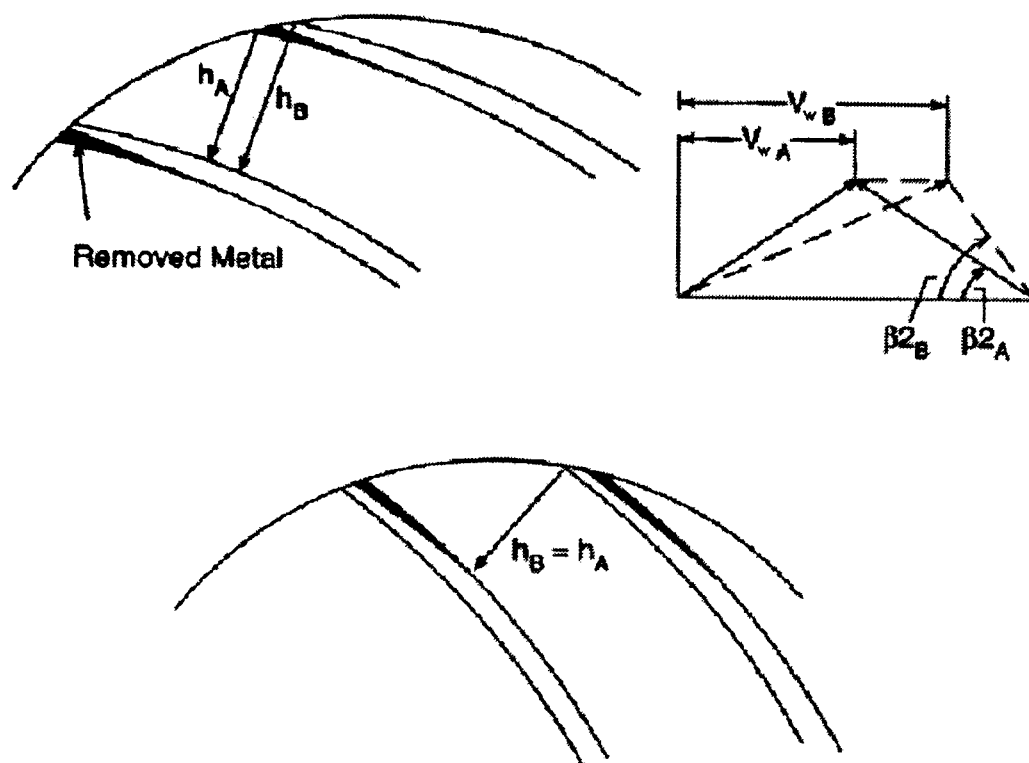


Figure 4.5 Under filling and over filling of blades (Nelik 1999)

4.4 Airflow around Disc

Convective heat dissipation from the brake disc is directly related to the airflow around the disc. Airflow enhances the heat transfer by bringing cooler air into contact with the disc surface. The rate of heat transfer is increased by an increase in air velocity. Measuring the airflow around the disc, and analysing the flow patterns, allows convective heat transfer coefficients (h_{conv}) to be more accurately calculated, in order to verify CFD results predicting h_{conv} values.

4.4.1 Experimental Measurements

The airflow velocity around the commercial vehicle (CV) and TGV railway disc (see Chapter 3) has been measured using the hand held hot wire anemometer described in Chapter 3. The anti-coning disc was analysed in the most detail, measuring surrounding air velocities for the disc only and the disc shrouded by the wheel assembly, with and without the SAF ventilated wheel carrier.

The measuring head of the anemometer was placed at the measurement point and supported by a retort stand as shown in Figure 4.6a. Figure 4.6a shows the measurement of air velocity at the anti-coning disc ventilation channel inlet, Figure 4.6b shows the measurement of air velocity at the ventilation holes of the SAF wheel carrier. The measurement head of the anemometer was adjusted until the maximum air velocity was measured; maximum velocity measurement is achieved when the anemometer head is inline with the airflow. Airflow velocity has been measured for various rotational speeds ranging from 150 to 1000 min^{-1} for the CV disc and 200 to 1800 min^{-1} for the TGV disc. All measurements were taken at room temperature; the average ambient temperature was 24°C with a relative humidity of 43%. It is understood that the anemometer head will influence the flow, reducing the measuring accuracy. However, no other equipment could be provided and measured data will be compared with other sources, to confirm equipment suitability and accuracy.

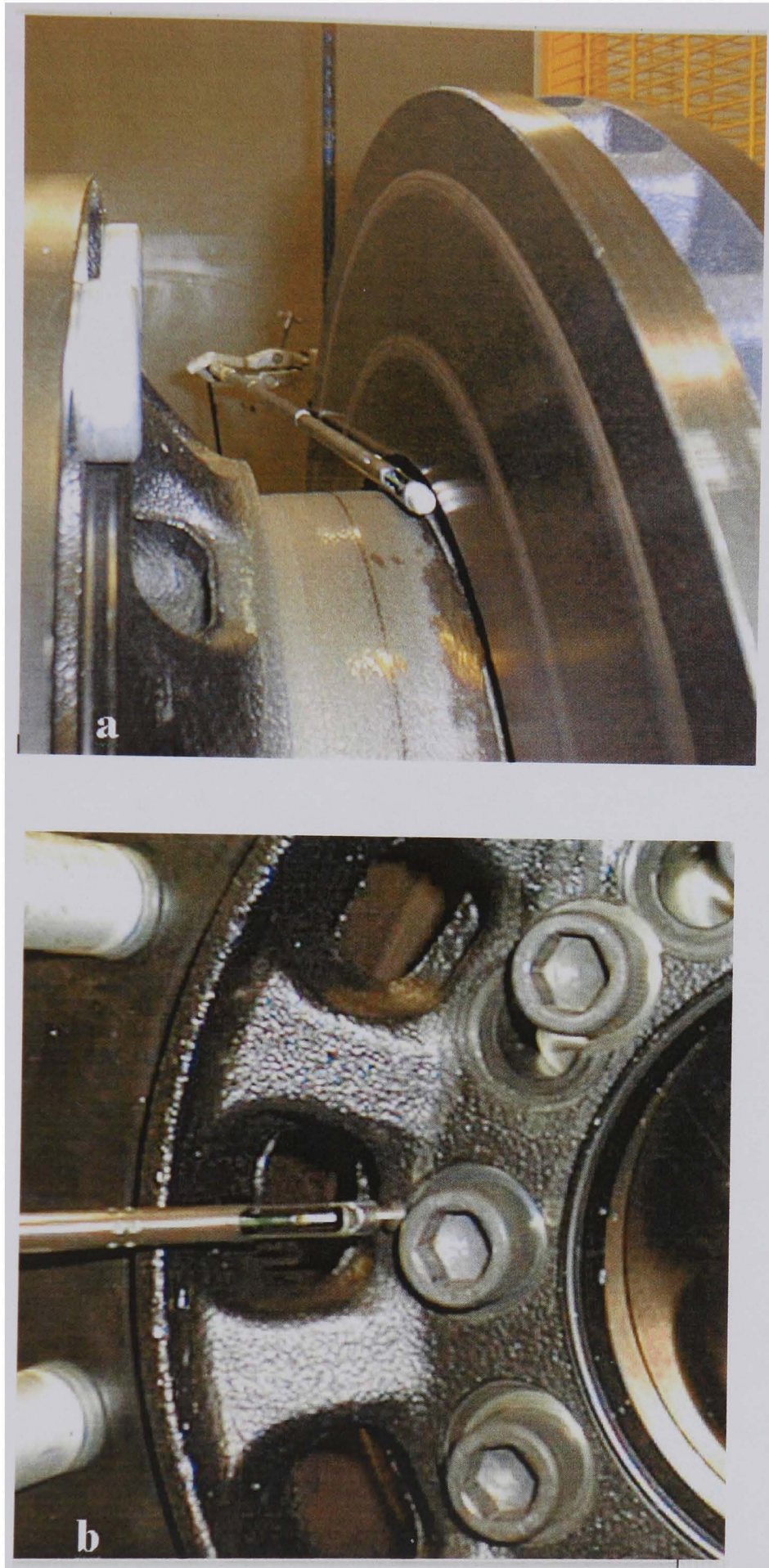
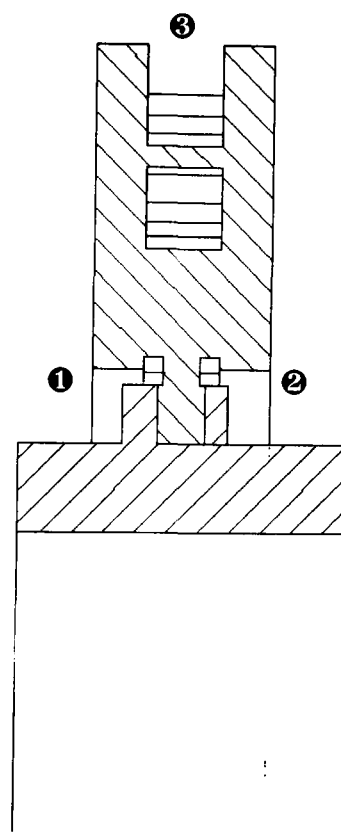
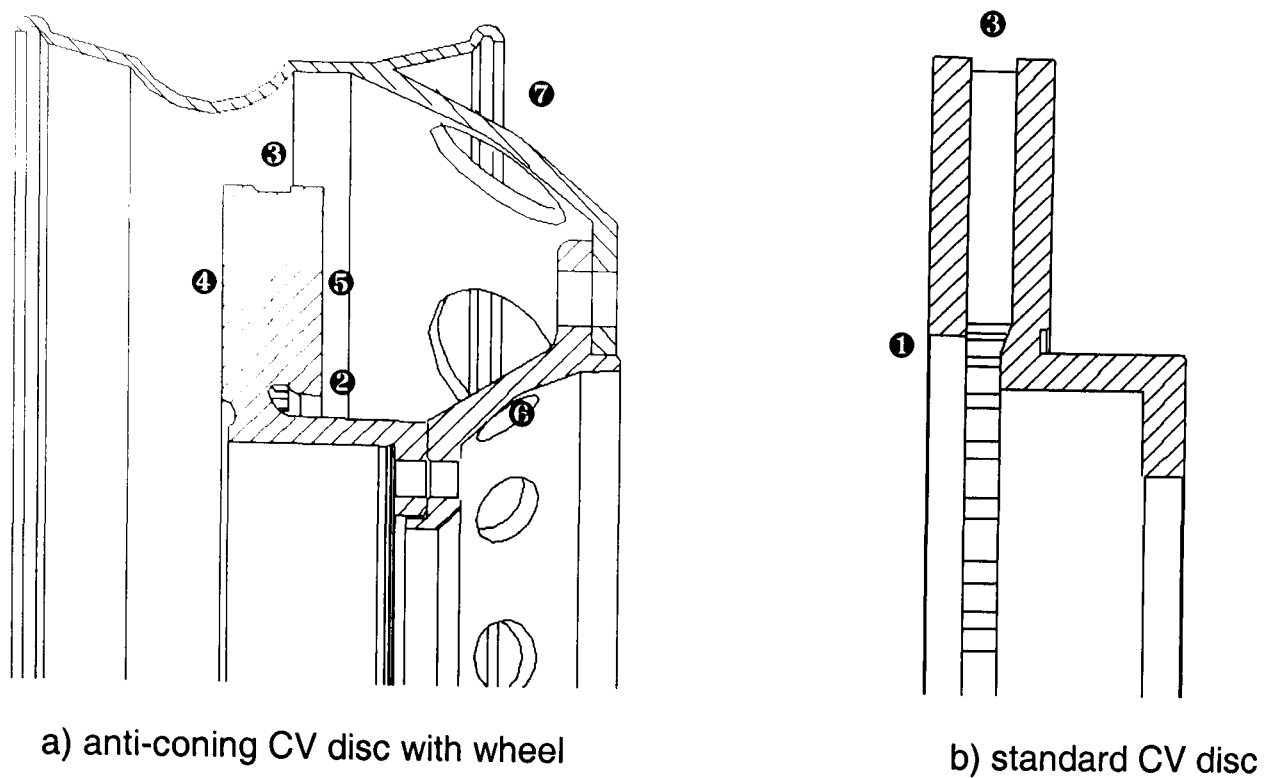


Figure 4.6 Measurement of air velocity using hot wire anemometer

More details of measurement points are given in Figure 4.7, measurements were taken at the channel inlets (1, 2), channel exit (3), the inboard and outboard rubbing faces of the disc at the mean radius (4, 5), the wheel carrier ventilation holes (6), and the wheel ventilation holes (7).



c) TGV disc

Figure 4.7 Air velocity measurement points for each brake assembly

Figure 4.8 shows the air velocity measured for the anti-coning radial vane CV disc as shown in Figure 4.7a but with the wheel and carrier removed. The curves show that the air velocities increase linearly with rotational speed, the highest velocity being at the channel exit (24 m/s at 1000 min⁻¹). High velocities are also measured at the rubbing faces due to the non-slip condition of the disc surface. The slope of the friction surface air velocity curve reduces at around 10 m/s. The Reynolds number at

10 m/s is 210000, which is in the laminar region. The transition between laminar and turbulent flow occurs at a Reynolds number of approximately 240000 at 11.5 m/s, which explains the change in air velocity slope.

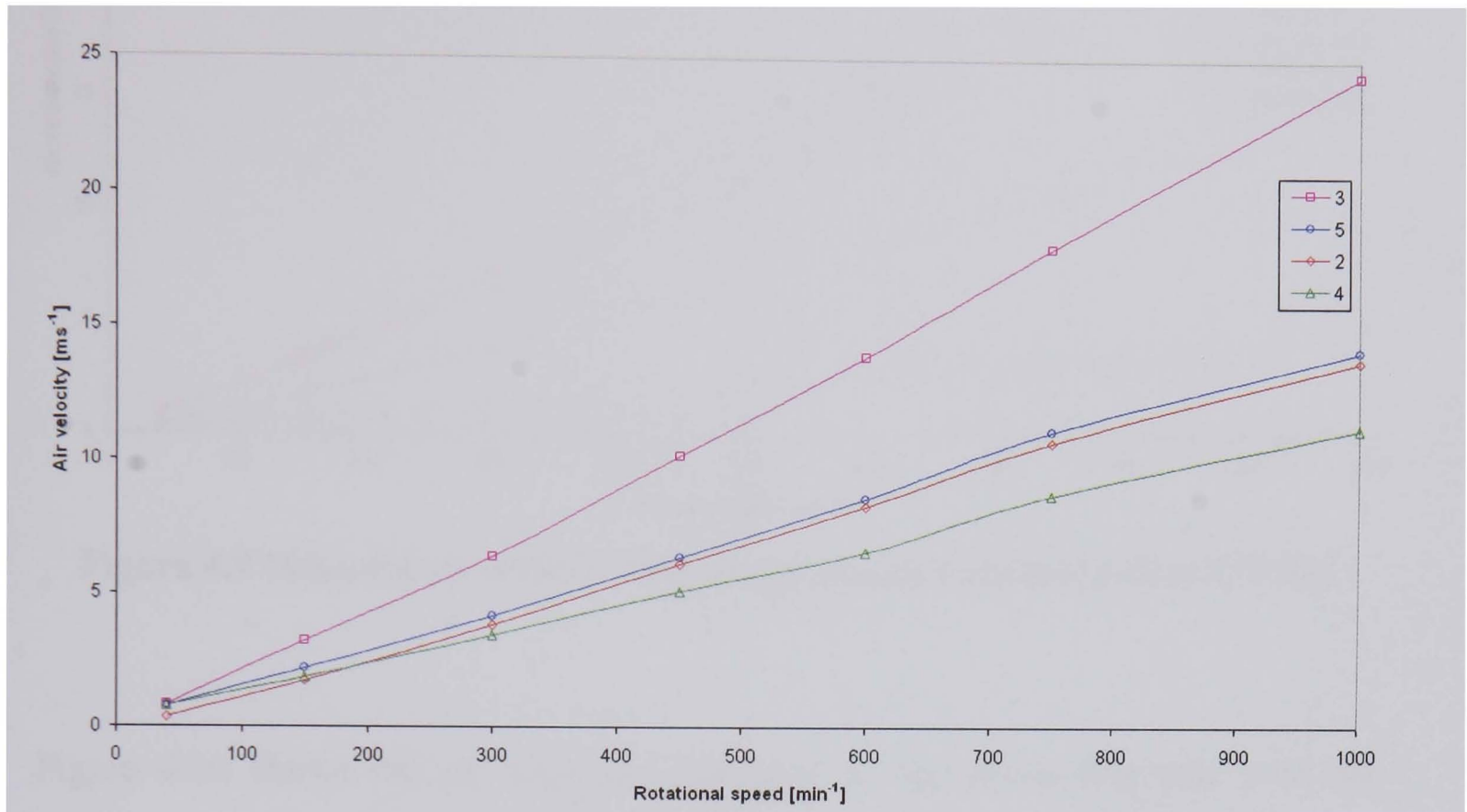


Figure 4.8 Measured air velocity for the CV anti-coning disc

Figure 4.9 shows the channel velocities for the standard (Figure 4.7b) and anti-coning disc (Figure 4.7a, wheel and carrier removed). Higher channel exit velocities have been measured for the standard disc; the channel inlet is less restricted for this disc design, which can be seen in Figure 4.7. It can also be seen that the channel inlet air velocity for the standard disc is lower, a result of the larger inlet area.

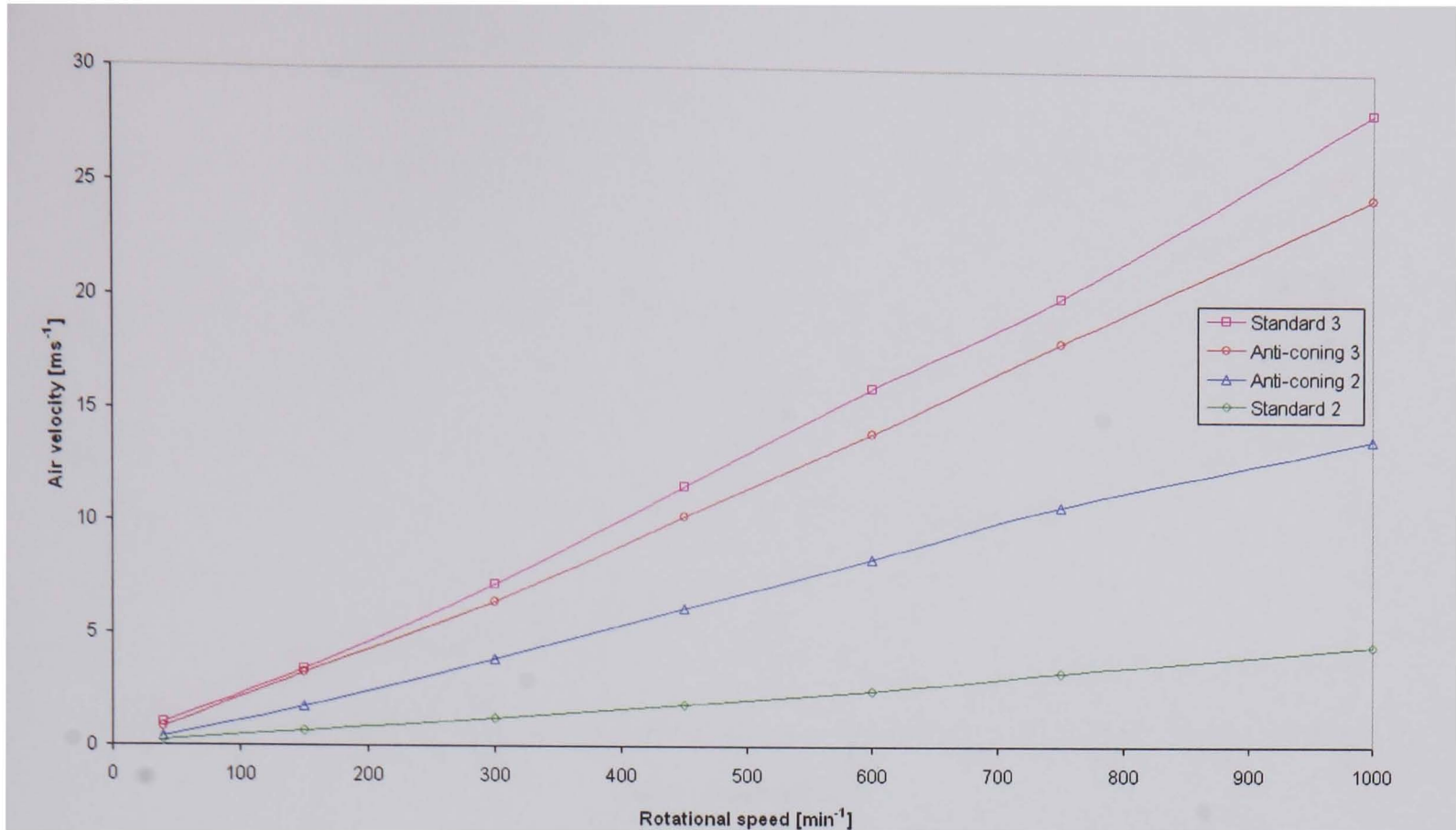


Figure 4.9 Measured air velocity comparison; standard and anti-coning CV disc

Figure 4.10 shows the air velocities measured at the anti-coning disc with the ventilated wheel carrier wheel assembly (as shown in Figure 4.7a). Only the channel exit (3), wheel (7) and wheel carrier (6) velocities could be measured because of the wheel assembly restricting access to the disc. Compared with the results shown in Figure 4.8, the wheel assembly reduces the channel exit velocities at 1000 min⁻¹ by 14%. Relatively high air velocities are measured at the wheel ventilation holes (7), this is air forced out of the wheel by the channel exit pressure. A lower air velocity is measured at the wheel carrier ventilation holes (6). The anemometer measuring head could not be placed directly at the ventilation hole because of the wheel carrier profile restricting access; the measurement is taken at a distance of 15 mm from the face of the hole.

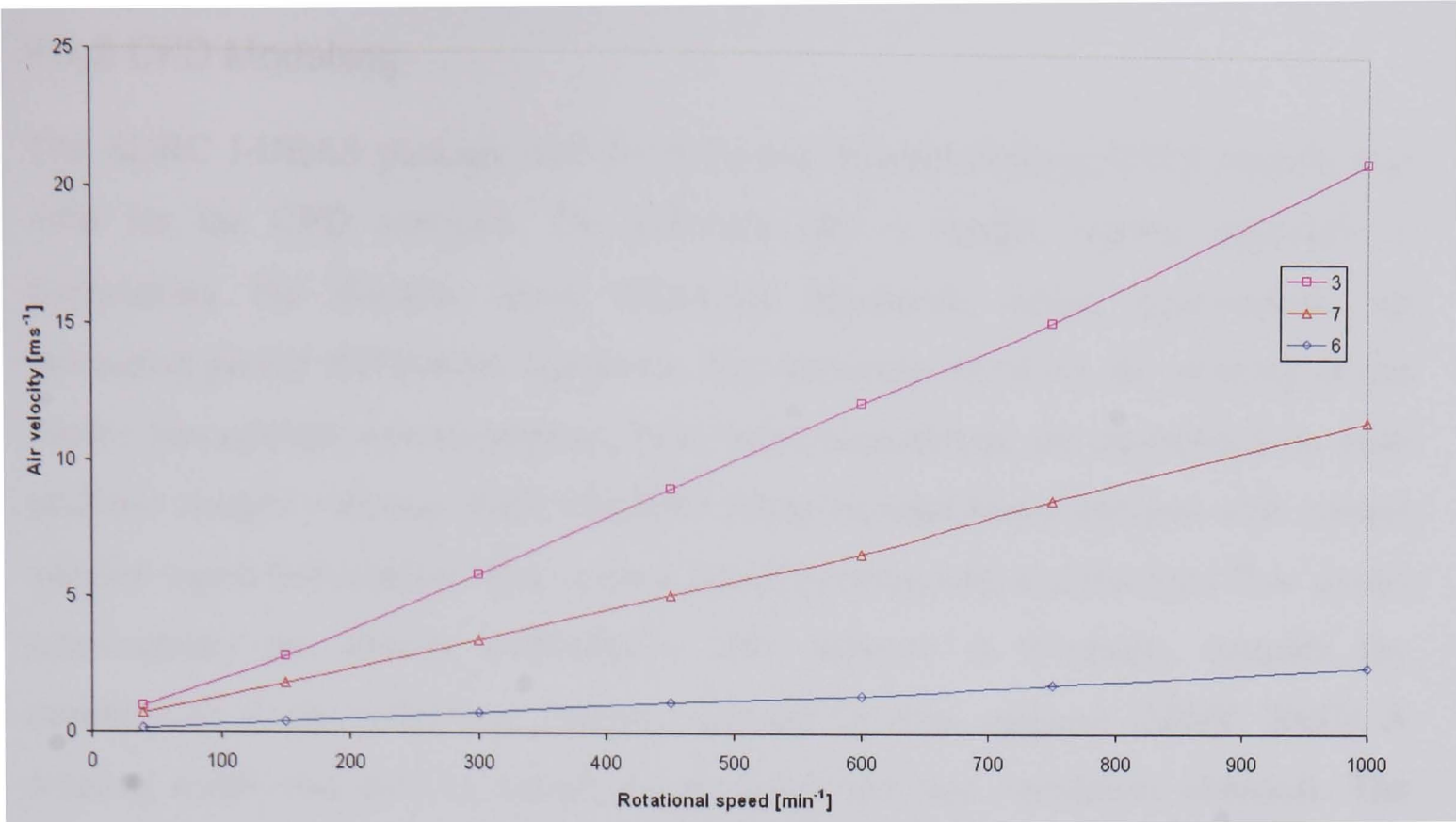


Figure 4.10 Measured air velocity for the CV anti-coning disc with ventilated carrier wheel assembly

The TGV railway disc (see Figure 4.7c) air velocities also show a linear characteristic relative to rotational speed. Figure 4.11 shows a maximum velocity of 44 m/s at the channel exit (3) when the disc is rotating at 1800 min⁻¹. The channel inlet velocity (2) is 10.3 m/s at 1800 min⁻¹, over 75% lower than the channel exit. The channel inlet velocity (1) on the retaining ring side, see Figure 4.7c, restricts flow by a further 60 % to 3.8 m/s, this is consistent throughout the velocity range.

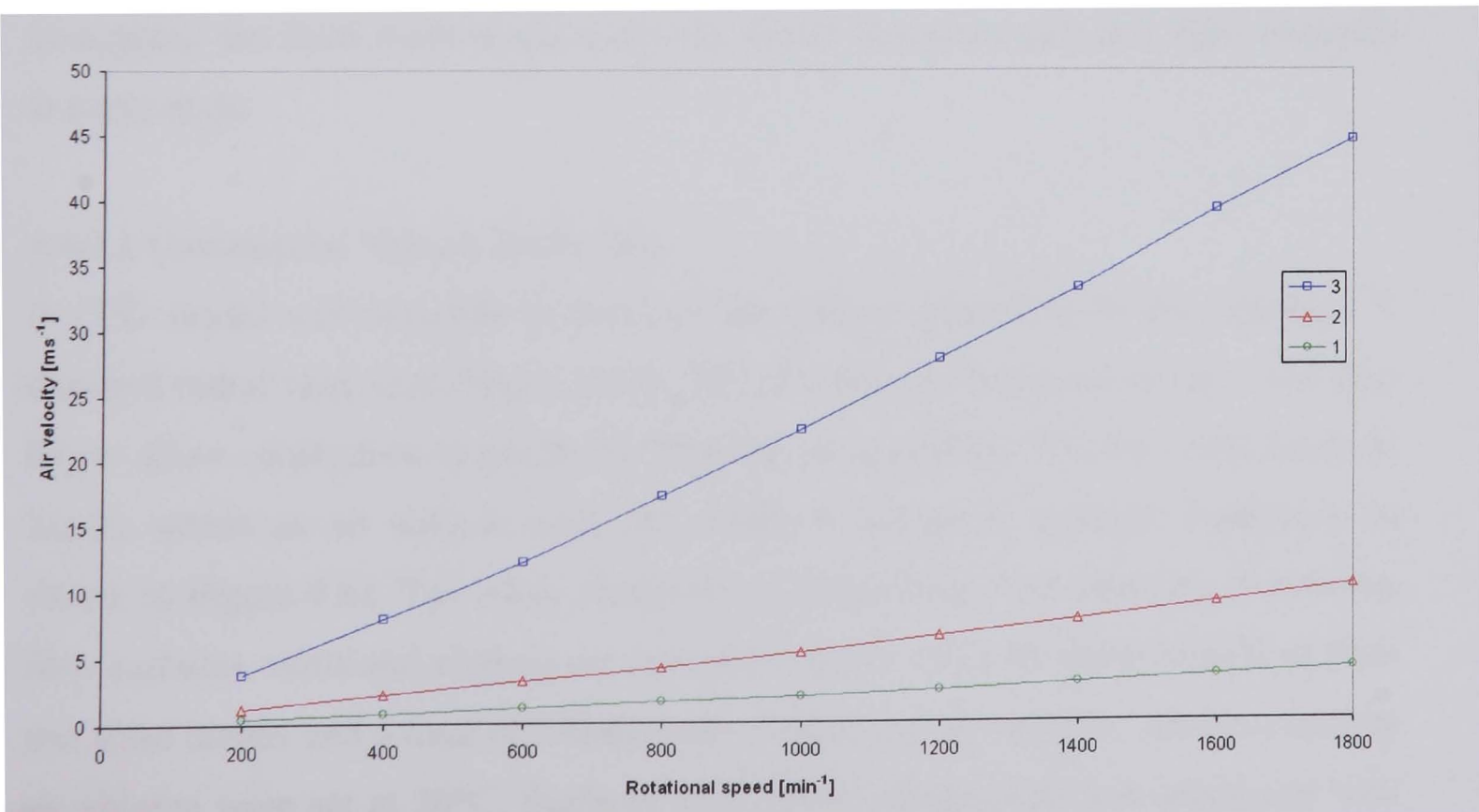


Figure 4.11 TGV railway disc ventilation channel velocity

4.4.2 CFD Modelling

The SDRC I-DEAS package and the electronic system cooling (ESC) module was used for the CFD analyses. The software uses a control volume approach in formulating the discrete finite difference equations, which approximate the governing partial differential equations. The technique involves the meshing of the model into control volume regions. Heat balance equations are established for each of these control volumes. ESC combines finite element-based analysis with control volume based formulation. The thermal model (conduction) and the fluid flow model (convection) are solved individually. The solution is thermally coupled (by convection) at the solid/fluid interface defined by flow surfaces (SDRC 2000). A rotating mesh was used to model the air inside the disc ventilation channels. The ESC analyses provided output results including airflow distribution and temperature, solid temperatures, h_{conv} distribution on solid surfaces, pressure distributions and torque on rotating flow surfaces. Post-processing allows the display of contour and arrow plots to view temperature and fluid flow directions and magnitude results for the model.

Turbulence is important for accurate simulation of airflow and convective heat transfer. A K-E turbulence model available within the ESC model has been used throughout the CFD analyses. The turbulent viscosity is not assumed constant throughout the fluid mesh domain and the model computes turbulent flow viscosity at every node.

4.4.2.1 Commercial Vehicle Brake Disc

A CFD model was designed to simulate the airflow generated by the rotating CV standard radial vane disc (Figure 4.7b). The disc was modelled mounted to the Spin Rig to allow verification of results by Spin Rig measurement. The disc solid mesh (a) rotates within an air volume mesh (b), which is vented to ambient conditions, as shown in Figure 4.12. The mesh comprises of 35915 thin shell elements (modelling flow surfaces, vents and rotating air screens), 140238 solid elements modelling fluid and solid bodies and a total of 73640 nodes. Initial temperatures for ambient and the air volume were set at 20°C. Surfaces were given perfectly smooth properties with zero surface roughness. Rotating surfaces were set to rotate about the shaft axis. The

fluid mesh within the channels was modelled as a rotating frame rotating about the shaft axis. Solid material properties are not required as the solid model only acts as a 3-D obstruction to fluid flow. The fluid elements were given standard air properties, shown in Table A5.

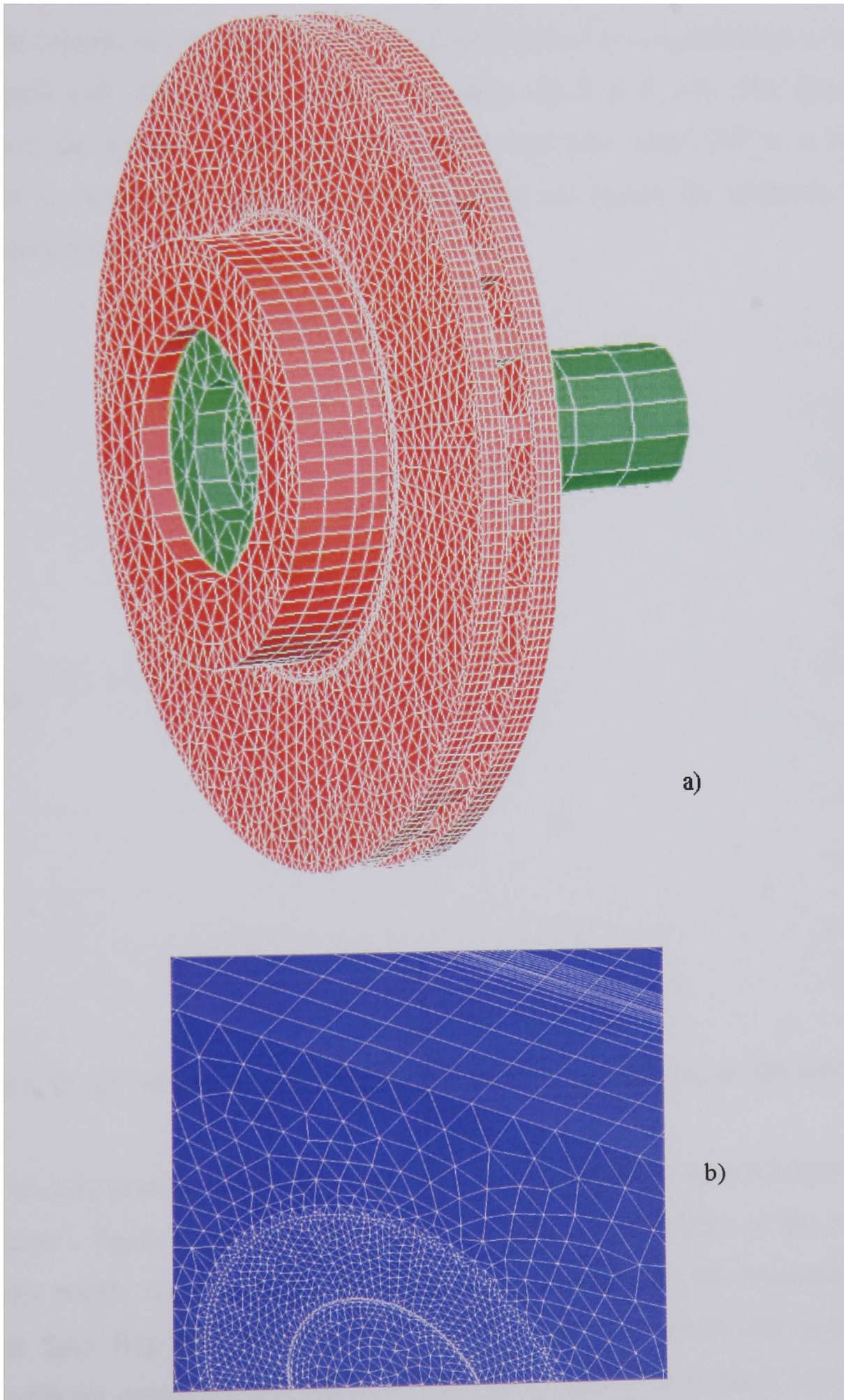


Figure 4.12 Standard radial vane CV disc CFD (a) solid mesh and (b) fluid mesh

The solution time increased with rotational speed and took between 18 and 24 hours to converge. Fluid turbulence and buoyancy were included in the analysis to give a much more accurate model of the flow. However, this added significant computational time to the solution. Figure 4.13 shows the arrow velocity plot for the standard radial vane CV disc mounted to the Spin Rig rotating at 450 min^{-1} . It can be seen that the velocity at the channel increases from 6 m/s at the channel inlet to 8 m/s at the channel exit. The rubbing surface velocities are 3 to 4 m/s. The direction arrows show the airflow enters the disc axially and then turns 90° to a radial direction as it enters the ventilation channels. The air leaves the channels in a tangential direction.

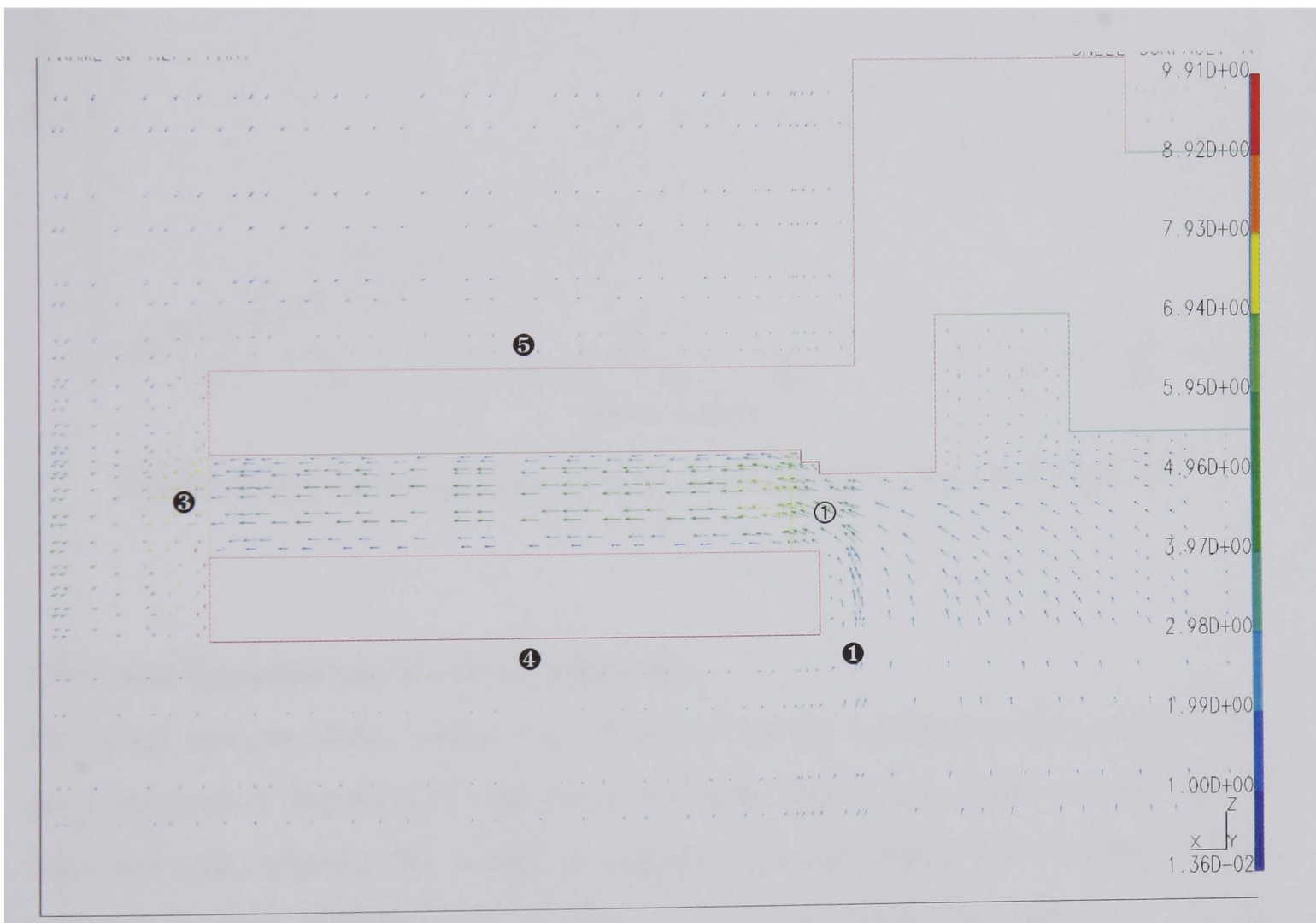


Figure 4.13 Air velocity profile for the standard CV disc rotating at 450 min^{-1}

From the velocity profiles of the CFD analyses for disc rotational speeds between 40 and 1000 min^{-1} , Figure 4.14 shows the air velocities at distinct points of the model. The velocity points are shown in Figure 4.13, coinciding with the measurements taken from Spin Rig tests (Figure 4.7b). Figure 4.14 also shows the predicted velocity as the air enters the channel. It can be seen that the air channel exit speed increases with rotational speed of the disc to a maximum of 21 m/s . Maximum

channel entry speed is slightly lower at approximately 16 m/s. It should be noted that these are not average velocities but point velocity vector values. The results for the friction surfaces and channel inlet indicate an increase with disc rotational speed as expected. The difference between the actual channel inlet (①) and the measuring point (①) is shown to be 1.5 m/s at 450 min^{-1} and increasing to 6.5 m/s at 1000 min^{-1} .

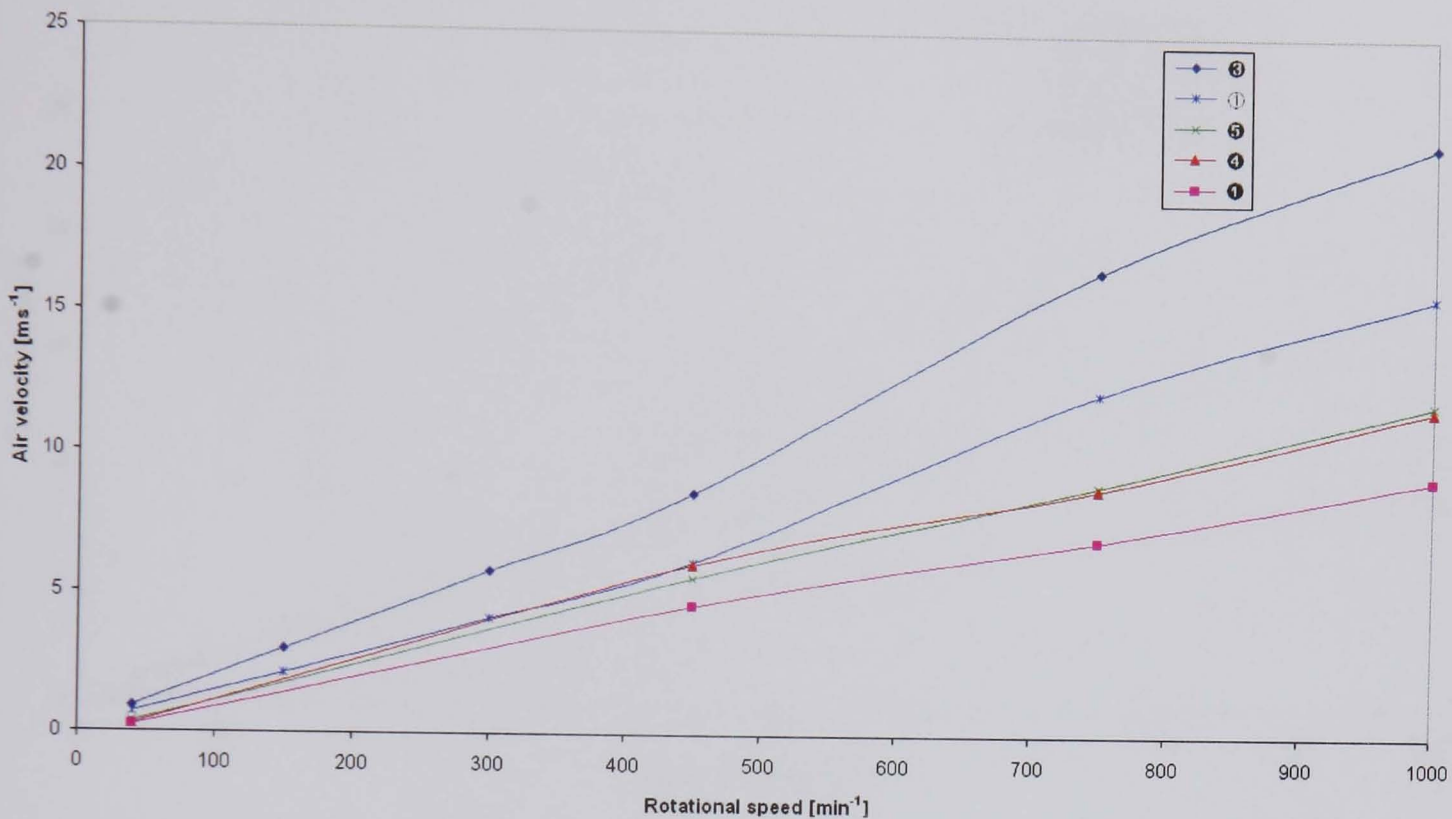


Figure 4.14 CFD air velocity results for the standard radial vane CV disc

CFD and Experimental Results Comparison

Measured and predicted channel air velocities for the standard radial vane CV disc are compared in Figure 4.15. Measured and CFD results are shown for the channel inlet and exit, whereas the analytical (equation (2.16)) results are available for the average channel velocity only. It can be seen that CFD and measured average velocities (average of channel exit and inlet) agree with the values predicted by equation (2.18) for average channel velocity. Throughout the speed range of the disc ($0 - 450 \text{ min}^{-1}$) CFD and measured values are in good agreement. At 150 min^{-1} (approx 30 km/h) CFD and measured values are within 10% of the maximum value. At 300 min^{-1} (approx 60 km/h) good agreement between CFD and measured results are shown, CFD predicts ventilation channel exits speed 18% lower than the measured value. At the maximum operating speed, 450 min^{-1} (approximately 90 km/h), the differences between measured and CFD results are within 25% of the

maximum value. CFD predictions do show lower velocities than those measured for the channel exit, however at the inlet higher velocities are predicted. CFD predictions show a large increase in inlet velocity between 300 and 450 min^{-1} . There is no obvious reason for the change in the rate of increase in velocity at this point and further analysis would be required to fully explain the irregularity.

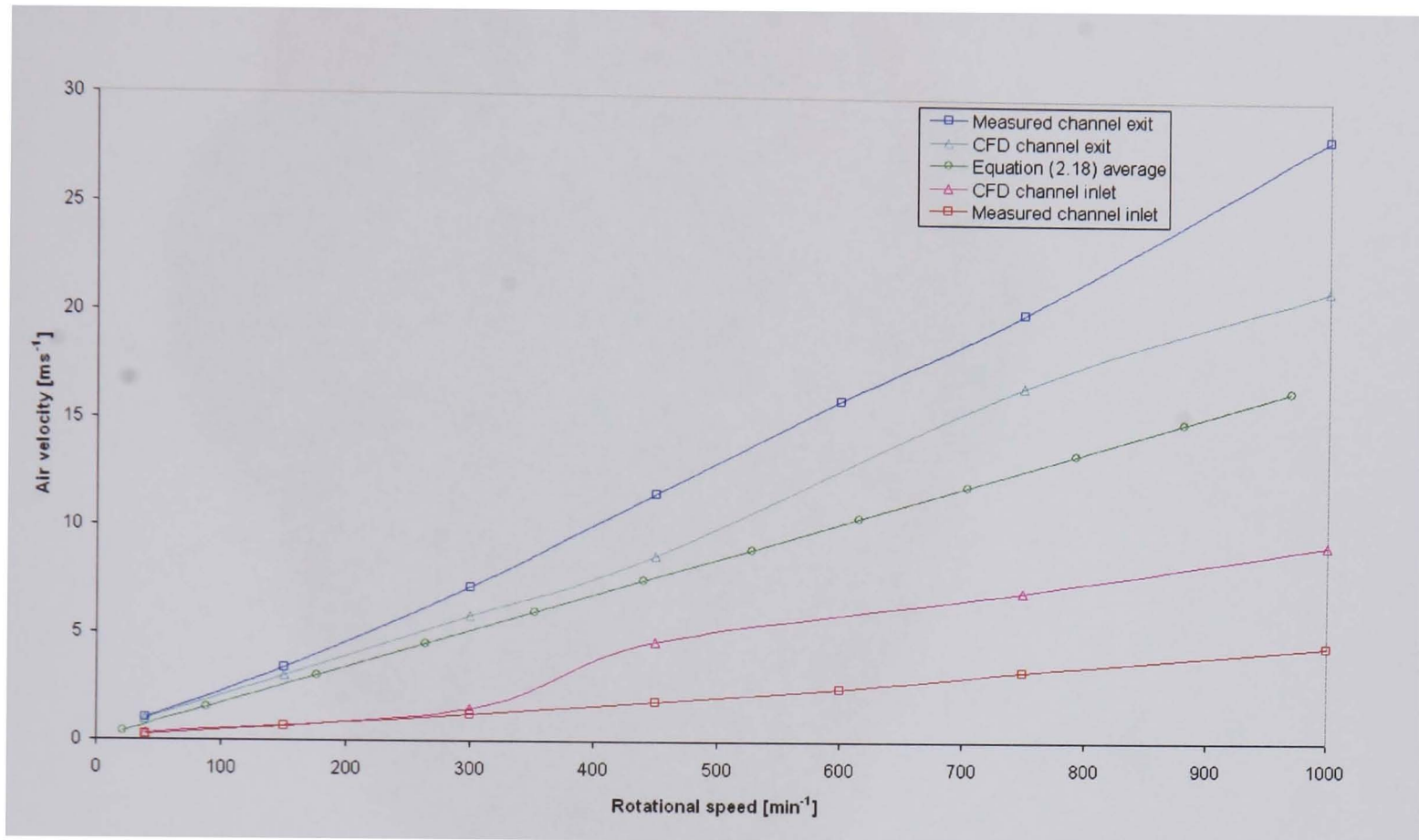
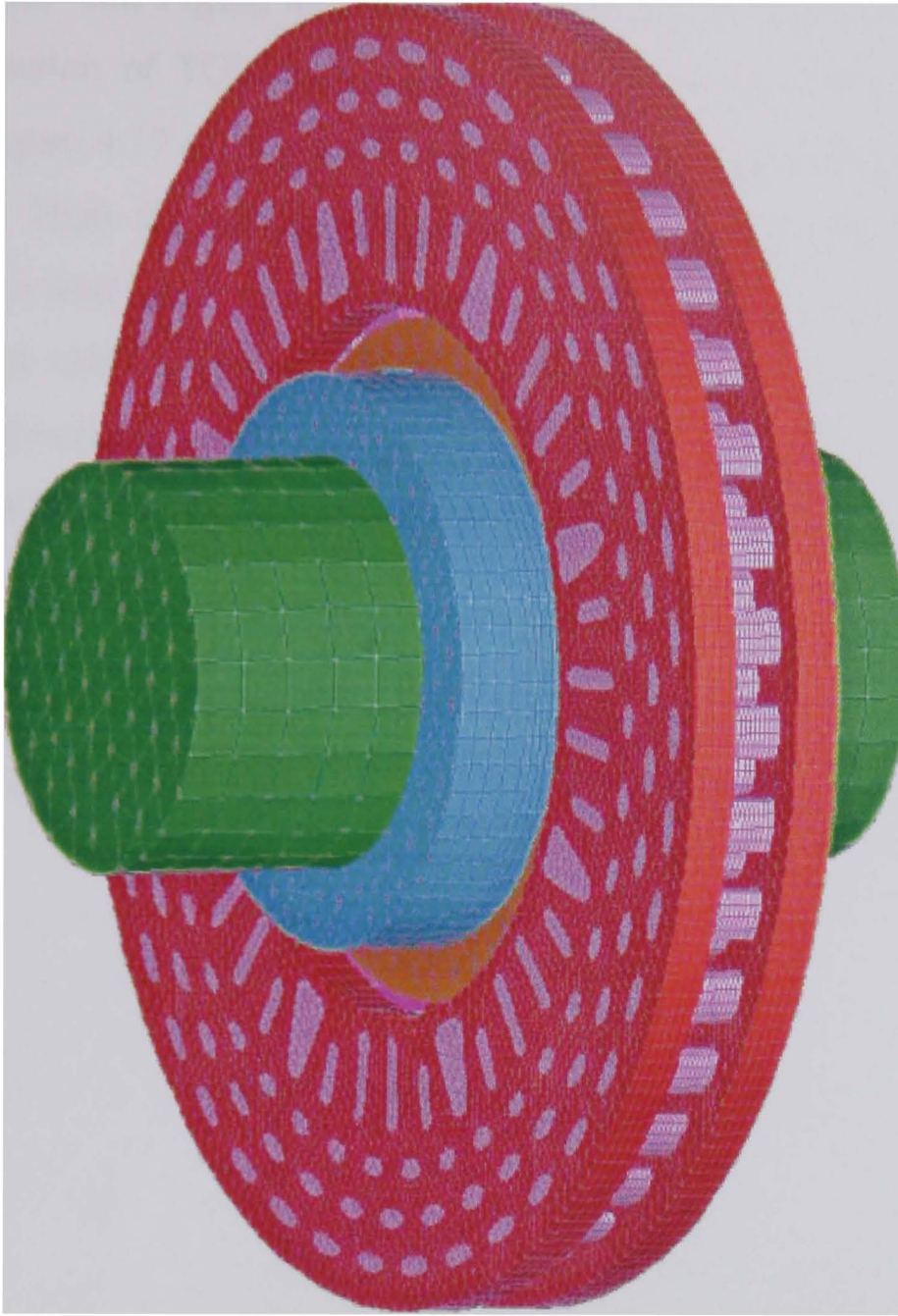


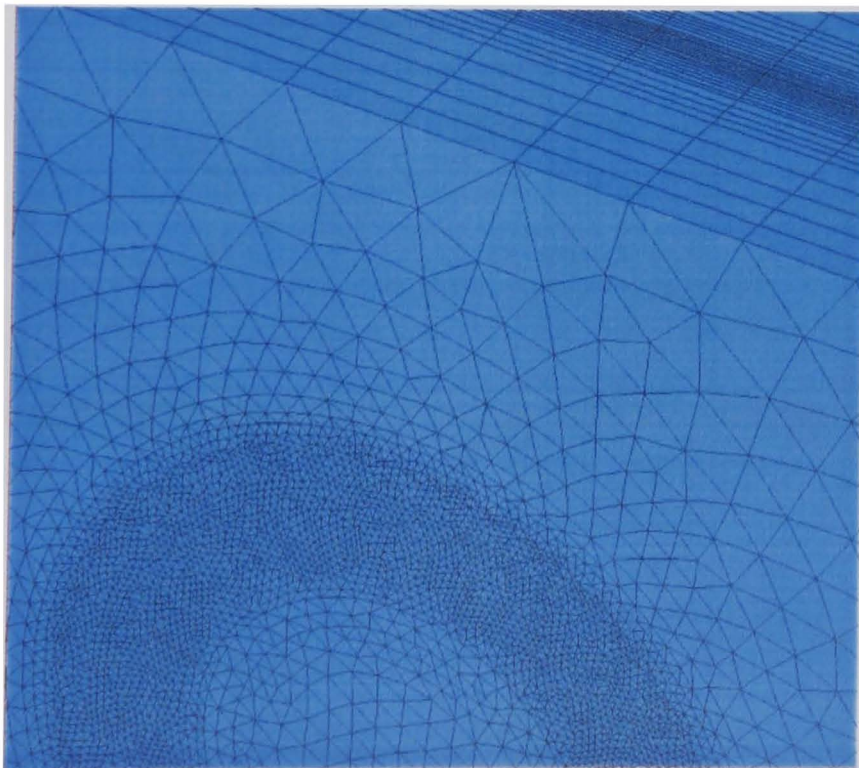
Figure 4.15 Ventilation channel air velocities; comparison of predicted and measured values for the standard radial vane CV disc

4.4.2.2 TGV Railway Brake Disc

CFD modelling has also been used to analyse the TGV railway disc. The same modelling methods described for the CV disc were used. Figure 4.16 shows the solid mesh (a) and fluid mesh (b). The mesh comprises of 90502 thin shell elements (modelling flow surfaces, vents and rotating air screens), 487840 solid elements modelling fluid and solid bodies and a total of 251043 nodes.



a)



b)

Figure 4.16 TGV railway disc (a) solid mesh and (b) CFD fluid mesh

Figure 4.17 and Figure 4.18 show velocity arrow plots of the airflow through the centre section of TGV disc rotating at 500 (Figure 4.17) and 1000 min^{-1} (Figure 4.18). Figure 4.17 clearly shows how the vane design influences the airflow through the disc. High air velocity is seen between the vane and front lug face area (a), stagnation and swirl can be seen at the back of the lug (b) indicating areas of inefficient vane design. It should be remembered that the disc must operate equally in both directions, making design improvements difficult. In Figure 4.18 the effect of the retaining ring on airflow is seen, with an uneven velocity profile across the ventilation channel.

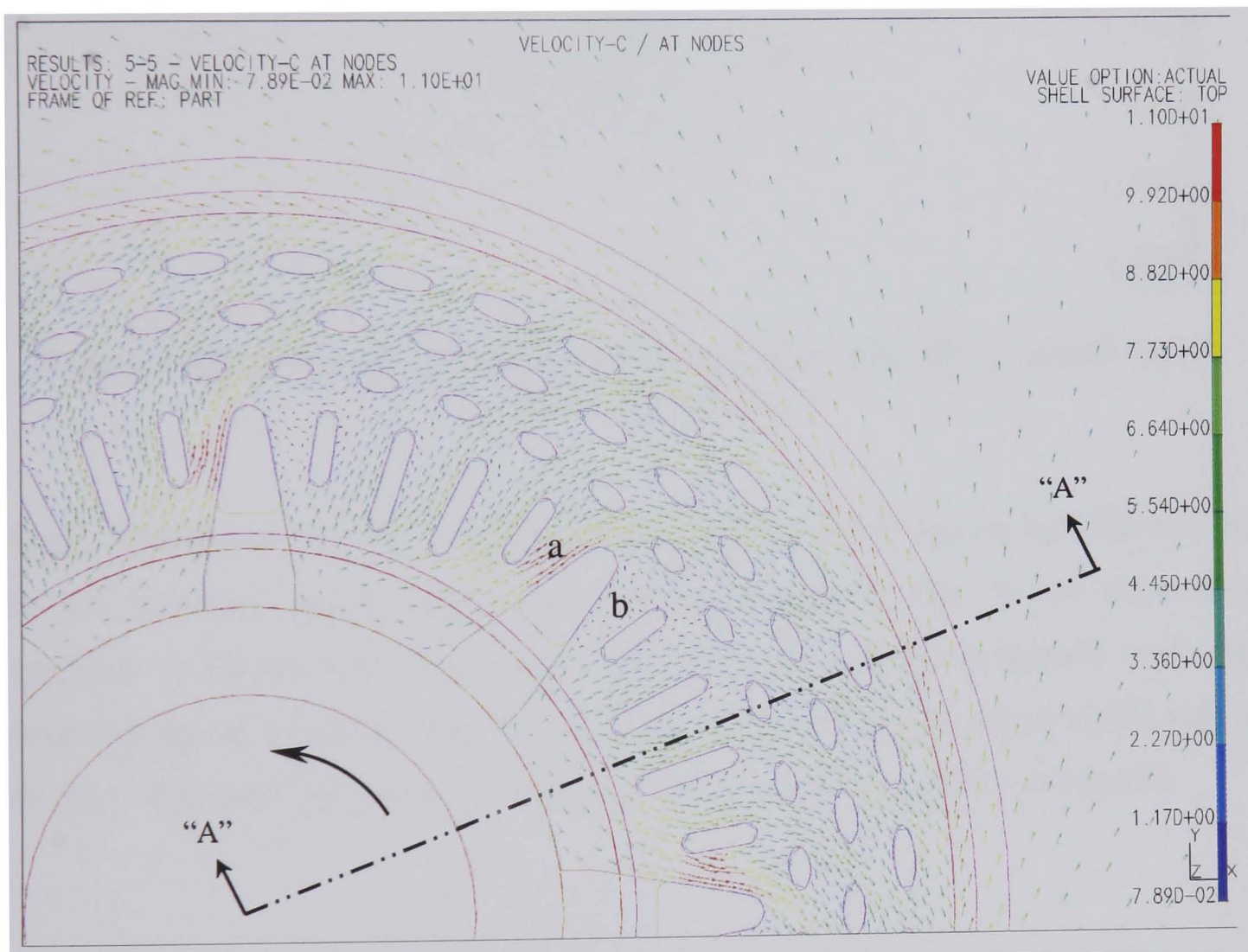


Figure 4.17 CFD velocity arrow plot of TGV disc rotating at 500 min^{-1}

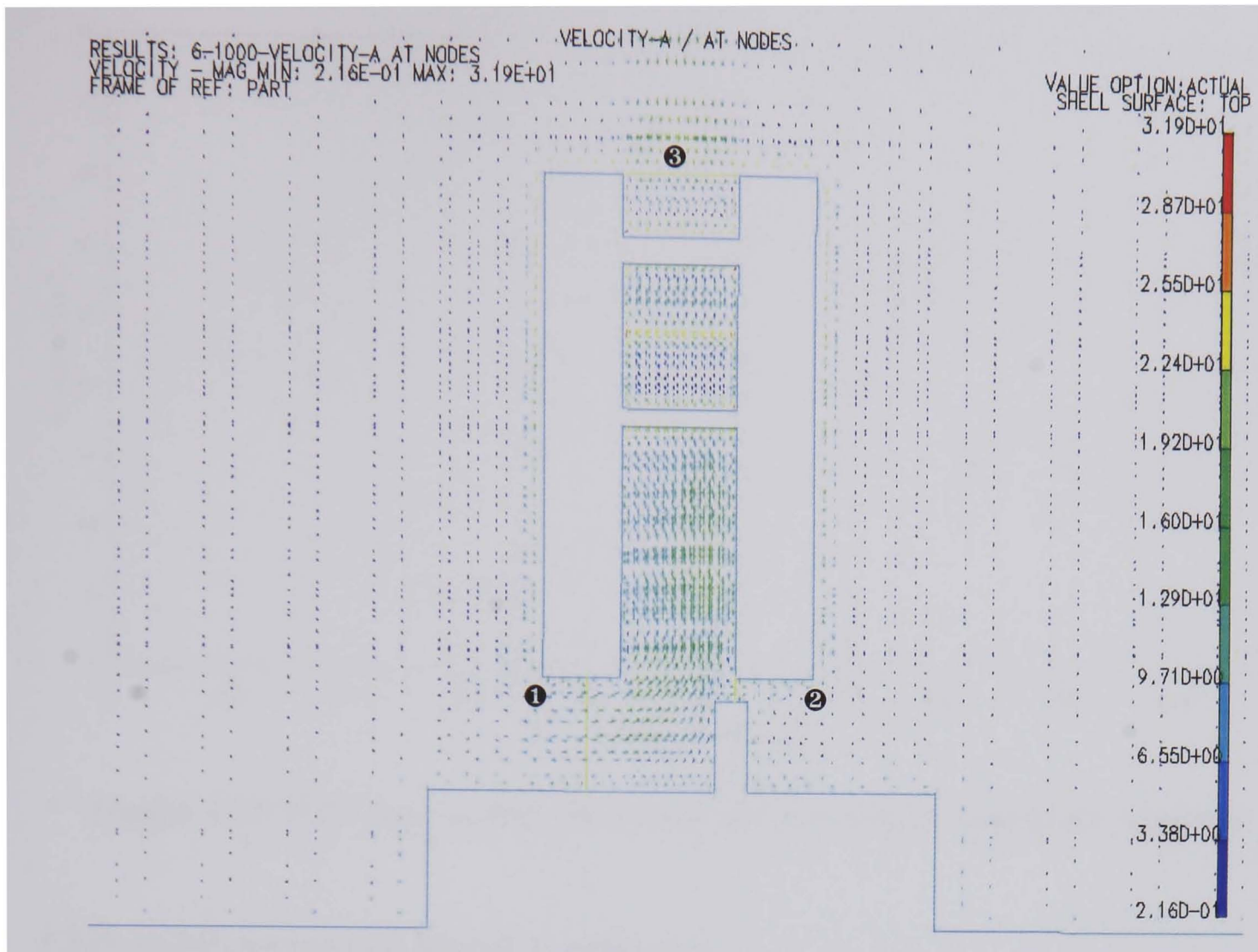


Figure 4.18 CFD arrow plot of TGV disc rotating at 1000 min^{-1} , section “A-A” (from Figure 4.17)

Figure 4.19 shows the TGV ventilation channel velocities predicted by CFD analysis for the rotational speeds ranging between 500 and 2000 min^{-1} in the three areas specified in Figure 4.18. Channel air velocities are increasing linearly with disc rotational speed. It can be seen that the fixing ring restricts air entering this side of the disc. Channel inlet speeds are typically 50% lower than channel exit speeds.

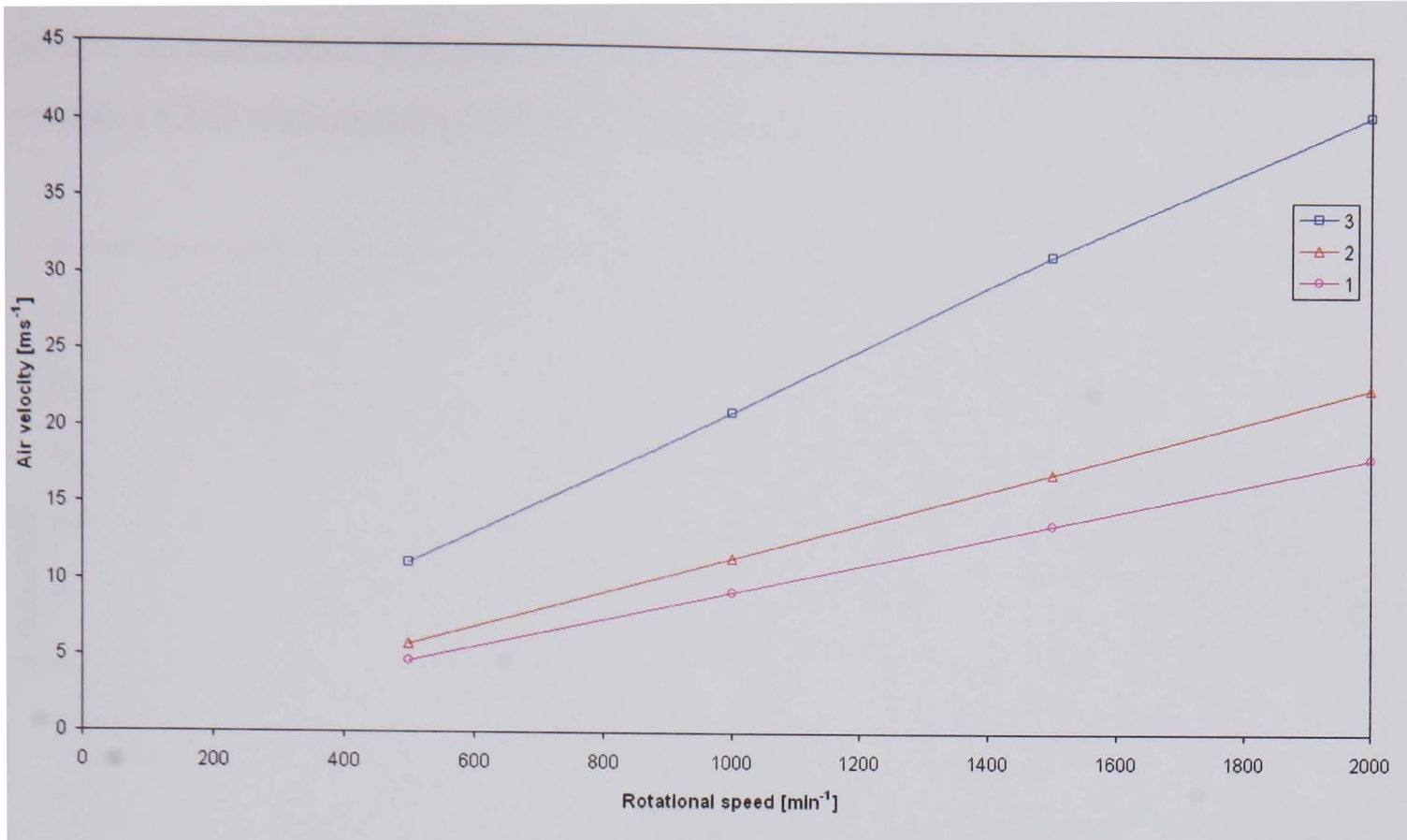


Figure 4.19 TGV railway disc CFD predicted ventilation channel air velocities

CFD and Experimental Results Comparison

Figure 4.20 shows the measured and CFD predicted air velocities for the TGV disc ventilation channel inlet and exit. CFD results predict exit speeds comparable to measured speeds; exit speeds are almost equal up to 1000 min^{-1} . At higher rotational speeds (above 1000 min^{-1}) predicted velocities are lower than those measured, at 1800 min^{-1} approximately 16%. CFD results predicted inlet speeds are approximately twice the measured value throughout the speed range. Comparable trends are predicted throughout the speeds range for the measured points and again good average velocity prediction is attained.

Due to the complexity of the TGV vane design, analytical formulae cannot be used to predict accurate channel velocities. Overall CFD channel exit velocity predictions are very close to measured values, for both the TGV and CV discs. However for both disc designs CFD inlet air velocities are approximately twice the measured speed. It can be seen in Figure 4.13 and Figure 4.18 that air approaching the ventilation channel inlet converges towards it. Because an instantaneous change in direction is impossible, streamlines do not become parallel until after entering the channel inlet, making airflow measurement difficult. At the channel exit airflow does not diverge until some distance away from the exit, the parallel streamlines providing good

airflow measurement. This phenomenon can explain the difficulties in comparing the complex CFD and measured channel velocity values.

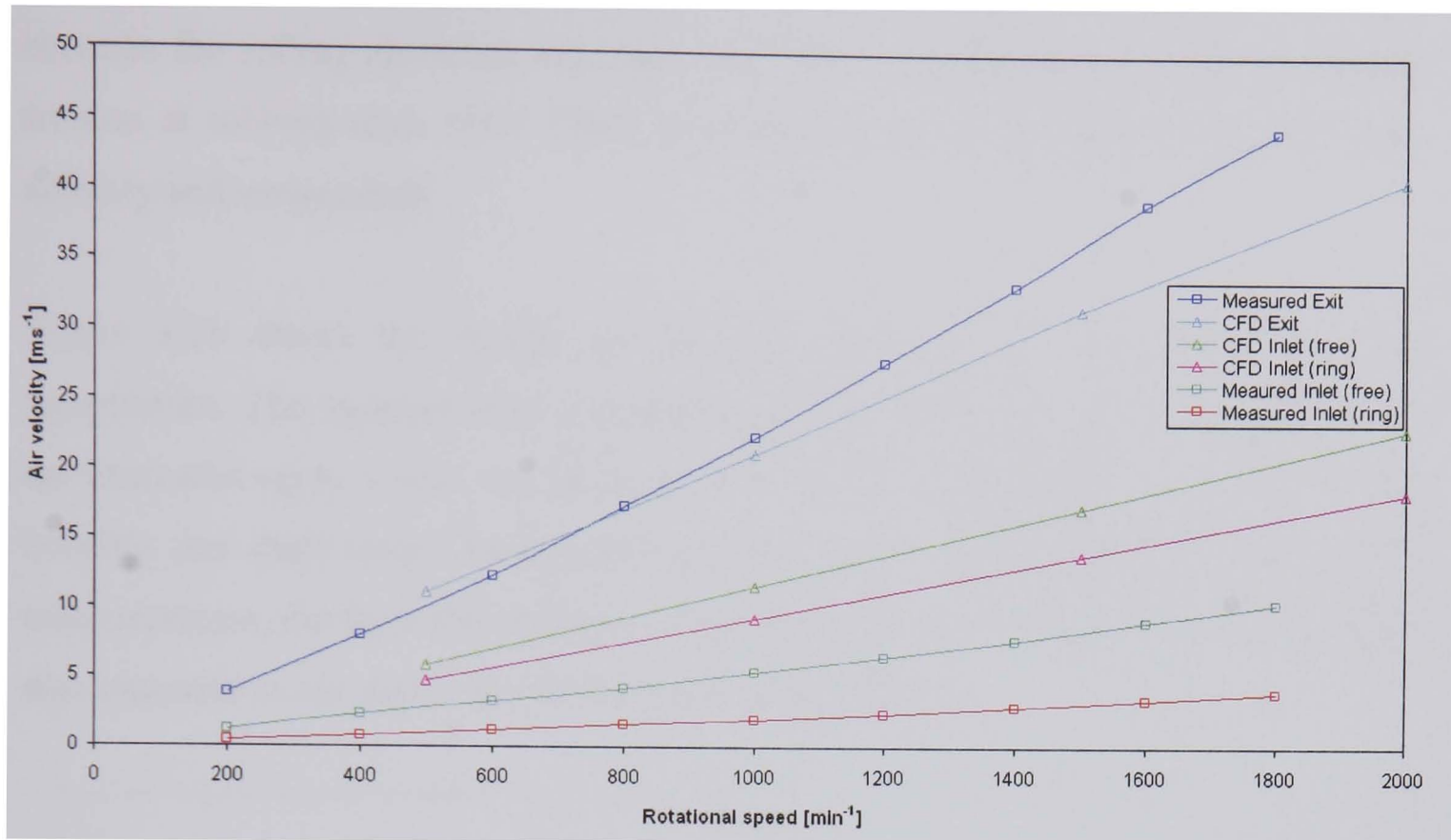


Figure 4.20 Ventilation channel air velocities; comparison of predicted and measured values for the TGV railway disc

4.5 Pumping Loss Measurement

The aim of the pumping loss measurement experiments is to determine vane design efficiency in providing high cooling but low energy consumption. The pumping loss of the disc is measured using the Spin Rig torque transducer, see Chapter 3. The shaft torque and rotational speed measurements are used to determine the power lost due to pumping and hydraulic losses (due to friction as airflow passes over the surface) in the ventilation channels (bearing and hydraulic losses from the other surfaces of the disc have also been measured). Various disc designs have been tested and pumping losses compared.

4.5.1 Experimental Procedure

The disc was rotated on the Spin Rig and the shaft torque measured at a fixed velocity to determine shaft power requirements. The torque transducer is located between the Spin Rig motor and shaft bearing, see Chapter 3. The transducer will

therefore measure the total torque, comprising of the pumping and hydraulic losses of the brake disc and bearing friction. The total resistance to rolling in a bearing is made up of the rolling and sliding friction in the rolling contacts, in the contact areas between the rolling elements and cage, the friction in the lubricant and the sliding friction of rubbing seals (SKF 1994). Bearing friction is a function of bearing load, velocity and temperature.

Figure 4.21 shows the change in Spin Rig shaft torque with bearing housing temperature. The measurement was taken with the standard CV disc. Measurements are from start-up to 1 hour and 20 minutes of running, after which time both bearing housing and shaft torque have stabilized. To ensure repeatability of pumping loss measurements, the Spin Rig must be run at maximum measurement velocity with the disc mounted to the shaft until the torque reading stabilizes.

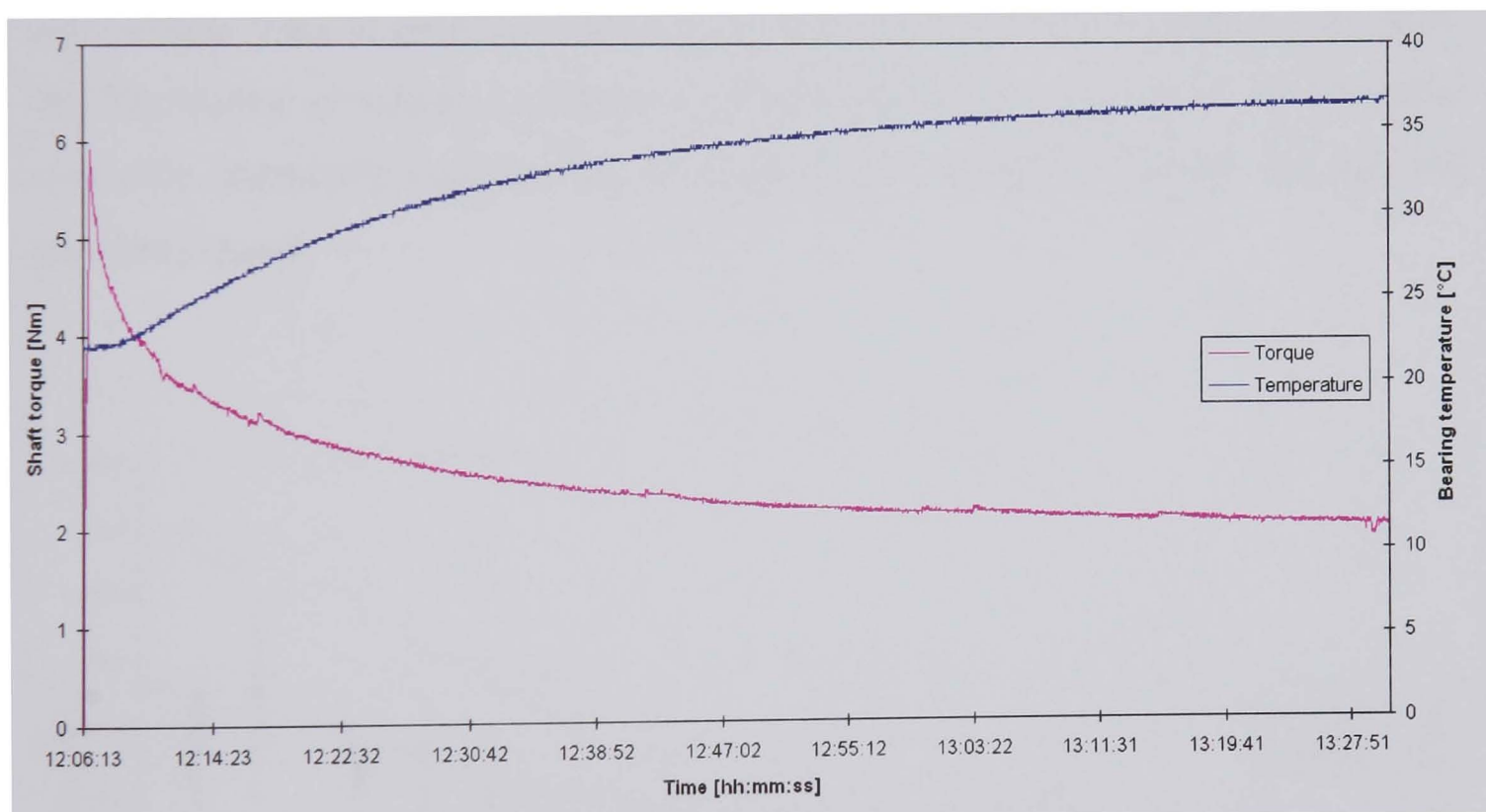


Figure 4.21 Stabilization of Spin Rig shaft torque and bearing housing temperature

To measure the losses incurred solely by the ventilation channels of the disc all tests consist of two measurements; one to measure the torque required to rotate the disc, through the velocity range, and the second, to measure the torque required to rotate the disc with the ventilation channels blocked, through the velocity range. The unblocked ventilation channel shaft power (Q_t) is subtracted from the blocked ventilation channel shaft power (Q_b) to derive the power lost by ventilation channel

pumping (Q_{pump}), see equation (4.31). The ventilation channel inlet and exit are blocked using industrial sealing tape.

$$Q_{pump} = Q_t - Q_b \quad (4.31)$$

When the shaft torque stabilized at the maximum test rotational speed, shaft torque and rotational speed data is logged at a frequency of 4 Hz for a period of 4 minutes. The velocity was then reduced by 100 min^{-1} and held for a further 4 minutes at constant velocity for data logging. The shaft rotational speed was reduced in increments of 100 min^{-1} to 0 min^{-1} . Figure 4.22 shows the torque and rotational speed of the shaft throughout the duration of the test for the TGV railway disc. It can be seen that the torque decreases with rotational speed and that the torque transducer is measuring some torsional vibrations. When the shaft rotational speed is reduced, the shaft torque reduces until the shaft has decelerated to the required rotational speed. The fluctuation of torque at constant rotational speed is a consequence of the motor controller constantly adjusting the frequency to the motor to maintain the required rotational speed.

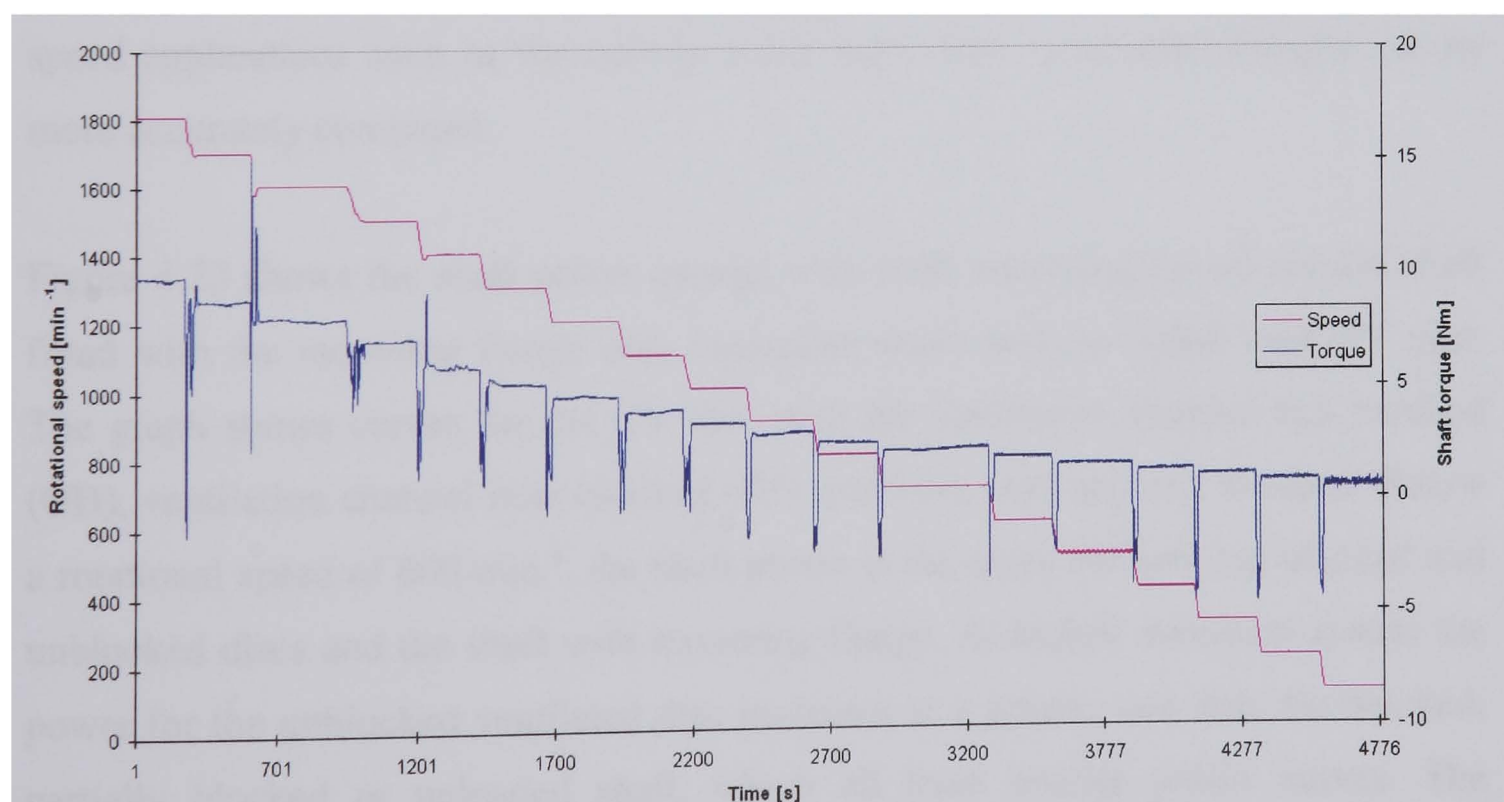


Figure 4.22 Spin Rig shaft torque and rotational speed measurement for a ventilated brake disc

The shaft power has been derived by multiplying the shaft torque by angular velocity, using the following equation:

$$Q_{shaft} = \frac{\pi\tau\omega}{30} \quad (4.32)$$

The torque and angular velocity used for calculation are average values taken at constant rotational speeds. A value for the shaft power is then derived for the range of rotational speeds.

4.5.2 Commercial Vehicle Brake Disc

Tests were carried out on four different ventilated CV brake disc designs, a standard radial vane disc, an anti-coning radial vane disc, a pillar vane disc and a curved vane disc (see Chapter 3 for disc design details). The velocity range of the CV disc brake is 0 to 450 min⁻¹, however measurements were taken at rotational speeds up to 1000 min⁻¹. It is apparent from the results shown in this section that pumping losses are very low at rotational speeds lower than 600 min⁻¹. The investigation of CV disc ventilation channel pumping losses at high rotational speeds are still valid as the findings can be applied to disc brake designs for vehicles with higher rotational speed applications such as the railway brake disc. Also, ventilation designs can be more accurately compared.

Figure 4.23 shows the shaft power change with shaft rotational speeds for the shaft fitted with the mounting flange only (unloaded shaft) and the radial vane CV disc. The graph shows curves for the CV disc with the ventilation channel exit blocked (OD), ventilation channel inlet blocked (ID), and both inlet and exit blocked. Below a rotational speed of 600 min⁻¹, the shaft power is the same for both the blocked and unblocked discs and the shaft with mounting flange. At higher rotational speeds the power for the unblocked ventilated disc increases at a greater rate than the blocked, partially blocked or unloaded shaft, which all have similar power curves. The maximum power required by the unblocked ventilated disc is 1 kW at 1000 min⁻¹. The shaft with flange requires similar power as the blocked channel disc (500 W

maximum) showing that the ventilation channel pumping loss is the primary mode of power loss.

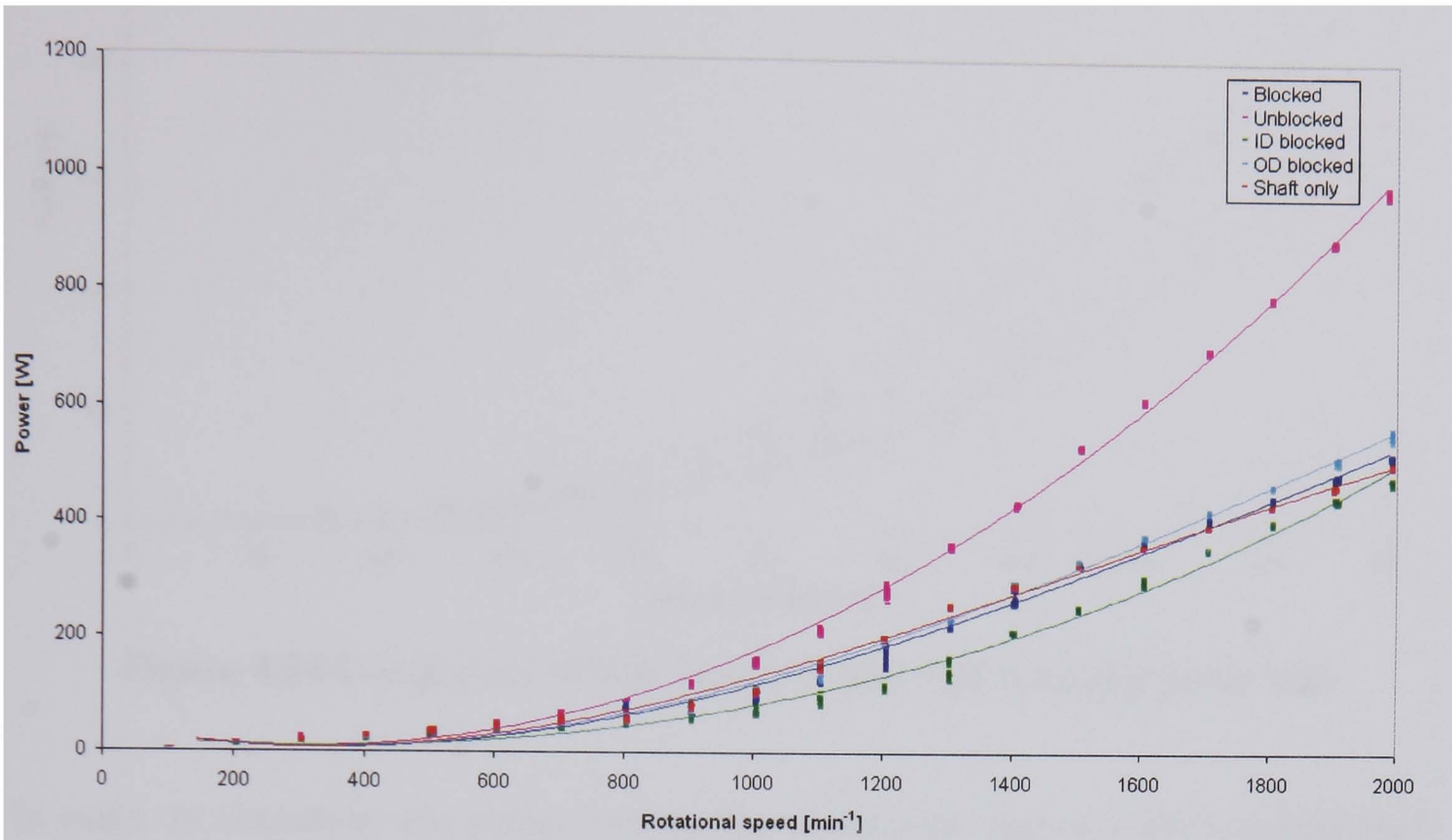


Figure 4.23 Pumping power curve for the standard CV disc channels blocked, unblocked and shaft with mounting flange

Figure 4.24 shows the shaft power change with rotational speed for the range of CV disc vane designs (unblocked). At rotational speeds over 500 min^{-1} , there is a clear distinction between the designs, the standard radial vane design showing the highest power requirement. The curved vane requires the second highest amount of power followed by the anti-coning disc. The pillared vane design requires the least amount of power for rotation. Less air is directed radially through this disc design reducing surface pressures. However, this is at the expense of airflow, as the disc will pump less without continual vanes, to guide the air and generate a centrifugal force on the air particles. The second lowest pumping loss is provided by the anti-coning disc. The channel inlet is reduced compared to the other designs, reducing the volume of air pumped by this design of disc. Maximum shaft power values range from 1 kW for the standard radial vane design to 650 W for the pillar vane design.

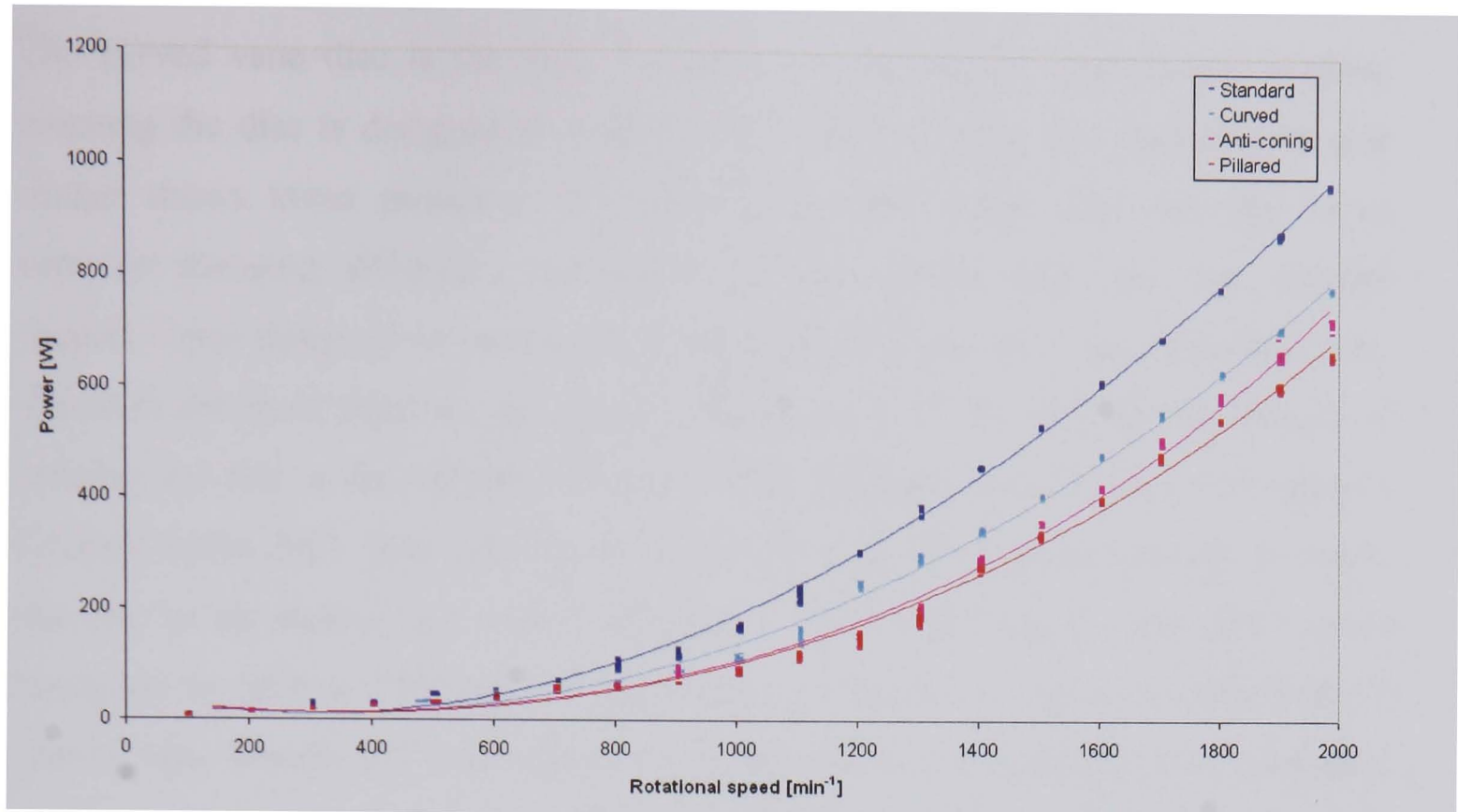


Figure 4.24 Comparison of ventilated CV disc total pumping power loss

In order to determine the power lost by the ventilation channels the required shaft power of the unblocked disc was subtracted from the blocked disc, the results are shown in Figure 4.25. The shaft power difference for each vane design is now more distinct, the standard radial vane design requiring the most power, 450 W at 2000 min^{-1} . The curved disc requires a power of 275 W, the anti-coning radial disc 250 W and the pillared vane disc 175 W. A large difference in power requirement is seen between the standard radial vane and pillar vane design, with the pillar disc requiring 40% of the power required by the standard radial vane disc.

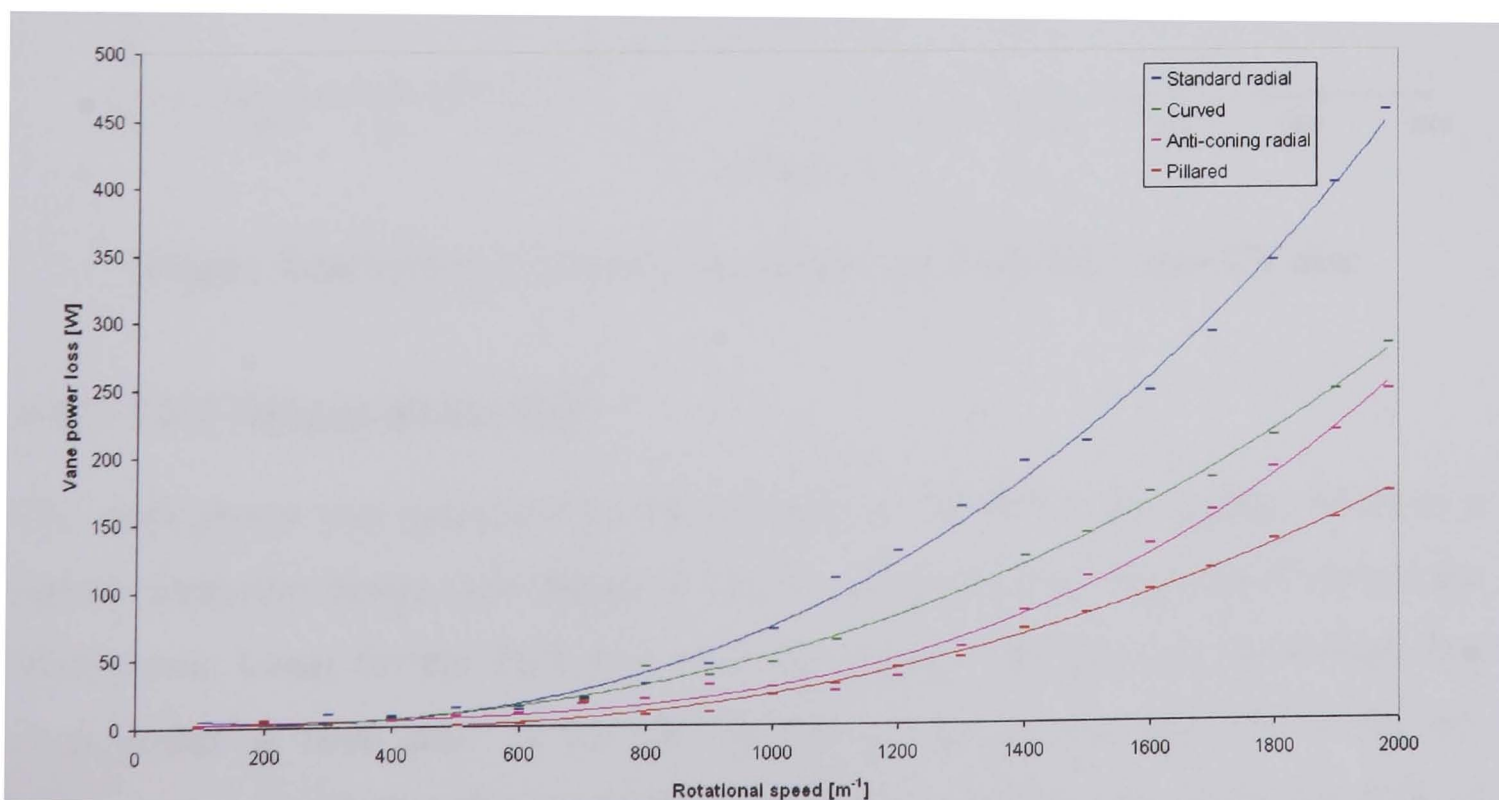


Figure 4.25 Comparison of ventilated CV disc channel power loss

The curved vane disc is the only ‘handed’ disc out of the vane designs studied, meaning the disc is designed to rotate in one direction only. The curved vane disc design shows lower pumping loss than the standard radial vane disc due to its superior pumping efficiency characteristics. The curved vane disc has aerofoil shaped vanes designed to operate as a backward curved (BC) vane centrifugal fan, which is the most efficient fan design (see Figure 4.1). To examine the effects of rotating the disc in the opposite direction to its designed direction, i.e. running as a forward curve (FC) vane fan, Figure 4.26 shows the shaft power required to rotate the disc in the normal and reverse direction. The curves show that the shaft power increases by 30% at 2000 min^{-1} when the disc is rotated in the reverse direction. It can be seen that the FC vane design has approximately the same power requirement to the radial vane design, when compared to Figure 4.25 (also shown by Figure 4.1).

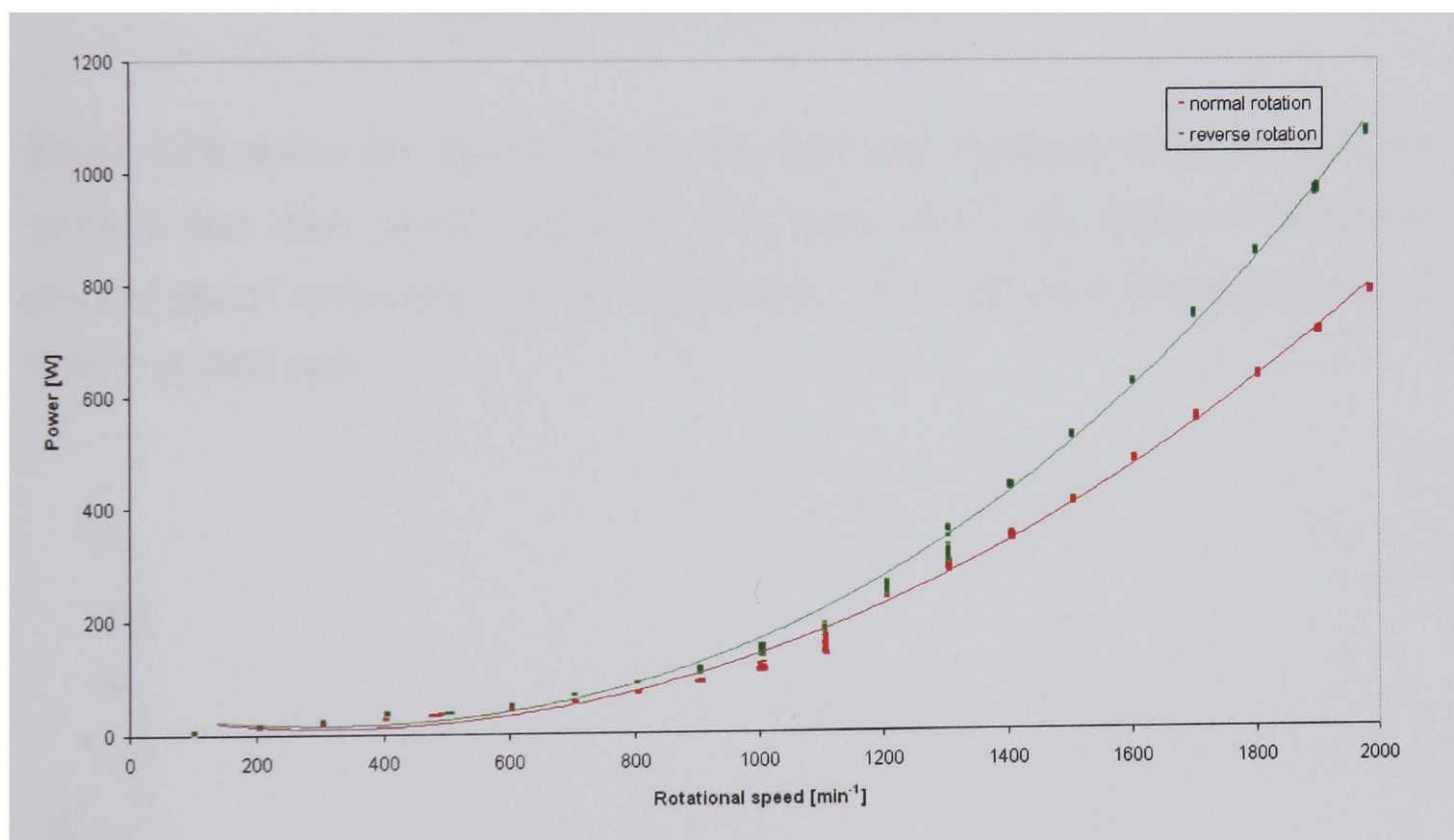


Figure 4.26 Effect of reverse rotation of the curved (BC) vane CV disc

4.5.3 TGV Railway Brake Disc

The shaft power was measured for the rotation of the TGV railway disc, which is a radial vane/pillar design (see chapter 3, for the design details). Figure 4.27 shows the shaft power losses for the TGV disc with the channels blocked and unblocked. The shaft power at 1800 min^{-1} is 1.9 kW for the unblocked disc and 950 W for the blocked disc, suggesting that ventilation channel pumping is responsible for 50% of the power loss at 1800 min^{-1} .

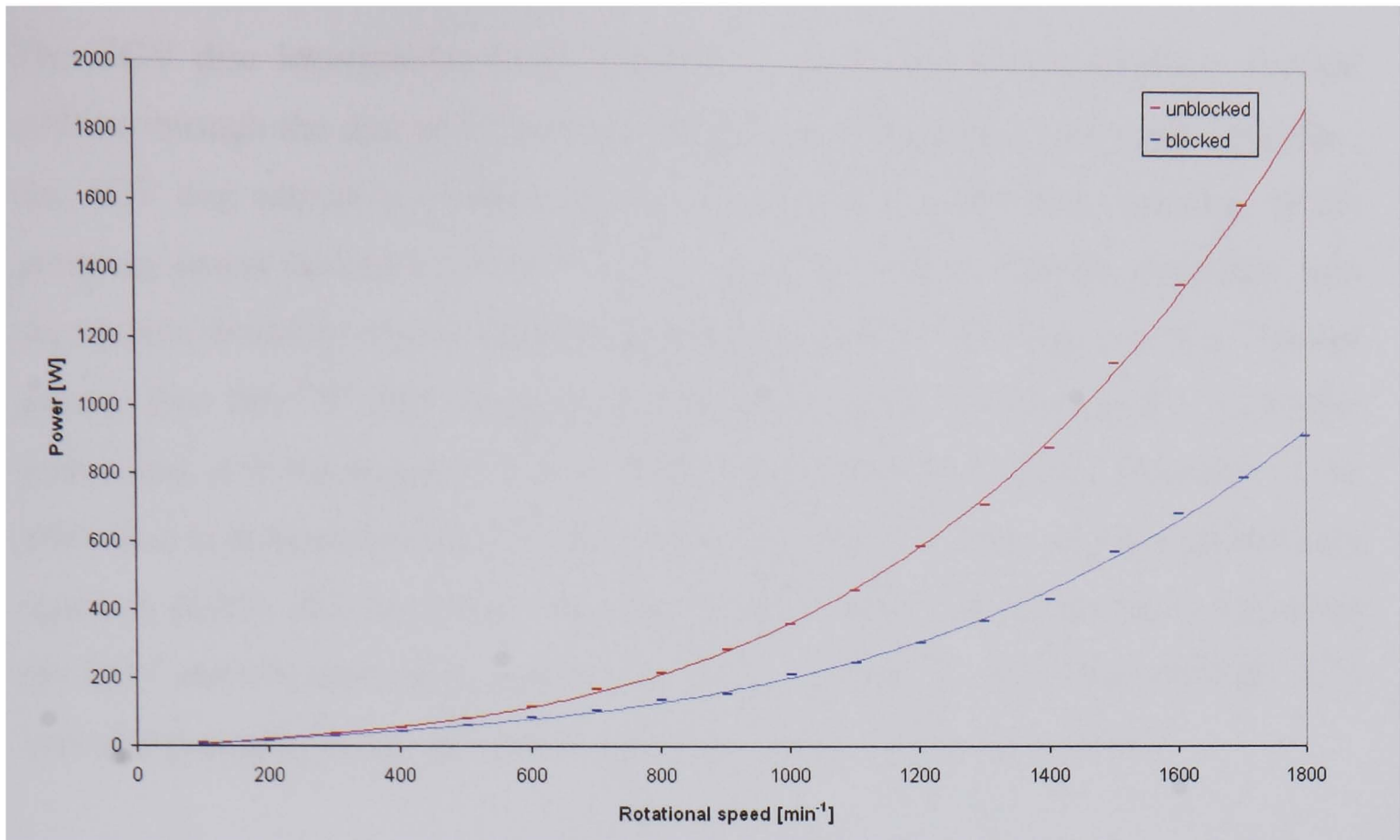


Figure 4.27 TGV disc total power loss

Figure 4.28 shows the shaft power for the TGV radial/pillared vane disc with the blocked disc shaft power subtracted. The curve shows the resultant ventilation channel power increasing with rotational speed. The maximum power produced is 970 W at 1800 min⁻¹.

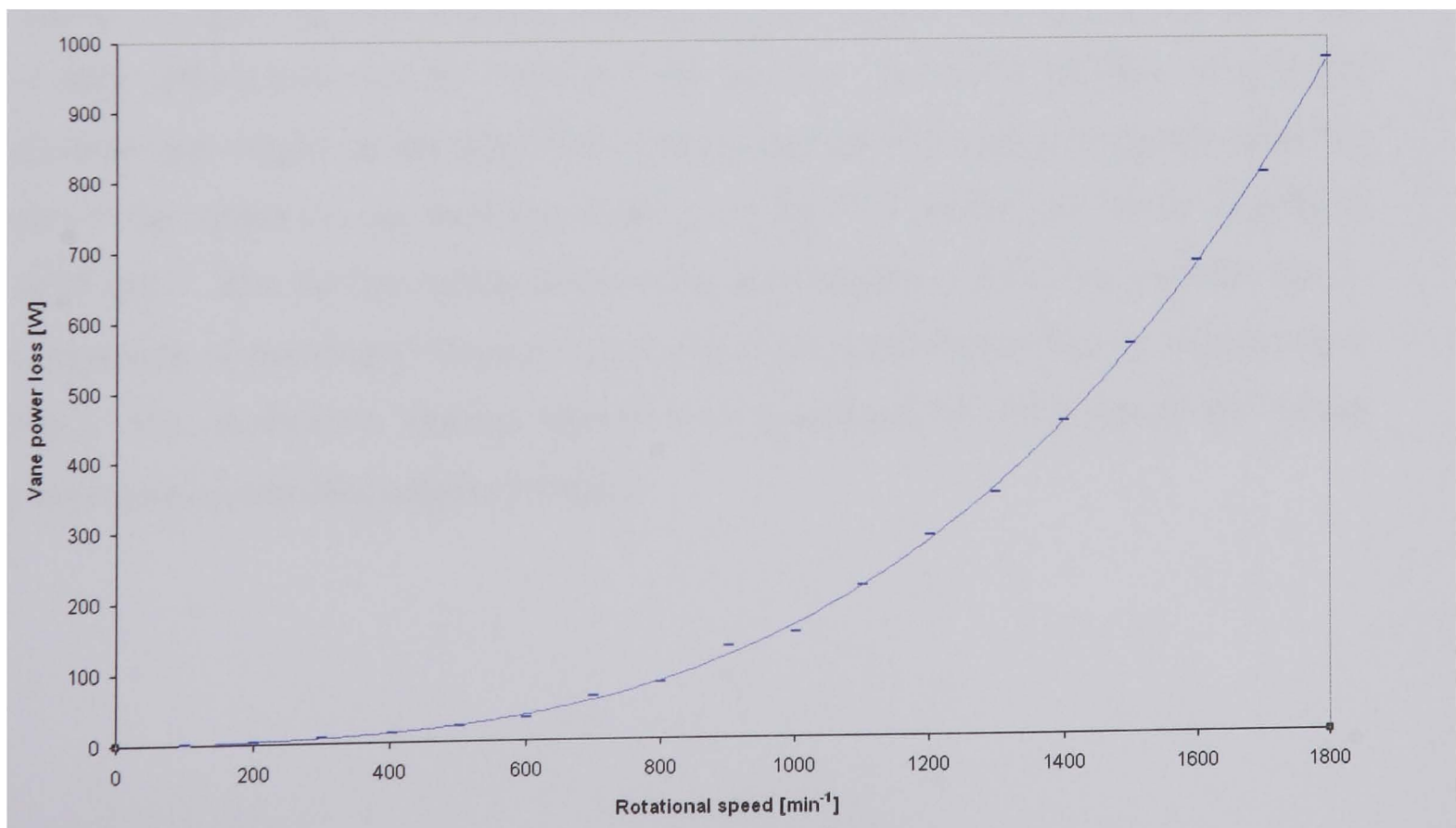


Figure 4.28 TGV disc ventilation channel power loss

The TGV disc incorporates a combination of radial vanes and pillars to provide airflow through the disc and reduce pumping losses. Because of the larger diameter, the TGV disc cannot be directly compared with the CV disc. From equation (4.25) pumping power increases to the 5th power of the ratio of the outside diameters, and therefore it would be expected that the pumping loss of the TGV disc would be 7 times greater than the CV disc. From the results presented in this section the TGV disc power loss is in the region of 3 to 4 times greater than the CV disc. Pumping of the TGV disc is reduced because the inside diameter also increases, not accounted for by equation (4.25), also the radial vanes are not full length (see Figure B8). Comparing the TGV and CV disc pumping losses it can be said that the TGV disc performs very well and pumping losses are relatively low for such a large diameter disc.

4.6 CFD Pumping Loss Prediction

To predict the pumping losses of ventilated disc designs a simulation method was developed. The SDRC I-DEAS ESC models used to determine airflow characteristics (described in Section 4.4.3) have been used for this. During model simulation the flow element mesh adapts and opens around the embedded flow surface creating a 3-D obstruction to fluid flow. Thin shell elements on the surface of the solid mesh are defined as spinning flow surfaces. Moving surfaces add momentum to the fluid due to drag effects between the fluid and the surface. The CFD program outputs the pressure and torque on spinning flow surfaces and for illustration purposes Table 4.1 shows the torque on the spinning surfaces of the TGV brake disc when rotating at 1000 min⁻¹. The Surface Inside Screen data corresponds to the vane surfaces, the z-component of the torque along the spin axis is the shaft torque due to vane pressure force. The ventilation channel power loss is derived by multiplying the torque component by the disc angular velocity.

Table 4.1 CFD output: torque on TGV spinning flow surfaces (1000 min^{-1})

| Torques on Spinning Flow Surfaces | x-comp | y-comp | z-comp | R |
|-----------------------------------|------------|------------|------------|-----------|
| ROTATING SURFACES | | | | |
| CG location (m): | 6.192E-08 | 2.170E-08 | 9.136E-04 | - |
| Pressure Force (N): | 2.204E-03 | 1.336E-03 | 4.390E-01 | 4.390E-01 |
| Torque along spin axis (Nm): | 0.000E+00 | 0.000E+00 | 1.430E-01 | 1.430E-01 |
| Torque normal to spin axis (Nm): | 1.961E-04 | -6.232E-05 | 0.000E+00 | 2.058E-04 |
| SURFACE INSIDE SCREEN | | | | |
| CG location (m): | 3.188E-08 | -9.136E-09 | -3.035E-03 | - |
| Pressure Force (N): | -3.484E-02 | 5.522E-03 | 3.661E-01 | 3.678E-01 |
| Torque along spin axis (Nm): | 0.000E+00 | 0.000E+00 | 2.028E+00 | 2.028E+00 |
| Torque normal to spin axis (Nm): | -1.824E-04 | 3.398E-05 | -4.057E+00 | 4.057E+00 |

4.6.1 Commercial Vehicle Brake Disc

CFD has been performed on the standard CV disc and pumping losses determined for the entire disc surface. Figure 4.29 shows the losses for rotational speeds up to 2000 min^{-1} (bearing losses are not modelled). The power increases with the third power of rotational speed agreeing with theory set out in Section 4.2.2. It can be seen that the vane surfaces account for almost all the pumping losses. The remaining disc surface account for only 1 to 2% of losses. The analysed rotational speed range coincides with the pumping loss measurement discussed in Section 4.5.2.

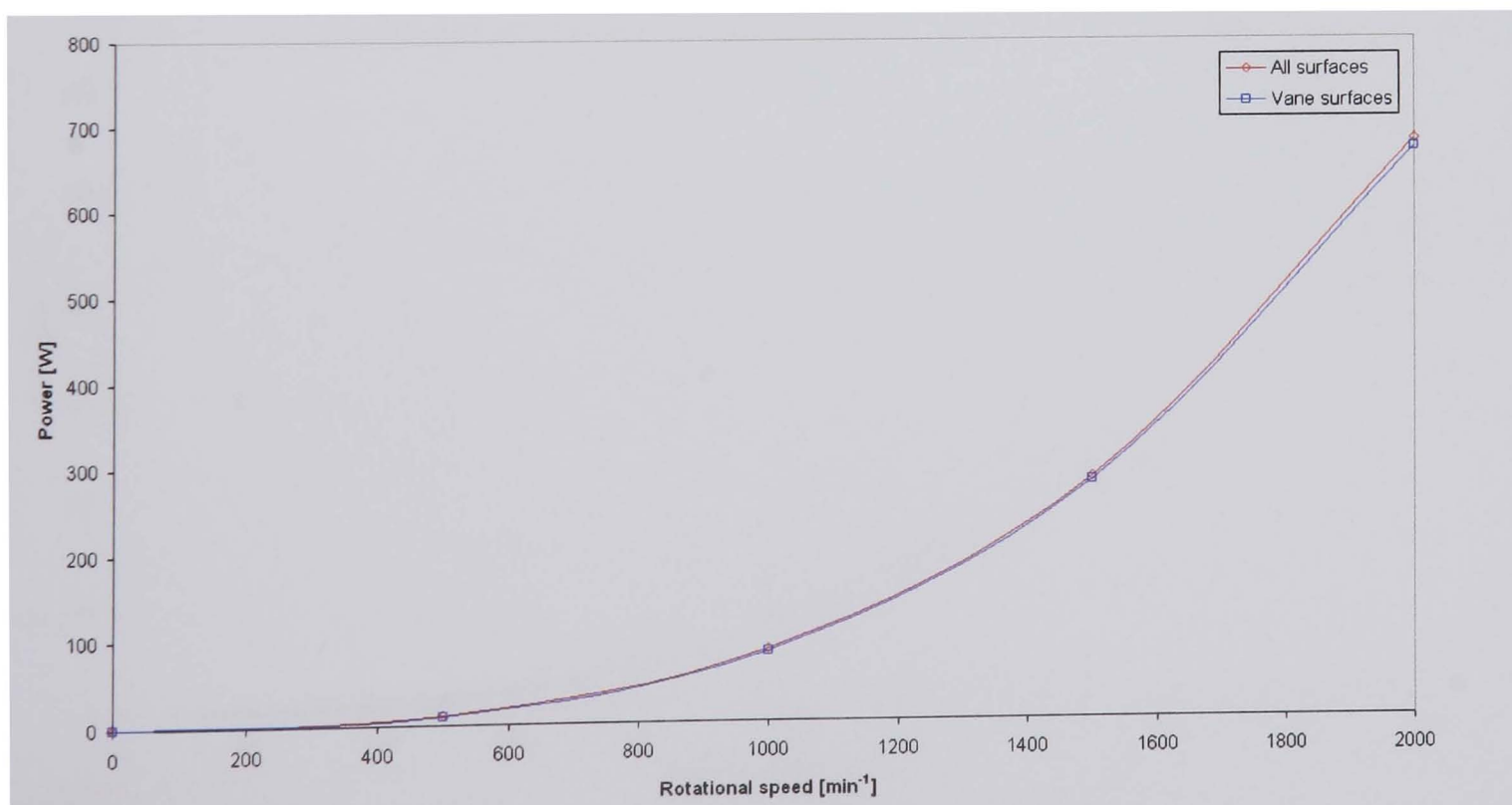


Figure 4.29 Standard CV disc CFD predicted power loss

Figure 4.30 shows a comparison of predicted and measured standard radial vane CV disc ventilation channel pumping loss. Good agreement of results was achieved with experimental values and theory. At 500 min^{-1} the predicted and measured values are in excellent agreement. Good agreement is shown at 1200 min^{-1} ; CFD values are 13% higher than measured and theoretical values. It can be seen that the theoretical results derived from equation (4.17) are higher than measured values above 1200 min^{-1} ; a maximum of 20% at 2000 min^{-1} . CFD values at 2000 min^{-1} are 16% higher than theoretical values and 30% higher than measured values. The lower measured pumping losses can be due to a reduction in airflow through the disc caused by crowding of the air (choking) in the ventilation channels and the inlet at high rotational speeds.

CFD provides detailed local air pressure values for the ventilation surfaces as well as airspeeds. Pumping power is a resultant of these factors, which generates torque about the axis of rotation. With the CFD data areas responsible for increasing power requirements (pumping losses) can be highlighted and design improvements can be investigated. Unfortunately restrictions (computing resources and time) prevented more CFD investigation into this phenomenon. Reliable prediction within the operating range gives confidence in comparing designs.

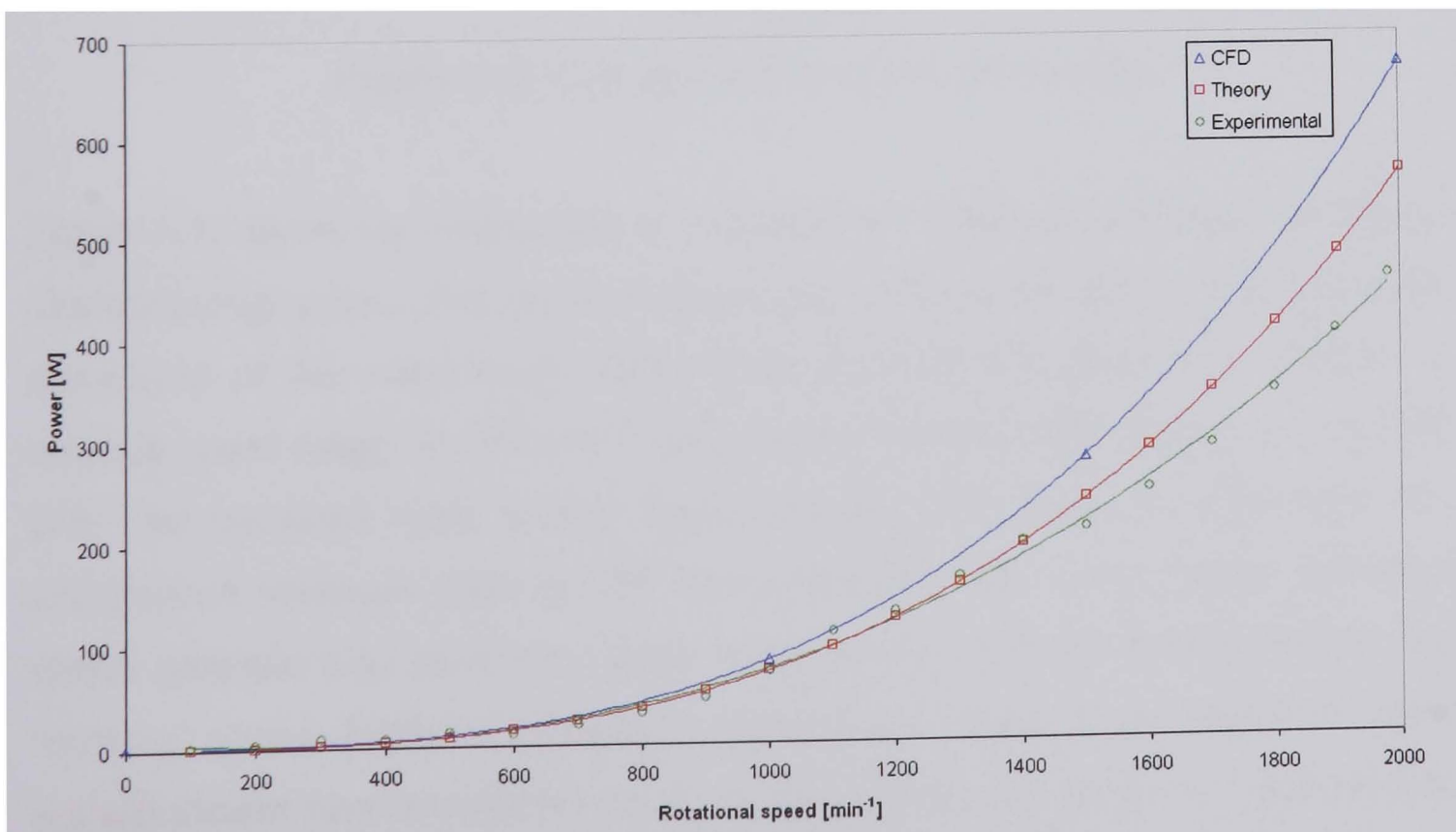


Figure 4.30 Comparison of predicted and measured standard radial vane CV disc ventilation channel pumping loss

4.6.2 TGV Railway Brake Disc

CFD analysis on the TGV disc has produced ventilation channel pumping loss results throughout the disc operating rotational speed. Figure 4.31 shows the power loss of the TGV disc by hydraulic losses of all the disc surfaces and the vane surfaces only. At maximum rotational speed (2000 min^{-1}) the power loss is 1.8 kW for all rotating surfaces, the ventilation channel surfaces account for 95% of the losses. Again, the power increase trend is to the third power of the rotational speed, agreeing with fan theory (Section 4.2.2).

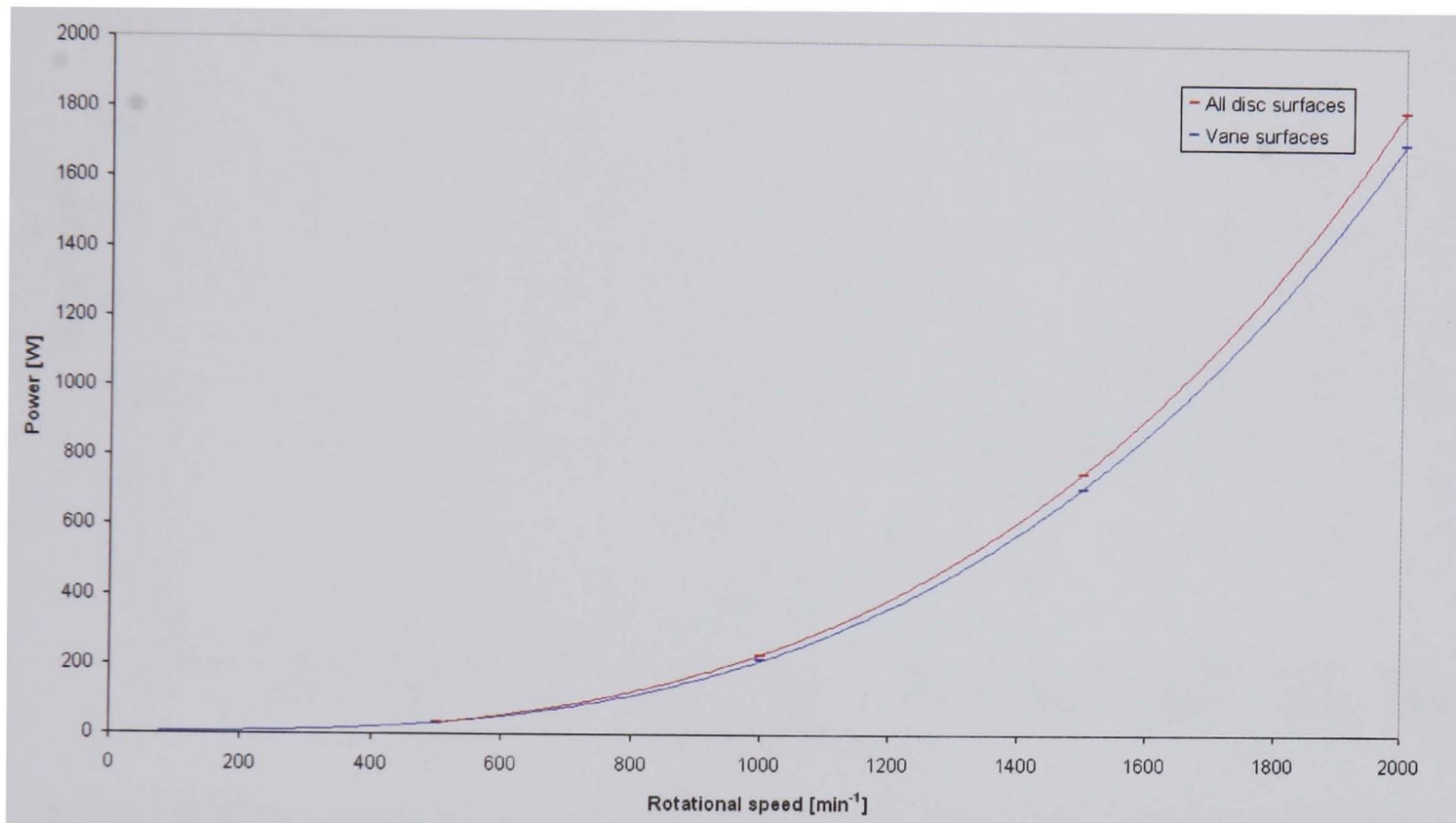


Figure 4.31 TGV disc CFD predicted power loss

Figure 4.32 shows the comparison of predicted and measured TGV disc ventilation channel pumping loss. The analytical procedure could not be implemented due to the complexity of the vane design. CFD values show good correlation at the low to medium speed range. At 700 min^{-1} values show less than 13% difference. At 1200 min^{-1} the measured value is 22% lower than the CFD value. At 2000 min^{-1} the extrapolated measured value is 23% lower than the CFD value. Higher rotational speeds generate over predicted values where airflows become more turbulent and ‘choking’ occurs. Predicted pumping loss trends are similar to the measured values and adjustment factors could be put in place to modify the predictions and provide good results at higher rotation speeds. The CFD analysis has been subject to computing limitations, which restricted the size and density of the air volume

element mesh surrounding the disc. The CFD analyses may not be accurately predicting the airflow through the complex vane and pillar disc ventilation design. A larger air volume and finer mesh may improve the CFD TGV disc results. Unfortunately restrictions (computing resources and time) prevented more CFD investigation into this phenomenon. But the good correlation of results has proven the CFD method to be a good practical tool.

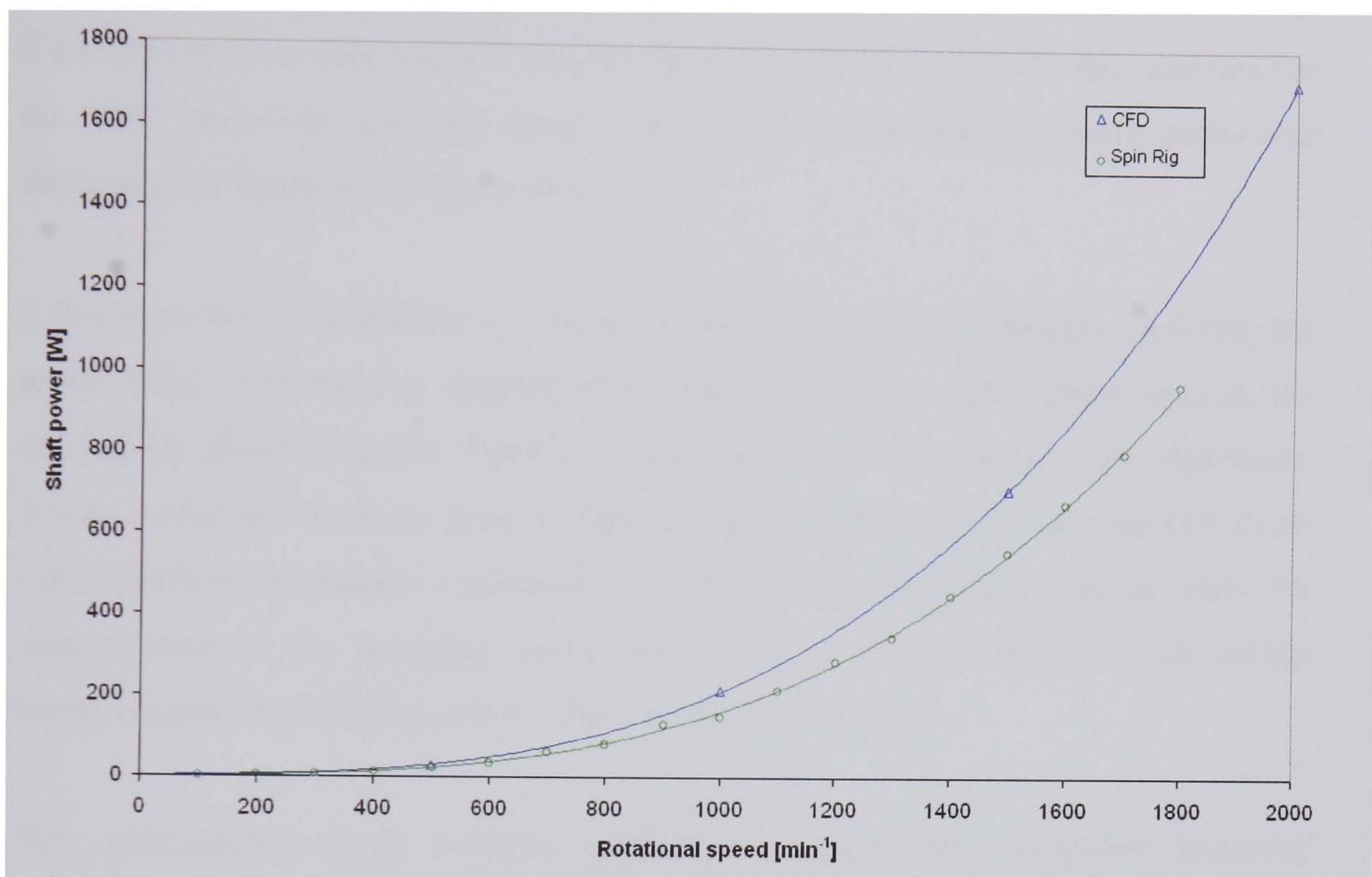


Figure 4.32 Comparison of predicted and measured TGV disc ventilation channel pumping loss

4.7 Summary

The ventilated brake disc provides increased convective cooling by pumping air through the cooling channels of the disc. The air flowing through the disc dissipates heat by forced convection, expelling heated air from the channel exit.

Disc ventilation channel velocity vector diagrams have been analysed to determine the velocity components of airflow and predict the power requirements for disc rotation. Experimental analysis included the use of a hotwire anemometer device to measure air velocities at specific areas of the disc and wheel assembly including the ventilation channel inlet and exit for a range of disc designs, allowing pumping

performance to be analysed. Torque measurements were also taken to determine the amount of power required to rotate ventilated discs. A range of disc designs were measured and compared with non-ventilated designs. CFD models have been developed to predict airflow around ventilated discs. The CFD models predicted the air velocity and pressure around and on the surfaces of the disc, which allowed the prediction of the power required for rotation. Over 20 Spin Rig pumping loss tests were performed on six disc designs involving 20 days of laboratory experiments. Two CFD models were created, one for the standard radial vane CV disc and one for the TGV frequently stopping disc, a total of 10 simulation runs were performed requiring 200 hours of computer time.

It has been shown that there is a range of ventilation channel designs available for brake discs, with varying degrees of pumping efficiency, their characteristics are defined by given formulae. Results of Spin Rig tests have shown that significant power is required to rotate discs at high speeds and also allowed comparisons to be made between the designs considered. A procedure has been developed to allow the measurement of the pumping losses due to the ventilation channels, eliminating losses incurred by bearings and the outer surfaces of the disc.

The comparisons made between predicted analytical and measured pumping requirements showed very good agreement for the radial vane disc. The comparisons made between the CFD and measured results are also in very good agreements for the CV and TGV disc airflow and pumping losses. The developed methodologies provide accurate and fast airflow and power requirement predictions that are suitable for comparing disc ventilation designs in an industrial environment.

Convective Heat Dissipation

5.1 Theoretical Background

Convection is the main mechanism of heat dissipation from brakes in most vehicle service conditions (Newcomb and Spurr 1967) and detailed experimental and numerical analysis of this mode of heat transfer is discussed in this chapter. Convection is a process of heat transfer through a fluid caused by fluid motion and conduction from a surface. The fluid motion enhances the heat transfer since it brings cooler air into contact with warmer air. The rate of heat transfer is increased by the increase in air velocity.

There are two types of convection, free (or natural) and forced, classified by air motion initiation. Natural convection results from the tendency of most fluids to expand when heated, thus becoming less dense and rising because of the increased buoyancy. Forced convection involves the transport of fluid by external means, such as a fan or pump. Forced convection is also classified as external or internal, depending on whether the fluid is forced over a surface or through a channel.

The rate of convective heat transfer (Q_{conv}) is proportional to the temperature difference of the surface and the air ($T_s - T_\infty$), the convective heat transfer coefficient (h_{conv}) and the surface area dissipating heat (A); this is expressed by Newton's law of cooling:

$$Q_{conv} = h_{conv} A (T_s - T_\infty) \quad (5.1)$$

When air flows over a flat plate the velocity decreases to zero at the plate surface, known as the no-slip condition. The surface heat transfer is by conduction (q_{cond}), between the surface and the adjacent fluid layer:

$$q_{cond} = -k \left. \frac{dT}{dy} \right|_{y=0} \quad (5.2)$$

As heat is conducted through the still air to the flowing air, it is convected away as shown in Figure 5.1. The situation for natural convection is similar except for the velocity profile. The velocity increases with reduced distance from the surface due to the decreased density of the warmed air. The velocity then decreases as the fluid density approaches the value of the surrounding fluid.

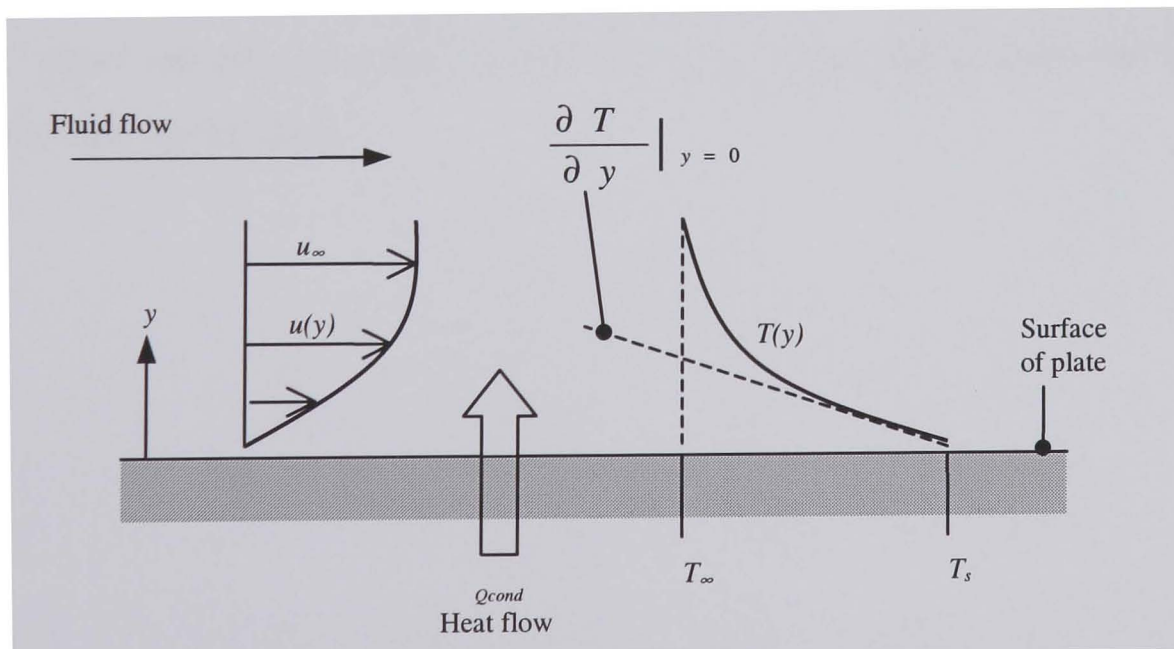


Figure 5.1 Temperature and velocity distributions in laminar forced convection flow over a heated flat plate (Kreith 1986)

The h_{conv} value can be determined from the following equation:

$$h_{conv} = \frac{-k \left(\frac{dT}{dy} \right)_{y=0}}{T_s - T_\infty} \quad (5.3)$$

Where h_{conv} is a function of fluid conductivity, the temperature gradient of the air close to the surface and the temperature difference between the ambient air and surface. The heat transfer coefficient is commonly non-dimensionalised with the Nusselt number (Nu), defined as:

$$Nu = \frac{h_{conv} l}{k} = f(Re, Pr) \quad (5.4)$$

Where, k is the conductivity of the air and l is the characteristic length. The Nusselt number represents the convective transfer through a fluid layer caused by convection relative to the conduction through the same fluid layer. The average value of the Nusselt number along a surface is a function of the Reynold (Re) and Prandtl number (Pr).

The internal flow of a fluid through a channel is somewhat different to external flow. The boundary layer growth is restricted by the inner surfaces of the channel. The velocity of the fluid changes from zero to a maximum at the centre of the channel, see Figure 5.2. Once the air enters the channel, the h_{conv} value reduces until the flow in the channel is fully developed.

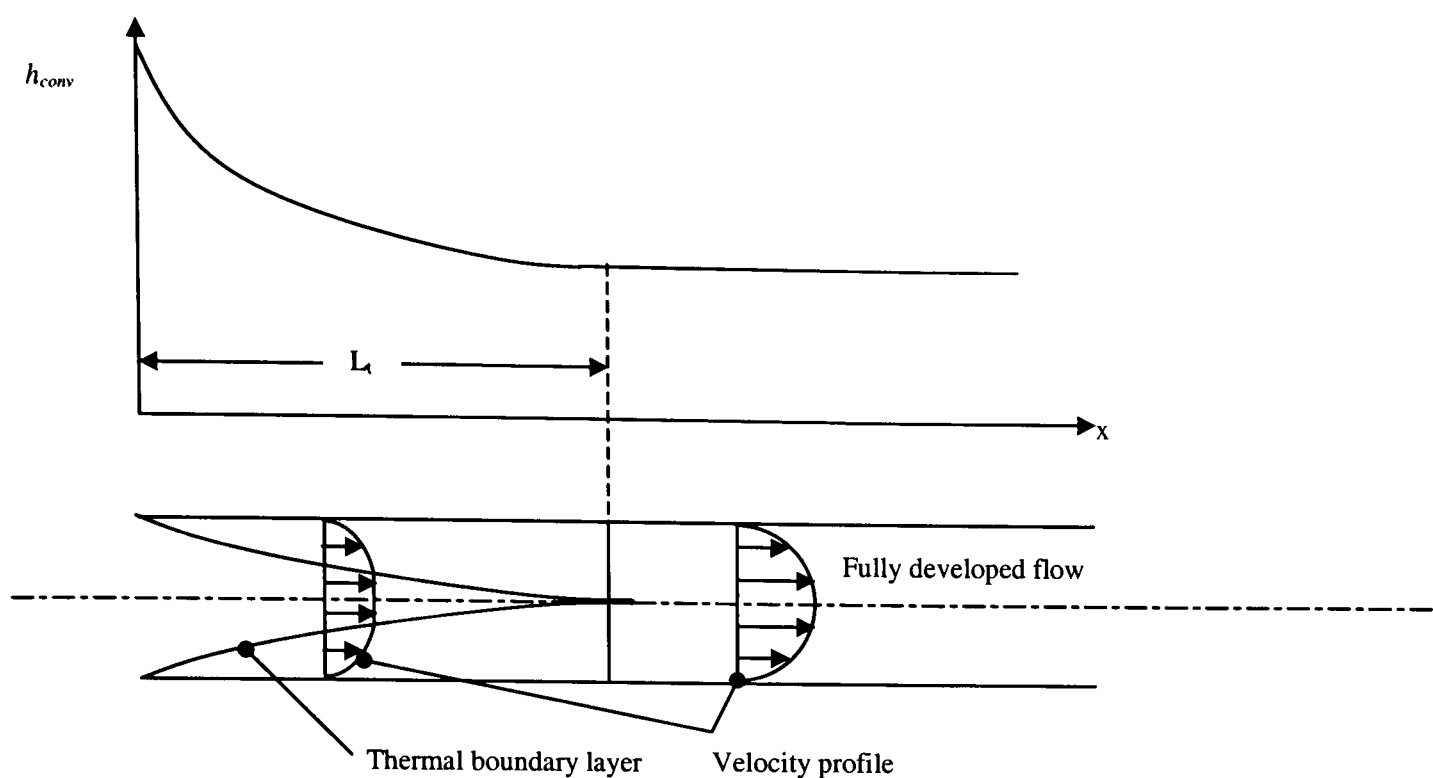


Figure 5.2 Variation of h_{conv} values in the flow direction for flow in a tube ($Pr > 1$) (Cengel 1998)

5.2 Convective Heat Transfer Coefficients and Relationships

Equations for the calculation of h_{conv} , available from literature are shown in Chapter 2. To use the equations effectively, the brake disc must be broken down into regions, which experience different airflow characteristics, as shown in Figure 5.3. The equations refer to a rotating cylinder (disc hat outside diameter, disc rim), rotating disc (friction surface) and ventilation channels. The h_{conv} equations are derived empirically and theoretically, showing good results for their respective experimental conditions.

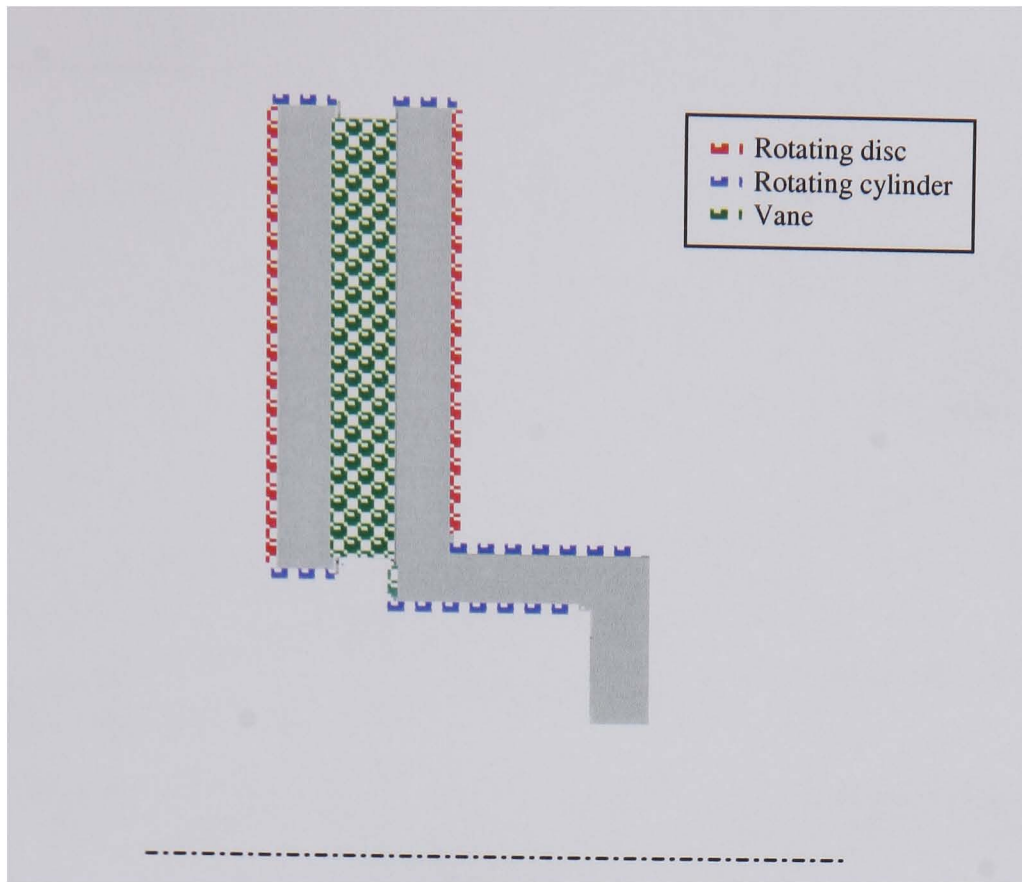


Figure 5.3 Brake disc regions for the h_{conv} calculations

To investigate the equations suitability, the calculated values of h_{conv} for a standard CV disc (see Chapter 3) are shown in Figure 5.4 to Figure 5.9. The differences in calculated h_{conv} can be very high, as shown in Figure 5.4. At 450 min^{-1} (maximum CV speed) h_{conv} values range from 16 to $60 \text{ W/m}^2\text{K}$. The h_{conv} values have been calculated using standard air properties at a temperature of 30°C , see Table 5.1.

Table 5.1 Air properties at 30°C (Rogers and Mayhew 1995)

| Property | Value |
|---|------------------------|
| Viscosity (kinematic) [m^2/s] | 15.68×10^{-6} |
| Thermal conductivity [W/mK] | 26.24×10^{-3} |

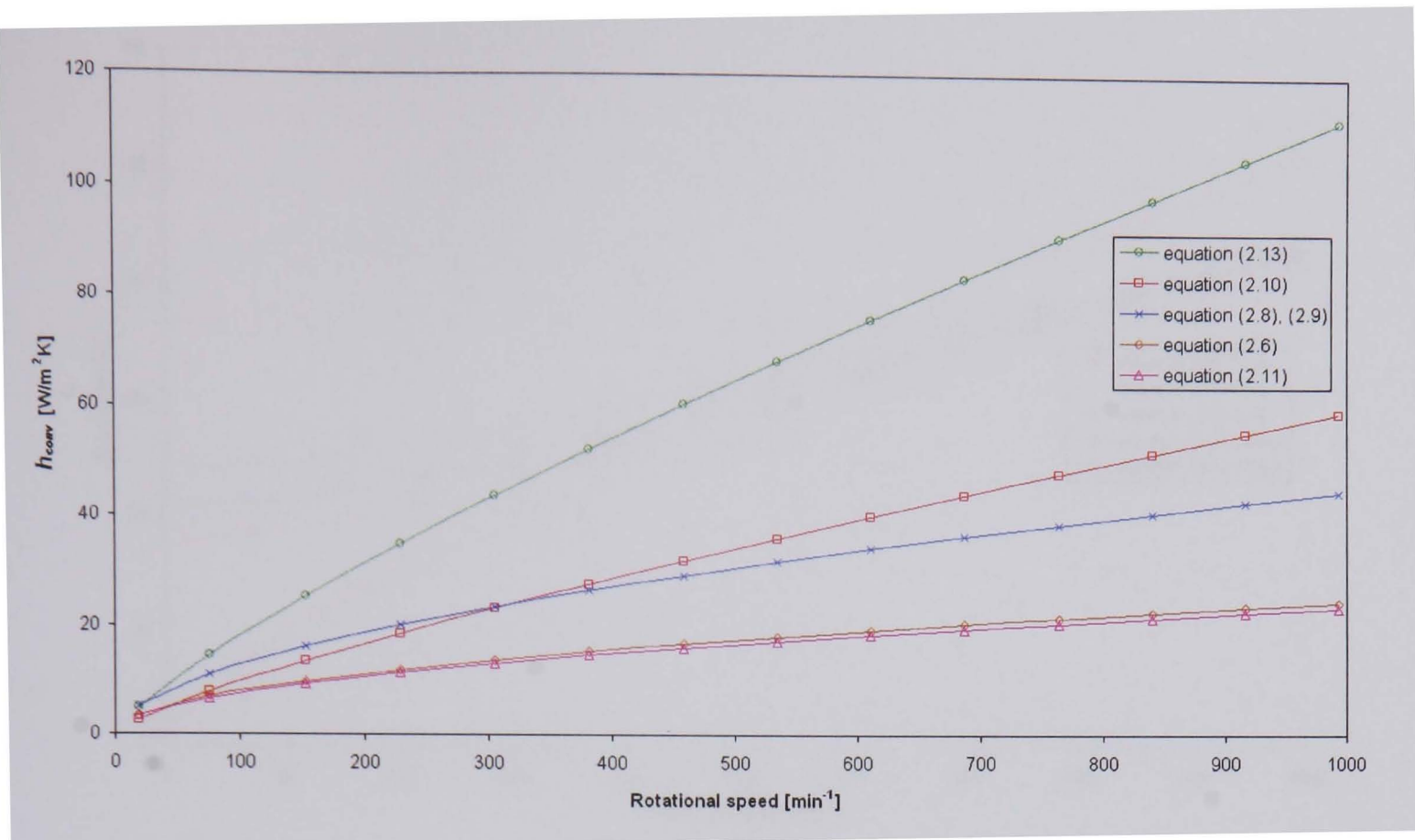


Figure 5.4 Rotating disc in still air, h_{conv} values for the standard CV disc

All the formulae show an increase in h_{conv} with increased rotational speed, formulae allowing for cross flow show further h_{conv} increase with an increase in cross flow velocity, as shown in Figure 5.5 and Figure 5.6.

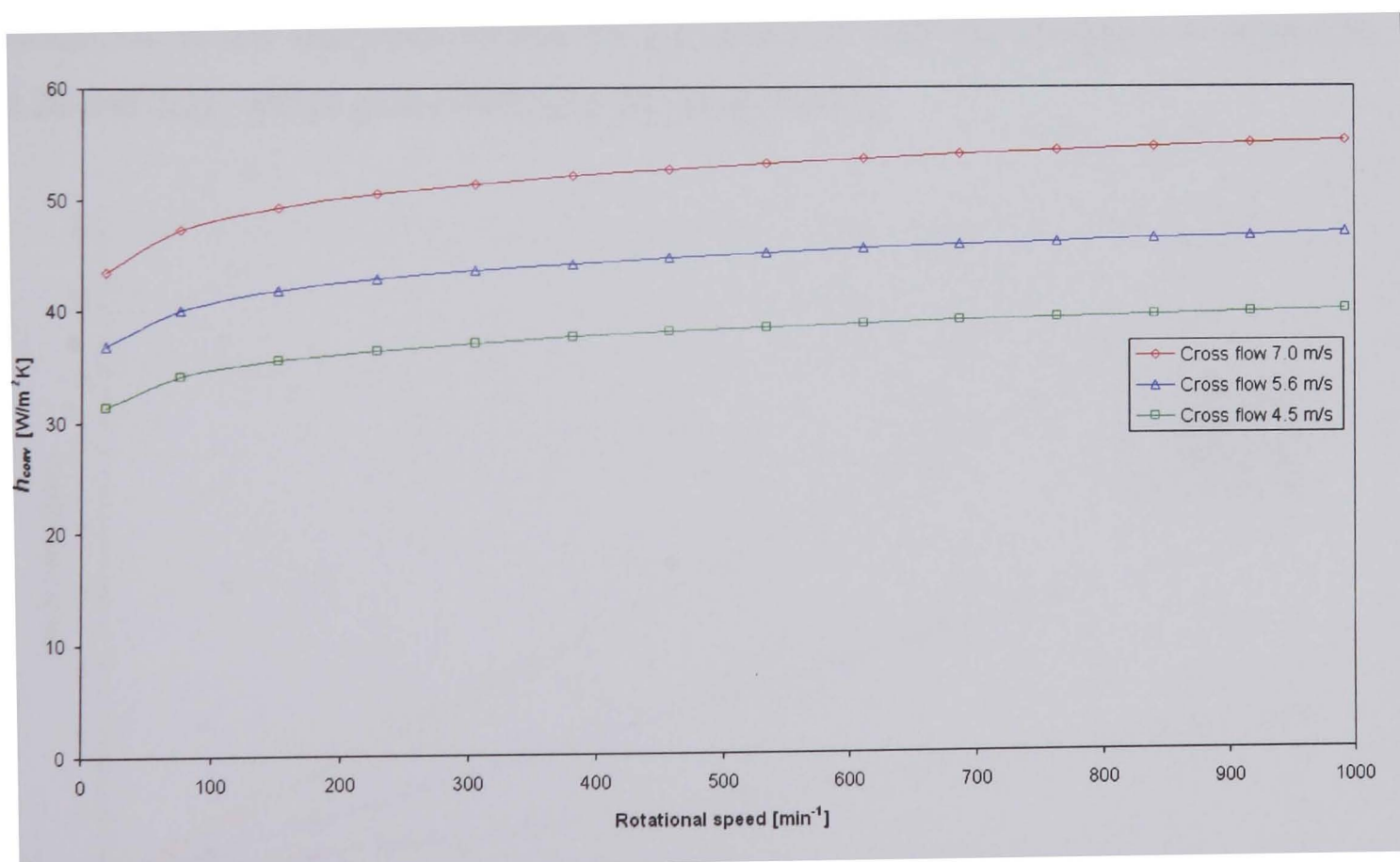


Figure 5.5 Comparison of rotating disc h_{conv} in cross flow using equation (2.12), for the standard CV disc

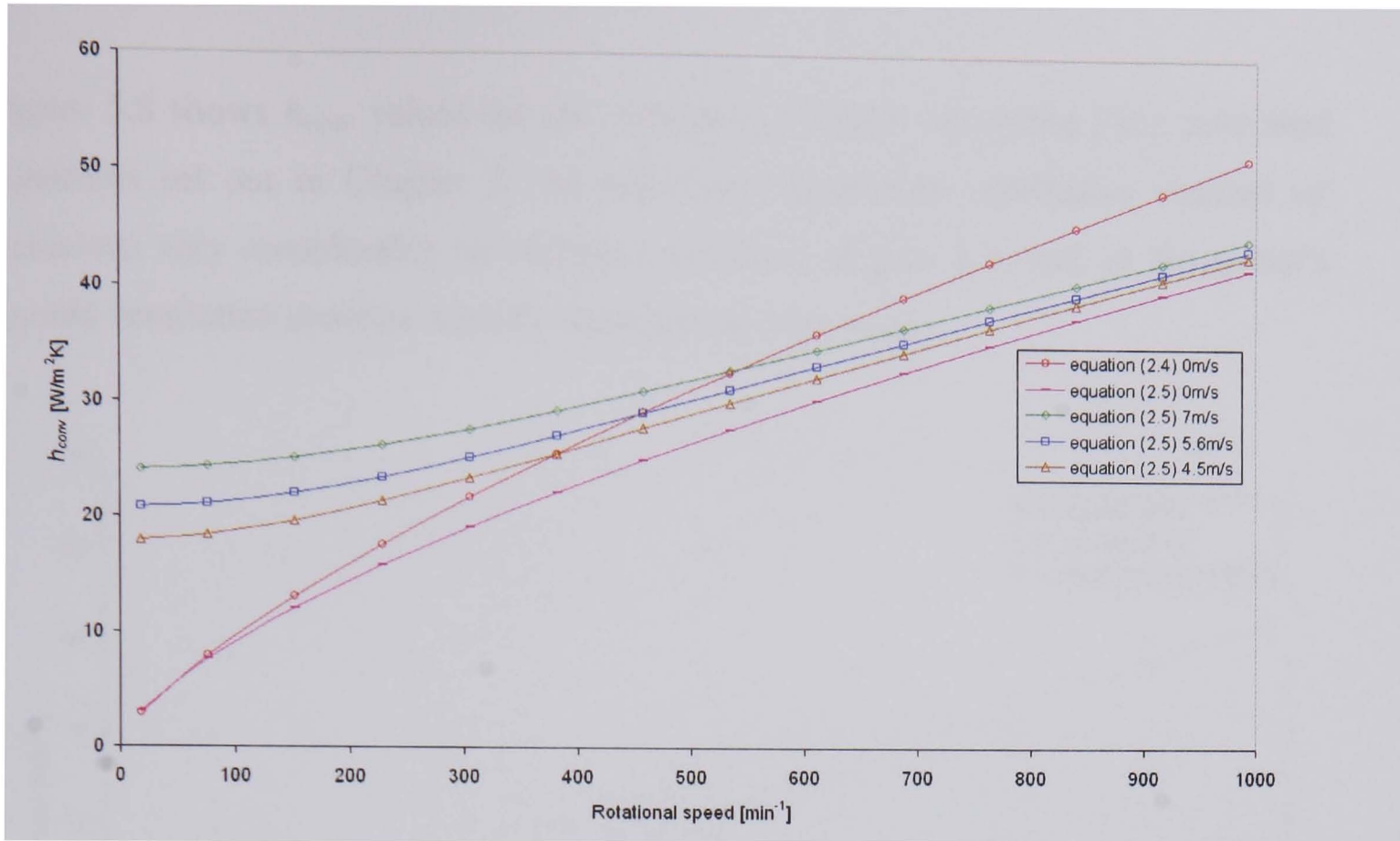


Figure 5.6 Rotating cylinder with and without cross flow, h_{conv} for standard CV disc

Further complications arise when considering the ventilation channels of the disc. The h_{conv} value is a function of velocity and, before it can be predicted, the airflow through the ventilation channel must be found. Literature equations for predicting ventilation channel airflow are given in Chapter 2 and Figure 5.7 shows a large difference in the velocities derived by the equation, with the exception of equations 2.20 and 2.21, which give practically the same results.

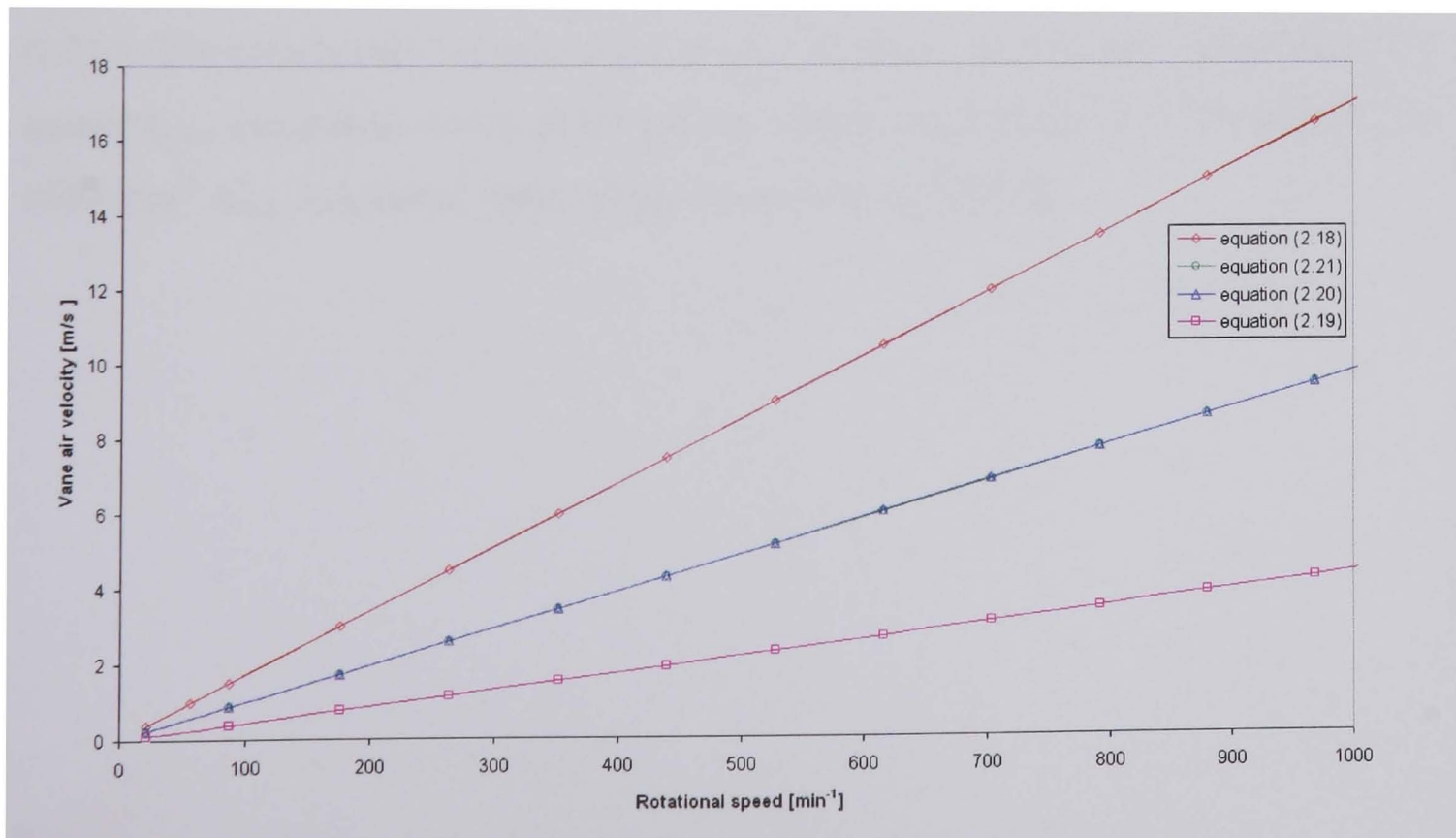


Figure 5.7 Comparison of standard CV disc vane air velocities using published equations

Figure 5.8 shows h_{conv} values for the ventilation channel calculated from published equations set out in Chapter 2. As previously mentioned ventilation channel air velocities vary considerably for different equations (Figure 5.7) and so the author's quoted ventilation channel velocity equation has been used.

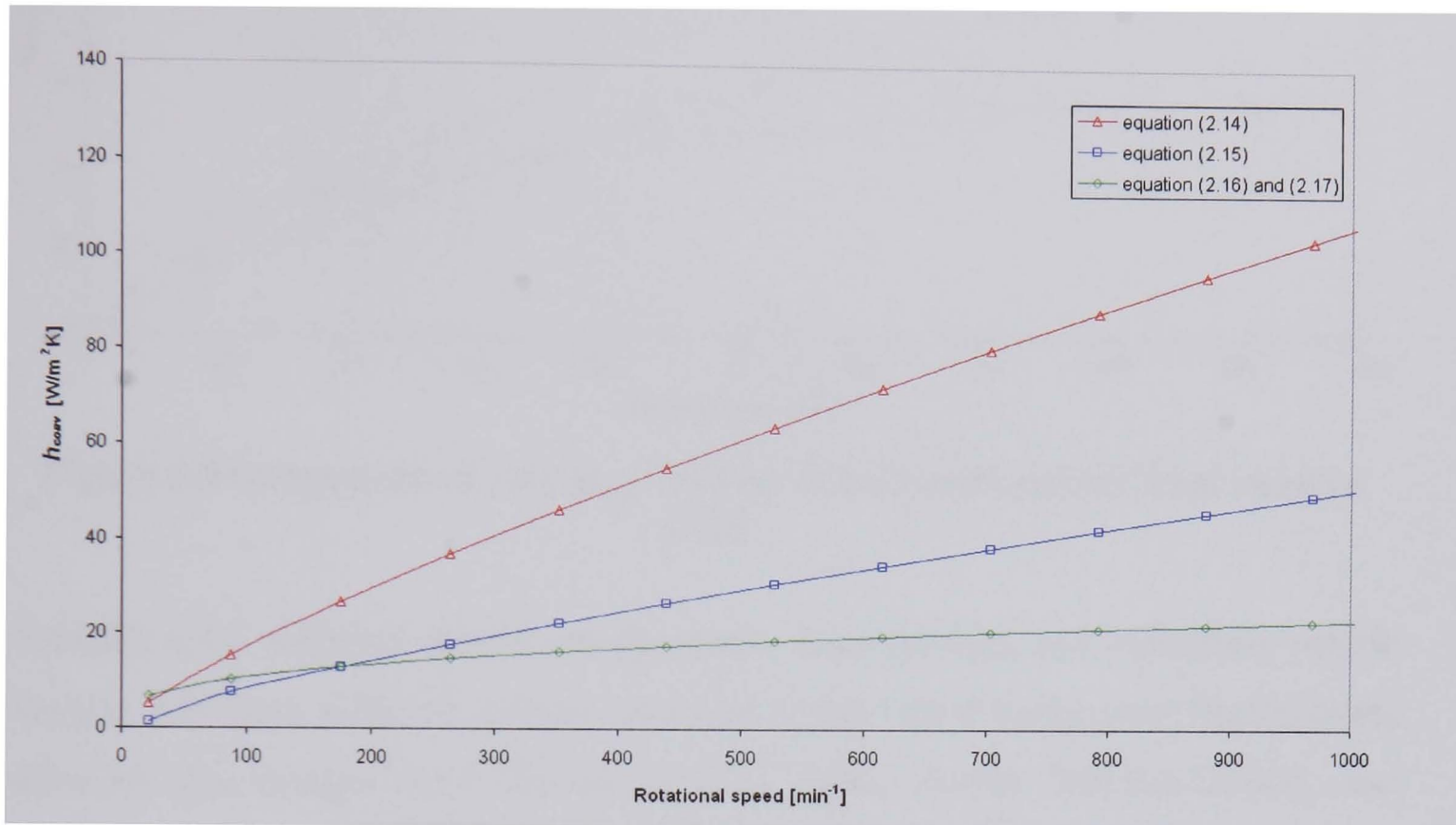


Figure 5.8 Comparison of vane h_{conv} with respective ventilation channel velocities

Figure 5.9 shows h_{conv} values calculated with a common velocity (from equation (2.21)). The results vary for each form of h_{conv} equation. At 450 min⁻¹ (maximum CV speed) h_{conv} calculated values differ greatly, values range from 18 to 35 W/m²K. At 1000 min⁻¹ h_{conv} calculated values range from 30 to 66 W/m²K.

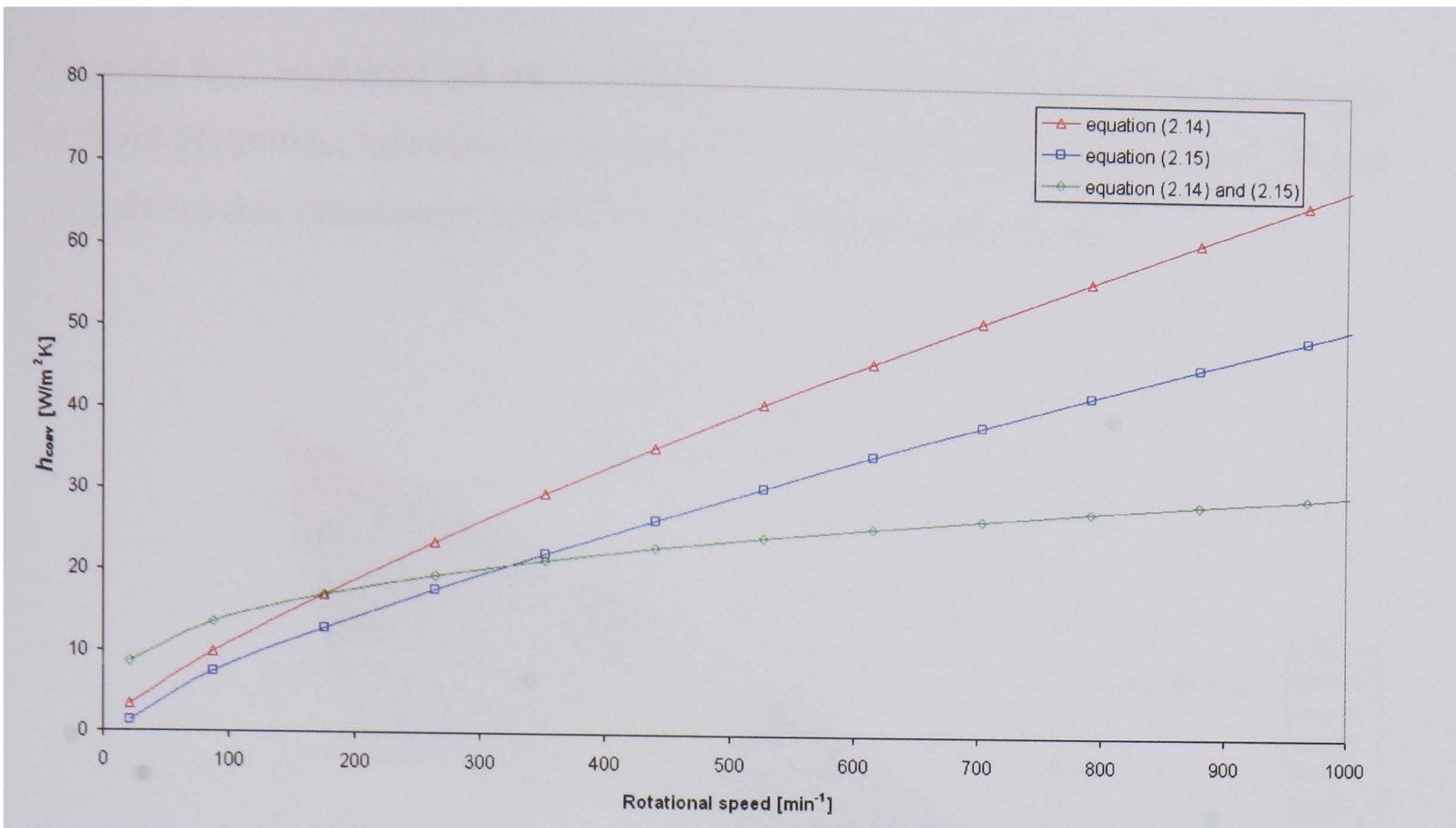


Figure 5.9 Comparison of vane h_{conv} with air vane velocity derived from equation (2.21)

Vehicles have different global aerodynamics characteristics and individual vehicle designs will have different airflow velocities in the wheel cavity area. Furthermore, different disc designs show different airflow characteristics. For this reason, care must be taken to choose the correct equation for the application.

When determining a value for h_{conv} , careful consideration of air properties must be made. From Newton's law of cooling, equation (5.1), T_{∞} is the temperature of the fluid sufficiently far from the surface. The thermal boundary layer varies from T_s , at the surface, to T_{∞} . Values of h_{conv} are sensitive to air temperature and to accurately determine h_{conv} values, the air properties must correspond to the correct air temperature, see Table 5.2. Fluid properties are usually evaluated at the film temperature (T_f), defined as (Cengel 1998):

$$T_f = \frac{T_s + T_{\infty}}{2} \quad (5.5)$$

Table 5.2 Computed relative h_{conv} variation with film temperature (Sheridan, Kutchey et al. 1988)

| | | | | | |
|---------------|------|------|------|------|------|
| T_f [°C] | 100 | 200 | 300 | 400 | 500 |
| h_{rel} [-] | 1.00 | 0.89 | 0.81 | 0.79 | 0.70 |

From the h_{conv} equations set out in Chapter 2, it can be seen that the h_{conv} is affected by fluid properties; however, some equations are more sensitive than others. Figure 5.10 shows this characteristic for CV vane h_{conv} using equation (2.14).

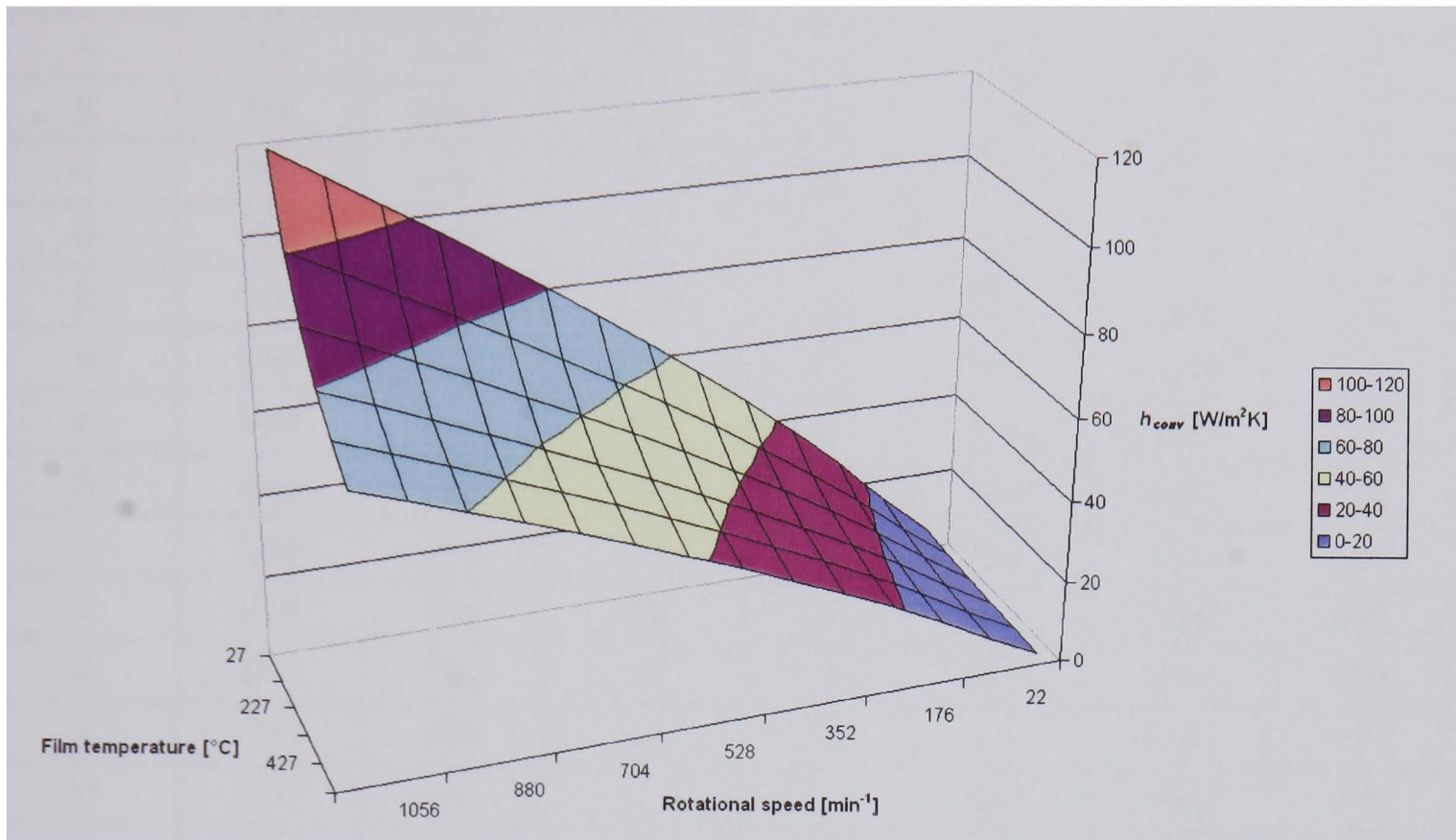


Figure 5.10 Change in standard CV disc ventilation channel h_{conv} with rotational speed and film temperature

5.3 Cooling Constants

An alternative approach to predicting cooling performance, developed by Newcomb (1965), defines brake cooling parameters and was introduced in Chapter 2. The cooling rate b can be determined from logarithmic plots of brake cooling. Results obtained when vehicles are driven at various speeds indicate that b can be expressed as:

$$b = b_o + Kv^{0.8} \quad (5.6)$$

The term b_o involves a conduction and natural convection component and the $Kv^{0.8}$ is the forced convection component, where v is the linear velocity [mile/h] of the vehicle and K is a constant relating to the geometry of the body, radiative heat dissipation is neglected. Table 5.3 shows empirical values for K and b_o , A is the total friction area for a disc and A_c is the area of disc in contact with the hub.

Table 5.3 Effective areas and cooling constants of the front discs or drums of various vehicles (Newcomb and Spurr 1967)

| Car | Engine capacity [cm ³] | Type of front brake | Front disc or drum weight [lb] | A [in ²] | A _c [in ²] | 10 ³ K | 10 ³ b _o |
|-----|------------------------------------|---------------------|--------------------------------|----------------------|-----------------------------------|-------------------|--------------------------------|
| A | 767 | Drum | 8.8 | 107 | 14.0 | 0.145 | 2.55 |
| B | 848 | Drum | 5.3 | 83 | 11.0 | 0.145 | 1.65 |
| C | 997 | Disc | 4.3 | 62 | 11.1 | 0.163 | 3.27 |
| D | 1098 | Disc | 5.3 | 81 | 6.8 | 0.150 | 1.30 |
| E | 1172 | Drum | 10.0 | 107 | 18.5 | 0.100 | 2.55 |
| F | 1340 | Disc | 12.0 | 99 | 23.4 | 0.100 | 2.20 |
| G | 1489 | Drum | 11.8 | 149 | 14.1 | 0.103 | 1.45 |
| H | 1592 | Disc | 6.8 | 69 | 6.6 | 0.107 | 1.20 |
| I | 1596 | Disc | 5.5 | 91 | 8.6 | 0.115 | 2.07 |
| J | 1798 | Disc | 10.0 | 113 | 5.7 | 0.088 | 0.90 |
| K | 2279 | Disc | 9.3 | 110 | 13.3 | 0.081 | 1.60 |
| L | 2553 | Disc | 8.3 | 112 | 8.1 | 0.095 | 1.22 |
| M | 2651 | Disc | 11.3 | 134 | 16.7 | 0.090 | 1.45 |
| N | 3770 | Drum | 17.0 | 282 | 32.3 | 0.198 | 0.80 |
| CV | 5416 | Drum | 54.5 | 316 | 54.5 | 0.040 | 1.10 |

To determine the cooling rate of a brake disc or drum a plot of K against A/w [in²/lbs] (based on Table 5.3), where w is the weight of the disc, gives (Newcomb and Spurr 1967):

$$K = 0.0094 \times 10^{-3} \frac{A}{w} \quad (5.7)$$

A plot of b_o against A_c/w gives a linear slope showing that:

$$b_o = 1.17 \times 10^{-3} \frac{A_c}{w} \quad (5.8)$$

The respective slopes of these plots show that b is given by:

$$b = \frac{1.17 \times 10^{-3} A_c + 0.0094 \times 10^{-3} A v^{0.8}}{w} \quad (5.9)$$

If the convective term is expressed as (Newcomb and Millner 1965):

$$b_c = \frac{Ah_{conv}}{wC_p} = Kv^{0.8} \quad (5.10)$$

Then the convective heat transfer coefficient can be expressed as:

$$h_{conv} = \frac{Kv^{0.8}wC_p}{A} \quad (5.11)$$

It should be noted that equation (5.11) considers the forced convection component only. Using equation (5.11) and the CV parameters of Table 5.3 ($K = 0.040 \times 10^3$), the h_{conv} values for a range of vehicle speeds have been determined for the standard CV radial vane disc and presented in Figure 5.11.

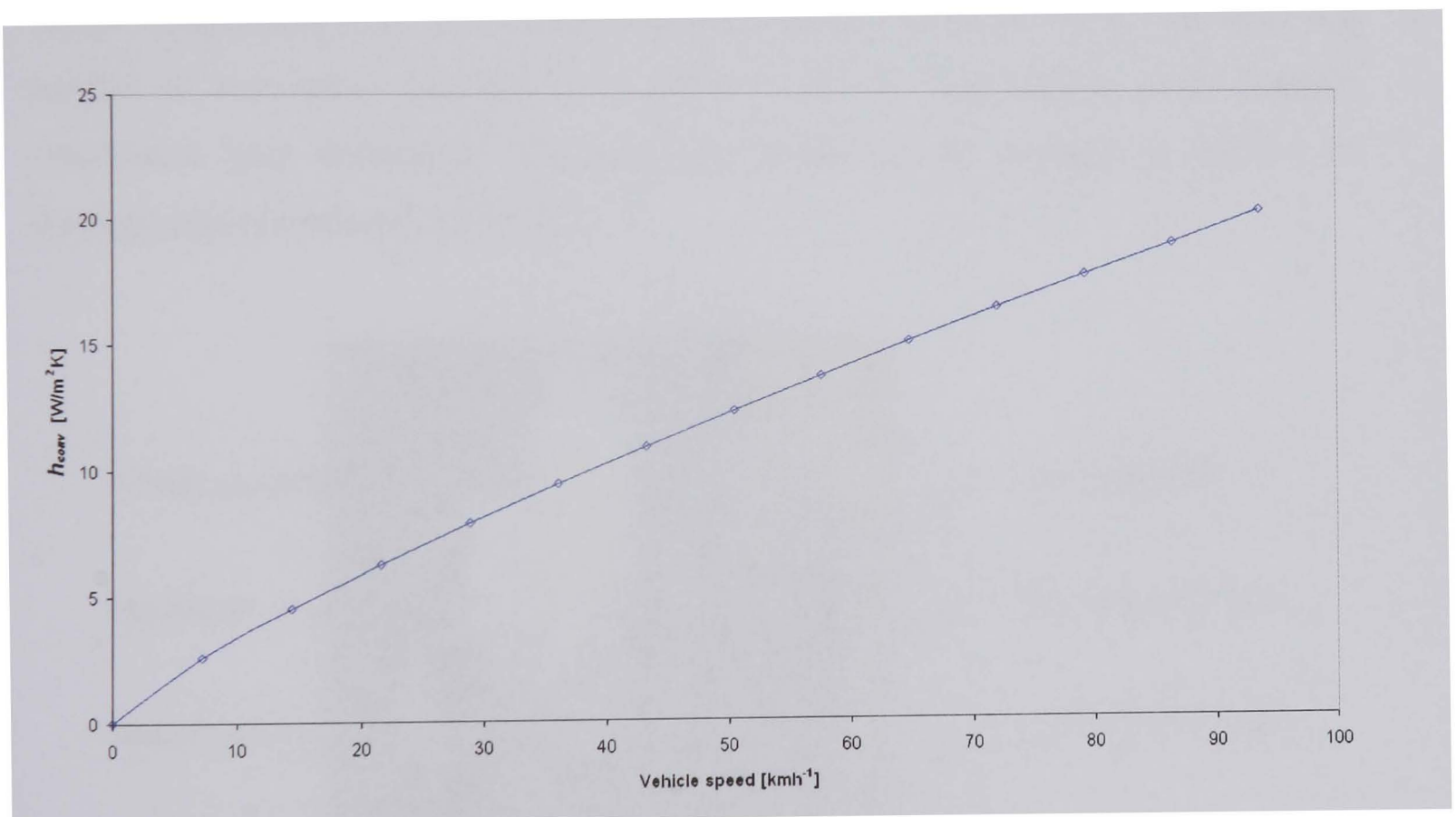


Figure 5.11 h_{conv} derived from cooling constants (Newcomb and Millner 1965) for standard CV disc

5.4 Measurement of Commercial Vehicle Disc Cooling

Experimental studies of convective heat dissipation have been conducted on the Spin Rig for the CV discs presented in Chapter 3. A range of brake disc designs and assemblies have been heated and the cooling measured. The brake disc was mounted to the Spin Rig shaft, which was fitted with a special flange adapter. The shaft adapter was insulated to prevent heat conducting back to the shaft. For studies of convection cooling with the wheel assembly included, the wheel carrier was also fitted to the disc and Spin Rig shaft during the heating phase. Figure 5.12 shows the CV disc and wheel carrier during the heating phase of the convective cooling test (with heater box and insulation on wheel carrier). The brake disc was heated using the heater box fitted with two additional electric air heaters (see Chapter 3) and the Spin Rig heater (Figure 5.12), the total heating power being 8 kW. The wheel carrier was insulated with fibreglass lagging during the heating phase. The Spin Rig air heater temperature was set to 600°C and the airflow set to 45 l/min, the disc was rotated at low speed (25 min^{-1}) to provide uniform disc heating and minimise convective heat dissipation. The disc was heated for 45 minutes to achieve an average disc temperature of 250°C.

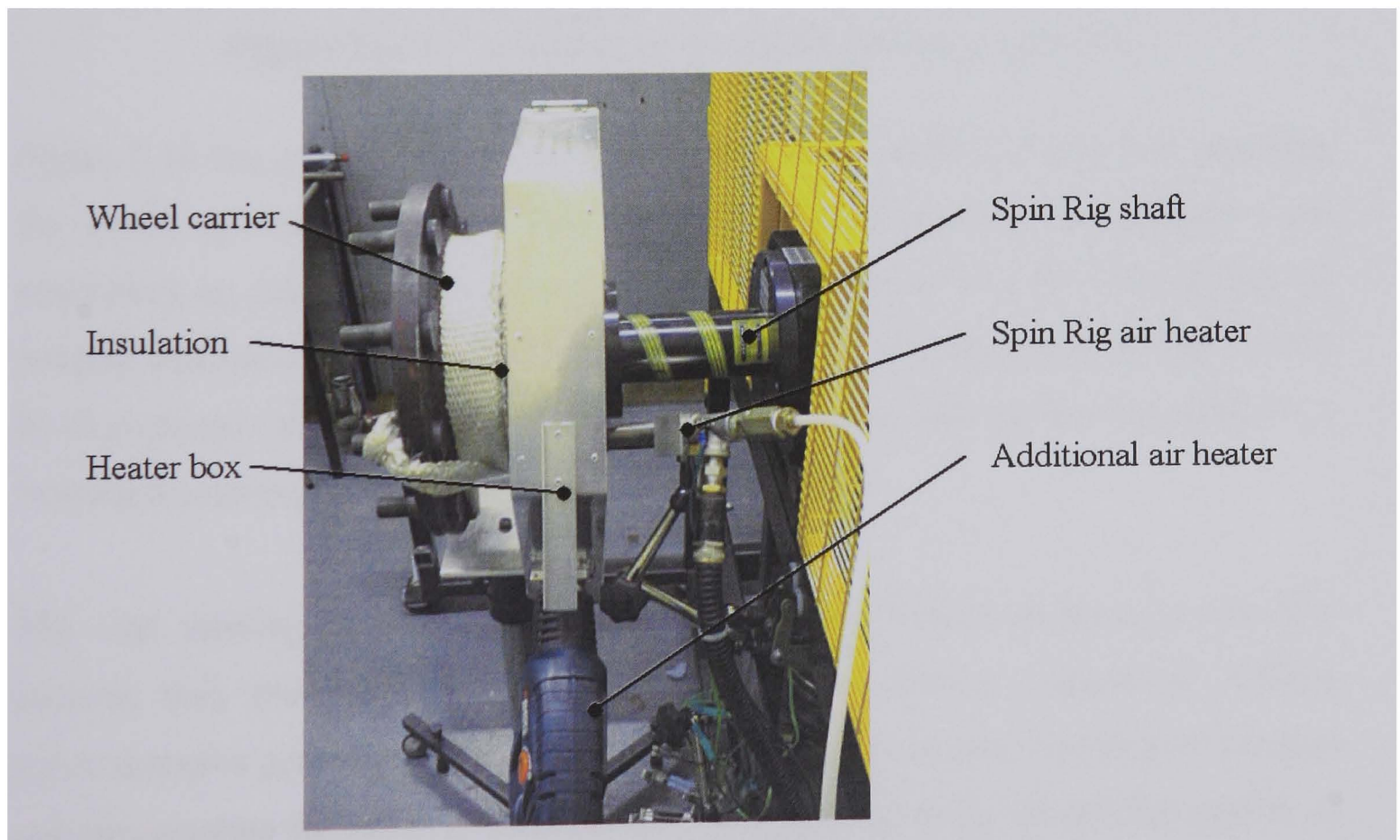


Figure 5.12 Heating of brake during convective cooling test

After the heating phase, the heater is switched off, disc rotation is stopped, and the insulation and heater box are removed. A series of rubbing thermocouples, see Chapter 3, are then placed on the disc and wheel carrier surface. The rubbing thermocouples are mounted to an arm profiled to fit around the disc and carrier, as shown in Figure 5.13. Welded tip thermocouples (see Chapter 3) are also fitted to the arm for measuring air temperatures. The arm is articulated with a centre lock that allows quick positioning of the thermocouples. Rubbing thermocouples were used in eight positions during the CV disc assembly tests.

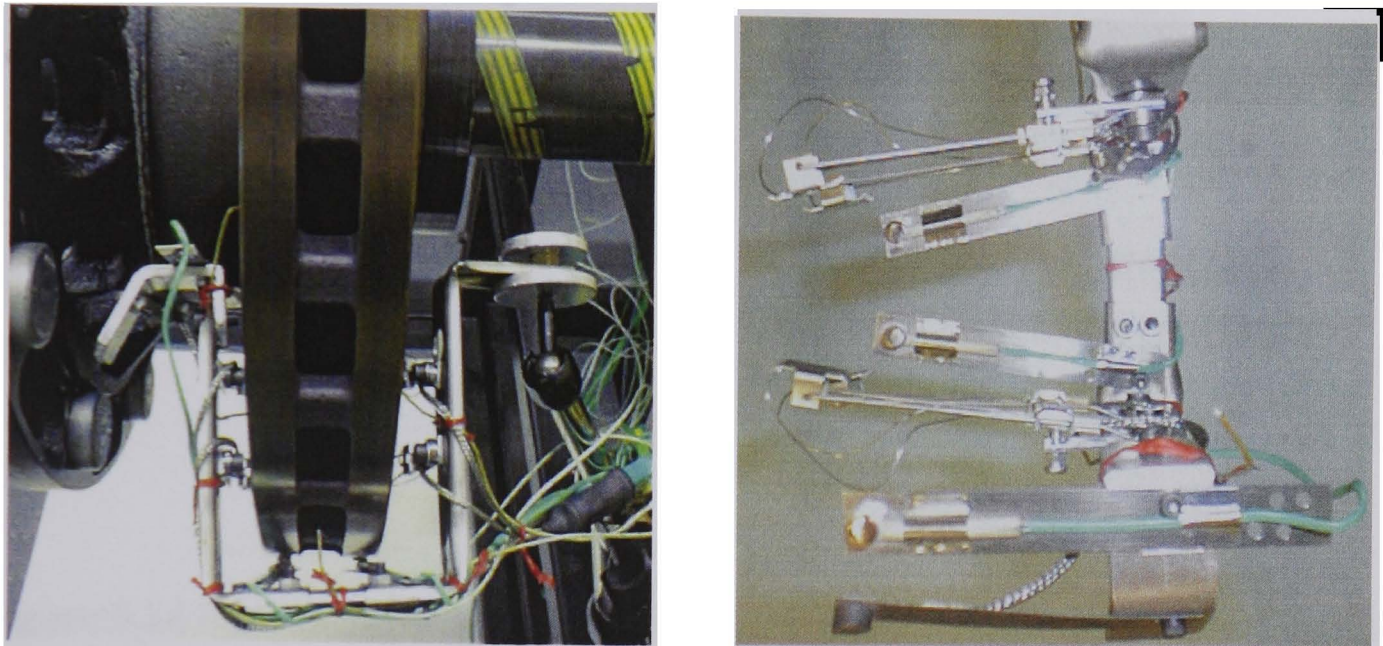


Figure 5.13 CV disc and carrier rubbing thermocouple arm

Figure 5.14 shows the positions of the thermocouples during cooling tests including the wheel carrier and wheel. Two low friction sled rubbing thermocouples are positioned on each friction surface of the disc ①, ②, ⑤ and ⑥. Two copper tip rubbing thermocouples are placed on the inboard and outboard rim of the disc, ③ and ④. One copper tip rubbing thermocouple is placed on the disc hat ⑦. One graphite tip rubbing thermocouple is located on the wheel carrier ⑧.

The sled rubbing thermocouples were used on the friction surfaces of the disc because they provided good contact with the flat surface. Copper tip rubbing thermocouples provided the best surface contact for the curved surfaces of the disc and the graphite tip rubbing thermocouple was profiled to fit the surface profile of the wheel carrier. The air temperature thermocouples measured the vane inlet ①, vane exit ③ and the film temperature 3 mm from the friction surface of the disc at the mean diameter (② and ④). The arrangement was established after many trials and

proved to give accurate and reliable results for all CV convection tests. From the boundary layer thickness equation given in Chapter 4, the boundary layer thickness ranges from 9.25 (high temperature low speed) to 1.50 mm.

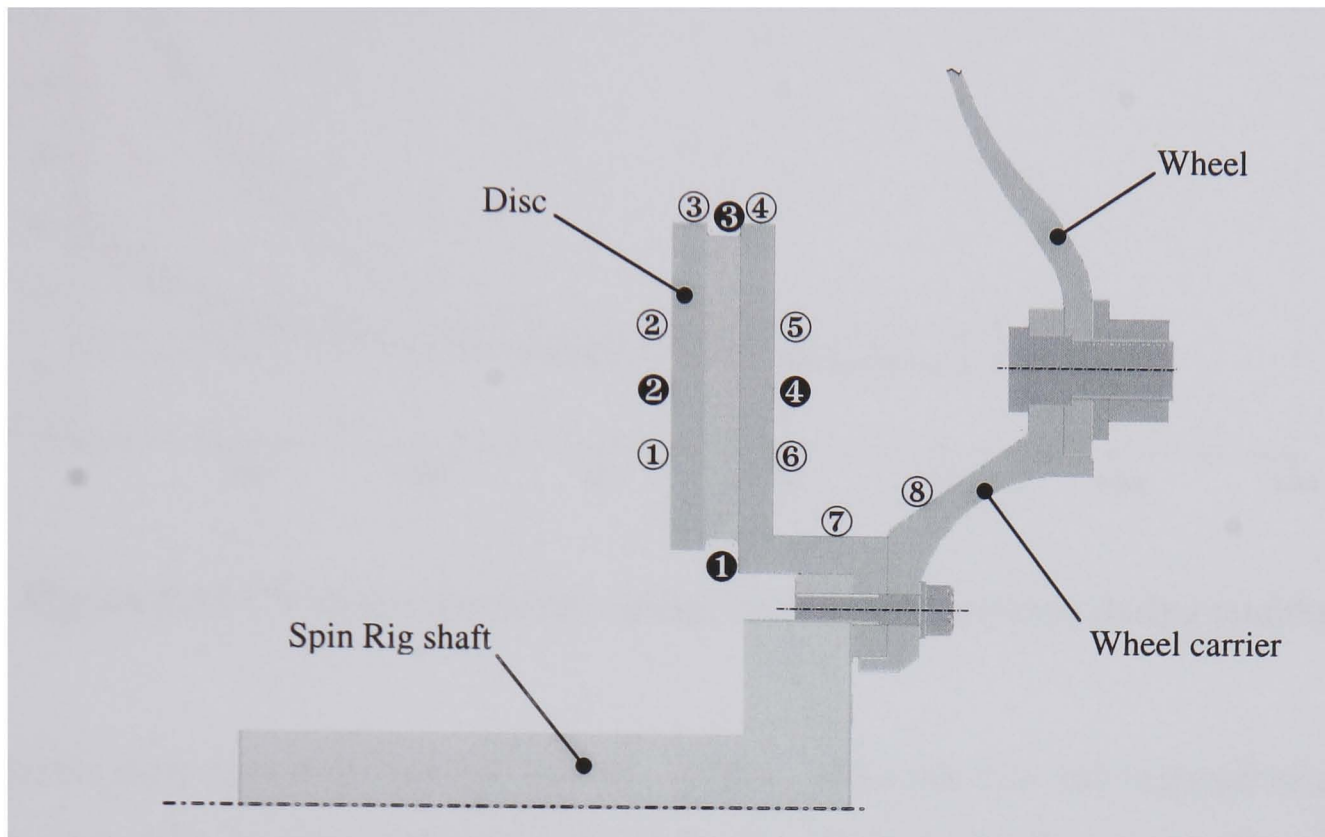


Figure 5.14 Position of rubbing (○) and air temperature (●) thermocouples for the CV disc and wheel assembly

After the thermocouples are positioned, the wheel is fitted if required. The disc is then rotated at the test speed and thermocouple measurements are logged, at a sample rate of 0.25 Hz. The brake assembly is rotated until surface temperatures drop to levels close to ambient temperature, (approximately 30°C). All the tests were performed in still air.

The heat dissipation characteristics of disc designs and configurations of disc and wheel assemblies can be compared using the cooling curves measured on the Spin Rig. Based on cooling curves the average heat transfer coefficient (h_{avg}) can be determined. Figure 5.15 shows the typical cooling curves and surrounding air temperatures for a brake assembly during Spin Rig cooling.

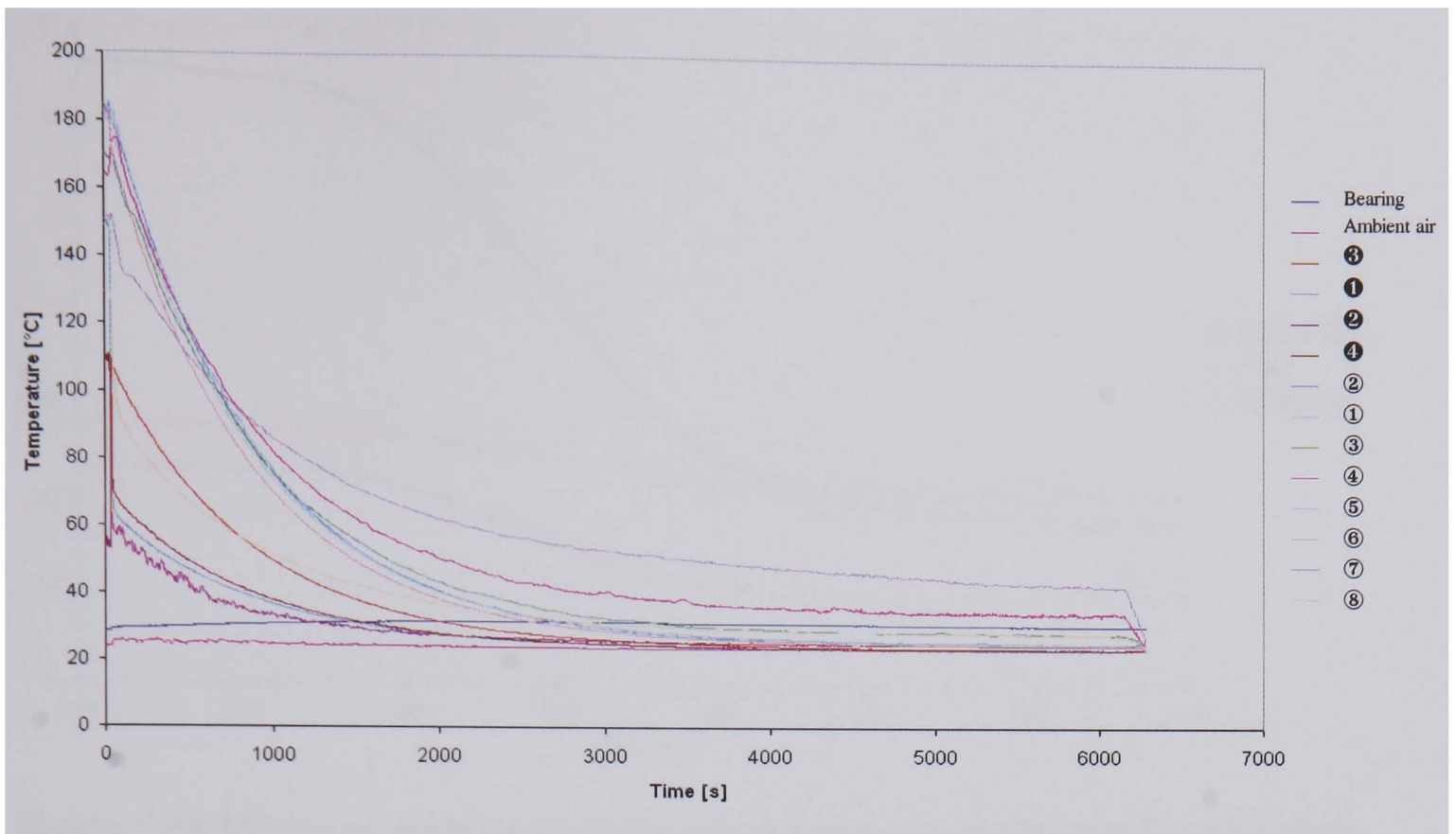


Figure 5.15 CV brake assembly, surface and air temperatures during cooling

It can be seen that at the end of the cooling test, when the disc has stopped rotating, there is a drop in temperature measured by the rubbing thermocouples. The spring force acting on the rubbing thermocouple contact area with the brake surface causes frictional heating during disc rotation. Precise adjustment of the rubbing thermocouple can minimise the frictional heating effect (shown by identical rotating and static temperature measurement). However, in practice, precise adjustment of contact force is not possible for the set-up procedure used (limited set-up time). It should be noted that the cooling tests are carried out at constant speed and therefore friction heat generation (being constant throughout the test) does not practically affect the cooling rate measured.

Figure 5.16 shows the measured temperature drop during brake disc deceleration from 450 to 0 min^{-1} . It can be seen that the copper tip thermocouple gives a temperature measurement 10°C higher than the actual surface temperature at 450 min^{-1} , the graphite tip thermocouple gives a temperature measurement 3°C higher and the sled type thermocouple gives a temperature measurement 1.5°C higher than the surface temperature.

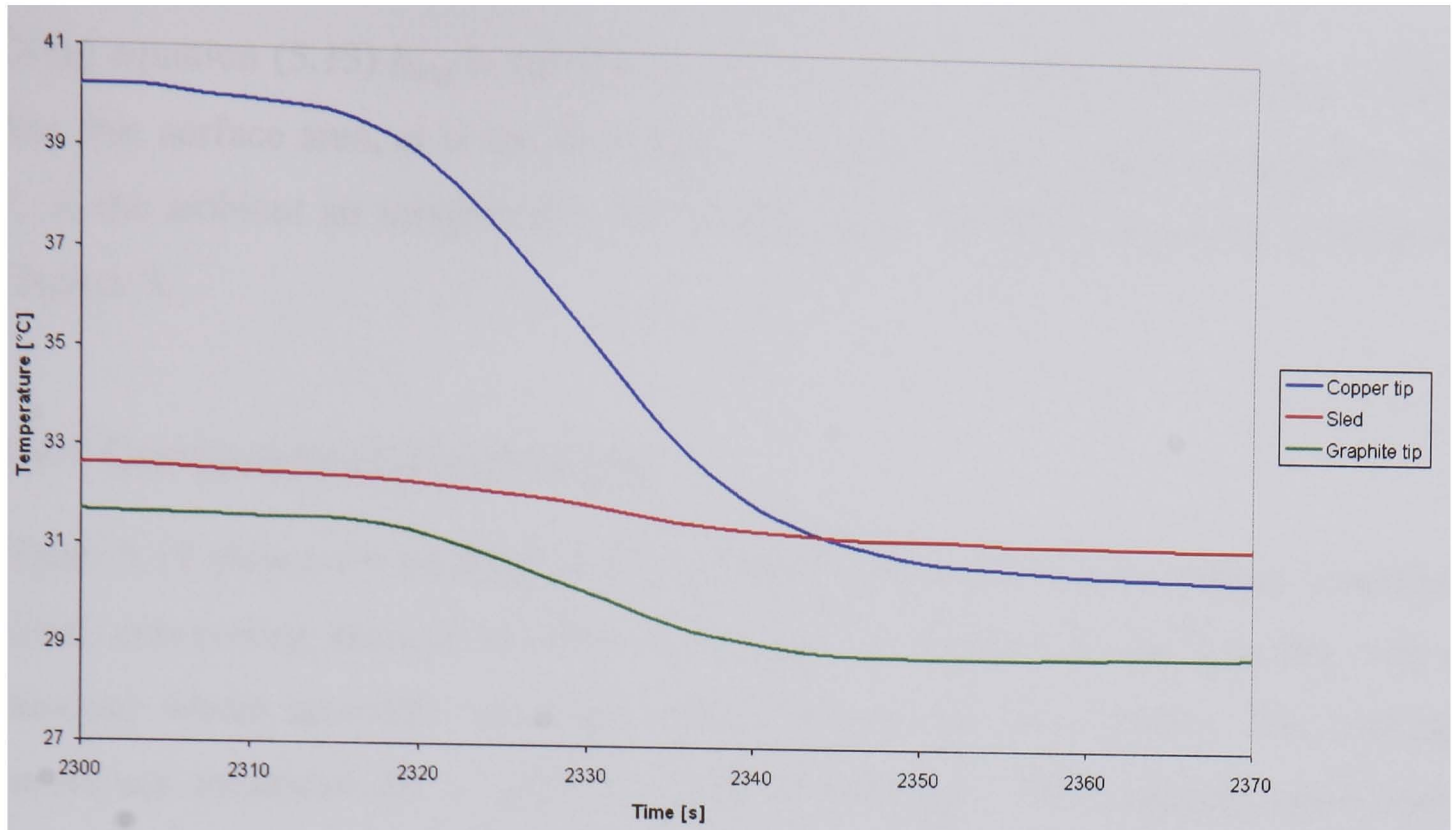


Figure 5.16 Measured rubbing thermocouple temperature during deceleration from 450 to 0 min⁻¹

Measuring the rate of cooling ($\Delta T/\Delta s$) of the brake disc allows average heat transfer coefficients (h_{avg}) to be determined. From equation (5.1) and the energy equation (5.12), equation (5.13) is derived. h_{avg} is a combined heat transfer coefficient incorporating all modes of heat transfer; conduction, convection and radiation.

$$Q = \frac{mc_p \Delta T}{\Delta s} \quad (5.12)$$

$$h_{avg} = \frac{mc_p \Delta T}{\Delta s A (T_s - T_\infty)} \quad (5.13)$$

The h_{avg} value has been determined for a range of disc rotational speeds and temperatures. Radiation and conduction are speed independent, which allows the cooling curves and h_{avg} values to be used to determine h_{conv} and compare the convective heat dissipation performance of the different brake assemblies.

The cooling rates are measured at a range of average disc surface temperatures between 200 and 75°C, using the slope of the cooling curves. The cooling curve used is the average friction surface temperature calculated from the four friction surface temperatures ①, ②, ⑤ and ⑥, as shown in Figure 5.14.

Using equation (5.13) h_{avg} is calculated where Δs is the cooling time period, A is the disc free surface area, m is the disc mass, T_s is the average surface temperature and T_∞ is the ambient air temperature. The surface areas of the CV discs are detailed in Chapter 3.

5.4.1 Comparison of Disc Designs

Figure 5.17 shows the cooling curves for three different CV disc designs (standard radial, anti-coning and curved vane, see Chapter 3) mounted on the Spin Rig with a standard wheel assembly (standard wheel carrier and steel wheel). The cooling curves are measured for a rotational speed of 450 min^{-1} . The standard radial vane disc has the highest cooling rate and the curved and anti-coning disc have very similar (lower) cooling rates.

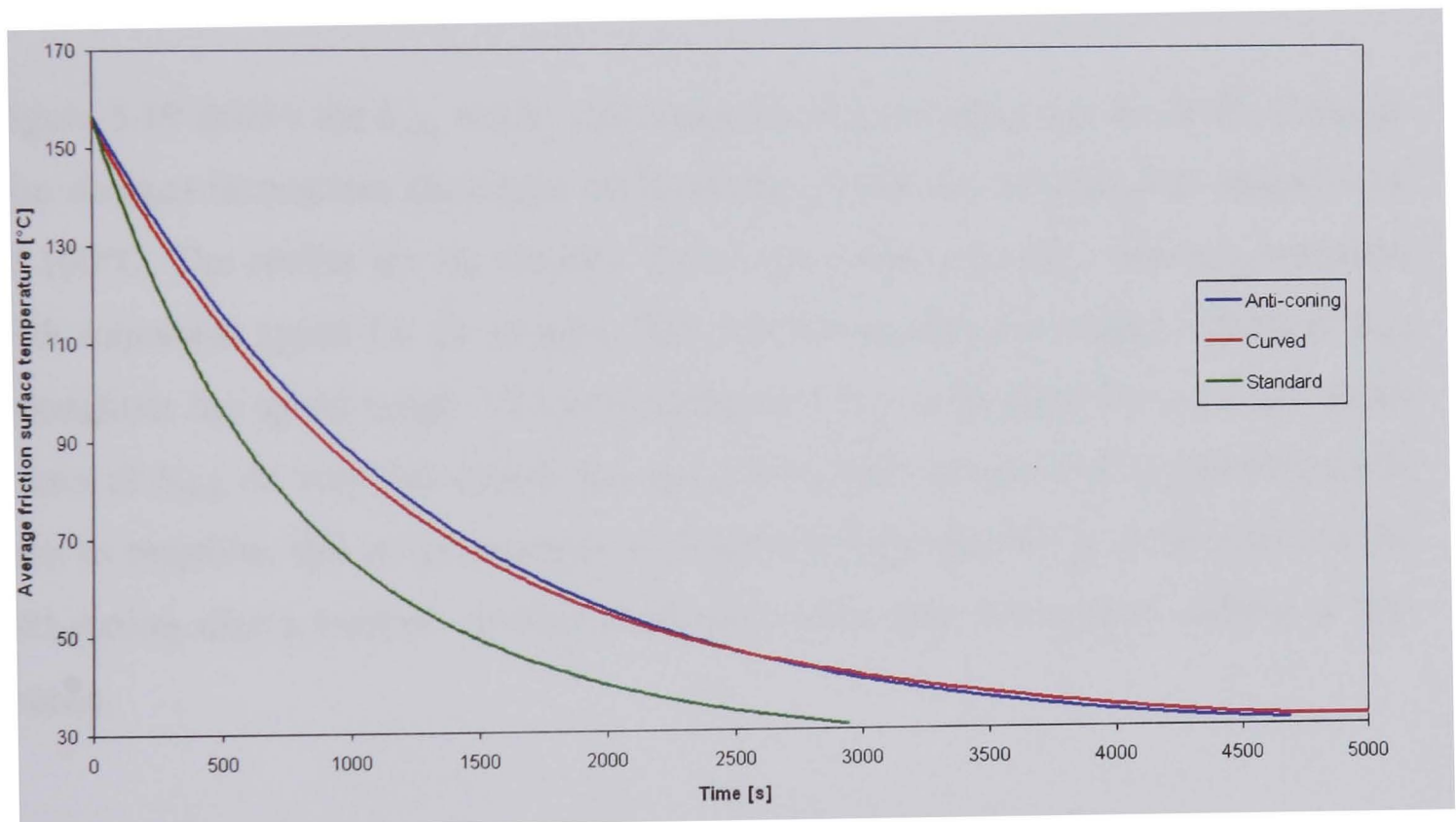


Figure 5.17 Comparison of CV disc vane design rotating at 450 min^{-1} with a standard wheel assembly

At lower rotational speeds, the disc cooling performance changes, from Figure 5.18 it can be seen that at a very low rotational speed (40 min^{-1}), the anti-coning disc has a cooling rate closer to that of the standard disc. Again, the curved vane disc has the lowest cooling rate. The curved disc design's cooling performance is severely reduced at lower rotational speeds. There is little airflow at low rotational speeds and natural convection is restricted by the curved vane design restricting rising air.

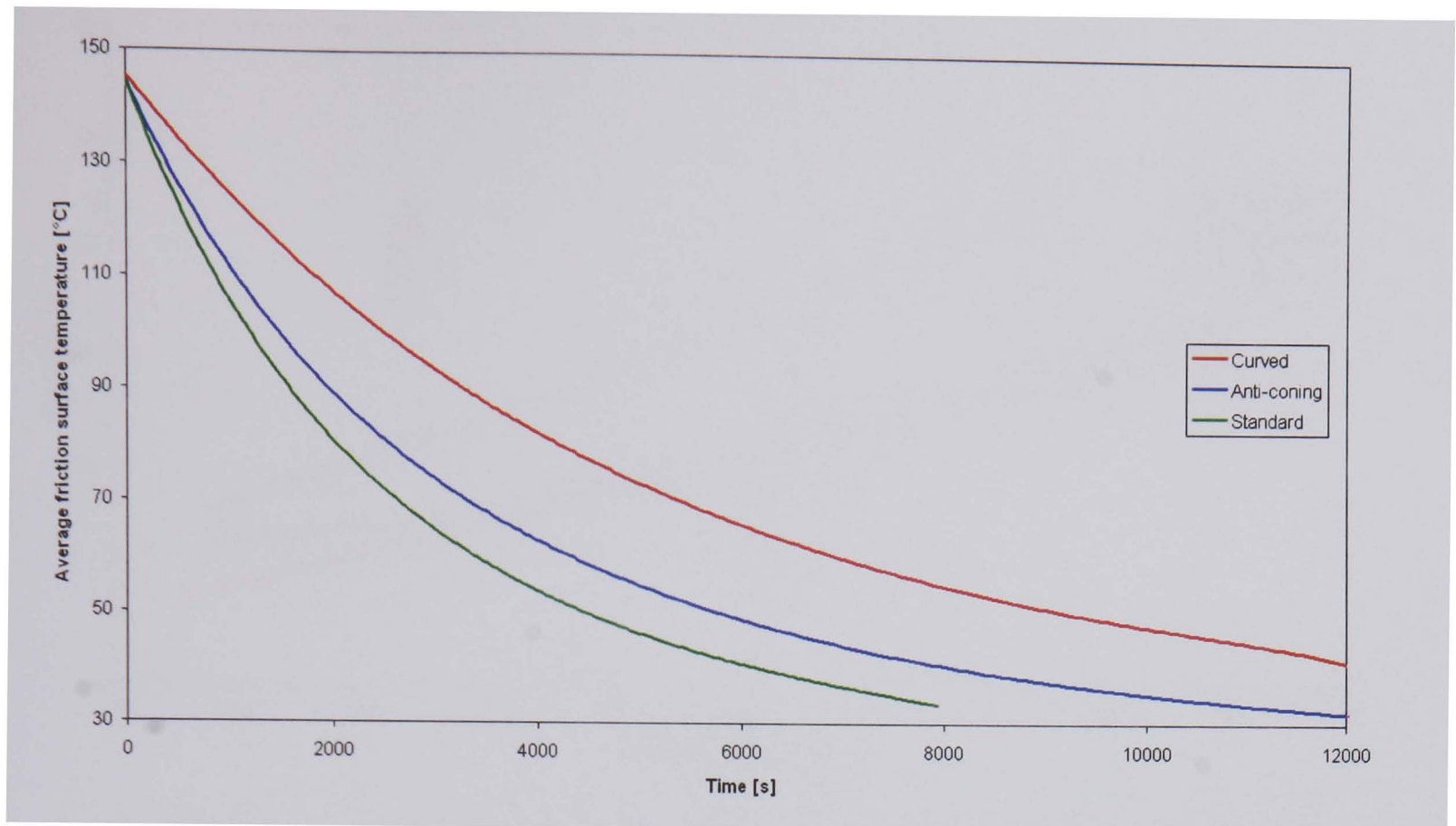


Figure 5.18 CV disc vane designs with standard wheel assembly (40 min^{-1})

Figure 5.19 shows the h_{avg} values calculated from the cooling curves of the different disc designs throughout the speed range of the CV for the average disc temperature of 100°C . The results are for the disc within the wheel assembly. The h_{avg} increases with rotational speed for all designs. The standard design has higher values of h_{avg} throughout the speed range. The anti-coning and curved designs have similar lower values of h_{avg} . At very low speeds the anti-coning disc design cooling performance is seen to improve, this is inconsistent with other measurements. It is thought that the anti-coning disc's smaller ventilation channel inlet does not restrict airflow at low speeds.

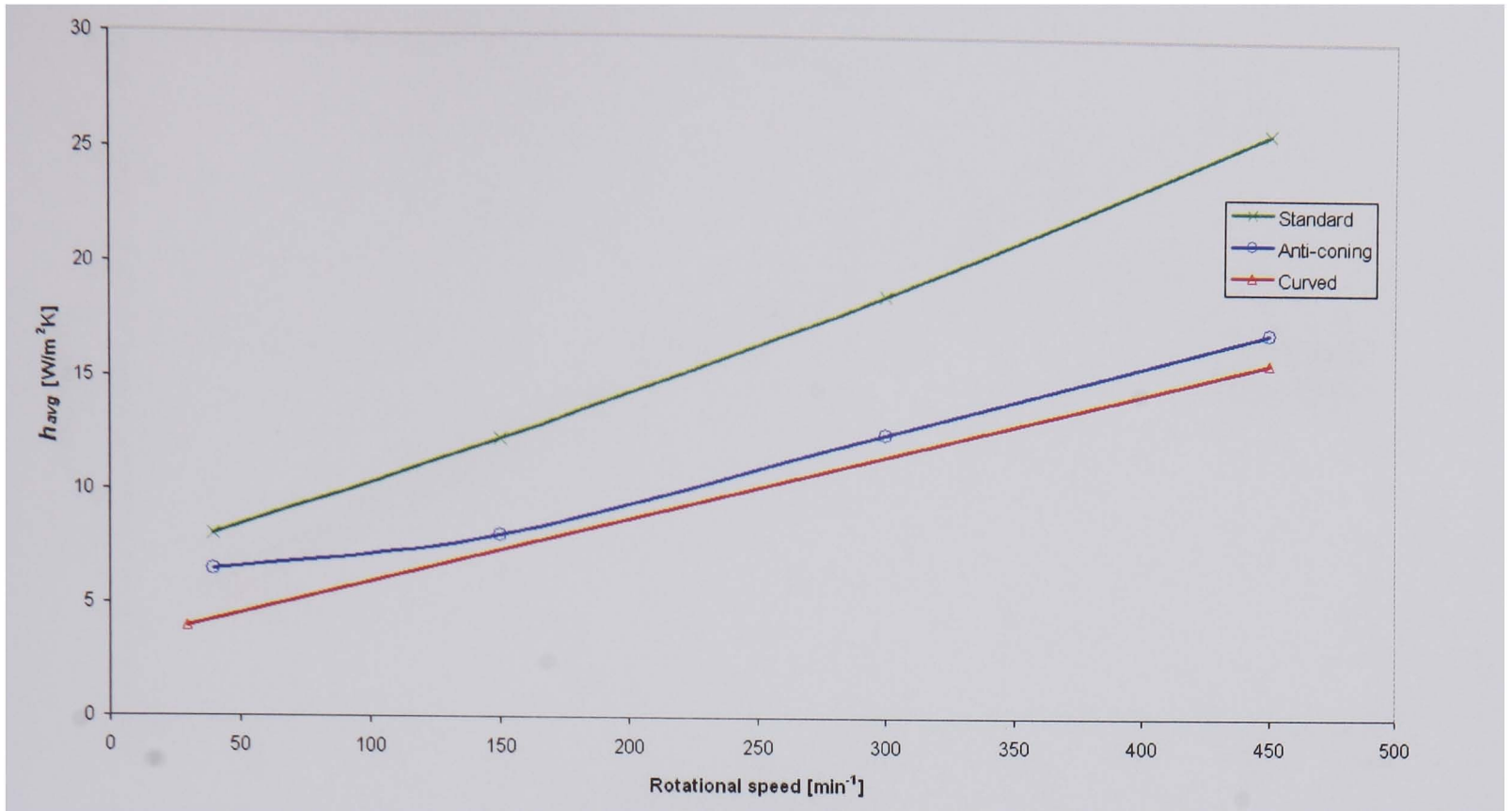


Figure 5.19 Effect of CV disc vane design on h_{avg} at 100°C, with wheel assembly

The results of Figure 5.17, Figure 5.18 and Figure 5.19 clearly show that the standard radial vane design CV disc cooling performance is superior to the anti-coning and curved vane designs. The standard disc draws air into the ventilation channel from the inboard side and therefore the wheel assembly has little effect on the cooling performance. The anti-coning design however, draws air into the ventilation channels on the outboard side and therefore the wheel assembly restricts air entering the ventilation channels. This is in agreement with air velocity measurements of Chapter 4.

Figure 5.20 shows a comparison of the h_{avg} for the standard and curved vane disc designs, measured for the disc only (wheel assembly removed). It can be seen that the two designs have similar cooling characteristics. The elaborate curved vane design does not improve cooling over the standard design and its performance deteriorates more with the wheel assembly fitted as shown in Figure 5.19.

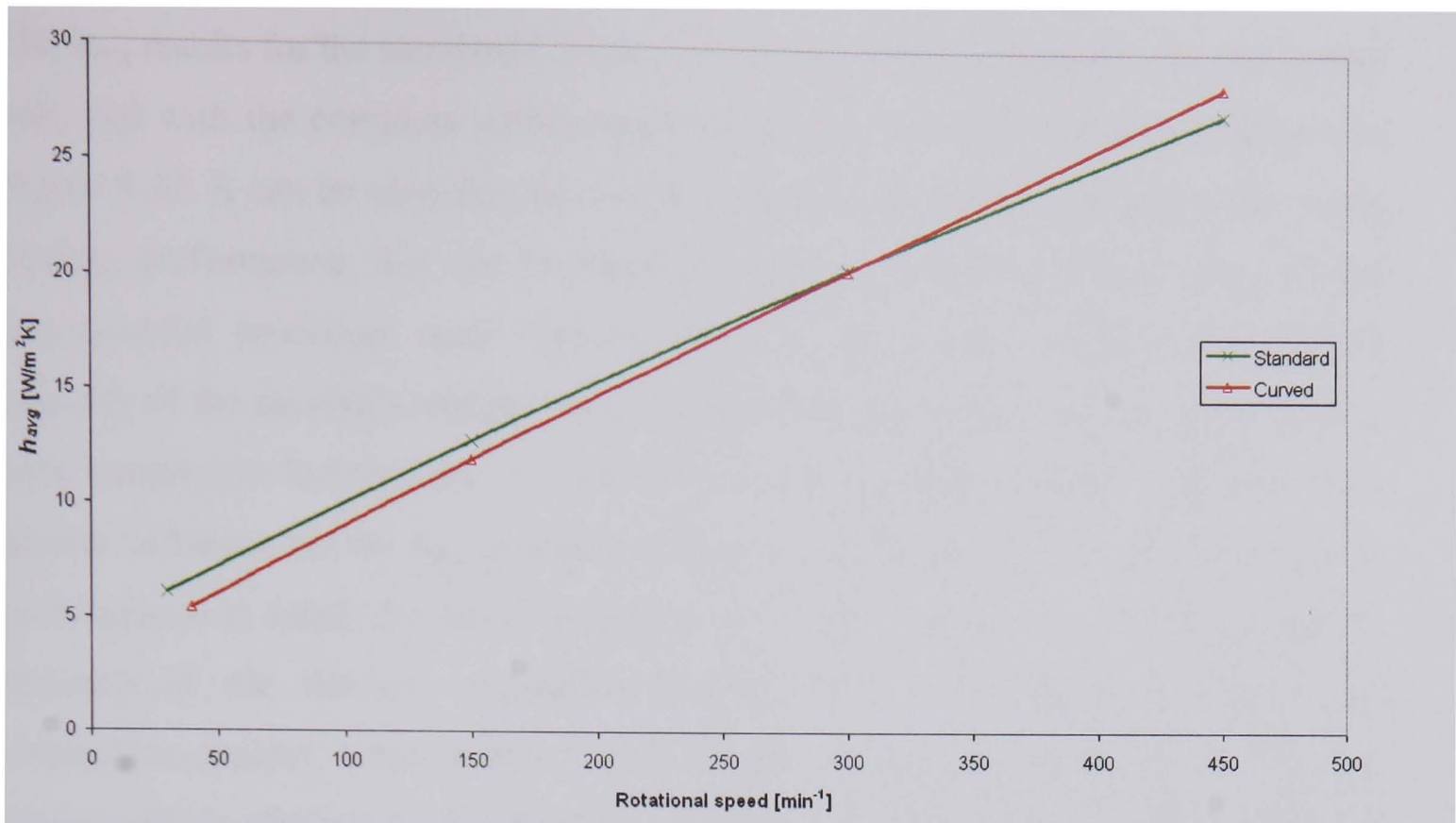


Figure 5.20 CV disc vane design comparison of h_{avg} values at 100°C, disc only

5.4.2 Influence of Wheel Assembly on Disc Cooling

Figure 5.21 shows the cooling curves for a standard CV disc with and without the standard wheel assembly rotating at 450 and 150 min^{-1} . It can be seen that reducing the rotational speed by 300 min^{-1} influences the cooling rate much more than ‘shrouding’ the disc with the wheel assembly.

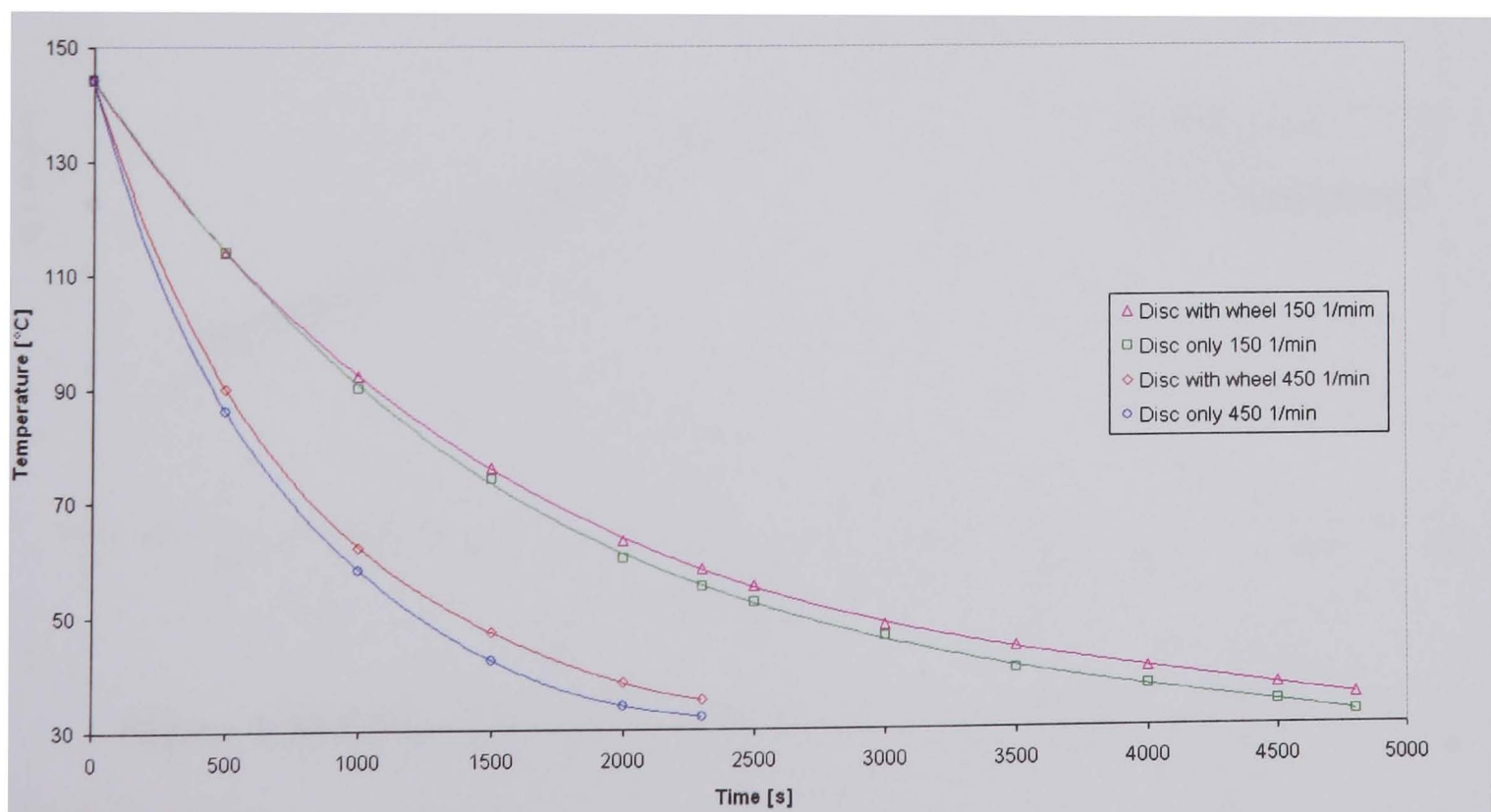


Figure 5.21 Cooling curves for a standard CV disc with and without wheel assembly

The h_{avg} results for the standard CV disc without the wheel assembly, with the carrier only and with the complete wheel assembly (carrier and steel wheel), are shown in Figure 5.22. It can be seen that the wheel carrier has no detrimental influence on the cooling performance; this can be expected, further confirming the accuracy of the experimental procedure used. The inclusion of the carrier increases the thermal capacity of the assembly and provides a larger cooling surface area, however there is little conduction between the two components. The complete wheel assembly has a greater influence on the h_{avg} at higher rotational speeds but the reduction in cooling performance is relatively small (reducing the value of h_{avg} by approximately 5%). Because of the inboard ventilation channel inlet, the wheel only affects the ventilation channel outlet airflow (reducing ventilation channel airspeed). The h_{avg} values will be affected by the reduction in surface airspeed (mainly in the ventilation channel) and a reduction in air supply to the outboard friction face. The film temperature at the disc surface will rise due to the wheel assembly shrouding the disc, reducing convective cooling.

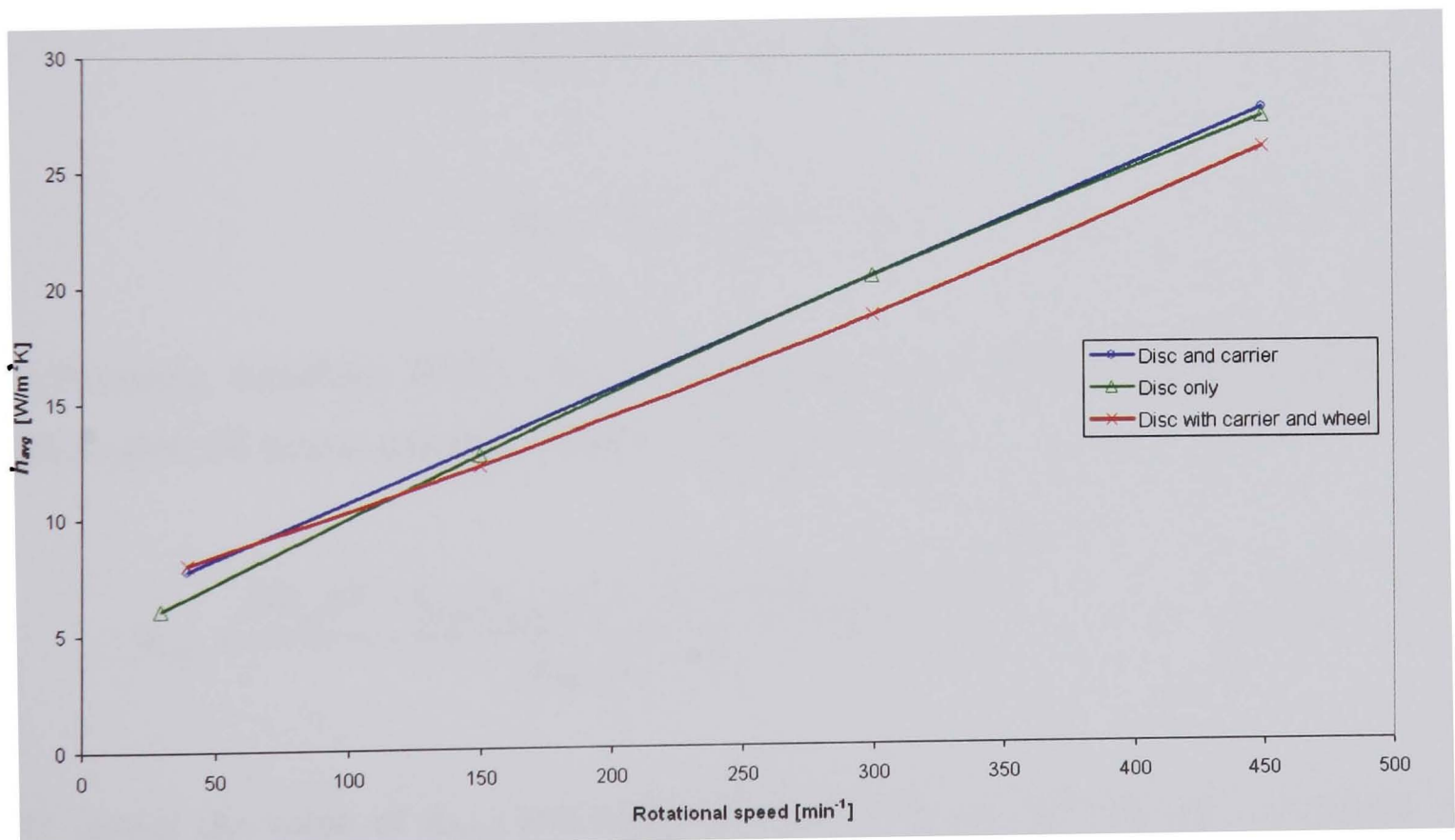


Figure 5.22 Effect of wheel assembly on standard CV disc h_{avg} at 100°C

5.4.3 Convective Heat Transfer Coefficients

The heat transfer coefficients determined from Spin Rig measurements are average ‘total’ heat transfer coefficients incorporating all three modes of cooling; convection, conduction and radiation. To determine the convective component, the heat dissipated by conduction and radiation components need to be subtracted from the total heat transfer coefficient h_{avg} . By modifying equation (5.1), h_{conv} can be determined by:

$$h_{conv} = \frac{Q_{total} - Q_{cond} - Q_{rad}}{A_{conv} (T_D - T_{\infty})} \quad (5.14)$$

The thermal power dissipated by conduction, radiation and convection can be calculated by equations (5.15), (5.16) and (5.17):

$$Q_{cond} = h_{cond} A_{cond} (T_D - T_C) \quad (5.15)$$

$$Q_{rad} = \sigma \epsilon A_{rad} (T_D^4 - T_{\infty}^4) \quad (5.16)$$

$$Q_{conv} = h_{conv} A_{conv} (T_D - T_{\infty}) \quad (5.17)$$

Substituting equations (5.12), (5.15) and (5.16) into equation (5.14) enables the calculation the convective heat transfer coefficient (h_{conv}):

$$h_{conv} = \frac{mc_p \Delta T - h_{cond} A_{cond} (T_D - T_C) - \epsilon \sigma A_{rad} (T_D^4 - T_{\infty}^4)}{A_{conv} (T_D - T_{\infty})} \quad (5.18)$$

By taking the value of h_{cond} and emissivity (ϵ) based on Spin Rig measurements detailed in Chapter 6 and 7, h_{conv} has been determined. An average value of 988 kW/m²K has been used for h_{cond} (the standard interface condition for 300 Nm bolt torque). The value of ϵ used is 0.2. The value of c_p is assumed constant with temperature; a standard value of 420 J/kgK is used (Kreith 1986). The mass used in

the determination of heat transfer coefficients is the combined mass of the disc and adapter (39.1 kg), see Chapter 3 for details.

The measured h_{avg} for the standard CV disc without wheel assembly (disc only) and the h_{conv} values throughout the CV speed range are shown in Figure 5.23. The average friction surface temperature is 100°C. It can be seen from the difference of the h_{avg} and the h_{conv} values, that the radiative and conductive components are speed independent and account for approximately 2 W/m²K of the total h_{avg} . At 450 min⁻¹ h_{conv} is 25 W/m²K dropping almost linearly to 4 W/m²K at 30 min⁻¹.

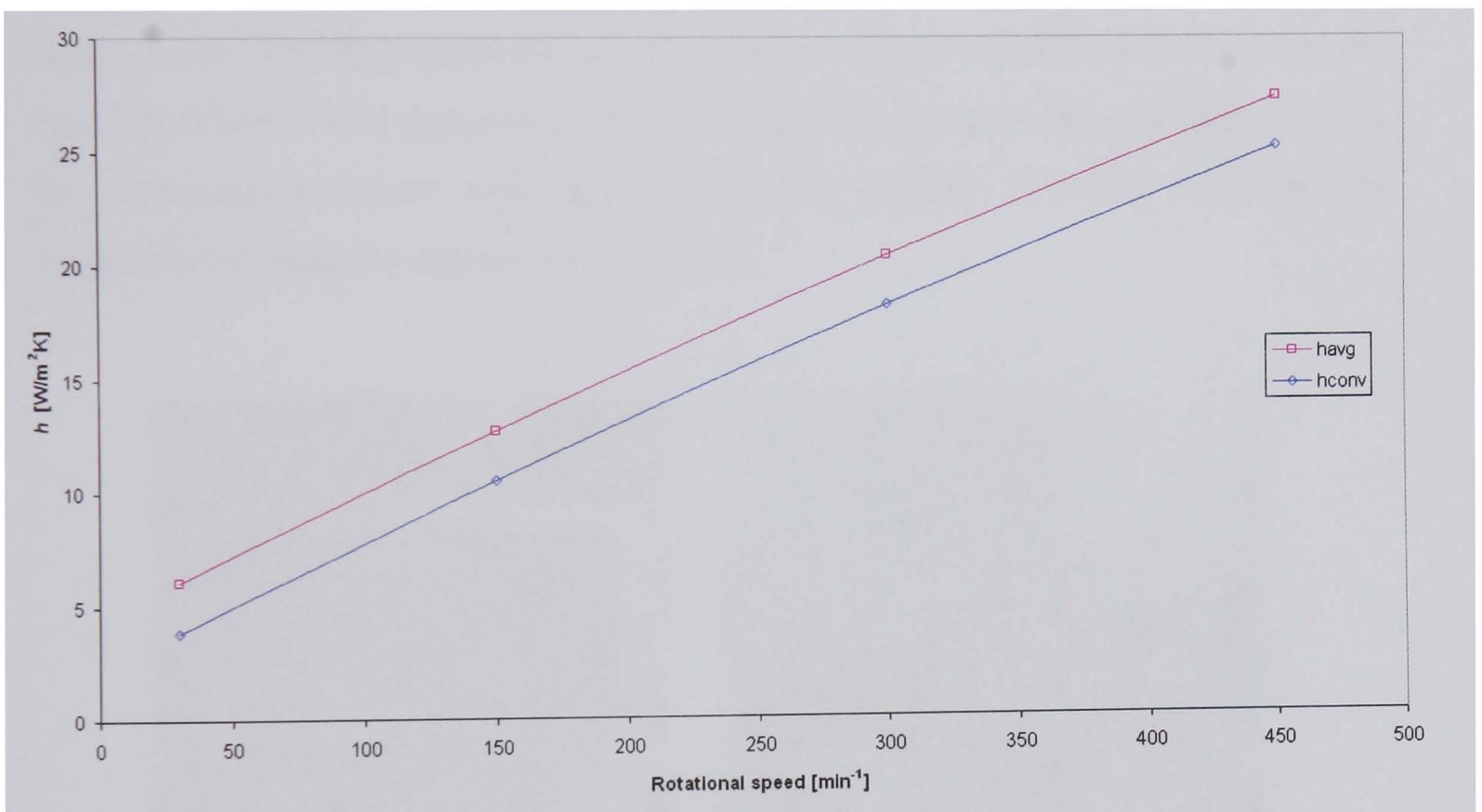


Figure 5.23 Measured h_{avg} and h_{conv} for the standard CV disc (disc only)

The h_{conv} function for the standard CV disc defining its relationship with angular velocity (ω [rad/s]) can be calculated by the equation of the h_{conv} curve of Figure 5.23 and is given by equation (5.19). Equation (5.19) shows a linear relationship, which compares well to the published equations given in Section 5.2:

$$h_{conv} = 0.484\omega + 2.64 \quad (5.19)$$

Examination of equation (5.19) provides the natural convective component (speed independent) value of 2.65 W/m²K.

5.5 Measurement of TGV Railway Disc Cooling

Experimental studies of convective heat dissipation of the TGV railway disc (see Chapter 3) were also conducted on the Spin Rig. The obtained cooling curves enable heat transfer coefficients to be derived and CFD results to be verified. The cooling tests were performed in a similar manner to the CV disc (see Section 5.4). However, the TGV disc has three times the mass of the CV disc and the hot air heaters could not be used because of insufficient power to heat the disc to test temperature. Therefore, an industrial oven was used to heat the disc, before it was mounted to the spin Rig shaft, as described in Chapter 3. The disc was positioned in a steel frame then placed in the oven and heated to 500°C (taking approximately three hours), see Figure 5.24a. The disc was removed from the oven with a forklift and moved to the Spin Rig where it was mounted to the Spin Rig shaft, using a crane, see Figure 5.24b. The mounting procedure took approximately 20 minutes, by which time the disc temperature dropped to approximately 300°C.

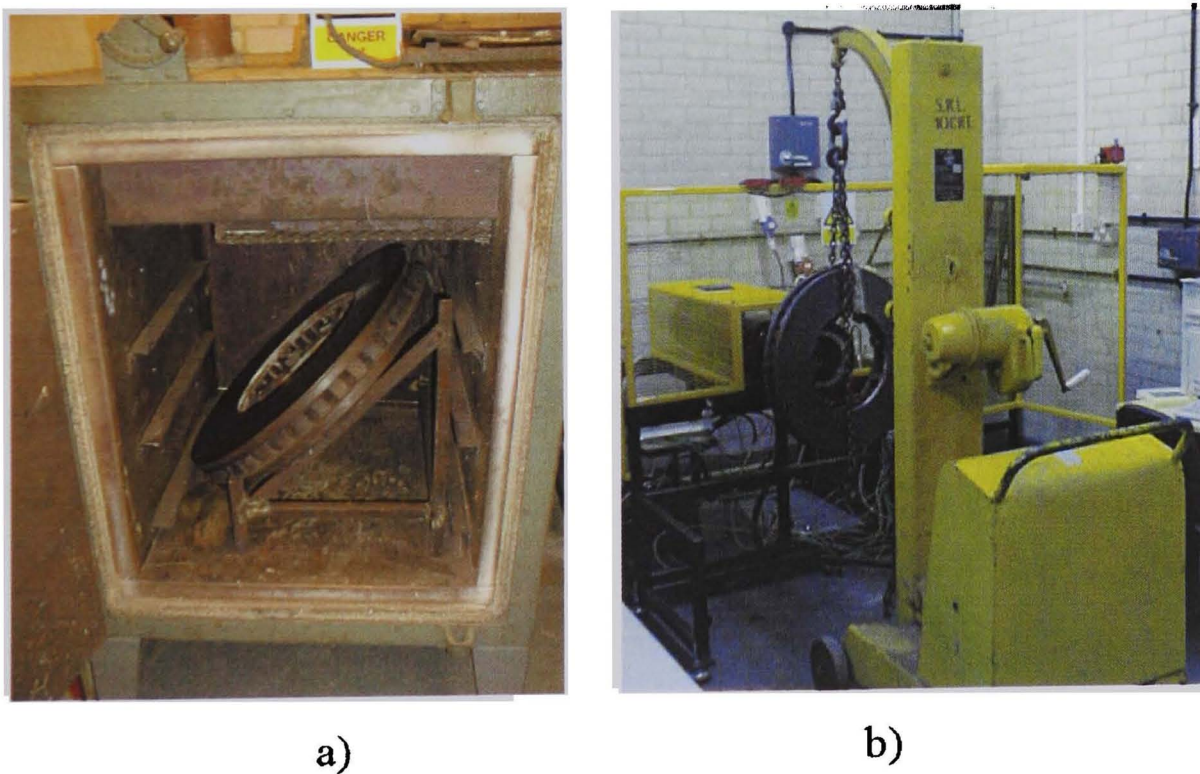


Figure 5.24 TGV disc (a) heated in oven and (b) mounted to Spin Rig shaft

A series of rubbing and welded tip thermocouples (see Chapter 3) were placed on and round the disc, as detailed in Figure 5.25 and Figure 5.26. The thermocouples were mounted to an articulated arm with a centre lock for quick positioning. Cooling measurements began at a disc surface temperature of approximately 250°C.

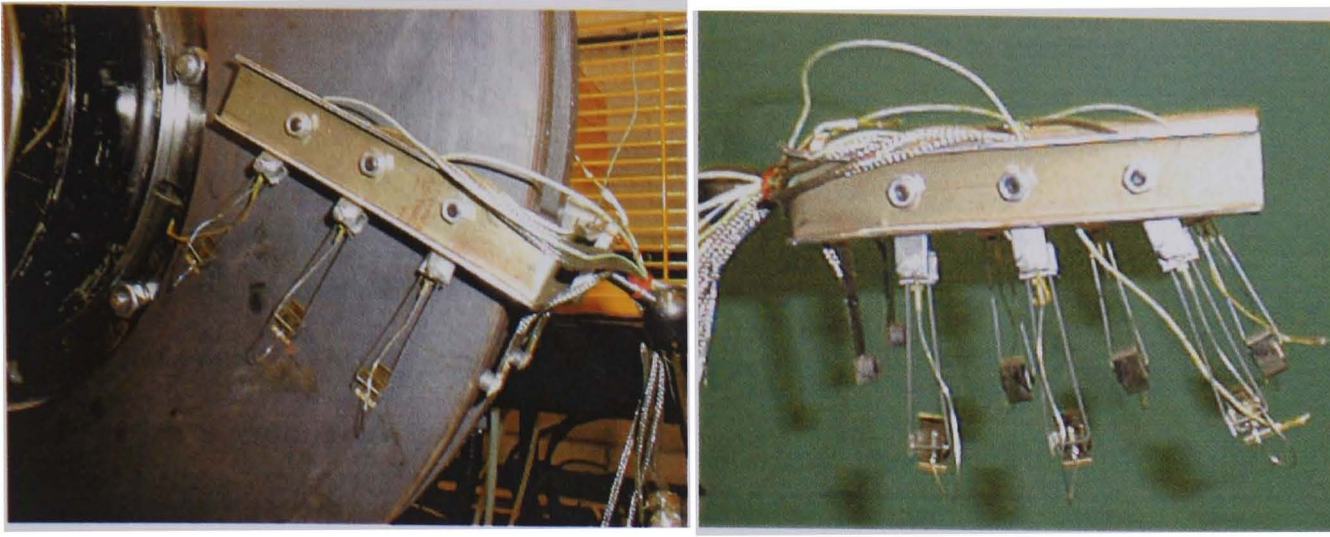


Figure 5.25 TGV disc rubbing thermocouple arm

Fourteen thermocouples measurements were taken during the cooling tests as shown in Figure 5.26 (the fourteenth thermocouple measured ambient temperature). Three low friction sled rubbing thermocouples (Figure 5.25) were positioned on each friction surface of the disc (①, ②, ③, ⑥, ⑦ and ⑧), two copper tip rubbing thermocouples were placed on the inboard and outboard rim of the disc (④ and ⑤). The sled rubbing thermocouples were used on the friction surfaces of the disc because they provided good contact with the flat surface. Copper tip rubbing thermocouples provided the best surface contact for the curved surfaces of the disc. Welded tip thermocouples measured air temperature at the vane outlet ③, and vane inlets ① and ⑤. The film temperature was measured 3 mm from the friction surface of the disc at the mean diameter, ② and ④. From boundary layer thickness equation (4.3) given in Chapter 4, the boundary layer thickness ranges from 9.25 (high temperature low speed) to 0.75 mm.

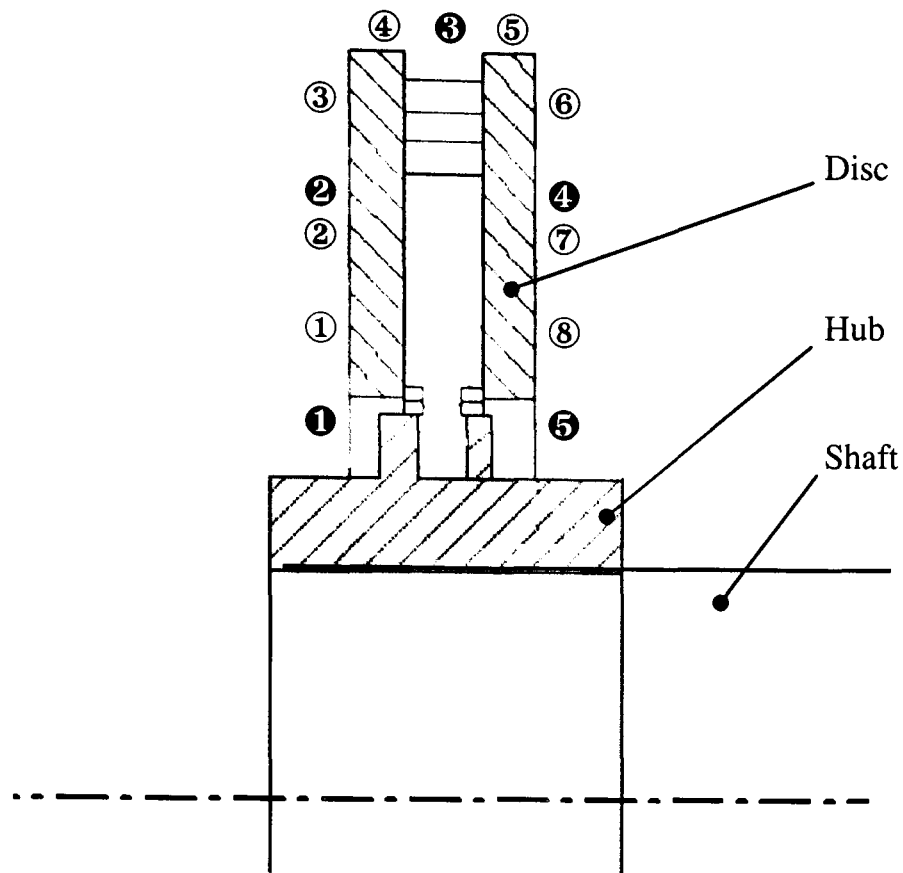


Figure 5.26 Position of (○) rubbing and (●) welded tip thermocouples used for the TGV disc experiments

After the thermocouples are positioned, the disc is rotated at the required speed and thermocouple measurements are logged, at a sample rate of 0.25 Hz. The brake assembly is rotated until surface temperatures reach levels approaching ambient temperature, (approximately 40°C). All the tests were performed in still air. Figure 5.27 shows the typical cooling curves and surrounding air temperature for a brake assembly during Spin Rig cooling tests.

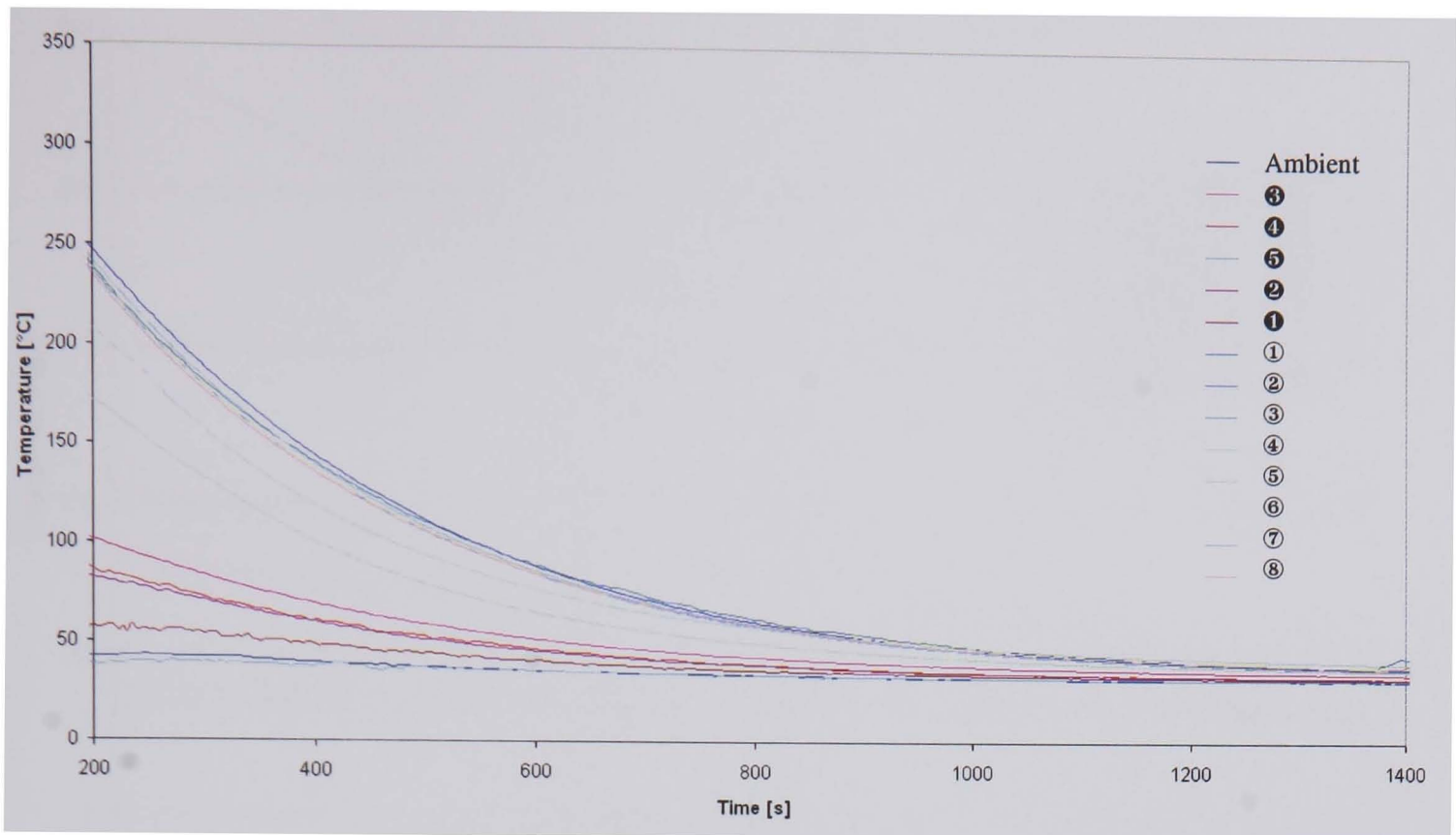


Figure 5.27 TGV disc typical surface and air temperatures during cooling

To calculate h_{avg} , the cooling rates are measured at a range of average temperatures using the slope of the cooling curves, as explained for the CV disc (Section 5.4). The ‘nominal’ cooling curve was calculated using the average value of the six friction surface temperatures (①, ②, ③, ⑥, ⑦ and ⑧), as shown in Figure 5.26, Figure 5.27 shows that the temperatures values are very close. Using equation (5.13) as described in Section 5.4, h_{avg} is calculated. The ‘wetted’ disc areas convecting heat are given in Chapter 3.

Figure 5.28 shows the cooling curves of the average friction surface and air temperatures when the disc is rotating at 1000 min^{-1} . The air temperature measurements are used to calculate h_{avg} and verify the CFD results (in Section 5.6). It can be seen that for an average friction surface temperature of 200°C the ventilation channel exit temperature (3) is 90°C , which is 50°C higher than the ventilation channel inlet temperature (5 and 1). The friction surface air temperature (2 and 4) is in the region of 70°C . Selected air temperatures are given later in Table 5.7 and are compared with CFD modelling results.

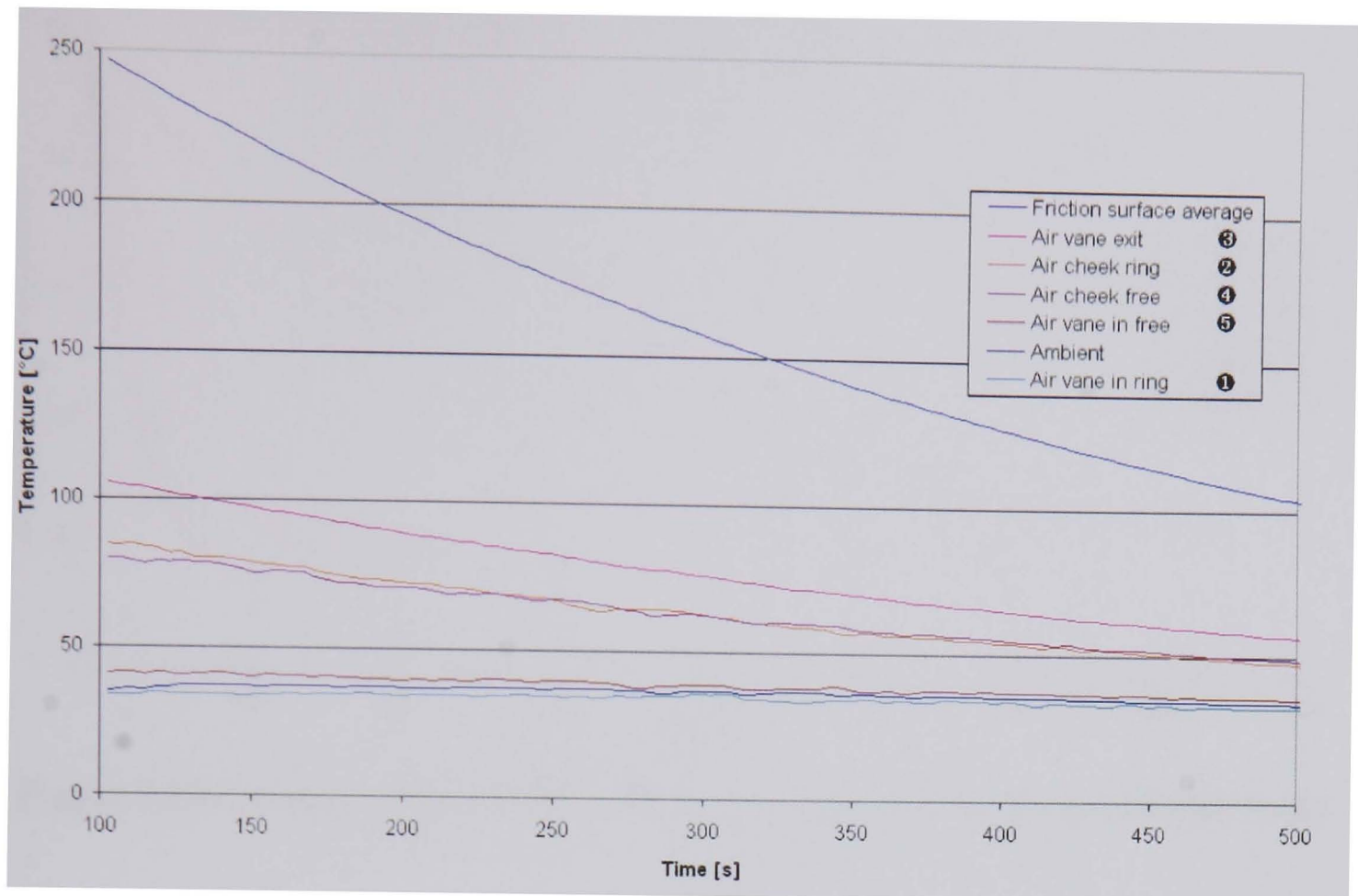


Figure 5.28 Average friction surface and air temperatures for a TGV disc rotating at 1000 min^{-1}

5.5.1 Influence of Rotational Speed on Disc Cooling

To investigate the influence of rotational speed on the cooling of the TGV disc, tests were conducted at rotational speeds ranging from 0 to 1800 min^{-1} on the Spin Rig. Figure 5.29 shows the cooling curves of the TGV disc for the speed range of the TGV train. The cooling curves also show the times for the disc to cool from 250°C , to near ambient temperature (40°C). The cooling rates increase with rotational speed. The disc takes 1000 seconds to cool from 250 to 40°C at 1800 min^{-1} (the top of the speed range), compared to 3000 seconds at 360 min^{-1} . Figure 5.29 also shows the cooling rate for the stationary disc, which as expected, shows the lowest cooling rate. After 3000 seconds, the stationary disc temperature is 75°C higher than the disc rotating at 360 min^{-1} .

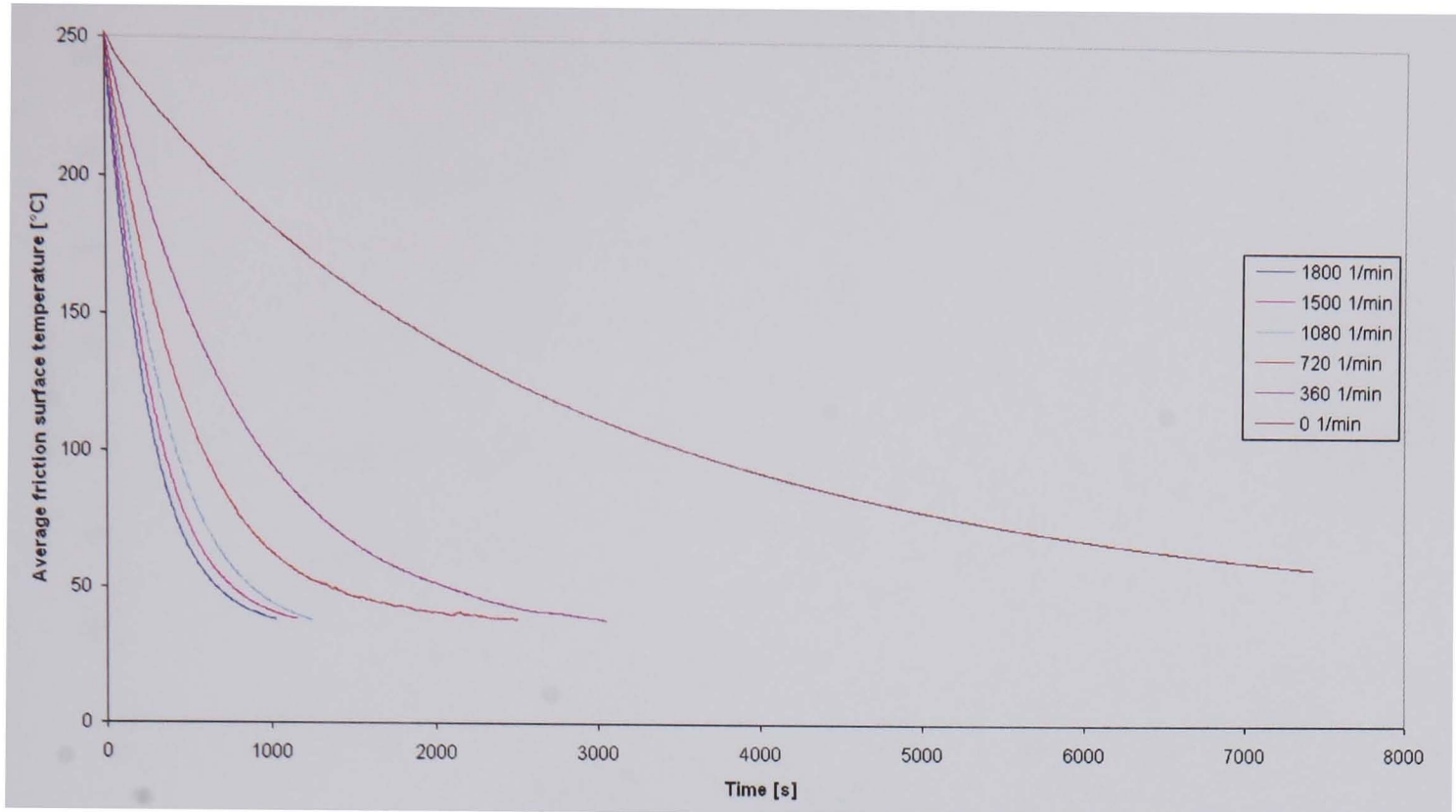


Figure 5.29 Cooling curves for the TGV disc, average friction surface temperatures

Based on the cooling curves the calculated h_{avg} values are shown in Figure 5.30. The h_{avg} values have been calculated for all the rotational speeds for a range of temperatures (100 to 225°C). The value of h_{avg} is approximately constant in the temperature range considered. A maximum value of 116 W/m²K for h_{avg} is calculated at 1800 min⁻¹, a minimum value of 7.5 W/m²K is calculated when the disc is stationary at 100°C. At 0 min⁻¹, where natural convection is dominant, h_{avg} values increase slightly with temperature, which can be expected as higher surface temperatures increase air buoyancy generating airflow.

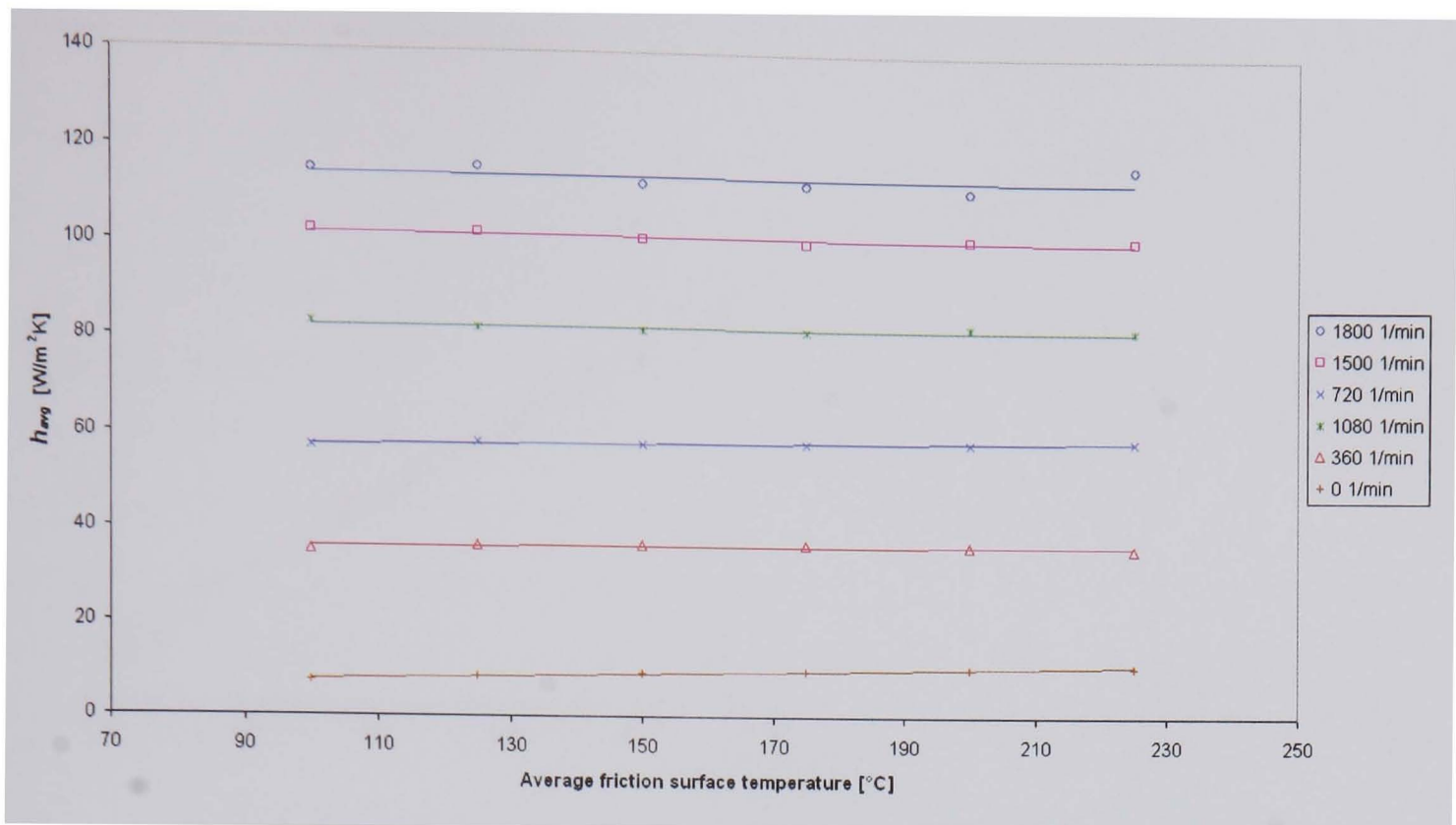


Figure 5.30 TGV disc measured h_{avg} comparison

The h_{conv} values are calculated from previous measurements using the same methodology described for the CV disc. Figure 5.31 shows the change of h_{avg} and h_{conv} with rotational speed for an average disc surface temperature of 200°C. The value of h_{avg} rises almost linearly from 10 W/m²K at 0 min⁻¹ to 112 W/m²K at 1800 min⁻¹, the rate of h_{avg} increase reduces above the rotational speed of 1200 min⁻¹. It can be seen from the graph that the radiative and conductive components are speed independent and account for approximately 3.5 W/m²K of the h_{avg} value. At 450 min⁻¹ the value of h_{conv} is 108 W/m²K dropping at the same rate as the h_{avg} curve to 6.4 W/m²K at 0 min⁻¹. These values show that natural convection for the TGV disc is higher than the CV disc.

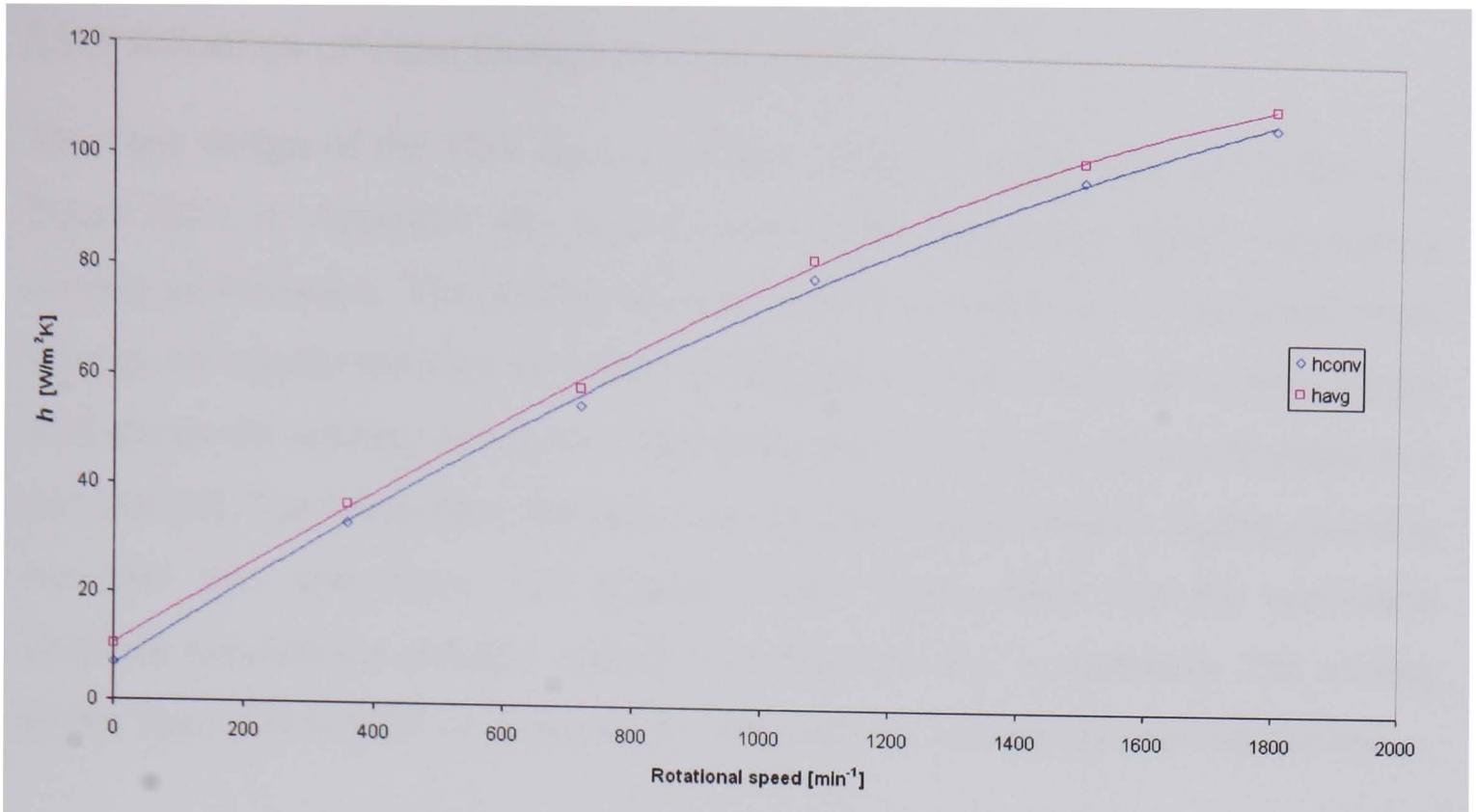


Figure 5.31 Measured h_{avg} and h_{conv} values for the TGV disc

The h_{conv} function for the TGV railway disc defining its approximate relationship with angular velocity (ω [rad/s]) can be calculated by the equation of the h_{conv} curve of Figure 5.31, giving a 2nd order polynomial trend:

$$h_{conv} = -1E-05\omega^2 + 0.0793\omega + 6.4 \quad (5.20)$$

Which, can be approximated by the linear function:

$$h_{conv} \approx 0.5417\omega + 11.77 \quad (5.21)$$

Examination of equation (5.21) provides the natural convective component (speed independent) value of approximately 11.8 W/m²K. The h_{conv} values for the TGV disc are higher than those of the CV disc at the same rotational speeds (Section 5.4.3), this is expected because of the larger diameter and hence surface speeds of the TGV disc surface. Similar trends to the theoretical values given in Section 5.2 can be seen. The TGV disc has a higher natural convection component than the CV disc, shown by equations (5.19) and (5.21). The radial vane/pillar design allows air to rise through the disc at low rotational speeds, improving low speed cooling characteristics. Also the large inside and outside radius of the disc provides large ventilation channel openings.

5.5.2 Influence of Vane Design on Disc Cooling

The vane design of the TGV disc is a combination of radial vanes and pillars (see Figure B2.1 in Appendix B), used to reduce pumping losses whilst maintaining cooling performance. The pillared section of the disc allows air to rise quite freely through the spaces between the pillars at stationary or low rotational speeds. Figure 5.32 shows the cooling curves for a stationary disc with the ventilation channels free and blocked. The ventilation channels were blocked with fibreglass lagging placed at the vane inlet and outlet. The cooling curves clearly show that the ventilation channels substantially aid disc cooling even when the disc is stationary. The cooling period from 250 to 60°C is increased by 20% with the cooling channels unblocked.

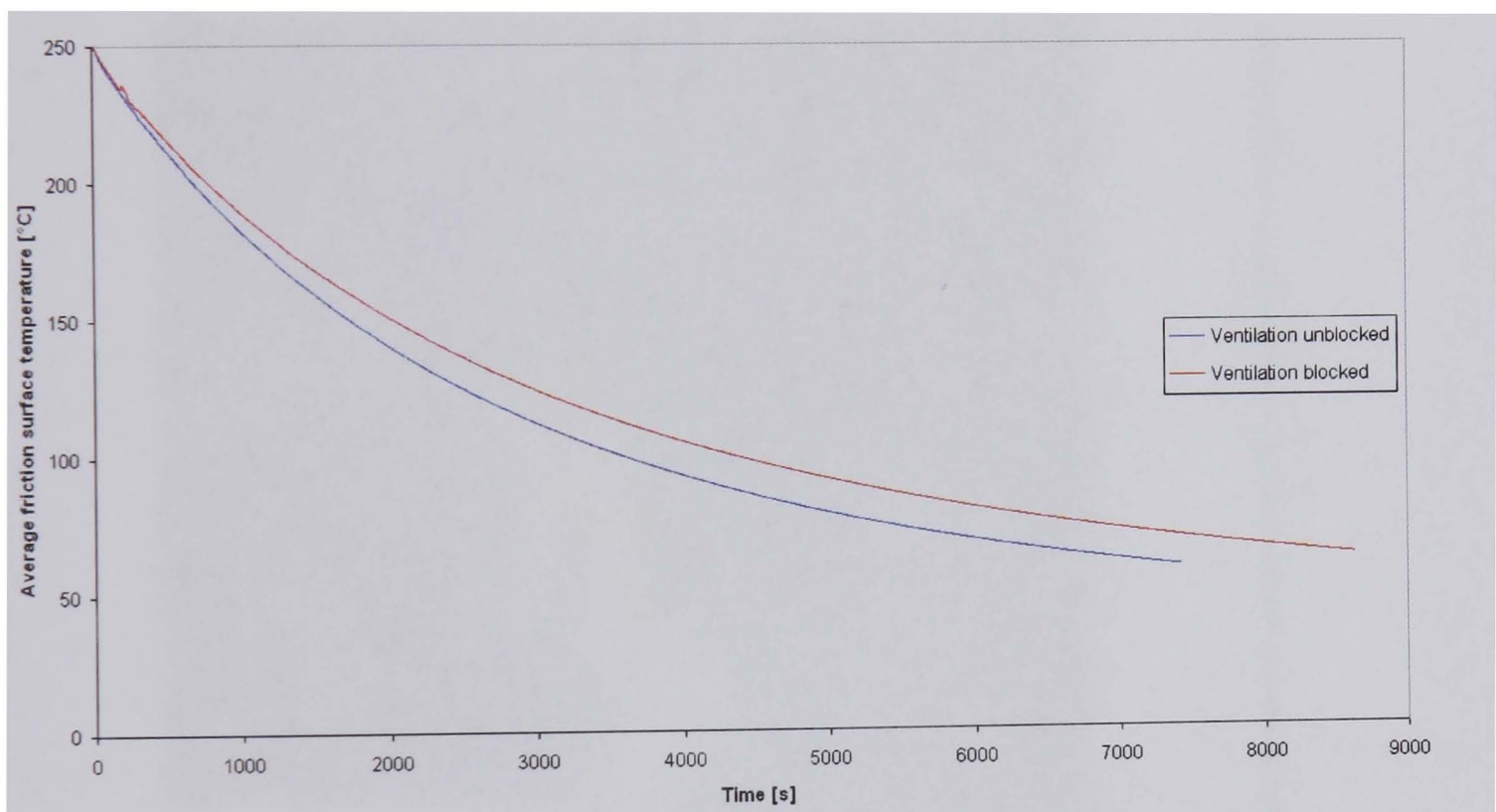


Figure 5.32 TGV disc cooling, average friction surface temperature, 0 min⁻¹

5.6 CFD Analysis of Convective Heat Transfer Coefficients

The SDRC I-DEAS package with the electronic system cooling (ESC) module was used for the CFD analyses. The CFD modelling methods are detailed in Chapter 4. The ESC analyses provided output results including h_{conv} distribution for all disc surfaces. The h_{conv} values are calculated by the temperatures of the model and the airflow in the region. To obtain h_{conv} values, a steady state model was analysed with

the solid disc elements set at a constant temperature and the disc rotated in a volume of still air that is vented to ambient.

5.6.1 Commercial Vehicle Disc

Based on the CFD model of Chapter 4 Figure 5.33 and Figure 5.34 show (two half-section) temperature contour maps of the fluid surrounding the standard CV disc mounted on the Spin Rig shaft, for the steady state condition. The discs are rotating at 450 min^{-1} and disc temperatures are 100°C and 600°C respectively. The ambient air temperature was set at 20°C . The model is of the 'disc only'.

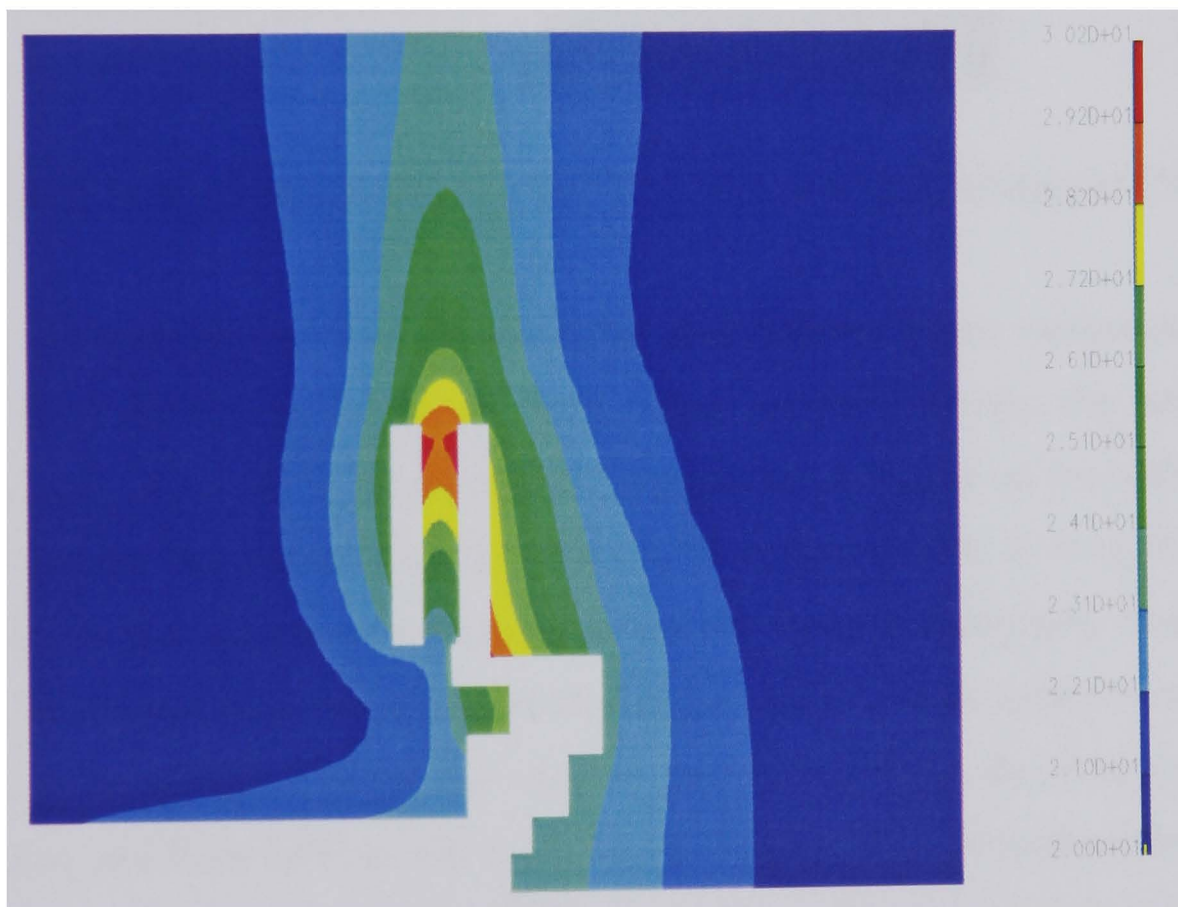


Figure 5.33 Air temperature for a 100°C standard CV disc rotating at 450 min^{-1}

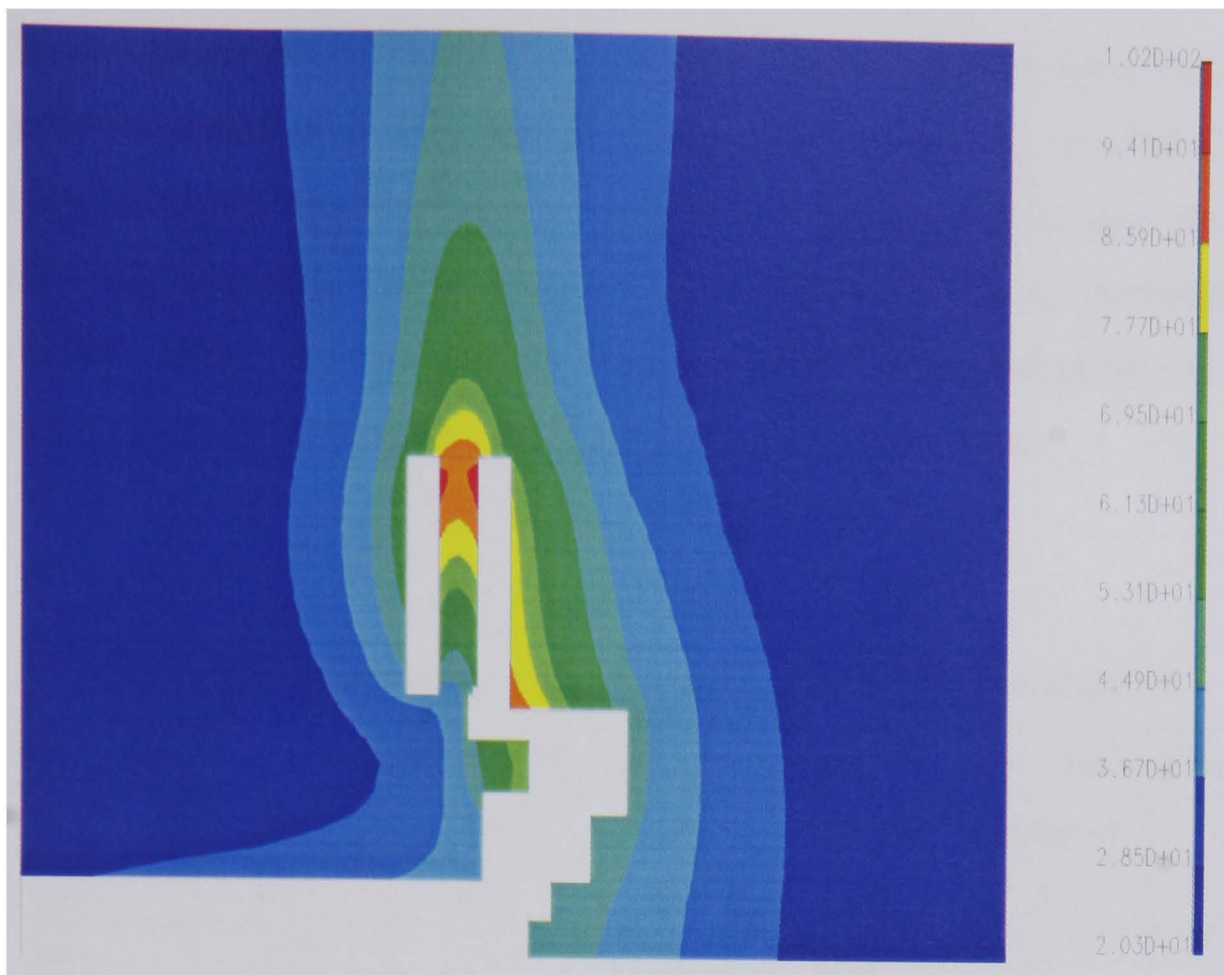


Figure 5.34 Air temperature for a 600°C standard CV disc rotating at 450 min⁻¹

Figure 5.33 and Figure 5.34 show similar distributions of air temperature. Both figures show differences in the air temperature contours between the inboard and outboard side of the disc. The average air temperature is higher on the outboard side (hat side) of the disc than the inboard side (in the region of 60°C at the surface of the 600°C disc). The temperature increase is caused by heat dissipation from the hat section. The air temperature in the ventilation channel shows an approximately linear increase, from around 23°C at the entry to just over 30°C at the vane exit for the 100°C disc, and from 50°C to 100°C for the 600°C disc. The air temperature increase through the vane is approximately 12% of the disc surface temperature for both disc temperatures.

Table 5.4 and Table 5.5 show the air temperatures for the disc at 100 and 600°C throughout the CV rotational speeds. It can be seen that vane exit air temperatures drop slightly with increased rotational speed of the disc. The higher velocity of the air flowing over the vane surface reduces the amount of heat the air can absorb. The larger temperature difference between the air and disc surface, increases the heat transfer at the surface, as defined by equation (5.17). The vane inlet air is drawn mainly from the surrounding air, as shown in Chapter 4, but higher disc temperatures

still influence the air temperature. The friction surface air temperatures are constant with rotational speed at a disc surface temperature of 100°C, at 600°C the air temperature increases with rotational speed. The air boundary layer near the surface of the disc will be at a higher temperature than the surrounding air temperature and the thickness of the boundary layer increases with surface temperature, causing higher temperatures at the measuring point, 3 mm from the surface.

Table 5.4 CFD air temperatures for the standard CV disc at 100°C

| Rotational speed [min ⁻¹] | Ventilation channel [°C] | | | Friction surface (mean radius) [°C] | | |
|--|--------------------------|------|-----|-------------------------------------|----------|-----|
| | Inlet | Exit | ΔT | Inboard | Outboard | ΔT |
| 40 | 23.1 | 32.6 | 9.5 | 26.2 | 28.2 | 2.0 |
| 150 | 24.7 | 30.0 | 5.3 | 24.9 | 27.2 | 2.3 |
| 300 | 22.6 | 29.2 | 6.5 | 25.0 | 27.7 | 2.7 |
| 450 | 22.6 | 28.9 | 6.3 | 25.0 | 27.8 | 2.8 |

Table 5.5 CFD air temperatures for the standard CV disc at 600°C

| Rotational speed [min ⁻¹] | Ventilation channel [°C] | | | Friction surface (at mean radius) [°C] | | |
|--|--------------------------|-------|------|--|----------|------|
| | Inlet | Exit | ΔT | Inboard | Outboard | ΔT |
| 150 | 35.0 | 104.0 | 69.0 | 52.0 | 52.0 | 0.0 |
| 450 | 39.3 | 90.6 | 51.3 | 56.7 | 82.1 | 25.4 |

CFD also enables the contour plot of the h_{conv} values. Figure 5.35 shows the h_{conv} values for a standard vane CV disc rotating at 450 min⁻¹ at a fixed temperature of 100°C. It can be seen that the h_{conv} values increase radially from the inside diameter to the outside diameter. The highest h_{conv} values are seen at the outer rim of the disc (the region with the highest surface speed). The h_{conv} values are shown to be higher at the vane inlet, where airflow entering the vane has not fully developed (as shown in Figure 5.2). The h_{conv} contour plots are useful for the examination of local h_{conv} values allowing the determination of areas dissipating heat inefficiently and allowing small design modifications to be directly evaluated.

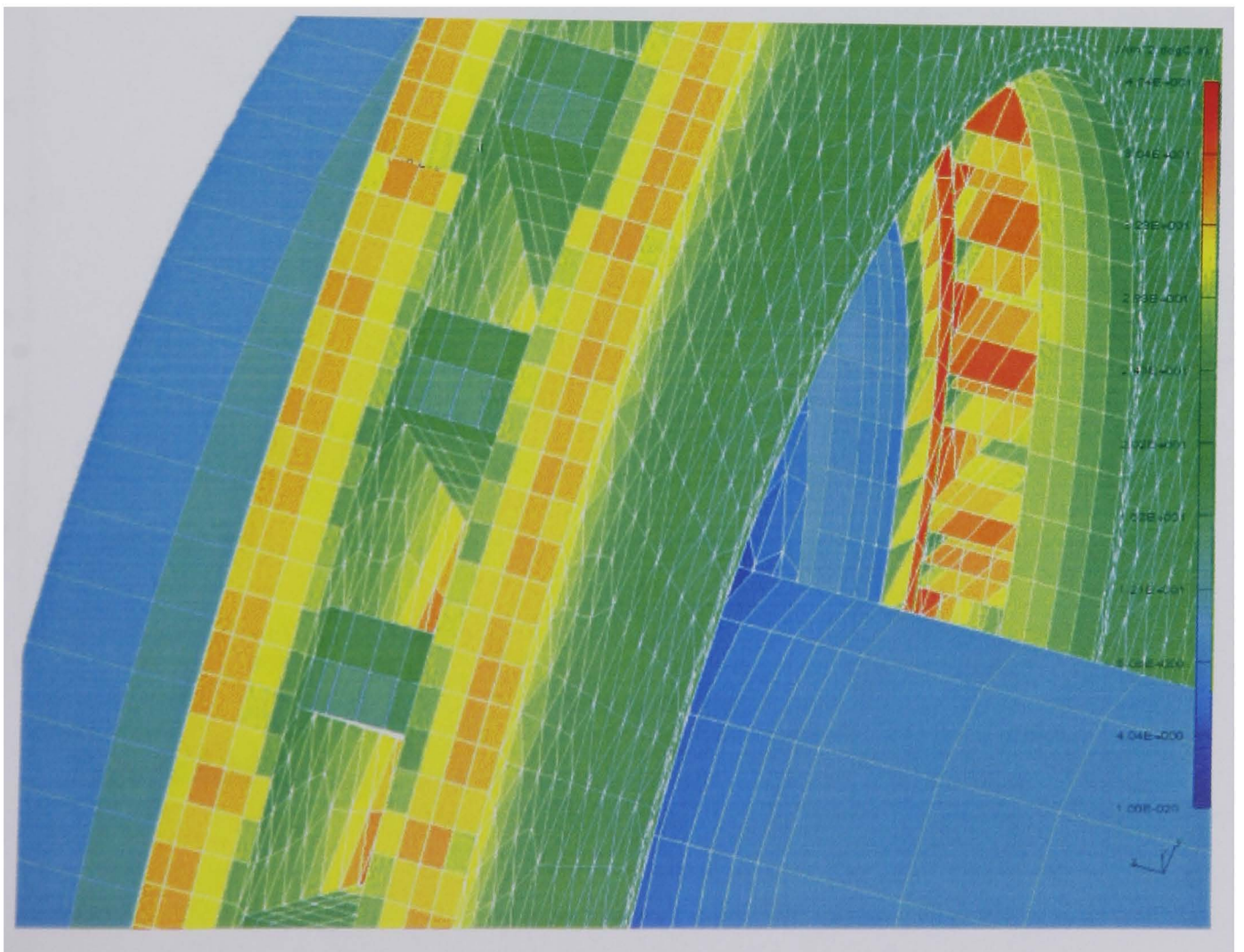
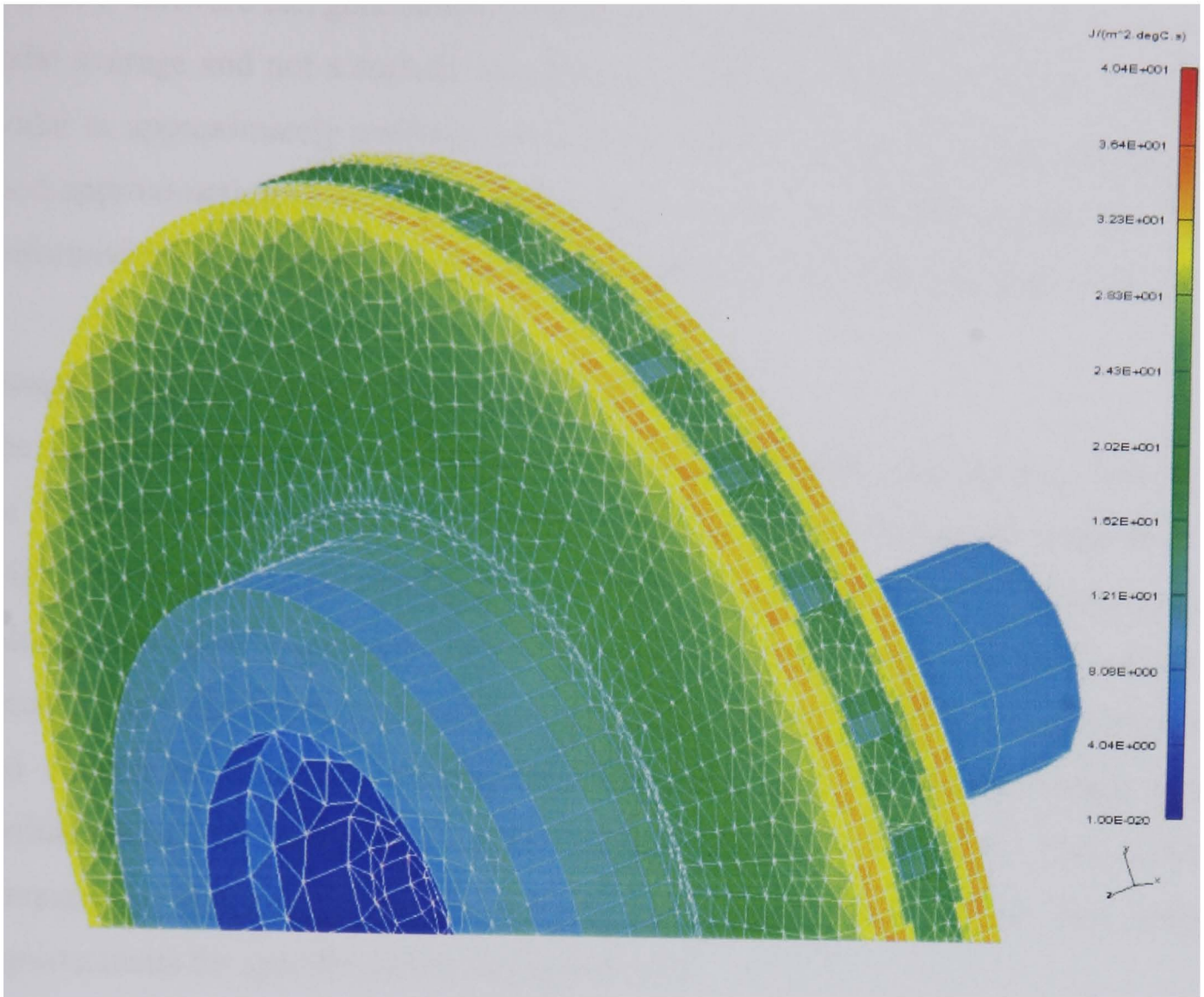


Figure 5.35 Standard CV disc CFD h_{conv} values rotating at 450 min^{-1} at 100°C

The ESC software can generate an average h_{conv} value for selected elements. This is a nodal average and not a surface area average. However, the element size of the disc model is approximately uniform (see Figure 5.35) and thus the nodal average is a good approximation of the average h_{conv} value. A number of CFD analyses have been performed for two disc temperatures, 100 and 600°C, for the speed range of the CV.

Comparison of Standard CV Disc h_{conv} Values

The values of average h_{conv} values are shown in Figure 5.36. Average h_{conv} values for the CFD model at 600°C are slightly lower throughout the speed range than at 100°C. CFD results are compared with Spin Rig results at 100°C. Experimental values show good agreement with CFD results, particularly at higher rotational speeds. The CFD modelling enables detail insight into local heat transfer coefficients and convective heat flux distribution. The good agreement of the results gives confidence in the local h_{conv} CFD predictions (see Table 5.6). This allows comparative analysis of design changes and determination of the best design improvements for specific duties and applications.

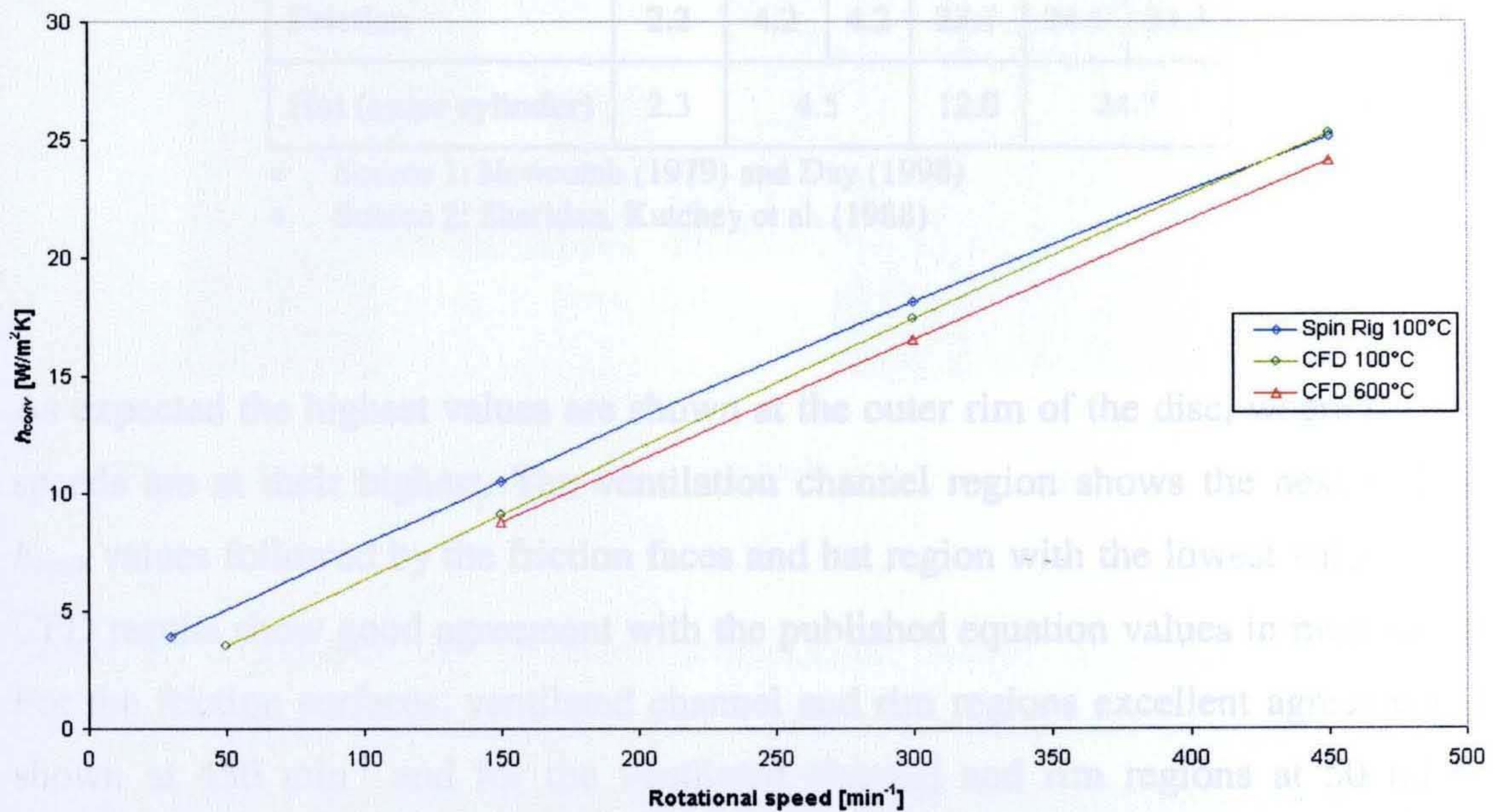


Figure 5.36 Average h_{conv} values for the standard CV disc (disc only)

The CFD h_{conv} values have been broken down into surface areas as shown in Figure 5.3 and presented in Table 5.6. The average CFD h_{conv} values are given for the outer rim, friction surface, ventilation channels, and hat regions for the rotational speeds of 50 and 450 min^{-1} , the results are compared with published h_{conv} equations presented in Section 5.2. The h_{conv} values calculated from equations used by Newcomb (1979) and Day (1998) are shown in column 1 and values from equations used by Sheridan, Kutchev et al. (1988) are shown in column 2. For the hat and rim regions identical equations are given.

Table 5.6 Comparison of CFD and published equation local h_{conv} values for the CV disc surfaces at 100°C

| Surface | Average h_{conv} [W/m ² K] | | | | | |
|-----------------------------|---|--------|-----|-----------------------|--------|------|
| | 50 min^{-1} | | | 450 min^{-1} | | |
| | CFD | Source | | CFD | Source | |
| | | 1 | 2 | | 1 | 2 |
| Rim (outer) | 4.3 | 5.6 | | 30.1 | 19.7 | |
| Ventilation channel | 4.2 | 10.8 | 4.0 | 26.9 | 63.1 | 27.0 |
| Friction | 2.2 | 4.2 | 4.2 | 23.1 | 24.1 | 31.3 |
| Hat (outer cylinder) | 2.3 | 4.5 | | 12.0 | 24.7 | |

- Source 1: Newcomb (1979) and Day (1998)
- Source 2: Sheridan, Kutchev et al. (1988)

As expected the highest values are shown at the outer rim of the disc, where surface speeds are at their highest. The ventilation channel region shows the next highest h_{conv} values followed by the friction faces and hat region with the lowest values. The CFD results show good agreement with the published equation values in most cases. For the friction surfaces, ventilated channel and rim regions excellent agreement is shown at 450 min^{-1} and for the ventilated channel and rim regions at 50 min^{-1} . However, the ventilated channel values of equation set 1 show very high values compared to CFD and other published equations (see Figure 5.8). The hat region equation h_{conv} values are double the CFD values, which are influenced by proximity of the friction surface modifying the airflow and heating air in the region. These factors are not accounted for by the published equations.

5.6.2 TGV Railway Disc

Base on the CFD model of Chapter 4, Figure 5.37 shows a half-section temperature contour map of the fluid surrounding the TGV disc (see Chapter 3), for the steady state condition. The disc is rotating at 1000 min^{-1} and the disc temperature 200°C . The ambient air temperature was set at 20°C . The plot shows differences in the air temperature contours close to the disc surface for the retaining ring side and ‘free’ side of the disc. The average air temperature is higher on the retaining ring side, which has restricting airflow into the vane (as shown in Chapter 4).

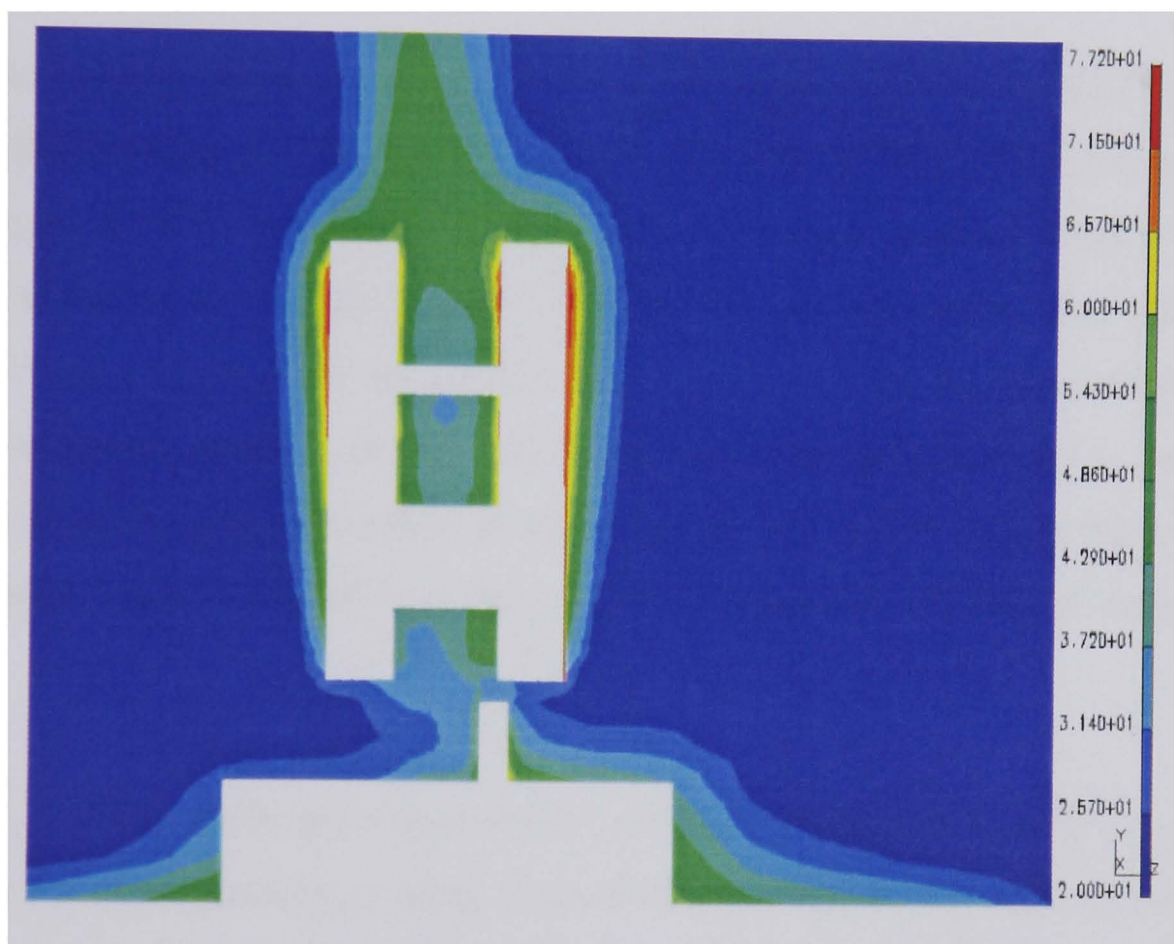


Figure 5.37 Air temperature for a 200°C TGV disc rotating at 1000 min^{-1}

Table 5.7 compares the predicted temperature change (Figure 5.37) with the measured temperatures change of Figure 5.28 relative to ambient temperatures, it can be seen that the predicted temperatures are of similar distribution and compare well at the ventilation channel inlets and rubbing surface. However, lower temperatures are predicted at the ventilation channel exit. It must be noted that ambient temperatures during testing were higher than the CFD ambient temperature, see Table 5.7.

Table 5.7 Comparison of measured and CFD change in air temperature, $\Delta T = (T_{air} - T_{\infty})$ for a 200°C TGV disc rotating at 1000 min⁻¹

| Position | Measured ΔT [°C] | Predicted ΔT [°C] |
|--|--------------------------|---------------------------|
| Ventilation channel exit | 53 | 30 |
| Ventilation channel inlet (free side) | 2 | 10 |
| Ventilation channel inlet (ring side) | -3 | 10 |
| Rubbing surface (free side, mean radius) | 34 | 43 |
| Rubbing surface (ring side, mean radius) | 36 | 45 |
| Ambient (T_{∞}) | 43 | 20 |

A contour map of the h_{conv} values are shown in Figure 5.38 for the TGV ventilated railway disc rotating at 1500 min⁻¹ at a fixed temperature of 200°C, with ambient air temperature at 20°C. It can be seen that the h_{conv} values increase radially from the inside diameter to the outside diameter with the disc surface speed. The highest h_{conv} values are seen at the outer rim surface (the region with the highest surface speed). The retaining ring restricts airflow into the vane and lower values of h_{conv} are shown on this side of the disc. The effect of the retaining ring is also seen at the ventilation channel exit, lower values of h_{conv} are seen on the retaining ring side of the disc outer rim.

The h_{conv} contour plots give great detail of local ventilation channel h_{conv} values allowing the determination of areas dissipated heat inefficiently and allowing small design modifications to be directly evaluated. Detailed contour plots are shown in Figure 5.39. High h_{conv} values are seen on the front (facing the direction of rotation) vane surfaces and on the vane surface at the outer diameter of the disc. Low h_{conv} values are seen on the back faces of the disc and in areas of air stagnation (it must be noted that the train disc is required to operate in both directions). The h_{conv} values are dependent on air speed and high h_{conv} values correspond to high air speeds (shown in Chapter 4).

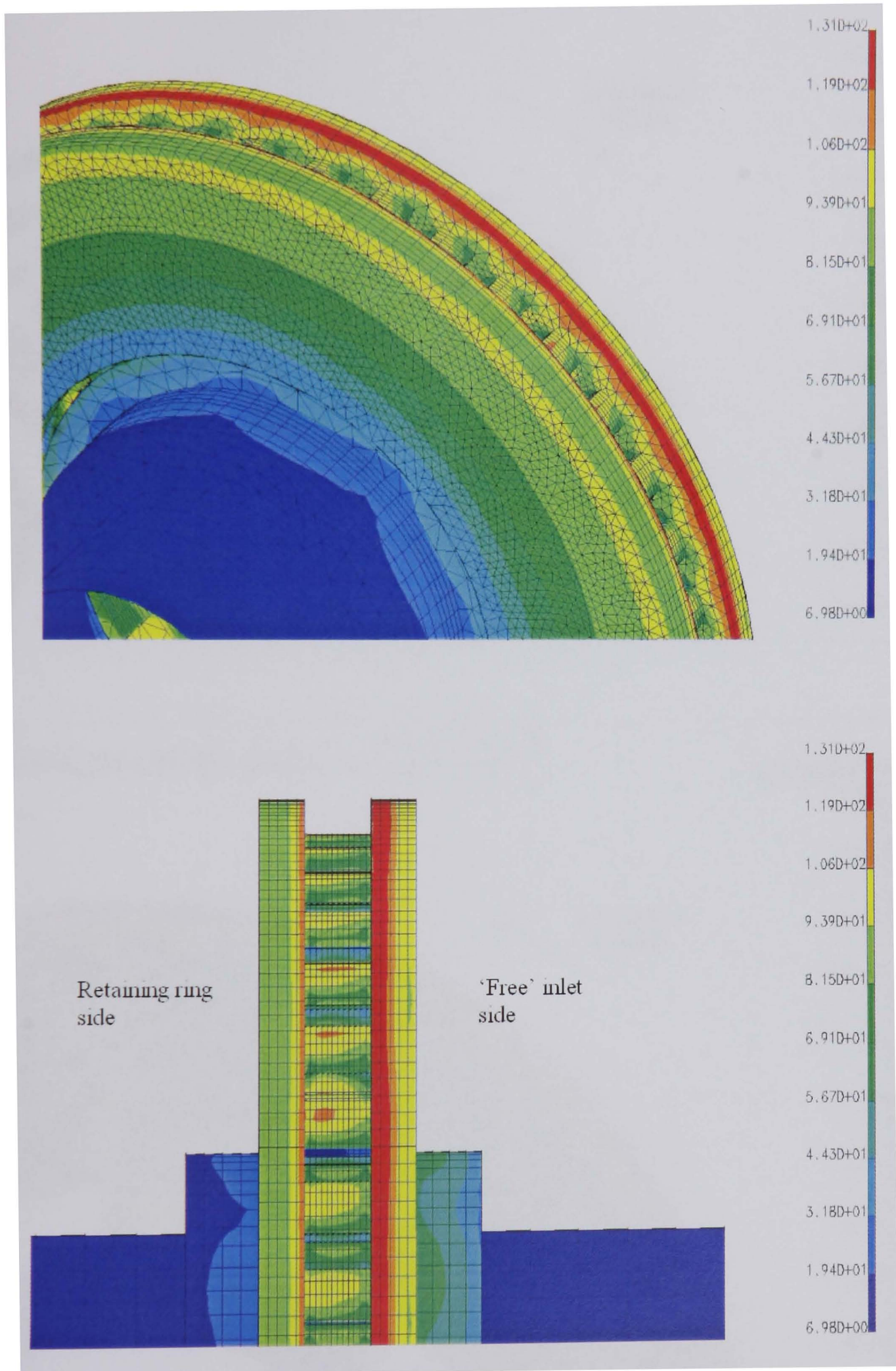


Figure 5.38 TGV disc CFD h_{conv} values, rotating at 1500 min^{-1} at 200°C

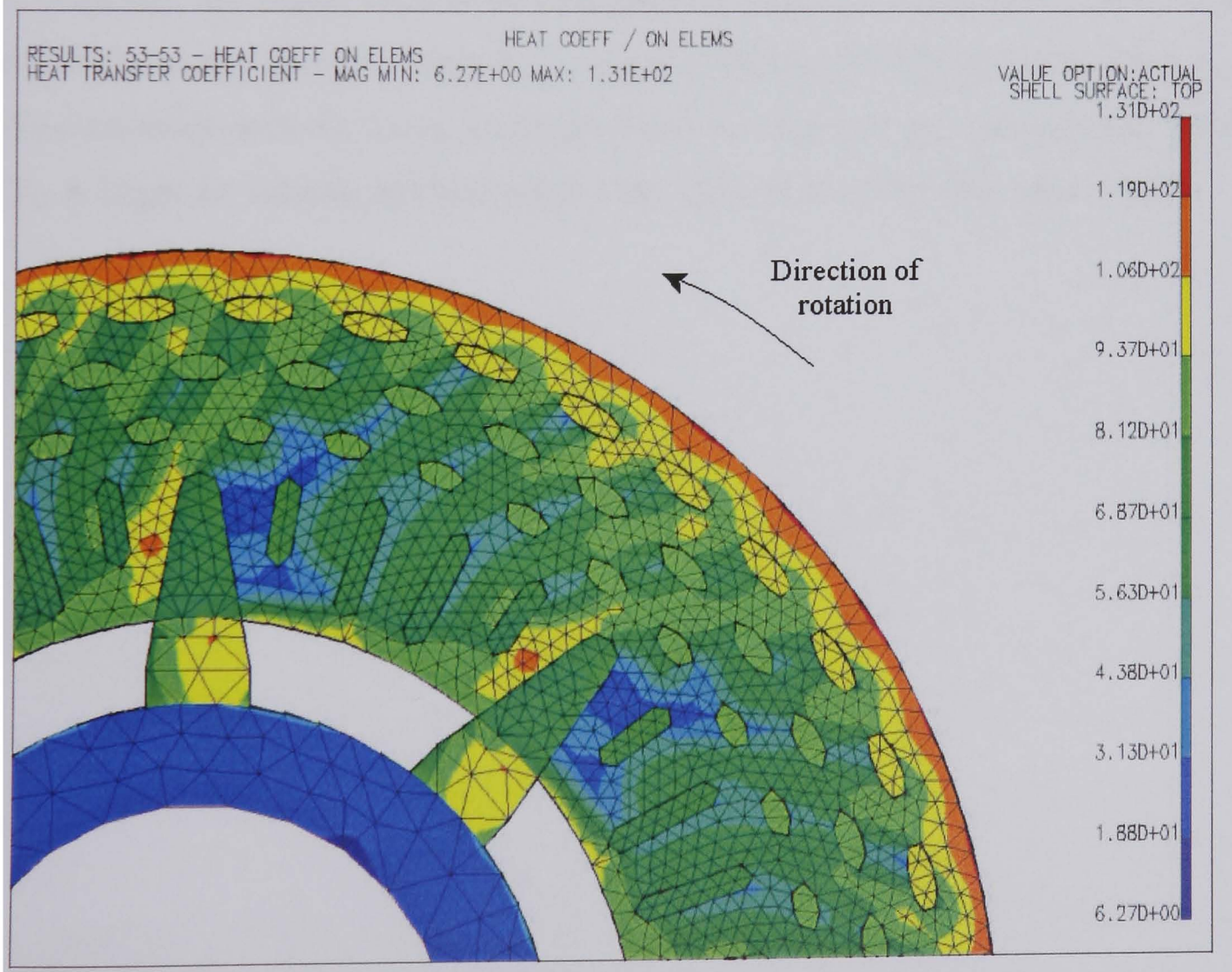
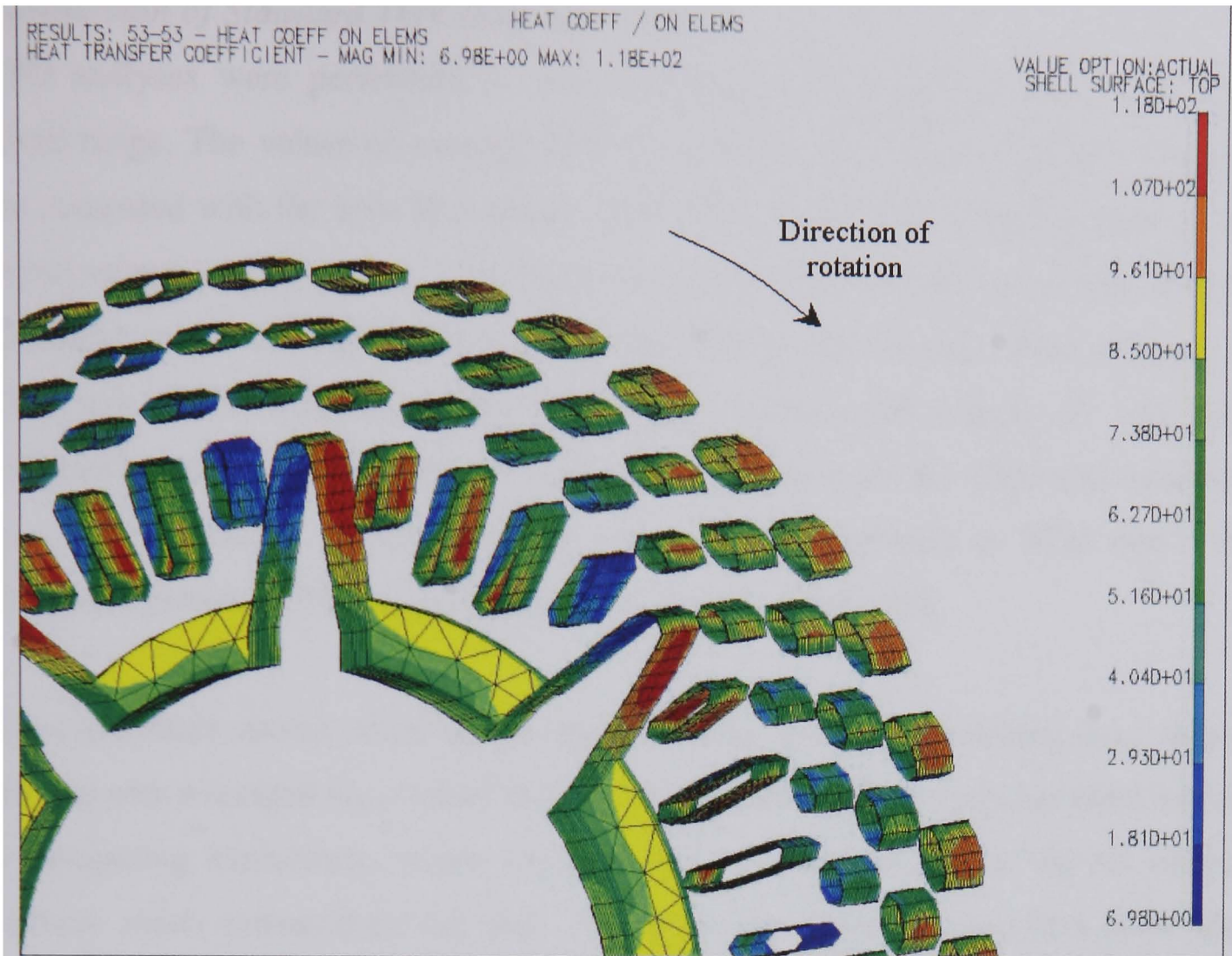


Figure 5.39 TGV disc detailed CFD h_{conv} values of the ventilation channels

Comparison of Standard TGV Disc h_{conv} Values

CFD analyses were performed at four rotational speeds spanning the TGV train speed range. The values of average CFD h_{conv} values are shown in Figure 5.40 and are compared with the Spin Rig results. The CFD results show a similar trend to the experimental values. At very low rotational speeds CFD results are within 10% of measured values. At higher rotational speeds CFD predicts lower values of h_{conv} . At 1500 min^{-1} CFD results are 24% lower than experimental values. At very high rotational speeds (above 1500 min^{-1}) the difference between the CFD and measured h_{conv} values reduces. When Spin Rig values are extrapolated to 2000 min^{-1} , the difference between CFD and measured results are less than 15%.

The differences shown could be the result of nodal averaging reducing h_{conv} values; the true area averaged h_{conv} values may be higher. The CFD analysis has been subject to computing limitations, which restricted the size and density of the air volume element mesh surrounding the disc. No doubt the complex vane and pillar disc ventilation design lead to increased errors in the CFD analyses. Measured vane exit air velocities are higher than those predicted by CFD (see Chapter 4), these under predictions would generate lower h_{conv} values in the model. Also the lower CFD h_{conv} values coincide with the lower air temperatures predicted at the vane exit (see Table 5.7). A larger air volume and finer mesh may improve the CFD TGV disc results.

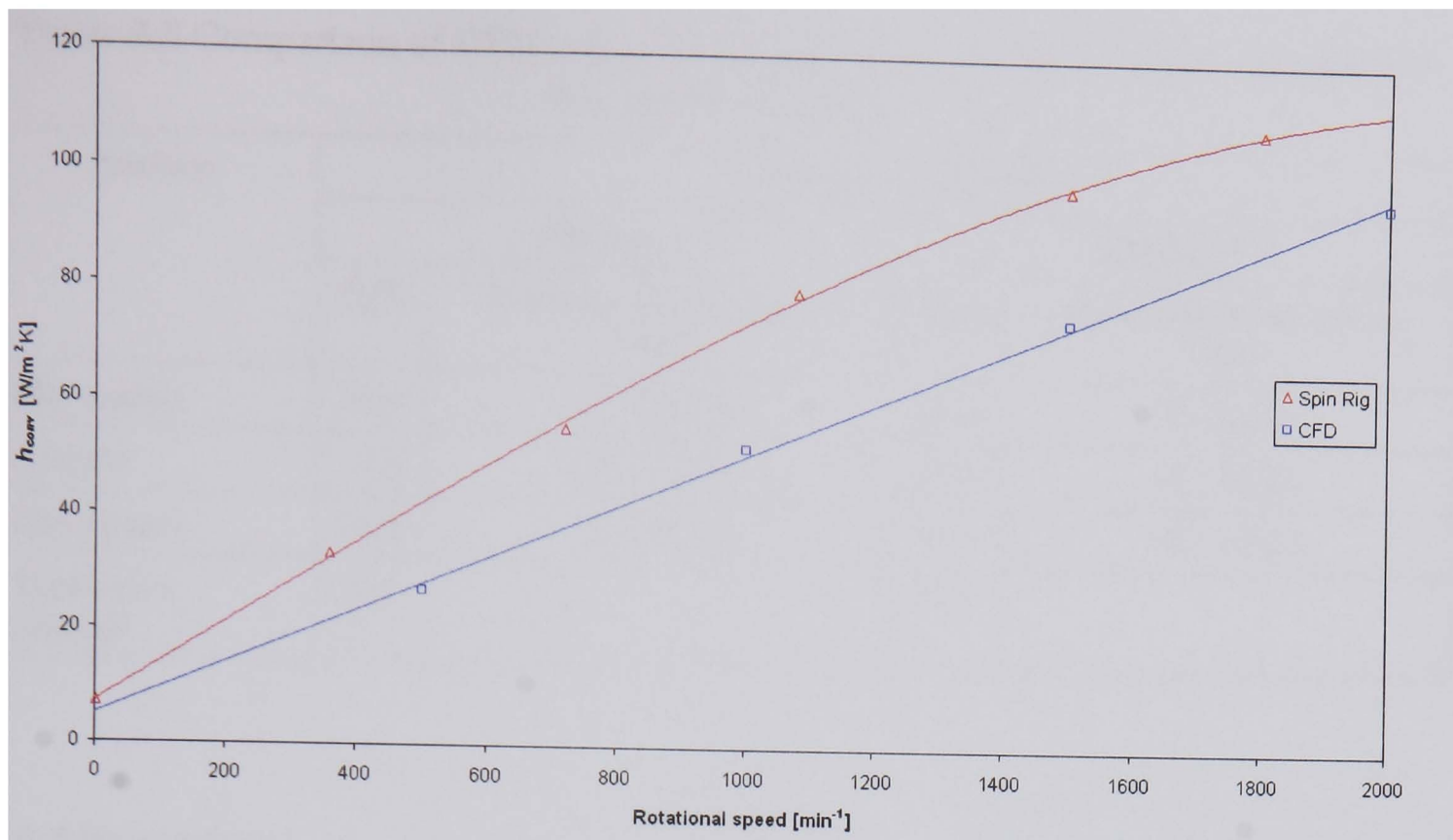


Figure 5.40 Average h_{conv} values for the TGV disc at 200°C

The CFD h_{conv} values have been broken down into surface areas as shown in Table 5.8. The average h_{conv} values are given for the friction surface, ventilation channel, outer rim and inner rim for the rotational speeds of 500 and 1500 min^{-1} , the results are compared with the h_{conv} values calculated from published equations used by Newcomb (1979) for railway brakes presented in Section 5.2. The ventilation channel results could not be compared due to the vane design complexity. The highest CFD values are shown at the outer rim of the disc, where surface speeds are at their highest. The friction surface has the next highest h_{conv} values followed by the inner rim and vane regions with the lowest values.

The CFD results show good agreement with the published equation values. For the friction surfaces at both speeds and the rim surfaces at 500 min^{-1} , excellent agreement is shown. However, the rim surfaces at 1500 min^{-1} show very high CFD values compared to the published equations. The lugs and ventilation channel inlet influence the h_{conv} value at in the inner rim region, which is not accounted for by the equation used. At the outer rim h_{conv} values are influenced by the ventilation channel outlet, also not accounted for by the equation used. The pillar/radial vane region of the TGV disc shows lower h_{conv} values than the radial vane design of the CV disc, the higher surface temperature of the TGV disc will reduce h_{conv} values.

Table 5.8 Comparison of CFD and published equation local h_{conv} values for the TGV disc surfaces at 200°C

| Surface | Average h_{conv} [W/m ² K] | | | |
|---------------------|---|------------------------------|------------------------|------------------------------|
| | 500 min ⁻¹ | | 1500 min ⁻¹ | |
| | CFD | Newcomb (1979) (rel. to CFD) | CFD | Newcomb (1979) (rel. to CFD) |
| Rim (outer) | 36.4 | 27.6 (0.76) | 102.8 | 57.4 (0.56) |
| Friction | 27.8 | 28.5 (1.03) | 79.5 | 68.7 (0.86) |
| Rim (inner) | 26.6 | 22.6 (0.85) | 74.2 | 46.9 (0.63) |
| Ventilation channel | 26.0 | - | 71.7 | - |

5.7 Summary

This chapter has introduced the convective mode of heat dissipation showing its contribution to brake cooling and examining influencing factors.

Theoretical convective heat transfer coefficient formulae have been studied and comparisons made with alternative approaches. The methods and effects of film temperature were also considered. The Spin Rig has been used to determine cooling curves for numerous CV disc designs and disc, wheel assembly arrangements; the TGV railway disc was also studied. From measured cooling rates, average heat transfer coefficients were determined. Repeatability tests were performed to ensure confidence in measurements. CFD models used to predict the airflow around ventilated discs have been further developed to calculate convective heat transfer coefficients at the brake disc surface for a range of speeds and temperatures. A total of 50 cooling tests were performed on the CV and TGV discs amounting to a total of 40 days of laboratory testing. A total of 16 computer simulation runs were performed requiring 300 hours of computer time.

When comparing the numerous convective heat transfer coefficient formulae, differences in results were occasionally very high and it has been shown that film temperature must be taken into consideration. Using the average heat transfer coefficients determined from Spin Rig measurements, cooling performance comparisons of disc designs has been made. Measured results show that the wheel

assembly can have detrimental effects on convective CV disc heat dissipation and ventilated disc designs used should be carefully considered. Using known heat transfer coefficients of conduction and radiation enabled the determination of convective heat transfer values, and functions are given defining the relationship with rotational speed. CFD analysis has enabled detailed analysis of local convective heat transfer coefficients and the influence of disc ventilation channel design.

The Spin Rig has been used to provide accurate temperature measurements during disc cooling. The comparisons with measured convective heat transfer coefficients and values published in the literature show very good agreement with CFD results. The developed methods of predicting convective heat transfer coefficient values of brake discs allows comparative analysis of design changes and determination of the best disc design improvements for specific duties and applications.

Conductive Heat Dissipation

6.1 Introduction

The aim of this chapter is to introduce the conductive mode of heat dissipation and determine values of thermal contact resistance at the interfaces of the brake components. In order to study conductive heat transfer clamping bolt forces were analysed experimentally and theoretically, interface pressure distribution was modelled and compared with measurements and temperature measurements were conducted at brake component interfaces.

The cross section through the commercial vehicle (CV) wheel assembly is shown in Figure 6.1. Heat is generated at the CV brake disc friction surfaces and conducted through the disc hat section to the flange area. The wheel assembly provides two areas of conductive heat dissipation from the disc, one through the bearing assembly, the other through the wheel carrier. Heat transfer from the brake disc to the bearing must be avoided to ensure bearing temperatures are kept low. However, the wheel carrier has a substantial mass of 21 kg, which is approximately 2/3 of disc mass, and therefore can provide a very desirable conduction path from the brake disc to the wheel of the vehicle. The outer faces of the wheel carrier and wheel have dir

ect contact with cool, fast flowing and turbulent air and these boundary conditions suggest that the wheel carrier and wheel can offer substantial potential for heat dissipation. It is important to consider tyre temperature, since overheating of the tyre can lead to extremely dangerous conditions and must be avoided.

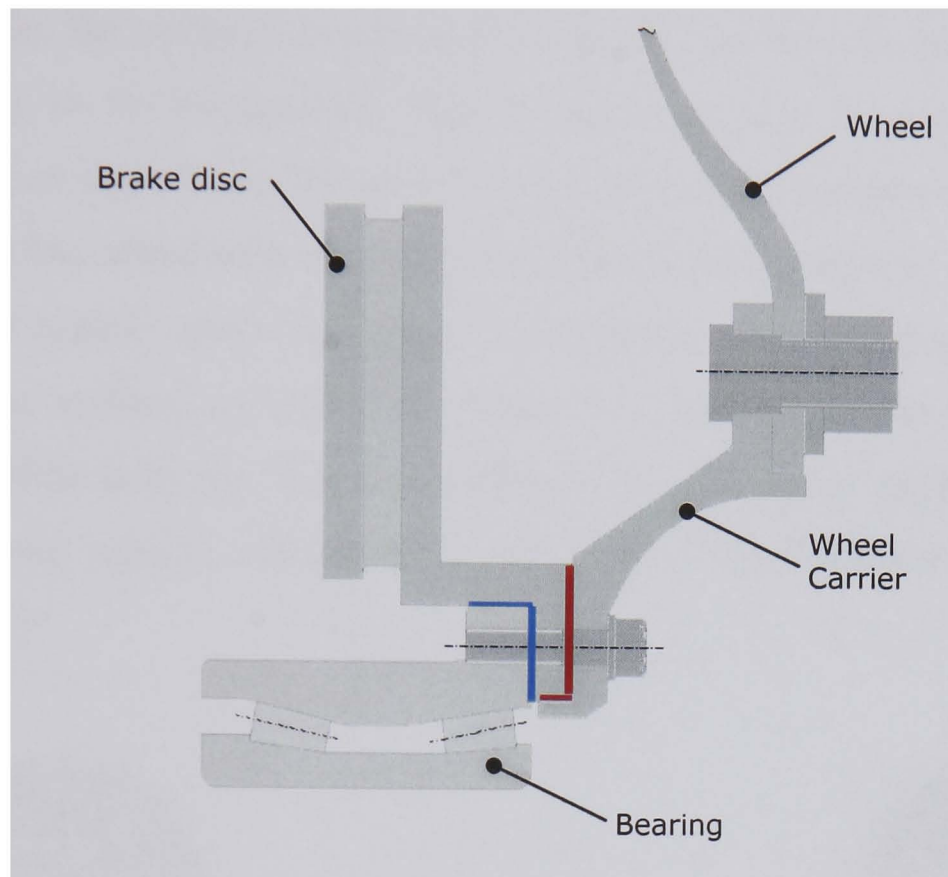


Figure 6.1 Cross section of wheel assembly

6.1.1 Theoretical Background

For thermal conduction to occur through a solid, a temperature difference is required. The difference in temperature causes the transfer of energy by the more energetic molecules to adjacent less energetic molecules and energy transport by free electrons, (Cengel 1998). The rate of heat conduction through a solid is governed by the cross section area, material thermal conductivity and temperature gradient. This is shown in Fourier's law of heat conduction:

$$Q_{cond} = -kA \frac{dT}{dx} \quad (6.1)$$

The equation above indicates that conductive heat transfer increases with cross section area (A), material conductivity (k) and temperature gradient (dT/dx).

Appendix A gives thermal conductivity values for materials commonly used in the brake assemblies.

To analyse the conduction of heat through multi-layer solids, (disc, wheel carrier and wheel), it cannot be assumed that the interfaces between layers are perfect. If this were the case, the surfaces would have to be microscopically and macroscopically flat resulting in no temperature drop between surfaces. In reality, no surface is perfectly flat or smooth and this causes a thermal contact resistance (R_{cond}). The R_{cond} is a result of the actual area of contact between layers being only a small fraction of the apparent contact area. The actual contact area being the micro-contacts at the peaks on the surfaces as shown in Figure 6.2. Valleys on the surface will form interstices filled with the ambient medium. The interstitial medium, which under normal ground vehicle conditions is air, acts as an insulator due to its lower conductivity.

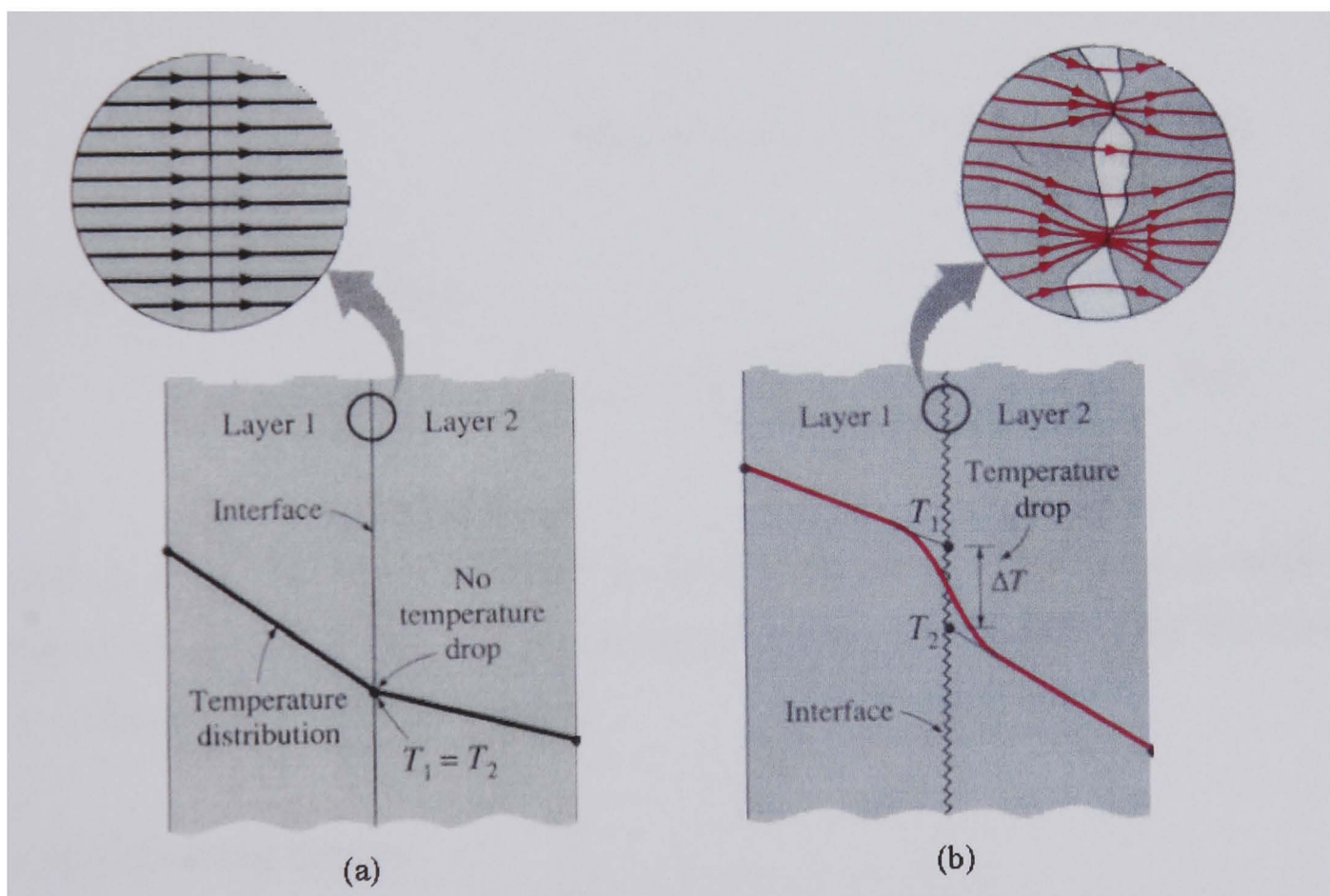


Figure 6.2 Ideal (a) and actual (b) thermal contact (Cengel 1998)

Conductive heat transfer (Q_{cond}) through the interface can be expressed as a sum of the conductive heat transfer ($Q_{contact}$) through the actual contact areas and the interstitial medium (Q_{gap}):

$$Q_{cond} = Q_{contact} + Q_{gap} \quad (6.2)$$

The average thermal contact conductance (h_{cond}) at the interface is the reciprocal of R_{cond} :

$$h_{cond} = \frac{1}{R_{cond}} \quad (6.3)$$

Q_{cond} can be expressed as:

$$Q_{cond} = h_{cond} A_{cond} \Delta T_{int} \quad (6.4)$$

For the CV brake (Figure 6.1) the temperature difference (ΔT_{int}) is the temperature difference between the disc interface surface (T_D) and wheel carrier interface surface (T_C). The interface area (A_{cond}) is the area of contact between the disc and the wheel carrier and equation (6.4) becomes:

$$Q_{cond} = h_{cond} A_{cond} (T_D - T_C) \quad (6.5)$$

Giving an expression for h_{cond} :

$$h_{cond} = \frac{Q_{cond}}{A_{cond} (T_D - T_C)} \quad (6.6)$$

Values of h_{cond} have been published in the literature for several materials under a range of conditions (temperature, pressure and surface conditions); Table A6 shows h_{cond} values for a range of metal pairs.

6.1.2 Influencing factors

The value of h_{cond} at the interface between two mating surfaces will increase with interface pressure, as discussed in Chapter 2. In the case of the brake assembly bolts are used to clamp the disc to the wheel carrier and wheel, making the interface pressure non-uniform, the highest pressure being near the bolt shank, and reducing with bolt radius. Components that are fastened together with bolts, such as the hub and brake disc (Figure 6.1), may experience changes in clamping force as a result of

removal and replacement during vehicle servicing. To determine the h_{cond} values as a function of interface contact pressure at the disc and wheel carrier the bolt force is first determined. Using an FE model of the interface, the pressure distribution is determined and confirmed by experimental measurement. The average h_{cond} values at the interface are determined by Spin Rig temperature measurements for a range of pressures and temperatures. From the results, expressions are determined for h_{cond} as a function of pressure.

6.2 Bolt Clamping Force Determination

The average interface contact pressure at the disc flange and wheel carrier can be calculated by dividing the total clamp force by the interface area, therefore it is crucial to accurately determine the force at the bolt. Experiments were conducted to determine the clamp force for a range of bolt torques between 50 and 300 Nm. The maximum considered value (300 Nm) being the nominal bolt torque specified by the vehicle manufacturer.

6.2.1 Theoretical Calculation

The bolt clamp force can be calculated using the theoretical bolt force equation (6.7) (Shigley and Mischke 1989).

$$\tau = \left[\left(\frac{d_m}{2d} \right) \left(\frac{\tan \phi + \mu \sec \phi}{1 - \mu \tan \phi \sec \phi} \right) + 0.625 \mu_c \right] F_i d \quad (6.7)$$

The term in brackets can be defined as a torque coefficient (K):

$$K = \left(\frac{d_m}{2d} \right) \left(\frac{\tan \phi + \mu \sec \phi}{1 - \mu \tan \phi \sec \phi} \right) + 0.625 \mu_c \quad (6.8)$$

Where, d is the thread outside diameter, d_m is the mean thread diameter, ϕ is the lead angle, μ is the coefficient of thread friction, μ_c is the coefficient of collar friction, Φ is the half apex angle of the thread and F_i is the preload. Equation (6.7) can now be written as:

$$F_i = \frac{T}{Kd} \quad (6.9)$$

Where T is the bolt torque and d is the nominal bolt diameter. Since all the parameters can vary considerably, a simplified approach is often used in engineering practice by using an average value of 0.2 for K (Shigley and Mischke 1989). Using equation (6.9) the following bolt forces have been calculated:

Table 6.1 Tensile stress at bolt

| Bolt Torque [Nm] | Nominal Bolt Dia. [mm] | K [-] | Bolt Force [kN] |
|-------------------------|-------------------------------|---------------------------|------------------------|
| 50 | 16 | 0.2 | 15.625 |
| 100 | 16 | 0.2 | 31.250 |
| 150 | 16 | 0.2 | 46.875 |
| 200 | 16 | 0.2 | 62.500 |
| 250 | 16 | 0.2 | 78.125 |
| 300 | 16 | 0.2 | 93.750 |

6.2.2 Experimental Measurement

The bolt clamp force versus torque relationship was measured with a low profile force washer load cell connected to a digital meter display detailed in Chapter 3, the load cell was calibrated in imperial tons.

An M16 bolt, of the same specification and surface condition as installed in the CV brake assembly and an appropriate nut were used to clamp the load cell. The bolt assembly was tightened up to the value of 200 Nm. Figure 6.3 schematically shows the test assembly.

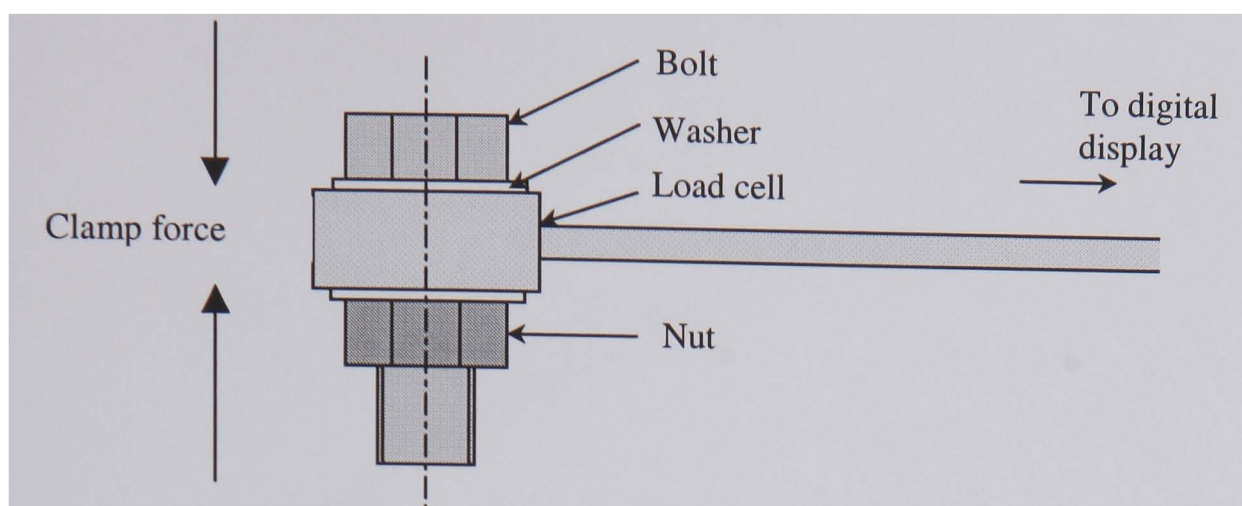


Figure 6.3 Clamp force measurement

Table 6.2 gives the measurement results and the average interface contact pressure at the interface (P_{avg}) calculated using equation (6.10). Six load measurements were taken for each bolt torque and the average force value (F) used in the calculation. The surface area at the disc/carrier interface (A_{int}) is $21.3 \times 10^{-3} \text{ m}^2$ and the number of bolts (n_b) clamping the interface is 10:

$$P_{avg} = \frac{n_b F}{A_{int}} \quad (6.10)$$

Table 6.2 Experimental clamp force and average interface contact pressure

| Torque [Nm] | Load [Imperial Ton] | | | | | | Average Bolt Force [kN] | Average Interface Pressure [MN/m ²] |
|----------------|---------------------|-----|-----|-----|-----|-----|----------------------------|--|
| | Measurement Number | | | | | | | |
| | 1 | 2 | 3 | 4 | 5 | 6 | | |
| 50 | 2.2 | 2.4 | 2.2 | 2.4 | 2.2 | 2.4 | 22.9 | 10.76 |
| 100 | 4.2 | 4.4 | 4.1 | 4.3 | 4.0 | 4.0 | 41.5 | 19.50 |
| 150 | 5.8 | 6.0 | 6.1 | 6.2 | 6.0 | 6.0 | 60.0 | 28.16 |
| 200 | 7.7 | 7.8 | 8.0 | 8.0 | 7.8 | 7.7 | 78.1 | 36.66 |

Tests were performed up to 200 Nm. The bolt torque has been plotted against the calculated average interface pressure in Figure 6.4. The results were extrapolated to determine the average interface pressures up to a torque of 300 Nm. The average interface contact pressure and total clamp force are detailed in Table 6.3.

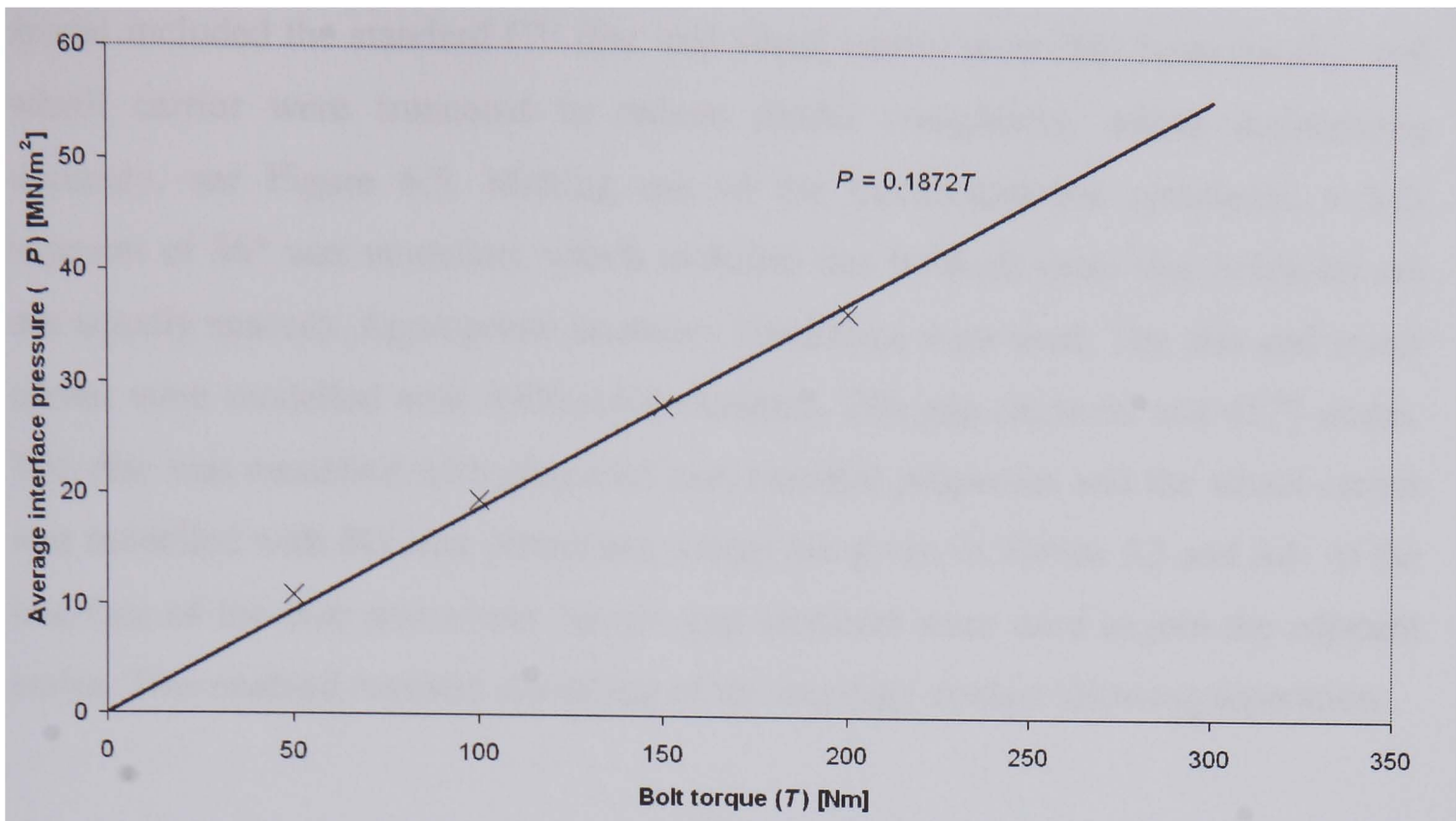


Figure 6.4 Wheel/carrier interface contact pressure increase with bolt torque

Comparing the measured results with the theoretically calculated bolt force (Table 6.3), the theoretically calculated values under predict the bolt force by approximately 25%.

Table 6.3 The six bolt tightening torques and average interface contact pressure

| | | | | | | |
|---|-----|------|------|------|------|------|
| Bolt Torque [Nm] | 50 | 100 | 150 | 200 | 250 | 300 |
| Measured total clamp force [kN] (10 bolts) | 200 | 399 | 600 | 798 | 999 | 1200 |
| Theoretical total clamp force [kN] (10 bolts) | 156 | 313 | 469 | 625 | 781 | 938 |
| Average interface pressure [MN/m²] (measured) | 9.4 | 18.7 | 28.1 | 37.4 | 46.8 | 56.2 |

6.3 FE Analysis of Contact Pressure

In the previous section, average contact pressure at the interface of the CV disc and wheel carrier was determined from the clamp bolt force and surface area. In order to study contact pressure in more detail an FE analysis model has been developed to predict the contact pressure magnitude and distribution. The ability to model the pressure at the interface of two bolted components will allow the prediction of the thermal contact resistance and in turn the conductive heat flow (Q_{cond}) from the disc to adjacent components. SDRC I-DEAS has been used to model the interface. The

model included the standard CV disc and wheel carrier assembly, both the disc and wheel carrier were truncated to reduce model complexity, whilst maintaining accuracy, see Figure 6.5. Making use of the circumferential symmetry, a 3-D segment of 36° was modelled, which included one bolthole (note that boltholes are not equally spaced). Appropriate boundary conditions were used. The disc and wheel carrier were modelled with 3900 solid elements, 286 gap elements and 4577 nodes. The disc was modelled with grey cast iron material properties and the wheel carrier was modelled with SG iron properties, values are given in Tables A3 and A4. At the interface of the disc and wheel carrier, gap elements were used to join the adjacent nodes. This enabled realistic modelling of the interface contact allowing separation.

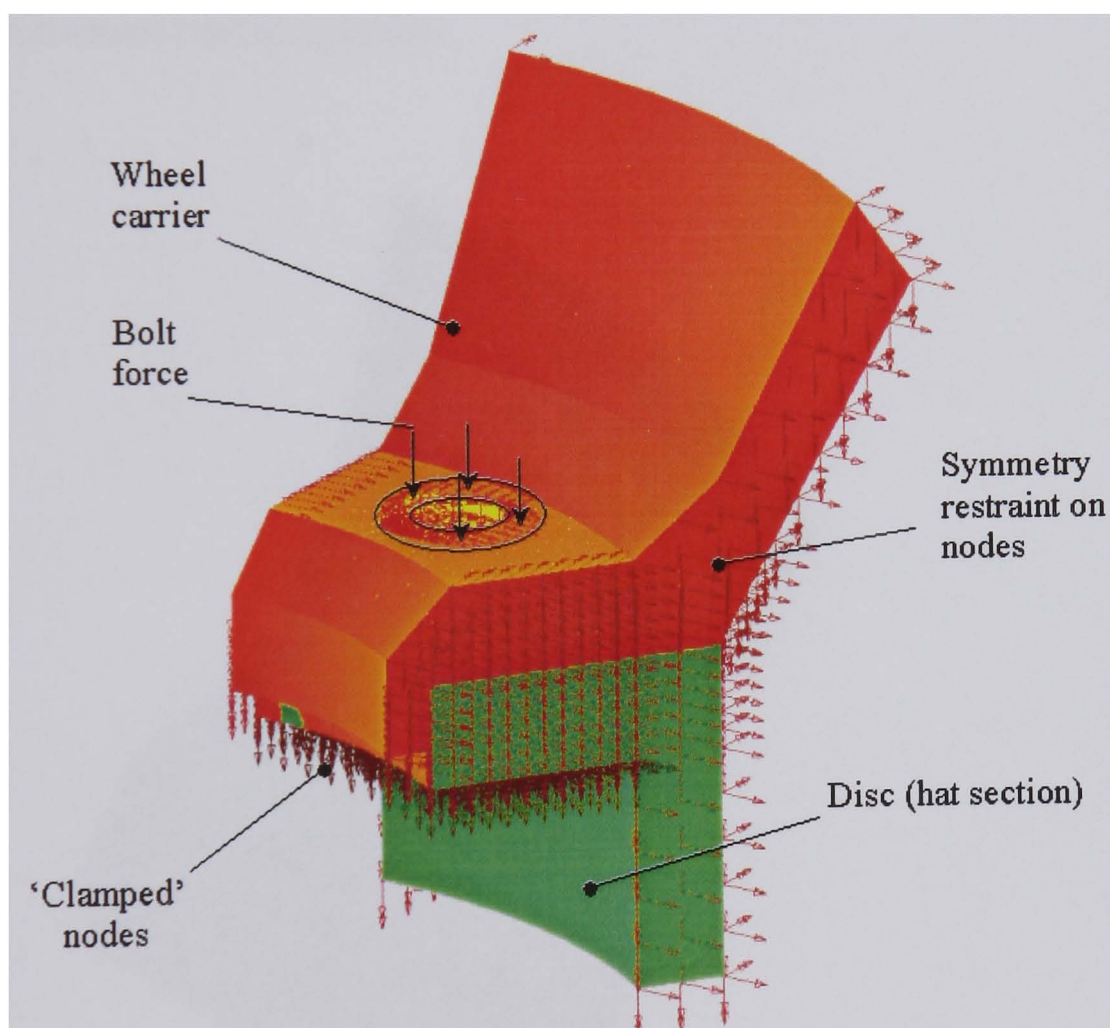


Figure 6.5 CV disc and wheel carrier interface pressure FE model boundary conditions

For Spin Rig measurement of interface pressure the disc and wheel carrier were bolted to the Spin Rig adapter (see Figure 6.15). This has been modelled by applying restraints to the nodes on the underside surface of the disc hat (see 'clamped' nodes, Figure 6.5). A continuous load (nodal forces) was then applied to the nodes under the bolt head on the surface of the disc, from the outside diameter of the bolt to a

diameter of 26 mm (outside diameter of washer under the bolt). At the symmetry planes of the model (36° apart), appropriate boundary conditions were introduced; ensuring nodes remained within these planes during loading. To control stability, nodes on the surface of the bolthole were only allowed to move axially in the direction of the applied bolt force.

Figure 6.6 shows the Von Mises stress and deformation of the disc and wheel carrier model for a simulated bolt force resulting from a torque of 300 Nm. The bolt force was equal to 120 kN (measured value, Table 6.3) and this was distributed over the 120 nodes under the bolt head washer (see Figure 6.5). High stress and deformation can be seen around the bolthole, under the washer. Deformation has also occurred at the disc and wheel carrier interface.

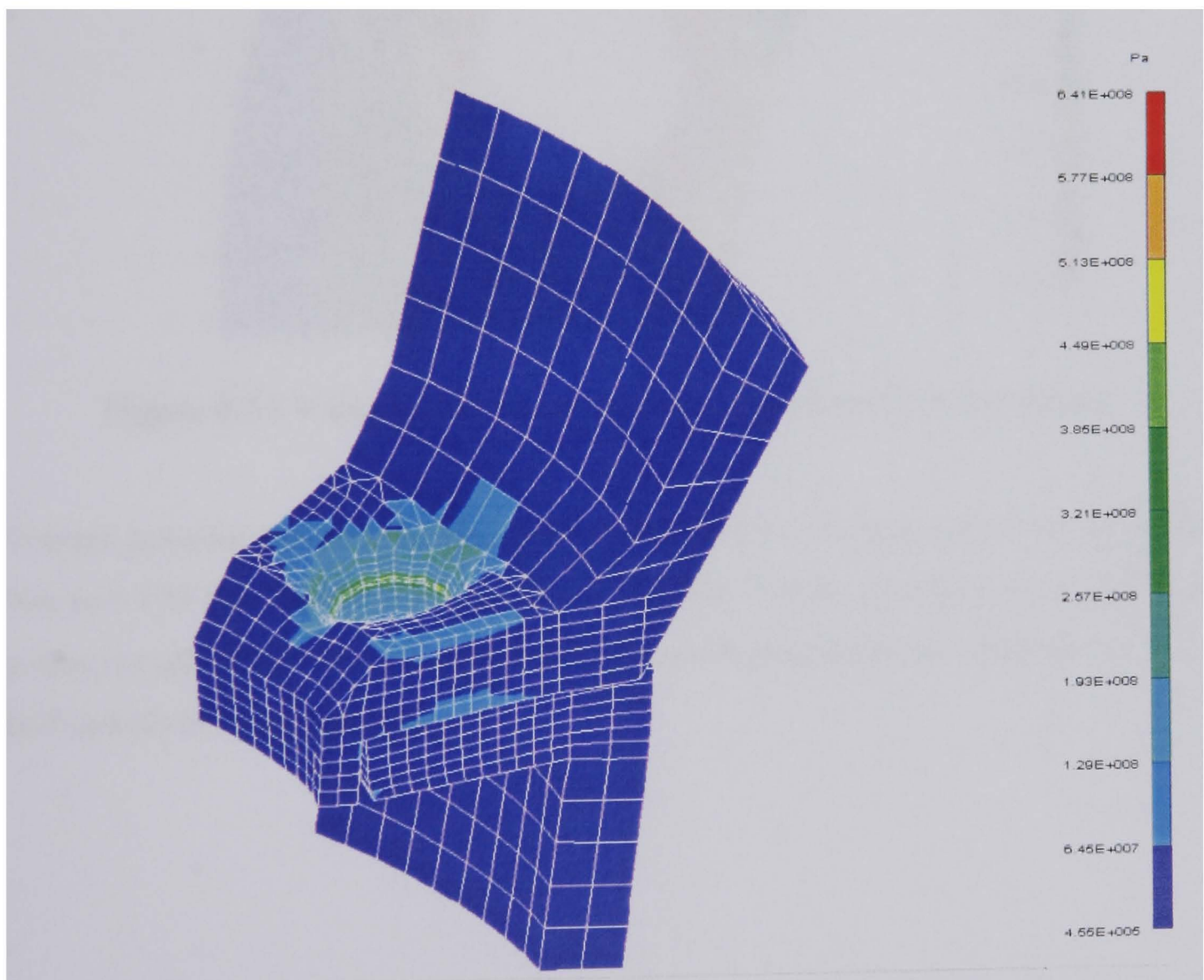


Figure 6.6 Von Mises stress of bolted CV disc and wheel carrier on deformed geometry

Figure 6.7 shows the zz-component (representing interface pressure direction) stress contour plot of the disc hat section under loading. High stresses can be clearly seen around the hole, reducing radially from the outside diameter of the hole. The

maximum pressure is 128 MN/m^2 and two distinctive areas can be noticed; under the bolt (1) the pressure is 95.0 MN/m^2 and between the bolts (2) the pressure is 32.3 MN/m^2 . This compares well with the average pressure of 56.2 MN/m^2 given in Table 6.3.

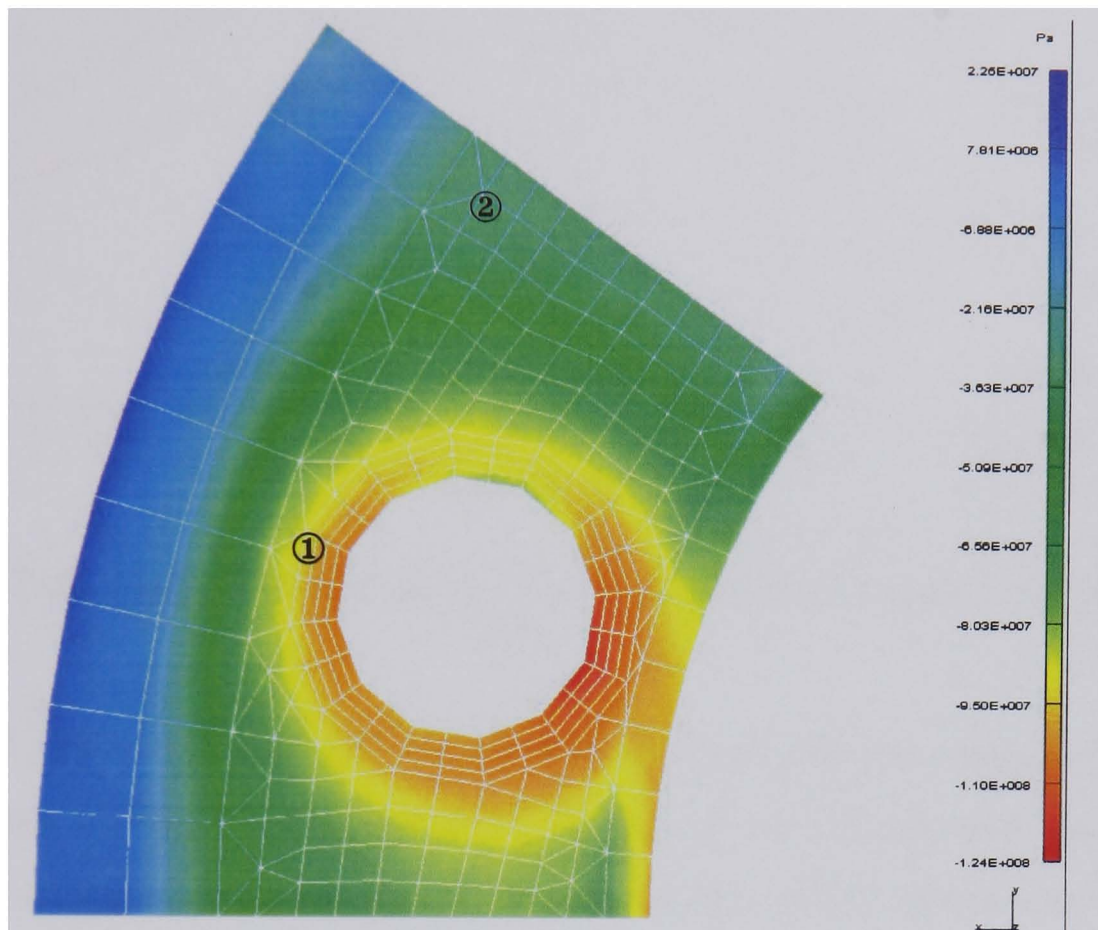


Figure 6.7 CV disc/wheel carrier interface contact pressure distribution

Contact pressure analysis has also been carried out for the bolt torque values of 200 Nm and 150 Nm. Figure 6.8 show local interface contact pressures at the radius of points (1) and (2) shown in Figure 6.7. The dashed lines show the positions (1) at the bolt and (2) between the bolts.

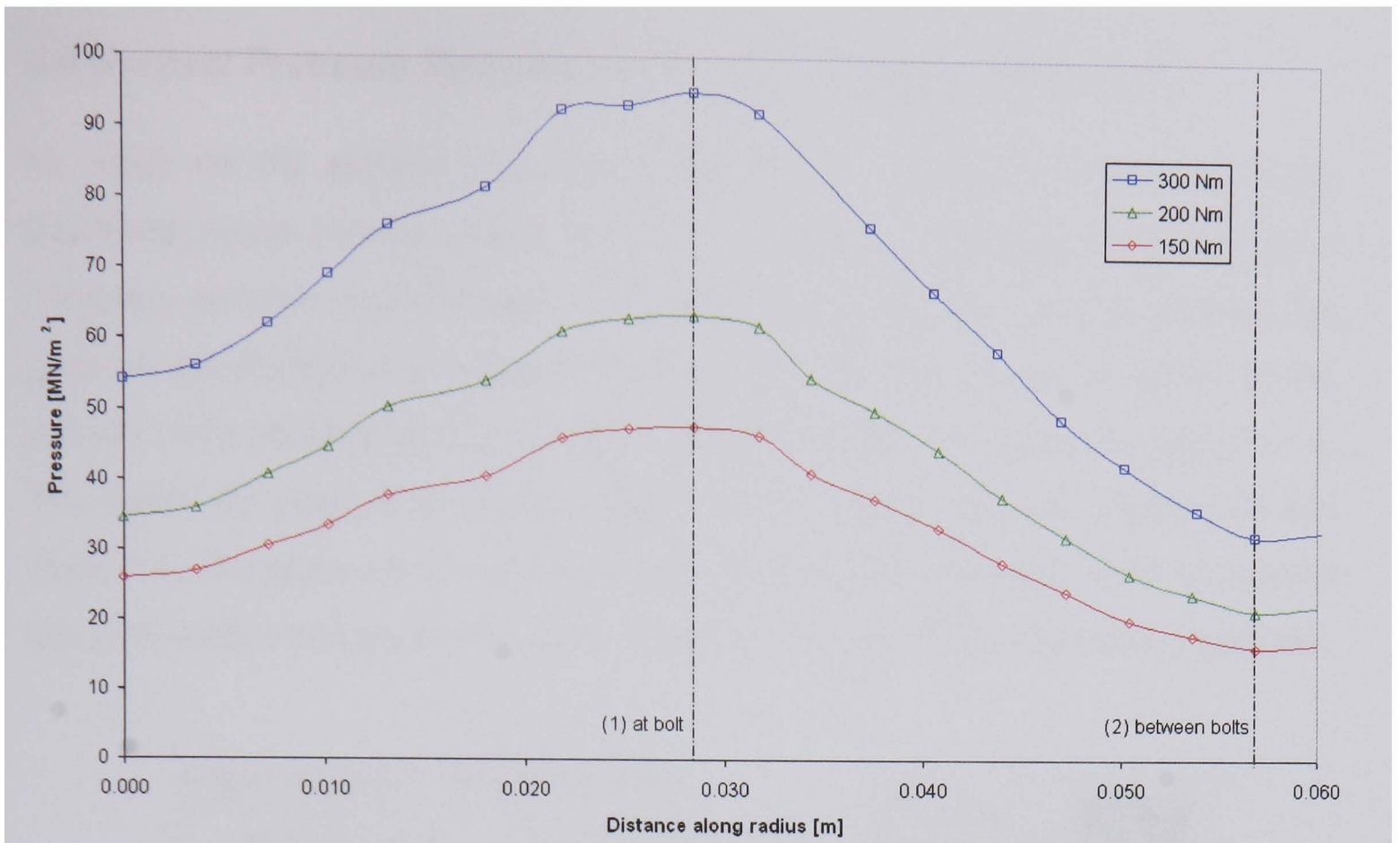


Figure 6.8 Local contact pressure along the radius of points (1) and (2), (see Figure 6.7)

From the FE results presented in Figure 6.8 the local pressure change with bolt torque is shown in Figure 6.9 for the two positions, at the bolt (1) and between the bolts (2). The expressions for local pressure as a function of bolt torque can be found from the curves (shown in Figure 6.9).

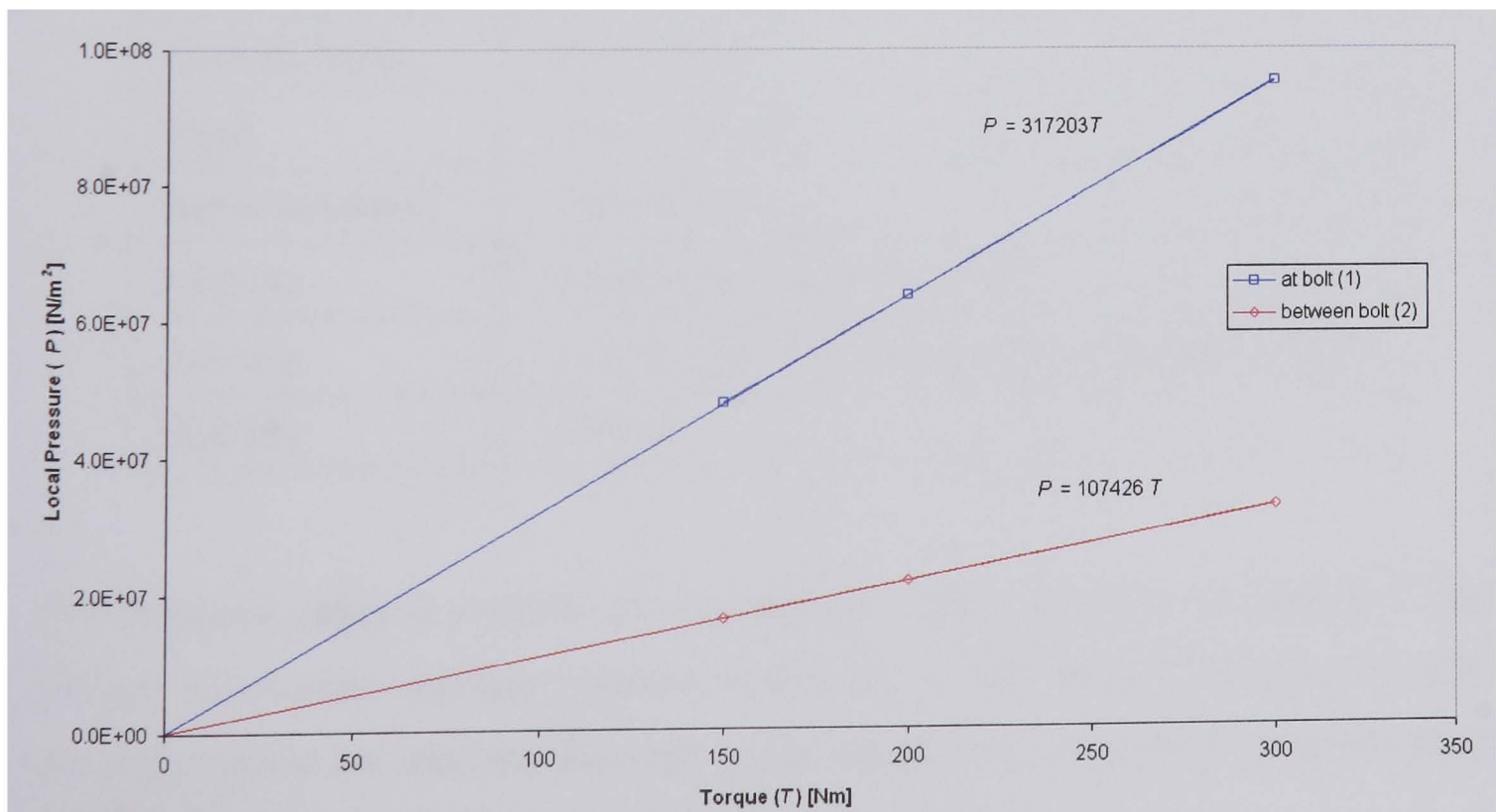


Figure 6.9 Local pressure change at positions (1) and (2) with bolt torque

6.4 Contact Pressure Measurement and FE Results Verification

To verify the FE analysis and further research the contact pressure at the brake disc/wheel carrier interface, measurements of the interface pressure were conducted. Pressurex pressure sensitive paper (Sensor Products Inc.) was used to measure the pressure distribution and magnitude at the interface. The change in colour of the initially white pressure sensitive paper is directly related to the pressure applied to it. The higher the pressure applied the higher the colour intensity, see Figure 6.10 and Table 6.4. The paper can be compared with the supplied correlation chart or scanned using specially developed software to determine pressure distribution and magnitude.

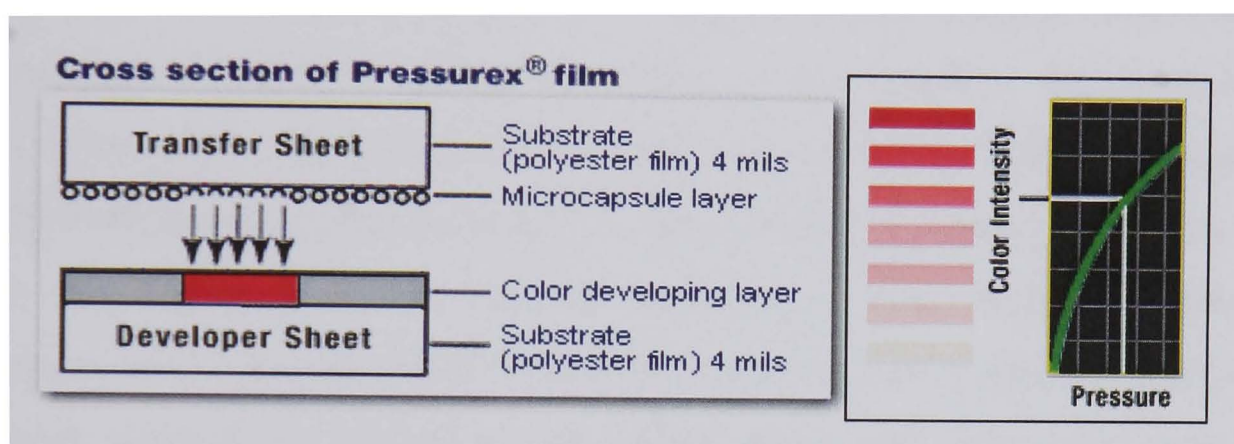


Figure 6.10 Pressurex structure and correlation chart (Sensor Products Inc. 2002)

Table 6.4 Pressurex specifications (Sensor Products Inc. 2002)

| | |
|---------------------------|--|
| Temperature Range | 5° - 35° C (Higher for brief exposure) |
| Humidity Range | 20 to 90% RH |
| Gauge | 25 to 50 microns |
| Spatial Resolution | 5 to 15 microns |
| Substrate | Polyethylene Terephthalate (PET) |
| Accuracy | +/-10% visual +/-1% utilizing optical measurement system |
| Shelf Life | 2 Years |

The Pressurex paper is available for six pressure ranges, as shown in Table 6.5. The average disc/carrier interface pressure at 300 Nm is 56.2 MN/m² (Table 6.3), with this information the medium and high grade papers were considered to be the most suitable for the interface pressure measurements.

Table 6.5 Pressurex paper sensitivities (Sensor Products Inc. 2002)

| Paper Type | Pressure Range [MN/m²] |
|-------------------|--|
| Ultra Low | 0.2 – 0.6 |
| Super Low | 0.5 – 2.4 |
| Low | 2.4 – 9.7 |
| Medium | 9.7 – 49.0 |
| High | 49.0 – 127.6 |

Measurements were conducted on a new brake disc and used (slightly corroded) wheel carrier. The clamping faces were cleaned and the pressure sensitive paper (requiring careful handling) cut to the profile of the interface. The humidity and ambient temperature was recorded as this affects the colour intensity of the paper and is required during the analysis of results. The pressure sensitive paper was placed between the clamping faces and the components were bolted together. The components were tightened first to 100 Nm, opposing bolts tightened alternately to avoid high pressure concentration and uneven tightening. The bolts were finally tightened to the nominal torque (300 Nm) in the same order. The pressure sensitive paper requires that the pressure be sustained for more than 10 seconds. After this period, the assembly bolts were loosened in the order described for tightening and removed, and then the pressure sensitive paper was removed.

Figure 6.11 shows the pressure sensitive paper colour change after being clamped between the disc and the wheel carrier. It can be clearly seen that the pressure is higher in the proximity of the fixing bolts, and reduces with increased distance from the bolts.

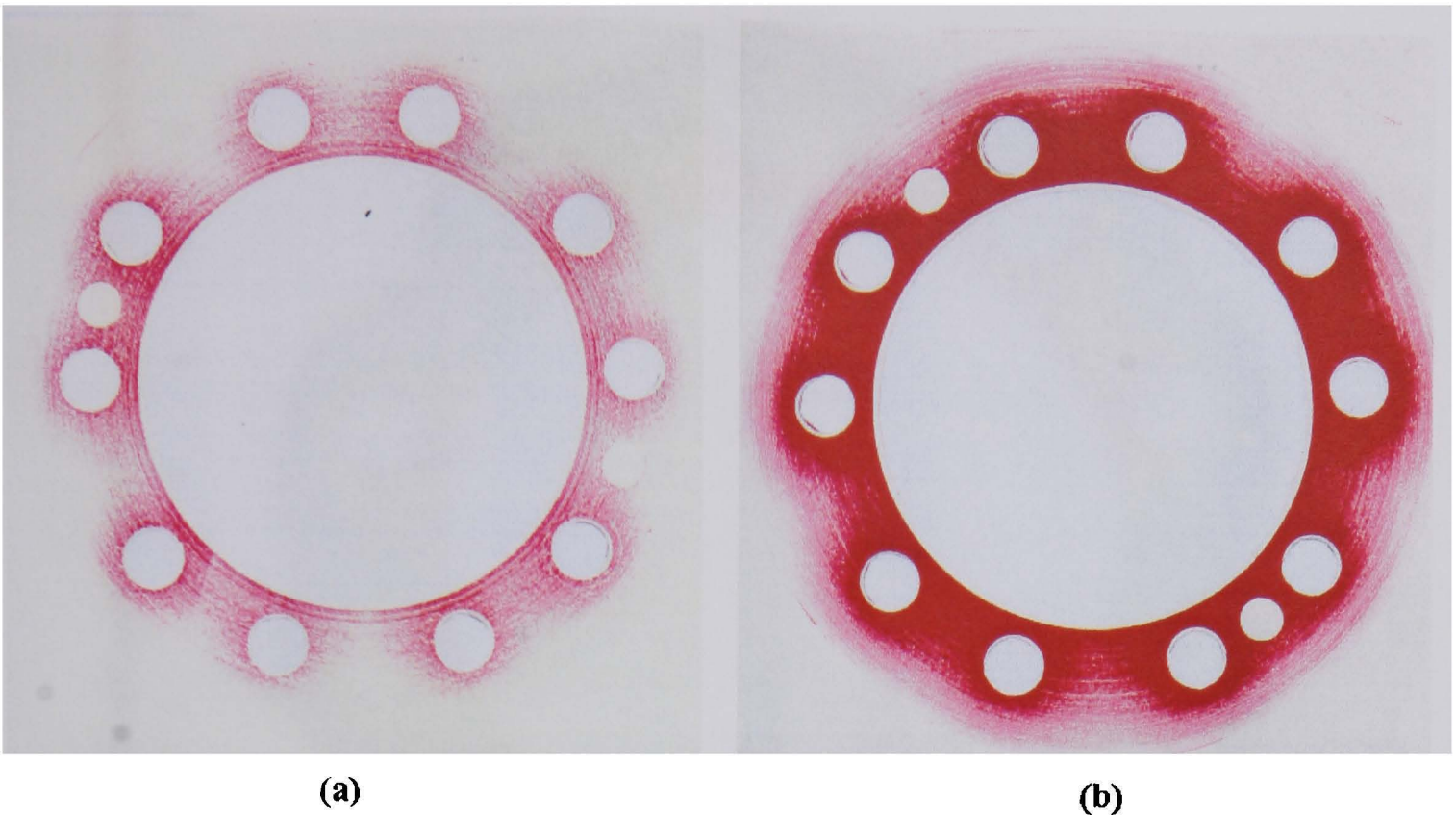


Figure 6.11 High (a) and Medium (b) pressure sensitive paper after pressure application at 300 Nm bolt torque

The pressure sensitive paper has been analysed using the Topaq pressure analysis system; a service provided by the supplier of the paper (Sensor Products Inc.). Used in conjunction with Pressurex pressure indicating papers, Topaq analysis provides computer analysis of the pressure distribution and magnitude. The system renders high resolution, colour-calibrated images that reflect how force is dispersed at the interface. The results obtained from the analysis include 2-D and 3-D contour plots, pressure line profiling to determine the pressure profile along a user-defined line, and a pressure histogram. The pressure histogram shows the percentage of plot area within a range of pressures (the 30 bars add up to 100% of area), displaying where pressure is concentrated. Figure 6.12 shows the High range paper results and Figure 6.13 the Medium range paper results. The pressure histogram plots are shown in Figure 6.14.

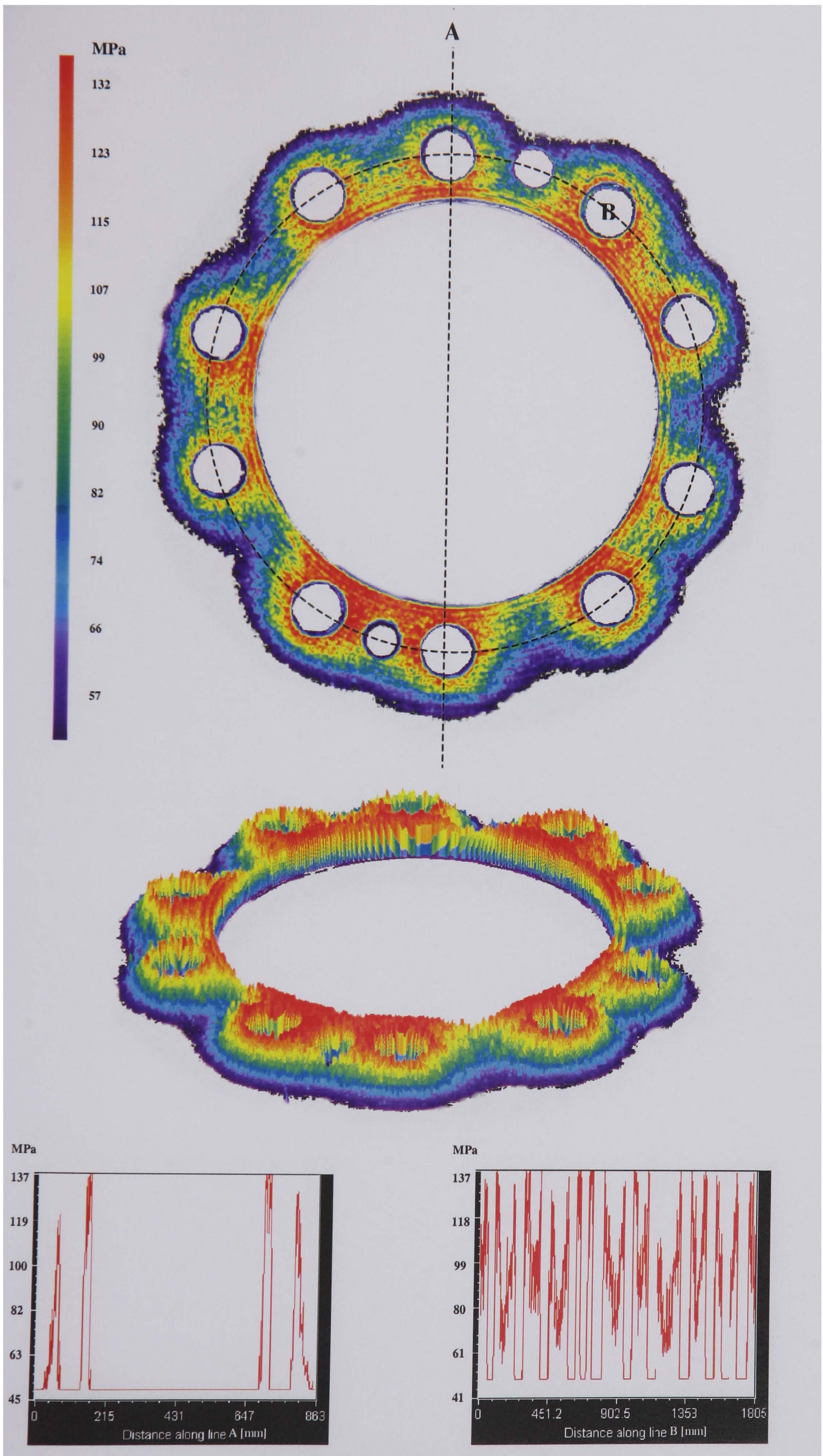


Figure 6.12 Pressurex High paper Topaq results

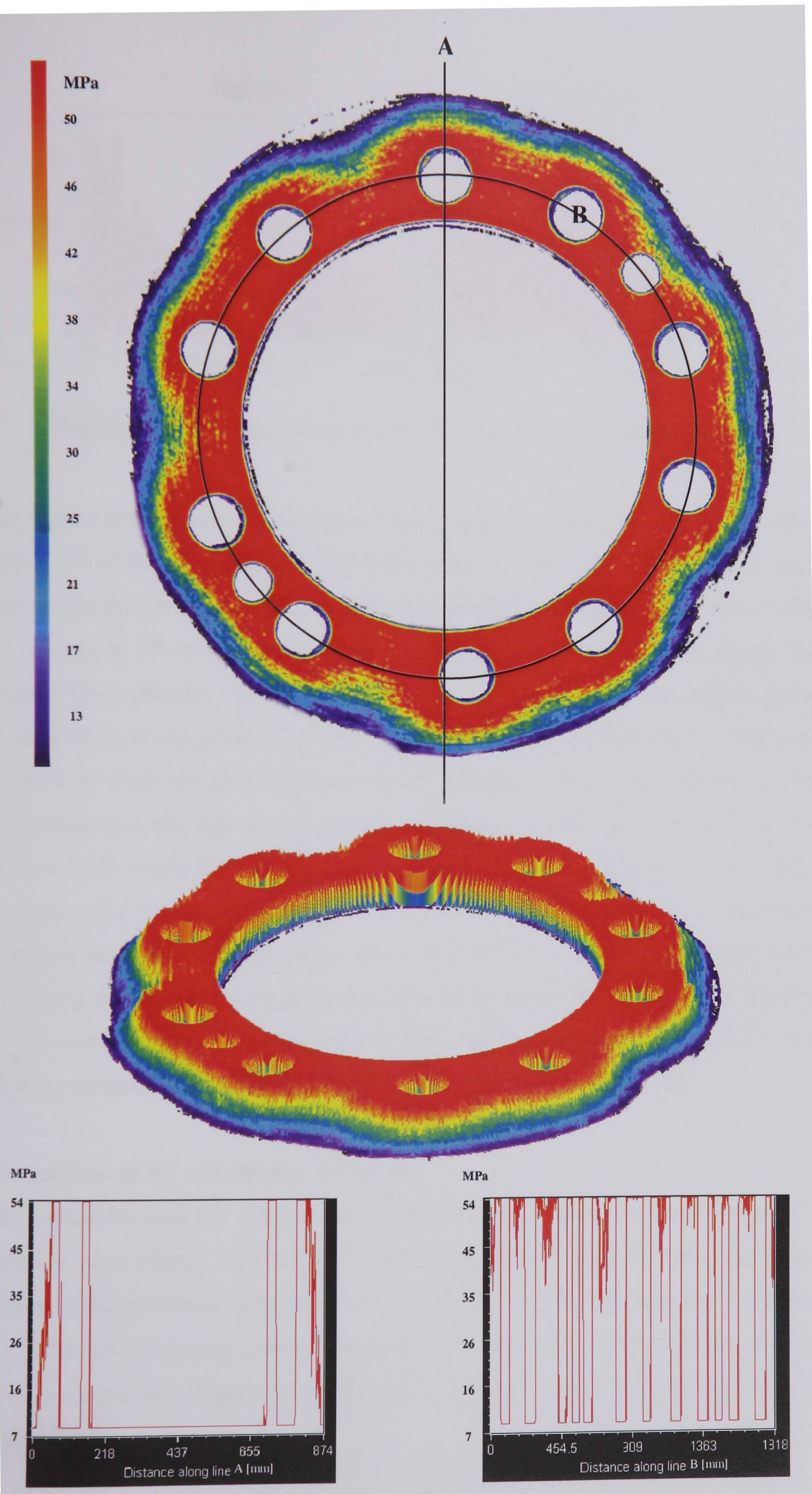


Figure 6.13 Pressurex Medium paper Topaq results

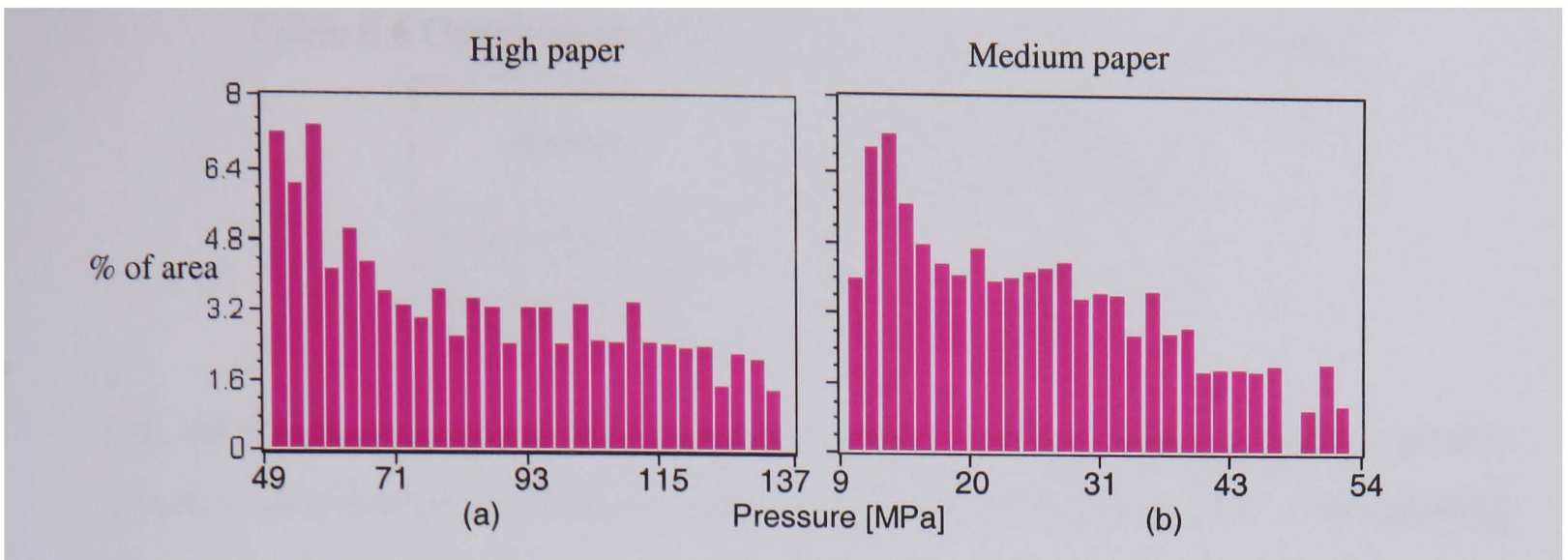


Figure 6.14 Pressure histogram plot for High (a) and Medium (b) paper

The Figure 6.14 shows that the maximum pressure (above 134 MN/m^2) is seen at only 1.2% of the measured area, the minimum pressure (below 9 MN/m^2) is seen at only 4% of the measured area, the predicted average pressure of 56.2 MN/m^2 (Table 6.3) is seen at 7% of the measured area. The high paper contour plots (Figure 6.12) reveal higher pressure evenly distributed around the boltholes, the highest pressure concentration at the group of two holes between the jacking hole, this is also shown by the Line Scan (B) plot. High pressure is also seen close to the internal diameter concentrating at the regions close to the boltholes. The Medium paper contour plots (Figure 6.13) reveal the pressure reducing from the internal diameter to the outside diameter, this is also shown by the Line Scan (A) plot. The boltholes continue to influence the pressure distribution close to the outside diameter. The low pressure in the region of the outside diameter between the groups of boltholes is not registered on the contour plots. The pressure in this region is below the threshold of the Medium pressure paper, that is to say it is below 9.7 MN/m^2 (Table 6.5).

Comparison of FE and Measured Results

The measured pressure sensitive paper results (see Figure 6.12 and Figure 6.13) coincide very closely with stress results from the FE analysis (see Figure 6.7). Almost identical stress distribution and magnitude has been predicted as shown in the Table 6.6 comparing contact pressure at positions (1) and (2) (see Figure 6.7) of the FE contour plot (Figure 6.7) and pressure sensitive paper results (Figure 6.12 and Figure 6.13).

Table 6.6 Comparison of FE and measured contact pressure results

| Position | Pressure [MN/m ²] | |
|-----------------------|-------------------------------|-----------------|
| | FE model | Pressurex Paper |
| At bolt proximity (1) | 95.0 | 107 |
| Between bolts (2) | 32.3 | 38 |

The results show that the FE modelling method can be reliably used to predict pressure distribution in bolted brake component interfaces. The corresponding thermal contact resistance can then be determined from the functions for thermal contact resistance with respect to contact pressure, which is detailed in the next section.

6.5 Measurement of Thermal Contact Resistance

To examine the effects of clamping pressure on the h_{cond} value a defined torque was applied to the clamping bolts and effects on (Q_{cond}) through the disc/wheel carrier interface measured. Changes in clamping force will affect the contact surface area of the components. Improvement of surface finish and the use of interstitial media to increase h_{cond} have been investigated in Chapter 9.

6.5.1 Experimental Set-up

Experiments have been conducted on the standard front CV brake disc and wheel carrier (see Chapter 3 for details). The h_{cond} value between the brake disc and the wheel carrier has been obtained as a function of contact pressure for the standard interface condition. Figure 6.15 illustrates a schematic of the Spin Rig test assembly.

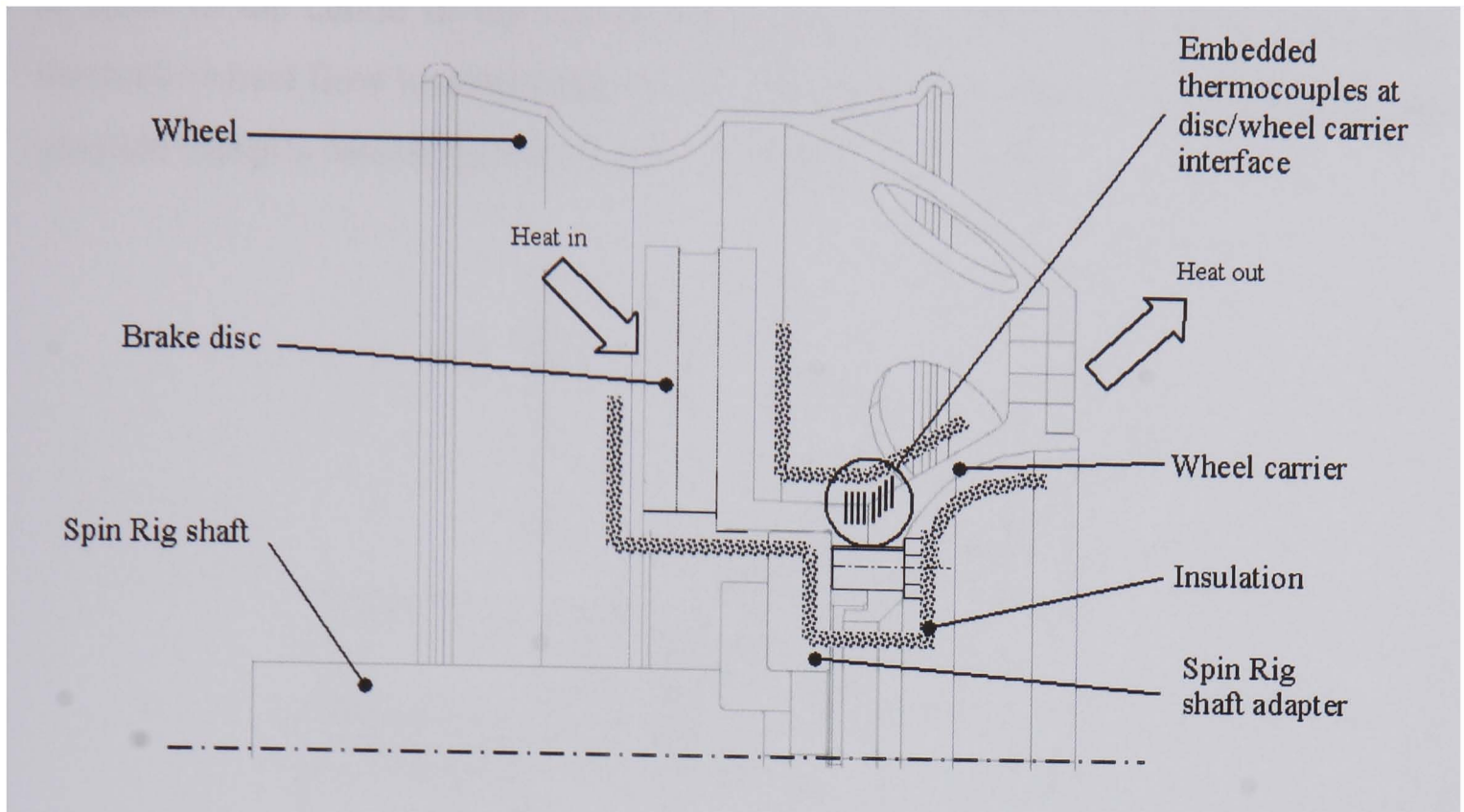


Figure 6.15 Thermal contact resistance experimental set-up

For the measurement of h_{cond} at the CV disc/wheel carrier interface, the brake disc, and wheel carrier were mounted to the Spin Rig shaft. The shaft adapter was insulated to prevent heat conducting back to the shaft. The brake disc was heated with two hot air guns fitted to the heater box (see Chapter 3 and Figure 6.18); the total heating power being 4 kW. The heater box allows hot air to flow over the surface of the disc providing uniform heating. The brake assembly was stationary during the heating phase.

Pressure distribution investigation, conducted in the previous section, indicate two distinctive areas; high pressure around the bolts, and low pressure between the bolts. Therefore, holes have been drilled into the disc and carrier in these two areas as shown in Figure 6.16 and Figure 6.17, and correspond to positions (1) and (2) shown in Figure 6.7. The holes are sized to allow secure fitting of the thermocouples. K-type welded tip glass fibre insulated thermocouples are used (describe in Chapter 3). For each area investigated the thermocouples measured the temperature gradient at eight points across the interface of the two components (disc and carrier). Heat sink compound is applied to the bottom of the drilled holes to improve the contact with the thermocouple tip. Measurements are taken when steady-state conditions were reached, allowing the thermocouple tip to reach the same temperature as the surrounding material, providing accurate results. The thermocouple hole depth was

as close to the centre of the components as possible, this was to ensure that only conductive heat flow was measured and not heat flow to the surface generated by any possible (despite insulation) convective or radiative heat loss.

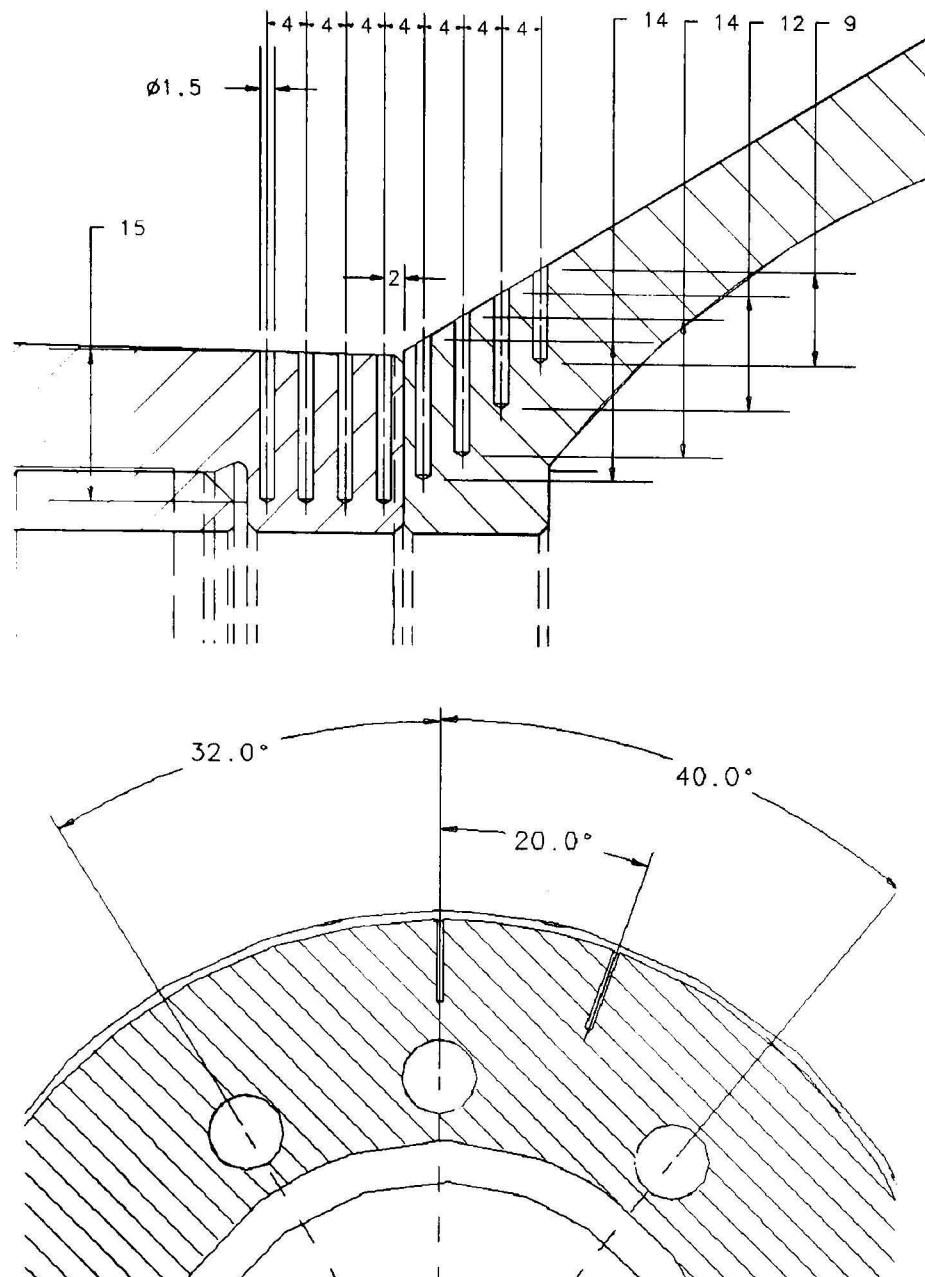


Figure 6.16 Position [mm] of drilled holes for embedded thermocouples

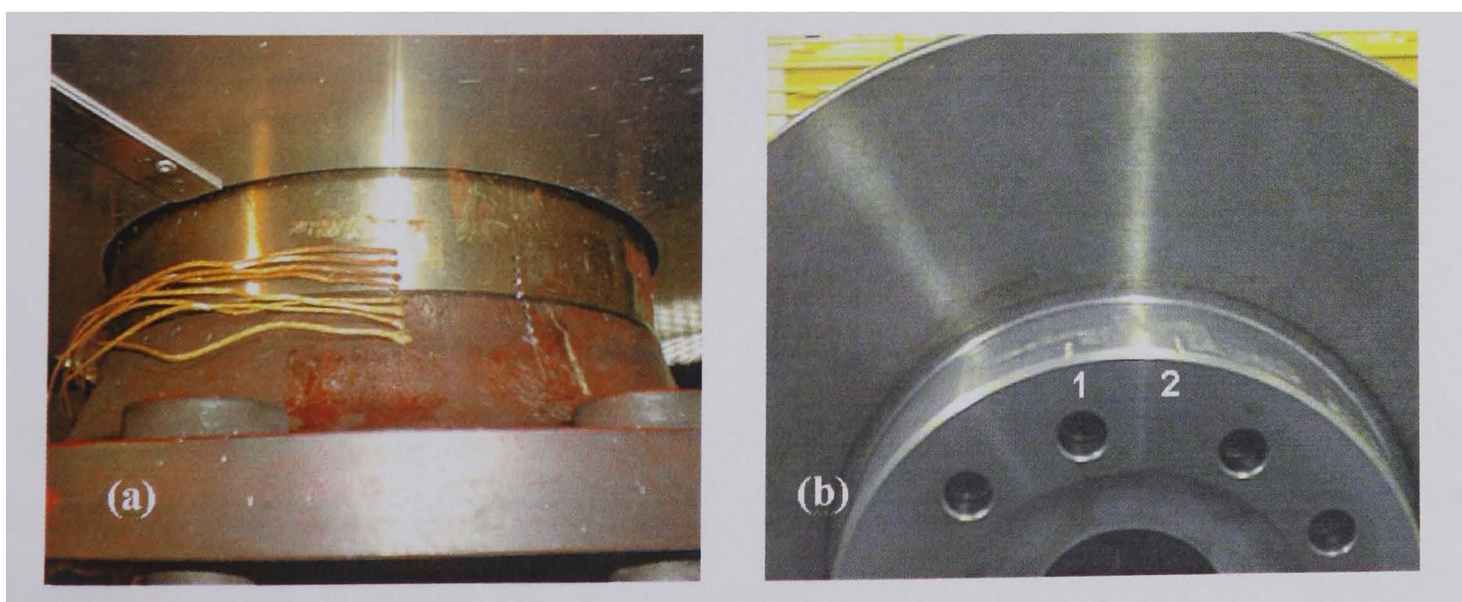


Figure 6.17 The measurement of h_{cond} . (a) The eight thermocouples (b) The two positions (disc only shown), at the bolt (1) and between the bolts (2)

Using the thermal conductivity of the disc material (grey cast iron, see Table A2) and the temperatures measured at known axial locations on the brake disc, the heat flow is determined. The heat flow is found using equation (6.1). Measuring the temperature difference at the interface, h_{cond} is determined with equation (6.6).

It is assumed that there are no heat losses and all heat is conducted from the disc to the wheel carrier. Losses have been kept to a minimum by keeping test temperatures relatively low (below 200°C). A thermal blanket is also placed over the test components to reduce heat losses by convection and radiation, as shown in Figure 6.18.

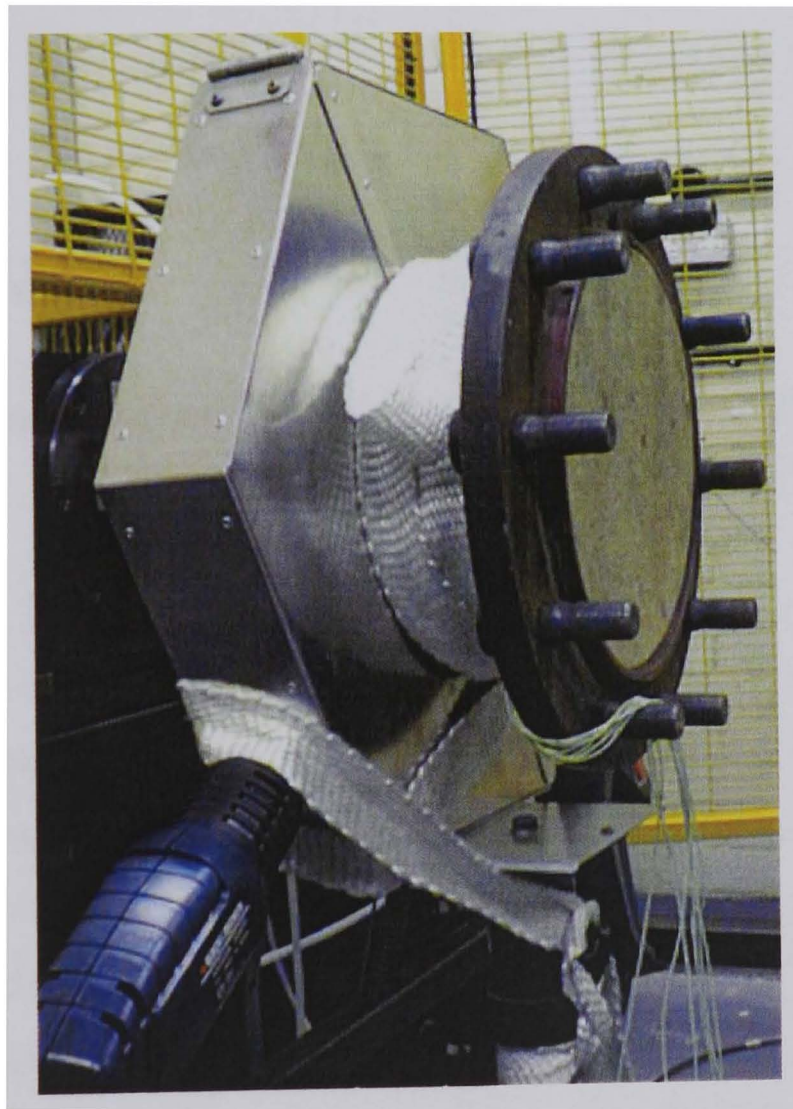


Figure 6.18 Thermal contact resistance test set-up showing; heater box, insulation and thermocouple wires

6.5.2 Experimental Procedure

The standard CV brake disc and wheel carrier are bolted together at the required torque as shown in Figure 6.15. The assembly was heated until steady-state conditions were achieved. By controlling the heater power, three temperature levels were achieved, in the regions of approximately, 80, 115 and 170°C. Figure 6.19 shows the 8 temperatures logged during a typical heating cycle.

Temperatures are logged at 0.25 Hz. The criteria for steady-state is a temperature change of less than 0.05°C after 400 seconds.

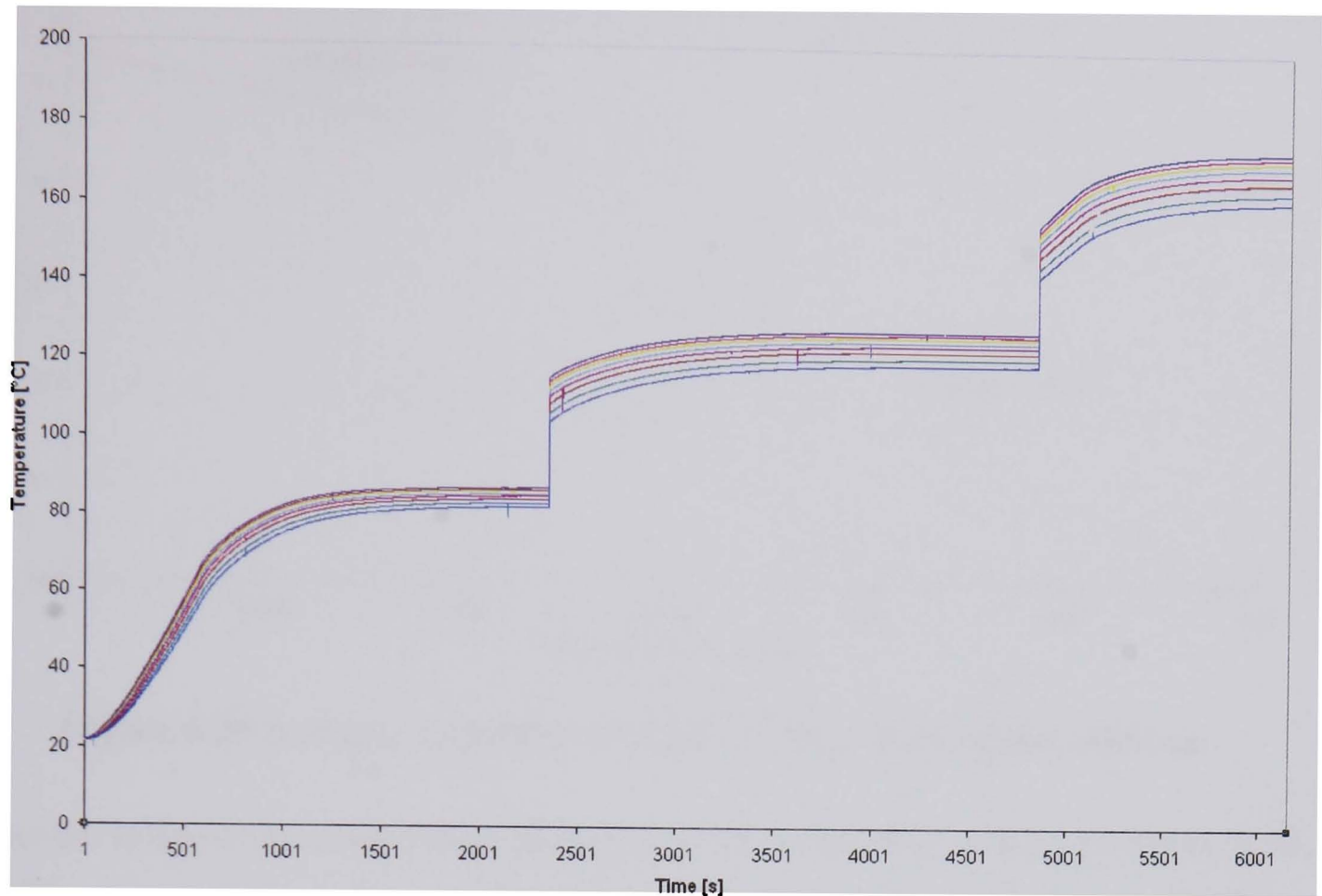


Figure 6.19 The typical temperature conditions, logged during experiment, showing three steady-state levels across the interface

Figure 6.20 shows the average steady-state temperatures at the eight points for the first test steady-state temperature of 80°C. The temperatures are averaged from 100 consecutive temperature values logged at 0.25 Hz. The distance of the thermocouple measurement from the interface is plotted on the x-axis of the graph. The temperature gradient at the disc (dT/dx) is 78.9°C/m and at the carrier dT/dx is 191.3°C/m. The temperature gradients are proportional to the conductivity of the material and the steeper gradient of the carrier is a result of its lower conductivity. The temperature drop at the interface is measured at the interface line shown on the graph; a temperature drop (ΔT_{int}) of 1.3°C is shown. Heat flow through the components is calculated from dT/dx . The R_{cond} value is calculated using ΔT_{int} .

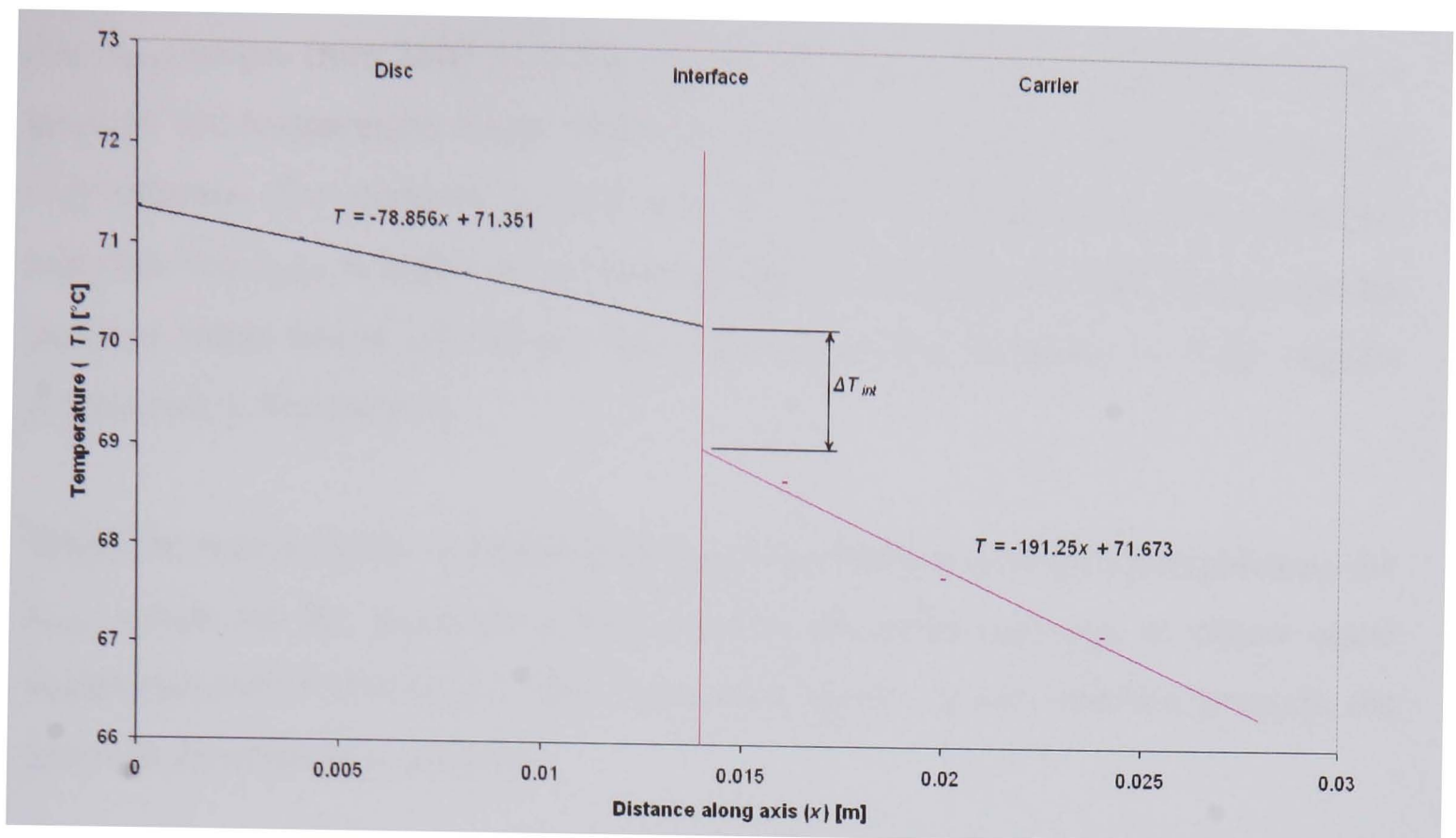


Figure 6.20 Average temperatures at the CV disc/wheel carrier interface

From the slope of the temperature distribution across the disc, shown in Figure 6.20, equation (6.1) gives a value, for the heat flow through the disc/wheel carrier interface, of 4140 W/m^2 . With the temperature drop at the interface equation (6.6) and (6.3) give an R_{cond} value of $0.0029 \text{ m}^2\text{K/W}$, or in the form of h_{cond} , $344.8 \text{ W/m}^2\text{K}$. The h_{cond} value will be used to compare interface conditions and applied to the numerical brake model during FE analysis.

6.5.3 The Influence of Interface Pressure and Temperature

Experiments have been conducted to examine the change in h_{cond} with contact pressure and temperature. A total of 15 tests were performed at three temperatures, each test requiring one day to perform. The disc used in the test was new and had a fine turned, machine finish ($R_a = 2 \mu\text{m}$), as shown in Figure 6.17(b). The carrier had been in service and some corrosion had formed from moisture penetration at the OD of the interface ($R_a = 1 - 3.3 \mu\text{m}$). The fixing bolts were tightened to six torque levels, all bolts to the same torque, gradually increasing from 50 to 300 Nm as shown in Table 6.3, the maximum value corresponding to the nominal bolt tightening torque.

Figure 6.21 shows the h_{cond} values for the two positions (close to the bolt and between the bolts), at the three temperature ranges and six pressures. It can be seen

that h_{cond} ranges from 2800 to 11400 W/m²K, increasing with the increase in contact pressure and temperature. Some results are scattered but the trend is a linear increase with pressure. The tendency is for h_{cond} to increase with temperature. The graph also indicates that h_{cond} is higher in the proximity of the bolts, this is seen throughout the pressure range tested and shows that contact pressure is higher in these regions (confirmed in Section 6.3).

When the results shown in Figure 6.21 are extrapolated to zero interface pressure, the h_{cond} values for the positions at and between the bolts converge to almost equal values (around 2333 W/m²K). This is expected because at zero interface pressure, the pressure distribution is uniform.

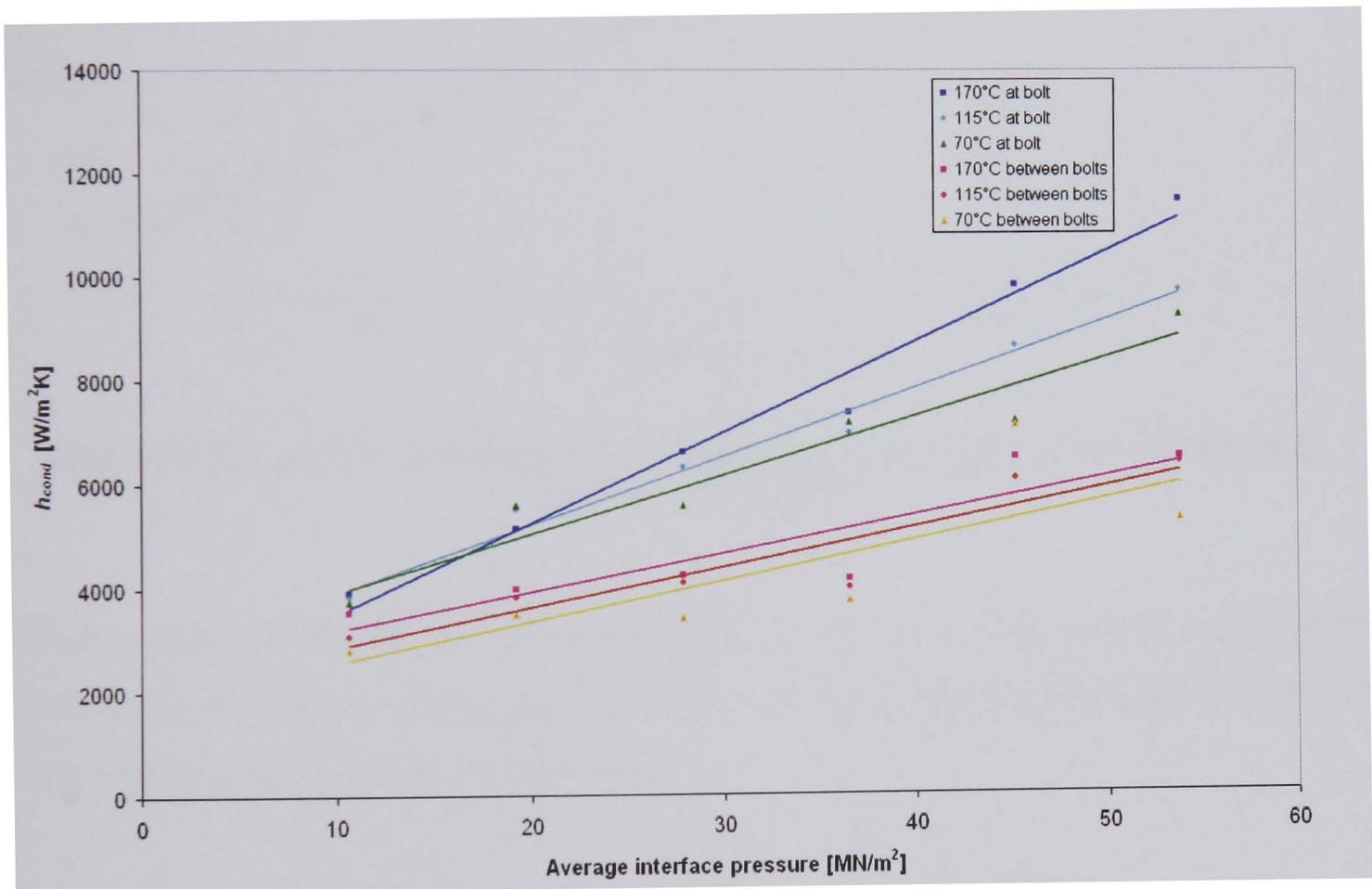


Figure 6.21 Thermal contact conductance at standard CV disc/carrier interface

The h_{cond} function for the standard interface of the disc and wheel carrier, defining its relationship with contact pressure, can be calculated by the equations derived from Figure 6.21, showing a linear trend:

$$\text{Between the bolts} \quad h_{cond} = 76 \times 10^{-6} P_{avg} + 2098 \quad (6.11)$$

$$\text{At the proximity of the bolts} \quad h_{cond} = 141 \times 10^{-6} P_{avg} + 2287 \quad (6.12)$$

Where P_{avg} is average contact pressure in N/m².

The local interface pressure results of the FE analysis presented in Figure 6.9 for the positions (1) at the bolt, and (2) between the bolts (corresponding to the thermocouple positions) are plotted against the average measured h_{cond} values given in Figure 6.21. This gives a function for the local h_{cond} value as a function of local interface pressure as shown in Figure 6.22.

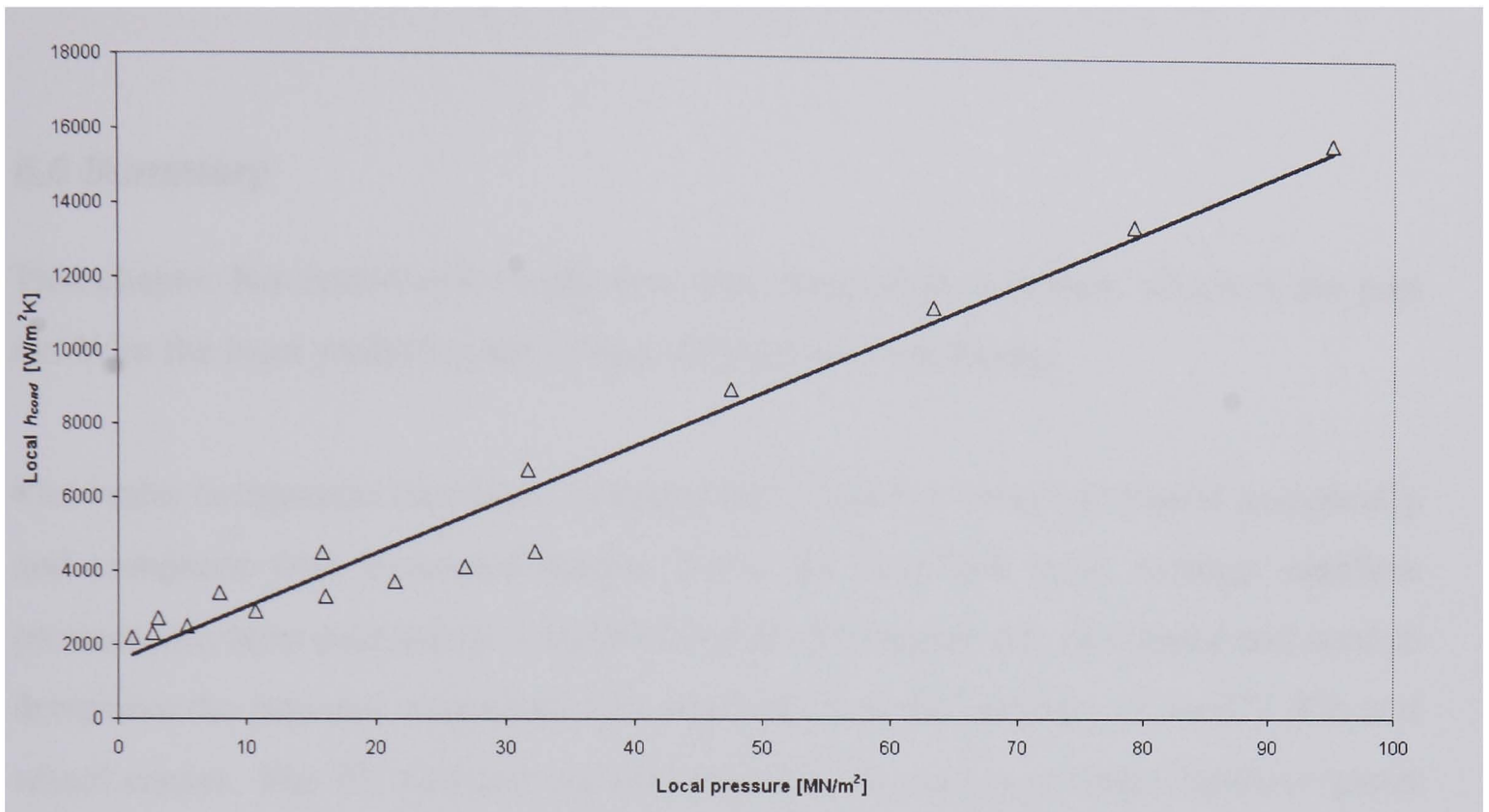


Figure 6.22 Local h_{cond} change with local interface pressure for the standard CV disc/carrier interface

The h_{cond} function for the standard interface of the disc and wheel carrier, defining its relationship with local contact pressure (P), can be calculated by the equation derived from Figure 6.22, showing a linear trend:

$$\text{Local value} \quad h_{cond} = 1 \times 10^{-4} P + 1560 \quad (6.13)$$

The results for the standard interface are in good general agreement with published h_{cond} values, as shown in Table 6.7. It should be noted that there is little published data for h_{cond} and the surface roughness, interface materials and clamping conditions are different for each value of h_{cond} given. The highest value for h_{cond} is for the aluminium interface as expected and the lowest value is given for the grey cast and SG iron materials with a poorer surface finish.

Table 6.7 Comparison of published and calculated h_{cond} values

| | Equation (6.13) | Mittelbach, Vogd et al. (1994) | Cengle (1988) |
|---------------------------------|----------------------|--------------------------------|---------------------|
| h_{cond} [W/m ² K] | 1760 | 5000 | 3800 |
| Pressure [MN/m ²] | 2 | 2 | 0.3 – 2.5 |
| Surface Finish | Ra = 1 – 3.3 μ m | Ra = 3.7 μ m | Ground |
| Material | Grey/SG cast iron | Aluminium | 416 stainless steel |

6.6 Summary

This chapter has introduced conductive heat dissipation in brakes, which in the past has been the least studied mode of heat dissipation from brakes.

The brake component interface clamping bolt force has been calculated analytically and compared with measured results. From the total bolt force, average interface pressure has been calculated. A bolted interface FE model was developed and used to determine the pressure magnitude and distribution at the interface of the CV disc and wheel carrier. The FE method was then verified by placing pressure sensitive paper at the interface of the brake assembly and further computer scanning and analysis of the paper.

Spin Rig measurement of CV disc and wheel carrier interface temperatures have enabled values of thermal contact resistance to be determined as a function of temperature and interface pressure. Over 12 Spin Rig thermal contact resistance measurements were conducted at three temperature ranges, requiring 15 days of laboratory testing.

Analytical methods for determining bolt force compare well with measured values. Comparisons with the FE interface pressure results and pressure sensitive paper measurements showed excellent agreement. The measured thermal contact resistance values compare well with the limited data published, determining the parameters influencing conductive heat dissipation.

Conduction cannot be neglected in brake cooling analysis and conductive heat dissipation for new brakes being designed can now be predicted. The FE analysis

conducted for new brakes in the design phase can be used to predict the thermal contact resistance, providing a powerful new tool for studying conductive heat dissipation. The phenomenon studied here is not limited to friction brake heat dissipation analysis; the thermal contact resistance results can be applied to similar multi-solid applications. Scope for further improvement to thermal contact resistance based on the findings of this chapter is studied in Chapter 9.

Radiative Heat Dissipation

7.1 Theoretical Background

Thermal radiation is the process by which heat is transferred from a body by virtue of its temperature, without the aid of any intervening medium (Kreith 1986). Radiation travels at the speed of light, which is a product of the frequency and wavelength of the radiation. Thermal radiation always encompasses a range of wavelengths. The amount of radiation emitted per unit wavelength varies with wavelength and is called monochromatic radiation. At temperatures below 2000 K the wavelength range covered by thermal radiation falls approximately between 0.1 and 100 μm . This range is divided into ultraviolet, visible and infrared. The wavelength for maximum monochromatic emissive power decreases with temperature, as shown in Figure 7.23.

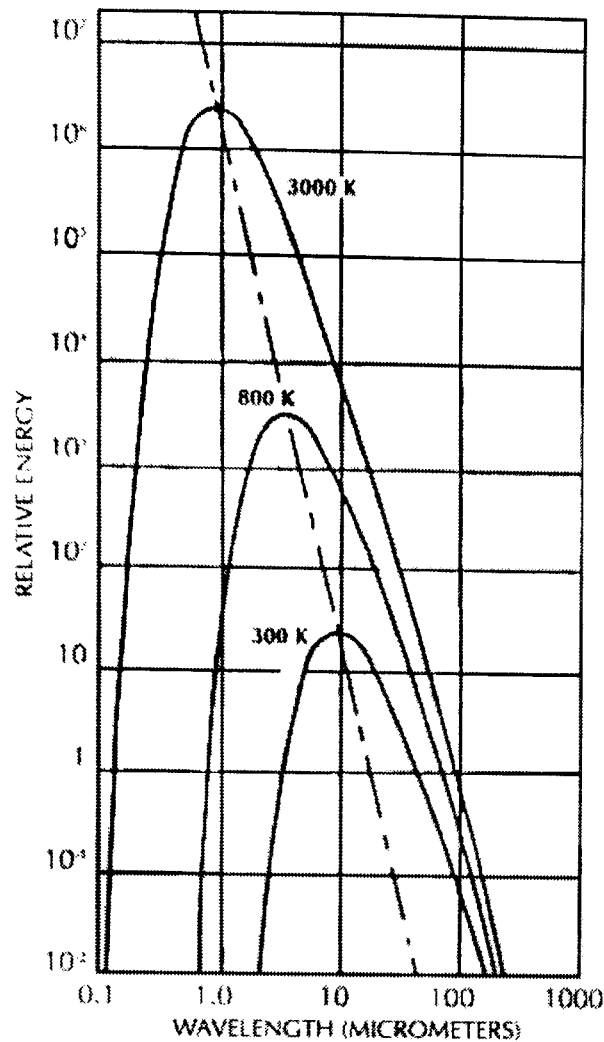


Figure 7.23 Radiation intensity as a function of wavelength and temperature (Planck's Law) (Mikron Instrument Company 2002)

A blackbody or ideal radiator is a body that emits and absorbs, at any temperature, the maximum possible amount of radiation at any given wavelength. It is a standard with which the radiation characteristics of other media are compared. The rate of radiation emission by a blackbody is equal to its rate of radiation absorption. The radiation energy emitted by a black body per unit time and per unit surface area was determined experimentally by Joseph Stefan in 1879 and this relation was theoretically verified in 1884 by Ludwig Boltzmann. It is expressed as the Stefan-Boltzmann law, as shown in equation (7.1):

$$q'_b = \sigma T^4 \quad (7.1)$$

Where q'_b is the energy flux emitted by the blackbody, σ is the Stefan-Boltzmann constant and T is the absolute temperature at the surface in Kelvin.

7.1.1 Emissivity

The emissivity of a surface is defined as the ratio of the radiation emitted by the surface to the radiation emitted by a blackbody at the same temperature (Cengel 1998). Black bodies have an emissivity of one, however most objects have a lower value of emissivity. The value of emissivity may change with temperature and wavelength for different objects. The effect of temperature on emissivity is shown in Figure 7.24, showing that the emissivity of most metals increases with temperature.

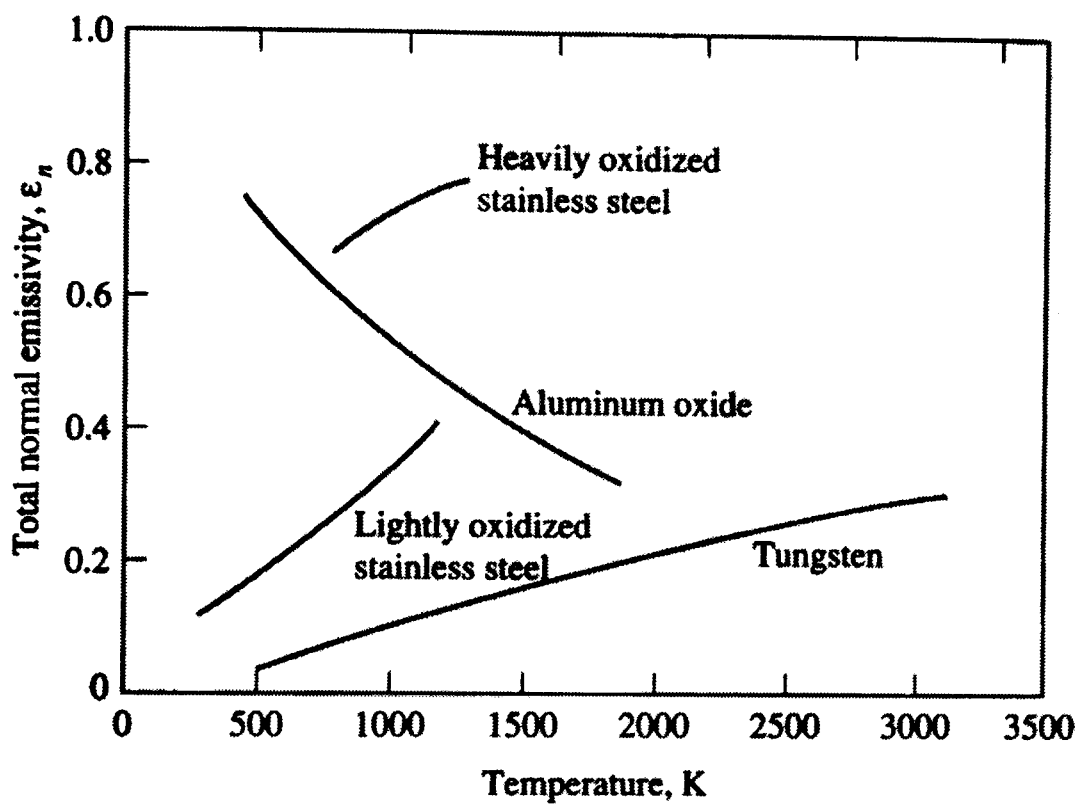


Figure 7.24 Variation of normal emissivity with temperature for various metals (Cengel 1998)

The emissivity values of common brake disc materials are listed in Table 7.8, showing that metals generally have low emissivity values, as low as 0.02 for polished surfaces; non-metals such as ceramics have higher values. Oxidisation causes significant increases in the emissivity of metals. Heavily oxidised metals can have emissivities comparable to those of non-metals. It is interesting to note that, for the highly polished cast iron surfaces, emissivity values of 0.05 to 0.07 are given for the temperature range 300 to 500K. For the oxidised cast iron surfaces, emissivity values are 0.64-0.78 (over 10 times higher) for the same temperature range.

Table 7.8 Emissivities of common metal surfaces (Cengel 1998)

| Material | | Temperature [K] | Emissivity [-] |
|-----------|------------------|-----------------|----------------|
| Aluminium | Polished | 300-900 | 0.04-0.06 |
| | Commercial | 400 | 0.09 |
| | Heavily oxidised | 400-800 | 0.20-0.33 |
| Iron | Highly polished | 300-500 | 0.05-0.07 |
| | Oxidised | | 0.64-0.78 |
| Steel | Polished | 300-500 | 0.08-0.14 |
| | Commercial | 500-1200 | 0.2-0.32 |
| | Heavily oxidised | 300 | 0.81 |

To determine heat losses by radiation, the values of emissivity must be known for each surface. Emissivity (ϵ) values will vary for different sections of the brake disc, mainly between the friction surface and other areas (e.g. the hat and rim). The energy emitted by radiation can be determined by equation (7.2):

$$Q_{rad} = \epsilon \sigma A (T_D^4 - T_\infty^4) \quad (7.2)$$

Where, A is the area emitting radiation, T_D is the surface temperature, T_∞ is the ambient temperature.

7.1.2 View Factors

Radiative heat transfer between surfaces is affected by the orientation of the surfaces relative to each other as well as their radiation properties and temperatures, as illustrated in Figure 7.25. To account for the effects of orientation on radiative heat transfer, the view factor parameter is used. This is purely a geometric quantity, also called the shape factor, configuration factor or angle factor. The view factor from a surface i to a surface j is denoted by $F_{i \rightarrow j}$ and is defined as (Cengel 1998):

$F_{i \rightarrow j}$ = the fraction of the radiation leaving surface i that strikes surface j directly

Radiation striking surface i does not need to be absorbed by the surface. In addition, radiation that strikes a surface after being reflected by other surfaces is not considered in the evaluation of the view factors. The underlying assumption is that

the radiation received from a source is directly related to the angle the surface subtends when viewed from the source. View factors for common geometry are evaluated and can be found in the literature (Cengel 1998).

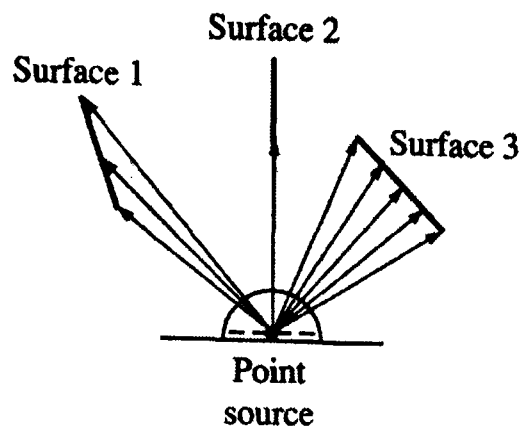


Figure 7.25 Radiation heat exchange between surfaces (Cengel 1998)

View factors must be considered when modelling heat transfer by radiation for the brake disc surface. Heat radiating from the surfaces will be absorbed and reflected by adjacent surfaces.

7.2 Surface Emissivity of Brake Discs

Measuring the emissivity of the brake surface and the radiative heat dissipation, is connected with numerous problems, including non-uniform temperature distribution and constant surface condition alteration (such as wear, pad deposits) during the brake application.

7.2.1 Literature Data

For the cast iron disc surface, different values for emissivity are quoted in literature, some of which are presented in the Table 7.9.

Table 7.9 Cast iron brake emissivity data

| Author | Emissivity |
|--------------------------------------|-------------|
| Limpert (1975) | 0.55 |
| Noyes and Vickers (1969) | 0.80 |
| Grieve, Barton et al (1998) | 0.40 |
| Eisengraber, Grochowicz et al (1999) | 0.15 – 0.90 |

Limpert (1975) has recommended an emissivity value of 0.55 for cast iron discs and Noyes and Vickers (1969) assumed all emissivities to be 0.8 with a background temperature of 38°C. No information was given on how emissivity values were determined.

From thermal imaging work carried out on a brake dynamometer, Grieve, Barton et al (1998) used an emissivity value of 0.4 for cast iron and MMC rotors. Eisengräber, Grochowicz et al (1999) showed that the surface emissivity needed to be constantly corrected during the braking application. Comparing IR sensor measurements with thermocouple readings to determine emissivity, values varied between 0.15 and 0.9 in different dynamometer tests. During a drag test, emissivity values increased from 0.4 to 0.7.

7.2.2 Emissivity Measurements

As shown in Section 7.2.1 values for surface emissivity of brake discs published in literature are limited, inconsistent and sometimes contradicting. A series of experiments aimed at providing accurate emissivity measurements for brake cooling analyses have been developed. To determine emissivity and radiative heat transfer coefficients, temperature measurements have been conducted on metal surfaces using infrared sensors and thermocouples. Comparing thermocouple measurements with infrared sensor measurements, the emissivity setting of the infrared sensor was adjusted until the infrared sensor measurement equalled the thermocouple temperature values. This emissivity value is then taken as the surface emissivity of the material.

Three experiments were conducted, one for the study of a new-machined cast iron disc at high temperature, the second measured a mild steel plate at high temperature, and the third measured the cast iron disc at lower temperatures. The third test was conducted at lower temperatures to avoid changing the surface properties due to high temperature oxidation and discolouration of the surface.

Experiment 1

A section of grey cast iron brake disc was heated with a gas flame; temperature measurements were taken on the opposite face using a thermocouple and infrared sensor, see Figure 7.26. The Raytec infrared sensor was used for the experiment (see Chapter 3) mounted to a camera stand. The measuring head was 200 mm away from the plate surface (x) giving a measurement spot diameter of 7 mm. The ground disc surface blackened at high temperature, the effect of emissivity setting on infrared sensor temperature measurement is shown in Figure 7.27. The infrared readings for emissivity set to values of 0.2, 0.6 and 1.0 are compared with a thermocouple temperature measurement. Figure 7.27 shows good correlation for the blackened disc surface when emissivity is approaching a value of 1.

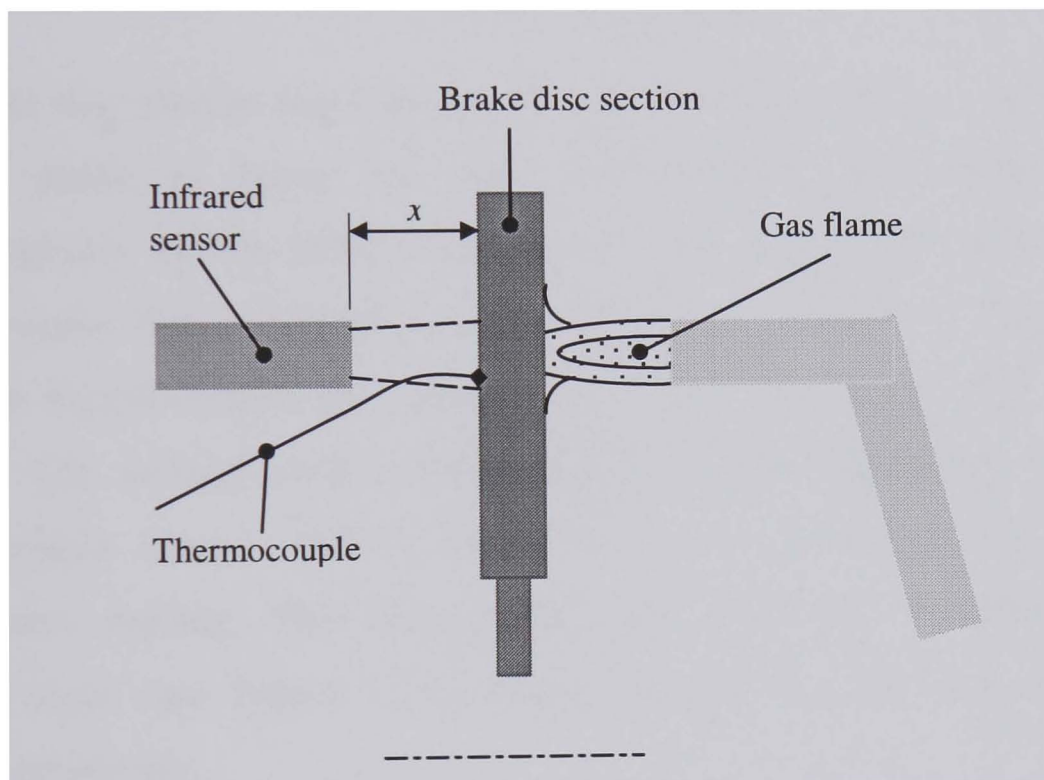


Figure 7.26 Gas flame heating of brake disc and combined infrared and thermocouple temperature measurement for assessing emissivity

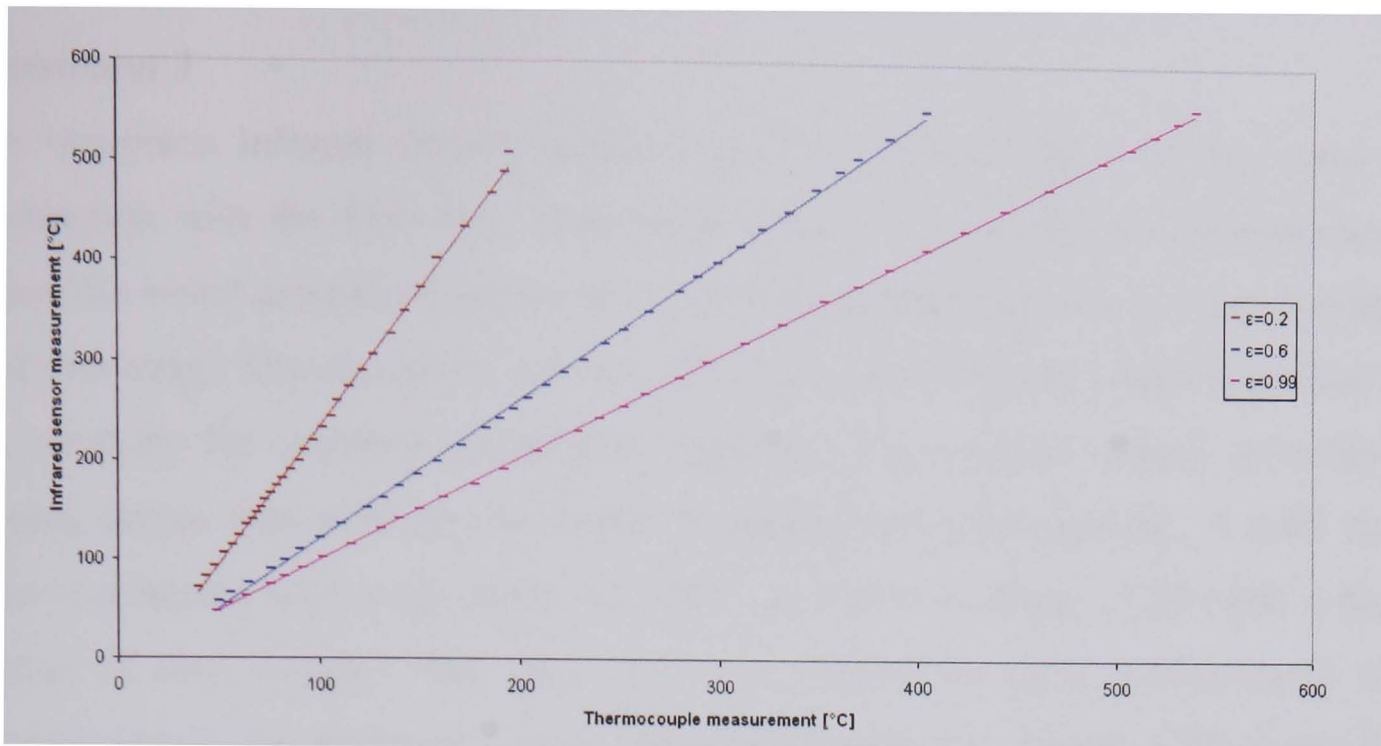


Figure 7.27 Infrared sensor and thermocouple measurement of grey cast iron disc surface temperature

The brake disc section was heated to 550°C and the temperature measured during the cooling phase to avoid hot spots. The surface temperature was measured simultaneously by the infrared sensor set to an emissivity value of 0.99 and the thermocouple. Figure 7.28 shows that the infrared sensor is in very good agreement with the thermocouple, this confirms the emissivity value 0.99 for the material surface. The infrared sensor shows slightly higher temperature readings than the thermocouple above 250°C, the temperature difference increases with the temperature reading. This indicates that the emissivity has increased during the cooling stage (see Figure 7.24), demonstrating the complexity of setting correct surface emissivity.

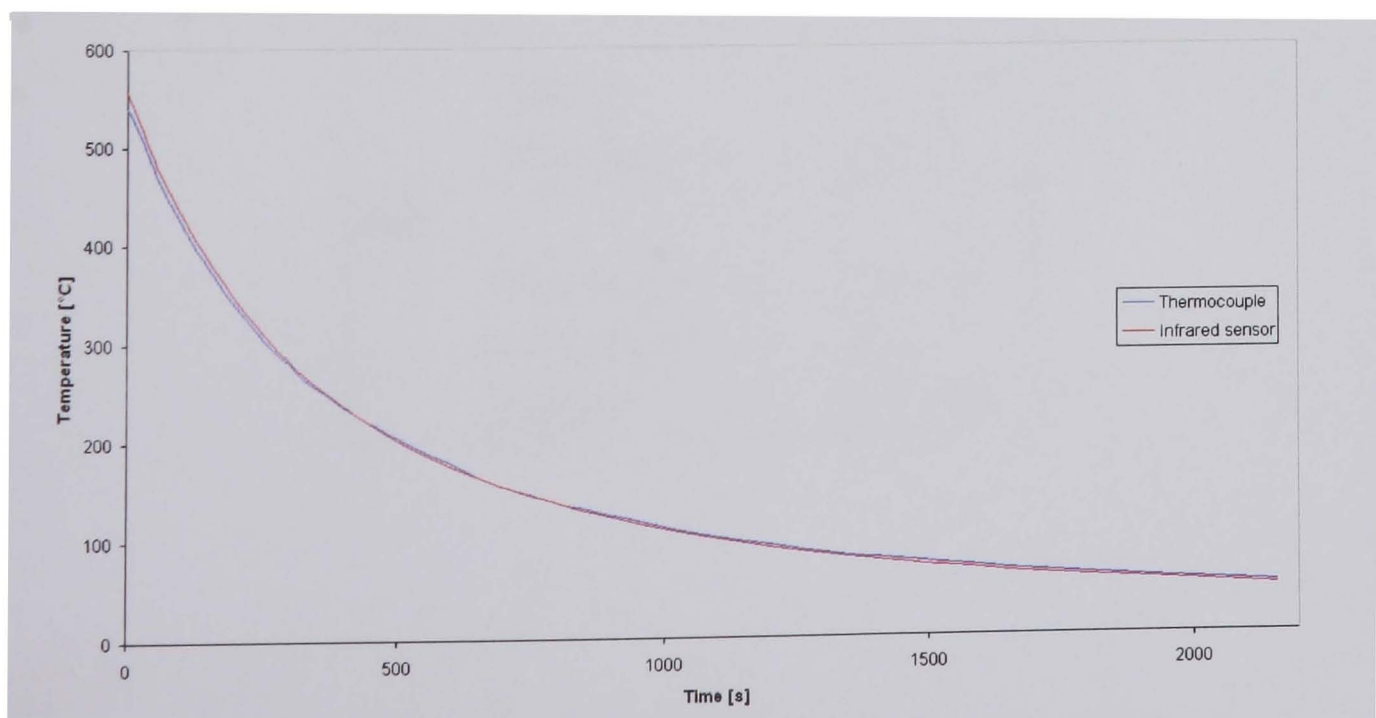


Figure 7.28 Thermocouple and infrared sensor measurement comparison for grey cast iron disc surface ($\epsilon = 0.99$)

Experiment 2

The two-piece infrared sensor supplied by Calex (see Chapter 3) was used in conjunction with the Spin Rig. This sensor type is more suited to laboratory tests within the wheel assembly because of its small measuring head size (14 mm diameter x 28 mm long). The emissivity value is also adjustable with this sensor and must be set correctly for accurate temperature readings. The infrared sensor provides a voltage output that must be calibrated for temperature measurement. A mild steel plate was heated with a gas flame to 500°C, as shown in Figure 7.26 (with a plate instead of disc section). The plate was then allowed to cool; thermocouple and infrared sensor measurements were taken simultaneously. Figure 7.29 shows the linear voltage output of the Calex infrared sensor when measuring the surface temperature; emissivity was set to 0.9, which is in the range recommended by the manufacturer (see Table 7.10). The sensor head was placed 25 mm from the plate surface, giving a surface measurement diameter of 12.5 mm. The voltage output curve was used to define temperature output.

Table 7.10 Typical emissivity values for metals, Calex Electronics Ltd.

| Materials | Emissivity |
|-----------------------|------------|
| Aluminium | |
| Un-oxidised | 0.02 - 0.1 |
| Oxidised | 0.2 - 0.4 |
| Alloy A3003, oxidised | 0.3 |
| Roughened | 0.1 - 0.3 |
| Iron, Cast | |
| Oxidised | 0.6 - 0.95 |
| Un-oxidised | 0.2 |
| Steel | |
| Ground sheet | 0.4 - 0.6 |
| Polished sheet | 0.1 |
| Oxidised | 0.7 - 0.9 |

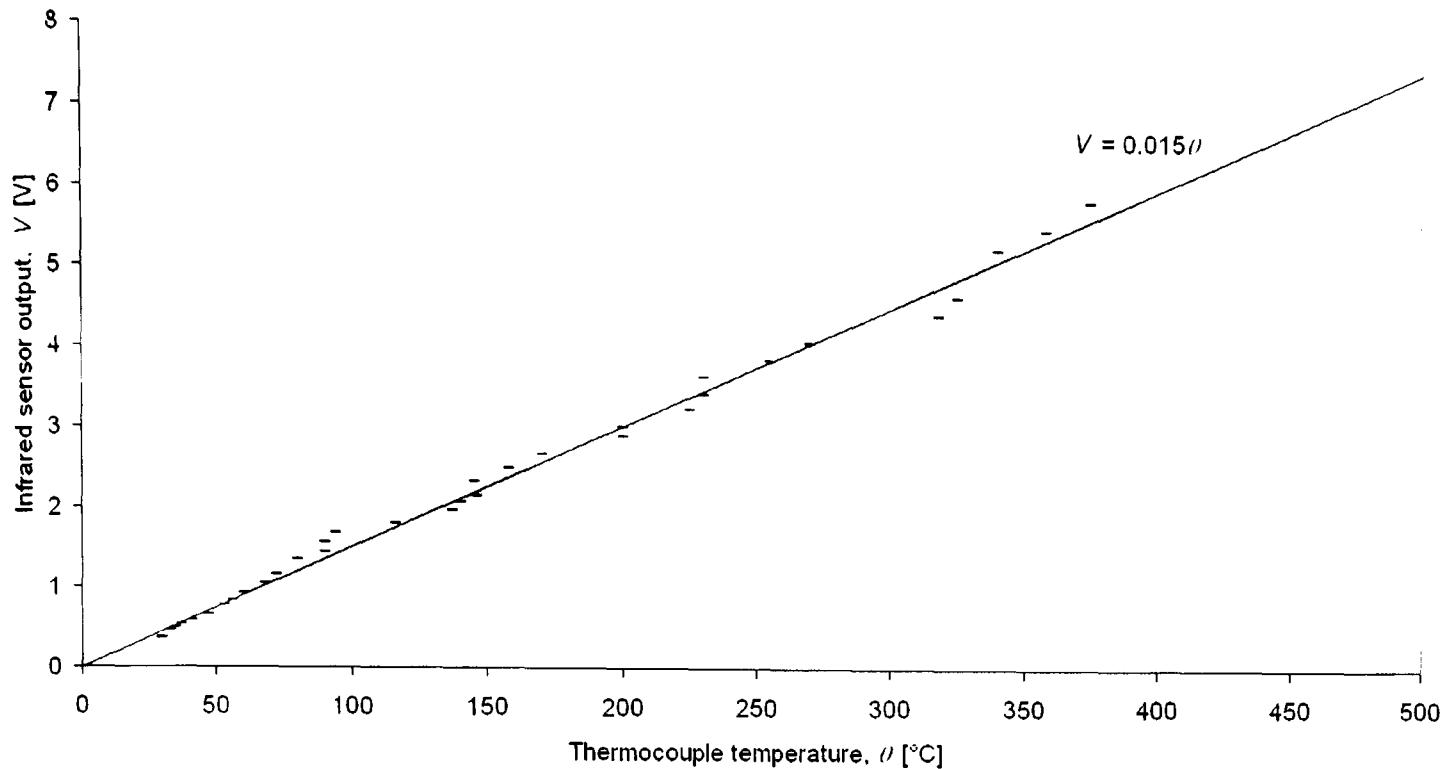


Figure 7.29 Calex infrared sensor voltage output, $\epsilon = 0.9$, oxidised mild steel

Experiment 3

Infrared measurements were conducted on the Spin Rig for a new CV disc using the Calex infrared sensor. The disc was heated using the Spin Rig air heater (see Chapter 3) and then allowed to cool at a constant rotational speed. Emissivity is set to 0.2 as recommended by the manufacturer, see Table 3.12, and the sensor head placed 4.5 mm from the surface giving a measurement spot diameter of 2.25 mm. Figure 7.30 shows the linear voltage output of the Calex infrared sensor for a temperature range of 30 to 100°C for the machined grey cast iron surface. It can be seen that the voltage output is a different function to that shown in Figure 7.29. It was found that the voltage output also changes with distance from the disc surface and surface condition. This can be due to atmospheric absorption and surface emissivity.

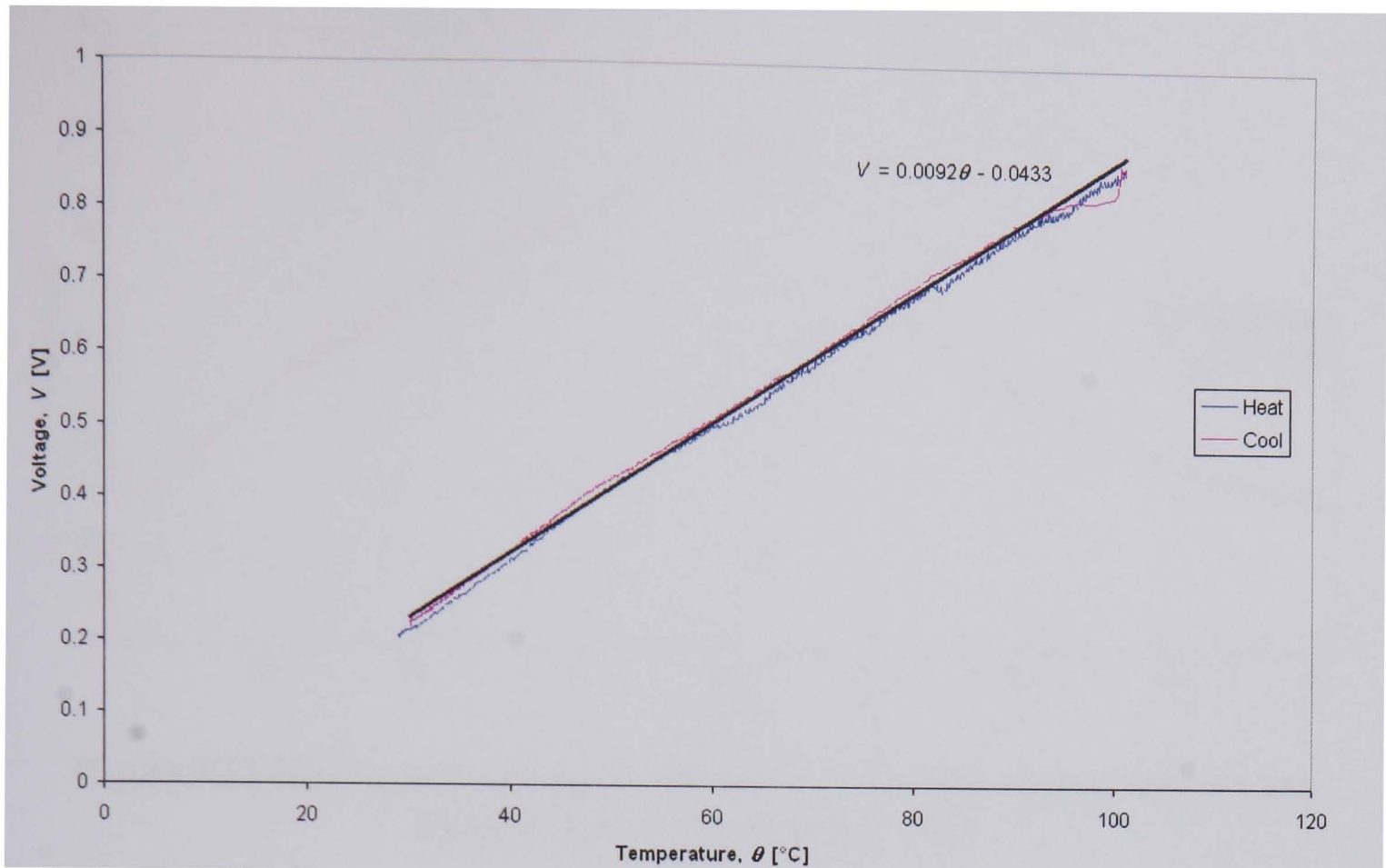


Figure 7.30 Infrared sensor voltage output during CV disc temperature rise, $\epsilon = 0.2$

After calibration of the infrared sensor, the temperature output of the infrared sensor is compared with the rubbing thermocouple during the CV disc heat and cool cycle (at 500 min^{-1}) as shown in Figure 7.31. Good correlation is achieved between the infrared sensor and the rubbing thermocouple temperature measurements. It can be seen from the plot that the infrared sensor is sensitive to the electric heater operation during the heating cycle, the temperature output being noisier than during the cooling phase. However, the infrared sensor readings compare reasonably well to the thermocouple readings during the heating phase, and the readings are much closer during the cooling phase.

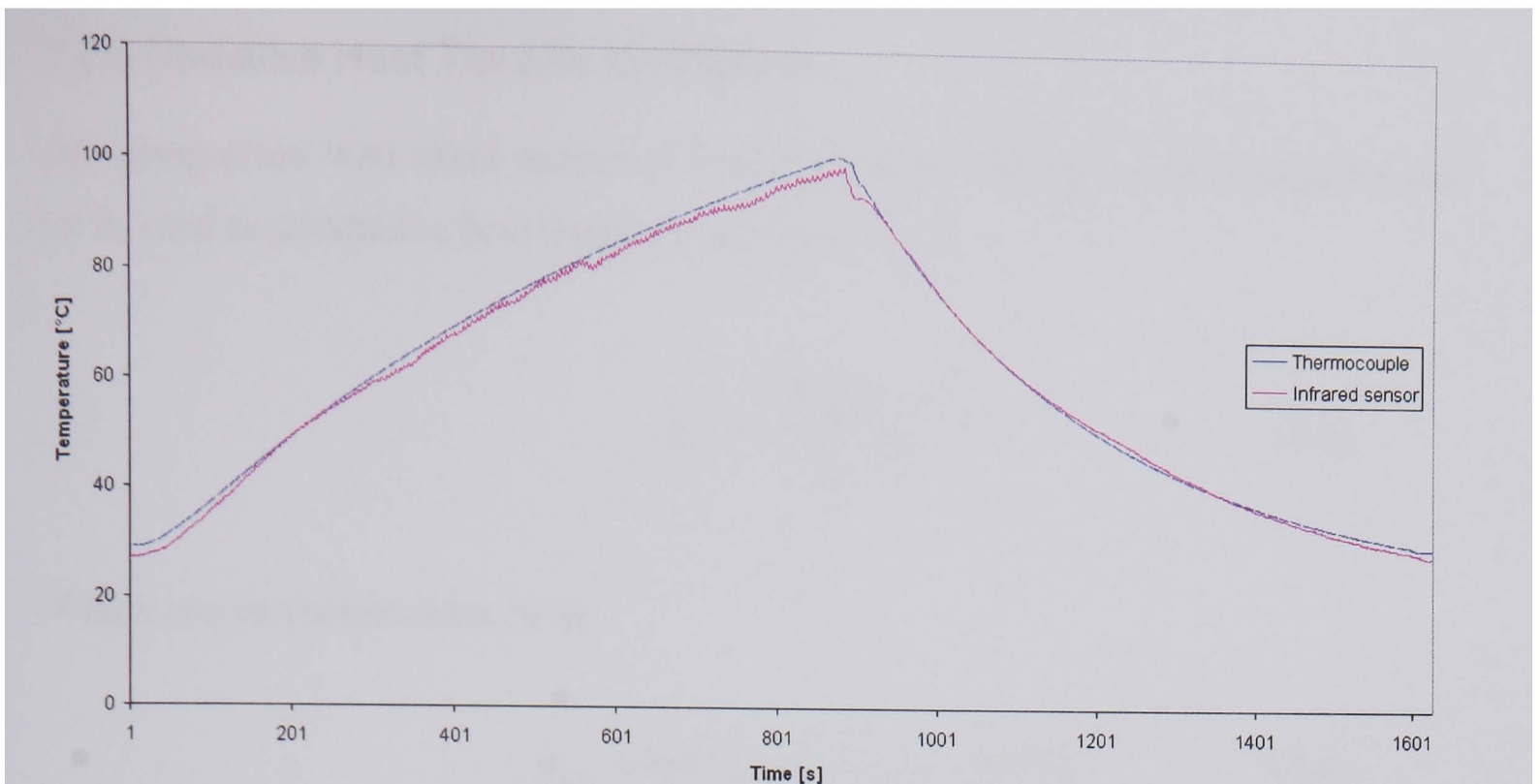


Figure 7.31 Heating and cooling (at 500 min^{-1}) of CV disc surface, infrared and thermocouple measurement, $\epsilon = 0.2$

Discussion of Results

The emissivity value corresponding to the new machined grey cast iron disc surface was 0.2 at temperatures between 20 and 200°C. For the oxidised ‘blackened’ disc surface, the emissivity value was much higher, around 0.99 for the wide temperature range between 20 and 600°C, as summarised in Table 7.11. The use of the infrared sensors proved difficult when compared to the rubbing thermocouple, each infrared sensor requiring individual calibration and the distance of the measuring head from the surface affected the output. Problems of emissivity changing with temperature are also difficult to compensate for. Infrared devices that are more sophisticated (and expensive) may prove more suitable. The infrared sensors used were particularly useful for measurement of uneven surfaces and the determination of non-transient emissivity values. Therefore, rubbing thermocouples are more suitable for Spin Rig measurements, when compared with infrared sensors, which were originally considered more useful for Spin Rig measurements.

Table 7.11 Measured emissivity values for cast iron, 20 – 200°C

| Surface condition | ϵ [-] |
|------------------------------|----------------|
| New machined ($R_a = 2.0$) | 0.20 |
| Oxidised (blackened) | 0.99 |

7.2.3 Radiative Heat Transfer Coefficients

For comparison with other modes of heat dissipation, radiative heat dissipation can be defined as a radiative heat transfer coefficient (h_{rad}):

$$h_{rad} = \frac{\varepsilon\sigma(T_D^4 - T_\infty^4)}{T_D - T_\infty} \quad (7.3)$$

Which can be further reduced to:

$$h_{rad} = \sigma\varepsilon(T_D^3 + T_\infty^3 + T_D T_\infty^2 + T_\infty T_D^2) \quad (7.4)$$

Evaluation of equation (7.4) yields an h_{rad} value as illustrated in Figure 7.32, which shows h_{rad} for an emissivity of 0.55. The value of h_{rad} increases rapidly at higher temperature when compared to convective and conductive heat transfer coefficients, which are nearly constant with temperature (as shown in Chapters 5 and 6). The curve shows that significant radiative heat dissipation occurs even at low temperatures; at 100°C, h_{rad} is equal to 5 W/m²K, comparable to natural convection. At 400°C, radiative heat dissipation becomes much more significant with h_{rad} equal to 16 W/m²K and at 600°C, h_{rad} rises to 31 W/m²K.

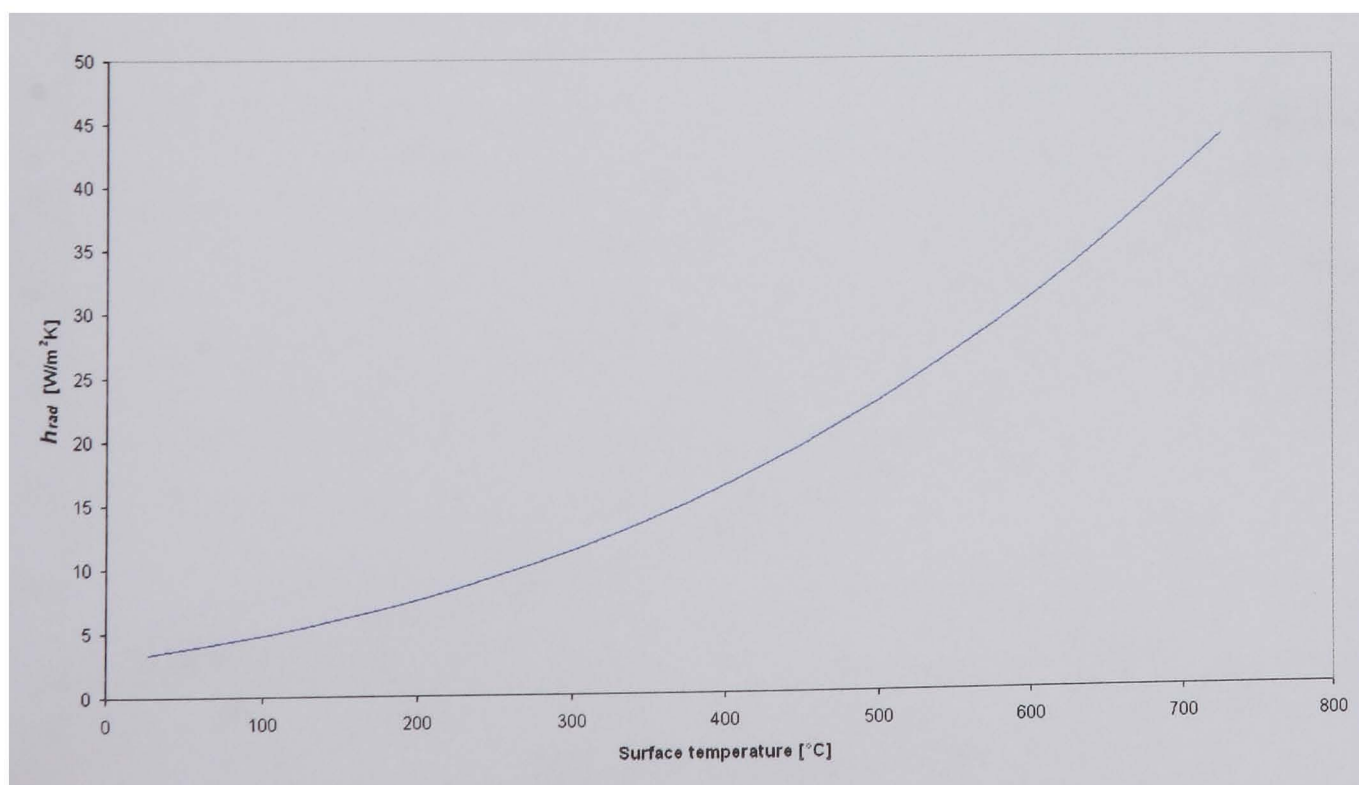


Figure 7.32 The h_{rad} increase with surface temperature for $\varepsilon = 0.55$

In order to observe how radiative heat dissipation changes during a brake application, Figure 7.33 shows the calculated h_{rad} values for the CV disc surface for the disc operating temperature range. The h_{rad} values are calculated using equation (7.3) and are based on measured and referenced emissivity values. The dashed line shows the h_{rad} values for a brake disc during a drag brake application, with emissivity change as per Eisengräber, Grochowicz et al (1999), see Table 7.9. The three solid lines indicate h_{rad} for fixed values of emissivity as indicated in Table 7.11 and Table 7.9. The curves show that significant radiative heat dissipation occurs even at low temperatures; at 100°C, h_{rad} is equal to 4 W/m²K for an emissivity of 0.55. At 400°C, radiative heat dissipation becomes very significant, h_{rad} values vary between 6 W/m²K for the lowest emissivity (0.2) and 27 W/m²K for the highest emissivity considered (0.9). At 600°C, h_{rad} varies between 12 and 52 W/m²K, for the lowest and highest emissivity values respectively.

The results illustrate the importance of correct emissivity values for reliable brake cooling prediction. Emissivity values will vary for different disc sections, mainly at the friction surface and the oxidised hat and rim areas. The friction surface experiences constant surface condition alteration during a brake application or series of applications.

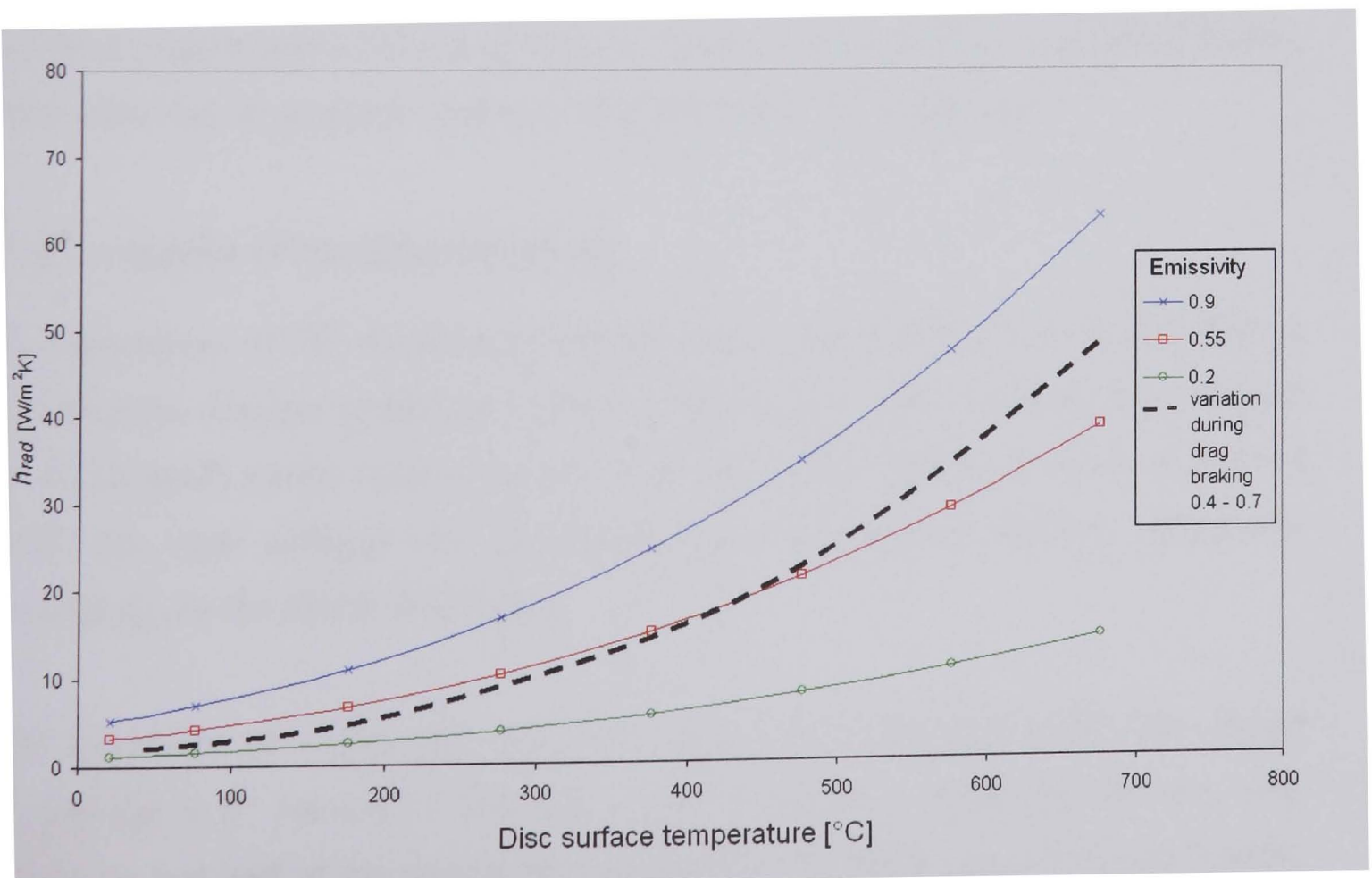


Figure 7.33 The h_{rad} increase with disc surface temperature

7.3 FE Modelling of Radiative Heat Dissipation

Radiation functions of the FE modelling package, SDRC I-DEAS TMG, enable heat transfer by radiation within the FE model. Radiation can be dissipated to ambient or adjacent surfaces. Upon a radiation request, TMG will detect enclosures, calculate view factors, perform shadowing checks, calculate diffuse and reflected radiative exchanges and compute radiative heating within the model. A surface layer of thin shell elements are required, defined with an emissivity value between 0 and 1.

All radiative exchange is calculated from one element to another element within an enclosure. If the model itself does not define an enclosure, then a Space Enclosure entity is created to absorb the energy lost from the model. In effect, a Space Enclosure creates one large tetrahedral element that encloses the model and the space around it. The software creates this element during the solve and deletes it afterward.

All elements that have an unobstructed view of each other will have their view factors computed first (see Section 7.1.2). Then, a shadowing check is performed on the remaining elements using element subdivision to evaluate what portion of the element's surface projection on another element's surface is obstructed by an obstacle. Radiation calculation can be very expensive in terms of computer time and memory requirements. To reduce expense surfaces that are known to radiate heat to each other can be grouped together, reducing view factor calculation.

7.3.1 Analysis of Modelling Methods

A comparison of FE modelling methods have been performed on a CV disc to optimise the analysis procedure and reduce computing costs. The ventilation channel is an enclosed cavity (except for the inlet and outlet), therefore radiation emitted from the vane surfaces will be absorbed by the opposite surfaces, effectively cancelling out the effect of radiation.

The symmetry of a grey cast iron brake rotor with a standard radial vane design allows for a 6° section of the disc to be considered, containing half the vane thickness and half of the ventilation channel between the vanes, see Figure 7.34(b). To ensure that modelling only half a ventilation channel provides accurate prediction

of the disc's temperatures the 6° model is compared with the 12° model, which contains a complete ventilation channel, see Figure 7.34(a). Both models have the same boundary conditions and the same heat flux applied; the material properties used are given in Table A3.

Convection coefficients were calculated using equations for convective heat transfer as discussed in Chapter 5 for the standard CV disc. A change was made to the inside of the ventilation channel of the 6° segment; radiation in this area was switched off due to the enclosed nature of the ventilation channel. A bi-linear heat flux (discussed in Appendix C) was applied to the rubbing surface representing a 0.5 second brake application time and a 2.83 second total braking time, the cycle time was 60 seconds. The power applied was equivalent to a 16.5 tonne lorry, with a front to rear braking distribution of 50:50, decelerating at 0.7g from 90 km/h on a level surface. Emissivity was set at 0.20 for the friction surfaces and 0.9 for the remaining surfaces (based on the values given in Table 7.11 for ground and oxidised cast iron).

The two models are shown with temperature contours in Figure 7.34. The 12° segment model (a) contains 4464 solid elements (eight node bricks), 2032 thin shell elements (4 node elements) and 6090 nodes. The 6° segment model (b) contains 2232 solid elements (eight node bricks), 966 thin shell elements (4 node elements) and 3410 nodes. Boundary conditions are applied to thin shell elements. The I-DEAS TGM was used for all analysis and I-DEAS was used for pre- and post-processing the analysis.

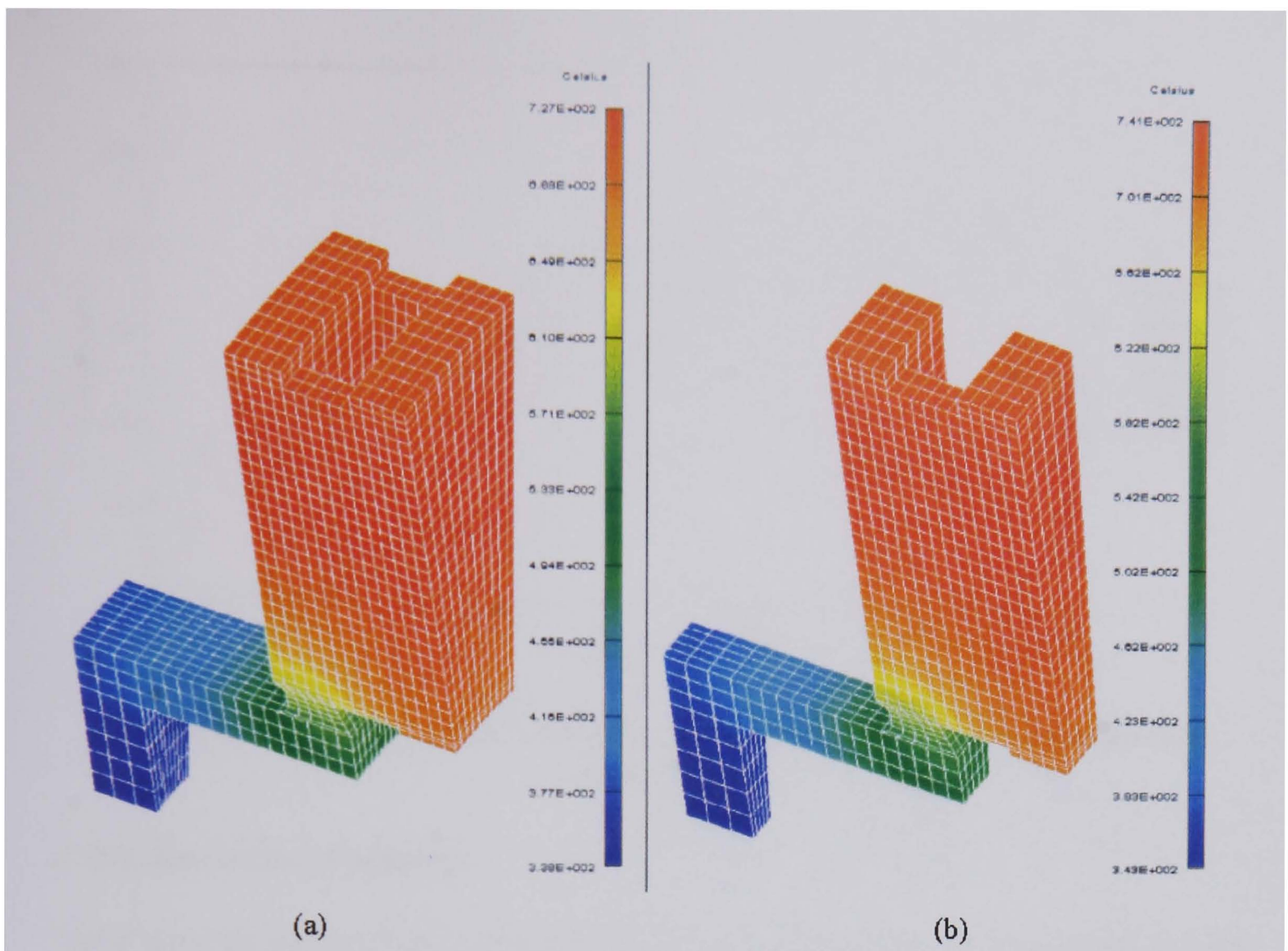


Figure 7.34 Whole (a) and half (b) ventilation channel CV disc FE model comparison of surface temperatures

The results shown in Figure 7.35 are the average maximum and minimum nodal temperatures during 20 repeated braking stops. The 6° segment gives only slightly higher temperatures, most probably the result of neglecting heat radiating from the inlet and outlet of the ventilation channel (radiation scatter). The maximum temperature difference, 13°C (958 – 945°C), is obtained after 1140 seconds, giving a maximum error of 1.4%. Considering the small temperature difference, these analyses showed that modelling only half a ventilation channel provides a reasonably accurate model. The run time for the half ventilation channel model was 25% shorter than that of the whole ventilation channel model.

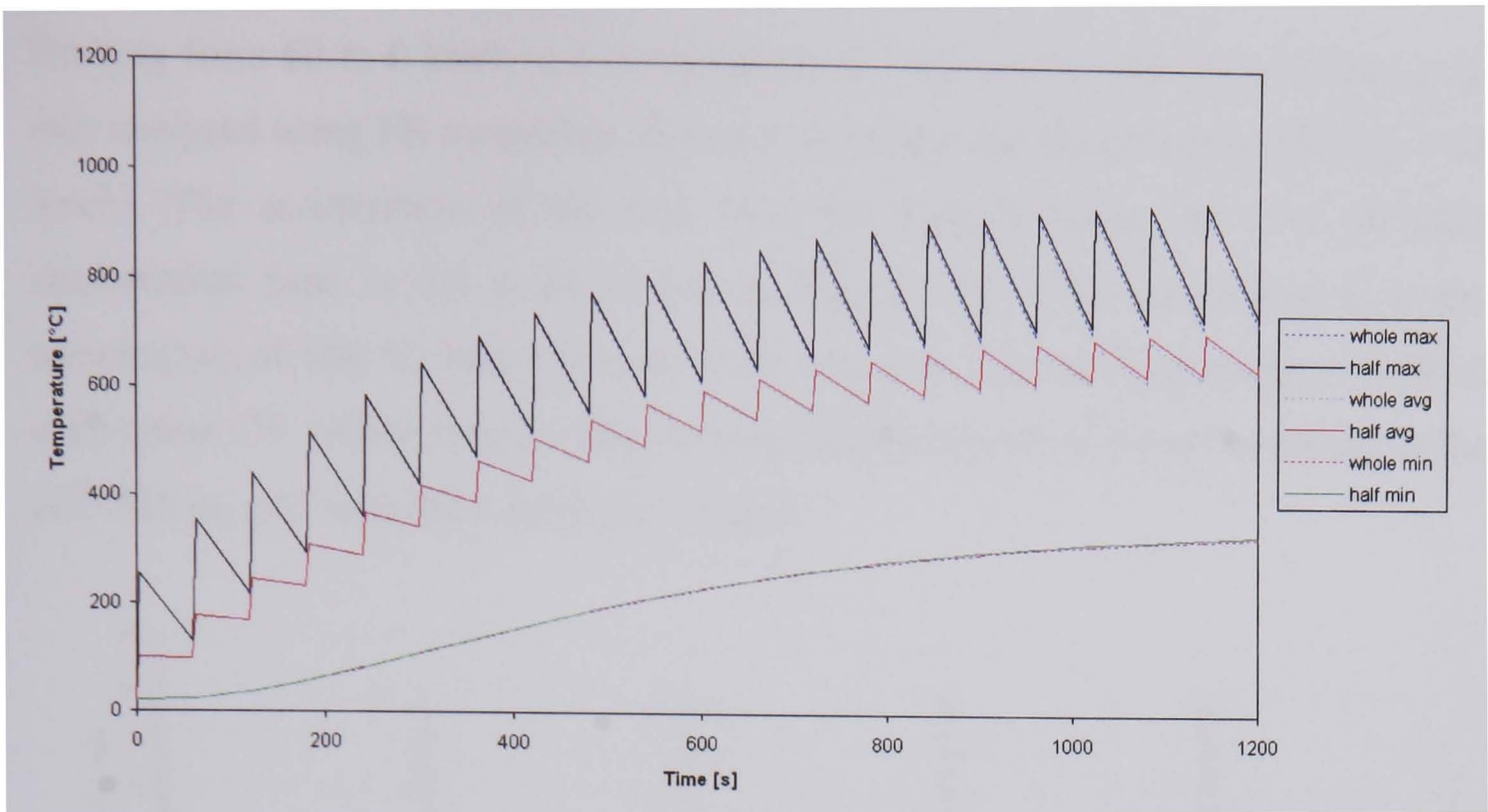


Figure 7.35 Whole and half ventilation channel CV disc FE model temperature comparison

7.3.2 Secondary Radiation

Total heat dissipation from the disc by radiation is defined by local temperatures, the emissivity of the surfaces and the amount of heat radiated (reflected) back to the disc from the surrounding components. The heat radiated back to the disc from surrounding components and the influence on disc temperatures need to be investigated. A solid CV disc has been modelled, see Figure 7.36, during a repeated brake application. The temperature predictions were compared for the disc only (with radiation dissipating to atmosphere) and the model including the wheel assembly, which will reflect back some of the radiation dissipated from the disc.

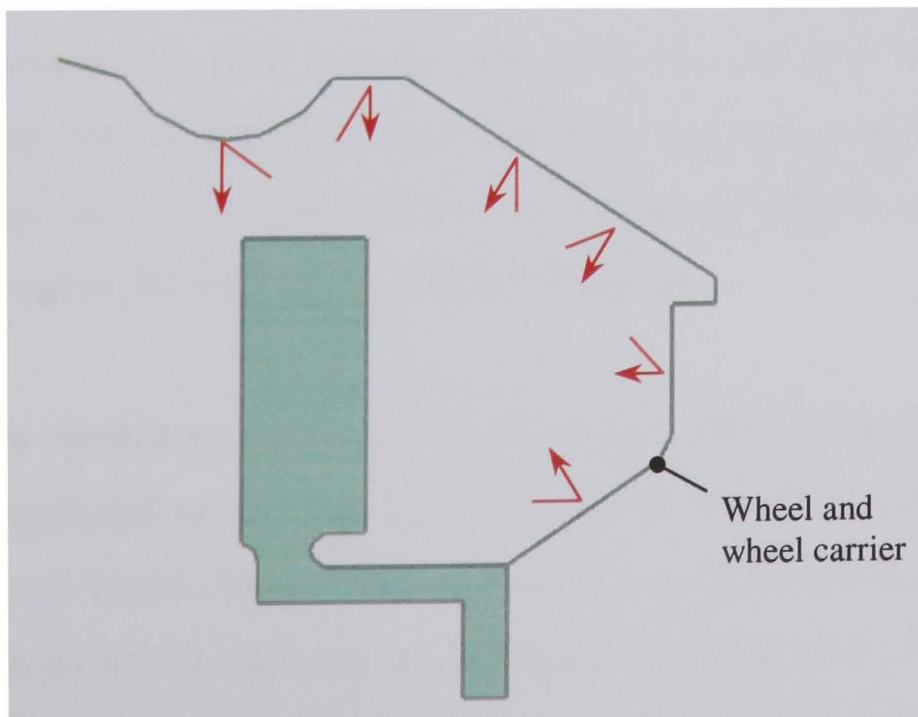


Figure 7.36 Reflection of radiative heat dissipated from the CV disc

Braking from 60 to 0 km/h at a deceleration of 5 m/s^2 with a 60 second time cycle, was analysed using FE modelling. Between the stops, the disc is run at 277 min^{-1} (60 km/h). The acceleration of the disc from the stop is linear; the 0 to 60 km/h deceleration time is 8.2 s, as shown in Figure 7.37. The test begins at a disc temperature of $100 \text{ }^\circ\text{C}$ from the start of the first stop. The braking energy is equal to a 19 tonne CV with a front to rear braking distribution of 50:50 and a rolling radius of 0.526 m, a 45 mm thick solid disc is used.

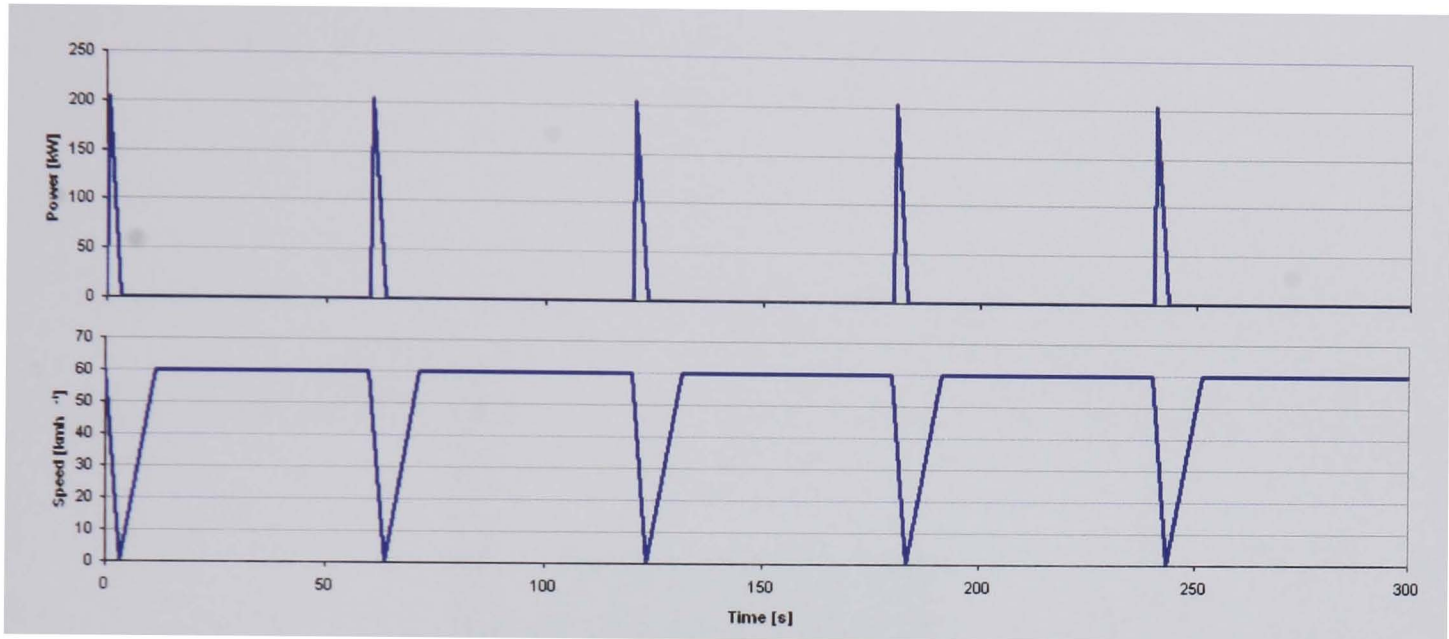


Figure 7.37 Vehicle speed and braking power to one front disc for the first five stops

Figure 7.38 shows the FE mesh of the CV solid disc brake assembly. The solid brake disc and wheel assembly are axisymmetric to a high degree (neglecting holes in the wheel) and therefore axisymmetric elements have been used in the model. Only the inner surface of the wheel carrier and wheel are meshed to reflect radiation, zero thickness axisymmetric shell elements are used, and therefore do not conduct any heat. Grey cast iron temperature dependent disc material properties were used, as listed in Table A2. The mesh consists of 128 axisymmetric shell elements, 652 axisymmetric solid elements and a total of 759 nodes.

The boundary conditions were applied to surface shell elements. Convection was modelled by applying an average h_{conv} value of $16 \text{ W/m}^2\text{K}$ to all surfaces except at the disc/hub and wheel carrier interface surfaces. Conduction to the hub and wheel carrier was modelled by applying an average h_{cond} value of $92 \text{ W/m}^2\text{K}$ to interface surface. Radiation was modelled on all free surfaces except the disc/hub and wheel carrier interface surfaces. Temperature dependent emissivity values from 0.4 to 0.7

were used for the disc friction surfaces and an emissivity of 0.9 was used for the remaining disc and inner wheel assembly surfaces (the high emissivity value representing heavily oxidised steel covered by brake dust). The temperature of the inner wheel carrier and wheel surface was kept constant, as emissivity will change very little during the brake application. A maximum heat flux of 2.1 MW/m^2 was applied to the rubbing surface representing the braking duty.

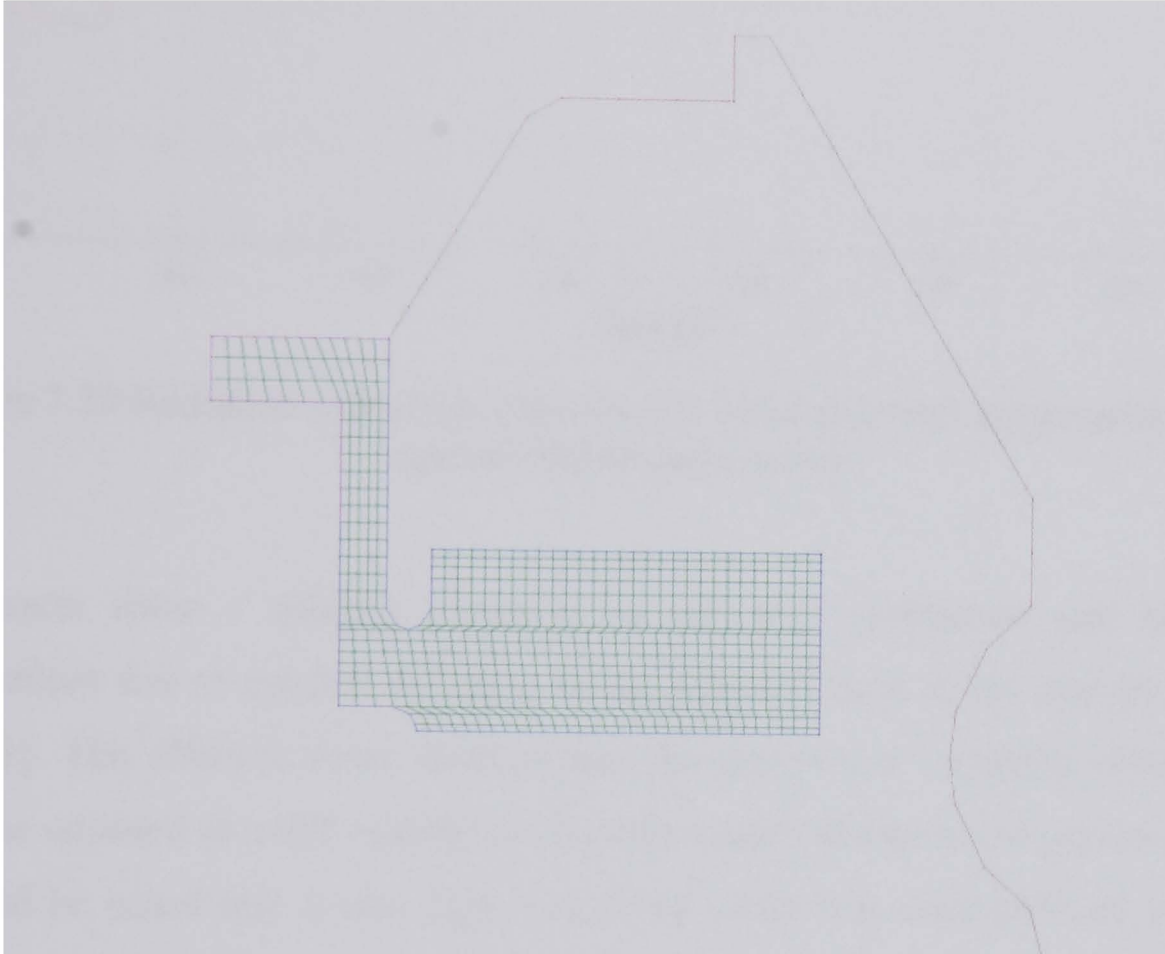


Figure 7.38 Axisymmetric FE mesh of the CV solid disc brake assembly

The route simulation was run for eleven repeated brake applications with (as shown in Figure 7.38) and without the wheel carrier and wheel modelled. Figure 7.39 shows the predicted disc bulk temperatures of the simulation. It can be seen that initially there is no effect from radiation reflection, however after the 4th stop the radiation reflection model shows a higher disc temperature. The temperature increase becomes greater as the disc temperatures rise and the effects are pronounced above bulk temperatures of 350°C . After the 11th brake application the bulk temperature of the radiation reflection model is 20°C higher than the disc only model.

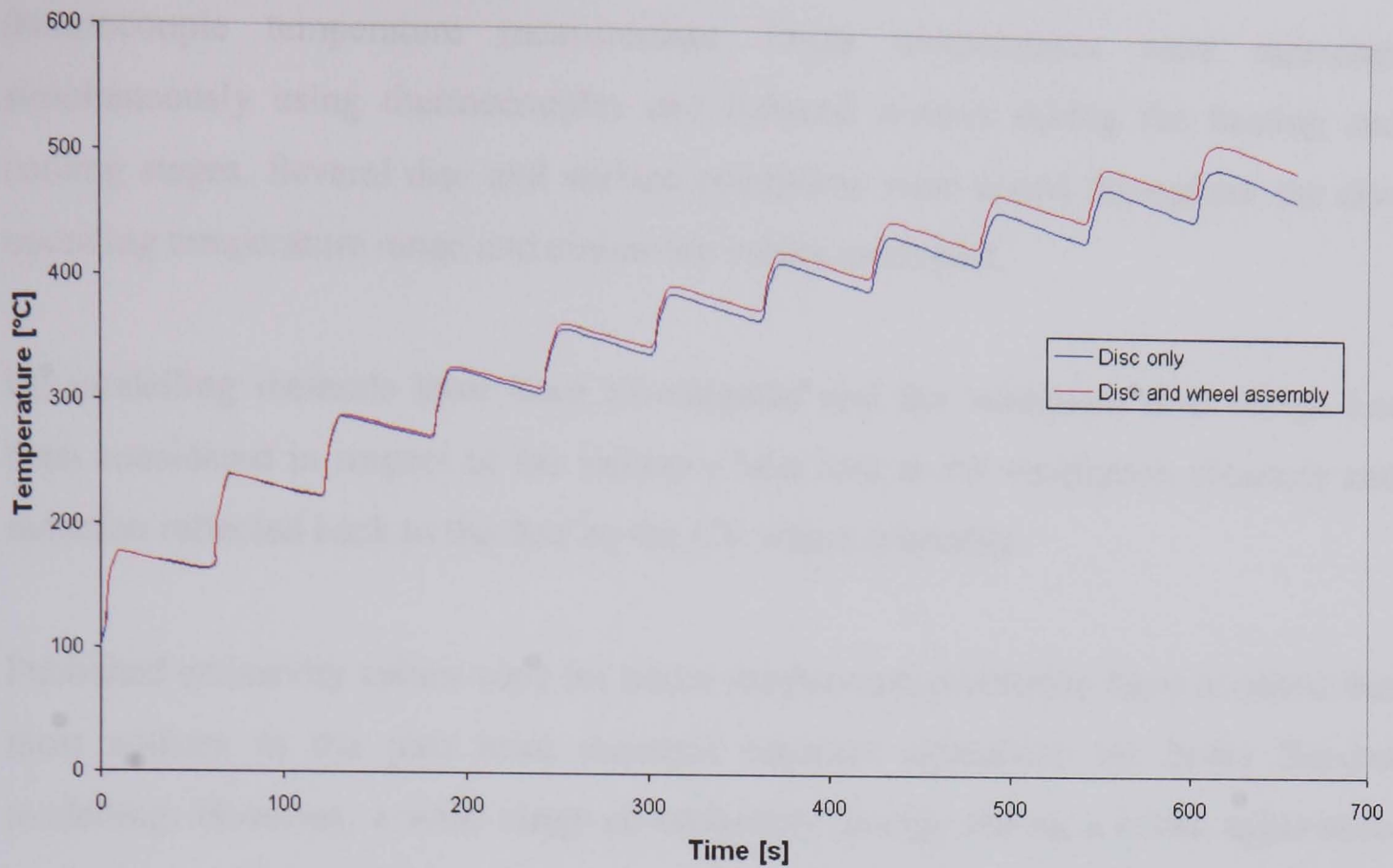


Figure 7.39 Radiation reflection effect on CV solid disc bulk temperatures during repeated brake applications

The results show a distinct reduction of the heat dissipation and higher disc temperatures due to emitted radiation being reflected back to the disc by the wheel assembly. The effect is more distinct than the use of a 6° segment ventilated disc model as opposed to a full ventilation channel model (shown in the previous section). It should be noted that a very high emissivity value was used (0.9), in some cases very low emissivity values are possible. A new aluminium wheel assembly emissivity can be in the region of 0.1 (Table 7.10) causing much more radiation reflection to take place, further increasing disc temperatures.

7.4 Summary

The theoretical background of radiation has been discussed, in particular the parameters that define emissivity and reflection. Radiative heat transfer coefficients have been used to study the relationships of radiative heat dissipation with temperature and surface conditions.

Radiative heat dissipation was studied experimentally on the Spin Rig by measuring brake temperatures using two types of infrared sensors and compared with

thermocouple temperature measurement. Discs temperatures were measured simultaneously using thermocouples and infrared sensors during the heating and cooling stages. Several disc and surface conditions were tested throughout the disc operating temperature range and emissivity values evaluated.

FE modelling methods have been investigated and the ventilated disc design has been considered in respect of the radiative heat loss at the ventilation channels and radiation reflected back to the disc by the CV wheel assembly.

Published emissivity values used for brake temperature prediction have revealed that most authors in the past have assumed constant emissivity for brake thermal modelling. However, a wide range of emissivity change during a brake application has been recently published, and the values of emissivity for the disc friction surface during a drag braking application are proposed. It has been shown that this is very important for brake heat dissipation analysis and cannot be neglected.

The advantages of infrared temperatures sensors were evaluated with the calibration requirements and necessity of correct emissivity setting. Thermocouples have been found to be more suitable for Spin Rig brake temperature measurements, however more expensive and sophisticated infrared sensor equipment may be more straightforward to use.

From the extensive FE modelling investigations, brake disc model complexity has been reduced along with analysis time. Reflection within the wheel assembly was found to noticeably reduce radiative heat dissipation from the disc. Disc bulk temperatures are shown to be higher when radiation reflection is modelled.

Radiation cannot be neglected due to its substantial influence at high temperatures and low rotational speeds. The change of emissivity during braking is an important conclusion. Using the developed modelling methods and proposed transient emissivity values will achieve efficient and more accurate brake temperature prediction.

Cooling Performance Simulation and Validation

8.1 Introduction

The heat dissipation from friction brakes has been studied in previous chapters by independently considering each mode of heat transfer; convection, conduction and radiation. Ventilated brake disc airflow has also been considered separately. The objective of this chapter is to bring all this research together, combining the modes of heat transfer to define their cumulative contribution to brake cooling. Real service duties of commercial vehicles (CV) and TGV trains are modelled. The model predictions are compared with experimental dynamometer test results, enabling the boundary conditions defined in previous chapters to be verified. The validated modelling methods will be used for cooling optimisation modelling in Chapter 9.

8.2 Modelling Methods

Simulation results have already been presented in previous chapters, however it is considered more suitable for the details of modelling methods to be given here. Appropriate finite element model representation will reduce effort required for model development, computing power, time and cost. The disadvantages of model

simplification include, the difficulty 'to picture' the model and sometimes the loss of peak values that may occur in simplified areas (Mottram and Shaw 1996). Therefore, one must be careful to ensure that the modelling techniques do not affect the required accuracy.

8.2.1 Software Packages

Two computer packages were available for use, SDRC I-DEAS-8 TGM and ABAQUS-5.9; both solve non-linear and transient heat transfer processes including conduction, radiation and free and forced convection. To choose the most suitable package for the project, an identical thermal model of a CV brake disc segment (described in Chapter 7) was solved using each package. The solution was transient, included distributed heat flux input and heat dissipation by convection, conduction and radiation. It should be noted that SDRC I-DEAS was used for pre- and post-processing of both the analyses because of its far superior solid modelling and results analysis facilities. This required the element mesh to be imported from SDRC I-DEAS to ABAQUS for solving by ABAQUS and after the solve it was necessary to export the results back to SDRC I-DEAS.

The computer time to solve the model using ABAQUS was twice that of SDRC I-DEAS. However, the run time cannot be directly compared as ABAQUS could only be run on a networked computer workstation, as opposed to SDRC I-DEAS, which was available on a more powerful stand-alone computer workstation (SGI-320). Very similar temperatures were predicted by both methods with temperature differences of less than 3°C. Therefore SDRC I-DEAS was chosen as the primary modelling package for this thesis taking advantage of using a single package, the speed, availability and reliability of a standalone installation.

8.2.2 Model Solution

Options for the method used by SDRC I-DEAS TGM to solve the transient thermal model must be selected by the user. There are four available solutions methods; Backward, Forward, Forward - Backward and Exponential Forward.

The Backward solution method has been used during the analysis, it is an implicit differencing scheme, where the element heat balance equations are evaluated at the end of the integration time step. Because the method is implicit, all element temperatures must be solved iteratively at every time step; this makes it less efficient than the Forward method for a given time step. However, the Backward technique is unconditionally stable (will not diverge) for any value of integration time step. This method is recommended for most applications (SDRC 2000); it is the most reliable and easy to use option. It is more accurate than the Forward-Backward method under conditions of rapid temperature change, such as those experienced during single or repeated brake applications.

Transient thermal models are solved by integrating over discrete time intervals. The Time Step is the time "mesh" for the transient solution. Smaller values (a finer mesh) will always give more accurate results at the price of increased computation time. Model solve time is inversely proportional to the size of the Time Step. Large or rapid temperature changes require a finer time step (SDRC 2000).

As a guide to the most suitable time step to be used with the implicit method, the well-known stability criterion, the mesh Fourier number (F_o) has been employed, expressed by equation (8.1) (Patankar 1980):

$$F_o = \frac{\alpha \Delta t}{(\Delta x)^2} \leq \frac{1}{2} \quad (8.1)$$

Where Δt is the time step value, Δx is the minimum element size and α is the thermal diffusivity of the material. From this initial value, the time step was increased when temperature changes were small or slow, i.e. during the cooling phase and low braking power input (heat flux).

8.2.3 Model Optimisation

In general, an accurate solution will only be obtained when the mesh is sufficiently fine. But there is no need to define a fine mesh where temperature (T) varies slowly with distance (x). A fine mesh is required where the $T \sim x$ variation is steep, therefore

the mesh spacing should directly relate to the T change with x . The mesh may be coarse in areas where detailed results are not necessary and the thermal behaviour is found to be non-influential to the rest of the model. The design of a suitable mesh for the FE models of this thesis has been guided by qualitative expectations and modification of preliminary coarse mesh solutions. The use of a non-uniform mesh enabled the computing power to be deployed effectively.

The choice of element types can be optimised; the higher the number of nodes present on an element, the more computer effort required. For pure thermal analysis a linear element is recommended (SDRC 2000), as a parabolic element will increase computational time without improving results.

The choice of an adequate geometry description is the most effective method of simplification. The physical problem being modelled may allow a reduction in the number of dimensions. If the problem has symmetry of material properties and boundary conditions, geometric symmetry may be exploited (Mottram and Shaw 1996):

If it is assumed that heat is generated uniformly over the entire disc friction surface and not just in the area of the friction pad, a uniform heat flux can be applied over the friction surface of the disc. Morgan and Dennis (1972) suggest previous work has shown that although large circumferential variations in temperature do exist in a disc brake, the mean surface temperature and bulk temperature are not affected by neglecting these circumferential variations.

The circumferential symmetry of the brake disc has been utilized throughout the FE thermal analysis of this thesis. For the solid disc a 2-D axisymmetric model has been used (Chapter 7). This significantly reduces run time and storage requirements allowing a more refined mesh to be used if required. The ventilated CV brake disc incorporates cooling vanes and channels that only allow for circumferential symmetry for each adjoined vane and cooling channel (see Figure 7.12 in Chapter 7), permitting modelling of an angular segment of 6° . For the ventilated TGV railway disc, an angular segment of 22.5° was analysed to account for the ventilation pillars and mounting lugs of the disc design, see Figure 8.11.

Problems may occur if the 3-D segment CV ventilated disc model is to be further simplified in order to increase speed and reduce model size. A 2-D axisymmetric model, shown in Figure 8.1, required the vane to be removed and thermo-coupling of the inboard and outboard cheeks, convective cooling in this area must also be increased to account for the reduced vane surface area dissipating heat (the vanes being removed). With the vanes removed the disc mass is substantially reduced, which in turn reduces the thermal capacity of the disc, causing further errors and must be adjusted accordingly.

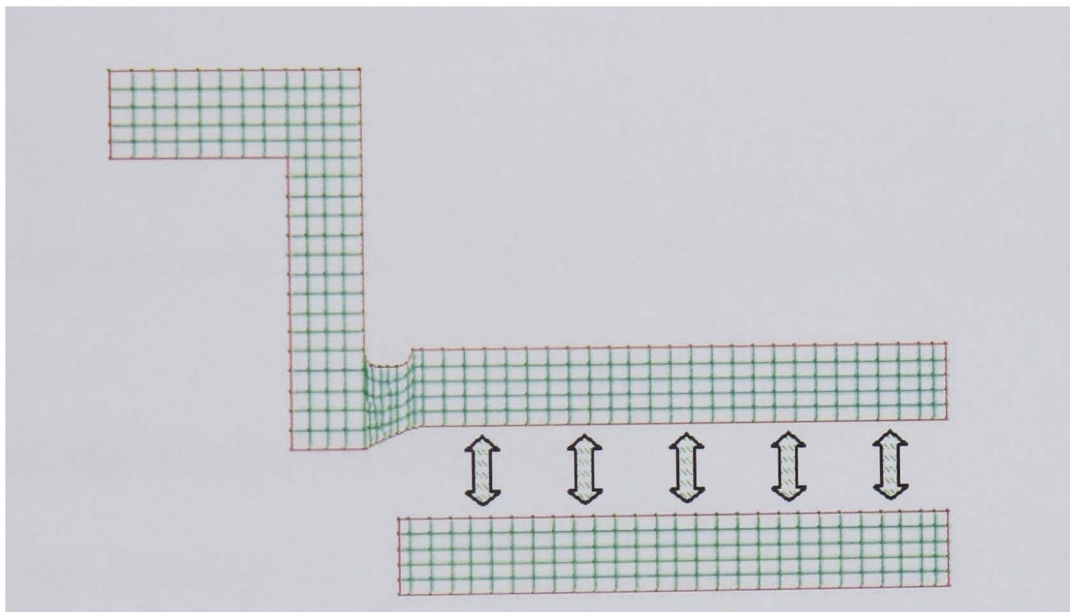


Figure 8.1 Thermal coupling of CV disc cheeks for 2-D axisymmetric representation

Figure 8.2 shows a comparison of the 2-D axisymmetric and 3-D segment models for 34 repeated braking applications. Identical results could not be achieved, due to inaccurate modelling of the vane and the reduced thermal capacity of the disc (shown by high temperatures during heat build up between 0 to 1000 seconds) but give the same steady-state condition. From the findings of this investigation it was decided to limit the 2-D axisymmetric modelling method to solid disc analysis only, with 3-D modelling for all ventilated discs.

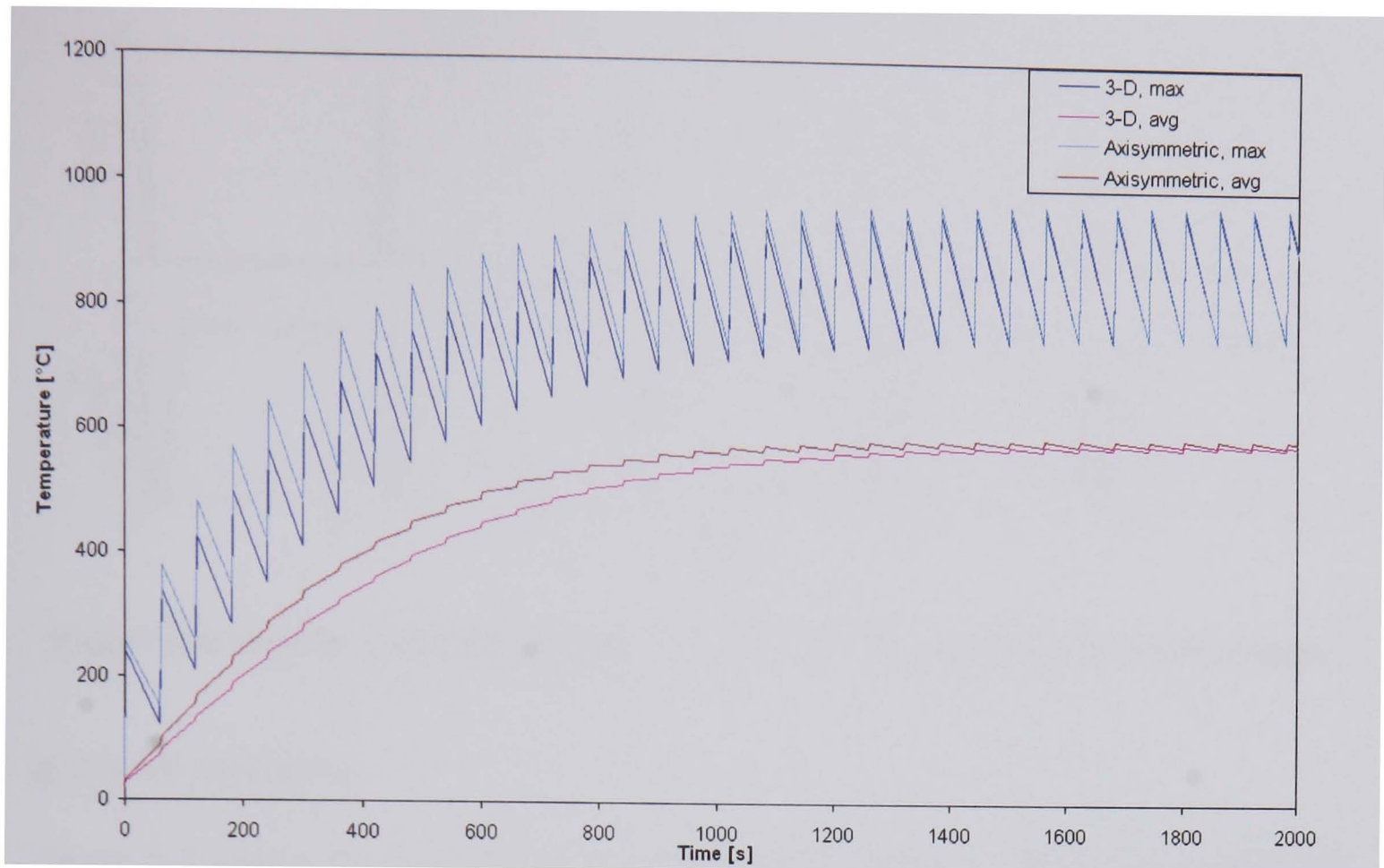


Figure 8.2 Axisymmetric and 3-D model temperature prediction comparison

8.3 Commercial Vehicle Route Simulation

To enable the prediction of brake disc temperatures for real vehicle service conditions, route simulations have been performed. A CV route simulation has been designed for the anti-coning brake disc (see Chapter 3). The disc model, which included all thermal boundary conditions taken from previous results, is compared with dynamometer test results.

8.3.1 Duty

The fade test comprises of repeated brake applications from 60 to 0 km/h at a deceleration of 5 m/s^2 (braking time is 3.33 seconds) with a 60 second time cycle. Figure 8.3 shows the vehicle speed and braking power to one front disc for the first five stops. There is no forced air cooling (cross flow) and between the stops the disc is run at 277 min^{-1} (60 km/h). The acceleration of the disc from the stop is linear; the 0 to 60 km/h acceleration time is 8.2 s. The initial disc temperature is $100 \text{ }^\circ\text{C}$, at the start of the first brake application. The braking energy represents a 19000 kg CV with a front to rear brake force distribution of 50:50, and a rolling radius of 0.526 m.

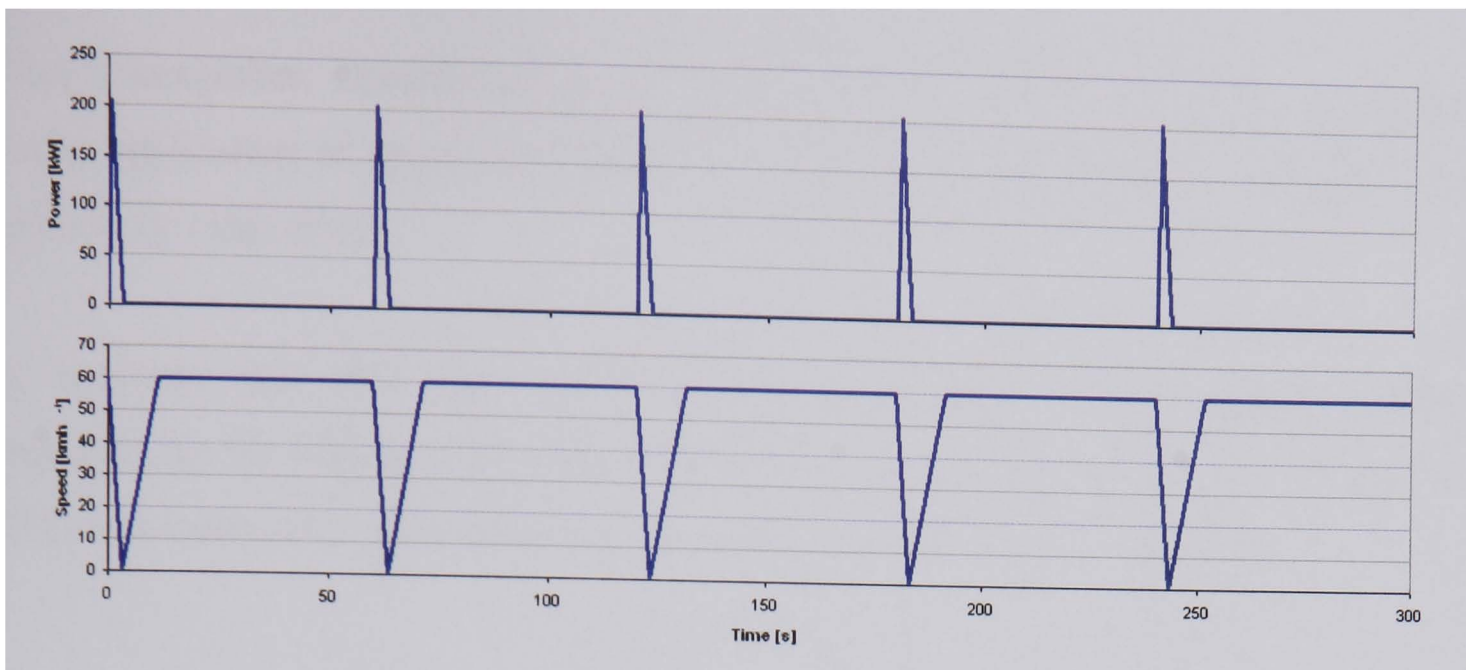


Figure 8.3 Vehicle speed and braking power to one front disc for the first five stops

8.3.2 FE Modelling

Figure 8.4 shows the mesh for a 6° section of the CV disc. The mesh consists of 3310 solid elements, 1278 thin shell elements (for the inclusion of boundary conditions), and a total of 4554 nodes. Grey cast iron temperature dependent material properties were used in the model, as listed in Table A2.

Convection was modelled by applying average h_{conv} values on all surfaces except the disc/hub interface surface. Speed dependent h_{conv} values were used, calculated using equation (5.14). A value of $17.8 \text{ W/m}^2\text{K}$ was used at the maximum speed (60 km/h) and $2.8 \text{ W/m}^2\text{K}$ at the minimum speed (0 km/h). At this stage pad and calliper components were not included. The friction surface area of the disc covered by the pad reduces the surface area available for convective and radiative cooling. This was outside the scope of the research and requires detailed analyses at a later date.

Conduction to the hub was modelled by applying an average h_{cond} value of $92 \text{ W/m}^2\text{K}$ to disc/hub interface surface. The h_{cond} value was calculated using equation (6.6) and Spin Rig thermal contact resistance test data (see Chapter 6). The measured heat flux (14518 W/m^2) at the interface (at 170°C and 300 Nm) was used with the ambient air temperature (20°C).

Radiation was modelled on all free surfaces except the vane and disc/hub interface surfaces. An emissivity change from 0.4 – 0.7 was used for the friction surfaces. These values are based on measured values and ‘enhanced’ by using measurements

from Eisengraber, Grochowicz et al. (1999). The change of emissivity during the brake application is shown in Figure 7.11. The remaining surfaces were given an emissivity value of 0.9.

A bi-linear heat flux (see Appendix C) was applied to the rubbing surface representing the braking duty, with a 0.5 second peak braking power time. Equation (C2) was used and a maximum heat flux value of 2.106 MW/m^2 calculated.

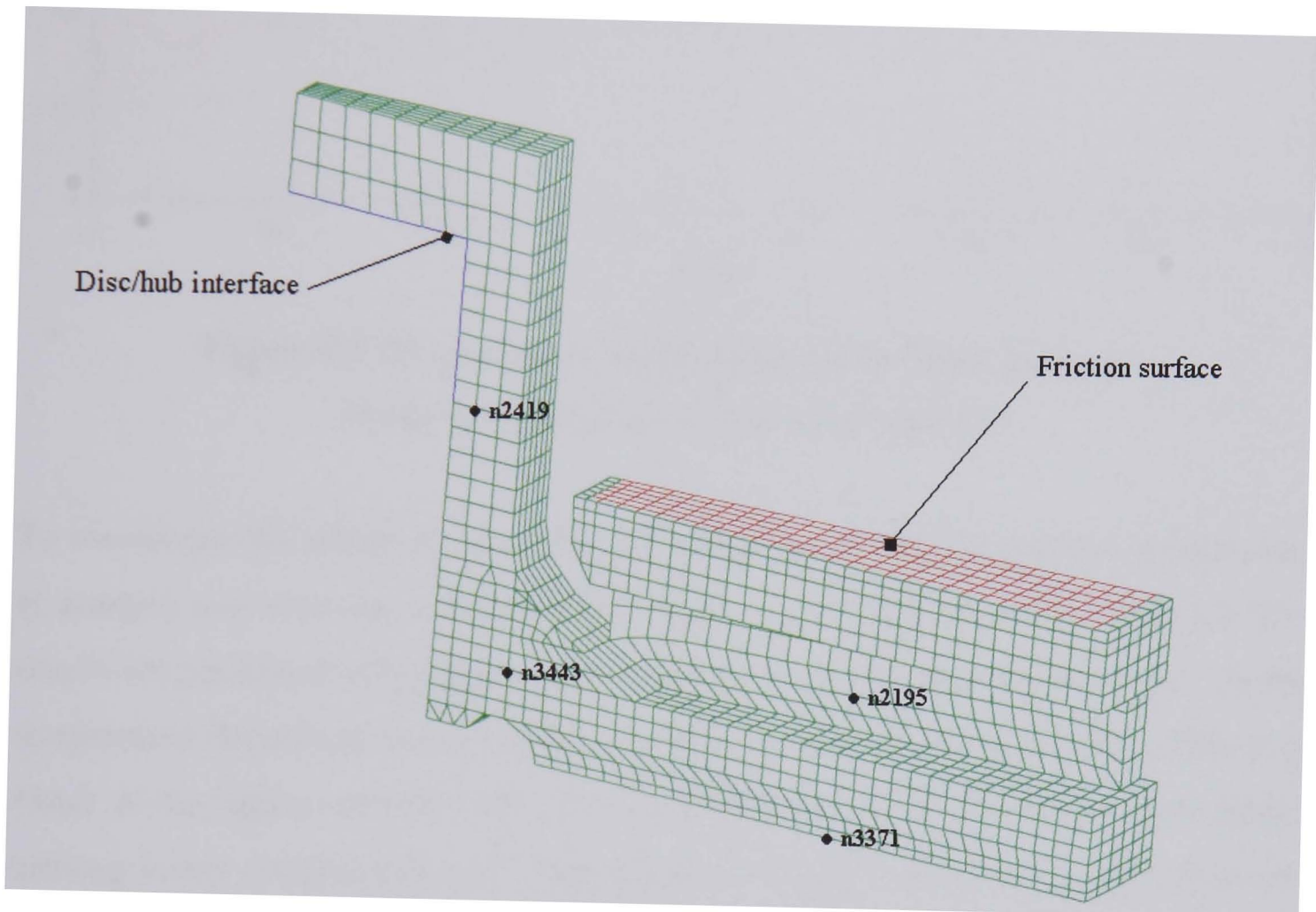


Figure 8.4 FE mesh of anti-coning CV brake disc

The route simulation was run for eleven repeated brake applications. Figure 8.5 shows the predicted disc temperatures for the repeated brake simulation, four nodal temperatures are shown; their positions within the model are given in Figure 8.4. The fade test applies a very high energy over a very short period, resulting in high peak temperatures being predicted. Bulk disc temperatures are in the region of the value shown for node 2195. It can be seen that the disc temperatures begin to plateau with maximum peak brake temperatures reaching 600°C .

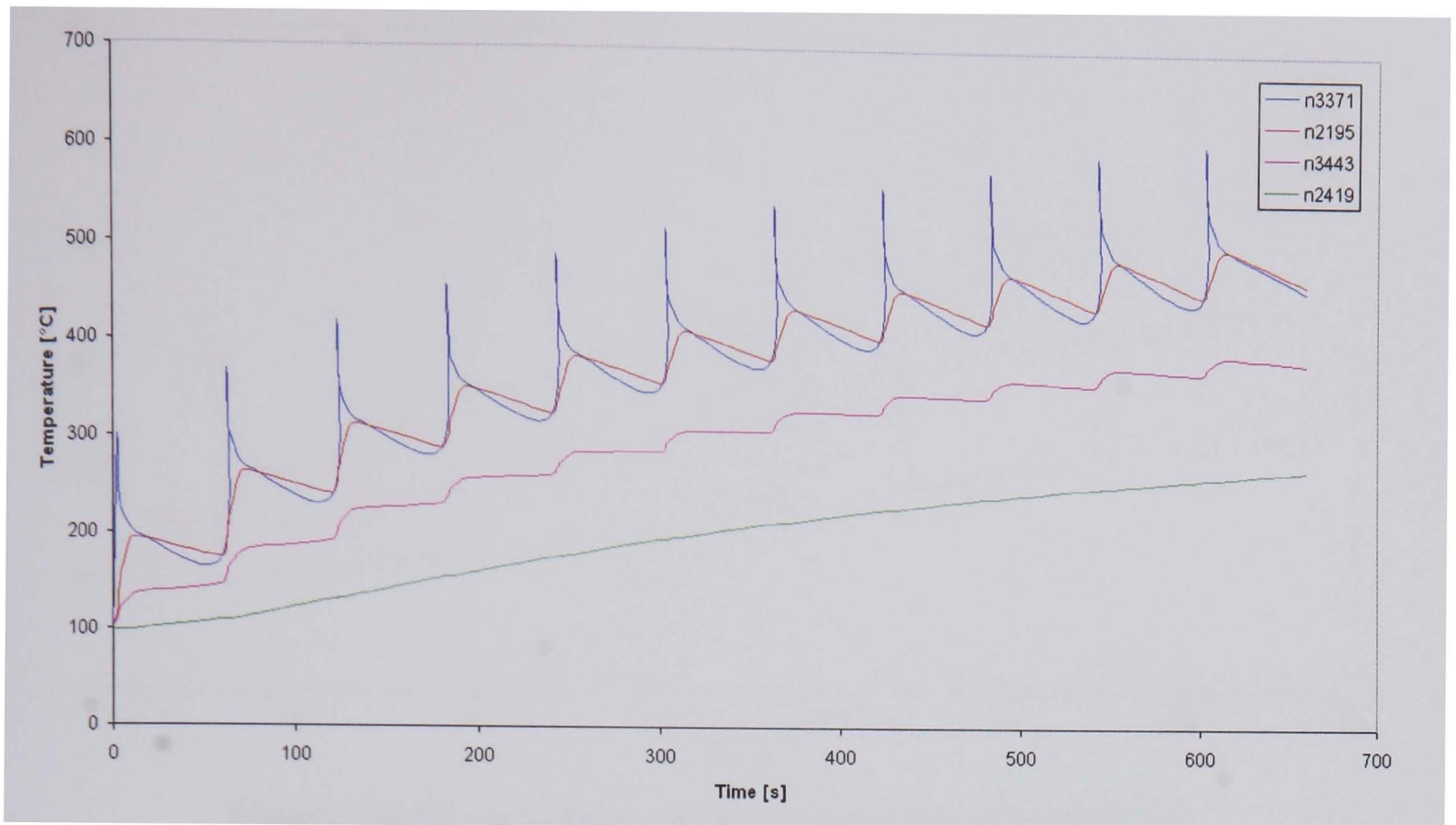


Figure 8.5 FE simulation temperatures for the brake fade test
(temperature dependent material properties)

To investigate the effect of fixed disc properties on the FE temperature predictions, an analysis was run with modified fixed material properties, shown in Table A3. The results are presented in Figure 8.6. The temperature predictions are lower than for the temperature dependent model. After eleven stops the difference is 35°C. This is a result of the higher specific heat value used throughout the disc temperature range, causing lower temperature rise. Temperature dependent values of specific heat are 40% lower at 100° when compared to the value at 600°C. The temperature dependent value of conductivity reduces with temperature, causing higher surface temperatures and combined with increasing emissivity should provide greater heat dissipation for the temperature dependent material properties model, but the effect is not so predominant as that of the specific heat values.

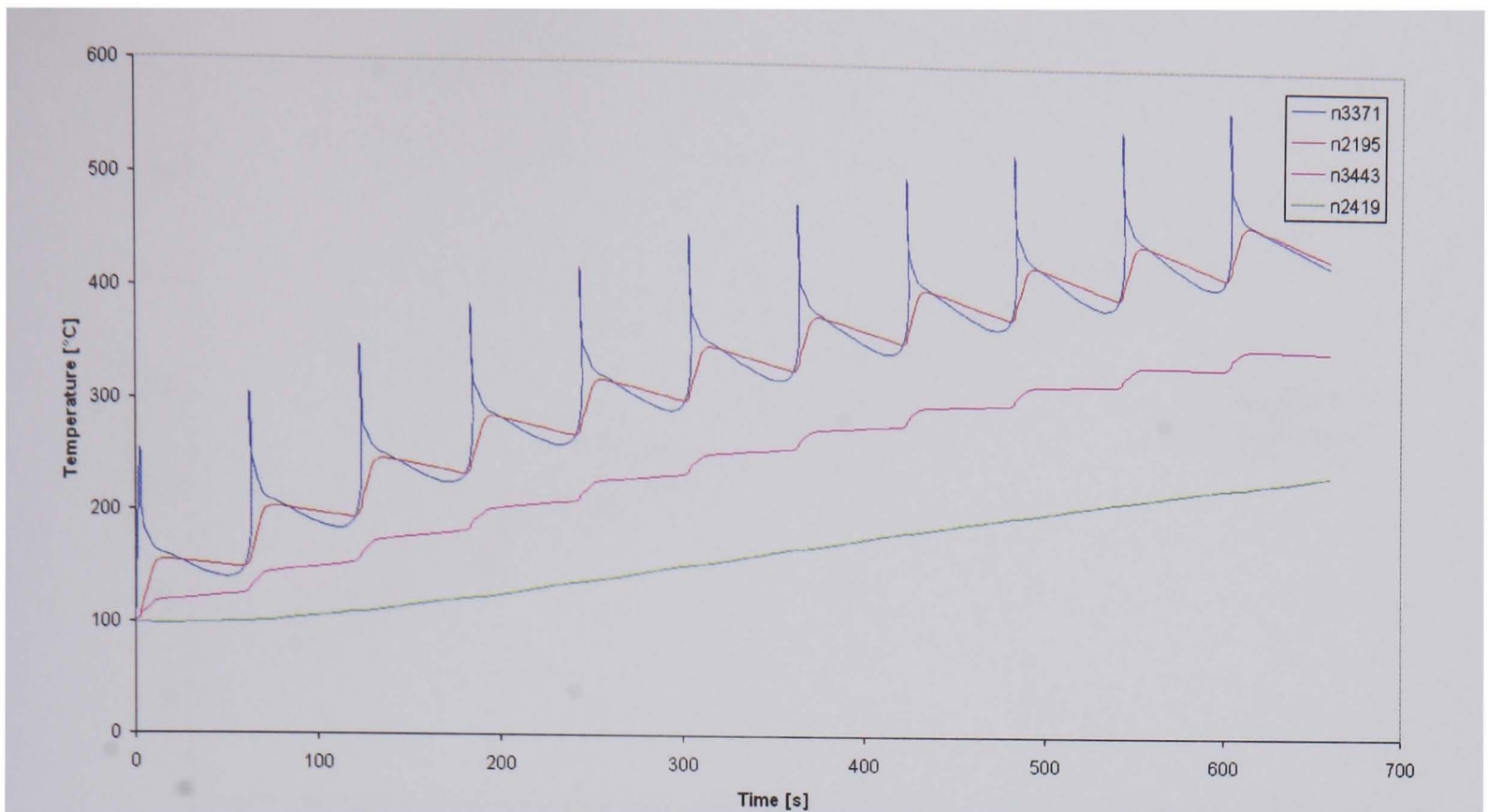


Figure 8.6 FE simulation temperatures for the brake fade test
(fixed material properties)

8.3.3 Analytical Temperature Prediction

Using equation (C17), (C18) and (C19) from Appendix C the analytical temperature predictions of bulk disc temperatures are shown in Figure 8.7 for the repeated brake application. Fixed material properties were used given in Table A3 and the cooling parameters are taken from Spin Rig cooling measurements of Chapter 5. Equation (C17) predicts the brake temperature after a series of identical stops. Equation (C18) and (C19) predict temperatures before and after the stop. The bulk temperatures of the analytical functions closely resemble the FE analysis results. Equation (C16) predicts temperatures approximately 70°C lower than equation (C19).

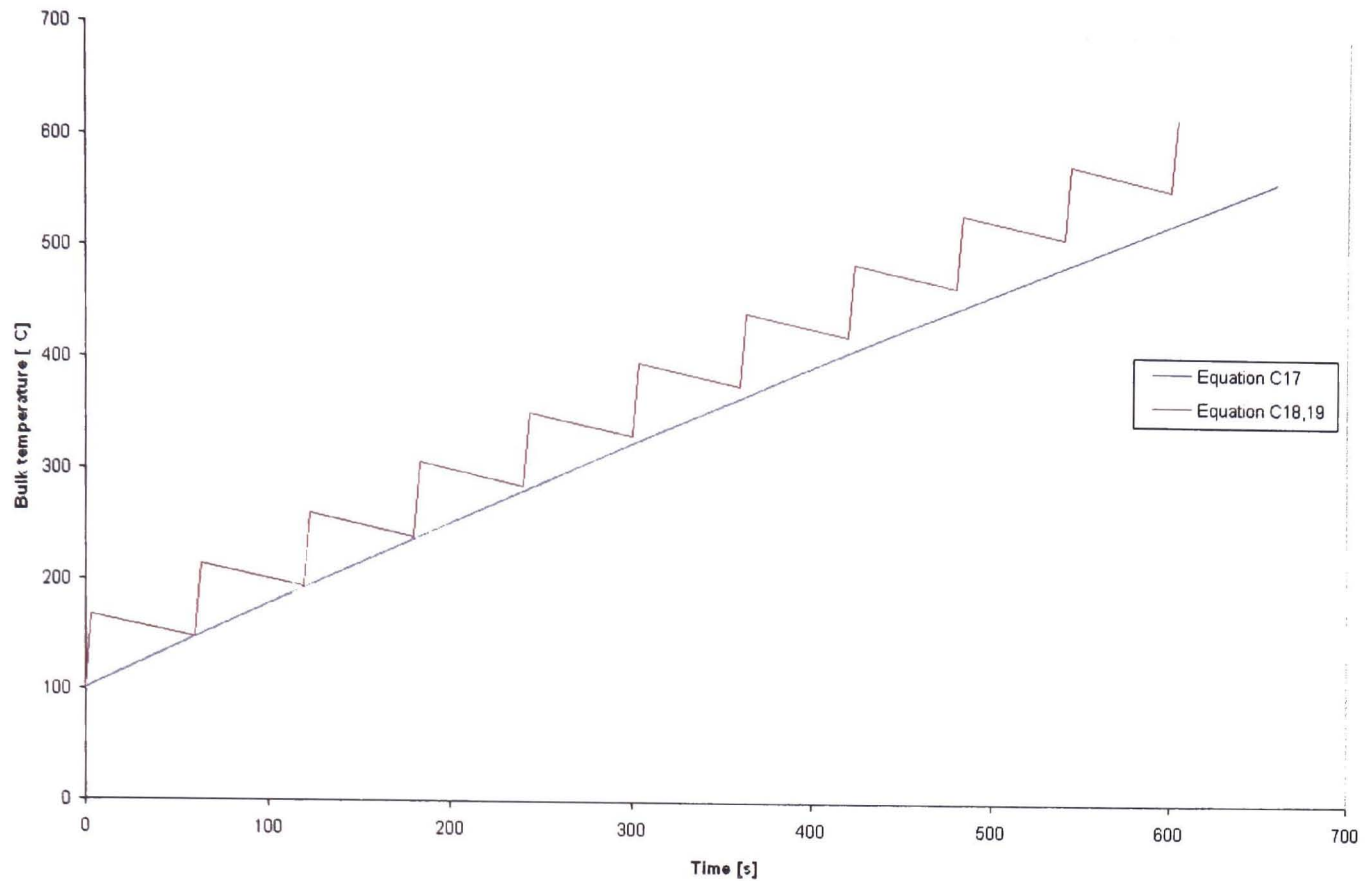


Figure 8.7 Analytical bulk temperature prediction of route simulation fade test

- Equation (C17) (Newcomb and Spur 1967)
- Equation (C18, C19) (Limpert 1999)

8.3.4 Dynamometer Test

Dynamometer tests were conducted at ArvinMeritor UK (see Chapter 3). The test is identical to modelled fade test. There was no cross flow in the dynamometer test, but an extraction fan is employed to remove brake dust particles, which is necessary for health and safety reasons. Figure 8.8 shows the friction surface temperatures measured during dynamometer testing.

Temperatures were measured using bronze, bead type thermocouples (see Chapter 3), one placed at the mean radius of the each friction surface. From Figure 8.8 it can be seen that temperature rise during the brake application is lower than expected for such a high deceleration. The position, adjustment and high thermal contact resistance of the rubbing thermocouples is most probably the cause of lower than expected measured temperatures. Also the large difference in temperature between the inboard and outboard friction faces is unexpected and can only be explained by poor rubbing thermocouple contact or uneven friction pad application. It should be noted that the test was performed with extremely worn friction pads that had been

used for previous high power braking tests. The main considerations for temperature measurement and prediction are investigated in Section 8.5.

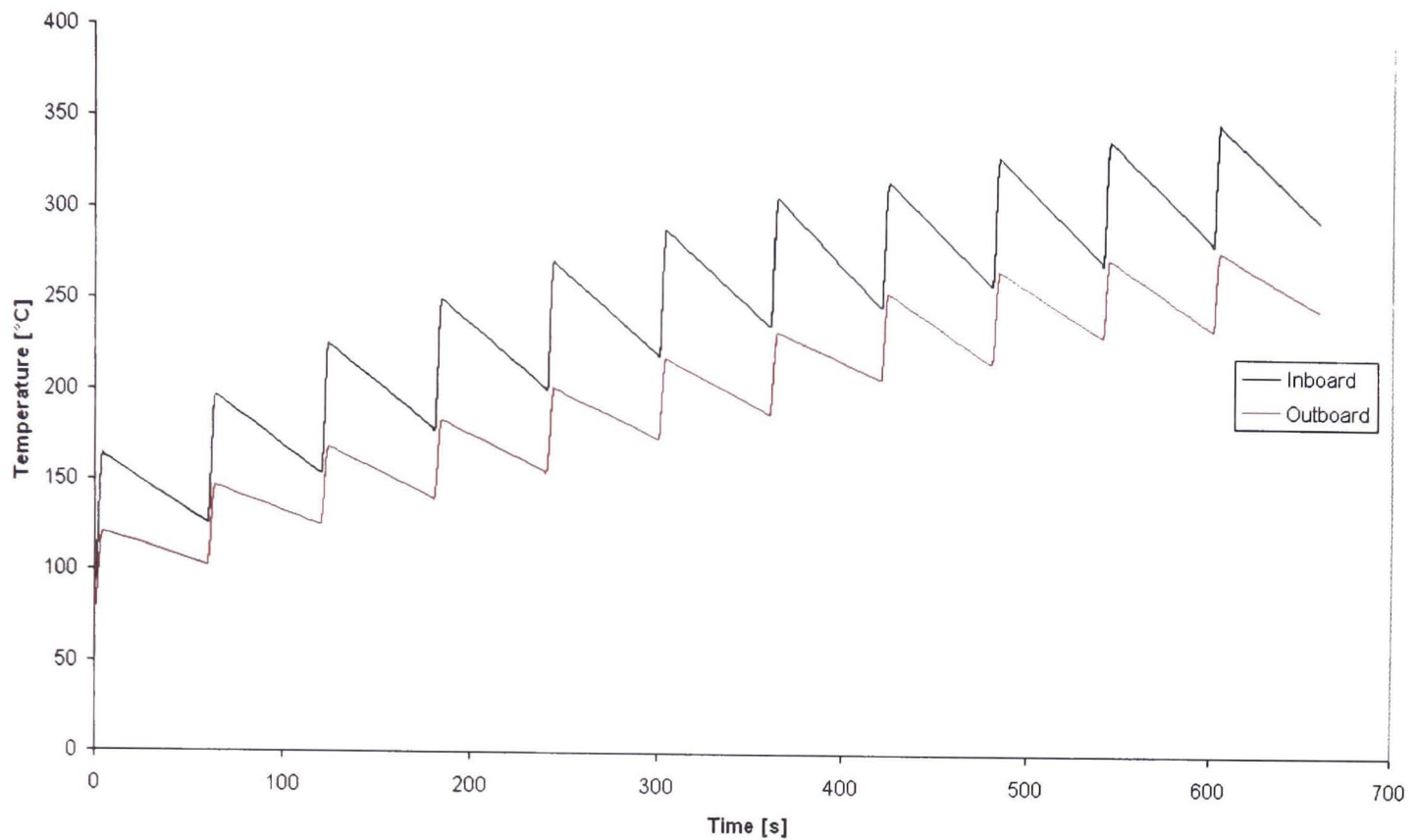


Figure 8.8 Repeated braking dynamometer test, friction surface temperatures at mean radius

8.3.5 Results Comparison

A comparison of FE (fixed and temperature dependent material properties), dynamometer and analytical results are presented in Figure 8.9. As mentioned before the dynamometer results show lower temperatures than the FE model, in order to predict temperatures in the same region as the dynamometer using FE methods a higher h_{conv} value was applied to the model. Higher emissivity and conductivity heat transfer coefficients could not be realistically increased, leaving convection as the variable mode of heat transfer. As mentioned previously, the dynamometer test was carried out with an extractor fan removing friction pad dust. The cross flow air velocity produced by the extractor is unknown but an increase in the convective cooling is expected. However, for the FE model to predict similar temperatures to those measured it was necessary to double the h_{conv} values. This is unrealistically high, equivalent to a cross flow of 4.5 m/s (according to the h_{conv} equation for the rotating disc in cross flow (Morgan and Dennis 1972). It is worth noting that Fukano and Matsui (1986) mentioned higher cross flow air velocities (7 m/s) for the passenger car brake during repeated high speed braking applications.

Comparing the predicted temperatures with the test results after the first stop they are approximately 50°C lower and they are in the region of 200°C lower at the end of eleven stops. The analytical equation (C17) shows very good agreement with FE results. These results highlight the problems of brake temperature measurement and prediction. This is discussed further in Section 8.5.

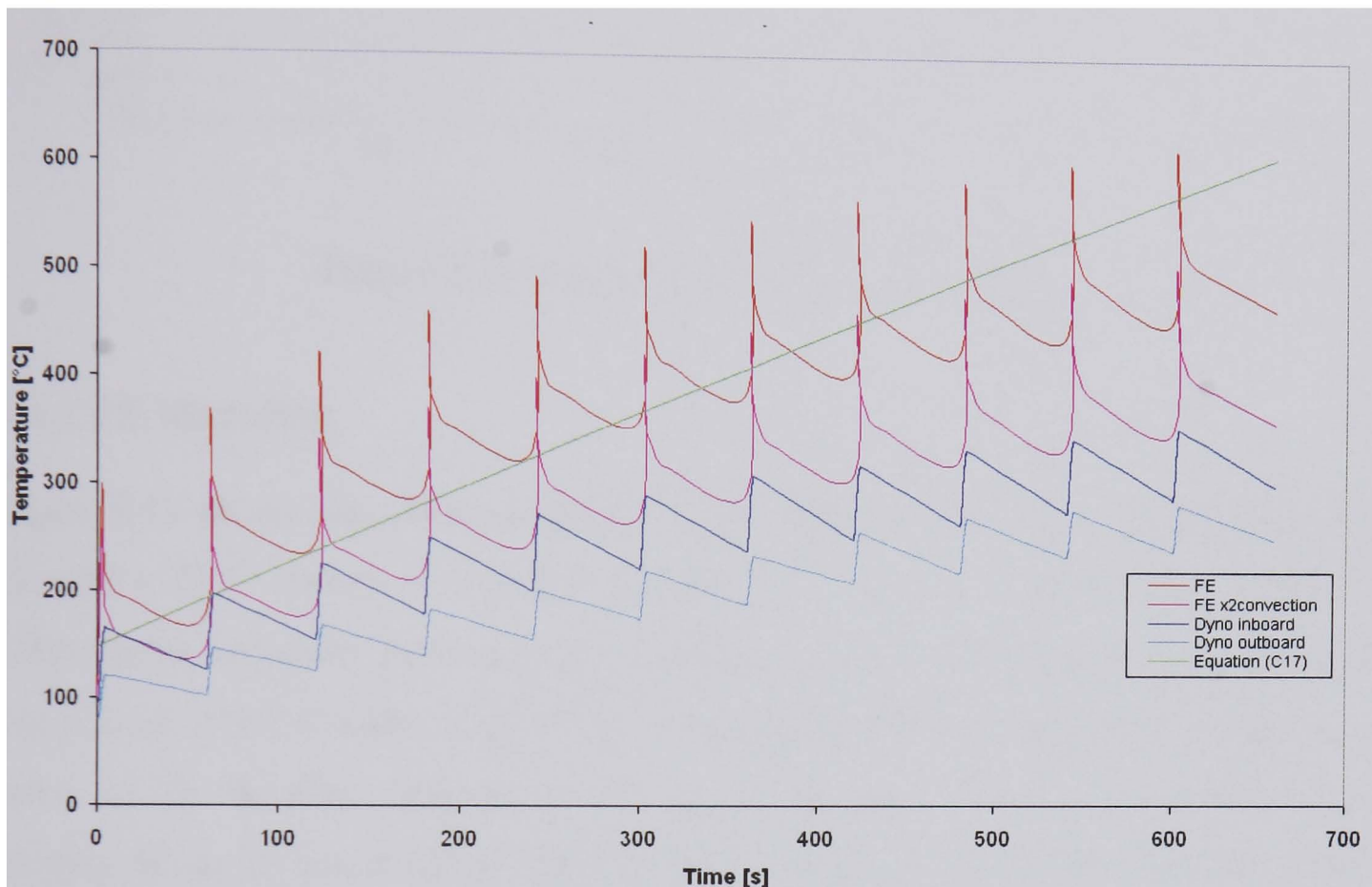


Figure 8.9 Comparison of measured and predicted CV disc surface temperatures

8.4 TGV Route Simulation

A route simulation has been studied for the ventilated TGV railway disc, this is a drag application to evaluate disc braking and thermal performance. Part of the test schedule is shown in Appendix E. Again, the disc model included thermal boundary conditions taken from previous results and predicted temperatures are compared with dynamometer test results.

8.4.1 Duty

The simulation comprises of a drag brake for 20 minutes at a vehicle speed of 60 km/h (358 min⁻¹) with a braking power equal to 21 kW, see Figure 8.10. After the drag application, the disc is allowed to cool for 20 minutes at a constant rotational

speed (358 min^{-1}), with no forced air cooling (cross flow). The drag braking power corresponds to a load of 4 tonnes per disc travelling at a constant speed (60 km/h) on a 3.2% gradient.

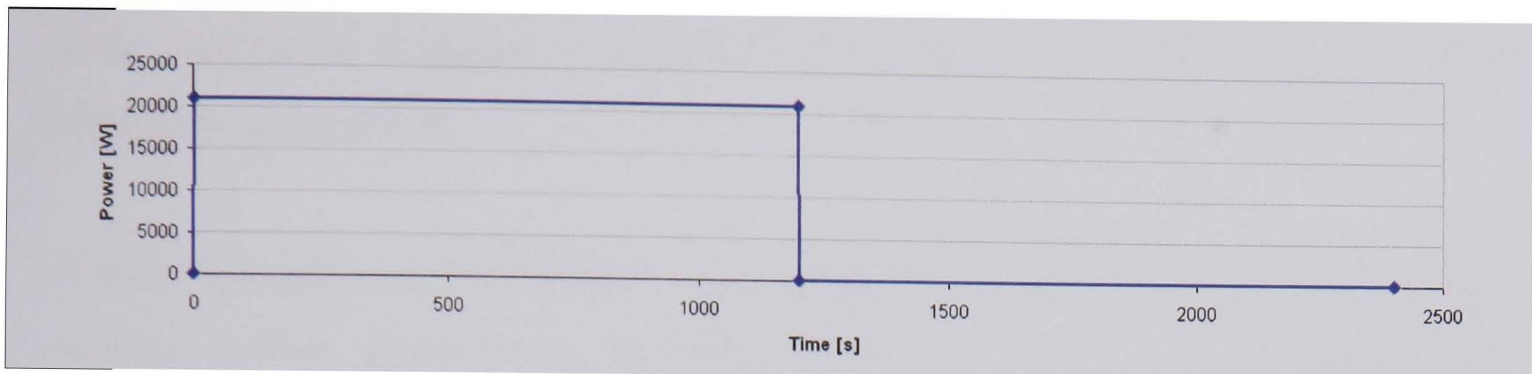


Figure 8.10 Drag braking power input to disc

8.4.2 FE Modelling

Figure 8.11 shows the element mesh for the TGV disc. Circumferential symmetry allowed a 22.5° section of the disc and hub to be modelled. The mesh consists of 13894 solid elements, 5997 thin shell elements (for applying boundary conditions) and a total of 9514 nodes. Convection was modelled by applying the average h_{conv} value of $32 \text{ W/m}^2\text{K}$, obtained from the convective cooling measurements (see Chapter 5), to all free surfaces. The friction surface area of the disc covered by the pad and calliper reduces the surface area available for convective and radiative cooling. This was outside the scope of this research and requires detailed analyses at a later date.

Conduction to the hub was modelled by applying an average h_{cond} value of $2500 \text{ W/m}^2\text{K}$ to disc/hub interface surface, using a layer of thin shell interface elements. The h_{cond} value was obtained from Spin Rig thermal contact resistance tests (see Chapter 6), using the h_{cond} value for a standard bolted interface with a 40 Nm bolt torque. Conduction from the hub to the shaft was modelled by applying an average h_{cond} value of $92 \text{ W/m}^2\text{K}$ to hub/shaft interface surface. The h_{cond} value was calculated using equation (6.4) and Spin Rig thermal contact resistance test data (see chapter 6). The pressure at the interface due to the interference fit was 50.6 MN/m^2 . The measured heat flux (14518 W/m^2) at the interface (at 170°C and 300 Nm) was used with the ambient air temperature of the model (20°C).

Radiation was modelled on all free surfaces except the vane and hub/shaft interface surfaces. An emissivity change from 0.4 – 0.7 was used for the friction surfaces. These values are based on measured values and ‘enhanced’ by using measurements from Eisengraber, Grochowicz et al. (1999). The change of emissivity during the brake application is shown in Figure 7.11. The remaining surfaces were given an emissivity value of 0.9.

A heat flux value of 52.1 kW/m^2 was applied during the drag application, to the rubbing surface representing the braking duty with a 3 second pressure rise (response). The Disc material, 15CDV 6 steel was modelled with temperature dependent material properties, as listed in Table A4.

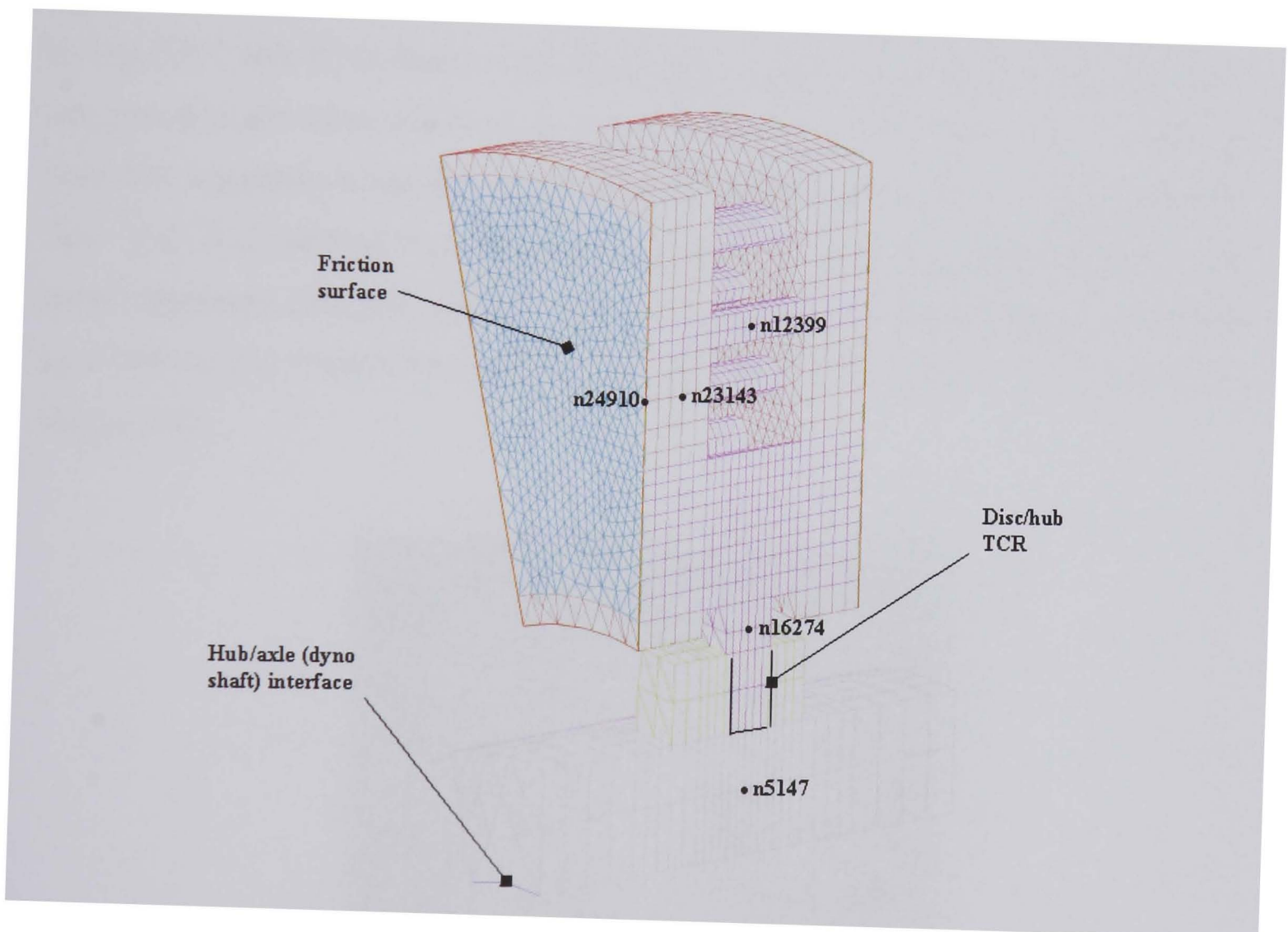


Figure 8.11 FE mesh of ventilated TGV railway disc

Figure 8.13 shows the predicted disc temperatures for the drag braking and cooling simulation together with the dynamometer temperatures, five nodal temperatures are shown; their positions within the model are given in Figure 8.11. For clarity, temperatures for only one side of the disc are given; the disc cheeks temperatures are very similar. Figure 8.13 indicates that the disc surface temperature rises to a

maximum of 330°C (at the end of the drag). After 20 minutes of cooling at a constant speed the disc surface temperature drops to 100°C. The hub temperature remains relatively low throughout the brake application reaching a maximum of 60°C, a result of the small disc lug/hub contact area.

8.4.3 Dynamometer Tests

Dynamometer tests were conducted with identical parameters to those modelled. The test was performed at SabWabco UK (see Chapter 3). Figure 8.12 shows a TGV disc under braking during a dynamometer test.

Figure 8.13 shows the friction surface temperatures measured during dynamometer testing (TC2 and TC5). Bronze, bead type thermocouples (see Chapter 3) were used, one placed at the mean radius of the each friction surface. From Figure 8.13 it can be seen that temperature rise during the brake application is not equal for each friction face. The TC2 rubbing thermocouple is probably measuring temperatures in a hot band (appearing after 150 seconds) and TC5 is probably measuring temperatures in a cool band of the friction area, an example of hot banding on a TGV disc is shown in Figure 8.12.

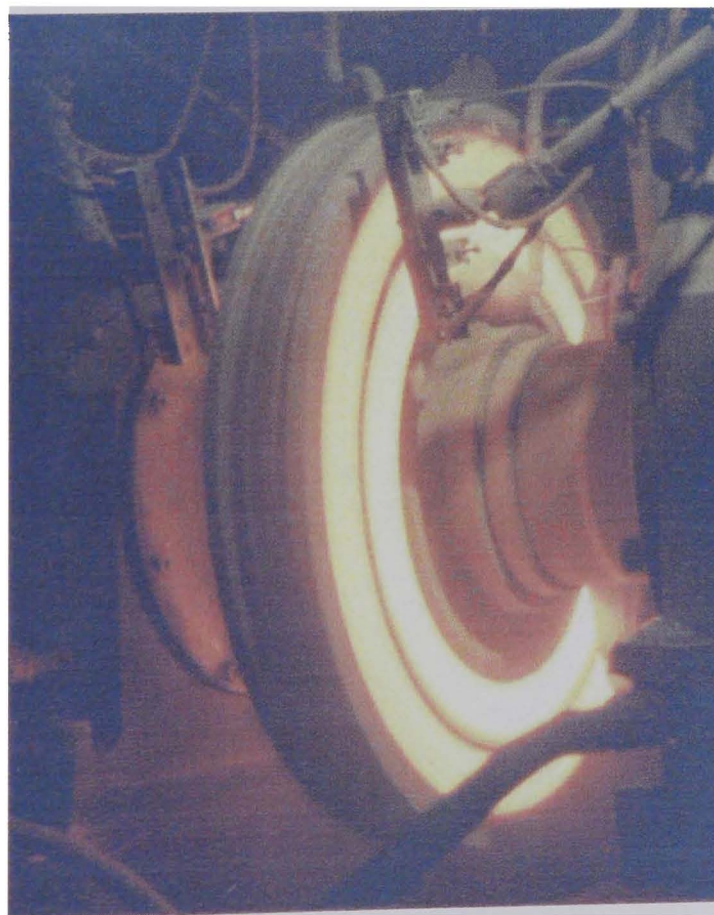


Figure 8.12 Hot banding of TGV disc friction surface, SabWabco Ltd.

8.4.4 Results Comparison

Comparing the predicted temperatures with the test results, the predicted surface temperatures are lying between the two measured temperatures and show a good correlation throughout the drag brake application and cooling period.

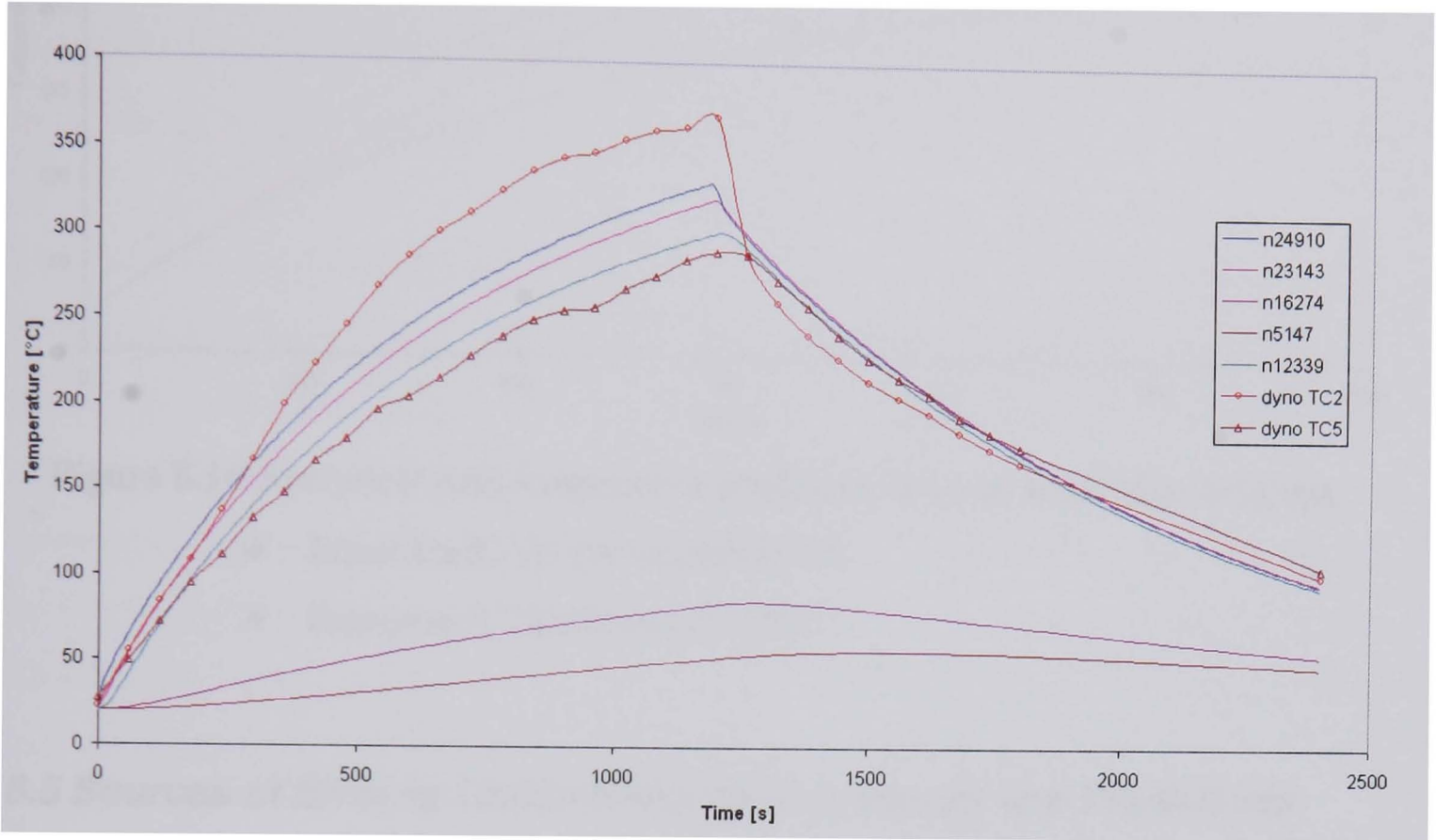


Figure 8.13 FE simulation and dynamometer temperatures during the drag and cool test

Using equation (C13) and (C15) from Appendix C, the analytical temperature predictions of bulk disc temperatures are shown in Figure 8.14 for the drag brake application. Fixed FE material properties at 200°C were used (Table A4) and the cooling parameters are taken from Spin Rig cooling measurements (see Chapter 5). It can be seen from the curves that equation (C15) predicts bulk temperatures close to the dynamometer and FE analysis results. Equation (C13) predicts temperatures approximately 100°C lower at the end of the drag.

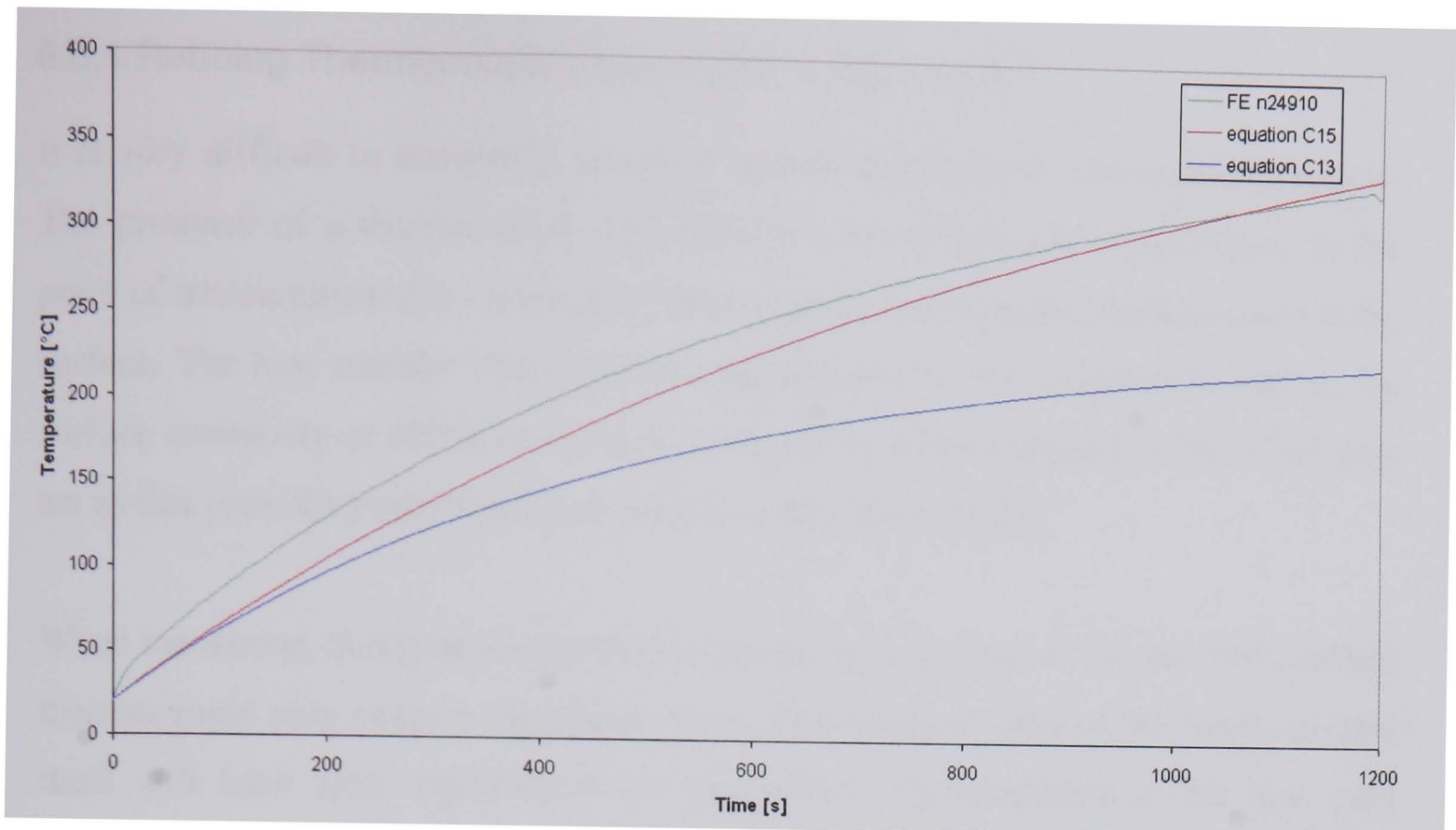


Figure 8.14 Analytical bulk temperature prediction of route simulation drag test

- Equation (C13) (Newcomb 1979)
- Equation (C15) (Limpert 1999)

8.5 Sources of Error in Temperature Measurements and Predictions

When evaluating route simulation FE predictions and experimental measurements (Sections 8.3.5 and 8.4.4) the limitations and difficulties of comparison can be appreciated. Several sources of error can be identified in temperature measurements and predictions. In temperature predictions, these include heat flux calculation; vehicle mass, deceleration, braking time and β values will not be identical to test values. Heat dissipation boundary conditions will also not be identical to those found under test conditions due to airflow caused by dust extraction. Furthermore, the effect of thermoelastic instability (TEI) on brake temperature measurement and the use of rubbing thermocouples make FE temperature prediction and measured temperature comparisons difficult. To investigate the main influencing factors of temperature measurement and prediction more inclusive, FE modelling has been conducted. This is to include rubbing thermocouple response and TEI influence on brake temperatures.

8.5.1 Rubbing Thermocouple Measurement Response

It is very difficult to accurately measure surface temperature with a thermocouple. The presence of a thermocouple will influence the temperature distribution at the point of measurement due a change of heat capacity and transfer characteristics at the surface. The heat transfer characteristics are changed by the installation, that is, the surface emissivity or effective thermal conductivity will be altered or the wires may act as fins providing additional heat transfer paths (Otter 1970).

When measuring changing surface temperatures, the response of the attached rubbing thermocouple may cause a significant error. The response time of the thermocouple itself will have little significance on the surface measurements if the heat path between the surface and the measuring junction is poor. The time required for the measuring junction to change temperature causes the thermocouple output to lag the surface temperature in time and decreases its amplitude. Thermal contact resistance between the junction and the surface will cause a temperature gradient that will prevent the measuring junction from attaining the surface temperature.

The measurement of moving surfaces by holding the thermocouple against the body results in errors caused by friction. This initially causes an increase in surface temperature by a few degrees. Figure 5.16 of Chapter 5 shows the copper bead thermocouple as used in the dynamometer tests, a decrease of 10°C during disc deceleration from 450 to 0 min^{-1} can be seen. Rubbing thermocouples are more suitable to determine cooling rates and heat transfer coefficients on the Spin Rig because low rates of temperature change are measured and not absolute values.

To investigate the rubbing thermocouple errors further and allow a closer correlation between rubbing thermocouple surface temperature measurements and simulation surface temperatures, FE modelling of the rubbing thermocouple and disc surface has been conducted. In particular, attention is paid to thermal contact resistance at the thermocouple and disc interface.

Figure 8.15 shows the axisymmetric FE mesh of a circular ‘cut-out’ section of the friction surface of the disc and copper rubbing thermocouple body. The tip of the

thermocouple is actually located 1 mm from the friction surface. The mesh consists of 96 axisymmetric solid elements, 24 axisymmetric shell elements (for the boundary conditions) and a total of 120 nodes. The mesh is simplified but sufficient for all the effects studied.

Boundary conditions are similar to the CV anti-coning disc model of Section 8.3.2. Convection was modelled at the disc surface by applying an average h_{conv} value of 17 W/m²K. Radiation was modelled on all free surfaces. An average emissivity value of 0.55 was used for the friction surfaces, based on own measurements and literature data (see Chapter 7), a value of 0.7 was used for the copper rubbing thermocouple body (Cengel 1998). A thermal contact resistance in the form a conductive heat transfer coefficient was applied to the axisymmetric interface elements at the disc and rubbing thermocouple interface. The temperature of the disc elements were set as a boundary condition, the rubbing thermocouple initial temperature was 20°C. Grey cast iron temperature dependent material properties were used for the disc, as listed in Table A2. The copper rubbing thermocouple body material properties are listed in Table 8.1.

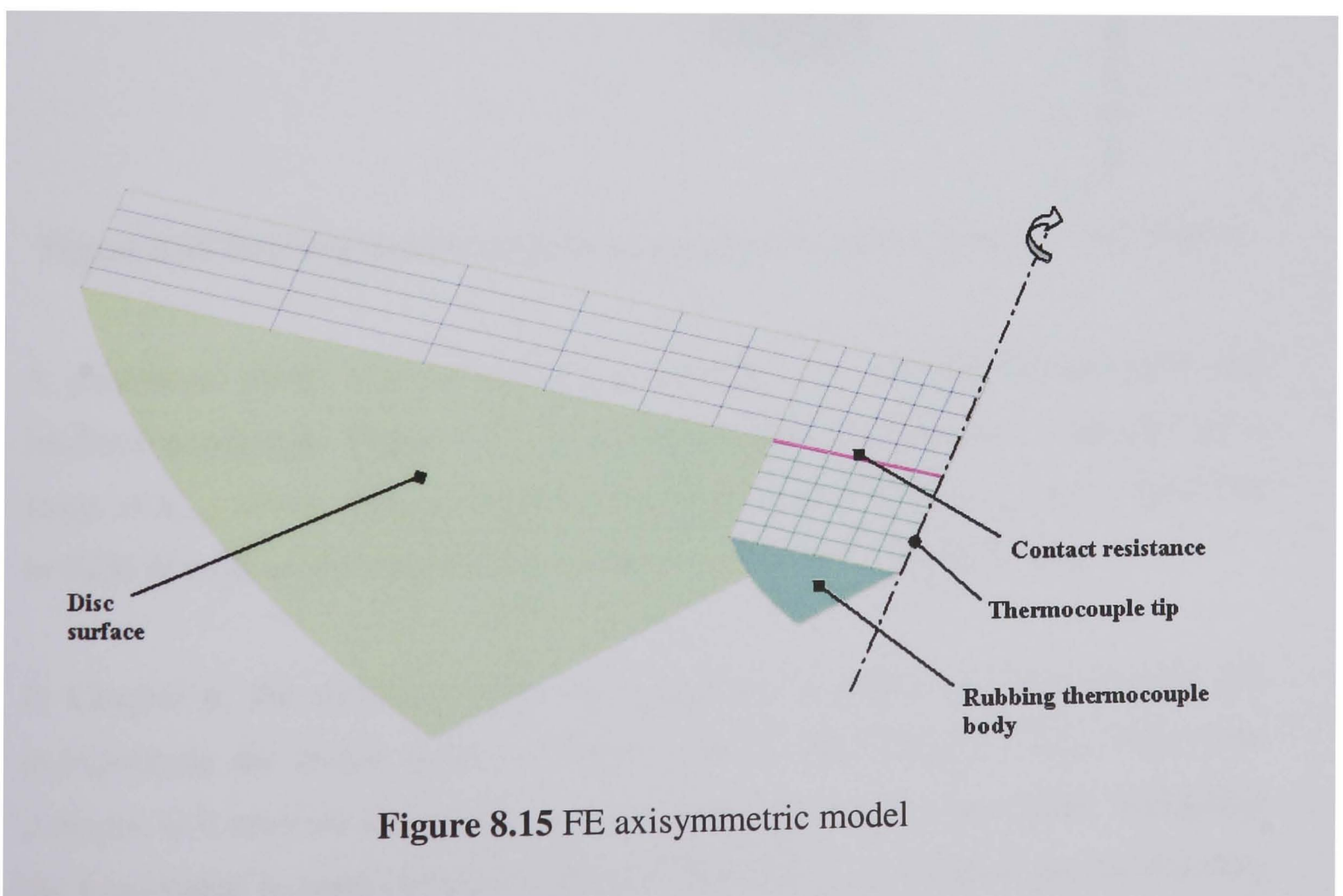


Table 8.1 Copper material properties for FE modelling (Cengel 1998)

| Property | Value |
|-----------------------------------|-------|
| Mass density [kg/m ³] | 8933 |
| Conductivity [W/mK] | 400 |
| Specific heat [J/kgK] | 385 |

Figure 8.16 shows the temperature contour plot for a 300°C disc temperature and an interface h_{cond} of 500 W/m²K, for the steady-state condition. It is shown that the thermocouple body temperature is uniform and a temperature gradient can only be seen at the interface.

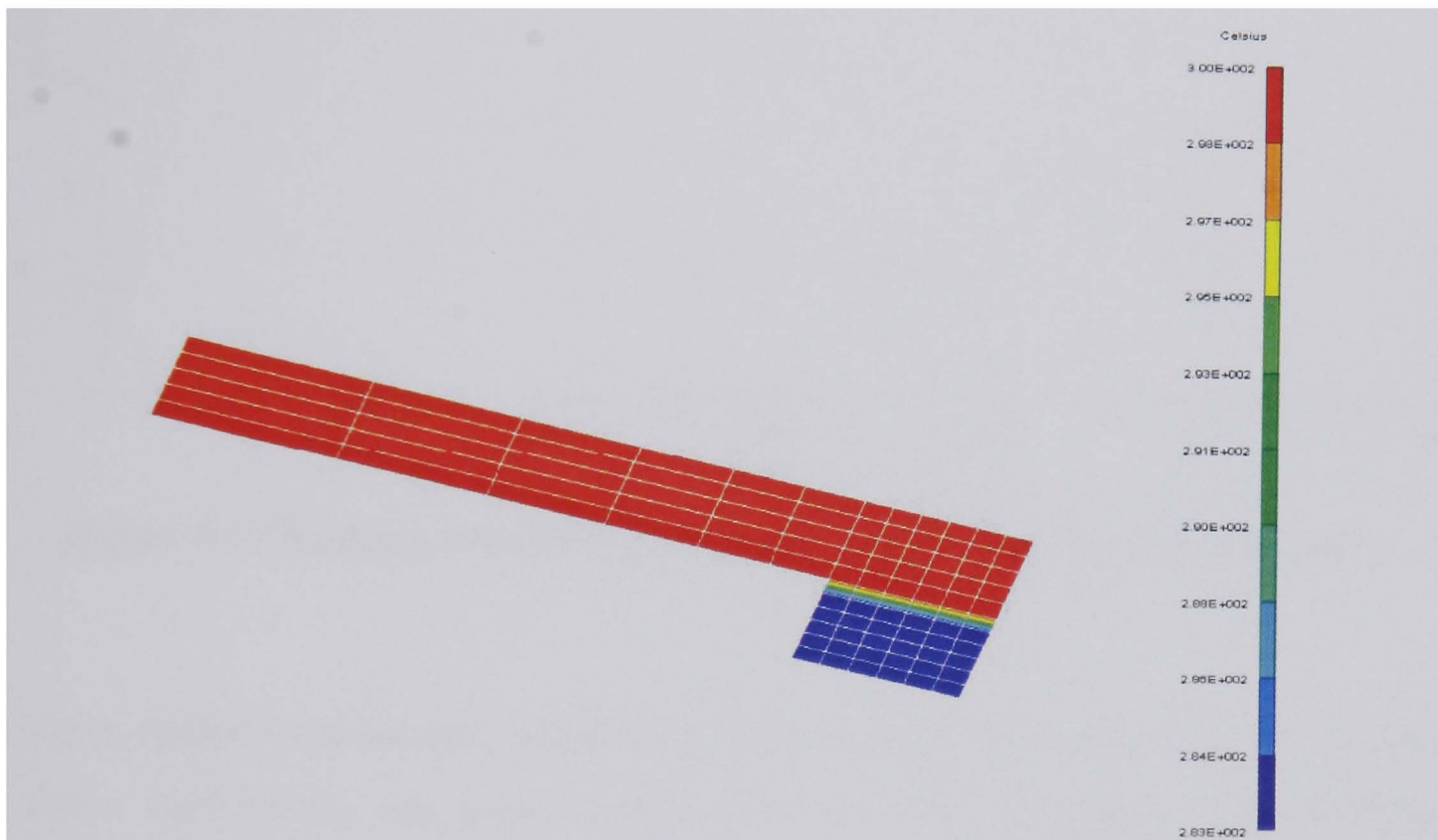


Figure 8.16 Rubbing thermocouple temperature distribution for $h_{cond} = 500$ W/m²K

A parametric study was conducted for various disc, rubbing thermocouple and interface conditions. Figure 8.17 shows the rubbing thermocouple response for a range of h_{cond} values. The curves show the effect of increasing h_{cond} values from 500 to 2000 W/m²K on the response time, which reduces with increased h_{cond} .

In Chapter 6, the thermal contact resistance was measured for bolted joints. By extrapolating the results given in Figure 6.22 for the change in h_{cond} value with pressure, at 0 pressure (the spring force of the thermocouple is practically negligible) the h_{cond} value is approximately 2000 W/m²K. The h_{cond} value at the disc/rubbing thermocouple interface is considered to be less than this due to friction pad deposits on the disc surface.

It should be noted here that an h_{cond} value of $3500 \pm 1000 \text{ W/m}^2\text{K}$ has been confirmed by Day (1990) in an experiment for the sliding contact of a specific friction material sliding on a cast iron mating surface.

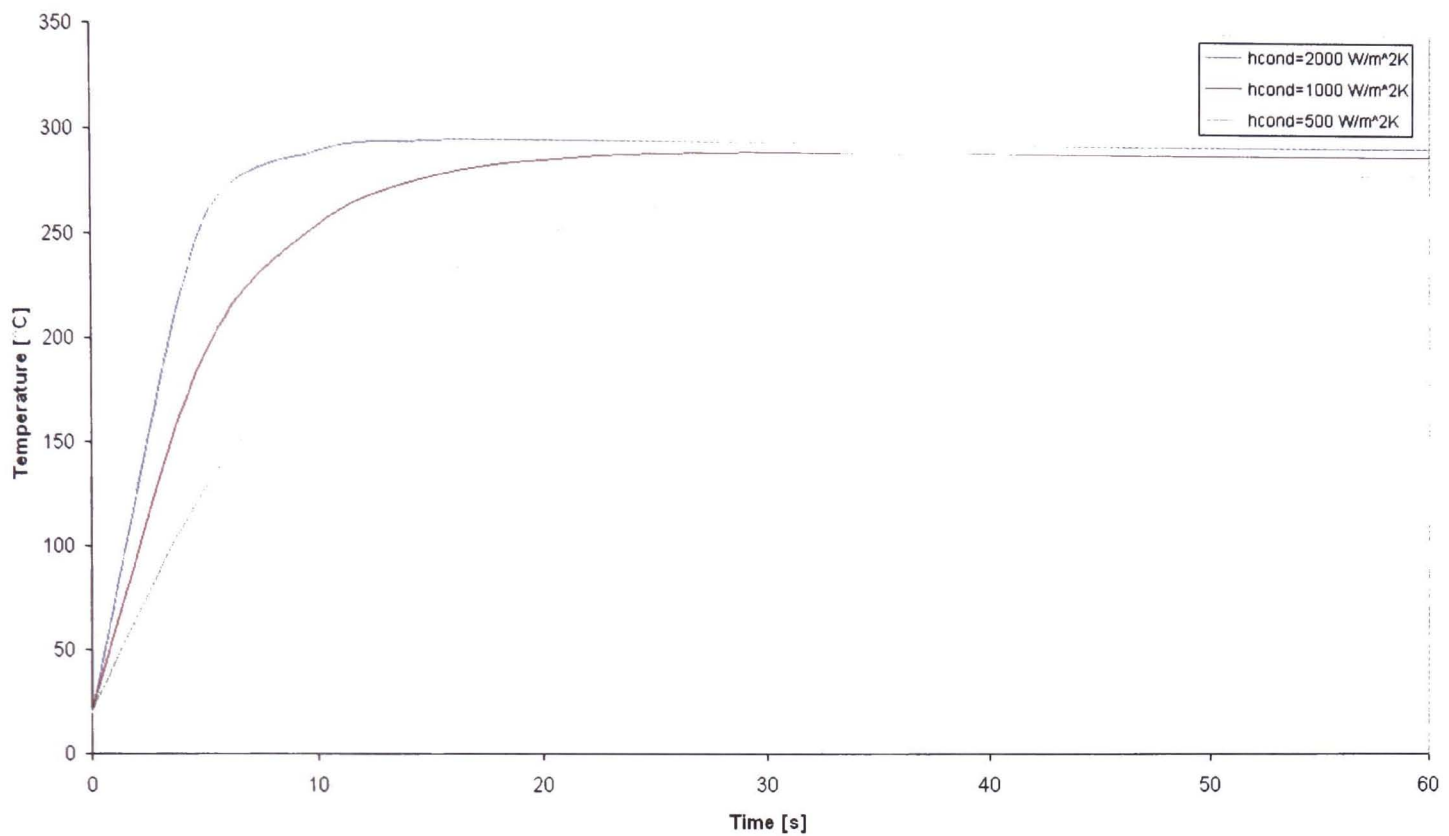


Figure 8.17 Rubbing thermocouple response and thermal contact conductance

Further studies included disc temperature, thermocouple position and convective heat transfer coefficients, and some of the results are shown in Figure 8.18. The blue curve shows the rubbing thermocouple response for the disc surface at 800°C , the rubbing thermocouple takes 30 seconds to reach a maximum temperature, which is 125°C lower than the actual surface temperature. The pink curve shows that the distance of the thermocouple from the surface does not practically affect its response, moving the thermocouple from 1 mm to 0.5 mm results in the same temperature prediction (disc surface 300°C). The red curve shows the effect of increased convective cooling of the thermocouple. Due to surface drag the airflow around the thermocouple will be similar to that of the disc surface and convective cooling of the rubbing thermocouple head will increase with the rotational speed of the disc. The increasing of the h_{conv} value by a factor of ten (from 5 to $50 \text{ W/m}^2\text{K}$) results in a temperature drop of 35°C for a disc surface temperature of 300°C .

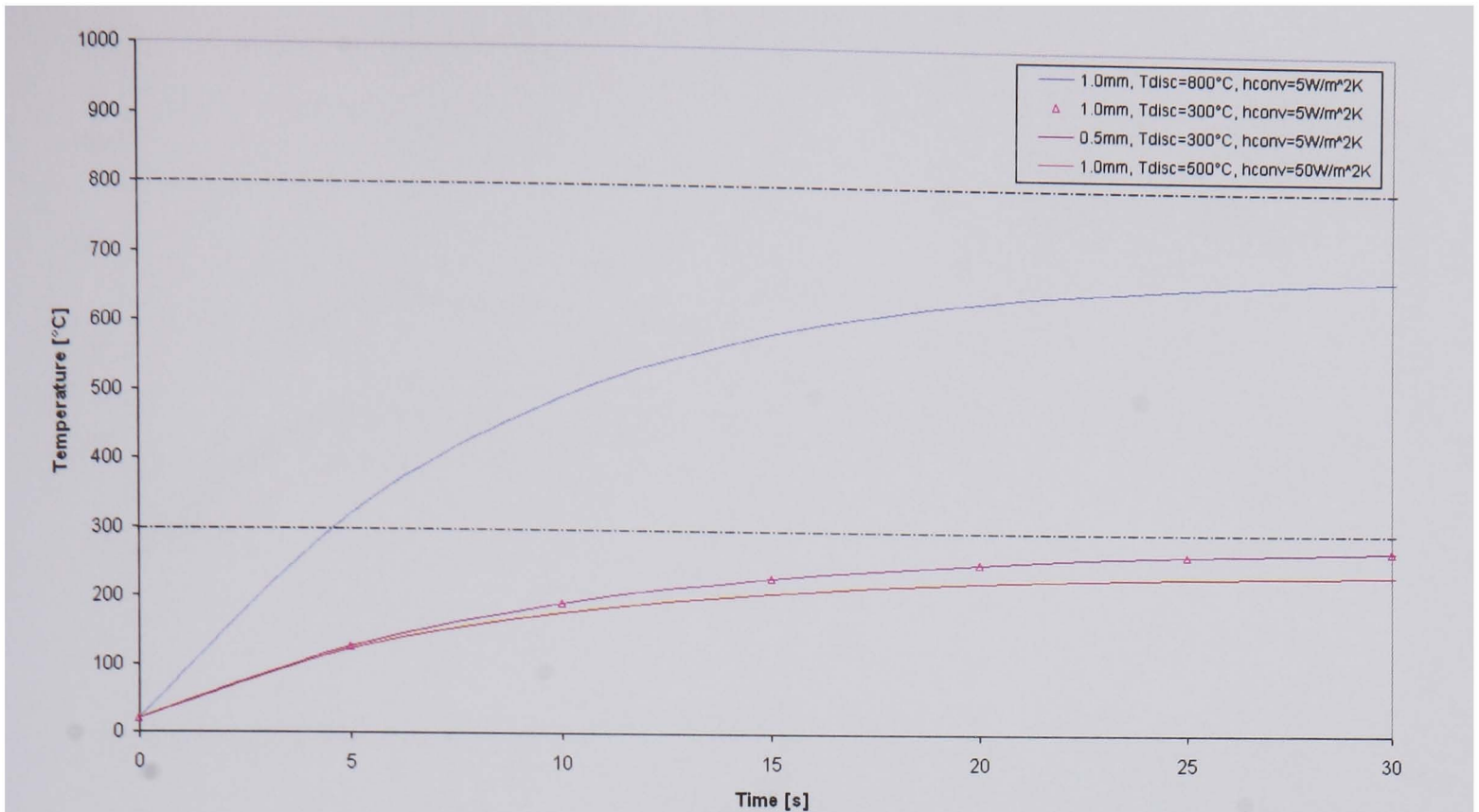


Figure 8.18 Rubbing thermocouple temperature response ($h_{cond} = 500 \text{ W/m}^2\text{K}$)

The analysis clearly demonstrated the sensitivity of the rubbing thermocouple to different influences. Substantially different readings are seen for identical temperatures, even during steady-state conditions. In reality transient conditions exist and Figure 8.19 shows the predicted rubbing thermocouple response for the transient disc surface temperatures (temperatures are from FE modelling of the anti-coning disc during repeated braking, see Section 8.3.2). The h_{cond} value at the interface is varied between 2000 and 500 $\text{W/m}^2\text{K}$, convective cooling of the rubbing thermocouple body is 20 $\text{W/m}^2\text{K}$. From the results it can be seen that an h_{cond} value of 1000 $\text{W/m}^2\text{K}$ shows a similar thermocouple response as seen during dynamometer tests.

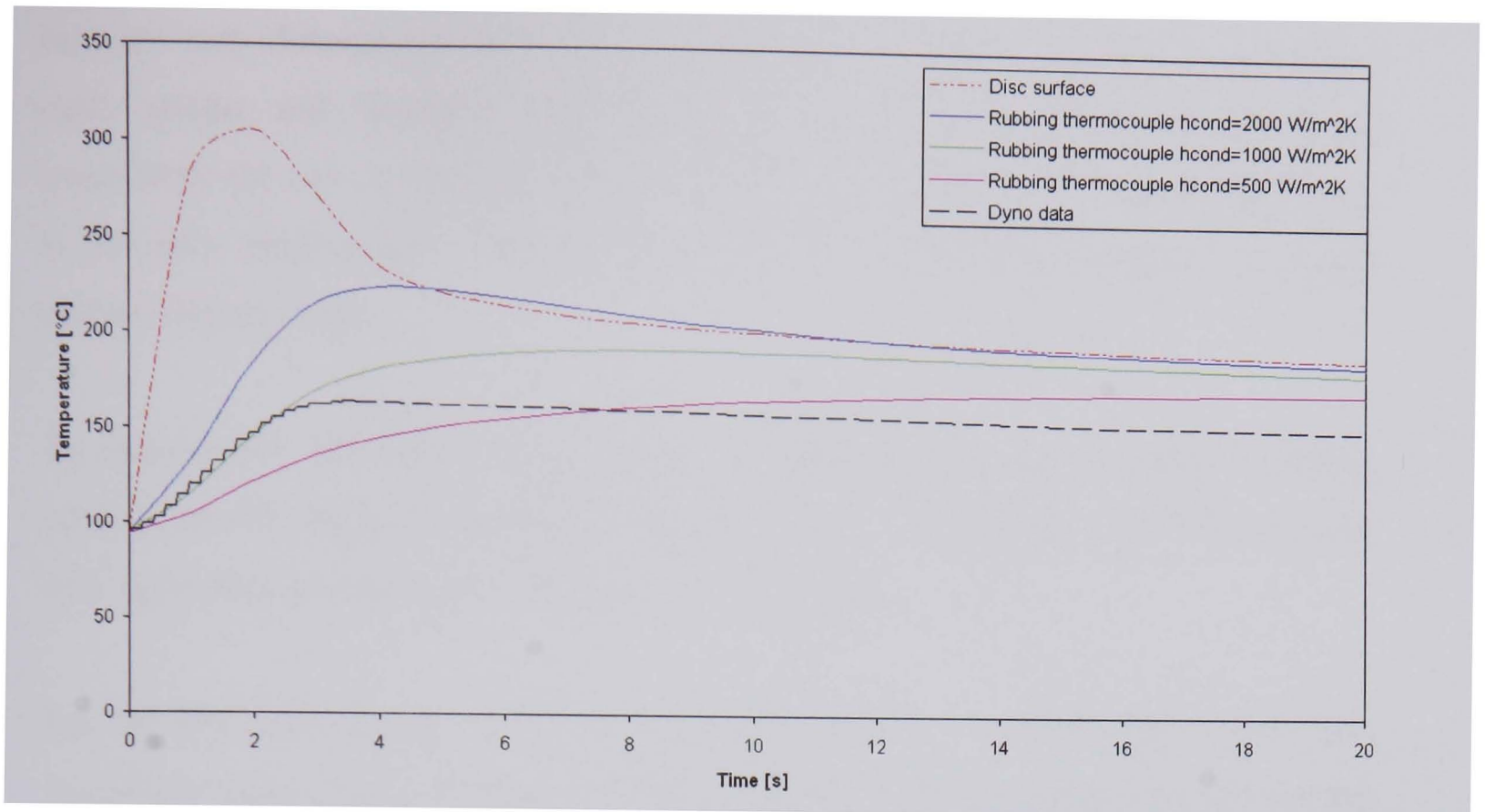


Figure 8.19 Modelled rubbing thermocouple response during a single stop brake application

The predicted rubbing thermocouple temperatures show that the time lag and amplitude reduction mean that the peak temperature seen during the brake application cannot be measured by using rubbing thermocouples. With these considerations in mind the FE predicted and measured repeated brake application temperatures given in Section 8.3 correlate well. If the thermocouple response factor is considered along with the increased cooling effect by the extraction fan used during the dynamometer test, predicted and measured temperatures of the repeated braking test show good agreement.

8.5.2 Thermoelastic Instability Influence on Brake Temperatures

The FE results of the CV route simulation (Section 8.3.2) were very close to dynamometer temperature measurements taking into consideration that a ‘perfect match’ is not possible due to complexity of the friction process. Practically all brake applications are conducted in the thermoelastic instability (TEI) regime (discussed in Appendix C), which means permanent change of interface pressure distribution, heat generation and wear on the friction surface. The state of the friction surface is also influenced by pad deposits. Furthermore, the studied brake applications are a transient heat transfer phenomenon, with rapid change of temperatures. As a result, during and for some time after braking, surface temperatures can substantially vary

between very close points on the disc surface. All this makes every brake application quite unique and ‘accurate’ temperature measurements impossible. Under these conditions, the use of relatively robust rubbing thermocouples in dynamometer tests is the only mechanically reliable option, enabling the measurements of ‘average’ surface temperatures.

To account for TEI effect on generated disc temperatures and indirectly on brake cooling, the FE analyses discussed in Section 8.3 were performed with both uniform heat input during braking and TEI simulated heat input.

For the TEI simulated heat input each friction surface area was divided up into four concentric areas (rings) as shown in Figure 8.20a. To simulate the hot bands of the TEI heat input the inner most ring and the 3rd ring (counting from ID to OD) have a heat flux increase 180% of the uniform heat input. The heat flux input of the other areas (rings) were reduced accordingly, to ensure adequate total heat (power) input. This ratio of heat flux was alternated for each area (ring) at each stop. Temperature dependent material properties were used, as shown in Table A2.

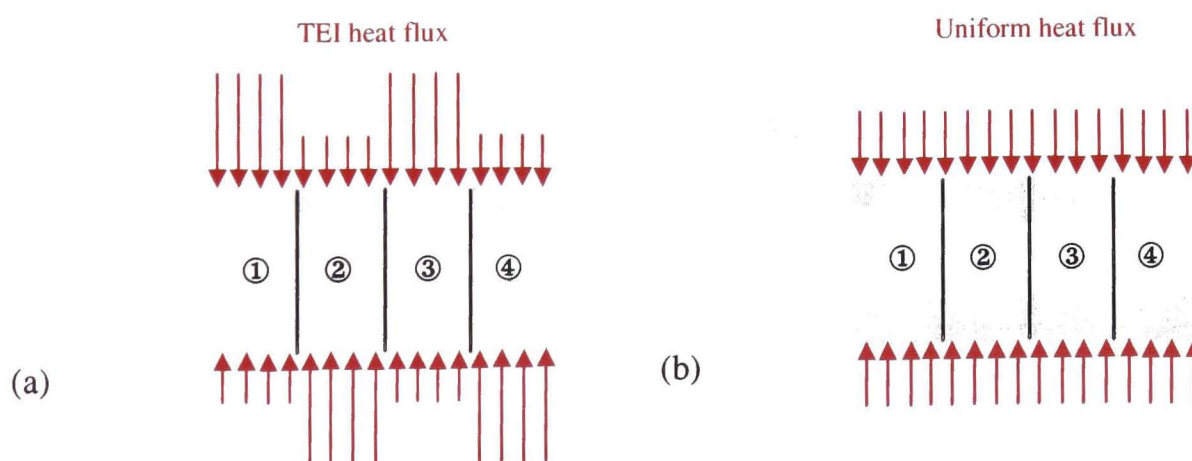


Figure 8.20 Assumed non-uniform TEI (a) and uniform (b) heat flux application

The temperature results are shown in Figure 8.21, the effect of the alternating heat flux is shown by the nodal temperatures (see Figure 8.4 for location of nodes), even at the disc hat. However, TEI heat input has a negligible effect on the disc bulk temperatures, since temperatures become quickly uniform during the cooling cycle.

Therefore, predicted temperatures incorporating TEI effects (Figure 8.21) are quite close to the uniform heat input disc bulk temperatures (shown in Figure 8.6).

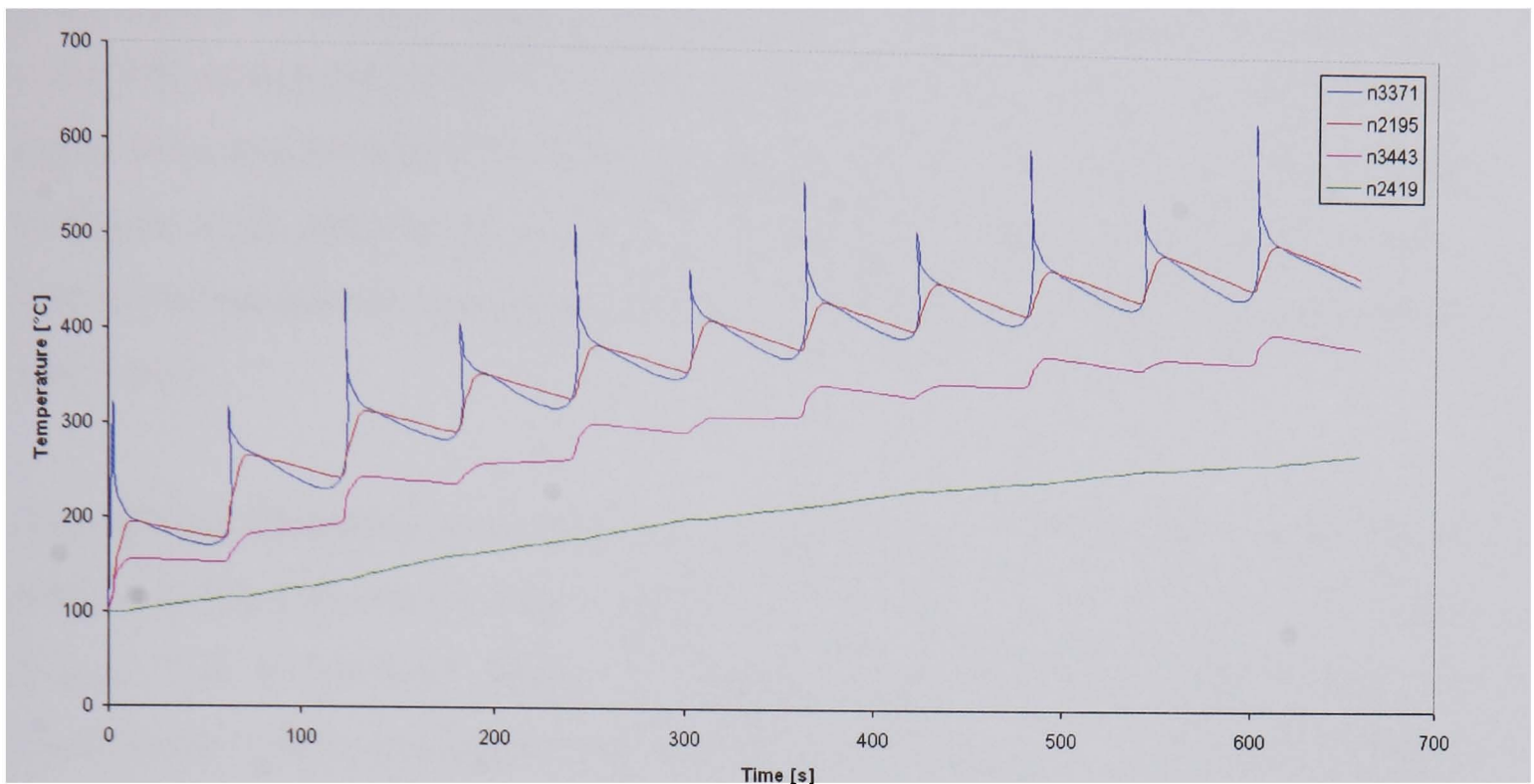


Figure 8.21 FE simulation temperatures for the dynamometer fade test, TEI simulated heat input

It would be expected that disc cooling increased with TEI heat input, in the areas of high heat flux input, surface temperatures are higher than for uniform heating (23°C for the first stop). At high temperatures radiative thermal power loss will be greater because it increases to the 4th power of temperature. However, the heat flux is applied only for a short period (3.33 seconds) and this effect is shown to be negligible. Increased cooling effects can be more prominent during a drag braking application where a constant heat flux is applied.

8.6 Contribution of Modes of Heat Transfer to Disc Heat Dissipation

So far the modes of heat transfer have only been considered individually. It is important to determine their contribution to disc heat dissipation to understand the complex cooling mechanism and the influence of temperature and vehicle speed. This understanding will provide the foundation for improvement and optimisation (see Chapter 9).

8.6.1 Commercial Vehicle Disc

To study the contribution of individual modes of heat transfer to brake cooling an FE brake model of the CV wheel assembly was created and a drag brake application modelled, as defined by ECE Directive 13 (type 2, 30 km/h on 6% incline). The FE model included the standard CV disc, wheel carrier and wheel (truncated), as shown in Figure 8.22. Making use of the circumferential symmetry, a 3-D segment of 6° was modelled. Material properties are given in Table A3 (disc) and A4 (wheel carrier and wheel).

Appropriate boundary and interface conditions were modelled as discussed in Section 8.3.2. Convection was modelled, for the ‘disc only’ in still air, as given in Figure 5.23. It has been shown in Chapter 5 that the wheel assembly does not significantly reduce convective heat transfer coefficients. An emissivity change from 0.4 – 0.7 was used for the friction surfaces. The change of emissivity during the brake application is shown in Figure 7.11. The remaining surfaces were given an emissivity value of 0.9. A layer of surface elements are used at the disc/wheel carrier interface to model the thermal contact resistance. A value of 7000 W/m²K was used for h_{cond} to model a standard interface (see Chapter 6).

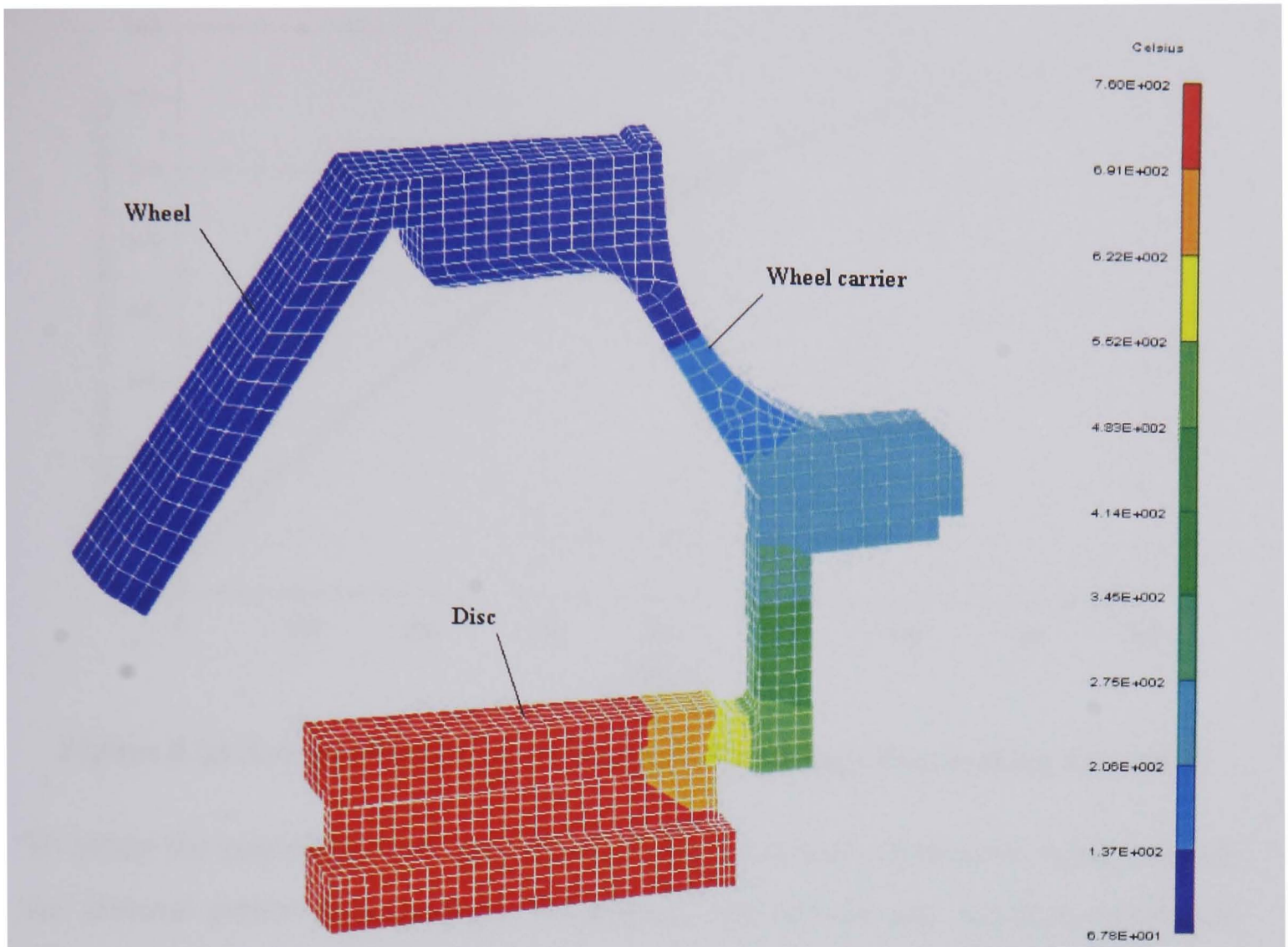


Figure 8.22 FE analysis temperature contour plot of CV disc brake with wheel and carrier

Transient thermal FE analysis of the drag brake application was performed and the average friction surface temperatures are shown in Figure 8.23. Temperatures increased throughout drag braking (not reaching steady-state conditions) rising to over 750°C at the end of the drag, at 720 seconds. The proportion of heat dissipated by conduction, convection and radiation were studied in detail when the average friction surface temperature is at 600°C. This temperature was reached after 430 seconds of drag brake application.

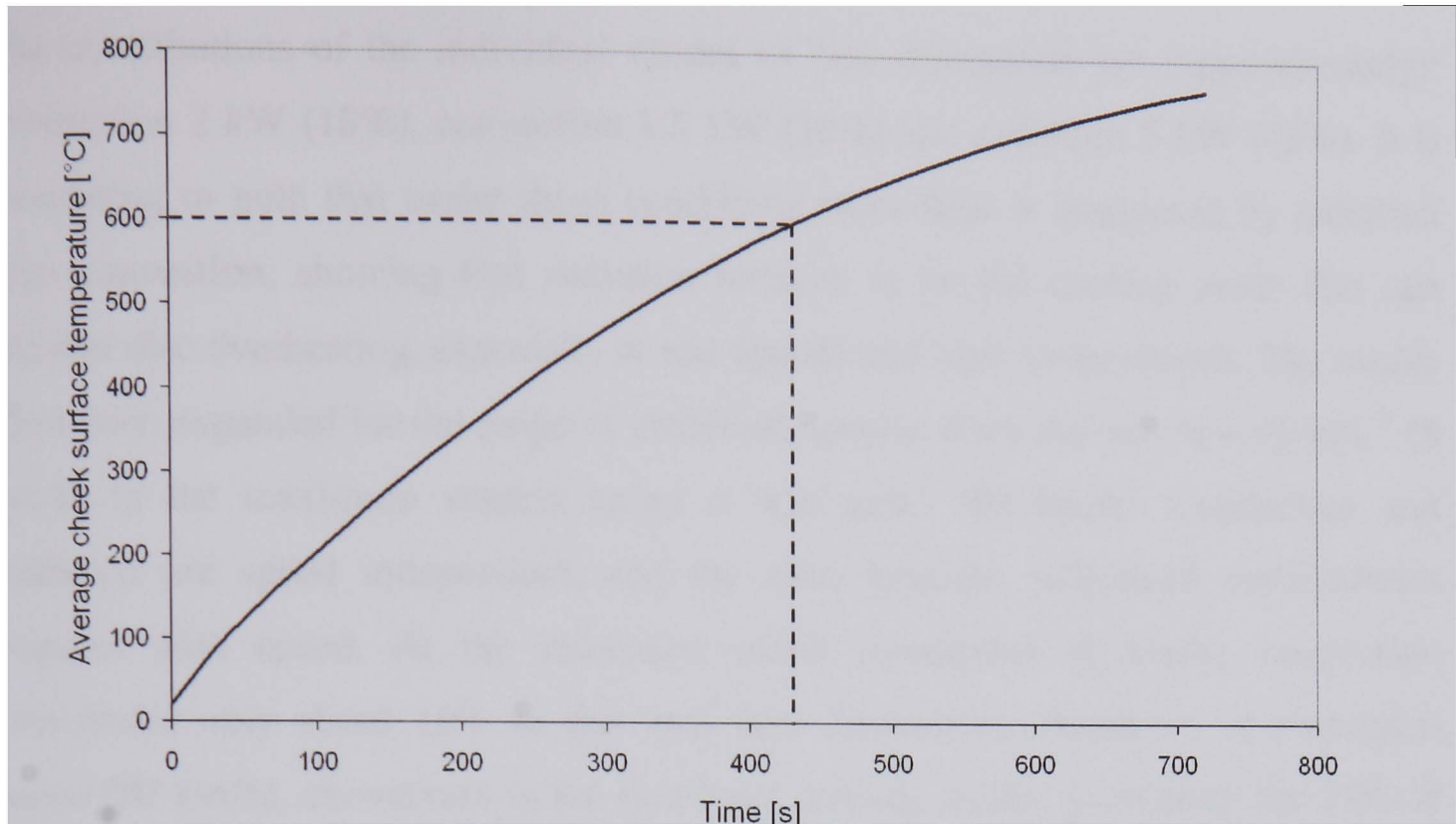


Figure 8.23 Average friction surface temperature during drag braking simulation

To study the contribution of individual modes of heat dissipation on brake cooling, the thermal power equations for conduction, convection and radiation (equations (5.15), (5.16) and (5.17)) are used. The vertical line shown in Figure 8.24 indicates the total thermal power loss and the contribution of the individual modes, for the drag braking application, when the average friction surface temperature is 600°C (rotational speed is 150 min⁻¹). The results show that the total heat dissipation from the disc is about 11.5 kW.

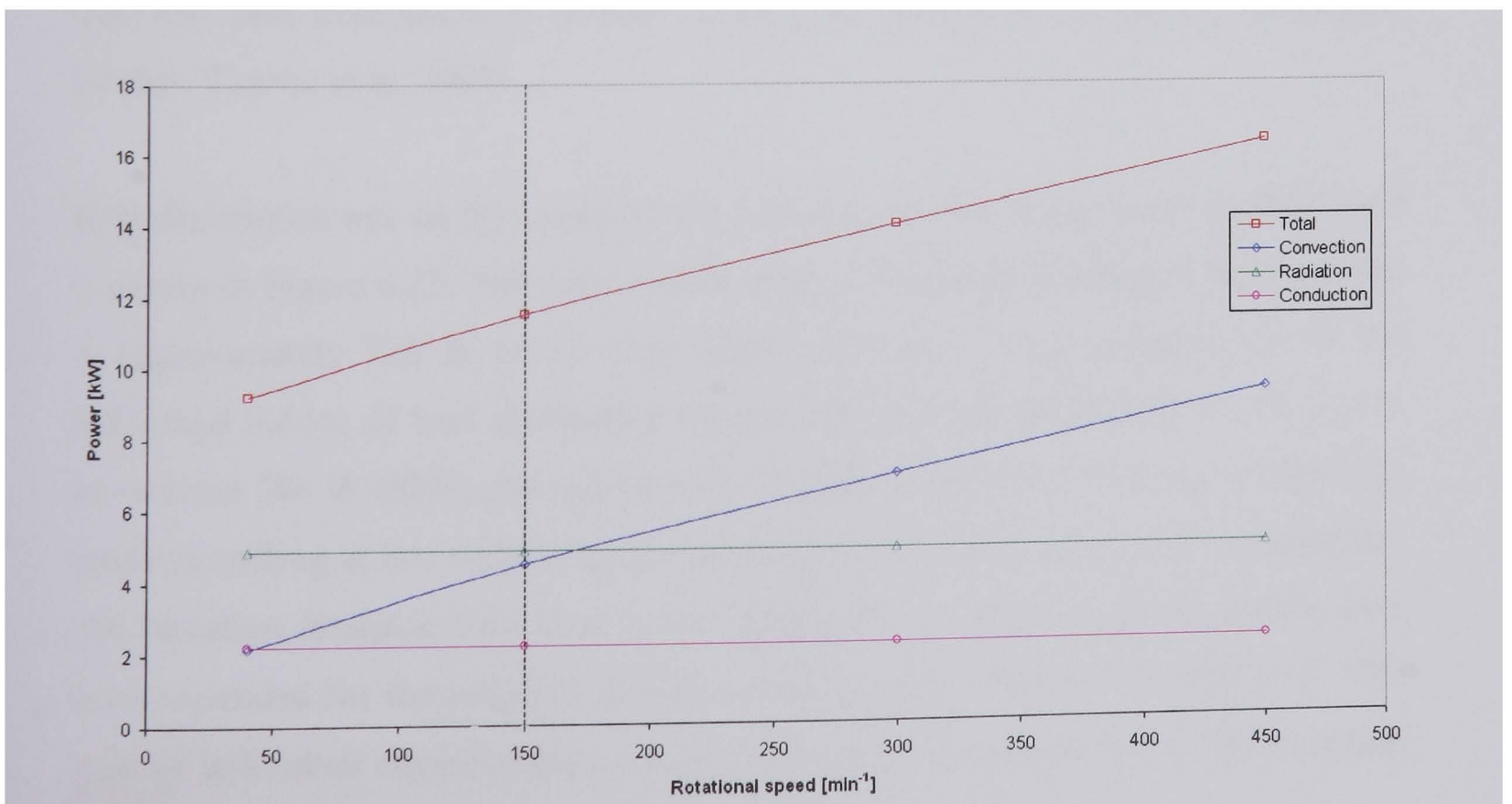


Figure 8.24 Heat dissipated by each mode of heat transfer for the standard CV disc at 600°C

The contributions of the individual modes of heat dissipation are (approximately): conduction 2 kW (18%), convection 4.5 kW (39%) and radiation 5 kW (43%). It is interesting to note that under these conditions more heat is dissipated by radiation than convection, showing that radiation remains to be the cooling mode that can prevent disc overheating, especially at low speeds and high temperatures. The results have been expanded for the range of rotational speeds, from the very low 40 min⁻¹ (8 km/h) to the maximum vehicle speed at 450 min⁻¹ (90 km/h). Conduction and radiation are speed independent, and the ratio between individual contributions changes with speed. At the minimum speed considered (8 km/h), convection contributes only about 18% to the total heat dissipation. However, at maximum speed (90 km/h), convection is the dominant cooling mode, accounting for 57% of total dissipated heat.

It has been shown that radiation is speed independent and can be the primary cooling mechanism at high disc temperatures when vehicle speeds are low. This situation is commonly found in braking from high speed or long downhill drag braking, when convection cooling is limited. Radiative heat dissipation is usually considered insignificant at lower temperatures, and neglected by many authors in brake analyses. This assumption cannot be accepted, since even at relatively low disc surface temperatures of 100°C to 150°C and at very low vehicle speeds, the amount of radiative heat dissipation is similar to the heat dissipated by natural convection (Voller, Tirovic et al. 2002).

Heat dissipation was further analysed for a friction surface temperature of 100°C and is shown in Figure 8.25. The results show that the total heat dissipation from the disc is approximately 722 W at the drag speed (150 min⁻¹). The contributions of the individual modes of heat dissipation are (approximately): conduction 76 W (10%), convection 596 W (83%) and radiation 50 W (7%). Convection is the most dominant mode of cooling at low surface temperatures (ten times that of radiation). Conduction and radiation dissipate little heat at low temperatures. Once again the results have been expanded for the range of rotational speeds, from 40 min⁻¹ to 450 min⁻¹. The ratio of individual contributions changes with speed but convection is the dominant mode throughout.

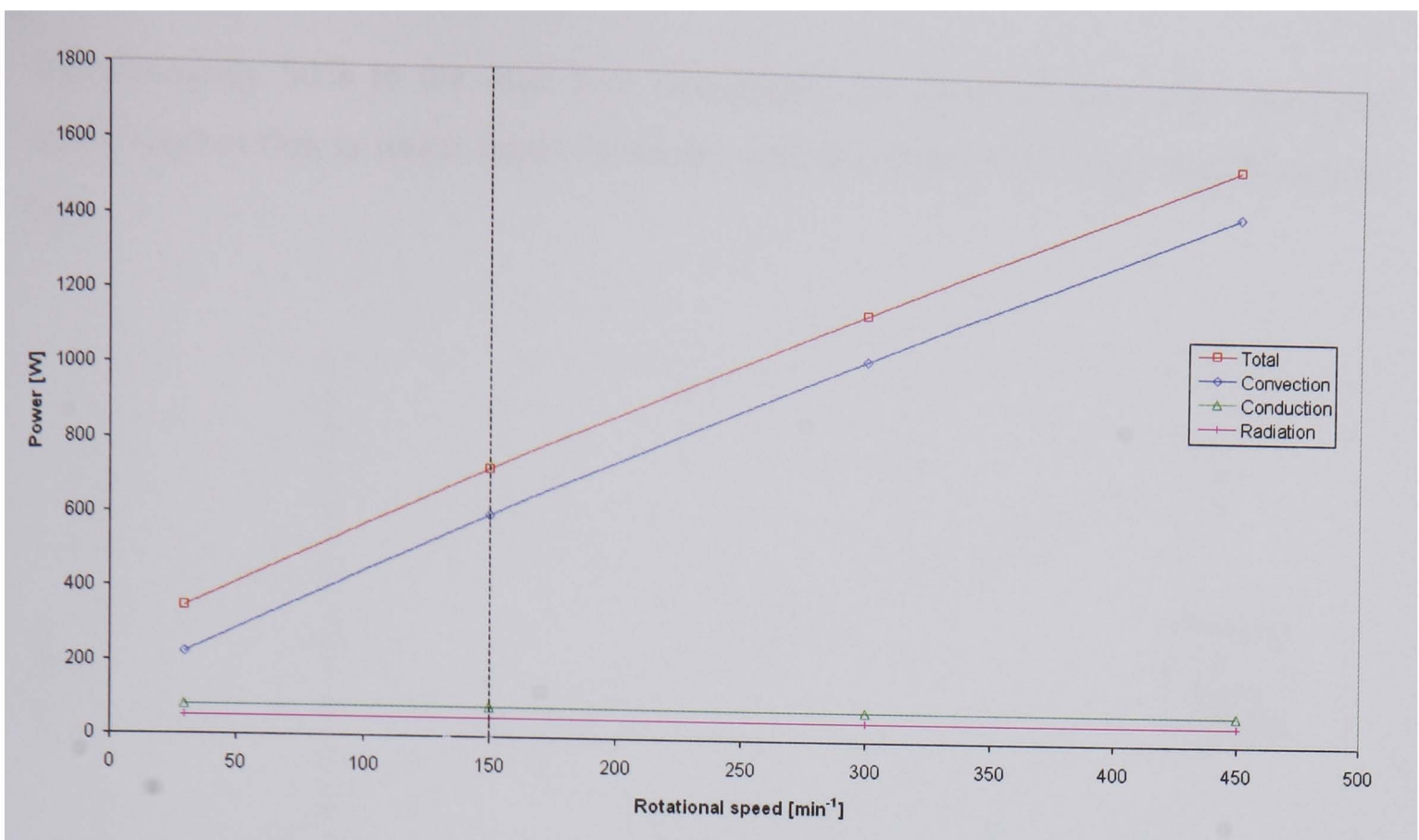


Figure 8.25 Heat dissipated by each mode of heat transfer for the standard CV disc at 100°C

8.6.2 TGV Disc

To study the contribution of individual modes of heat transfer during high speed railway brake cooling, the TGV disc route simulation results (see Section 8.4) have been used to calculate the thermal power dissipated by conduction, convection and radiation. The same methods as described for the CV disc have been used to determine the distributions of thermal power. The results are shown in Figure 8.26 for an average surface temperature of 300°C (achieved at approximately 1000 seconds into the drag, see Figure 8.13). The vertical line (Figure 8.26) indicates the total thermal power loss and the contribution of the individual modes, for the drag braking application, at drag speed (358 min⁻¹). The results show that the total heat dissipation from the disc is about 14.7 kW. The contributions of the individual modes of heat dissipation are (approximately): convection 12.1 kW (82%), radiation 2.2 kW (15%) and conduction 0.4 kW (3%). In this condition convective cooling is dominant, however at higher temperatures radiation will play a larger role (as shown in Figure 8.24 for the CV disc). Conductive heat dissipation is very low due to the small contact surface area of the lugs, which conduct heat to the hub and axle.

The results are again expanded for the range of rotational speeds, from 0 min⁻¹ to 1800 min⁻¹ (300 km/h). When the disc is stationary, convection contributes

approximately 50% to the total heat dissipation. However, at maximum rotational speed, convection is much more dominant, and accounts for 87% of total dissipated heat.

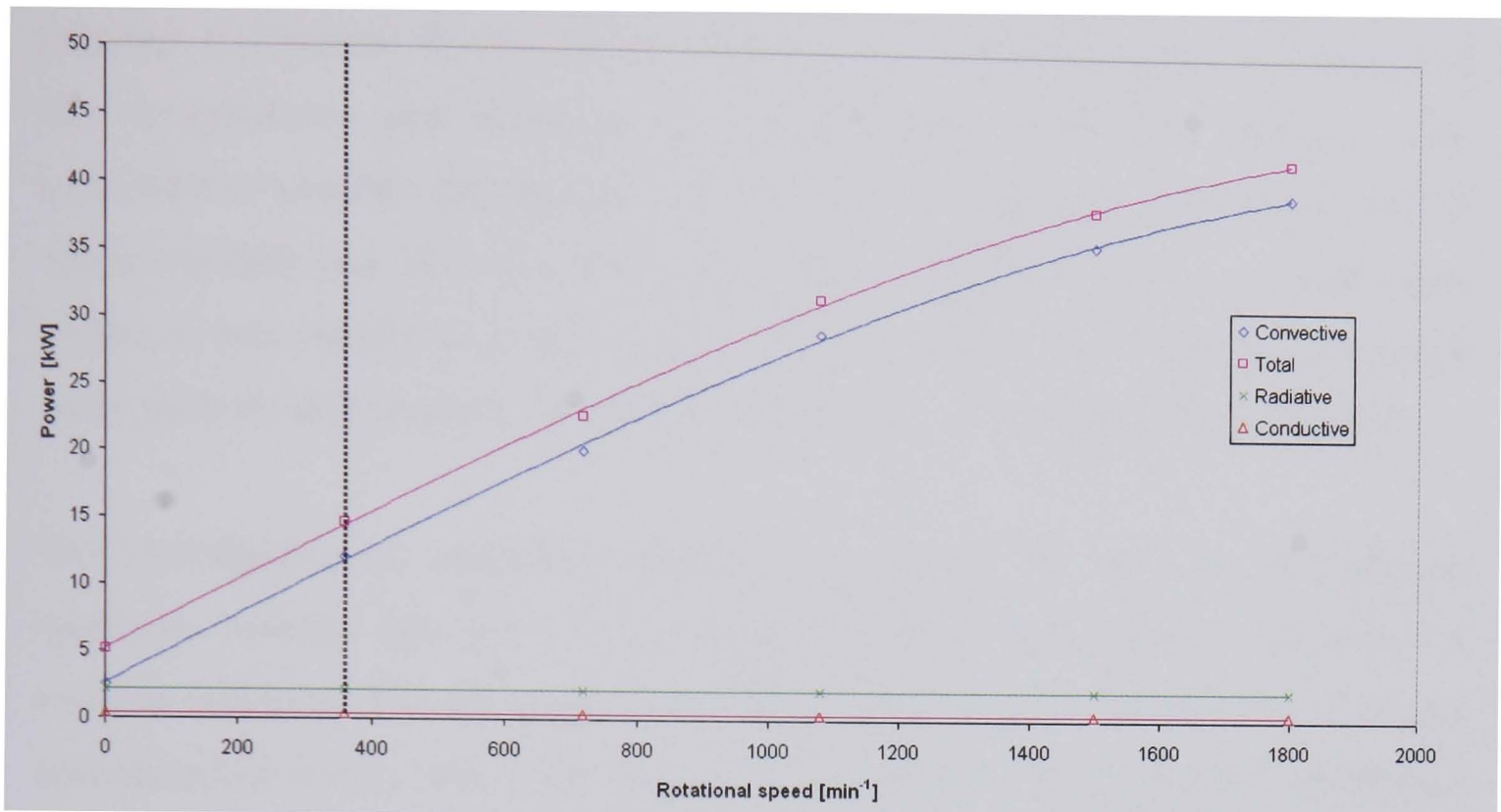


Figure 8.26 Heat dissipated by each mode of heat transfer for the TGV disc at 300°C

The analyses shown in this section and literature data, suggest that in most vehicle service conditions the majority of heat is dissipated from brakes by convection. Since convection is the dominant mode of heat dissipation, it potentially offers most scope for further improvement. However, other modes must not be neglected in brake thermal analysis.

8.7 Summary

This chapter has investigated modelling methods to enable confident modelling of heat dissipation optimisation solutions. Route simulations have been performed to validate the overall work of the previous chapters.

FE software has been carefully selected and modelling methods have been discussed, investigating simplification techniques. Route simulations have been performed for the CV and TGV railway brake discs for repeated and drag braking applications and validated using analytical calculations and dynamometer test measurements. The

results of Spin Rig experiments and CFD modelling were used to provide the boundary conditions. The effect of temperature dependent material properties on the brake temperature predictions were investigated and compared with fixed property values. The use of rubbing thermocouples has been investigated, to determine their response limitations. To account for thermoelastic instability effects on generated disc temperatures and indirectly on brake cooling, further FE analyses were performed to simulate this phenomenon. Finally, drag braking simulations of the CV wheel assembly and TGV disc have been used to study the contribution of individual modes of heat transfer to brake cooling. The proportions of heat dissipated by each mode were studied in detail for a range of brake temperatures and rotational speeds.

The investigation of modelling methods has ensured the best use of computer resources, making best use of simplification techniques to provide efficient but accurate solutions. The FE temperature predictions compare well with dynamometer and analytical results and it has been shown that the use of temperature dependent material properties has a substantial influence on predicted temperatures. The study of thermocouple response has shown that peak surface temperatures cannot be measured with used equipment during the repeated braking simulation studied. It has also been shown that thermoelastic instability simulated heat input does not have a significant effect on the predicted bulk temperatures or mean surface temperatures during cooling.

A more accurate evaluation of route simulation predictions and measurements can now be accomplished and the limitations and difficulties of comparison are more fully understood, giving confidence in future brake temperature prediction. The detailed analysis of the contribution of the modes of heat transfer to brake heat dissipation allows areas with potential for improvement to be established and provides a good foundation for the investigation of heat dissipation optimisation (in Chapter 9).

Heat Dissipation Improvement and Optimisation

9.1 Objectives

The objective of this chapter is to investigate the ways of increasing disc brake thermal performance by improving conductive, convective and radiative heat dissipation. To achieve this, influencing factors, design modifications, the gains, limits and practical aspects are considered to provide technically acceptable and commercially viable recommendations for higher performance brake designs. Experiments have been conducted to examine the influence of modifications designed to improve heat dissipation. Their cumulative effects are further investigated in FE simulations. FE modelling of route simulations were successfully conducted in Chapter 8 and in this chapter, FE models have been modified to include the specific effects to increase heat dissipation. The final temperature results have enabled the evaluation of actual gains in brake cooling.

9.2 Analysis of Methods to Improve Heat Dissipation

The commercial vehicle (CV) disc has potential for an increase in conductive heat transfer coefficient with modification of the disc/wheel carrier interface. Convection can be increased by improving the airflow around the disc within the wheel assembly. Increasing radiation cooling is limited because of the difficulties in modifying the surface emissivity of the disc and wheel assembly.

The TGV railway disc also has limited scope for the improvement of radiative heat dissipation. This is also true for conductive heat dissipation, as the contact area for conduction is relatively small (0.2% of the total surface area). The TGV railway disc is axle mounted and airflow is not affected by the wheel (as for the CV disc) and in order to increasing convective heat dissipation the disc ventilation design must be studied. However, increasing airflow through the disc ventilation channels can lead to serious pumping losses (discussed in Chapter 4) and therefore the ventilation design must be carefully considered. A method for assessing 'ventilation design efficiency' has been developed.

9.2.1 Airflow and Convection

Airflow and convection are very closely linked. Convective heat transfer coefficients (h_{conv}) increase with air velocity (cross flow), more so than with rotational speed, as shown in Chapter 5. Convective heat dissipation (Q_{conv}) increases with temperature difference between the brake surface (T_s) and surrounding air (T_∞). If air is allowed to flow over the disc (cross flow) then the surrounding air heated by the disc is transported away and replaced by cooler air, reducing T_∞ .

Disc ventilation has been the subject of much focus as a method of increasing convective heat dissipation, however for large discs fitted to high speed vehicles the power to rotate the ventilated disc can be very high leading to much energy loss, as shown in Chapter 4. An efficient pump design is not necessarily an efficient heat dissipater, for example, the high pumping efficiency curved vane CV disc has cooling rates that are very similar to the standard radial vane disc (shown in Chapter 5).

As the high pumping efficiency value of the curved disc design suggests airspeed through the ventilation channels is greater than the radial vane design for the same rotational speed. From the h_{conv} equations (2.14) to (2.17) of Chapter 2, which state that h_{conv} increases with air velocity; Q_{conv} would be expected to be higher for the curved vane disc. However, the poorer than expected cooling rate of the curved vane design is due to the flow pattern through the ventilation channel. The high pumping efficiency of the design is achieved by encouraging the airflow to follow the contours of the vane, providing laminar flow within the channel. The airflow remains attached to the walls of the vanes. This results in a low temperature difference between the air at the surface and the wall surface because the film of air is heated but not transported away from the wall, only along it, see Figure 9.1. This reduces heat transfer as demonstrated by Newton's law of cooling (equation (5.1)). This suggests that to increase ventilated disc cooling, turbulent flow must be encouraged, to transport heat dissipated (initially by conduction) to the surface film of air, away from the surface and introducing cooler air to the surface of the ventilation channel. Design considerations (discussed in Chapter 4) such as blade (vane) angles, blade width, number of blades, filleting radii and filling increase airflow but should be considered carefully, as encouraging laminar airflow may not increase heat dissipation.



Figure 9.1 (a) Laminar and (b) turbulent airflow heat dissipation of the ventilation channel

The radial vane design offers the best overall cooling characteristics, as shown in Chapter 5. However, at very low rotational speeds, the pillared disc design has higher convective cooling, due to good natural convection characteristics. The pillared vane design also requires the least power to rotate from the designs tested in Chapter 4. For large discs rotating at high speeds, there must be a compromise between good cooling characteristics and low pumping losses, this is clear in the studies of Chapters 4 and 5. The required heat dissipation must be decided upon and efficient

disc ventilation designed accordingly. Any cooling above requirements will increase pumping losses unnecessarily.

9.2.2 Conduction

To increase the average conductive heat transfer coefficient (h_{cond}) at the CV disc/wheel carrier interface a higher bolt torque and thus clamping pressure can be applied. However pressure differences also increase with increased bolt torque. Increasing the bolt torque can therefore produce reduced clamping pressure at the areas between the bolts, reducing h_{cond} in that area (a result of increased bolt torque and deformation at the interface). If high bolt torques are used in order to increase h_{cond} then it would also be necessary to increase the number of bolts used. Increasing the number of bolts used to clamp the components would provide a more uniform pressure distribution and an overall higher magnitude of pressure. The resulting reduced area of contact and the conductance through the bolts must be considered when the number of bolts is increased, along with structural integrity, assembling and maintenance issues.

Conductive heat transfer at the interface can also be increased by improving the interface surface finish, increasing the actual contact area. Improving the surface finish of the components increases their manufacturing costs and is not feasible with the manufacturing methods used. Alternatively, thermal contact conductance can be increased by replacing the air within interstitial areas at the contact interface with a medium of higher conductance. As discussed in Chapter 2 interstitial fillers may take the form of grease, metal foil, wire screens or powders, this is investigated further in Section 9.3.2.

The studied railway brake designs are of a 'slip joint' type connection between the disc and the hub (see Chapter 3). In such designs, disc/hub contact areas are very small and conductive cooling is very limited despite the high thermal conductivity bronze washers (used to reduce friction) applied at the interface. This is clearly shown in the contributions of modes of heat transfer to heat dissipation in Chapter 8.

9.2.3 Radiation

Most authors in the past have assumed constant emissivity for brake thermal modelling. However, emissivity change on the disc surface has been measured, shown in Chapter 7. Only very recently, during the course of this project, other data on this phenomenon has been published (Eisengraber, Grochowicz et al. 1999). The wide range of emissivity values (0.2 to 0.9) is in agreement with the findings of Chapter 7. The change of emissivity in such a wide range is a very important conclusion, and care must be taken to ensure adequate values are used in brake thermal modelling to avoid large errors in temperature predictions. There is a distinct reduction in the heat dissipation, leading to higher disc temperatures, due to emitted radiation being reflected back to the disc by the wheel assembly. This is shown in the results of simulations presented in Chapter 7. Therefore, the effect of radiation being reflected back to the disc by the wheel carrier, wheel and dust shield must also be considered in the analysis of brake disc heat dissipation.

The design and surface condition of surrounding components must be very carefully considered, when designing a vehicle wheel assembly. Using wheels of low emissivity (such as aluminium) can mean that more of the heat radiated from the disc surface is reflected back to the disc, increasing disc temperature. However, the increased conductivity of aluminium may provide thermal benefits from heat conduction, this is investigated further in Section 9.3.3. The steel wheel carrier and wheel can absorb more of the radiated heat from the disc because of the material's higher emissivity value. However, in real life conditions, the inside surface of the wheel assembly will be coated by a layer of brake and road dust. An increased emissivity value is expected on this dull, blackened surface allowing more heat to be absorbed by radiation. But, its low conductivity (and thermal capacity) will limit thermal energy that the dust can absorb and transmit to the wheel assembly.

Under the circumstances, there is not much that the brake or vehicle designers can do to improve radiation from the friction surface or even non-friction disc surfaces. The friction surfaces are large, but their characteristics not favourable. The non-friction surfaces are relatively small and exposed to corrosion that increases radiative losses.

Probably, the only solution in increasing emissivity of disc friction surface is a 'special pad formulation' that would 'condition' disc surface.

9.3 Commercial Vehicle Brake Assembly

Various methods aimed at improving heat dissipation from the disc have been implemented based on the results of the research presented so far. Gains in convective and conductive heat transfer coefficients have been measured experimentally and the cumulative effects of these gains are investigated in numerical route simulations.

9.3.1 Wheel Carrier Ventilation

The standard CV wheel carrier was modified with the aim of increasing the airflow in order to improve convective cooling of the CV disc. Ten 35 mm diameter ventilation holes were machined in the standard wheel carrier, as shown in Figure 9.2.

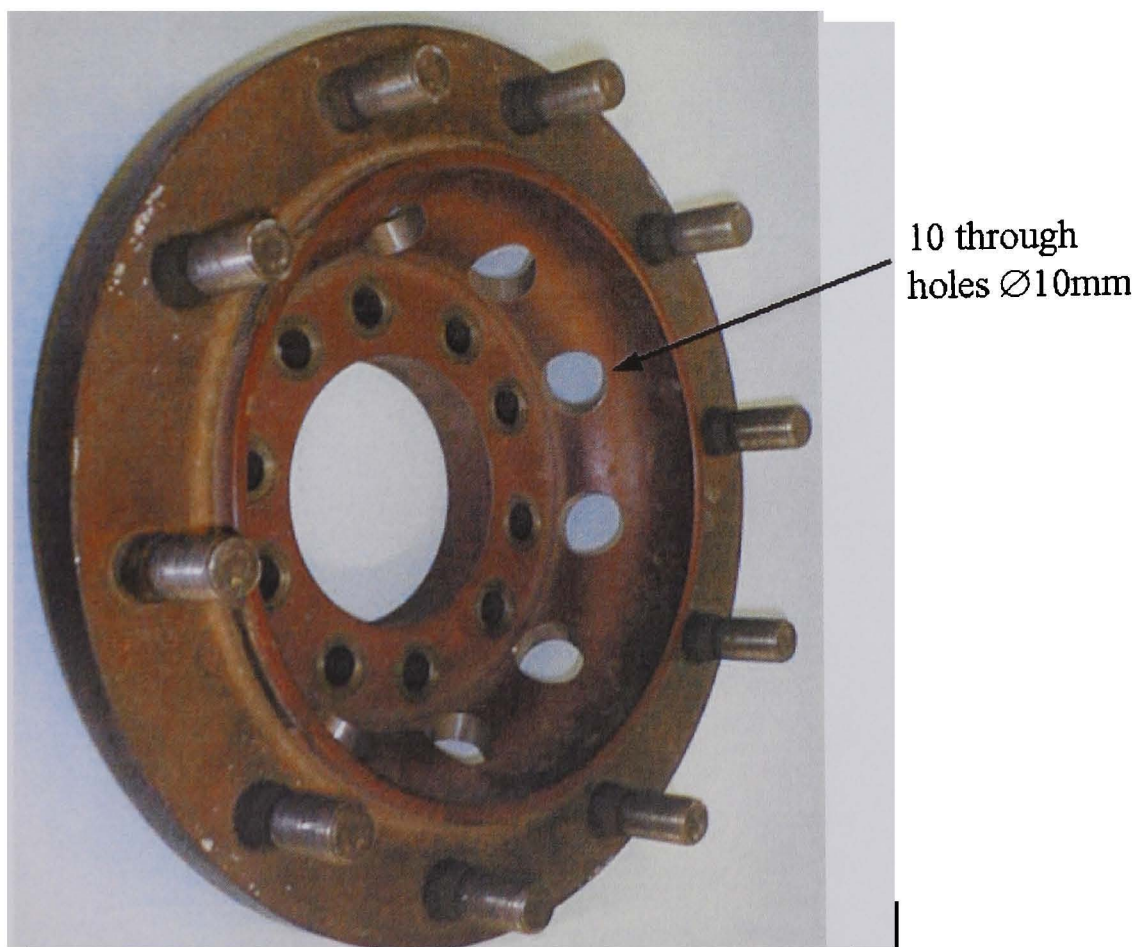


Figure 9.2 Modified CV wheel carrier

The standard wheel assembly shrouds the disc and can restrict airflow to and from the ventilation channel inlet and exit (measured in Chapter 4). However, the standard radial disc ventilation channel inlet is on the inboard side and is not restricted by the wheel assembly, as shown in Figure 9.3.

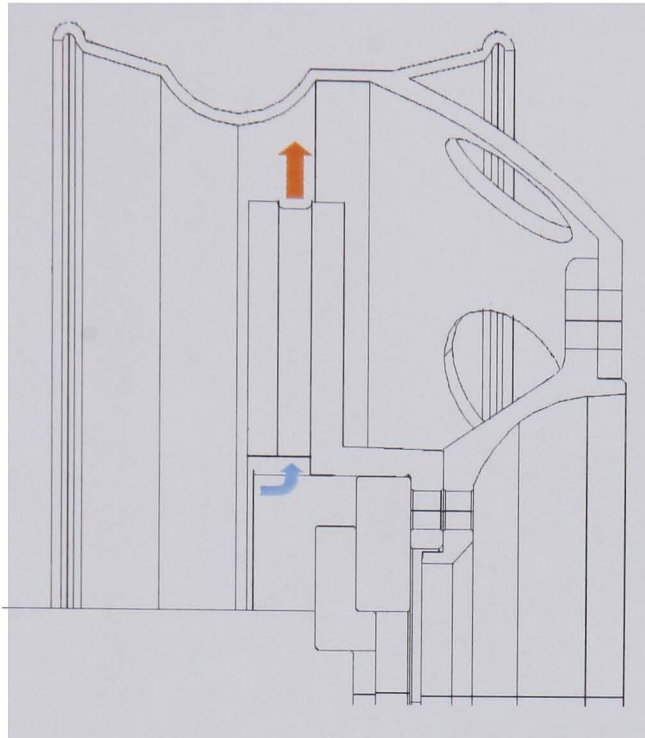


Figure 9.3 Standard disc and wheel assembly

However, for the anti-coning disc, which has the ventilation channel inlet on the outboard side, the wheel assembly seriously restricts the airflow of the disc ventilation channel inlet, shown in Figure 9.4. This reduces the cooling performance of the disc as shown in the measurements of Chapter 5.

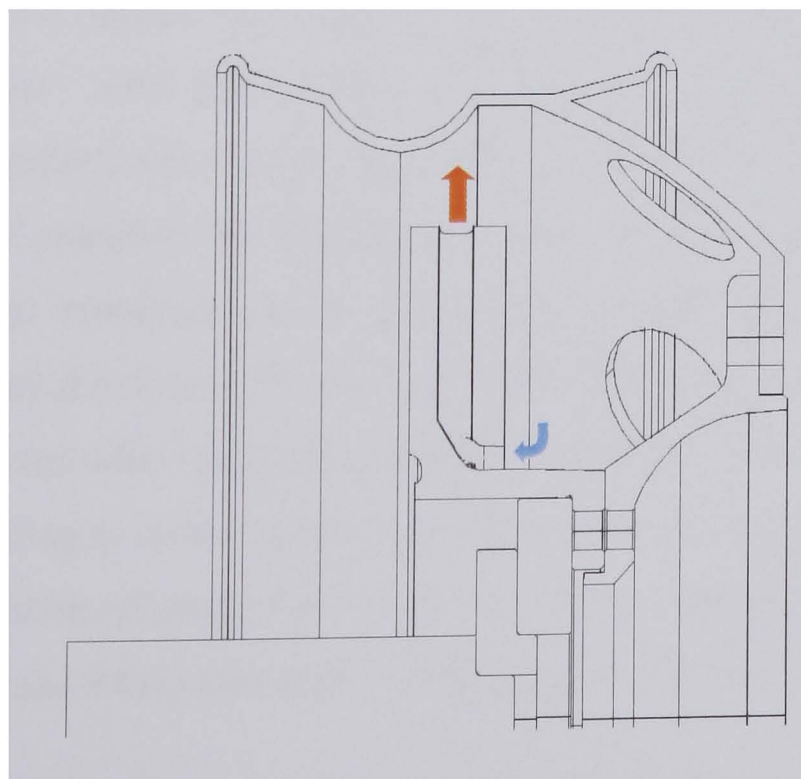


Figure 9.4 Anti-coning disc and standard wheel carrier

Modifying the wheel carrier and introducing ventilation holes improves airflow to the disc ventilation channel inlet. The aim is to allow air to be drawn from outside of the wheel assembly and through the wheel carrier ventilation holes by the pumping action of the disc ventilation channels, as shown in Figure 9.5. This will increase airflow through the disc ventilation channels, improving convective heat dissipation.

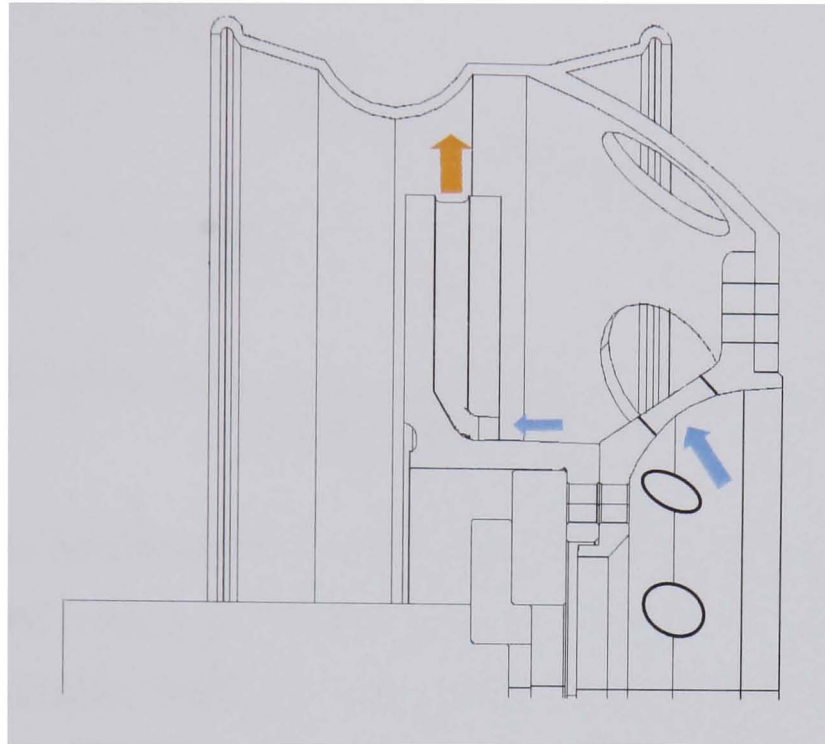


Figure 9.5 Anti-coning disc and modified wheel carrier

The cooling rates of the disc fitted with the modified wheel carrier assembly were measured on the Spin Rig (procedures described in Chapter 5). Six wheel assembly configurations were tested at four speeds; the 24 tests required twenty days to complete. Figure 9.6 shows the cooling rates for the standard radial vane disc rotating at 450 min^{-1} with three wheel assembly types. The unventilated wheel assembly is the standard wheel assembly with the wheel ventilation holes blocked. The standard wheel assembly has ventilation provided by the holes in the wheel only (see Chapter 3). The ventilated wheel carrier wheel assembly provides ventilation at the wheel carrier and the wheel. The cooling curves show that the introduction of the ventilation holes to the wheel assembly has very little effect on the cooling rate of the standard disc, resulting in only a small improvement in cooling performance. This is because the ventilation channel inlet is on the (free) inboard side. Blocking the ventilation holes of the wheel also shows little effect on the disc cooling rate.

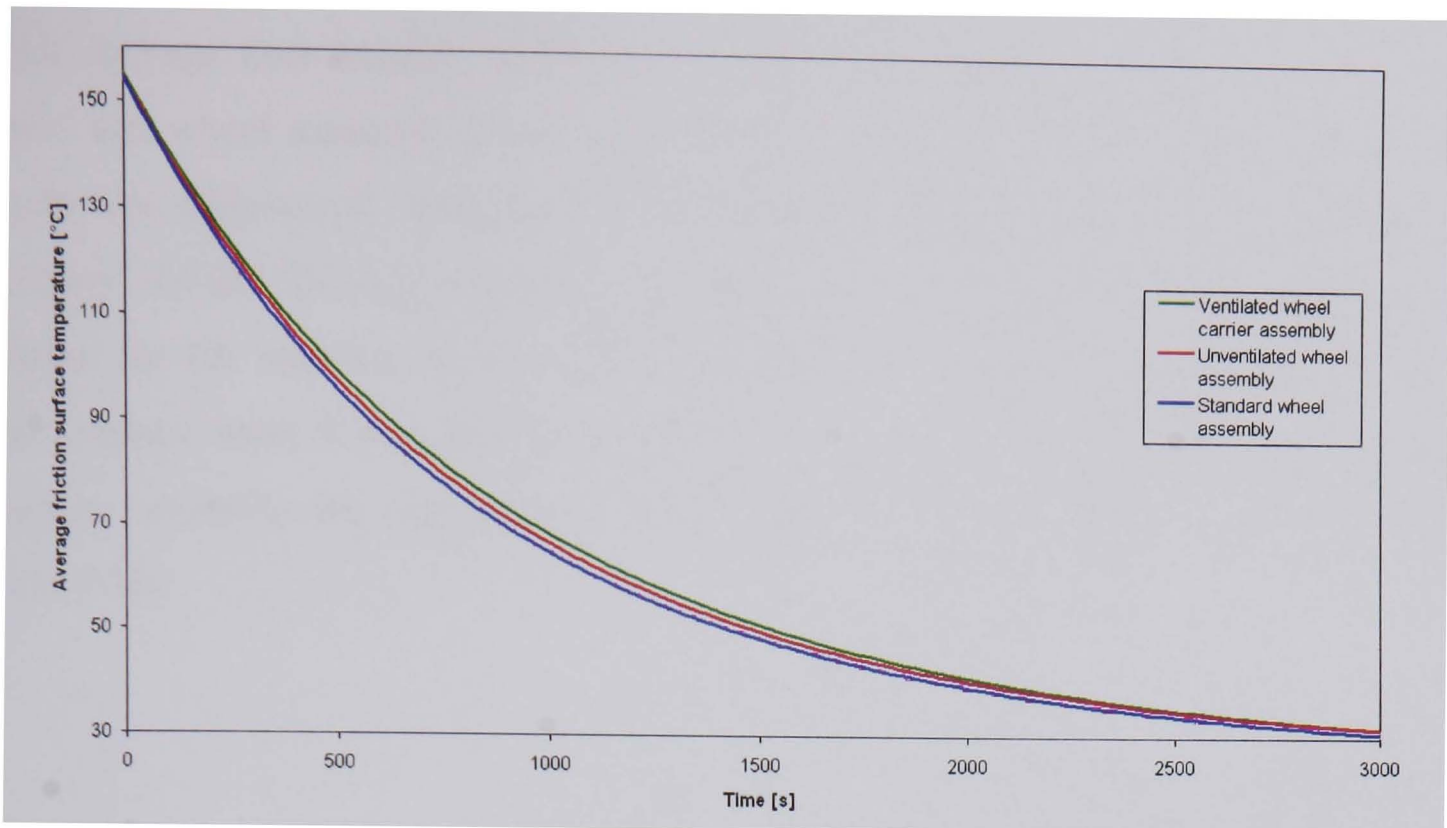


Figure 9.6 Effect of wheel assembly ventilation on standard CV disc cooling, rotating at 450 min^{-1}

Figure 9.7 shows the cooling rates for the anti-coning disc rotating at 450 min^{-1} with the standard and the ventilated wheel carrier assembly. It can be seen that the introduction of ventilation holes has a much more prominent effect on the cooling rate of the anti-coning disc. The ventilation holes provide improved air supply to the (outboard) ventilation channel inlet of the anti-coning disc (see Figure 9.5). Blocking the ventilation holes of the wheel have been shown to have little effect on the disc cooling rate (Figure 9.6) and has not been investigated for the anti-coning disc.

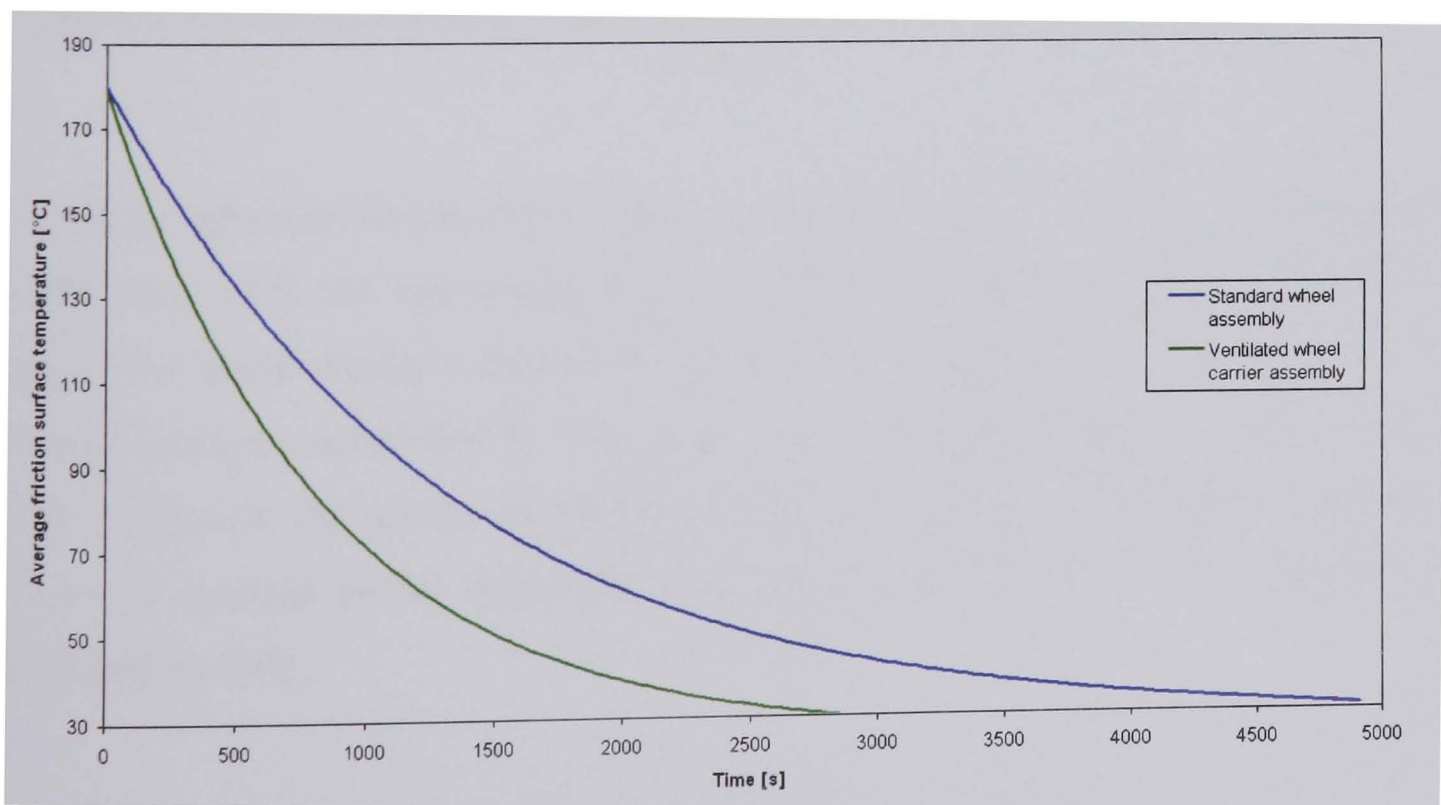


Figure 9.7 Effect of ventilated wheel carrier on the anti-coning CV disc cooling, rotating at 450 min^{-1}

The average heat transfer coefficient values (h_{avg}) values for different anti-coning disc and wheel assemblies are compared in Figure 9.8. The improved cooling rate with the addition of ventilation holes to the anti-coning disc wheel assembly is clearly visible. The h_{avg} values for the ventilated wheel carrier are 64% higher than those for the standard wheel carrier at 450 min^{-1} . Increased performance is seen throughout most of the speed range. The h_{avg} values of the disc with the ventilated wheel assembly are approaching those measured for the disc without the wheel assembly.

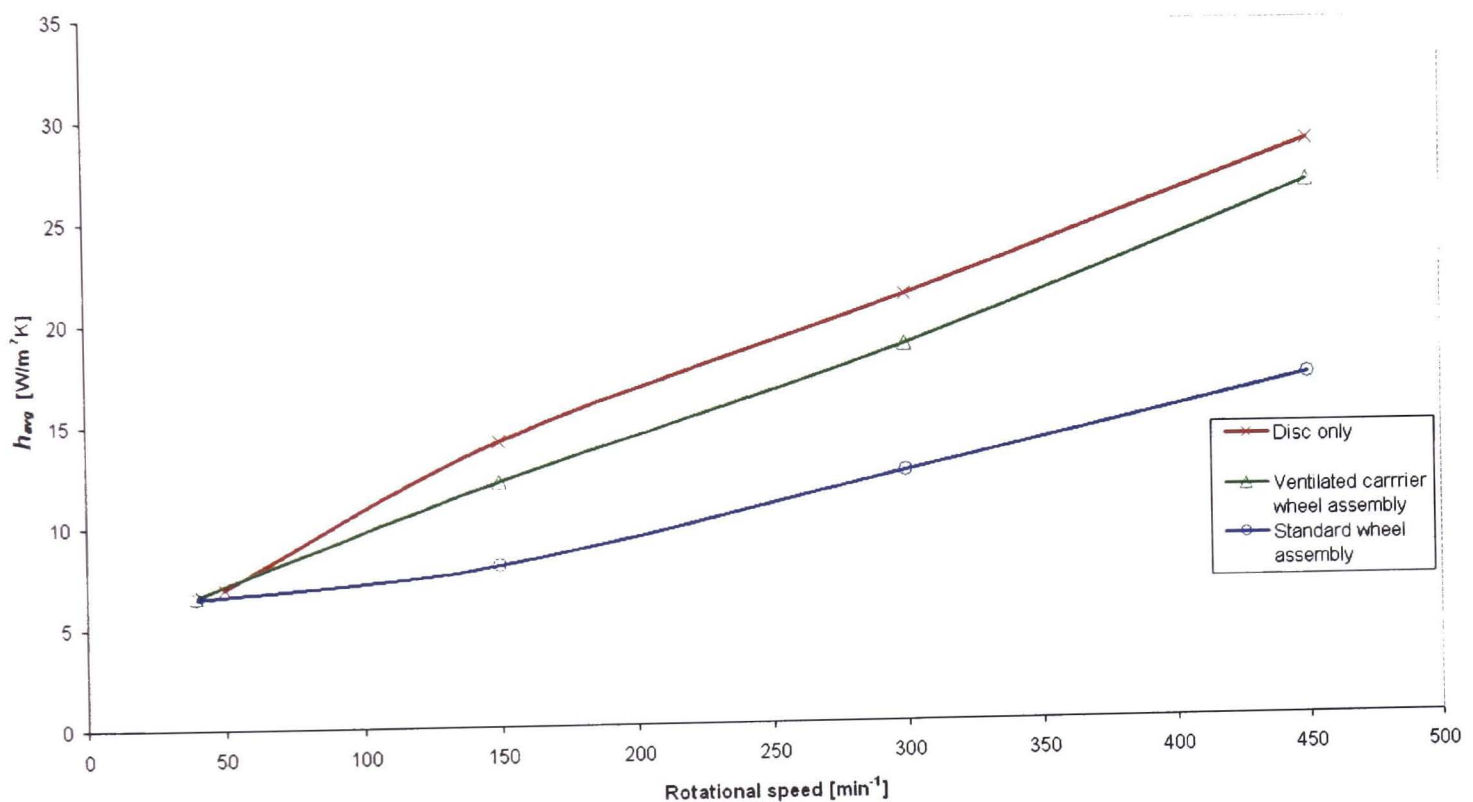


Figure 9.8 Total heat transfer coefficient values for the anti-coning disc assemblies at 100°C

To further demonstrate the effectiveness of the ventilated wheel carrier when used in conjunction with the anti-coning disc, the chart of Figure 9.9 shows the thermal power dissipated during a drag brake application at 30 km/h (150 min^{-1}) when the friction surface reaches 600°C . The chart shows the contributions of each mode of heat dissipation, the results are obtained using the methods developed in Chapter 8. The total thermal power dissipated when using the modified wheel assembly is increased by 14%.

Standard wheel assembly

Total heat dissipation $Q_T = 9.4\text{kW}$

Modified wheel assembly

Total heat dissipation $Q_T = 10.9\text{kW}$

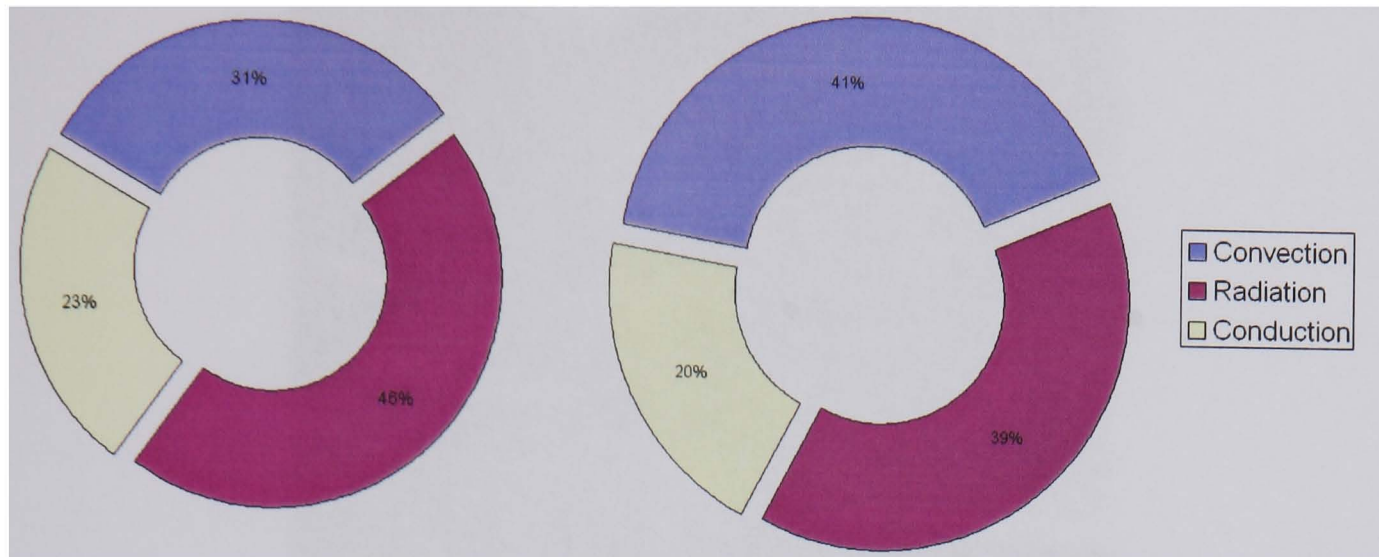


Figure 9.9 Thermal power distribution of the anti-coning disc at 600°C rotating at 150 min^{-1}

Airflow Visualisation

Flow visualisation provides qualitative global pictures of the flow without introducing probes, which invariably disturb the flow. Single component air velocity measurement gives no indication of flow patterns and direction; to study these details a smoke machine has been used (described in Chapter 3).

Smoke tests were conducted at 50 min^{-1} ; a relatively low rotational speed is necessary to avoid a break up of smoke particles in turbulent flow. Smoke was introduced to the anti-coning radial vane CV brake assembly with the SAF ventilated wheel carrier (similar to the modified standard wheel carrier, see Chapter 3 for details), to visualise the flow pattern at the ventilation holes of the wheel assembly and the ventilation channel inlet. Figure 9.10 shows, (a) the airflow into wheel carrier ventilation holes, (b) airflow exiting wheel ventilation holes, and (c) airflow into vane inlet. It is clear from Figure 9.10a, that air is drawn into the wheel assembly through the ventilation holes of the wheel carrier. Air is drawn into the wheel assembly by the ventilated disc, which is acting as a centrifugal pump as shown in Figure 9.10c. Figure 9.10b shows that air is exiting the wheel assembly through the wheel ventilation holes; this air is forced out of the wheel cavity by the air exiting the disc ventilation channel.

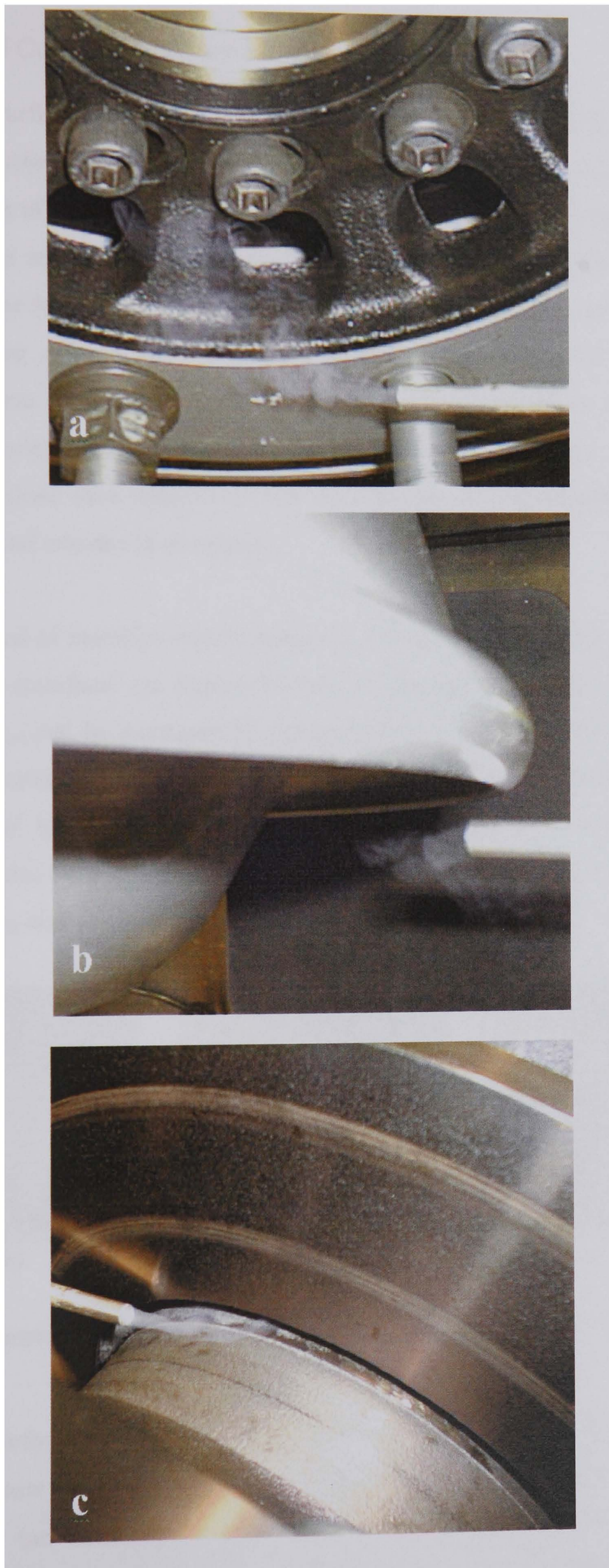


Figure 9.10 Airflow visualisation tests around the anti-coning CV disc

9.3.2 Thermal Contact Resistance

The interface surfaces of the disc and wheel carrier are not perfectly flat or smooth, causing a reduction in the conductive heat transfer coefficient (h_{cond}). The influence of the condition of contact surfaces on h_{cond} has been studied for newly machined and 'normal vehicle service state' (somewhat corroded) disc/carrier contact surfaces. In order to increase h_{cond} , high thermal conductivity paste is available and similar effect maybe achieved using a thin aluminium gasket. These interstitial materials can increase the area of micro contact and fill the surface interstices as discussed in Chapter 6. In order to increase h_{cond} at the disc/wheel carrier interface, three modified interface conditions were tested. Six tests were performed at three disc temperatures, each test required one day to complete.

The first method of interface conditioning was the insertion of a thin aluminium foil 'gasket' at the interface; see Figure 9.11(c). As discussed in Chapter 2 it has been shown that h_{cond} can be increased by a factor of up to seven by inserting a metallic foil at the interface. Aluminium foil is made from 99.5% aluminium (European Aluminium Foil Association 2002) and is of high conductivity as shown in Table A1, aluminium is also very soft providing good contact at the interface surface. The foil used in the tests was 15 μ m thick, standard kitchen foil.

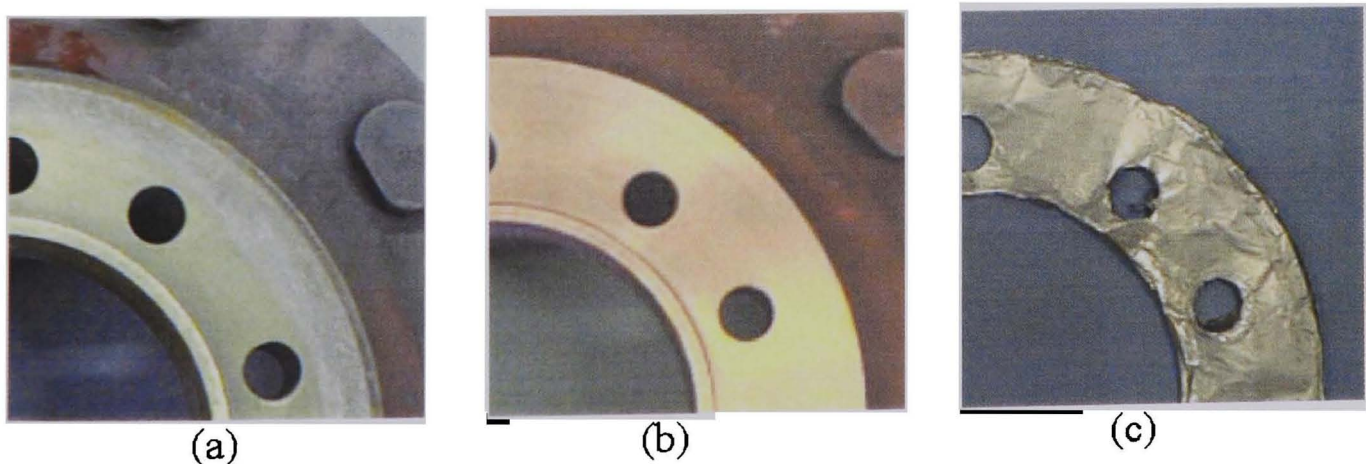


Figure 9.11 Interface conditions, (a) corroded (b) new machined (c) aluminium foil gasket

The second method of interface conditioning involved the use of a high thermal conductivity paste to increase h_{cond} , this has the added benefit of easy application by brush or spay (an advantage in the vehicle servicing environment). A heat sink compound has been used in the experiments; a two metal oxide filled paste of high

thermal conductivity, approximately 35 times higher than air at 20°C. The paste is commonly used to improve heat transfer between semiconductor devices and heat sinks. The paste is chemically inert, shock absorbent, and moisture repellent with long-term stability. The compound contains a silicone base reducing any contamination risk. The manufactures specification is shown below in Table 9.1, unfortunately specific heat and density values were not available.

Table 9.1 Technical specification of heat sink compound

| Property | Silicone Heat Sink Compound |
|----------------------|-----------------------------|
| Dielectric strength | 18 kV/mm |
| Volume resistivity | 10^{15} W cm |
| Thermal conductivity | 0.9 W/mK |
| Temperature range | -100 to +200°C |

The third method tested for improving conduction across the interface was the machining of the interface surfaces (shown in Figure 9.11b). This allows the measurement of h_{cond} for an ‘as new’ interface condition. This process permits the removal of corrosion on the surface and a reduction of the surface roughness. Improving the surface finish increases the contact area at the interface. Table 9.2 shows the measured surface finish for the two test specimens, at the disc and carrier interface

Table 9.2 Brake assembly interface surface finish

| Component | Surface Condition | Surface Finish, Ra, [μ m] |
|---------------------------|--|--------------------------------|
| Front CV disc | As supplied (new machined) | 2.0 |
| Standard CV wheel carrier | As supplied (some corrosion), Figure 9.11(a) | 1.0 – 3.3 |
| | Machined, Figure 9.11(b) | 2.1 |

Measurements of h_{cond} were taken at three temperatures, in the range of 70 to 180°C for all three modified interface conditions, using the same procedure as described in Chapter 6. Average h_{cond} values have been used to compare the modification techniques. Figure 9.12 compares the average h_{cond} at this temperature range for the

four interface conditions tested at the nominal interface pressure (at a 300 Nm bolt torque). The chart clearly shows the increase in average h_{cond} for the modified interface conditions. The average h_{cond} values range from 7 to 67 kW/m²K. All three interface modifications increased h_{cond} . The ‘base’ corroded condition has an h_{cond} value of 7 kW/m²K. The use of aluminium foil provides the highest increase in h_{cond} (approximately 10 times higher) with an average value of 67 kW/m²K. Next, is the use of heat sink paste with an average value of 59 kW/m²K (approximately 9 times higher). Finally, the machining of the disc surface increased h_{cond} with an average value of 12 kW/m²K (approximately 40% higher). The sequence shown in Figure 9.12 indicates the possible variation in h_{cond} for the life of the vehicle, from the new interface to the corroded interface.

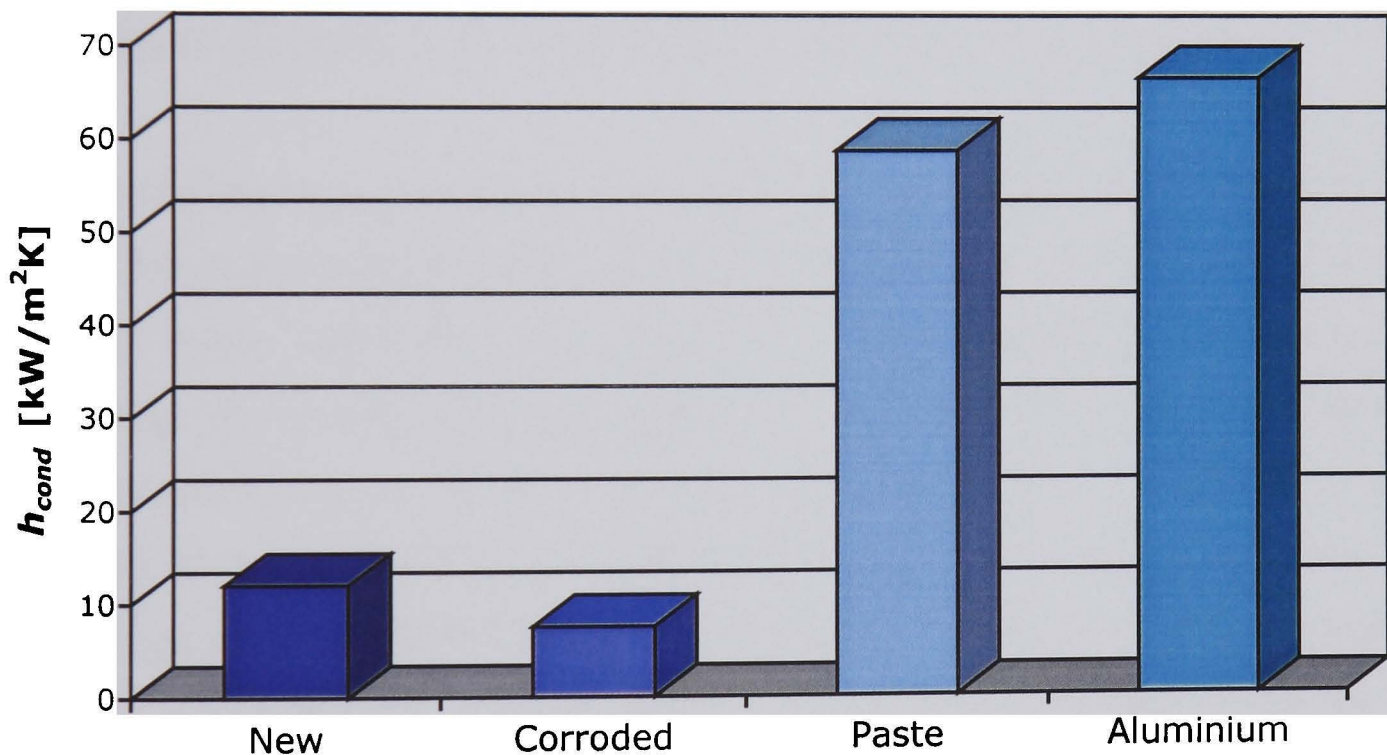


Figure 9.12 Average h_{cond} at the CV disc/wheel carrier interface at the nominal bolt torque (300 Nm)

9.3.3 Simulation of Modified CV Wheel Assembly

The influence of the above methods of improving convective and conductive heat dissipation on disc temperatures during braking has been examined. The standard CV brake assembly has been modelled for two different ECE Directive 13 brake tests. Seven route simulations were performed, requiring 40 hours of computer time.

9.3.3.1 Component Materials

Conduction plays an important role in brake disc heat dissipation, especially at high disc temperatures and low vehicle speeds, as shown in the contribution of the heat dissipation mode charts of Chapter 8. Conduction is increased with increase in material conductivity, contact area and temperature gradient (as defined in Chapter 6). Contact area and temperature gradient cannot be easily increased to improve conductive heat dissipation and a more feasible option is to select a material with higher conductivity. Aluminium is widely used as an engineering material, having a good strength to weight ratio and casting and machining properties. Aluminium also has a high conductivity compared to cast irons and steels (3 to 4 times higher, see Appendix A). An aluminium wheel carrier with the same thermal capacity as the standard CV SG iron wheel carrier has only half its mass, corresponding to the saving of 21 kg/axle. Aluminium wheels are widely available and an aluminium wheel carrier design has been considered to optimise brake heat dissipation.

To examine the influence of the use of an aluminium wheel carrier and wheel on conductive heat dissipation from the disc and ultimately on disc temperatures, a repeated brake application was modelled. Three assemblies were modelled comprising of a standard CV grey cast iron brake disc with steel and aluminium wheel assemblies. In the analysis it was assumed that there is no thermal contact resistance at the component interfaces (since h_{cond} is very high) to allow the full potential of the aluminium components to be appreciated. The repeated braking analysis follows the requirements of the ECE Directive 13 Type 1 test for the effectiveness of hot brakes. The energy to the disc corresponds to a deceleration of 3 m/s² from 60 to 30 km/h, with a cycle time of 60 seconds for 37 stops (ECE requires only 20 stops), based on a 16500 kg CV. The front brake was considered and the effects of rolling and air resistance, engine braking and retarder engagement have not been included. The analysis is therefore braking under extreme conditions. The front to rear brake force distribution was assumed to be 50:50.

The FE analysis was based on the model used in Chapter 8 (see Figure 8.22) for the standard CV disc and wheel assembly. The material properties used for the aluminium components are given in Table A1. The lower strength of aluminium (compared with steel) requires an increase in component wall thickness to keep

stresses within safe limits. The wall thickness of the aluminium components was increased by a factor of 1.5 to model more closely, real component geometry. The emissivity value of aluminium is very low compared to steel (up to 10 times lower). This will increase the amount of heat radiated from the disc surface reflected by the wheel carrier and wheel, as discussed in Chapter 7. Further research into the emissivity of aluminium has shown that the values can be as low as 0.04 for a polished plate and 0.07 for a rough plate (Kreith 1986). Higher values are also published; 0.2 to 0.33 for heavily oxidised surfaces (Cengel 1998)). A heavily oxidised aluminium surface has been considered, which is blackened with brake dust, much higher values of emissivity are expected and an estimated value of 0.5 has been used.

Figure 9.13 shows the friction surface temperatures during the brake application for three wheel assemblies, a standard CV grey cast iron brake disc with an all steel wheel assembly, a combination assembly of SG iron wheel carrier and aluminium wheel, and an all aluminium wheel assembly. A small reduction in friction surface temperature is gained from the use of an aluminium wheel but temperatures eventually equal the standard steel assembly. The conduction path from the disc friction surface to the wheel is very long and temperatures at the carrier/wheel interface are relatively low, in the region of 60°C. Therefore, little heat can be absorbed by the wheel. The addition of an aluminium wheel carrier initially increases friction surface temperatures. This is seen during the first 15 stops where temperatures are increased by up to 30°C (a results of radiation reflection). As the heat generated in the disc conducts through the disc hat and into the wheel carrier, temperatures eventually become lower to those found for the standard steel assembly. Eventually a temperature reduction of 10°C is seen after 37 stops. These findings suggest that the aluminium wheel assembly would provide lower friction surface temperatures during long brake applications, e.g. mountain descents.

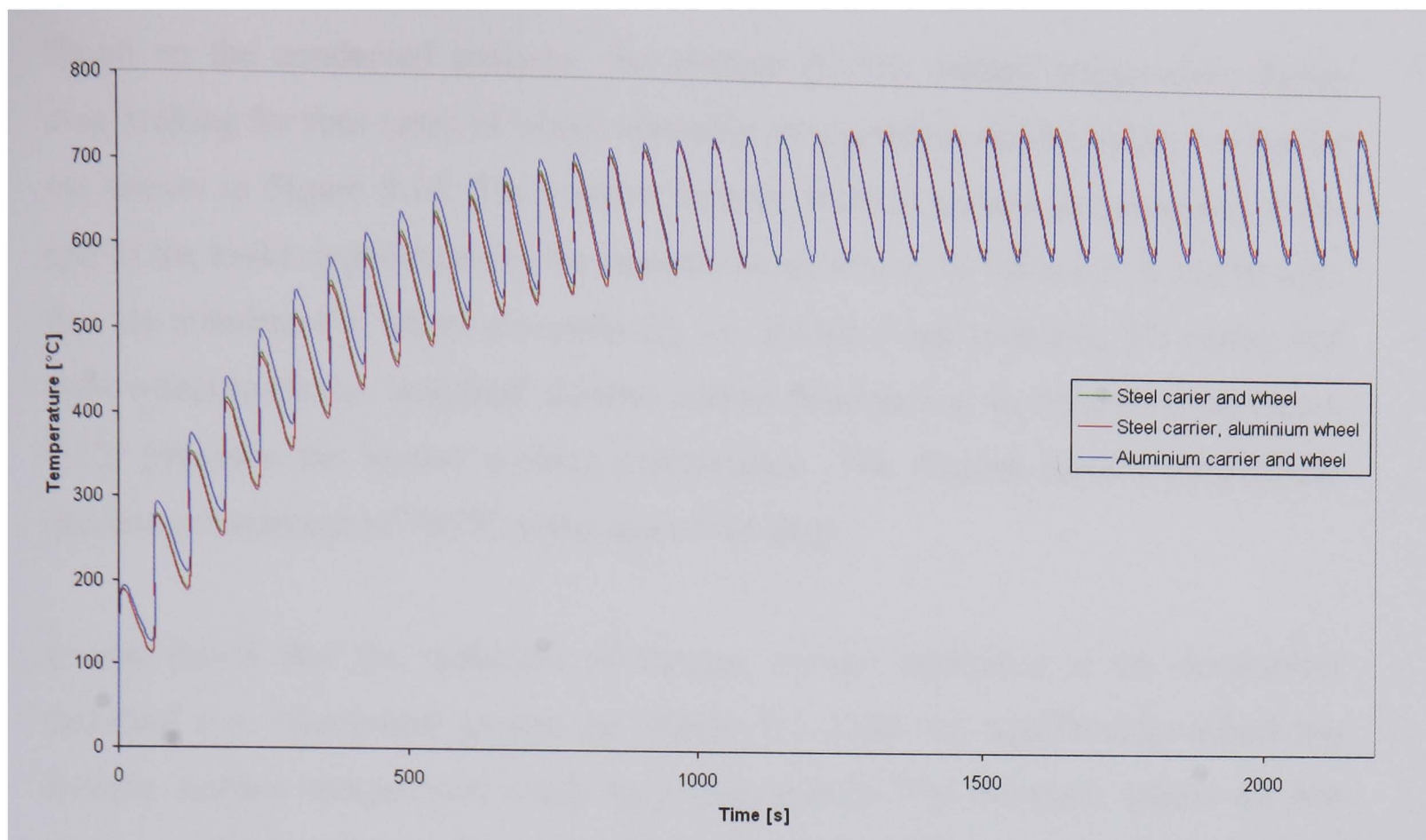


Figure 9.13 Standard CV disc friction surface temperatures with aluminium and steel wheel assemblies

9.3.3.2 Thermal Contact Resistance and Cross Flow

To further examine the influence of thermal contact resistance and wheel carrier ventilation on the heat dissipation and disc temperatures, a drag brake application has been modelled. The drag braking analysis follows the requirements of ECE Directive 13 Type 2 test for the effectiveness of hot brakes following long inclines. The braking energy corresponded to 6 km drag braking at 30 km/h on a 6% incline, based on a 16500 kg CV. The front brake was considered and the effects of rolling and air resistance, engine braking and retarder engagement have not been included. The analysis is therefore drag braking under extreme conditions. The front to rear brake force distribution was assumed to be 50:50.

To model the drag application, an FE model of the wheel assembly has been used, as shown in Chapter 8, with the addition of a layer of interface elements at the component interfaces to model the thermal contact resistance. Numerous analyses have been conducted for different disc, wheel and carrier materials and designs, investigating the influence on temperature rise.

Based on the conducted analyses, the average friction surface temperature during drag braking for four cases of wheel assembly arrangements and boundary conditions are shown in Figure 9.14. The relative average friction surface temperatures at the end of the brake application for the assemblies are shown in Table 9.3. It can be seen that the standard CV wheel assembly (1), i.e. standard cast iron disc, SG carrier and steel wheel (with the 'standard' thermal contact resistance at the interface, see Figure 9.12) provides the lowest cooling performance. The friction surface temperature reaches a maximum of 765°C at the end of the drag.

It was found that the reduction of thermal contact resistance at the disc/carrier interface (i.e. aluminium gasket, see Figure 9.11) did not significantly reduce the friction surface temperature (only by approximately 7°), therefore results are not shown in Figure 9.14 or Table 9.3. However, the modified carrier with ventilation holes (2), combined with aluminium gasket at disc/carrier interface and 2 m/s cross flow reduces the temperature by 72°C. It should be noted that the gains would be much higher with the anti-coning disc fitted.

The use of an aluminium wheel assembly (wheel and carrier) (3) offers some further improvements, although very small. The h_{cond} value was set to the values of the aluminium gasket measurements (see Figure 9.12). The high thermal conductivity of aluminium carrier did improve the conduction heat transfer, but the effect was limited due to relatively low disc material (grey cast iron) conductivity, leading to low disc flange temperatures. Final temperatures are reduced by 79°C, to 90% of the standard assembly.

A more dramatic increase in cooling performance is achieved when the cross flow is further increased to 3.5 m/s (4). Final friction surface temperatures reached were 630°C, a reduction of 135°C on the standard SG/steel wheel assembly. The cross flow value of 3.5 m/s is not considered to be excessive. It is believed that this value can be achieved if the modified wheel carrier with ventilation holes is used. Published airspeed values for cross flow by Fukano and Matsui (Fukano and Matsui 1986) are twice as high (7 m/s) for the passenger car brake during repeated high speed braking applications.

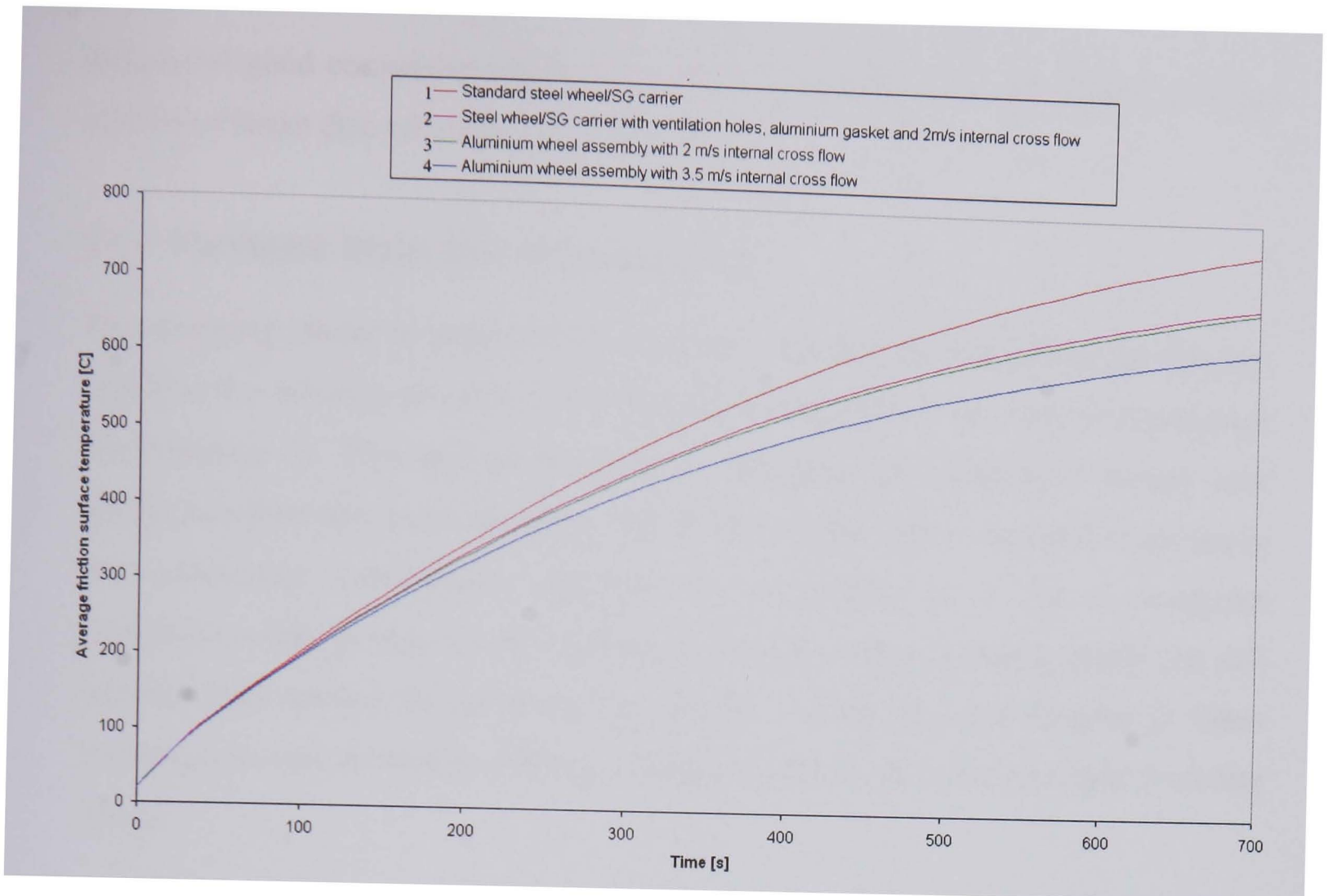


Figure 9.14 Effect of wheel assembly on disc friction surface temperature during drag braking

Table 9.3 Average friction surface temperatures (T_{avg}) and relative temperatures (T_{rel}) values at the end of the drag application

| Assembly | T_{avg} [°C] | T_{rel} [-] |
|----------|----------------|---------------|
| 1 | 765 | 1.00 |
| 2 | 693 | 0.91 |
| 3 | 686 | 0.90 |
| 4 | 631 | 0.82 |

9.4 TGV Railway Disc

Pumping loss is insignificant for commercial vehicles but for the high speed train this is a very important issue, as shown in Chapter 4. Low ventilated disc pumping power loss (Q_{pump}) is necessary for the economic operation of high speed vehicles. Pumping losses can be reduced by restricting airflow through the disc ventilation system but this is at the expense of convective cooling performance (Q_{conv}), which decreases with reduced ventilation airflow. Therefore, a good balance is required and disc design efficiency determined. Different designs are compared based on low pumping

losses and good convective cooling. In order to quantify the above requirement, the ventilated brake disc efficiency ratio is proposed.

9.4.1 Ventilated Brake Disc Efficiency Ratio

The pumping power is proportional to the V_w component of the absolute velocity, which is the velocity of whirl in the direction tangential to the vane circumference (see Chapter 4). This can be reduced by incorporating a backward curved vane design, however this is not an option for the railway disc that is required to operate in both directions. SabWabco's approach to the problem is to use a vane/pillar combination that pumps air onto pillars, the pillars reduce pumping power but still provide good cooling by increasing the 'wetted' surface area (see Chapter 3). Other manufactures use somewhat different designs based on the same principle (avoiding vanes).

To aid the design of large high speed ventilated discs a method to compare the efficiency of ventilation designs with regards to thermal and pumping efficiency an efficiency ratio has been developed. The ventilation system of a ventilated disc affects only the convective component of thermal power loss (radiation is enclosed within the vane channel and conduction is minimal). The ventilation efficiency ratio η_v has been defined as the ratio of convective power dissipation (Q_{conv}) and pumping power (Q_{pump}), by the following equation:

$$\eta_v = \frac{Q_{conv}}{Q_{pump}} \quad (9.1)$$

The ratio η_v increases with increase in convective thermal power dissipation and reduces with increase in pumping power. That is to say, the higher the ratio the more energy efficient the ventilation system is in dissipating heat. The thermal and pumping power are functions of rotational speed; the thermal power dissipation is also a function of disc surface temperature. The ratio η_v for a particular ventilated disc is thus a function of rotational speed and temperature.

Figure 9.15 shows the ratio η_v for the TGV pillared/radial vane disc with a surface to ambient temperature difference ($T_D - T_\infty$) of 170°C, based on Spin Rig results. Thermal power dissipation increases with rotational speed at much lower rate than the pumping power loss, therefore there is a sharp increase in η_v at low speeds.

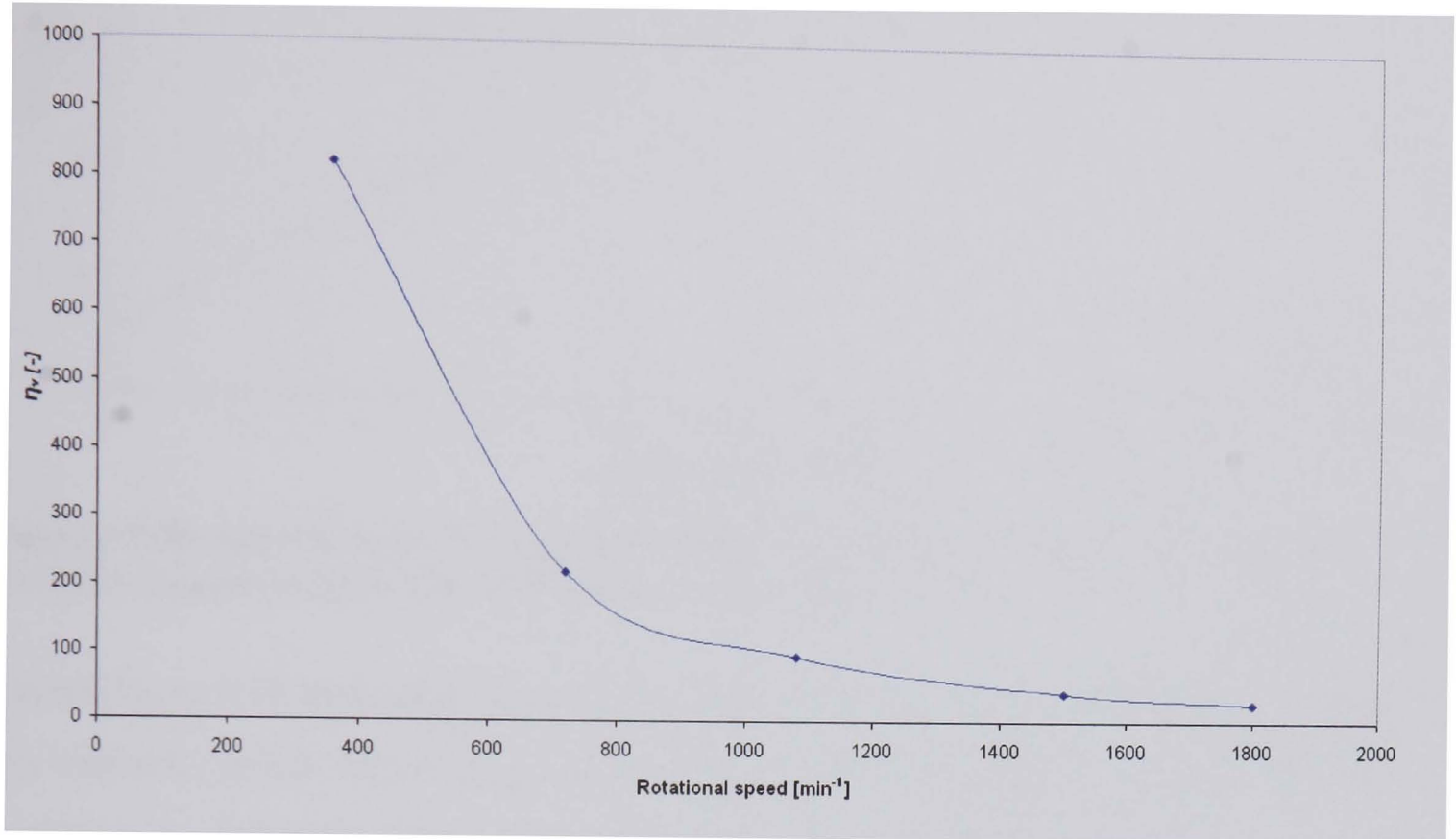


Figure 9.15 TGV pillared/radial vane disc ventilation efficiency ratio η_v

The h_{conv} value can be considered (for the purpose of this ratio) to be a linear relationship with disc angular velocity (shown in Chapter 5). Figure 9.16 shows the equation of the curve for h_{conv} with respect to angular velocity.

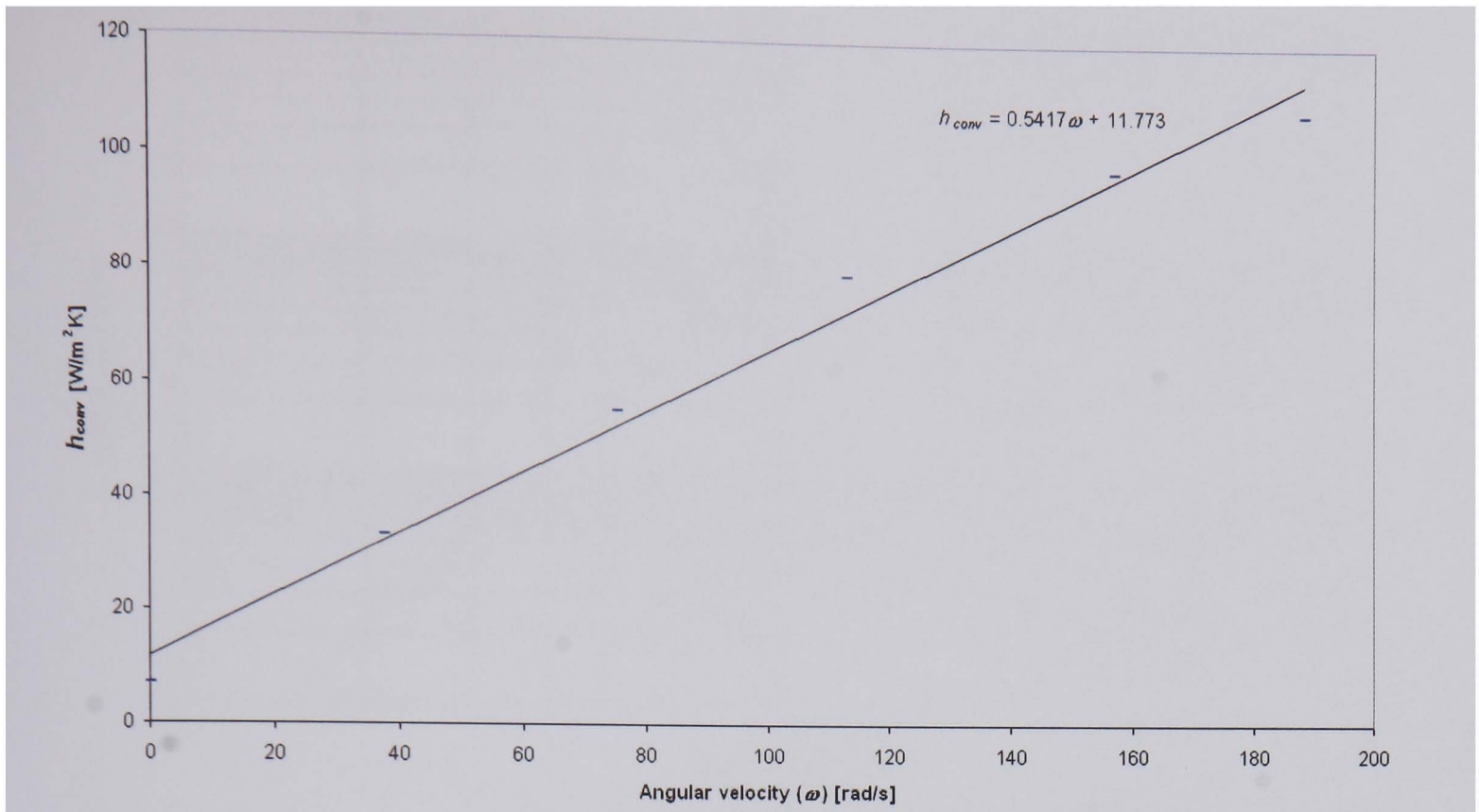


Figure 9.16 Approximate TGV pillared/radial vane disc h_{conv} change with angular velocity (based on Spin Rig TGV disc measurements)

From Figure 9.16 and using equation (5.17) for Q_{conv} the empirical equation (9.2) can be defined, which allows Q_{conv} to be determined from angular velocity and the temperature difference between the disc surface and ambient air ($T_D - T_\infty$).

$$Q_{conv} = (0.5417\omega + 11.77)A_D(T_D - T_\infty) \quad (9.2)$$

If pumping losses are assumed to be constant throughout the operating temperature range (Chapter 4 shows surrounding air temperatures between 20 and 100°C), then Q_{pump} can be found as a function of disc angular velocity only. The Q_{pump} value has a non-linear relationship with angular velocity (see Chapter 4). The relationship can be determined from a logarithmic plot of Q_{pump} , as shown in Figure 9.17.

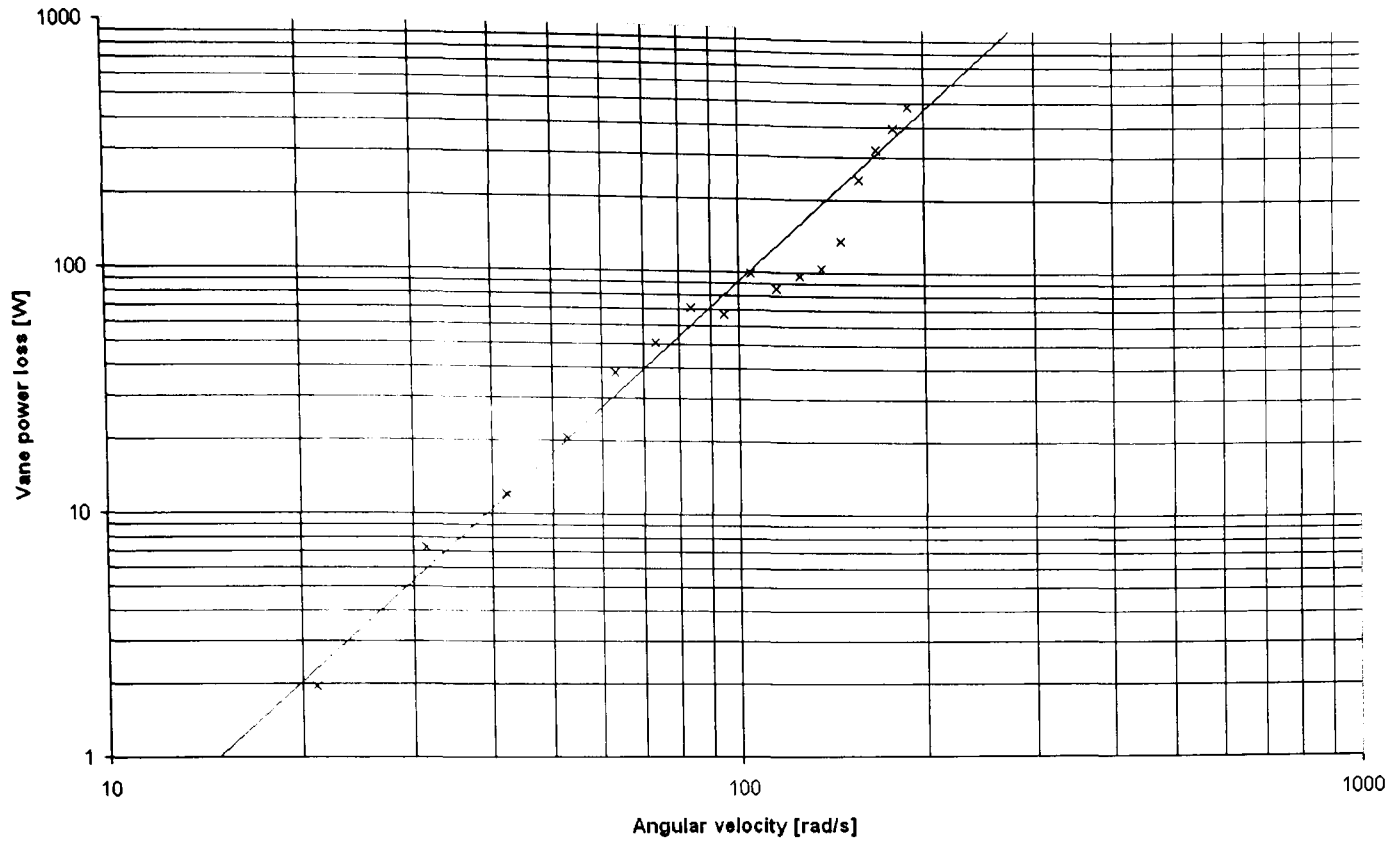


Figure 9.17 Logarithmic plot of TGV pillared/radial vane disc pumping power loss (based on Spin Rig TGV disc measurements)

From Figure 9.17 the empirical equation (9.3) has been determined for Q_{pump} with respect to angular velocity. Equation (9.3) shows that Q_{pump} has an angular velocity relationship of approximately the 3rd power, which is in agreement with the fan theory of Chapter 4.

$$Q_{pump} = 1.946 \times 10^{-4} \omega^{2.94} \quad (9.3)$$

Substituting equations (9.2) and (9.3) into equation (9.1) and eliminating the known surface area of the TGV pillared/radial vane disc that dissipates heat by convection, equation (9.4) can be derived to empirically determine η_v :

$$\eta_v = \frac{(0.7207\omega + 16.4855)(T_D - T_\infty)}{1.946 \times 10^{-4} \omega^{2.94}} \quad (9.4)$$

This can be simplified to equation (9.5):

$$\eta_v = \frac{(3703.49\omega + 84714.78)\Delta T}{\omega^{2.94}} \quad (9.5)$$

Where:

$$\Delta T = (T_D - T_\infty) \quad (9.6)$$

The general form of the η_v ratio equation (9.5) can be written as:

$$\eta_v = \frac{(a\omega + b)\Delta T}{\omega^c} \quad (9.7)$$

Where a , b and c are constants specific to disc design, a is the forced convection component (a function of rotational speed), b is the natural convection component (independent of rotational speed) and the exponent c is the pumping power relationship with rotational speed (a value of 3 for the radial vane design, see Chapter 4).

The ratio η_v is a useful measure of disc ventilation design performance, with high η_v values showing good cooling and low pumping loss. Figure 9.18 shows a comparison of the measured values of η_v for the TGV pillared/radial vane disc and the calculated values of η_v using the empirical formula given by equation (9.5). A good approximation is made for η_v , throughout the speed range of the disc. At very low speeds the calculated values of η_v tend to be lower than measured values of η_v .

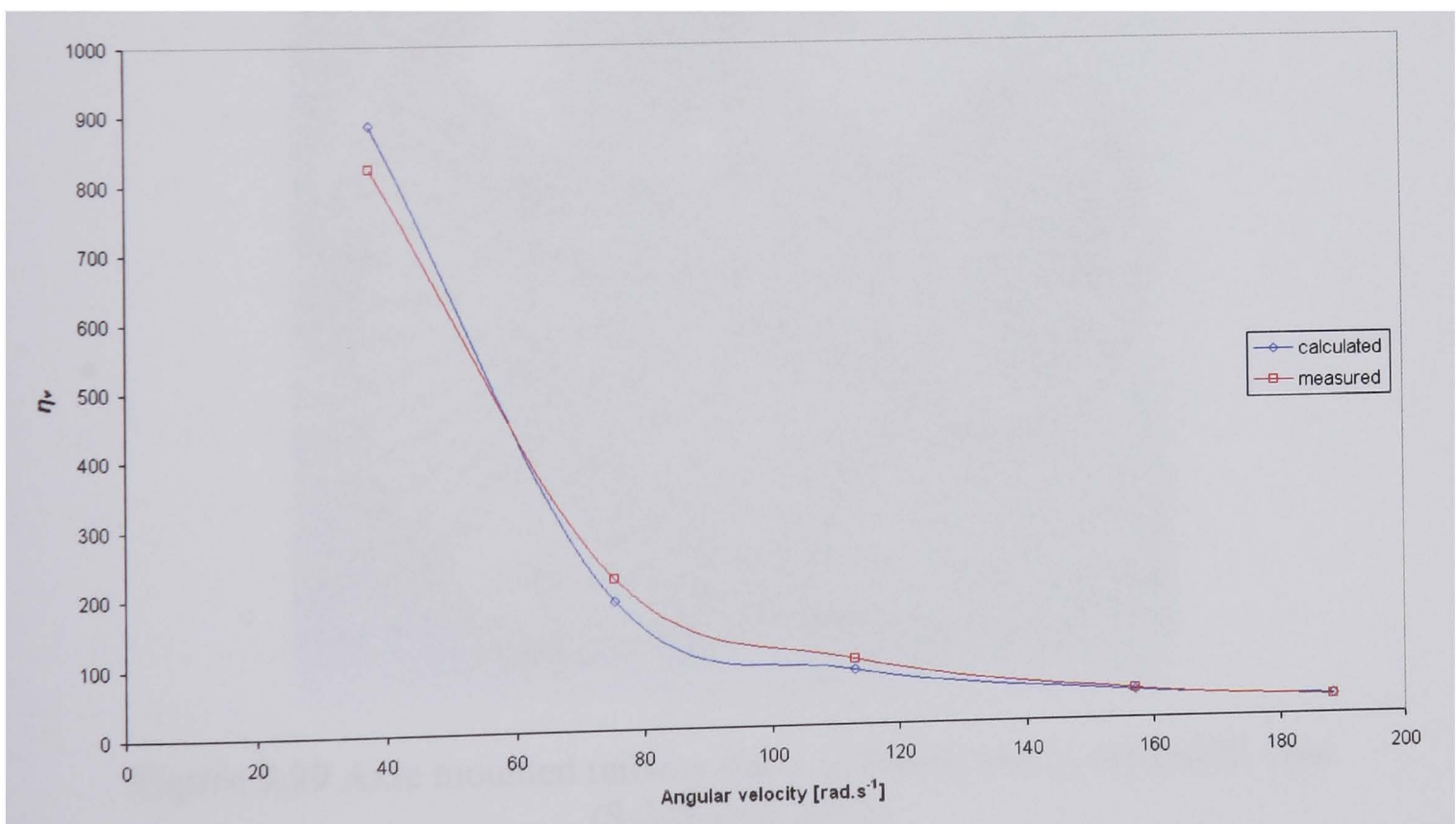


Figure 9.18 Comparison of equation (9.5) and measured η_v values for the pillared/radial vane TGV disc ($T_D - T_\infty = 170^\circ\text{C}$)

9.4.2 Disc Design Comparison

To demonstrate the new vane efficiency ratio (η_v), four axle mounted railway disc designs (radial/pillared vane, radial vane, tangential vane, and solid disc) have been investigated and η_v has been compared for the operating speed range. Details of the radial/pillared vane disc are given in Chapter 4. The (a) radial and (b) tangential vane discs are shown in Figure 9.19. The solid disc is not shown but has the same internal and outside diameters as the other three discs. The pumping and convective cooling losses for the ventilated discs are based on data published by SabWabco (Watson 2002), which give cooling rates and pumping losses for each ventilation design up to a rotational speed of 1600 min^{-1} . Pumping loss data for the solid disc is based on Spin Rig data by blocking the inlets and outlets of the radial/pillared disc ventilation channels (see Chapter 4). Convective thermal power loss for the solid disc is based on heat transfer coefficients calculated for the disc surface, equations for a rotating disc and cylinder (Morgan and Dennis 1972) have been used (see Chapter 2).

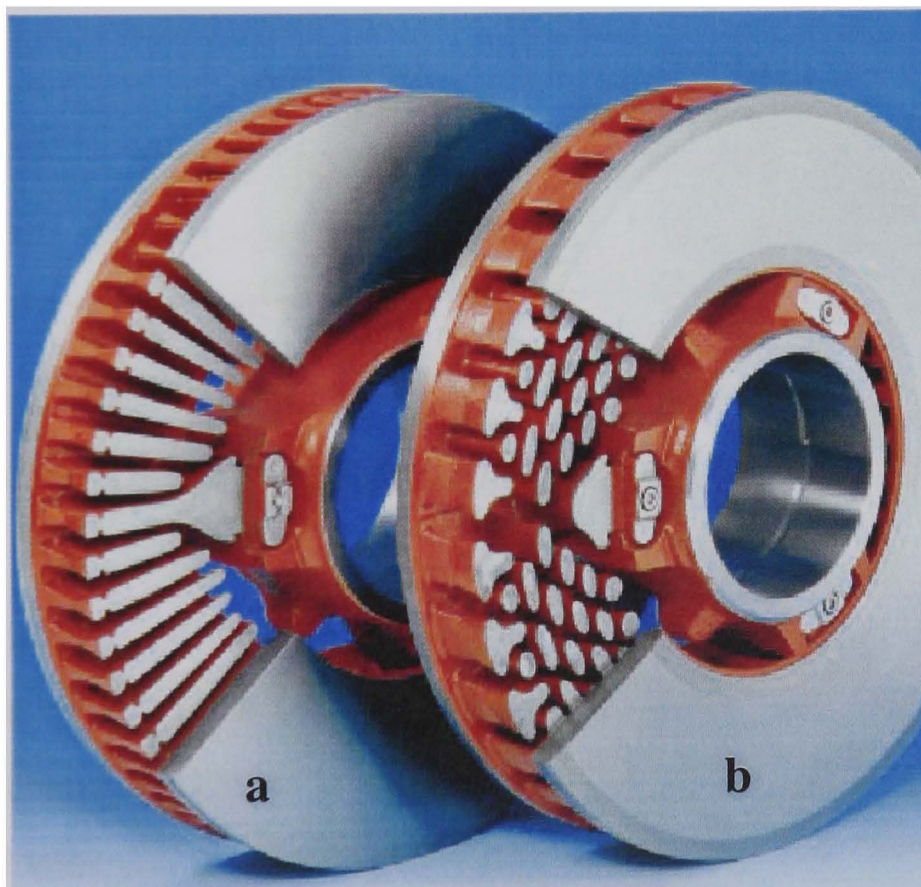


Figure 9.19 Axle mounted railway discs, a) Radial and b) tangential vane (SabWabco 2002)

Figure 9.20 shows the pumping losses (Q_{pump}) for each disc design, Q_{pump} is mainly due to ventilation channels and increases with rotational speed. The radial vane disc shows very high losses, 4.92 kW at 1600 min^{-1} . The solid disc (unventilated disc)

shows relatively low Q_{pump} values of 0.32 kW at 1600 min^{-1} , resulting from surface drag and resistance at the mounting bolts and lugs. The radial/pillared disc shows the lowest Q_{pump} values for the ventilated discs, showing a value of 0.82 kW at 1600 min^{-1} . The tangential vane disc has a higher Q_{pump} value, 1.63 kW at 1600 min^{-1} .

At 600 min^{-1} the radial vane disc still shows a high Q_{pump} value of 0.24 kW, Q_{pump} values of the other designs become negligible below this speed. Below 500 min^{-1} all designs show negligible Q_{pump} values.

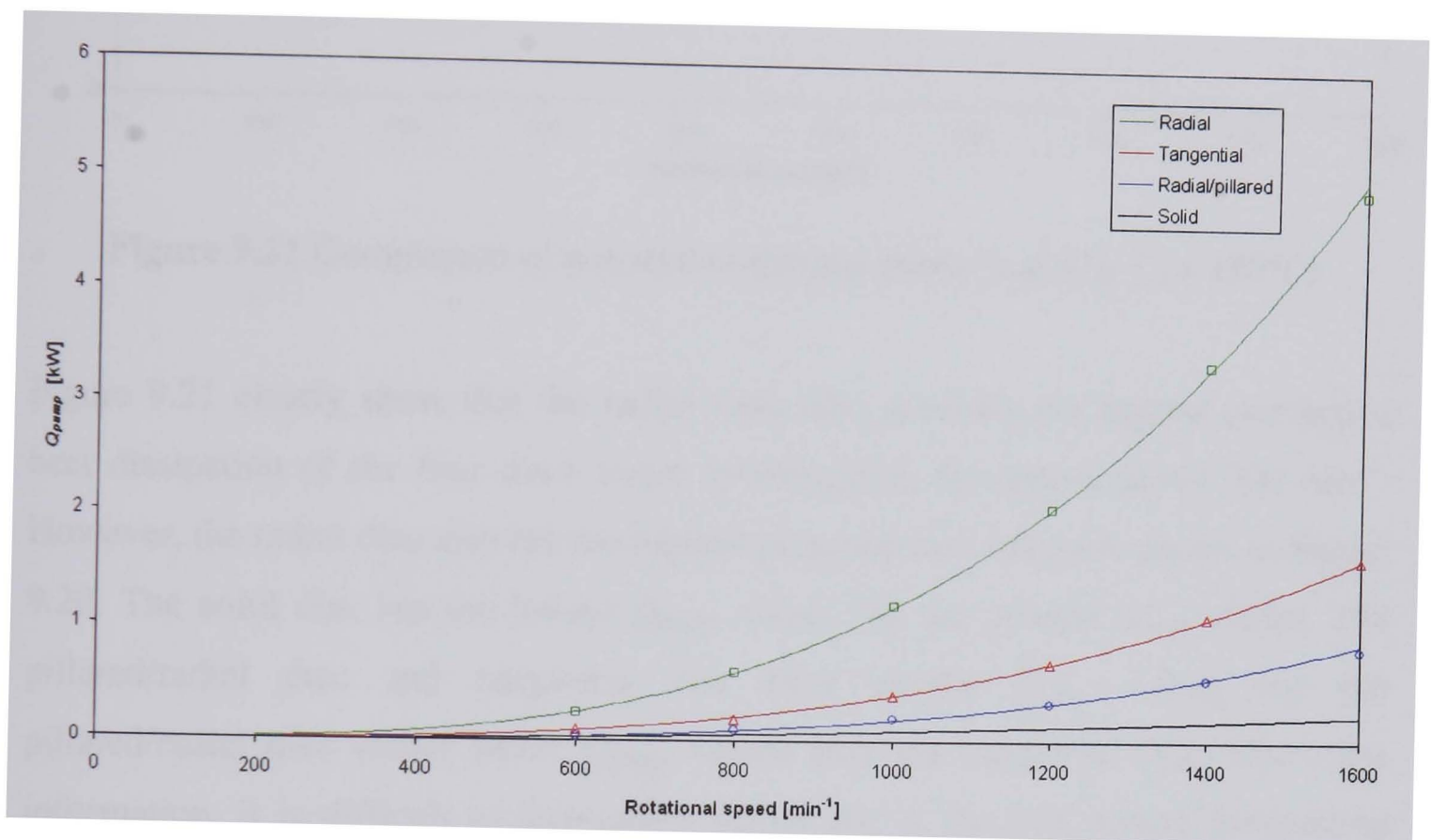


Figure 9.20 Comparison of disc design pumping losses

Figure 9.21 shows the convective cooling losses (Q_{conv}) for each disc design for a disc temperature of 200°C . It can be seen that the radial vane disc has the highest Q_{conv} values, reaching 75 kW at 1600 min^{-1} . At low rotational speeds, less than 300 min^{-1} , the radial vane disc design blocks natural convection and does not cool as well as the other ventilated discs (pillared/radial and tangential vane). The pillared/radial and tangential vane discs show very similar cooling characteristics throughout the speed range. The radial/pillared vane disc has a higher (1.3%) Q_{conv} value (56.6 kW) than the tangential vane disc at 1600 min^{-1} . The solid disc shows the lowest Q_{conv} values, with a Q_{conv} value of 39 kW at 1600 min^{-1} , which is 48% lower than the radial vane disc.

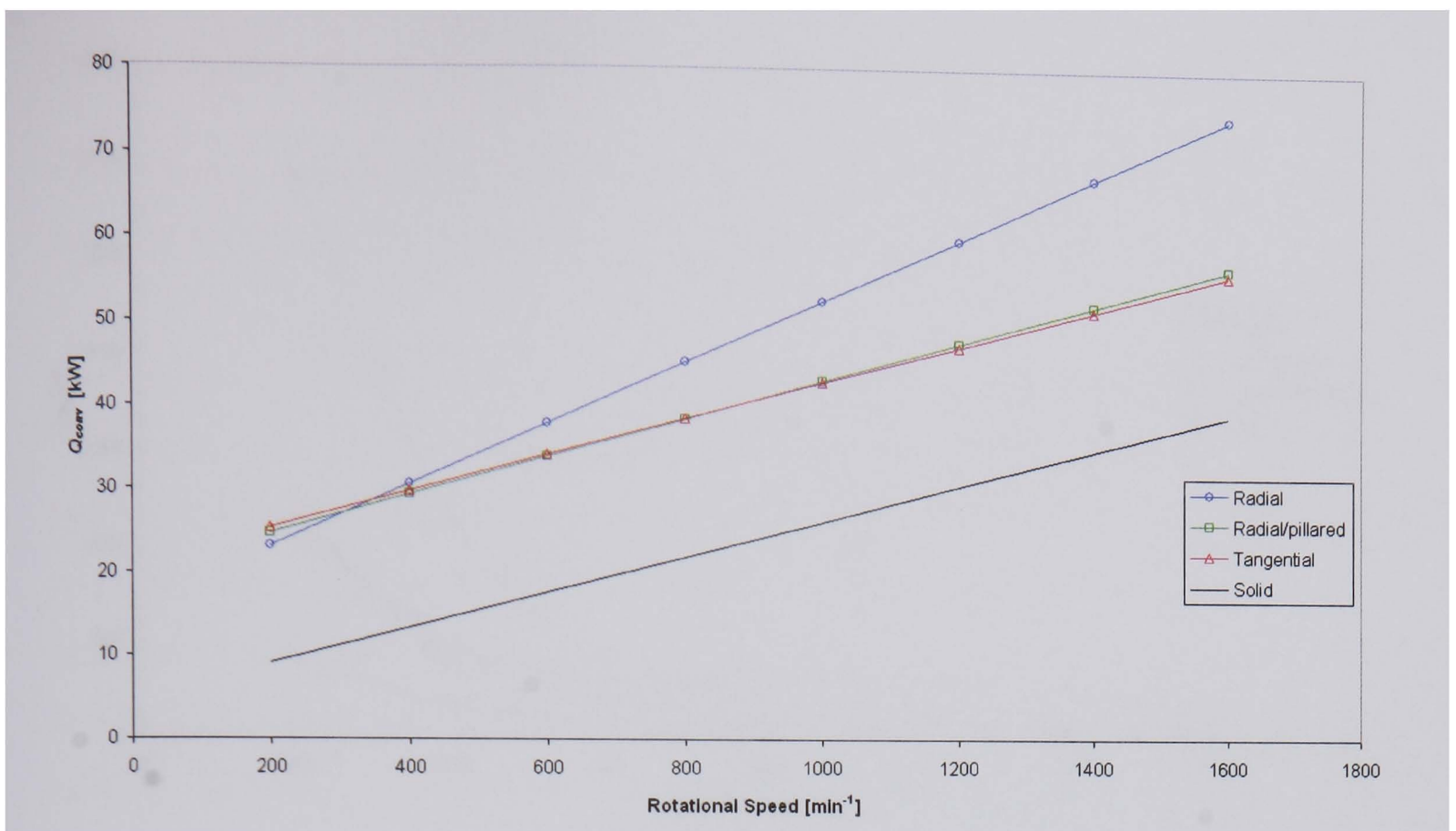


Figure 9.21 Comparison of convective thermal power loss ($T_D - T_\infty = 180^\circ\text{C}$)

Figure 9.21 clearly show that the radial vane disc provides the highest convective heat dissipation of the four discs under investigation, for speeds above 300 min^{-1} . However, the radial disc also has the highest pumping loss values as shown in Figure 9.20. The solid disc has the lowest Q_{pump} values but the poorest Q_{conv} values. The pillared/radial disc and tangential disc have similar Q_{conv} values but the pillared/radial disc shows better Q_{pump} values than the tangential disc. From this information, it is difficult to distinguish which disc is the best overall performing disc (most energy efficiently dissipating heat). This is where the η_v ratio can help; Figure 9.22 shows the η_v ratio calculated using equation (9.1) for each disc based on the Q_{conv} and Q_{pump} values. The η_v ratio clearly shows that the pillared/radial vane disc provides the best overall performance at rotational speeds below 800 min^{-1} . At higher speeds the solid disc has the highest η_v value, this is a result of the low pumping losses compared to the high pumping losses of the ventilated discs.

Below 800 min^{-1} , η_v values increases, with a reduction in rotational speed, for all disc designs. At 400 min^{-1} the pillared/radial disc has an η_v value of 2915. The tangential vane and solid discs show lower values (approximately 60% lower) of 1185 and 1110 at the same speed. The radial vane disc is least efficient (86% lower than the pillared/radial disc) with an η_v value of 405 at 400 min^{-1} .

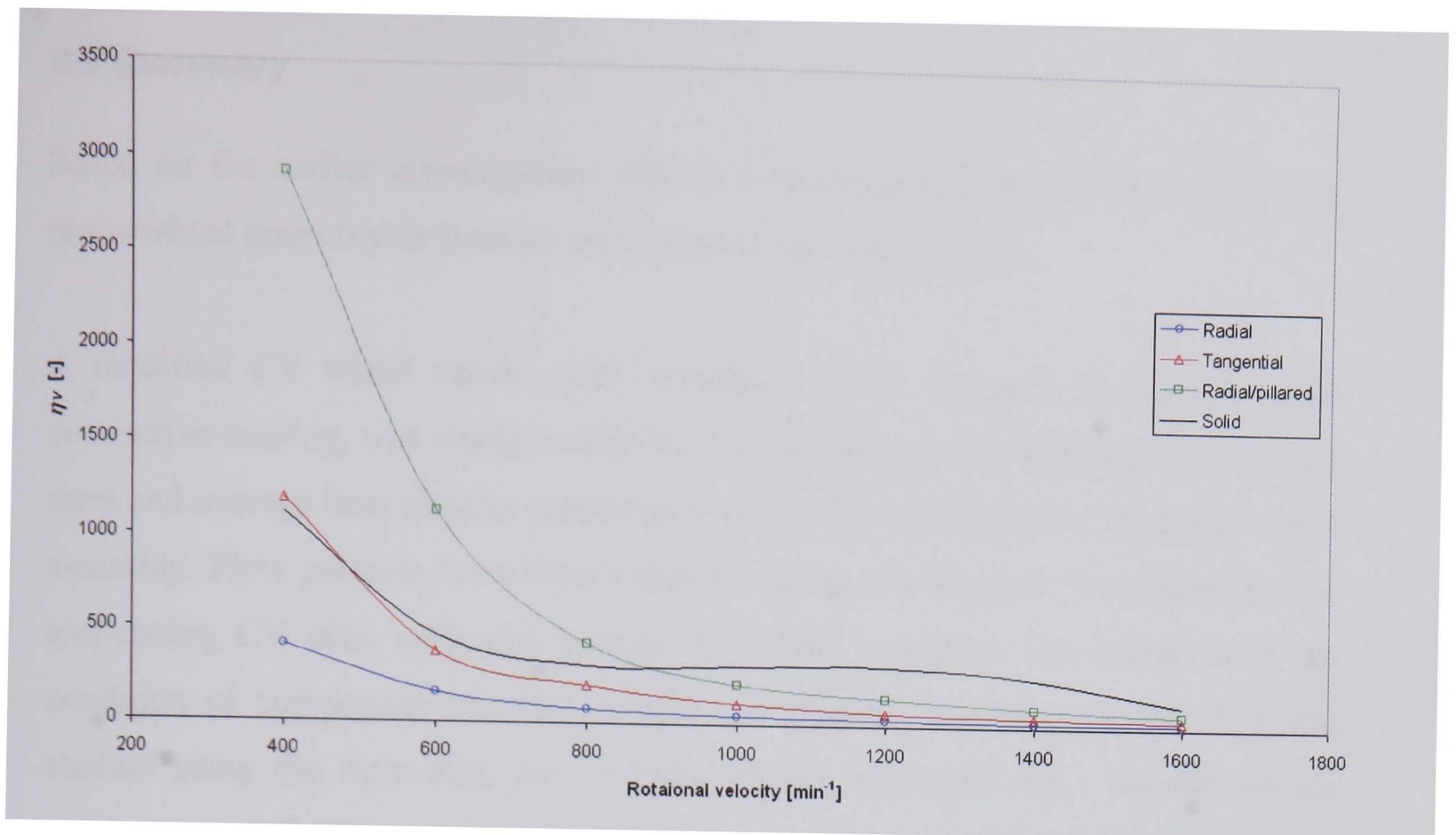


Figure 9.22 Comparison of ventilation design efficiency ratios

Figure 9.22 shows the η_v ratio to be very useful as a method of ranking ventilation designs throughout the speed range. This is highlighted in the case of the pillared/radial and tangential discs. Both discs dissipate heat equally well (see Figure 9.21), but when considered along side the pumping losses it is clear that the pillared/radial disc is far superior in overall performance. This is shown for the speed range of the disc in Figure 9.22.

The η_v ratio provides a method of selecting the best ‘overall’ performing disc for the required speed range. It should be noted that the cooling requirements must be first considered before consulting the η_v ratios. Another consideration is disc thermal capacity, assuming the compared disc designs are of the same material, the disc mass will have an effect on the disc cooling rate.

It must be emphasised that η_v , particularly when discs with similar characteristics are compared, can be determined based on CFD analysis. This can be done in the early design stages before any prototypes are made.

9.5 Summary

Based on the earlier investigations effective modifications have been made to the brake/wheel assembly to increase and optimise heat dissipation.

A modified CV wheel carrier with ventilation holes, designed to increase brake convective cooling, was studied with two disc designs on the Spin Rig. The cooling rates and average heat transfer coefficients were compared with the 'standard' wheel assembly. Flow patterns have been examined using visualisation techniques for the anti-coning CV disc, with and without the wheel assembly. The influence of the condition of component interface surfaces on thermal contact resistance was also studied using the Spin Rig, and included newly machined and 'normal vehicle service state' disc/carrier contact conditions. In order to increase conductive heat dissipation, high thermal conductivity paste and the use of a thin aluminium gasket at the interface have been tested. FE route simulations of the modified CV wheel assembly have been performed to study the effect on brake temperatures.

It has been shown that the novel ventilated wheel carrier vastly improves the cooling rate of the anti-coning CV disc and can also improve the cross flow over the disc surface. The measurement of thermal contact resistance for the modified interface conditions showed that very substantial improvements in the conductive heat transfer coefficient can be achieved. FE simulations studying the influence of proposed design modifications have demonstrated that heat dissipation can be substantially improved. Very good agreement has been achieved when comparing the calculated and measured ventilated disc efficiency values.

The final FE temperature results have enabled the evaluation of actual gains in brake cooling for the braking duties modelled, as a result of introduced design changes. It has been shown that proposed methods provide real improvement of heat dissipation. A method for ranking ventilated disc performance using efficiency ratios, based on heat dissipation and pumping efficiency, has been developed. This is a particularly important parameter for large and fast rotating high speed vehicle discs such as the high speed train TGV disc. Appropriate mathematical relationships established for convective heat and pumping losses, lead to the equation for ventilated disc

efficiency, as a function of disc rotational speed and temperature. Four types of disc design have been evaluated using this proposed ranking method.

Conclusions and Recommendations

10.1 Introduction

This thesis presents research into the understanding and improvement of heat dissipation from friction brakes. The problems of adequate brake cooling are associated with all brake types and despite the very practical aspects of this research, a ‘generic heat transfer approach’ was applied, not restricting the findings to friction brakes, or specific brake designs. All relevant parameters were considered, measured and recorded in order to provide a wider knowledge base for all modes of heat transfer. As a result, methodologies have been developed for determining disc brake airflow and cooling characteristics both experimentally (Spin Rig, dynamometer) and theoretically (analytically, CFD, FE). These generic methods are effective design tools for the development of new disc brakes.

10.2 Conclusions

Spin Rig

A dedicated Spin Rig, designed, built and commissioned for the measurement of brake heat dissipation and airflow characteristics, proved to be very valuable equipment, enabling accurate and repeatable tests to be performed. This facilitated the establishment of the differences in performance between very similar brake designs and the analysis of all modes of heat transfer.

Airflow

A procedure has been developed for pumping losses and airflow measurements, for a variety of brake discs, on the Spin Rig. Experiments clearly showed the differences in flow characteristics for the compared CV discs, which rotate at relatively low speeds. The anti-coning disc design is frictionally the most desirable, low coning enabling equal pad/disc wear and judder free operation. Its cooling characteristics are similar to the standard disc when rotating in free air, but when considered within wheel assembly (as used on the vehicle), its cooling characteristics are affected due to restricted air supply. Experiments conducted on the TGV frequently stopping disc (incorporating radial vanes and pillars) provided valuable data concerning pumping losses and air speeds. This, large railway disc for high speed trains, requires particular attention regarding airflow, since high rotational speeds result in considerable pumping losses.

Prediction of airflow characteristics using analytical methods can be very fast and relatively accurate for discs with continuous (from ID to OD) vanes. CFD has shown to be a very powerful tool for studying airflow for discs with different ventilation system designs (vanes, vanes and pillars). Experimental verifications proved that accurate CFD prediction of disc aerodynamic characteristics is possible at moderate costs. The developed methodologies provide effective airflow and power requirement predictions.

Convective Heat Dissipation

An accurate and very efficient procedure has been developed for establishing convective cooling characteristics in Spin Rig tests. Calculated average heat transfer coefficients, as a function of temperature and rotational speed, enabled comparison of convective cooling for variety of CV discs. This showed that literature claims of the superiority of discs with curved vanes are untrue for commercial vehicle applications, where vehicle speeds are quite low. It must be noted that the wheel assembly (compared to free air cooling) has the most detrimental effect on convective cooling of the anti-coning disc design. This negative effect can be rectified by using a ventilated wheel carrier, which dramatically improves cooling, up to the levels for the disc rotating in free air. TGV disc measurements also provided valuable information, the high disc thermal capacity requiring a different disc heating method.

Developed CFD methodologies showed that efficient cooling predictions can be made in an economical way. Predicted average convective heat transfer coefficients were very close to the values measured on the Spin Rig. The advantage of the CFD modelling is the ability to investigate local heat transfer coefficients and airflow, to improve cooling. The biggest advantage is that CFD modelling can be performed in the design stages, for efficiently generating novel disc designs.

Based on performed experiments, literature studies and CFD analyses, the most suitable procedures and formulas have been recommended for determining convective heat transfer coefficients. This allows comparative analysis of design changes and the determination of the most efficient design improvements for specific duties and applications.

Conductive Heat Dissipation

The review of published work has shown that conduction is the least studied mode of heat transfer, leading to often crude and inadequate brake thermal modelling. Performed research, which included temperature measurements, interface pressure distributions studies (measurements and FE analyses) and surface conditioning of the disc/wheel carrier interface, vastly improved the knowledge and understanding of

this heat transfer mode. Conduction can be a very important cooling mode and certainly should not be neglected. Interface conditioning offers an inexpensive way of substantially increasing this mode of heat dissipation, which should be exploited (if found appropriate), in variety of brake designs and applications.

Conducted research resulted in the development of the procedure for studying this mode of heat transfer. Equally importantly, a generic formulae for calculating conductive heat transfer across a bolted joint, has been established. Based on theoretical (FE) prediction of the interface pressure distribution, conductive heat transfer can be accurately predicted for a variety of brakes and general engineering assemblies, at the very early design stages. This offers a variety of possibilities for design enhancements.

Radiative Heat Dissipation

Experimental studies, performed on the Spin Rig, showed a substantial variation of emissivity values, not only for different disc surface conditions, but also for different temperatures. This confirmed the results of a recent published work about the emissivity variations during a drag brake application. Investigations showed the importance of adequate emissivity values for accurate temperature predictions. Finite element modelling showed that a substantial part of energy emitted by radiation can be reflected back to the brake disc.

Based on research findings, recommendations have been made for radiative heat dissipation modelling by including adequate emissivity values and variations with surface condition and temperatures, as well as the effect of surrounding components.

Cooling Performance Simulations

The integration of the findings for the individual modes of heat transfer enabled the conduction of route simulations in order to validate the overall research work. The comparison of the analytical and FE temperature predictions with the dynamometer data showed very good overall agreement. However, the complexity of temperature measurements at the friction surface and variety of influencing factors cause

difficulties in conducting these comparisons. A methodology for addressing the performance of rubbing thermocouples has been developed.

It has been shown that the use of temperature dependent material properties has a substantial influence on predicted temperatures. It has also been shown that thermoelastic instability simulated heat input does not have a significant effect on the predicted heat dissipation. This is the result of small amount of heat dissipated during braking and fast disappearance of the 'hot spots' due to relatively high disc thermal conductivity. Even for drag brake applications, the influence of thermoelastic instability effects on brake cooling is very limited.

The measurements and analyses enabled accurate determination of the contribution of individual heat transfer modes in total heat dissipation. In most vehicle service conditions, the majority of heat is dissipated by convection. However, conduction and radiation must not be neglected, as they can be the primary modes of heat dissipation at low vehicle speeds and high temperatures. Detailed studies of all modes of heat dissipation enabled accurate temperature predictions in all braking conditions. Brake design features which have scope for improvement, were established, providing a good foundation for further investigation into heat dissipation optimisation.

Heat Dissipation Optimisation and Improvement

Based on conducted research, effective modifications have been made to the brake and wheel assembly to increase and optimise heat dissipation. A modified CV wheel carrier, with ventilation holes, designed to increase brake convective heat dissipation, demonstrated the highest overall gain in heat dissipation. Conditioning of the CV disc/wheel carrier interface is inexpensive and practical method for dramatically reducing thermal contact resistance and increasing conductive cooling. However, to achieve the full potential, this method should be combined with an aluminium wheel carrier and ideally, higher conductivity disc material (such as aluminium MMC's).

For the high speed ventilated railway disc brake, the balance of pumping losses and convective heat dissipation is shown to be the main area of potential improvement.

The development of an original ventilated disc design efficiency ratio has allowed disc designs to be accurately and efficiently evaluated and compared, even for small differences in heat dissipation and/or cooling characteristics.

The conducted research enables more efficient disc designs to be developed in much shorter time and at lower costs.

10.3 Recommendations for Further Work

Further research work is envisaged in several areas of heat dissipation from friction brakes. Firstly, the practical application of the conducted research is going to take place in a Life Cycle Cost Prediction Project, the process is shown in the form of the flowchart in Figure 10.1. In this Project, currently being established with a railway brake manufacturer, the heat dissipation forms a central part, defined as ‘Thermal Route Simulation’ (Figure 10.1). The project aims to fully define life and cost characteristics of friction pair components, enabling the most cost effective solutions (combinations) to be chosen. Heat dissipation has a crucial role in ensuring, initially, that the friction pair operates within acceptable thermal limits. If this requirement is satisfied, pad and disc lives are predicted for the given operating route. Providing the lives are acceptable, cost optimisation can be conducted by choosing the most cost effective solution.

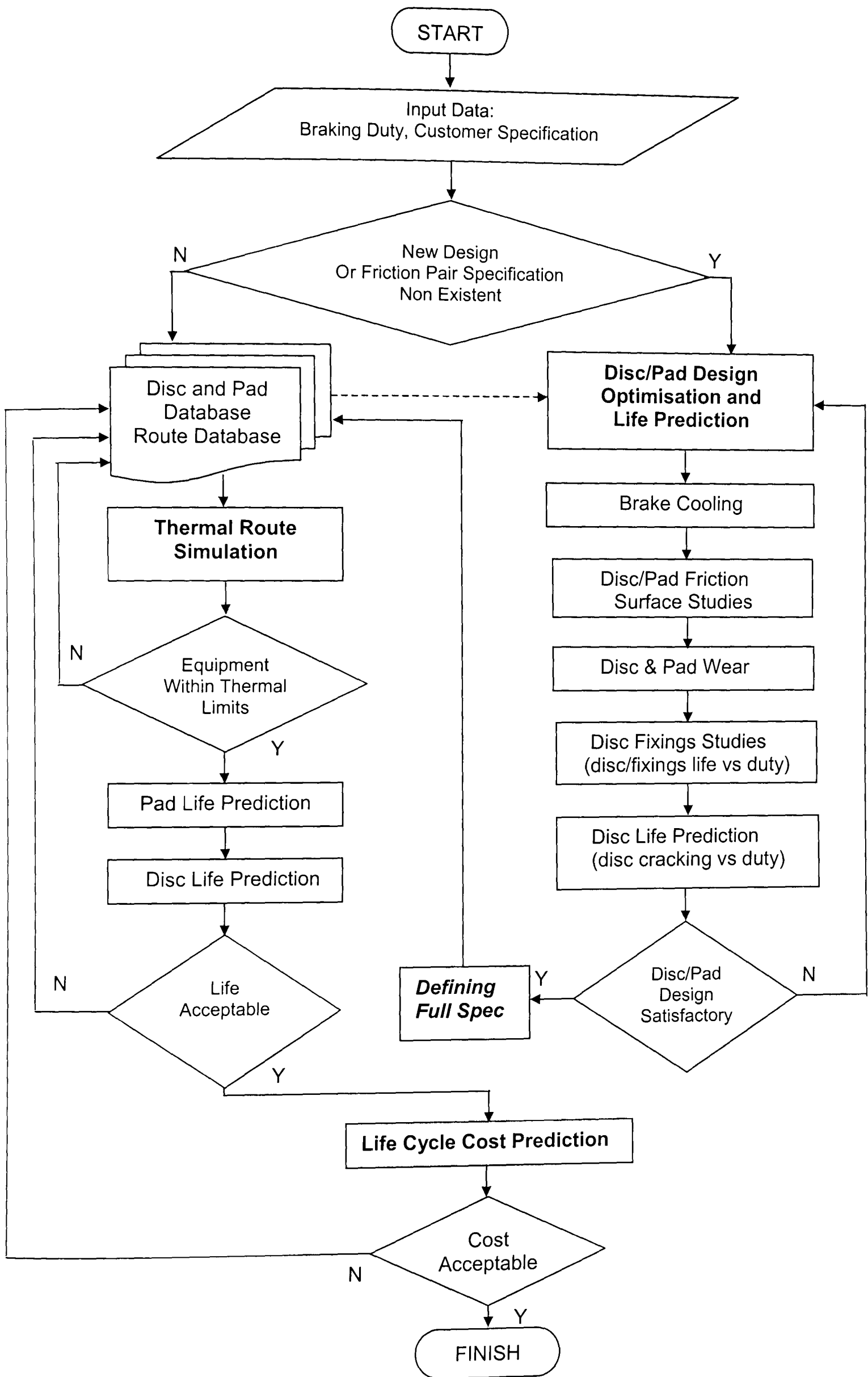


Figure 10.1 Life cycle cost prediction process

Apart from this immediate application, the following areas of heat dissipation from friction brakes are considered to be of prime interest for further research: cross flow investigations, novel disc designs, development of advanced wheel carriers for CV vehicles, road and rail vehicle ventilated disc aerodynamic studies and route simulations. Further work is also envisaged in the study of radiative heat dissipation.

These studies will require further development of the testing facilities, the Spin Rig would require updating to include a more powerful heating system, rotational telemetry and cross flow. Also, development of CFD analyses will improve accuracy and speed of obtaining results. CFD codes are developing fast and part of the further research would require assessment of the most suitable code to be used.

The research presented in this thesis has considered heat dissipation in still air conditions. Although cross flow has no influence on conductive and radiative heat transfer, its influence on convective heat transfer can be substantial. It must be noted that for railway application, the most widely accepted dynamometer procedure is testing in still air, which represents the most demanding environment. This is justified by the very different flow conditions that may exist on brake discs installed in different position on the train rake. However, there is no doubt that cross flow has substantial influence, in particular for high speed trains, therefore further research of complete vehicle aerodynamics combined with disc flow analyses will be required.

Automotive disc cooling characteristics are more sensitive to cross flow, as a result of disc position (within the wheel) and lower rotational speeds. Obviously, cross flow increases convective heat dissipation, however, the cross flow speed around the disc is lower than vehicle speed, and many other factors influence the flow (suspension components etc.). Therefore, the cross flow studies of discs will be only the first step in addressing this issue. Vehicle aerodynamics and flow around the wheels and brakes must be fully understood to provide adequate inclusion of this effect on brake cooling. The research should also investigate the influence of brake callipers (and pads) and dust shields; ventilated CV wheel carrier designs are being addressed by Odell (2003).

Research into novel heat dissipation efficient disc designs, is another important area of future work. The analyses of four different types of CV discs showed the limitations of addressing the problem by investigating only disc flow characteristics. A much more global, combined flow-thermal, vehicle and ‘wheel end’ approach is required. The potential benefits are clearly demonstrated in this thesis.

The four railway disc brakes analysed, showed considerable differences in cooling and pumping characteristics. The developed approach in determining ‘ventilated brake disc efficiency coefficient’ (pumping efficiency) is a good foundation of objectively assessing new disc designs, even with small differences in heat dissipation and/or cooling characteristics. Further work is required to fully explore this approach. The development of a new disc design with adequately ‘balanced’ pumping and cooling characteristics is possible at very little cost, as a result of validated theoretical procedures developed in this project.

Further research is also envisaged for radiative heat transfer. The research presented in this thesis clearly defines a practical approach and gives general guidance in choosing suitable values of surface emissivity. The radiative heat dissipation would require more research to examine emissivity and its variation with temperature and friction surface condition.

Heat dissipation research is also required to better understand the cooling characteristics of brakes made from novel materials, such as carbon fibre ceramic composites. These materials have very different properties from commonly used friction pairs (cast iron, steel and aluminium MMC’s discs combined with sinter or organic pads). Therefore, all modes of heat transfer; conduction, convection and radiation must be carefully studied, taking into consideration issues specific to these materials. It must be noted that fundamentally different material properties and manufacturing methods will result in different optimised disc designs. Until now, the designs of these brake assemblies were led by ‘copying’ existing, commonly used designs. The design changes were mainly influenced by manufacturing method limitations and specific design problems (failures). The process of disc and friction pair design optimisation, to fully explore the advantages and address limitation of these new materials, is still to be performed. The research results obtained in this

thesis are of fundamental value in maximising heat dissipation, but future work is required to provide optimal solutions for novel designs.

List of References

- Abbas, S. A., N. J. Cubitt, et al. (1969). "Temperature distributions in disc brakes." Proc. Instn. Mech. Engrs. Vol 184 Part 2A No. 9.
- Aikawa, T., Winer, W. O. (1994). "Thermal contact conductance across Si_3N_4 - Si_3N_4 contact." Wear 177/1.
- Anderson, A. E. and R. A. Knapp (1990). "Automotive friction system hot spots." Wear 135: 319-337.
- Antonetti, V. W. and M. M. Yovanovich (1985). "Enhancement of thermal contact conductance by metallic coatings: Theory and experiment." ASME-Journal of heat transfer 107 (August).
- Axon, L., K. Garry, et al. (1999). "The influence of ground condition on the flow around a wheel located within a wheelhouse cavity." SAE 1999-01-0806.
- Bailey, T. P., J. T. Buckingham, et al. (1991). "Optimisation of brake design using thermal imaging and finite element techniques." Autotech 91. Birmingham, UK.
- Baker, R. C. (2001). An introductory guide to flow measurement. Towbridge, Professional Engineering Publishing Ltd. ISBN 0-85-29867-0.
- Barozzi, G. S., E. Nobile, et al. (1989). "Study of the thermally induced tensions within brake discs for railway applications." Technical report.
- Basara, B., D. Beader, et al. (2000). "Numerical simulation of the flow around a rotating wheel." MIRA 2000, UK.
- Basch, R. H., J. Fash, et al. (2000). "Initial dynamometer and laboratory evaluations of thermally sprayed aluminium brake discs." Brakes 2000, Leeds, UK.
- Bleier, F. P. (1998). Fan handbook: selection, application, and design, McGraw-Hill. ISBN 0-07-005933-0.
- Çengel, Y. A. (1998). Heat transfer: A practical approach, WCR/McGraw-Hill. ISBN 0-07-115223-7.
- Centinkale, T. N. and M. Fishenden (1951). Proc. of general discussion on heat transfer. IME Conference, London.
- Cobb, E. C. and O. A. Saunders (1955). "Heat transfer from a rotating disc." ASME 236 A.
- Daudi, A. R. (1998). "Hayes high airflow design rotor for improved thermal cooling and coning." SAE 982248.
- Daudi, A. R. (1999). "72 curved fins and air director idea increase airflow through brake rotors." SAE 1999-01-0140.
- Daudi, A. R. and M. Narain (2000). "CAE prediction and experimental verification of maximum temperature of cool running 72 curve fin brake rotor design." Brakes 2000, Leeds, UK.
- Day, A. J. (1990). "Brake interface temperature prediction." Second Brakes Workshop, University of Bradford, UK.
- Day, A. J. (1998). "Thermal effects in brakes." Short course on the braking of road vehicles, University of Bradford, UK.
- Day, A. J., Tirovic, M., et al. (1991). "Thermal effects and pressure distribution in brakes." Proc. Instn. Mech. Engrs. Vol 205.
- D'Cruz, A. (1989). "Thermal stress evaluation in ventilated disc brakes for the Rover 200 vehicle." Autotech 1989, Birmingham. UK. Paper No. C399/31.
- D'Cruz, A. H. (1989). "Surface crack initiation in ventilated disc brakes under transient thermal loading." Proc. Instn. Mech. Engrs. C328/053.
- Dennis, R. W., C. Newstead, et al. (1970). "The heat transfer from a rotating disc in an air cross flow." Proceedings of the 4th International heat transfer conference, Paris, France.
- Dorfman, L. D. (1963). Hydrodynamic resistance and the heat loss of rotating solids. Oliver and Boyd.
- Dubensky, R. G. (1986). "Experimental techniques for rotor performance measurements." SAE 950078.

- Dufrenoy, P. and D. Weichert (1995). "Prediction of railway disc brake temperatures taking the bearing surface variations into account." Proc. Instn. Mech. Engrs. Vol 209.
- Eisengräber, R., J. Grochowicz, et al. (1999). "Comparison of different methods for the determination of the friction temperature of disc brakes." SAE 1999-01-0138.
- European Aluminium Foil Association (2002). www.alufoil.org.
- Fec, M. C. and H. Sehitoglu (1985). "Thermal-mechanical damage in railroad wheels due to hot spotting." Wear 102: 31-42.
- Freudenberger, B. (1999). "Brake Hydraulic System Principles & Service Tips." Auto & Truck International. Sept-Oct, 1999.
- Fukano, A. and H. Matsui (1986). "Development of the disc-brake design method using computer simulation of heat phenomena." SAE 860634.
- Goldstein, R. J. (1996). Fluid mechanics measurement. Taylor and Francis. ISBN 1-56032-306-X.
- Gilbert, G. (1977). Engineering data on grey cast irons -SI units. Birmingham, BCIRA.
- Goto, A., M. Nohmi, et al. (2002). "Hydrodynamic design system for pumps based on 3-D CAD, CFD, and inverse design method." Journal of Fluids Engineering-Transactions of the ASME 124 (2): 329-335 JUN.
- Greenwood, J A, Williamson, J B P (1966). "Contact of nominally flat surfaces." Proc. R. Soc. Lond. A295
- Grieve, D. G., D. C. Barton, et al. (1998). "Design of a light weight automotive brake disc using finite element and Taguchi techniques." Proc. Instn. Mech. Engrs. 212, Part D.
- Hamkins, C. P. and S. Bross (2002). "Use of surface flow visualization methods in centrifugal pump design." Journal of Fluids Engineering-Transactions of the ASME 124 (2): 314-318.
- Hartsock, D. L., R. L. Hecht, et al. (1999). "Parametric analysis of thermoelastic instability in disc brakes." Int. J of Vehicle Design 21(4/5).
- Hausen, H. (1950). Wärmeübertragung im Gegenstrom, Gleichstrom und Kreuzstrom. Springer-Verlag, Berlin.
- Kao, T., J. W. Richmond, et al. (1994) "The application of predictive techniques to study thermoelastic instability of brakes." SAE 942087.
- Kao, T. K., J. W. Richmond, et al. (2000). "Brake disc hot spotting and thermal judder: an experimental and finite element study." International Journal of Vehicle Design 23(3-4): 276-296.
- Kármán, T. (1946). "Zeits. f. angew." Math. u. Mech. 1, 233 (1921) (NACA Technical Mem. No. 1092).
- Kennedy, F. E. (1984). "Thermal and thermomechanical effects in dry sliding." Wear 100: 453-476.
- Hitachi Chemical (2002). Hot bands on disc surface caused by hot spotting. www.hitachi-chem.co.jp.
- Koetnilyom, S., P. C. Brooks, et al. (2000) "Finite element prediction of inelastic strain accumulation in cast-iron brake rotors." Brakes 2000, Leeds, UK.
- Kohts, Y. (1984). An outline of Heat Transfer, Yokendo.
- Kreith, F. (1986). Principles of heat transfer, Harper and Row. ISBN 0063503883
- Krüger, L. K., Boss, K., et al. (1990) "Brake test rig for operating load simulation." Fisita 90, Torino, Italy. Paper number 905171.
- Krusemann, R. and G. Schmidt (1995). "Analysis and optimization of disk brake cooling via computational fluid dynamics." SAE 950791.
- Kubota, M., T. Hamabe, et al. (2000). "Development of a lightweight brake disc rotor: a design approach for achieving an optimum thermal, vibration and weight balance." JSAE Review 21: 349-355.
- Lambert M A, Marotta, E E, et al. (1995). "The thermal contact conductance of hard and soft coat anodized aluminium." Journal of Heat Transfer-Transactions of the ASME 117(2).
- Lee, K. and J. R. Barber (1994). "An experimental investigation of frictionally-excited thermoelastic instability in automotive disc brakes under a drag brake application." Journal of Tribology 116.
- Lee, K. (1999). "Numerical prediction of brake fluid temperature rise during braking and heat soaking." SAE 1999-01-0483.

- Limpert, R. (1972). "An investigation of thermal conditions leading to surface rupture of cast iron rotors." SAE 720447.
- Limpert, R. (1975). "Cooling analysis of disc brake rotors." SAE 751014.
- Limpert, R. (1975). "The thermal performance of automotive disc brakes." SAE 750873.
- Limpert, R. (1999). Brake design and safety, 2nd Ed. SAE. ISBN 1-56091-915-9.
- Madhusudana, C. V. and L. S. Fletcher (1986). "Contact heat transfer-The last decade." AIAA 24: 510-523.
- Massey, B. and Ward-Smith (1998). Mechanics of Fluids, Stanley Thornes Ltd. ISBN 014234804.
- Materials, A. S. f. T. a. (1970). Manual on the use of thermocouples in temperature measurement, ASTM. ISBN 0-8031-0060-4.
- McCool, J. I. (1986). "Comparison of models for the contact of rough surfaces." Wear 107: 37-60.
- McWaid, T. H. and E. Marschall (1992). "Application of the modified Greenwood and Williams contact model for the prediction of thermal contact resistance." Wear 152: 263-277.
- McWaid, T. and E. Marschall (1992). "Thermal contact resistance across pressed metal contacts in a vacuum environment." International Journal of Heat and Mass Transfer 35(11).
- Mian, M. N., F. R. Al-Astrababi, et al. (1979). "Thermal resistance of pressed contacts between steel surfaces: Influences of oxide films." Journal Mechanical Engineering Science 21(3).
- Mikic, B. and G. Carnasciali (1970). "The effect of thermal conductivity of plating material on thermal contact resistance." ASME-Journal of heat transfer. Vol. 92 (August).
- Mikron Instrument Company, I. (2002). www.mikroninst.com.
- Mittelbach, M., C. Vogd, et al. (1994). "The interfacial distribution and thermal conductance of bolted joints." Journal of heat transfer- ASME 116 (November).
- Morgan, S. and R. W. Dennis (1972). "A theoretical prediction of disc brake temperatures and a comparison with experimental data." SAE 720090.
- Morris, A. M. (1993). Principles of measurement and instrumentation, Prentice Hall International. ISBN 0-13-489709-9.
- Motor Vehicle Research Institute. (2002). www.uvmv.cz.
- Mottram, J. T. and C. T. Shaw (1996). Finite Elements in Mechanical Design, McGraw Hill. ISBN 0-07-709093-4.
- Nelik, L. (1999). Centrifugal and rotary pumps: Fundamentals with applications. London, CRC Press. ISBN 0-8493-0701-5.
- Newcomb, T. P. (1958-9). "Transient temperatures in brake drums and linings." Proc. Auto. Div. Instn. Mech. Engrs. No.7.
- Newcomb, T. P. (1960). "Temperatures reached in disc brakes." J. of Mech. Eng. Sci. Vol 2 No 3.
- Newcomb, T. P. (1961). "Interfacial temperatures and the distribution of the heat between bodies in sliding contact." International heat transfer conference, ASME.
- Newcomb, T. P. (1979). "Thermal aspects of railway braking." Proc. Instn. Mech. Engrs. C154/79.
- Newcomb, T. P. and N. Millner (1965). "Cooling rates of brake drums and discs." Proc. Instn. Mech. Engrs. Vol 180 Pt 2A No 6.
- Newcomb, T. P. and R. T. Spurr (1967). Braking of road vehicles, Chapman and Hall, London.
- Newcomb, T. P. and R. T. Spurr (1970). "Background to brake design." The Journal of Automotive Engineering, (Oct).
- Noyes, R. N. and P. T. Vickers (1969). "Prediction of surface temperatures in passenger car disc brakes." SAE 690457.
- Odell, C., (2003) "Commercial Vehicle Wheel Carrier-Novel Materials and Designs." Final year project, Department of mechanical engineering, Brunel University, UK
- Otter, A J (1970) "Installation effects Manual on the use of thermocouples in temperature measurement" ASTM. ISBN 0-8031-0060-4.
- Patankar, S. V. (1980). Numerical heat transfer and fluid flow, Hemisphere Publishing Corporation. ISBN 0-89116-522-3.

- Qi, H. S., K. Noor, et al. (2002). "Interface temperatures in friction braking." Braking 2002, Leeds, UK.
- Renault Truck (2002). www.renault-trucks.com.
- Rogers, G. F. C. and Y. R. Mayhew (1995). Thermodynamic and transport properties of fluids. Oxford, Blackwell Publishers Ltd. ISBN 0-582-04566-5.
- Russell, D. F. and A. J. Williams (1990). "The design and development of a brake disc for high-speed trains." Proc. Instn. Mech. Engrs. 204.
- Sabwabco (2002). Brake discs, www.sabwabco.com.
- Sarwar, G. A. (2002). Design optimisation of wheel mounted railway disc brakes. PhD Thesis, Department of Mechanical Engineering, Brunel University, UK.
- Schwartz, H. W., L. L. Harter, et al. (1975). "Evaluation of gray cast iron brake discs for trucks by thermal modelling." SAE 751013.
- SDRC (2000). I-Deas-8 online Help. www.eds.com.
- Sensor Products Inc. (2002). East Hanover, USA.
- Sheridan, D. C., J. A. Kutchev, et al. (1988). "Approaches to the thermal modelling of disc brakes." SAE 880256.
- Sherrate, F. (1990). Modern fatigue analysis. Sheffield, John Draper and Associates.
- Shigley, J. E. and C. R. Mischke (1989). Mechanical engineering design, McGraw-Hill. ISBN 0-07-100607-9.
- Sisson, A. E. (1978). "Thermal analysis of vented brake rotors." SAE 780352.
- SKF (1994). SKF General catalogue, Gerber + Bruckmann.
- Slevin, E. J. and H. Smales (2002). "Towards more accurate brake testing." Braking 2002, Leeds, UK.
- Sulciner, J. (1999). "Choosing RTDs and thermocouples." Control Engineering (Feb 99).
- Tirovic, M. (1998). "Development of a wheel mounted disc brake for a high-speed train." Proc. Instn. Mech. Engrs. Vol 212 Part F.
- Tirovic, M. and A. J. Day (1991) "Disc brake interface pressure distributions" Proc. Instn. Mech. Engrs. Vol 205.
- Tirovic, M. and G. Voller (2002) "Optimisation of heat dissipation from commercial vehicle brakes." FISITA 2002 World Automotive Congress, Helsinki, Finland.
- Tirovic, M. and G. Voller et al. (2002) "Improving cooling of commercial vehicle brakes.2 Brems.Tech 2002, TÜV Akademie GmbH, Munich, Germany.
- Voller, G., M. Tirovic et al. (2002). Analysis of Automotive Disc Brake Cooling Characteristics. Braking 2002, Leeds, UK.
- Wagner, C. (1948). "Heat transfer from a rotating disk to ambient air." Journal of Applied Physics 19.
- Watson, J. (2002). "Save today-Pay tomorrow? Life cycle costing will help." JEF 2002, Lille, France.
- Wild, P. M., (1989) Air flow and cooling of a ventilated disc. Project Report, Department of Mechanical Engineering, University of Bradford, UK.
- Yevtushenko, A. and E. Ivanyk (1995). "Determination of heat and thermal distortion in braking systems." Wear 185:91-2): 159-165.
- Yevtushenko, A. and E. Ivanyk (1997). "Determination of temperatures for sliding contact with applications for braking systems." Wear 206: 53-59.
- Young, A. (2000). Infrared thermometer selection basics, Raytek Corp. www.process-heating.com.

Appendix A

Material Properties

Table A1 Aluminium, temperature dependent material properties (Cengel 1998)

| Property | 100°C | 200°C | 400°C | 600°C |
|-----------------------------------|--------------|--------------|--------------|--------------|
| Mass density [kg/m ³] | 2702 | 2702 | 2702 | 2702 |
| Specific heat [J/kgK] | 482 | 798 | 949 | 1033 |
| Conductivity [W/mK] | 302 | 237 | 240 | 231 |

Table A2 Grey cast iron, temperature dependent material properties (Gilbert 1977)

| Property | 100°C | 200°C | 300°C | 400°C | 500°C | 600°C |
|-----------------------------------|--------------|--------------|--------------|--------------|--------------|--------------|
| Mass density [kg/m ³] | 7050 | 7050 | 7050 | 7050 | 7050 | 7050 |
| Conductivity [W/mK] | 52.5 | 51.5 | 50.5 | 59.5 | 48.5 | 48.5 |
| Specific heat [J/kgK] | 265 | 265 | 355 | 400 | 425 | 445 |

Table A3 Grey cast iron, fixed material properties (Kreith 1986)

| Property | Value |
|--------------------------------------|-------|
| Mass density [kg/m ³] | 7050 |
| Conductivity [W/mK] | 50.5 |
| Specific heat [J/kgK] | 445 |
| Elastic Modulus [GN/m ²] | 100 |
| Poisson's ratio [-] | 0.26 |

Table A4 15CDV 6 steel, temperature dependent material properties (Sarwar 2002)

| Property | 20°C | 100°C | 200°C | 300°C | 400°C | 500°C |
|--------------------------------------|------|-------|-------|-------|-------|-------|
| Mass density [kg/m ³] | 7830 | 7830 | 7830 | 7830 | 7830 | 7830 |
| Conductivity [W/mK] | 42.3 | 42.3 | 41.9 | 40.2 | 36.8 | 34.8 |
| Specific heat [J/kgK] | 420 | 440 | 499 | 568 | 617 | 637 |
| Elastic Modulus [GN/m ²] | 226 | 224 | 192 | 188 | 182 | 162 |
| Poisson's ratio [-] | 0.28 | 0.28 | 0.28 | 0.28 | 0.28 | 0.28 |

Table A5 Standard ESC air properties (SDRC 2000)

| Property | Value |
|---|------------|
| Mass density [kg/m ³] | 1.207 |
| Coefficient of thermal expansion [K ⁻¹] | 3.41 E -03 |
| Thermal conductivity [W/mK] | 2.63 E -02 |
| Specific heat at constant pressure [J/kgK] | 1.007 E+03 |
| Viscosity (dynamic) [kg/ms] | 1.85 E -05 |
| Specific heat at constant volume [J/kgK] | 7.19 E+02 |
| Prandtl number [-] | 7.15 E -01 |
| Gas constant [J/kgK] | 2.87 E+02 |

Table A6 Thermal contact conductance of metal surfaces (Cengel 1998)

| Material | Surface condition | Roughness Ra [μm] | Temperature [°C] | Interface pressure [MN/m ²] | h_{cond} [W/m ² K] |
|-------------------------------|-------------------|-------------------|------------------|---|---------------------------------|
| Identical metal pairs | | | | | |
| 416 Stainless Steel | Ground | 2.54 | 90-200 | 0.3-2.5 | 3800 |
| 304 Stainless Steel | Ground | 1.14 | 20 | 4-7 | 1900 |
| Aluminium | Ground | 2.54 | 150 | 1.2-2.5 | 11400 |
| Copper | Ground | 1.27 | 20 | 1.2-2.0 | 143000 |
| Copper | Milled | 3.81 | 20 | 1-5 | 55500 |
| Copper (Vacuum) | Milled | 0.25 | 30 | 0.7-7 | 11400 |
| Dissimilar Metal Pairs | | | | | |
| Stainless Steel-Aluminium | - | 20-30 | 20 | 10 | 2900 |
| | | | | 20 | 3600 |
| Stainless Steel-Aluminium | - | 1-2 | 20 | 10 | 16400 |
| | | | | 20 | 20800 |
| Steel Ct-30-Aluminium | Ground | 1.4-2.0 | 20 | 10 | 50000 |
| | | | | 15-35 | 59000 |
| Steel Ct-30-Aluminium | Milled | 4.5-7.2 | 20 | 10 | 4800 |
| | | | | 30 | 8300 |
| Aluminium-Copper | Ground | 1.3-1.4 | 20 | 5 | 42000 |
| | | | | 15 | 56000 |
| Aluminium-Copper | Milled | 4.4-4.5 | 20 | 10 | 12000 |
| | | | | 20-35 | 22000 |

Appendix B

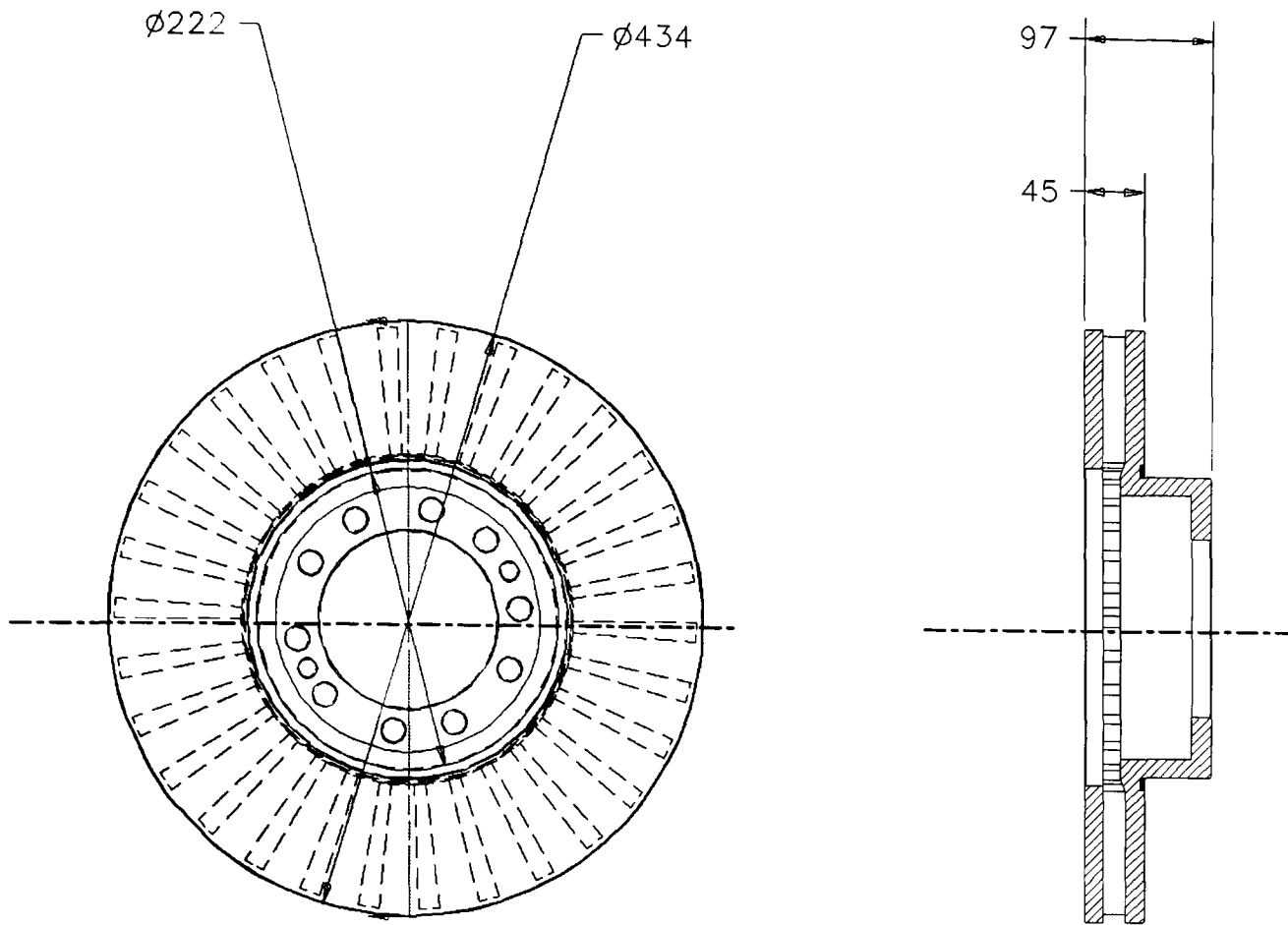
Brake Components

B1 Commercial Vehicle

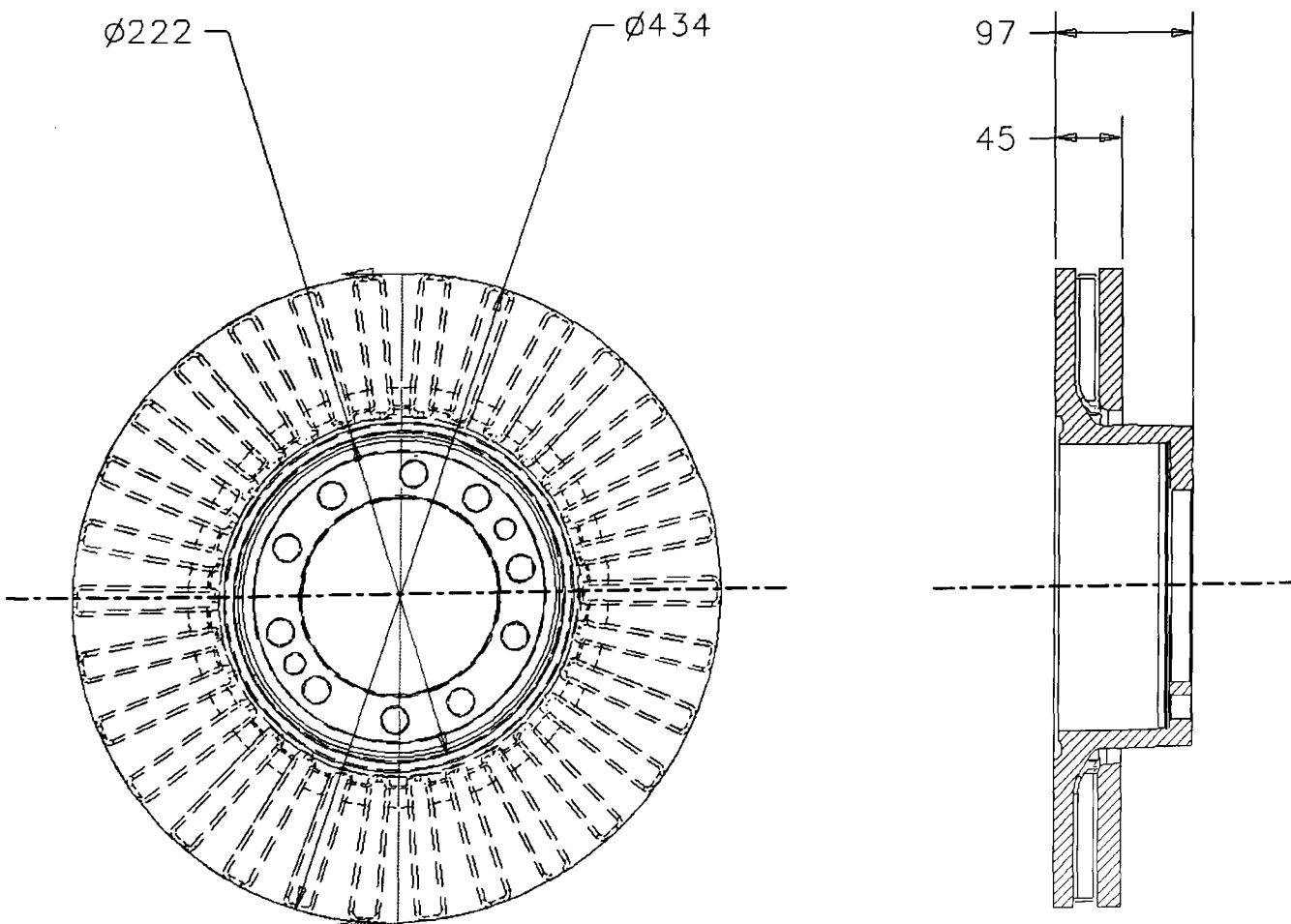


Figure B1 Renault 18 tonne commercial vehicle, supplied with ArvinMeritor brake discs (Trucks 2002)

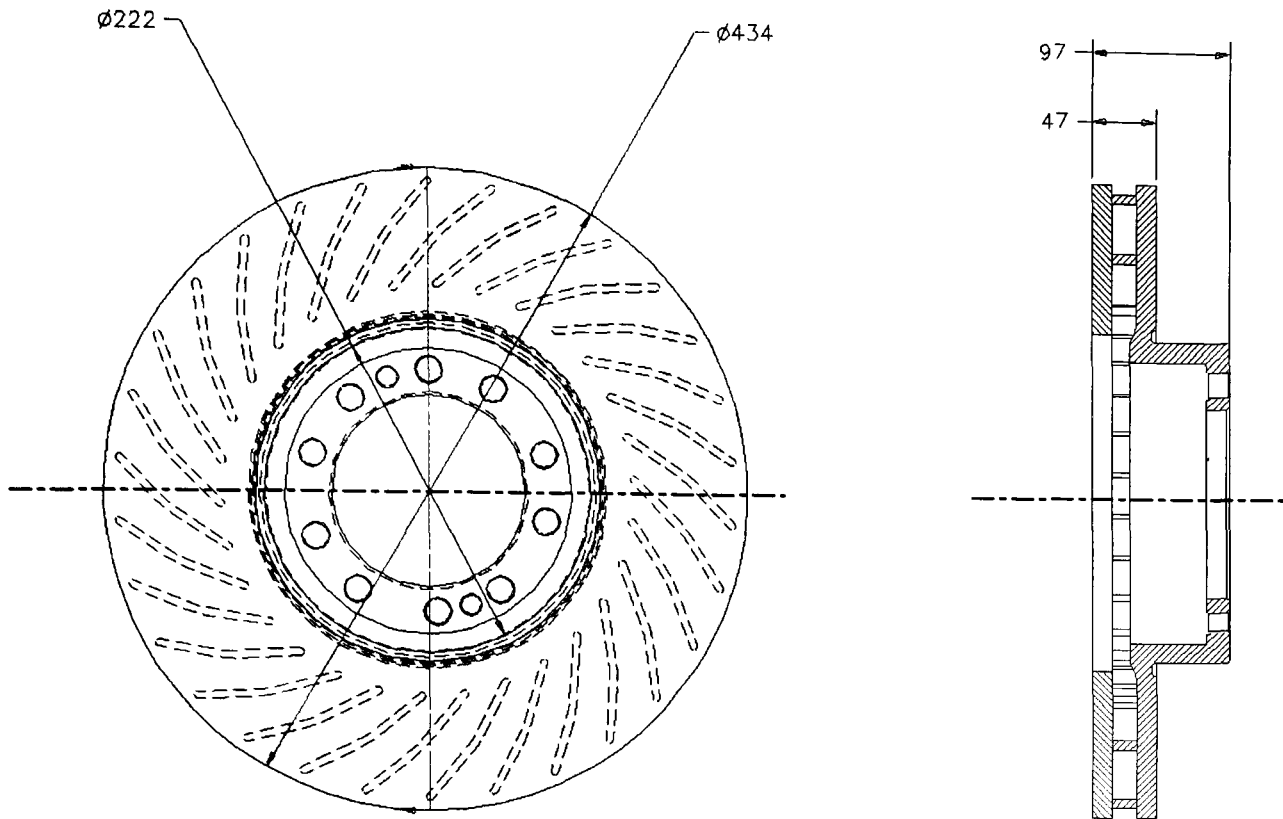
B1.1 Standard disc (all dimensions in mm)



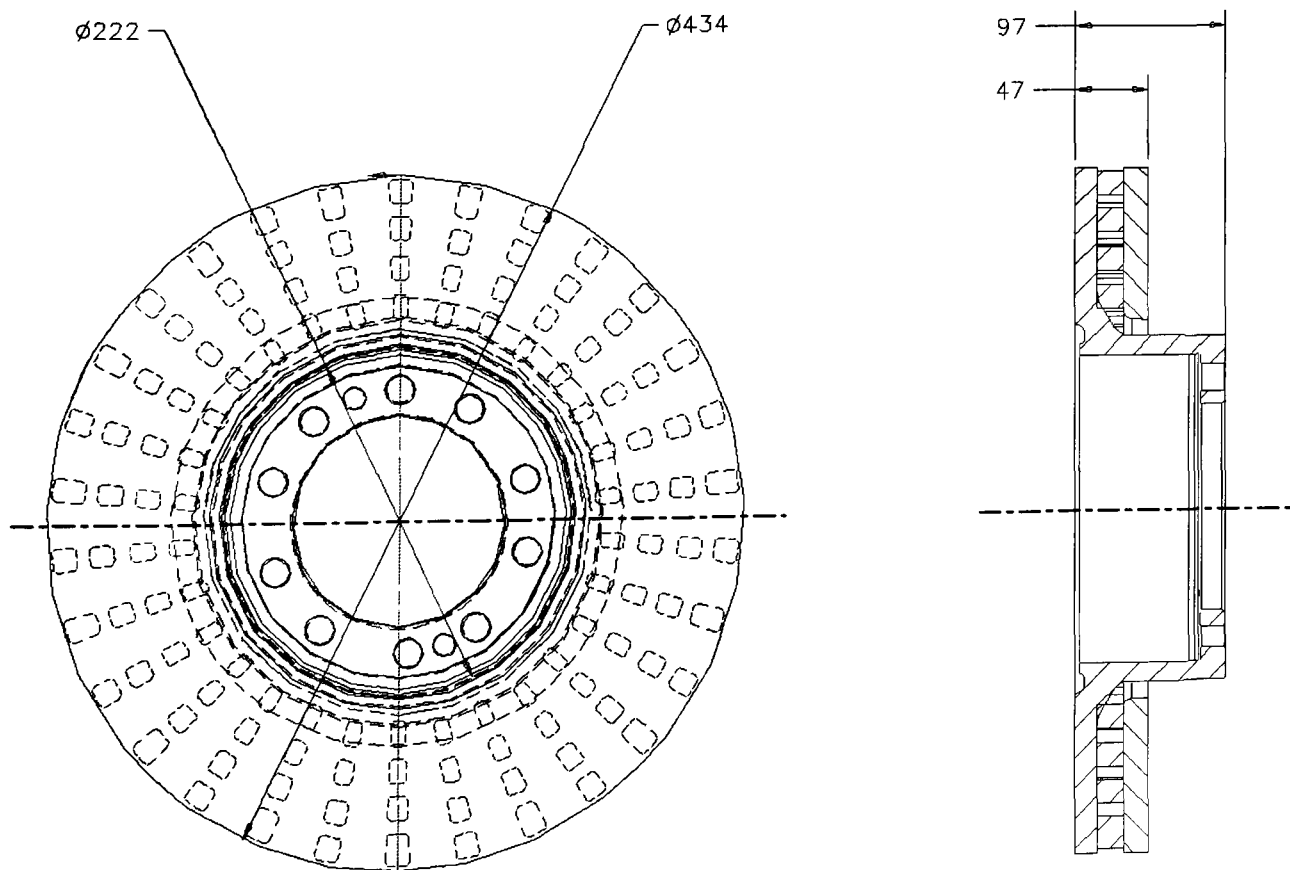
B1.2 Anti-coning disc



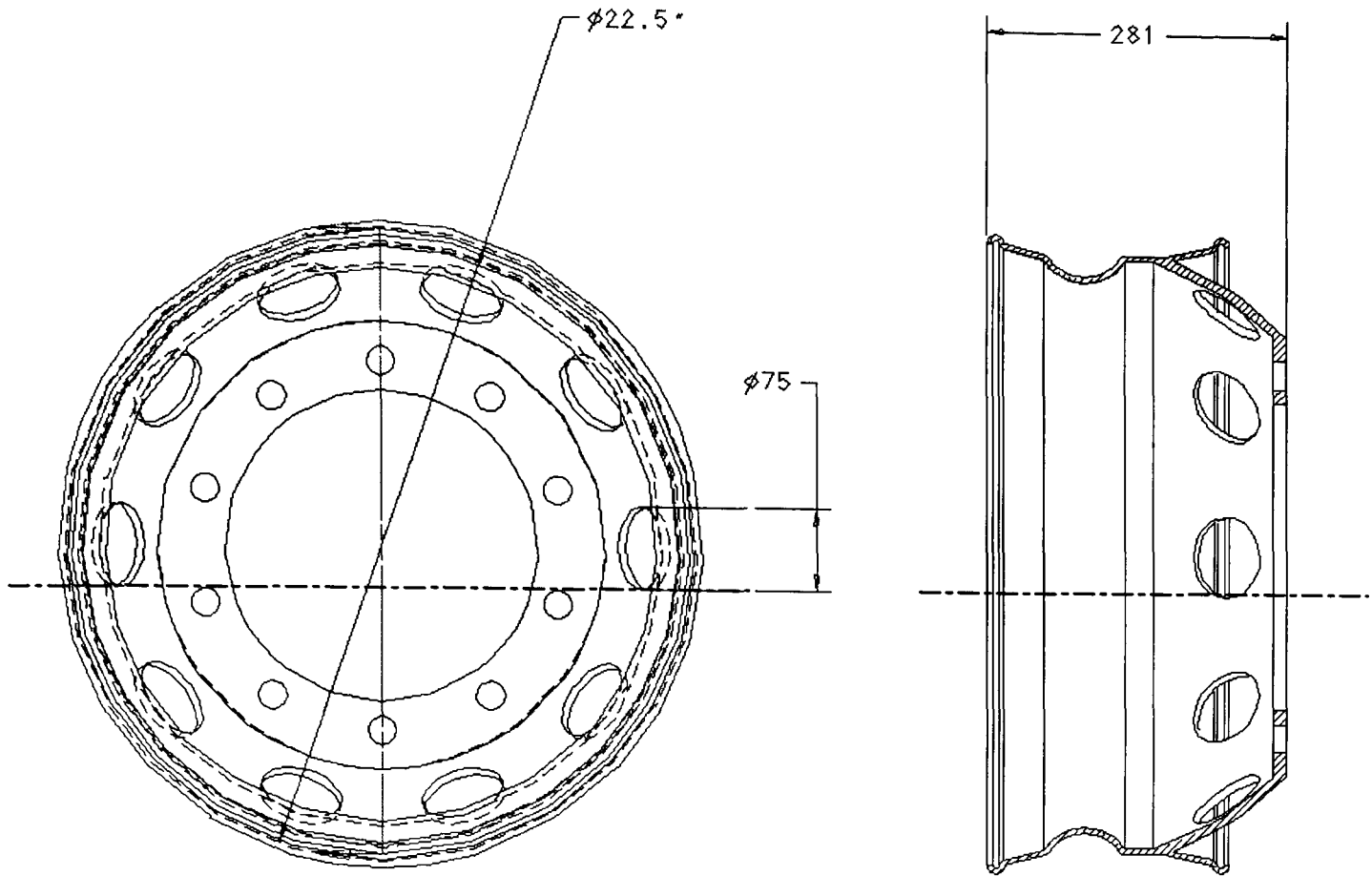
B1.3 Curved disc



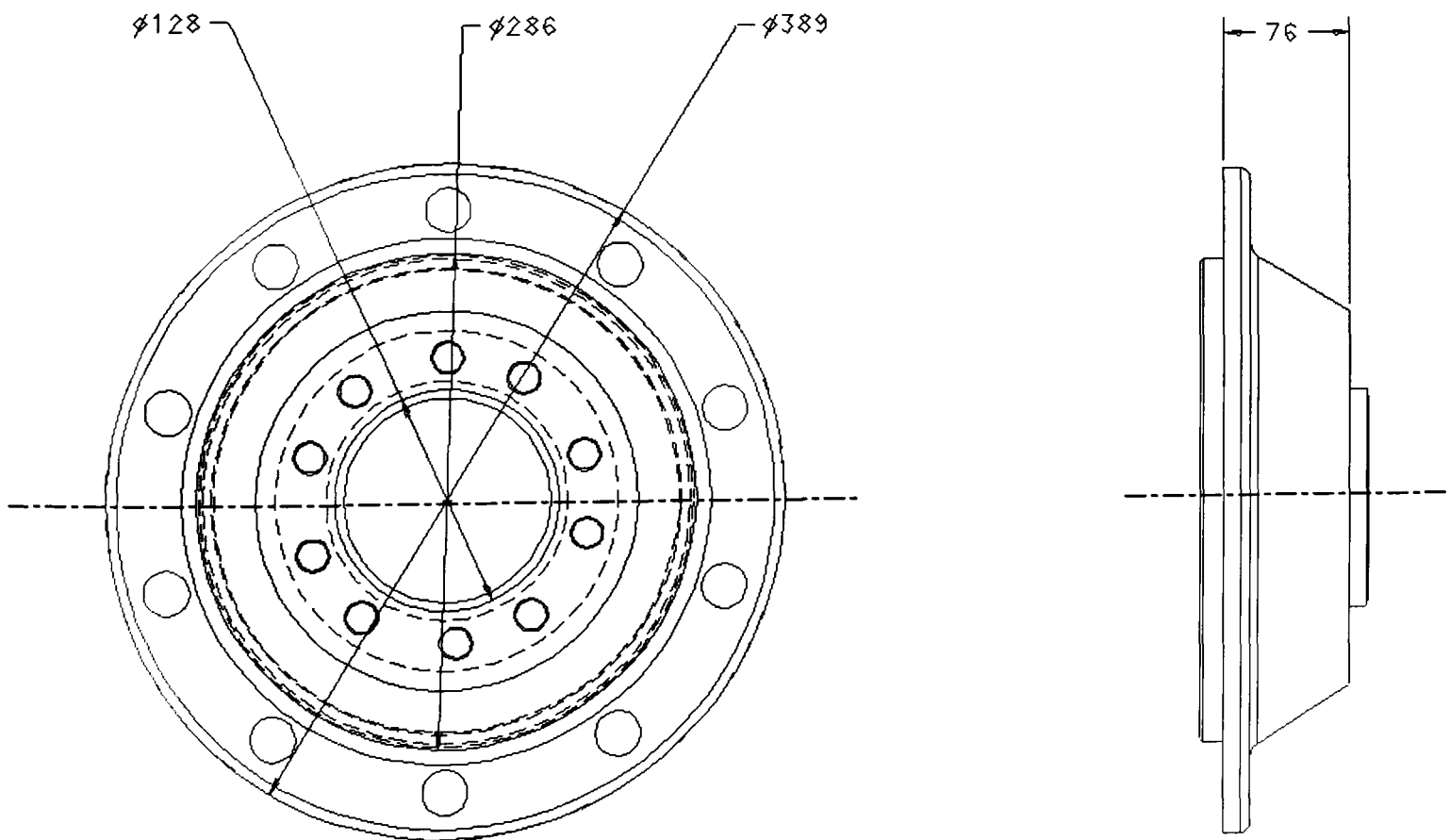
B1.4 Pillared disc



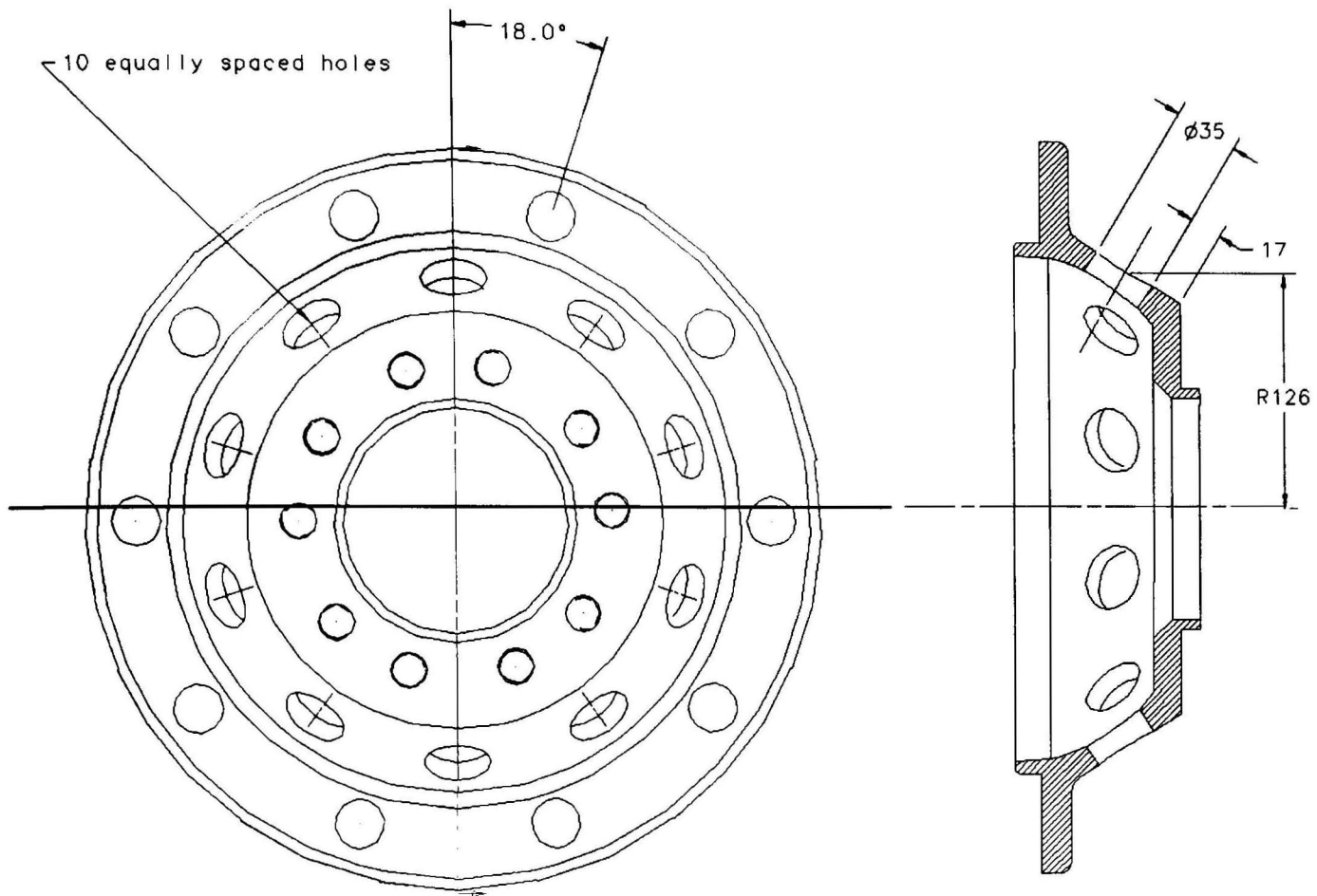
B1.5 Steel wheel



B1.6 Wheel carrier



B1.7 Modified wheel carrier (ventilation holes added)



B2 TGV High Speed Train



Figure B2 TGV high-speed trains supplied with SabWabco brake systems

B2.1 TGV ventilated axle mounted brake disc assembly

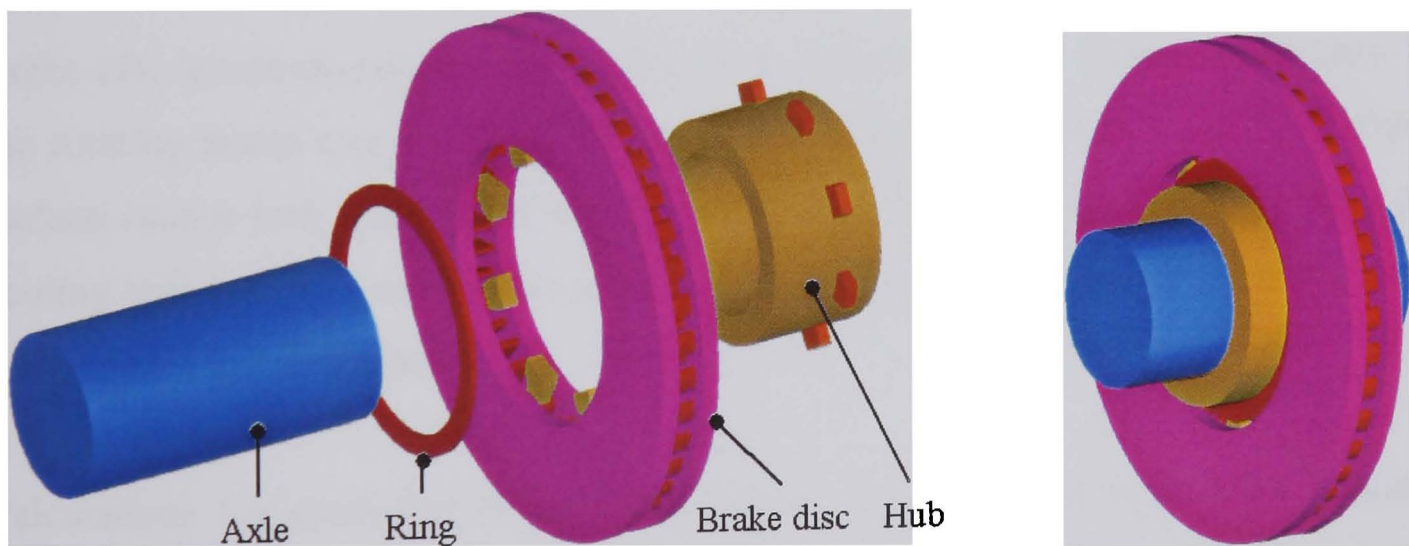
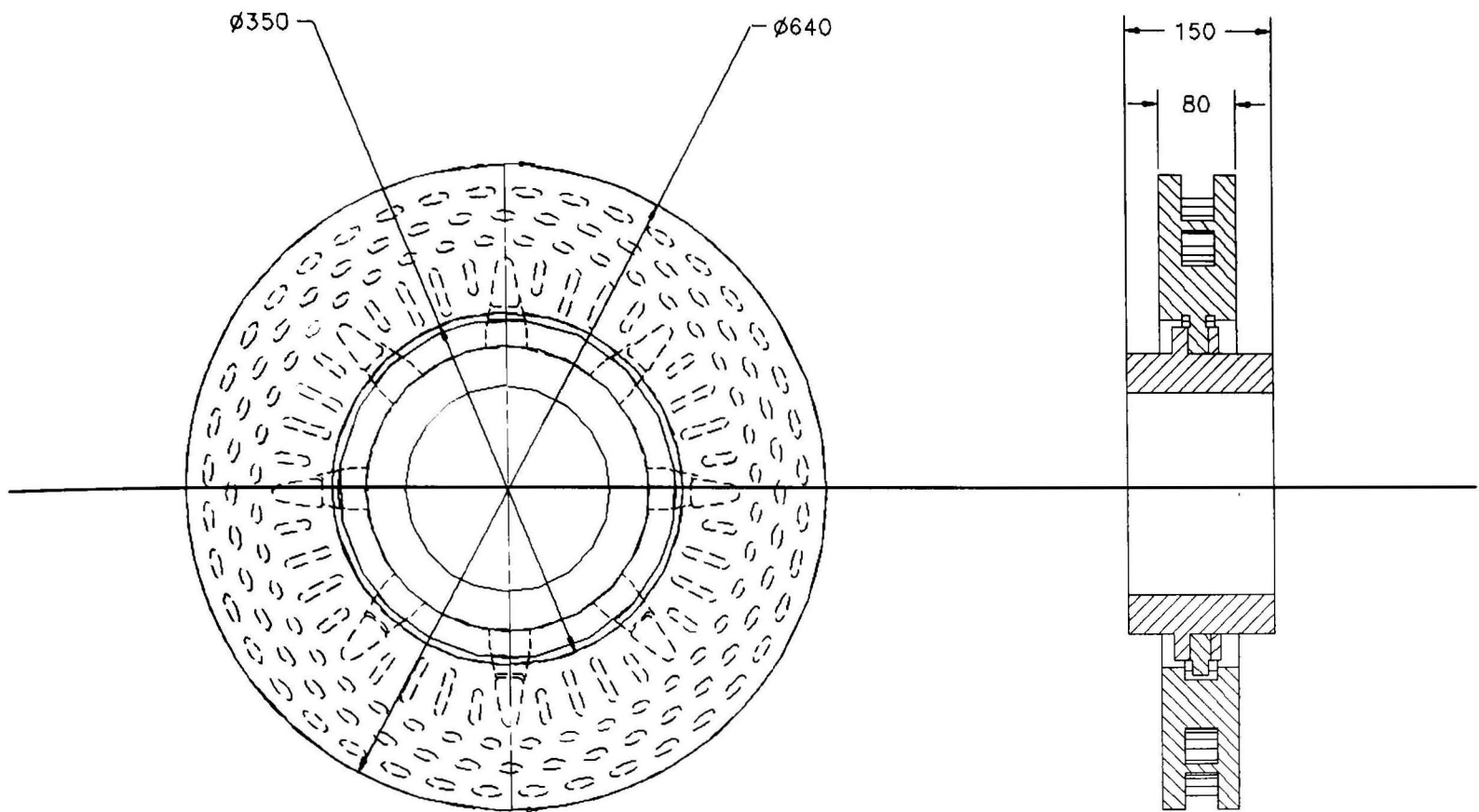


Figure B3 TGV axle mounted brake disc assembly

Temperature Prediction

C1 Braking Energy

Brake disc temperatures rise due to the friction force applied at the friction area of the rotating brake disc by the brake pads. The temperature increase at the friction surface causes heat conduction through the disc or drum. Convection and radiation cooling will lose part of the heat produced, heat will also be transmitted to adjacent components by conduction.

Calculations for predicting brake temperatures were first applied to drum braking (Newcomb 1958-9). Single stop temperatures and regular repetitive stop transient temperatures were determined. In the 1960's when the use of disc brake systems began to increase methods for determining the temperature distributions in brake discs were published. Newcomb (1960) developed equations to enable calculation of the temperatures reached during single stop braking and transient temperatures reached in during repeated braking. Typical curves are given showing the agreement between temperatures determined theoretically and experimentally at the friction surface during single and repeated brake applications.

C1.1 Heat Generation

If a vehicle decelerates at a uniform rate, kinetic and potential energies are converted into thermal energy through the pad and disc interface. The heat generated is proportional to the work done by the friction pair. When considering braking on a level surface from the initial velocity (u_2) to a lower velocity (u_1) the approximate (neglecting any losses) braking energy (q) for a vehicle of mass (m) is given by:

$$q = \frac{m(u_2^2 - u_1^2)}{2} \quad (C1)$$

To determine the energy input to the brake friction surface the average heat flux can be calculated. The equation (C2) is used by Day (1998) and gives the average braking heat flux (q') on a level surface:

$$q' = \frac{\beta\gamma m(1 + \zeta)u^2}{2As} \quad (C2)$$

Where, ζ is a fraction of 0.05 for rotational energy to kinetic energy of vehicle, γ is the front to rear brake distribution and β is the proportion of energy absorbed by the disc. The equation neglects aerodynamic and rolling resistance and therefore gives an over estimated energy input value. Energy entering the disc is assumed uniform over the friction area.

Figure C4, shows a graph of the bi-linear braking power graph; the first period of the graph corresponds to the time taken to develop the nominal pressure value. The rising braking power is assumed linear. The falling braking power is due to the deceleration, which is assumed constant (the friction coefficient is considered as constant during the whole brake application).

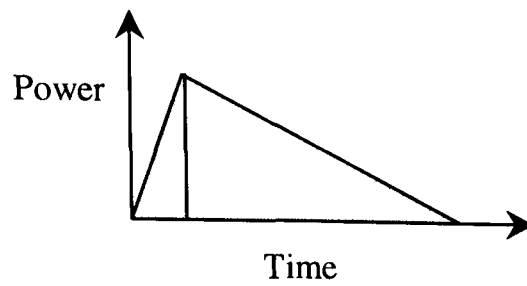


Figure C4 Brake friction surface pressure and braking power

C1.2 Energy Partition

The braking power developed at the disc/pad interface is distributed between the pad and the disc, is directly related to the thermal resistance of the interfacing materials, their thickness and their surface area. Newcomb (1960) has derived equations to determine the proportion entering the disc (β). Equation (C3) assumes that the two bodies are of infinite thickness:

$$\beta = \frac{k_D (\alpha_D)^{1/2}}{k_P (\alpha_P)^{1/2}} \quad (\text{C3})$$

If the distribution is required for longer braking periods the proportion of heat generated entering the disc can be obtained from the equation (Newcomb 1961):

$$\beta = \left(1 + \frac{A_P k_P (\alpha_P)^{1/2}}{A_D k_D (\alpha_D)^{1/2}} \right)^{-1} \quad (\text{C4})$$

Equation (C4) will give reasonable results for friction materials of low conductivity.

Other formulae proposed for predicting the distribution of energy can be found for short brake applications and continued braking, the following authors finding them satisfactory (Limpert 1972; Fukano and Matsui 1986; Sheridan, Kutchev et al. 1988):

Short application times:

$$\beta = \frac{q'_D}{q'_D + q'_P} = \frac{1}{1 + \left(\frac{\rho_P c_P k_P}{\rho_D c_D k_D} \right)^{1/2}} \quad (C5)$$

Repeated or continued braking:

$$\beta = \frac{q'_D}{q'_D + q'_P} = \left(1 + \frac{h_P k_P k_{pS} A_P}{h_D A_D (k_P k_{pS} + t_P k_P k_{pS} + t_{pS} k_P k_P)} \right)^{-1} \quad (C6)$$

Equation (C6) accounts for pad thickness and surface heat transfer.

Work by Day and Ahsi (1990) on heat flow and temperatures in friction material during braking indicates that the interface thermal contact conductance ranges from 1000-10000 W/m²K for resin bonded composite friction material sliding on cast iron. The values are expected to depend on the friction material, mating surfaces and also the conditions of frictional contact. A value of 3500 ± 1000 W/m²K has been confirmed by Day (Day 1990) in an experiment for the sliding contact of a specific friction material sliding on a cast iron mating surface.

Values for β are typically between 0.90 and 0.99. For asbestos-free materials of the semi-metallic type sliding against cast iron discs, $\beta = 0.98$ when $A_P/A_D = 1.00$ (Day 1998).

C1.3 Disc/Pad Interface Energy Distribution

Most friction brake applications are performed in the thermoelastic instability (TEI) regime, which causes variation of interface pressure and heat generation over the nominal disc/pad contact area. Irregularities in the surface will cause the pressure distribution to be non-uniform. Barber (1969) showed experimentally the formation and movement of these areas are determined by the thermo-mechanical process of thermal deformation and wear. The highest part of the surface will carry the greatest pressure, reach the highest temperature and consequently expand more than the surrounding surface. Thus the thermal expansion tends to exaggerate the initial

irregularity of the surface. The wear at the interface has an opposite effect, but under suitable conditions the process can be unstable.

The higher temperatures in these areas cause the material to expand and rise above the level of the surrounding surface, which increase pressure and thermal loading. High thermal stresses produced in these areas can cause surface cracking.

Work on various brake types has shown that hot spots are a very common occurrence in disc brakes. Fec and Sehitoglu (1985) examined the thermal-mechanical damage in train wheels due to hot spotting; constraints and thermal expansion cause stresses that eventually initiate and propagate fatigue cracks.

Anderson and Knapp (1990) studied various types of hot spots in detail and described different types of hot spots found in automotive brakes. It is suggested that the most critical operating conditions involve high sliding speeds, low bulk temperatures, long friction contacts, thick materials and low material wear rates.

In the study of brake interface pressure distributions by Tirovic and Day (1991) the thermal effects on brake performance are discussed describing how the pressure and contact at the brake friction interface can be broken down into three levels. The first relates to large scale pressure variation over the full rubbing surface, induced by bulk deformations and application of actuating forces. The second relates to 'macroscopic' interface pressure variation, arising from localised deformations or distortion of the rubbing surfaces. High peaks of interface pressure cause high rates of localised frictional heat flux generation, which initiate heat spotting, banding and ultimate cracking, crazing and failure. The third level represents frictional contact on the microscopic scale, fundamental to the study of friction and wear.

Lee and Barber (1994) have investigated TEI experimentally showing that the onset of instability is clearly identifiable through the observations of non-uniformities in temperatures measured using imbedded thermocouples.

Hot spots from TEI are usually anti-symmetric (Hartsock, Hecht et al. 1999), and will not occur below a critical speed. This speed is dependent on the disc and pad

material properties, pad/disc relative size, pad thickness, disc thickness, and the coefficient of friction. Results show that critical speed is a weak function of the number of hot spots per revolution, which means the number of hot spots obtained in a practical brake system will be sensitive to initial conditions.

Kao, Richmond et al. (2000), has demonstrated experimentally and theoretically that in addition to the thermal growth the thermoelastic unstable warping or buckling induces excitation to hot spotting and disc cracking, as well as torque variation and hot judder. The non-uniform heat distribution caused by hot spots result in higher than expected surface temperatures, effecting convective and radiative heat dissipation.

C2 Predicted Temperatures during Braking

Disc temperatures can be calculated based on braking energy and disc and pad geometry and materials. For short braking applications (a single stop) cooling can be neglected. For longer braking applications (repeated and drag) brake cooling must also be considered. The temperature prediction equations given in this section have been used in Chapter 8 for comparison with dynamometer test measurements and route simulations. From the experience of the author and other brake designers, it is always worth checking the bulk brake temperature with the simple energy equation:

$$q = mc_p \Delta T \quad (C7)$$

C2.1 Single Stop Braking

When a vehicle brakes to rest at a high deceleration, heat dissipation can be neglected. The braking application time is less than the time required for heat to be dissipated. Under these conditions, it is assumed all braking energy is absorbed by the disc and brake. If it is assumed that heat is generated uniformly over the disc surface and not just in the area of the friction pad, a 2-D heat equation can be formulated to find the temperatures within the disc. This will only cause very small errors; the rotational speed of the disc is very high except at the end of braking when heat developed is very small (Newcomb 1979). Two forms of solution are given depending on the value of the parameter λ , where t_D is the disc thickness:

$$\lambda = \frac{t_D}{(\alpha s_b)^{1/2}} \quad (C8)$$

If $\lambda \geq 1.21$ the disc can be considered to be infinitely thick and the mean temperature rise at a given time, s , is given by:

$$T = \frac{2q's^{1/2}}{\pi^{1/2}(k\rho c_p)^{1/2}} \left(1 - \frac{2s}{3s_b}\right) \quad (C9)$$

Where, s_b is the stopping time. The maximum temperature reached is:

$$T = 0.53q' \left(\frac{s_b}{k\rho c_p}\right)^{1/2} \quad (C10)$$

If $\lambda \leq 1.21$ the disc can no longer be considered infinitely thick and the mean temperature rise is given by:

$$T = \frac{\alpha q'}{t_d k} \left\{ \left(1 - \frac{s}{2s_b}\right) + \frac{t_D^2}{3\alpha} \left(1 - \frac{s}{s_b}\right) + \frac{t_D^4}{45\alpha^2 s_b} \right\} \quad (C11)$$

Limpert (1972) has derived an equation that computes temperatures at any location beneath the friction surface (z) as a function of time (s); convection cooling is also included:

$$T = \frac{q'}{h} \left[2 \left(\frac{T_i h}{q'} - 1 \right) \sum_{n_b=1}^{\infty} \frac{\sin(\Psi_{n_b} t_d / 2)}{(\Psi_{n_b} t_d / 2) + \sin(\Psi_{n_b} t_d / 2) \cos(\Psi_{n_b} t_d / 2)} \times e^{-a \Psi_{n_b}^2 t} \cos(\Psi_{n_b} z) + 1 \right] \quad (C12)$$

Where n_b is the number of stops. The values of $\Psi_{n_b} t_d / 2$ is determined from the transcendental equation:

$$\left(\Psi_{n_b} t_d/2\right) \tan\left(\Psi_{n_b} t_d/2\right) - \frac{h t_d/2}{k} = 0 \quad (\text{C13})$$

A few common solutions for values of $\Psi_{n_b} t_d/2$ for the above equation are given in Table C7. For most analyses, only three terms are required.

Table C7 Values of $\Psi t_d/2$

| $h t_d/2/k$ | $\Psi_1 t_d/2$ | $\Psi_2 t_d/2$ | $\Psi_3 t_d/2$ | $\Psi_4 t_d/2$ | $\Psi_5 t_d/2$ | $\Psi_6 t_d/2$ |
|-------------|----------------|----------------|----------------|----------------|----------------|----------------|
| 0.01 | 0.0998 | 3.1448 | 6.2848 | 9.4258 | 12.5672 | 15.7086 |
| 0.02 | 0.1410 | 3.1479 | 6.2864 | 9.4269 | 15.5680 | 15.7092 |
| 0.04 | 0.1987 | 3.1543 | 6.2895 | 9.4290 | 12.5696 | 15.7105 |

C2.2 Drag Braking

Drag braking occurs when the brakes are applied during a downhill decent to keep the velocity constant. The duration of the application is long and cooling must be considered in temperature analysis. Cooling increases with brake disc temperature increase (discussed in Chapter 2), and the brake disc will reach a state of equilibrium, where the generated thermal power equals the thermal power dissipated. Newcomb (1979) gives an expression for the excess brake temperature at the end of the braking time, which applies Newton's law of cooling and gives reasonable accuracy:

$$T = \frac{q'}{Ah} \{1 - \exp(-bs_b)\} \quad (\text{C14})$$

Where the cooling rate b can be found experimentally (see Chapter 2) or by equation (C15) (Newcomb and Millner 1965):

$$b = \frac{Ah}{v\rho c_p} \quad (\text{C15})$$

In a continuous brake application braking power (Q) is constant. Limpert (1999) has also published an equation for the temperature response during continuous braking:

$$T_s = \left[\frac{T_i - T_\infty - Q}{hA} \right] e^{\frac{-hAs}{\rho c_p v}} + T_\infty + \frac{Q}{hA} \quad (C16)$$

Where, Q is the braking power absorbed by the disc and s is the time during which the brakes are applied.

C2.3 Repeated Braking

As with drag brake applications, cooling must be considered. The temperature for the first brake application is calculated as outlined in Section C2.1, cooling is then considered up until the next brake application. Newcomb and Spur (1967) give an expression for the brake temperature after a series of identical stops, also applying Newton's law of cooling:

$$T_{n_b} = T_i + \Delta T \left\{ \frac{1 - \exp(-nbs_0)}{1 - \exp(-bs_0)} \right\} \quad (C17)$$

Where, s_0 is the regular interval time between braking and ΔT is the increase in bulk temperature of the disc, equation (C7). The value of b can be determined from the heat transfer coefficient, h , see equation (C15), or from cooling parameters based on cooling tests on a brake assembly as discussed in Chapter 2.

Limpert (1999) also developed an equation to calculate brake temperatures during repeated braking assuming the disc is a lumped system and heat transfer coefficients and material properties are constant. The relative brake temperature before (1) the n_b^{th} brake application is:

$$[T_s - T_\infty]_1 = \frac{\left\{ 1 - e^{[-(n_b-1)hAs_0]/[\rho c_p v]} \right\} \left\{ e^{(-hAs_0)/(\rho c_p v)} \right\} \{ \Delta T \}}{1 - e^{-(hAs_0)/(\rho c_p v)}} \quad (C18)$$

The relative brake temperature after (2) the n_b^{th} brake application is:

$$[T_s - T_\infty]_2 = \frac{\left\{1 - e^{(-n_{b1}hAs_0)/(\rho c_p v)}\right\} \{\Delta T\}}{1 - e^{(-hAs_0)/(\rho c_p v)}} \quad (C19)$$

C4 Temperature Measurements

In the literature some of the measured temperatures are given for various braking applications. For a cast iron rotor at 725°C the hub temperature was found to be 175°C (Sisson 1978). A vented rotor undergoing a 97 km/h fade stops reached a maximum temperature of 500°C at the disc surface and a maximum temperature of 100°C at the mounting flange (Noyes 1979). During a transient simulation disc surface temperatures reached a maximum of 145°C and the pad backing plate reached a maximum shown temperature of 65°C, this value however continued to rise. Measured temperatures of a passenger car brake during repeated braking gave maximum disc surface temperatures of 525°C and maximum calliper bridge temperatures of 160°C after 2000 seconds (Lee 1999). These results give good indications of the temperatures that can be expected during braking.

Spin Rig Design

D1 Initial Design

From the design brief detailed in Chapter 3 an initial design was chosen for the Spin Rig and included a schematic detailing the location of various components, see Table D8 and Figure D5. Calculations performed to determine the parameters of the component specifications are detailed in Sections D1.1 to 1.6. The initial specification is detailed in Table D12.

Table D8 Spin Rig components

| Position | Component |
|-----------------|-------------------------|
| 1 | Electric motor |
| 2 | Bearing housing |
| 3 | Slip rings or telemetry |
| 4 | Torque transducer |
| 5 | Wheel assembly |
| 6 | Platform |
| 7 | Base |
| 8 | Motor control |
| 8 | Data acquisition system |
| 9 | Rubbing thermocouples |
| 10 | Wheel |
| 11 | Brake disc |
| 12 | Imbedded thermocouples |
| 13 | Electric heater |

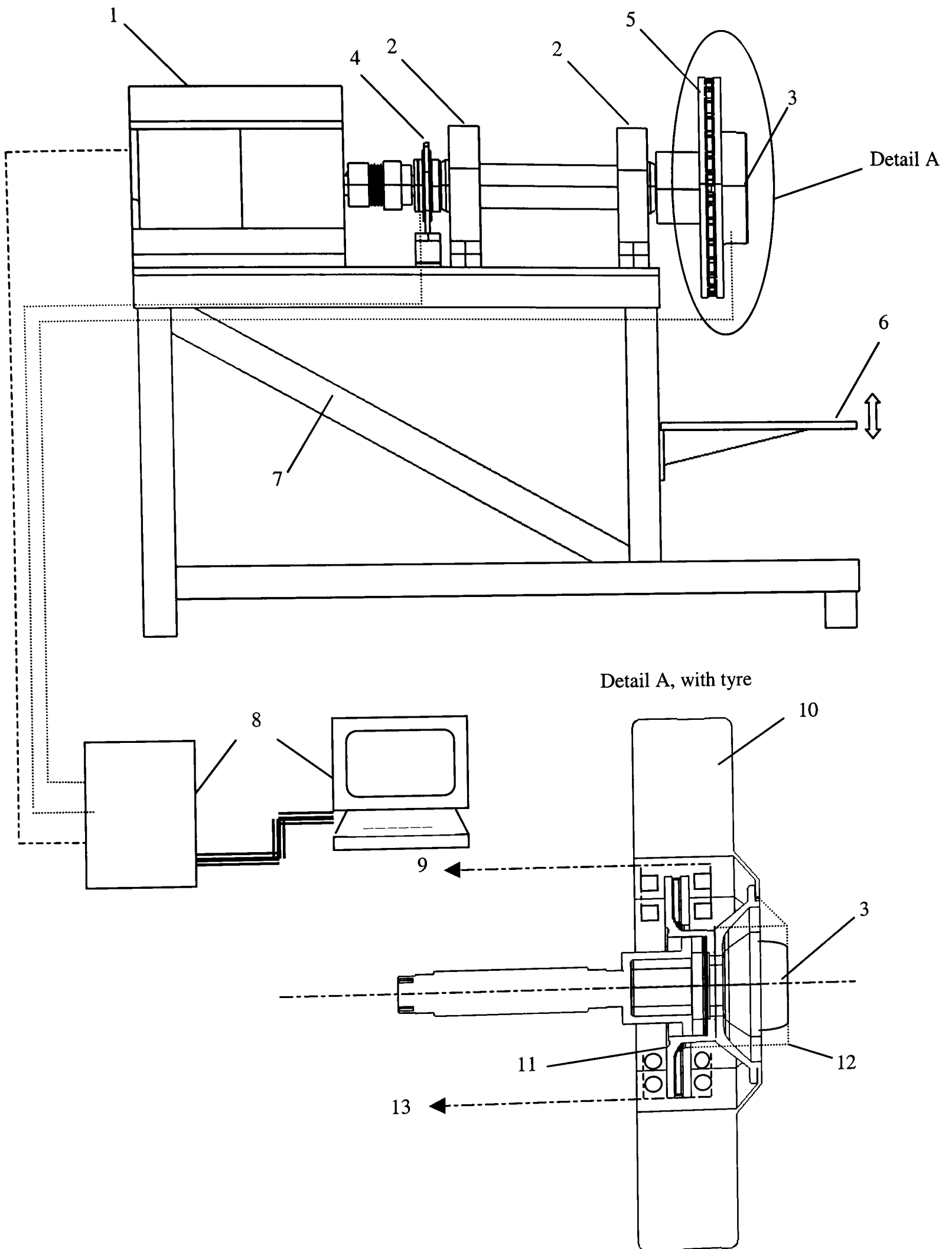


Figure D5 Initial design, schematic drawings

D1.1 Motor

Motor selection is based on torque and speed requirement, calculations have been performed to determine these requirements. The two applications requiring the highest rotation speed were considered, the brake disc of a single seat race car and the brake disc of a high speed train.

1. Maximum rotational speed of FSAE race car wheel travelling at 160 km/h

$$160 \text{ km/h} = 44.7 \text{ m/s}$$

$$\text{wheel diameter} = 520 \text{ mm}$$

$$\text{therefore, } \omega = v/r = 44.7/0.26 \text{ m} = 171.94 \text{ rad/s}$$

$$171.94 \text{ rad/s} = 171.94 \times 60/2\pi = 1642 \text{ min}^{-1}$$

2. Maximum rotational speed of train wheel travelling at 300 km/h

$$300 \text{ km/h} = 83.3 \text{ m/s}$$

$$\text{train wheel diameter} = 0.9 \text{ m}$$

$$\text{therefore, } \omega = v/r = 83.3/0.45 = 185.11 \text{ rad/s}$$

$$185.11 \text{ rad/s} = 185.11 \times 60/2\pi = 1768 \text{ min}^{-1}$$

Calculations 1 and 2 show that a rotational speed of 1800 min^{-1} is sufficient for simulations. A design specification of 2000 min^{-1} is adequate for the maximum angular velocity.

Ventilated disc brakes on trains can cause considerable energy loss, Russell and Williams (1990) stating each disc absorbs 3 kW of power when running at 270 km/h. The Spin Rig therefore requires a motor with sufficient power to overcome and accelerate the disc. A 7.5 kW motor is a standard size and is sufficient for this application. To determine how quickly the motor can accelerate a disc up to speed, the acceleration has been estimated for the rotation of a TGV disc and hub, this is the largest disc to be used on the rig.

Rotating mass

$$\text{Disc mass} = 120 \text{ kg}$$

$$\text{Hub mass} = 55 \text{ kg}$$

$$\text{Total Mass} = 175 \text{ kg}$$

Radius of gyration

$$\text{Radius of gyration for disc, } J = mr^2/2 = 120 \times 0.35^2/2 = 7.35 \text{ kg.mm}^2$$

$$\text{Radius of gyration for hub, } J = mr^2/2 = 55 \times 0.05^2/2 = 0.069 \text{ kg.mm}^2$$

$$\text{Total } J = 7.42 \text{ kg.mm}^2$$

Max torque available, 48 Nm (7.5 kW motor) – 15 Nm (losses)

Acceleration

$$\text{Max acceleration} = \text{Torque/Radius of gyration}$$

(D1)

$$= 33/7.42$$

$$= 4.45 \text{ rad/s}^2$$

To reach 1750 min^{-1} , 183.3 rad/s from 0 rad/s:

$$\text{Speed/acceleration} = 183.3/4.45 = 42.3 \text{ seconds}$$

A time of 43 seconds is thought to more than adequate for the disc to reach maximum speed and so a 7.5 kW motor is sufficient.

D1.2 Shaft Analysis

The shaft and bearings are required to support a maximum load of the TGV train disc, hub and shaft adaptor. The total mass is 250 kg rotating at a maximum speed of 2000 min^{-1} .

To determine the size of shaft required the ASME design code for transmission shafting has been used. First, a nominal diameter of 75 mm was chosen for the shaft and bearing. The stress and deflection calculations were performed; see Figure B6 and Figure D7.

Bending Moments

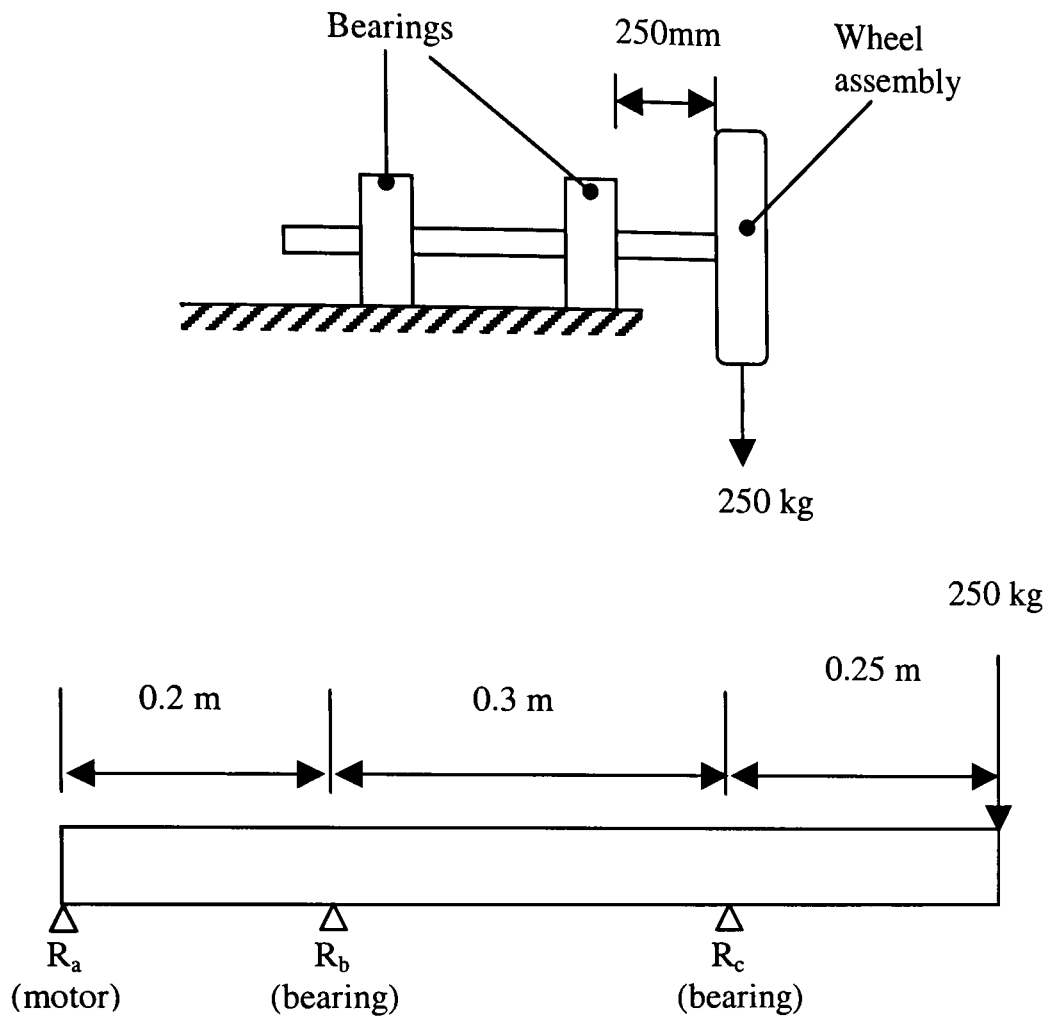


Figure B6 Bending moments of shaft at wheel/brake bearing assembly

$$M = 250 \times 9.81 \times 0.25 \quad (R_a = 0 \text{ N})$$

$$= 613.1 \text{ Nm}$$

Taking moments about R_b :

$$0.55 \times 250 \times 9.81 + 0.3 \times R_c = 0$$

$$R_c = \frac{-0.55 \times 250 \times 9.81}{0.3}$$

$$R_c = -4496 \text{ N}$$

Taking moments about R_c :

$$0.25 \times 250 \times 9.81 - 0.3 \times R_b = 0$$

$$R_b = \frac{0.25 \times 250 \times 9.81}{0.3}$$

$$R_b = 2044 \text{ N}$$

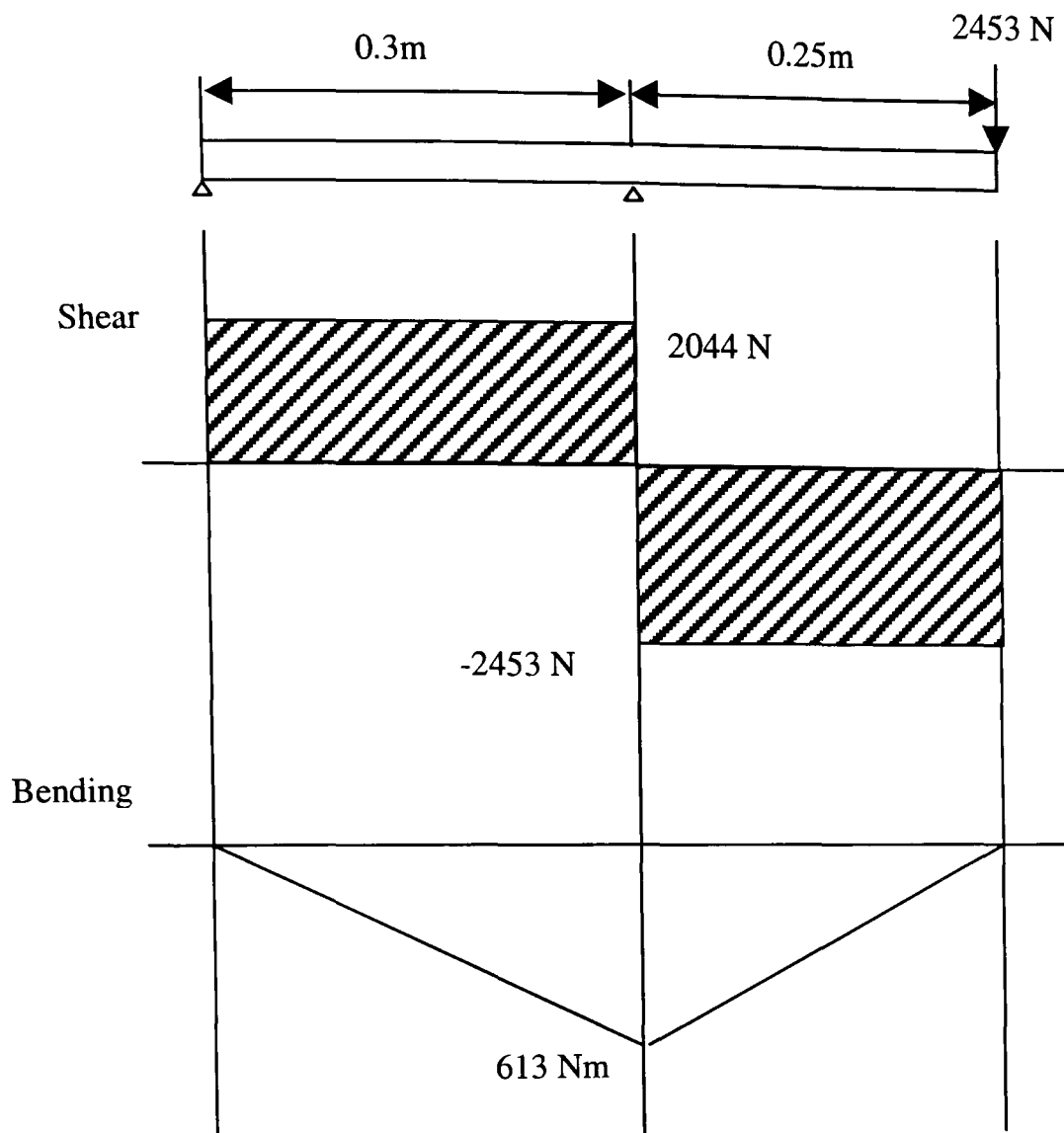


Figure D7 Bending moment diagram for Spin Rig shaft

Bending Stress

$$\sigma = \frac{Mc}{I} \quad \text{where } I = \frac{\pi r^4}{4} \quad (\text{D2})$$

For max stress c = radius of shaft

For \varnothing 50 mm shaft:

$$I = \frac{\pi 0.025^4}{4} = 306 \times 10^{-9} \quad \sigma = \frac{613 \times 0.025}{306 \times 10^{-9}} = 50 \text{ MN/m}^2$$

For \varnothing 75 mm shaft:

$$I = \frac{\pi 0.0375^4}{4} = 1.553 \times 10^{-6} \quad \sigma = \frac{613 \times 0.0375}{1.553 \times 10^{-6}} = 15 \text{ MN/m}^2$$

Taking the yield strength of steel to be 300 MN/m², the bending stresses found in the shaft are small for static loading with safety factors over 6.

Radius of Curvature

$$\text{Curvature} = \frac{1}{e} = \frac{M}{EI} \quad (D3)$$

$$\text{Radius of Curvature, } e = \frac{EI}{M} \quad (D4)$$

For steel $E = 200 \text{ GN/m}^2$

For $\varnothing 50\text{mm}$ shaft:

$$e = \frac{200 \times 10^9 \times 306 \times 10^{-9}}{613} = 100\text{m}$$

For $\varnothing 75\text{mm}$ shaft:

$$e = \frac{200 \times 10^9 \times 1.553 \times 10^{-6}}{613} = 500\text{m}$$

Deflection

Maximum deflection at wheel/brake assembly

$$y = \frac{-PL^3}{3EI} \quad (D5)$$

For $\varnothing 50\text{mm}$ shaft:

$$y = \frac{-250 \times 9.81 \times 0.25^3}{3 \times 200 \times 10^9 \times 306 \times 10^{-9}} = -2.1 \times 10^{-4} \text{m}$$

For $\varnothing 75\text{mm}$ shaft:

$$y = \frac{-250 \times 9.81 \times 0.25^3}{3 \times 200 \times 10^9 \times 1.553 \times 10^{-6}} = -4.1 \times 10^{-5} \text{m}$$

The radius of curvature and deflection of shaft are found to be small even when a 50 mm diameter shaft is considered. However, for out of balance calculation clearance tolerance must also be considered (0.05 mm).

Angle of Twist

$$\frac{T}{J} = \frac{G\theta}{l} \therefore \theta = \frac{Tl}{GJ} \quad \text{Where } J = \frac{\pi r^4}{2} \quad (D6)$$

For steel $G = 77 \times 10^9 \text{ N/m}^2$

Max torque on shaft = 50 Nm

Length of shaft = 0.7 m

For Ø50 mm shaft:

$$J = \frac{\pi 0.025^4}{2} = 613.59 \times 10^{-9} m^4$$

$$\theta = \frac{50 \times 0.7}{77 \times 10^9 \times 613.59 \times 10^{-9}} = 740.80 \times 10^{-6} \text{ radians} = 0.042^\circ$$

For Ø75 mm shaft:

$$J = \frac{\pi 0.0375^4}{2} = 3.106 \times 10^{-6} m^4$$

$$\theta = \frac{50 \times 0.7}{77 \times 10^9 \times 3.106 \times 10^{-6}} = 146.33 \times 10^{-6} \text{ radians} = 0.008^\circ$$

Angle of twist found in the shaft at maximum torque is very small for both the 50 and 75 mm diameter shaft.

Shear Stress

$$\tau = \frac{Tc}{J} \tag{D7}$$

For Ø50 mm shaft:

$$\tau = \frac{50 \times 0.025}{613.59 \times 10^{-9}} = 2.04 \text{ MN/m}^2$$

For Ø75 mm shaft:

$$\tau = \frac{50 \times 0.0375}{3.106 \times 10^{-6}} = 0.60 \text{ MN/m}^2$$

The shear stress calculations show that the shear stress in the shaft at maximum static load is negligible.

Fatigue

The shaft analysis so far has been for static loading. However during shaft rotation dynamic loads occur. For sinusoidal stress, the suggested fatigue limit is UTS/2 for smooth steel specimens of less than 1000 MN/m² (Sherrate 1990). All the stresses calculated in the Spin Rig shaft are well below this value.

The ASME design code for transmission shafting equation for determining the diameter of a solid shaft is:

$$d = \left[\frac{32n_s}{\pi} \sqrt{\left(\frac{M}{\sigma_e}\right)^2 + \frac{3}{4}\left(\frac{T}{\sigma_y}\right)^2} \right]^{1/3} \quad (D8)$$

where, n_s is the factor of safety and $\sigma_e = k_a k_b k_c k_d k_e k_f k_g \sigma'_e$

Table D9 Shaft material data, 817M40 hot rolled alloy steel

| Property | Value |
|--------------------------------|----------|
| UTS | 1000 MPa |
| σ_y | 770 MPa |
| Min shoulder radius at bearing | 1.5 mm |
| Torque | 50 Nm |
| Bending moment | 490.5 Nm |
| Reliability | 99.9% |
| Expected diameter, constant | 75 mm |

Where:

k_a = surface factor $k_a = a\sigma_{UTS}^b$

for hot rolled steel $a = 57.7$, $b = -0.718$

$$\therefore k_a = 57.7(1000)^{-0.718} = 0.405$$

k_b = size factor

assumed dia. 75 mm shaft

For $d > 50$ mm, $k_b = 1.85d^{-0.19}$
 $k_b = 0.815$

k_c = reliability factor

for 0.999 nominal reliability $k_c = 0.753$

k_d = temperature factor

for temperature between -57 °C and $+204$ °C $k_d = 1$

k_e = duty cycle factor

value of 1 for, no shock loads or high stop/starts, $k_e = 1$

k_f = fatigue stress concentration factor

$$k_f = \frac{1}{K_f}$$

$$K_f = 1 + q(k_t - 1)$$

q = notch sensitivity, from table

for 1 mm notch radius and UTS of 100 MPa, q = 0.85

k_t = geometric stress concentration factor, from table

for a dia. Ratio D/d = 100/75 = 1.333 and radius/dia. Ratio r/d = 1.5/75 = 0.02, k_t = 2.8

$$k_f = \frac{1}{1 + 0.85(2.8 - 1)}$$

$$k_f = 0.395$$

k_g = miscellaneous effects factor

The miscellaneous factor is taken as 1, k_g = 1

σ'_e = endurance limit of test specimen (N/m²)

Solution:

$$\text{Endurance limit, } \sigma'_e = 0.504\sigma_{UTS} \leq 1400 \text{ MPa}$$

$$\sigma'_e = 0.504 \times 1000 = 504 \text{ MPa}$$

Therefore,

$$\sigma_e = 0.405 \times 0.815 \times 0.753 \times 1 \times 1 \times 0.395 \times 1 \times 504 \times 10^6$$

$$\sigma_e = 49.48 \text{ MPa}$$

Material and loads are known thus n_s = 2

$$d = \left[\frac{32 \times 2}{\pi} \sqrt{\left(\frac{490.5}{49.48 \times 10^6} \right)^2 + \frac{3}{4} \left(\frac{50}{770 \times 10^6} \right)^2} \right]^{1/3}$$

$$d = 58.668 \times 10^{-3}$$

Therefore from the ASME design code the nominal shaft diameter = 58.67 mm, this gives the chosen shaft diameter of 75 mm a safety factor of 2.5.

D1.3 Wheel Assembly

The Spin Rig is required to rotate a wheel assembly up to the size of a commercial vehicle, this type of vehicle has a standard wheel diameter of 22.5", the tyre diameter measures 1.050 m and has a width of 0.250 m. The Spin Rig and its guarding must

have clearance for this. The maximum expected mass of this assembly including the shaft adaptor is 200 kg, see Chapter 3. A specification mass of 250 kg is sufficient to accommodate any future requirements.

D1.4 Frame

The Spin Rig frame is required to support the loaded shaft when rotating at maximum speed. The frame must be sufficiently heavy and stiff to support the overhanging weight of the wheel assembly at the end of the shaft. Vibrations need to be controlled to reduce fatigue problems and protect instrumentation. To aid manufacture the framework will be design using welded steel square section tubing. The frame will stand on anti-vibration feet, bolted to the floor.

D1.5 Instrumentation

The Spin Rig is used for measurements of brake and air temperatures, shaft torque and shaft speed, airflow measurements are measured using a handheld velocity meter as described in Chapter 3. These measurements are to be logged on computer for processing and analysis, the airflow measurements are logged separately. The speed of the Spin Rig shaft needs to be controllable requiring the use of a motor controller this should be operated using the 'logging' computer. A torque transducer is required to measure shaft torque; this is to be fitted in-line between the motor and the bearings. The ideal position for the torque transducer is in-line between the bearing and the wheel assembly. This would eliminate measurement of losses generated by the bearings. However, the torque traducer would be unable to support the dynamic loads of the wheel assembly and should be located between two bearings (motor and shaft bearings). The losses from the bearing assembly will therefore be measured and subtracted from the measurements. From the motor analysis, a torque measurement range of 0 to 50 Nm is required and for speed measurement a range of 0 to 2000 min^{-1} .

For measurement of temperature different types of sensors are to be used, rubbing thermocouples, embedded thermocouples and infrared sensors. It was envisaged that up to 16 embedded thermocouples and 16 surface temperature measurements would be required using rubbing or infrared sensors. The rubbing thermocouples and

infrared sensors can measure surface temperature of a rotating or moving surface, the embedded thermocouple however rotates with the material being measured and the thermocouple output need to be transmitted to the data acquisition device using a wireless system. The two methods are available to transmit thermocouple data from a rotating shaft, slip rings and telemetry.

Slip rings use contact rings and brushes to transmit data from a rotating shaft to the data acquisition device, see Figure D8. A ring is required for each channel. The problems associated with slip rings are noise and wear. Though they have been use for brake temperature measurement in the past (see Chapter 2) the output from a thermocouple is small, in the range of $40 \mu\text{V}/^\circ\text{C}$ for the K-type thermocouple. For this reason a more robust method of data transfer is desired.

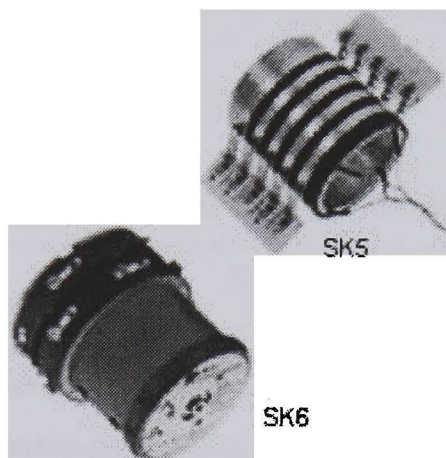


Figure D8 Slip ring assemblies to transmission electrical signals from rotating shafts, HBM Mess- und Systemtechnik GmbH, Germany

To avoid the problems of noise and wear a non-contacting means of transmitting measurement data to stationary and data processing equipment is available. Several devices are available on the market today. The sensor outputs are connected to a miniature transmitter, power pick up loop or battery pack are attached to the rotating shaft or component. The transmitter converts the transducer outputs into a form that enables transfer from the rotating shaft to a stationary pickup. Transmission options include inductive, infrared, radio and capacitive. A pickup, combined with an energising head in the case of inductively powered systems, collects the data and re-transmits via cable to the system demodulator and readout. The received data is decoded into analogue voltage or current form, or alternatively converted to serial data for input into a PC, see Figure D9. Table D10 shows the Spin Rig telemetry

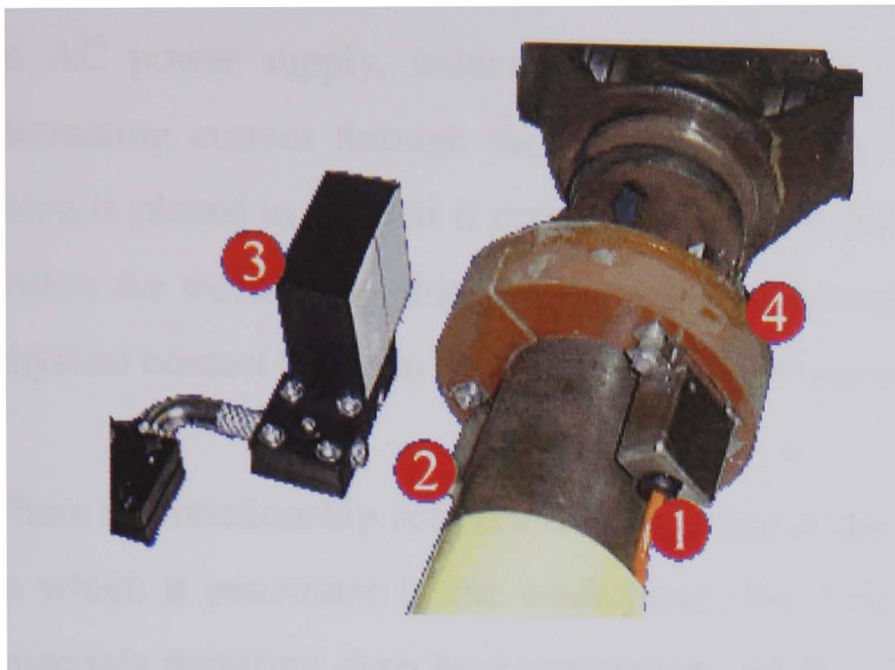
requirements. Three companies have quoted for a 16-channel thermocouple telemetry system to be fitted to the Spin Rig; details are shown in Table D11.

Table D10 Telemetry specification

| | |
|-------------------------------|--------------------------------|
| Capacity: | 16 ungrounded thermocouples |
| Sample rates: | 2.5 seconds per channel |
| Thermocouple type: | K-type |
| Measurement range: | 0 – 600 °C |
| Accuracy: | 0.5% of measurement range |
| Operating temperature: | 0 - 75 °C |
| Operating time: | 2 hours maximum |
| Dimensions: | To fit on 75 mm diameter shaft |
| Environment: | Dry, clean |

Table D11 Telemetry system suppliers

| Company | Specification | Cost, £ (+VAT) |
|--|--|---------------------------|
| Accumetrics Associates, Inc. NY, USA | 16 thermocouple inputs Induction powered shaft collar transmitter Inductive pickup loop 16 channel receiver | 10,125 |
| Astech Electronics Ltd. Hampshire, UK | 16 channel battery powered shaft collar transmitter Inductive pickup loop 16 channel receiver | 14,450 |
| SRC/ PMD Inc. Florida, USA | 1.75" diameter 16 channel digital transmitter 16 channel digital receiver Digital telemetry software | 6,657 |



1. Low-profile transmitter
2. Transmitter counterweight to balance assembly
3. Combined power source & signal pickup
4. Split-ring shaft clamp assembly incorporating transmitter and power pickup loop

Figure D9 Wireless telemetry system to transmit measurements from a rotating shaft, Astech Electronics Ltd., UK

D1.6 Brake Disc Heater

To determine cooling characteristics of the brake disc, the disc must be heated to sufficient temperatures. Bulk operating temperatures of brake disc can be as high as 600°C with surface temperature reaching much higher. The largest disc to be used on the Spin Rig has a mass of 90 kg. In order to increase the disc temperature by 600°C in 30 minutes the power requirement is (excluding losses):

$$Q = \frac{mc_p \Delta T}{t} \quad (D9)$$

$$Q = \frac{90 \times 419 \times 600}{30 \times 60}$$

$$Q = 12.6 \text{ kW}$$

The heating system needs to be adaptable for heating the range of discs to be tested, motorbike disc (1 kg) to the train disc (90 kg). The heater is required to heat the disc quickly and also must be removed quickly to allow cooling measurements to commence. Various heating systems were considered.

D1.6.1 Induction

Induction heating is a method of providing fast, consistent heat to metals or other electrically conductive materials. The process uses electrical currents within the material to produce heat. The basic components of an induction heating system are

an AC power supply, induction coil, and work piece. The power supply sends alternating current through the coil, generating a magnetic field. When the work piece is placed in the coil it enters the magnetic field and eddy currents are induced within the work piece, this generates precise amounts of localized heat without any physical contact between the coil and the work piece.

There is a relationship between the frequency of the alternating current and the depth to which it penetrates in the work piece; low frequencies are effective for thicker materials requiring deep heat penetration, while higher frequencies are effective for smaller parts or shallow penetration. Power levels and heating times are closely related to the characteristics of the work piece and the design of the induction coil. Coils are normally made of copper with appropriate water cooling and are shaped to suit the application.

This method of heating has the advantage of providing controlled high power heating enabling quick heating of the disc. The company CIH Ltd UK provided a proposal to supply a suitable system, including a water cooler and heating head, the price quoted was £34, 506 + VAT. Induction heating may be the best method for disc heating but it is also the most expensive, it could not be used since it was outside the project budget. A cheaper version was tested but proved to be unsuitable, lacking power and generating high electrical interference.

D1.6.2 Radiative

Heating by radiation can be achieved using heating elements including quartz short wave infrared, shown in Figure D10, and ceramic long wave infrared. Elements can be supplied providing up to 1 kW of power. The quartz heater, though more expensive than other radiation heaters has high efficiency and fast response time. The surface condition of the brake disc makes the radiation heater is unsuitable. The low emissivity of the disc surface means the majority of the thermal radiation from the heater will reflect back to the heater, causing over heating of the element.

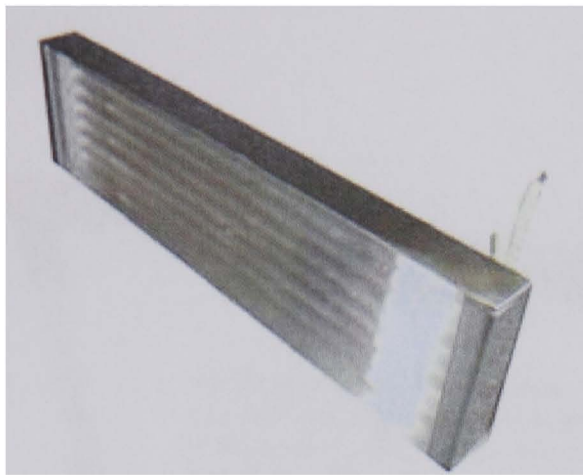


Figure D10 Quartz infrared heater, Hawco Ltd, UK

D1.6.3 Cartridge

A wide range of cylindrical stainless steel cartridge heaters are available giving a maximum surface temperature of around 700°C providing localised heat with good thermal control, shown in Figure D11. Tube heaters can be formed to a desired shape and can provide up to 3 kW of power. Both of these methods require fixing or inserting the element into the disc. The disc can not rotate when the heaters are fitted and must be removed before cooling measurements conducted. Uniform heating will be difficult when the disc is stationary.

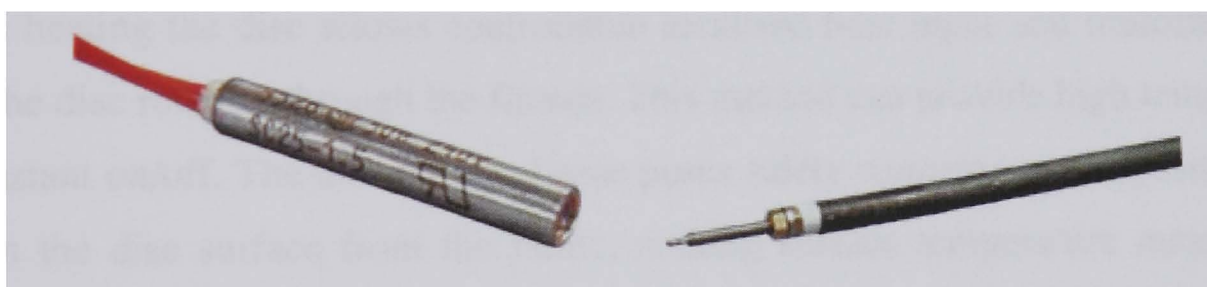


Figure D11 Cartridge and tube heater, Hawco Ltd, UK

D1.6.4 Air

Industrial high temperature air heaters (Figure D12) are designed for continuous high temperature operations up to 650°C, supplying an airflow rate up to 1400 l/min. Hot air flowing over a rotating disc provides uniform heating and can be switched off instantly, ready for cooling measurement. This method of heating will work best with the ventilated disc, which has a large surface area for heating.

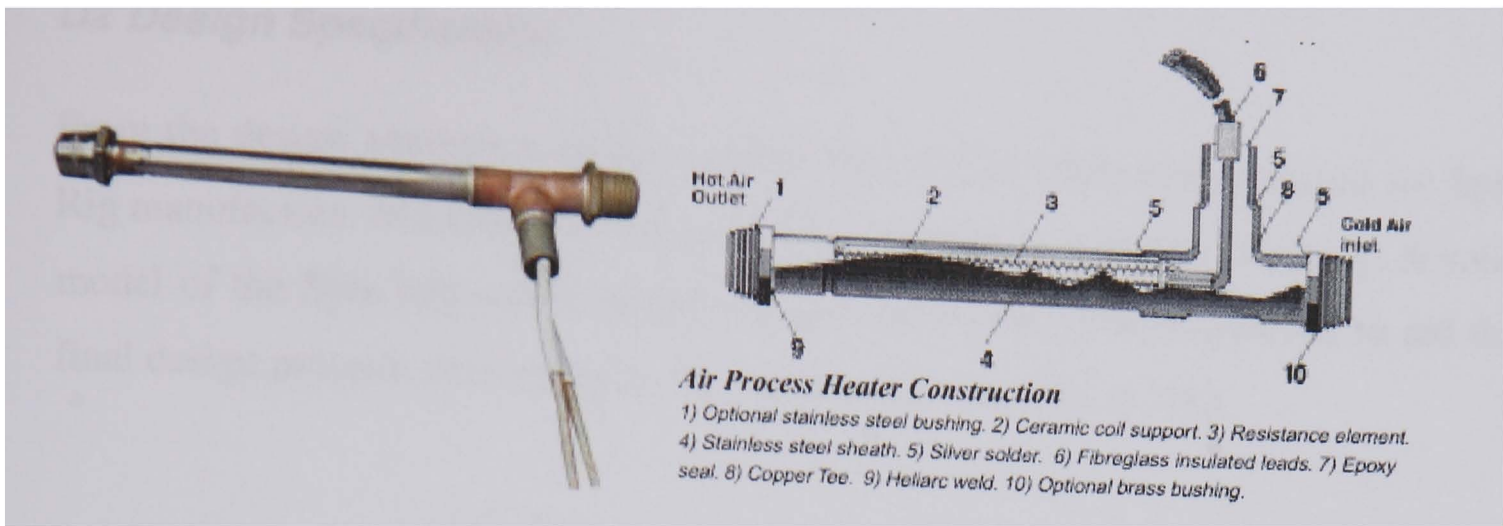


Figure D12 Hot air heater, Hawco Ltd, UK

D1.6.5 Industrial Oven

An industrial oven has been used in the past for disc heating experimental work on disc brake cooling. This requires the removal of the disc from the Spin Rig for heating then handling of the hot disc when taken from the oven and mounting to the Spin Rig. High disc temperatures can be achieved but handling problems arise and the time to mount the disc to the Spin Rig allows substantial heat loss before measurements can start.

D1.6.6 Gas Flame

Flame heating the disc allows controllable localised heat input and uniform heating with the disc rotating through the flames. This method can provide high temperatures and instant on/off. The use of a gas flame poses safety concerns and deposits will be left on the disc surface from the flame, making surface temperature measurement difficult.

D1.6.7 Heater Selection

From the study of disc heating methods it became clear that the best method is induction heating, providing localized heat quickly and efficiently. The high cost of such a system makes it unfeasible at this stage; budgets require a low cost system. Therefore, a hot air heating system providing uniform heating, taking advantage of the brake disc's heat dissipating design is the preferred method of disc heating, with a gas flame heater for higher temperature studies and industrial oven for large discs.

D2 Design Specification

From the design analysis a design specification (Table D12) was produced for Spin Rig manufacture. Manufacture was to be carried out by a specialist company. A solid model of the Spin Rig initial design was produced using SDRC I-DEAS to aid the final design process, performed by the manufacture, see Figure D13.

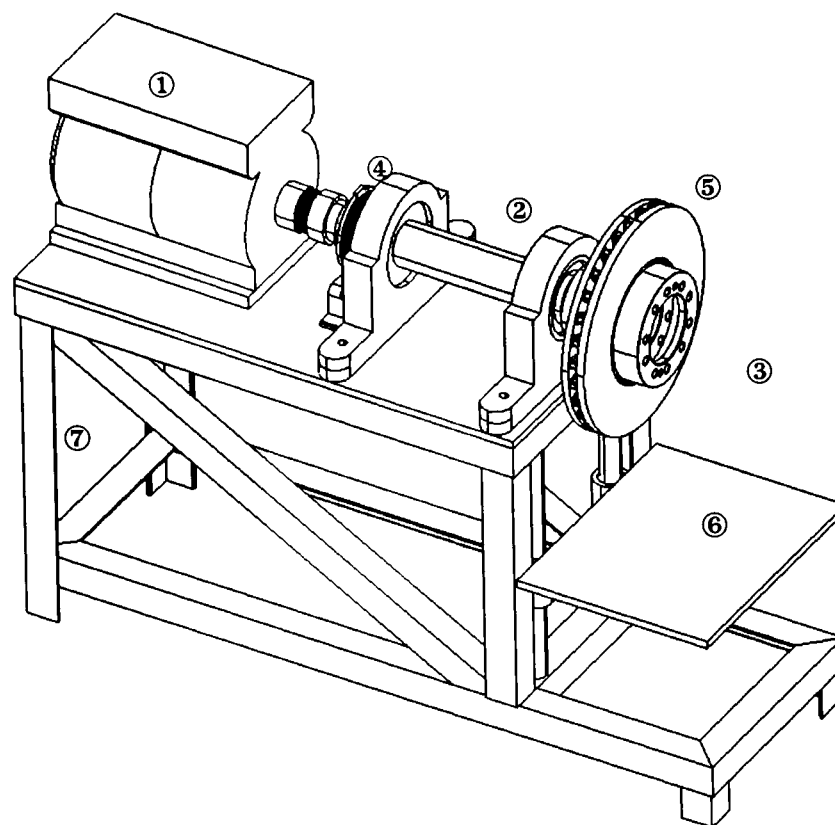


Figure D13 Solid model of initial Spin Rig design

Table D12 Spin Rig design specification

| Position | Component | Specification |
|-----------------|-----------------------------------|---|
| 1 | Electric motor | Power 7.5 kW, Torque 50 Nm, Speed control 0 – 2000 min ⁻¹ , reversible rotation |
| 2 | Shaft assembly | 2 bearings to support 75mm dia. shaft and wheel assembly |
| 3 | Telemetry | To carry 16 thermocouples |
| 4 | Torque transducer | Maximum torque corresponding to maximum torque of motor |
| 5 | Brake assembly | Maximum mass 250 kg, maximum diameter 1.05 m |
| 6 | Platform | Height adjustable by hand to simulate ground effect |
| 7 | Base | Heavy frame with flat steel machined top |
| 8 | Data acquisition system | To condition and acquire data from torque transducer, speed sensor, 16 thermocouples infrared sensors |
| 8 | Computer + software | Data logging and processing and motor control |
| 9 | Brake surface temperature sensors | 16 sensors, temperature range 0 - 500 °C |
| 10 | Wheel | Motorbike, car or lorry wheel, mounted to removable hub |
| 11 | Brake disc | Motorbike, car, lorry, and railway brake mounted to shaft adaptor |
| 12 | Imbedded thermocouple | 16 imbedded thermocouples in rotating components, temperature range 0 – 500 °C |
| 13 | Electric air heater | To heat disc to 300°C |

D3 Manufacture and Commissioning

Three test rig design and manufacture companies in the UK were approached and given the opportunity to prepare a quotation for the Spin Rig project. The Table D13 shows a summary of their proposals.

Table D13 Quotations for the design and manufacture of the Spin Rig

| Company | Cost, £ (+VAT) |
|--|----------------|
| BEL Developments Ltd., Chessington, Surrey, KT9 1SZ, UK | 92,000.00 |
| Rivercircle Ltd., Peterborough, Cambs., PE1 5TA, Peterborough, UK | 92,000.00 |
| Industrial Measurements Ltd. (IML), Derby, DE74 2NP, UK | 48,300.00 |

All three companies produced proposals based on the same design specification. On examining the companies it was considered that all three companies had facilities capable of delivering the Spin Rig. All three companies were located within reasonable distance from Brunel University, the deciding factor therefore was cost and Industrial Measurements Ltd (IML) won the Spin Rig contract.

From the initial budget of £50,000 a reduced budget of only £20,000 was finally allocated for the total cost of the Spin Rig. This allocation required the revision of the Spin Rig specification. The possibility of several build stages were discussed with IML, each stage with its own cost including design and assembly. IML provided a revised quotation, shown in Table D14.

Table D14 Build stages for Spin Rig

| | | |
|----------------|----------------------------|---------|
| Phase 1 | Framework | £13,800 |
| | Shaft and bearings | |
| | Guard | |
| | Motor and controller | |
| | Torque transducer | |
| | Temporary data acquisition | |
| Phase 2 | Telemetry system | £19,500 |
| Phase 3 | Disc heating system | £15,000 |
| | Data acquisition system | |

It is clear from Table D14 that a telemetry system and full data acquisition system are outside the scope of the given budget. Phase 1, with the addition of the disc

heating system would provide a functional Spin Rig within the given budget, the data acquisition system being obtained at a later date. A revised quotation for Phase 1 was prepared by IML providing an operational Spin Rig with a basic data acquisition system and disc heating system, shown in Table D15. The proposal for Phase 1a and 1b of the build was agreed and the final design and manufacture of the Spin Rig began.

Table D15 Revised Spin Rig phase 1 quotation

| | | |
|-----------------|-----------------------------------|-----------------|
| Phase 1a | Framework | £ 16,968 |
| | Shaft and bearings | |
| | Guard | |
| | Motor and controller | |
| | Torque transducer | |
| | Basic 16 channel data acquisition | |
| | Configuration of free issue PC | |
| Phase 1b | Air heater | £ 2,250 |
| | Controller | |
| | Air ducting | |
| Total | | £ 19,218 |

D4 Modifications

It was necessary to modify some aspects of the Spin Rig during the final design and manufacture. The ground effect platform presented clearance and mounting problems for the commercial vehicle wheel assembly. A decision was made to remove this from the design as ground effect on cooling performance was considered very small and a platform could be added at a later stage if necessary. The data acquisition and logging PC was linked to the motor controller to provide a simple on/off control of the motor via the PC.

The most significant modification was to the Spin Rig heater system. In initial tests, the air heater was located at the inlet of the CV disc cooling vanes, see Figure D14. With the heater air temperature set to 600°C, airflow set to 45 l/min and disc rotating at 25 min⁻¹. A 30 minute heating cycle produced an average disc temperature of 40°C with the temperatures reaching a steady state condition. This was a temperature rise



Figure D14 Heating of ventilated CV disc with air heater

The problem with the air heater method was the high heat loss. Hot air flowed through the disc vanes to the vane exit. Very little of the heat had transferred from the air to the disc, the vane exit air temperatures being very high. Also the disc dissipated heat to the atmosphere and to adjacent components during the heating phase, these losses made the air heater very inefficient. To use the heated air more efficiently it must flow over more of the disc surface to transfer heat to the disc and the disc requires insulating to avoid heat loss during the heating phase. A special enclosure was therefore developed, as shown in Chapter 3.

